The Effect of Salt Concentration on Aqueous Strong Acid, Carbon Dioxide, and Hydrogen Sulfide Corrosion of Carbon Steel

A dissertation presented to
the faculty of
the Russ College of Engineering and Technology of Ohio University

In partial fulfillment
of the requirements for the degree
Doctor of Philosophy

Fazlollah Madani Sani
December 2021

This dissertation titled

The Effect of Salt Concentration on Aqueous Strong Acid, Carbon Dioxide, and Hydrogen Sulfide Corrosion of Carbon Steel

by

FAZLOLLAH MADANI SANI

has been approved for

the Department of Chemical and Biomolecular Engineering

and the Russ College of Engineering and Technology by

Srdjan Nesic

Professor of Chemical and Biomolecular Engineering

Mei Wei

Dean, Russ College of Engineering and Technology

Abstract

MADANI SANI, FAZLOLLAH, Ph.D., December 2021, Chemical Engineering

The Effect of Salt Concentration on Aqueous Strong Acid, Carbon Dioxide, and Hydrogen Sulfide Corrosion of Carbon Steel

Director of Dissertation: Srdjan Nesic

Aqueous brines are often produced during hydrocarbon recovery from geological reservoirs as an unwanted by-product. Degree of salinity is always an issue in produced water. In the USA, salt concentration in waters produced from conventional oil and gas wells falls in the range of 1 g/l (~ 0.1 wt.%) to 400 g/l (~ 28 wt.%). Besides salts, CO_2 and H_2S are ubiquitous in the production stream. Dissolution of these gases in produced waters results in evolution of corrosive species, such as $CO_{2(aq)}$, $H_2S_{(aq)}$, $H_2CO_{3(aq)}$, $H^+_{(aq)}$, $HCO^-_{3(aq)}$ ion, and $HS^-_{(aq)}$ that cause severe corrosion problems for carbon steel; primary material used in the construction of oil and gas pipelines. Combination of aqueous salts with dissolved $CO_{2(aq)}$ and $H_2S_{(aq)}$ and their related species, has always been a great concern for pipeline operators in terms of corrosion problems. A large body of research exists on CO_2 and H_2S corrosion of oil and gas facilities, mostly at low salt concentrations; up to 3 wt.%. However, only a limited number of studies has investigated CO_2 corrosion at high salt concentrations and to the best of this author's knowledge, this number is zero for H_2S corrosion.

In the present study, the effect of salt (NaCl) concentration on aqueous uniform strong acid, CO_2, and H_2S corrosion of carbon steel is investigated. The key parameters in the corrosion process that are influenced by salt concentration are identified: transport

phenomena (solution density, solution viscosity and diffusion coefficients of dissolved species), solution chemistry, and electrochemistry of the underlying reactions. Models have been reproduced and developed to account for the effect of salinity (up to ~ 5 m NaCl) on transport phenomena and solution chemistry. The Smolyakov and the square root (Kohlrausch law) equations were chosen for correcting the diffusion coefficients for the effect of temperature, and salt concentration, respectively, using new coefficients obtained in this study. The mixed solvent electrolyte (MSE) model, which is the only comprehensive solution chemistry model available in the literature for the H_2O-NaCl-CO_2-H_2S systems is reproduced. The MSE model is used to calculate the equilibrium activity and activity coefficients of dissolved species important in aqueous strong acids, CO_2, and H_2S corrosion of carbon steel.

pH measurements at 1 bar total pressure and temperatures below 80°C showed that the autogenous pH of aqueous CO_2- and H_2S-saturated solutions decreased with increasing NaCl concentration. The reason for the decrease in the solution pH was attributed to the increase in the activity coefficient of the H^+ ion.

The effect of salt concentration on electrochemistry and rate of strong acid, CO_2, and H_2S corrosion was studied by performing eight sets of experiments in aqueous N_2-, CO_2-, and H_2S-satuared solutions at temperatures below 80°C, 1 bar total pressure, solution pH values between 3 to 5, and different NaCl concentrations, ranging from 0.1 wt.% (0.017 m) to 20 wt.% (4.27 m).

The weight loss and linear polarization resistance corrosion rate measurements showed that the corrosion rate for all three types of corrosion generally decreased with increasing NaCl concentration. The analysis of potentiodynamic polarization sweeps indicated that increasing NaCl concentration decreased the rate of the cathodic H^+ ion reduction reaction continually, while the rate of the cathodic water reduction reaction was mostly increased. The rate of anodic dissolution of iron in the active region increased at lower NaCl concentrations and then switched trend and decreased at higher NaCl concentrations. In strong acid corrosion, salt concentration seemed to have no effect on the mechanism of active dissolution of iron. However, it apparently altered the mechanism of the H^+ ion reduction reaction. In CO_2 corrosion, both mechanisms of active dissolution of iron and H^+ ion reduction remained unchanged with respect to NaCl concentration. Similar Tafel slopes (indication of the mechanism of an electrochemical reaction) were found for strong acid and CO_2 corrosion. In H_2S corrosion, the Tafel slopes for cathodic H^+ ion reduction and anodic iron dissolution were different from those found in strong acid and CO_2 corrosion. However, the H_2S corrosion Tafel slopes for both H^+ ion reduction and anodic iron dissolution were not affected by salt concentration.

The experimental results are used to quantify the effect of salt concentration on kinetic parameters needed for the development of an electrochemical model. The electrochemical model is completed by implementing new limiting current density equations proposed in this study. Ultimately, the models for transport phenomena and solution chemistry (the MSE model) are coupled with the electrochemical model to build the final corrosion rate prediction model.

In development of the new limiting current density equations for CO_2 and H_2S corrosion, the H^+ ion reduction reaction is considered as the only cathodic reaction. Comparisons with the experimental limiting current density values demonstrated that the new equations are applicable to ideal, near ideal and non-ideal solutions with an acceptable accuracy.

The final corrosion rate prediction model is valid for the H_2O-NaCl-CO_2-H_2S system, temperatures above the water freezing point and below its boiling point, pressures up to a few bars, solution pH values from 1.0 up to 6.5, and NaCl concentrations between 0 wt.% to 20 wt.% (~4.3 m). The model is also applicable to CO_2 and H_2S partial pressures between 0 bar to 1 bar. It is expected that the model works for higher pressures up to the critical pressure of $CO_{2(g)}$ (~ 73 bar). The corrosion rate prediction model could predict the experimental corrosion rates measured in this study with an average absolute accuracy of 13.5%.

Dedication

To my father, Hassan Madani Sani who taught me that working hard pays off

To my mother, Raziyeh Alirezaee who showed my passion in my life

To my girlfriend, Athena Ghiasi who supported me during writing this document

Acknowledgments

It has been a great privilege to pursue my Ph.D. degree at the Institute for Corrosion and Multiphase Technology (ICMT) at Ohio University. I would like to express my deepest gratitude to my Ph.D. advisor, Professor Srdjan Nesic for his continuous support, guidance, and encouragement in both my academic and my personal life. Professor Srdjan Nesic has given me valuable suggestions on my career, shared his incredible expertise and experience with me, taught me to look at things from a different perspective, and inspired me to always think positive. Under his guidance, I have become a more professional, mature, and patient person.

I would like to thank my project leader, Dr. Bruce Brown, for always being there when I needed help throughout my Ph.D. research. I also appreciate Dr. David Young for always assisting me with reviewing and revising my proposal, papers, essays, and dissertation.

I would like to give special thanks to Dr. Andre Anderko and Dr. Peiming Wang from OLI Systems, Inc. who helped me to reproduce the mixed solvent electrolyte water chemistry model used in corrosion rate prediction model described in this dissertation.

My accomplishments would not be possible without the help and support of fellow lab mates and collaborators at ICMT. I was fortunate to work with our administrative coordinator Ms. Becky Matthews, lab technician Mr. Alexis Barxias, research engineer Mr. Cody Shafer. Additionally, I would like to thank the students and staff at ICMT for providing much needed assistance to buddy me during my tough H_2S experiments.

Finally, I would like to express my appreciation to my committee members, Dr. Marc Singer, Dr. Sumit Sharma, Dr. Rebecca Barlag, and Dr. Katherine Fornash for their interest in my work and willingness to be on my committee.

Table of Contents

Page

List of Tables

List of Appendix Tables

Page

List of Figures

Page

List of Appendix Figures

Chapter 1: Introduction

Water is ubiquitous in fluids produced during hydrocarbon extraction from both conventional and unconventional oil and gas wells. The technical term used in the oil and gas industry for this water is “produced water”. According to some sources, for every barrel of crude oil extracted from conventional oil reservoirs, about 7 to 10 barrels of water are produced on average [1–3]. This amount is usually lower for gas reservoirs. Produced water can be injected into wells for enhanced oil recovery. The amount of produced water in primary production increases over time when reservoirs age and this amount can be even higher if secondary or tertiary recovery methods are used. Dissolved salts are always present in produced water. It is reported that, in the USA, salt concentration (salinity), can vary from 1 g/l (~ 0.1 wt.%) to 400 g/l (~ 28 wt.%) in water produced from conventional oil and gas wells, with about half of the wells producing water containing more than 10 wt.% salt. For the unconventional wells, the salinity is generally less than 50 g/l (~ 5 wt.%), with 86% of the wells producing water containing less than 0.5 wt.% salt [4].

Other than salts, corrosive gases such as CO_2 and H_2S can be abundant in the production stream. Dissolution of CO_2 and H_2S gases in produced water generates corrosive species such as $H_2CO_{3(aq)}$[1], $H_2S_{(aq)}$ and $H^+_{(aq)}$, which can lead to severe corrosion of carbon steel equipment including oil and gas pipelines. A large body of research exists on CO_2 and H_2S corrosion of oil and gas facilities, mostly at low salt concentrations; up to 3 wt.%. However, only a limited number of studies has investigated

---

[1] The subscript (aq) denotes aqueous species.

CO_2 corrosion at high salt concentrations and to the best of author knowledge, no study exists for H_2S corrosion; most probably due to the toxicity of H_2S gas. In the case of strong acid corrosion[2], there are numerous studies on the effect of chloride ion concentration on the electrochemistry of the anodic dissolution of iron. However, as described in Section 5.1, most of these studies were done at low pH values (< 2) and their primary emphasis was studying the mechanism of anodic dissolution of iron in the presence of chloride. Therefore, no study found in the literature that investigated the effect of salt concentration on the rate of corrosion in strong acid solutions. Furthermore, a critical review of the existing studies on the effect of salt concentration on CO_2 corrosion is presented.

Fang *et al.* [5,6] (2006) studied the effect of salt concentration on uniform CO_2 corrosion of C1018 carbon steel using a rotating cylinder electrode (RCE) at 5°C, 1 bar total pressure, in CO_2-saturated aqueous solutions, pH 4 (adjusted) in a range of NaCl concentrations, from 3 wt.% to 25 wt.%. Their LPR[3] results showed a factor of two reduction in the corrosion rate when NaCl concentration was increased from 3 wt.% to 10 wt.%, and similarly another factor of two when NaCl was increased further from 10 wt.% to 20 wt.%. No further decrease in the corrosion rate was reported with the addition of NaCl from 20 wt.% to 25 wt.%. According to Fang *et al.* [5,6] there was no flow sensitivity of the corrosion rate at any NaCl concentration, which suggests that the corrosion process was not under mass transfer control.

---

[2] The definition is given in Section 5.1.

[3] Linear polarization resistance technique used to measure the corrosion rate

Han *et al.* [7] (2011) measured the corrosion rate of J55 mild steel by LPR in CO_2-saturated aqueous solutions at 25°C, 1 bar total pressure, pH adjusted to 4, and NaCl concentrations ranging from 0.5 wt.% to 20 wt.%. They used hanging rectangular electrodes in their experiments and produced flow by a magnetic stirrer, which is not the best choice when compared to the rotating disc electrode (RDE) and the RCE systems. The water chemistry in their 3-4 days long experiments was not controlled and the final pH increased from initial pH 4 to pH 5.5 at the end of their experimentation, which is a significant change. Han *et al.* [7] reported that the corrosion rate decreased as NaCl concentration was increased from 0.5 wt.% to 20 wt.%, which agrees with Fang *et al.* [5,6]. Han *et al.* [7] mentioned that below 20 wt.% NaCl, increasing the rotational speed of the magnetic stirrer led to higher corrosion rates, and therefore, unlike Fang *et al.* [5,6], they concluded that the corrosion process was mass transfer controlled. At 20 wt.% NaCl, Han *et al.*[7] postulated that the corrosion process became flow independent due to the formation of magnetite on the steel surface, which acted as a diffusion barrier. However, their XRD analysis did not clearly indicate the presence of magnetite. Considering the low temperature and the relatively low pH in their experiments, it is unlikely that the conditions were favorable for the formation of magnetite.

Elyian *et al.* [8] (2012) examined the effect of salt concentration on corrosion of API X100 carbon steel in CO_2-saturated solutions containing 5-80 g/l (~ 0.5-7.5 wt.%) NaCl at 20°C, 1 bar total pressure, and autogenous pH. They used hanging specimens and stirred the solution during the experiments with a magnetic stirrer. They reported a range of initial solution pH from pH 4.2 to pH 4.8, which is moderately higher than that reported in other studies [6,9,10]. As pH was not adjusted in their experiments, given their experimental conditions, it is not clear how pH values more than pH 4 were measured. Regardless, they reported that the corrosion rate obtained from the potentiodynamic polarization (PD) experiments reached a maximum at NaCl concentration of 15 g/l (~ 1.5 wt.%), then decreased with the addition of NaCl to 40 g/l (~ 4 wt.%) and became insensitive to NaCl concentration in more concentrated solutions. Eliyan *et al.* [8] suggested that the observed trend in the corrosion rate was due to acceleration of the anodic reaction at low NaCl concentrations and deceleration of the cathodic reactions at higher NaCl concentrations. These conclusions are not fully supported by their reported data. It is unclear from the provided PD sweeps that potentials were corrected for the solution resistance, which is particularly problematic in low conductivity solutions (at low salt concentrations). This could be the reason that the sweep conducted without NaCl seemed to be shifted towards lower currents and lacks any of the electrochemical characteristic features seen in the PD sweeps at higher NaCl concentrations.

Liu *et al.* [11] carried out weight loss (WL) corrosion rate measurements on N80 carbon steel exposed for 72 h to aqueous solutions at 100°C, CO_2 partial pressure of 20 bar, and an NaCl concentration range of 0 to 247.18 g/l (~ 20 wt.%). Their results showed a maximum in the corrosion rate at 41.20 g/l (~ 4 wt.%) NaCl concentration. As the NaCl content was increased further to 123.59 g/l (~ 11 wt.%), the corrosion rate decreased sharply and beyond that NaCl concentration, the change in the corrosion rate was small. Liu *et al.* [11] stated that at low NaCl concentrations, increasing NaCl content promoted

CO_2 corrosion by acting as catalyst for the iron dissolution reaction and by impairing the protective iron carbonate corrosion product layer accelerated the anodic reaction. Beyond the peak, they explained that CO_2 corrosion was retarded with increasing NaCl content due to a reduction in CO_2 solubility and concentration of corrosive species such as H^+ ion, $H_2CO_{3(aq)}$ and HCO_3^- ion. Liu *et al.* [11] reported an increase in pH with increasing NaCl concentration, which is the opposite of what is observed in this study. Moreover, their PD sweeps showed retardation of the anodic reaction (at NaCl concentrations above ~ 4 wt.%) and a general acceleration of the cathodic reactions with increasing NaCl concentration. The latter observation contradicts the findings reported in the studies described above, as well as the results of the present study.

Zeng *et al.* [12,13] (2016, 2019) investigated the effect of salt concentration on the corrosion rate of carbon steels in CO_2 saturated aqueous solutions at a temperature range of 25-80°C and an NaCl concentration range of 0.001-10 wt.%. They used two types of specimens: C1018 rectangular specimens for LPR corrosion measurements and surface analysis, and C1010 microwire specimens for PD experiments. With increasing NaCl concentration, their LPR results showed a continuous decrease in the corrosion rate for temperatures below 60°C and an opposite trend for temperatures above 60°C. The latter is attributed to the effect of NaCl on the protectiveness of $FeCO_3$ formed on the metal surface at high temperatures, which was apparently compromised in the presence of NaCl. However, caution is required when interpreting their LPR results, as they carried out long term experiments (100 h) in a small vessel (200 ml) with relatively large rectangular specimens in quiescent conditions. This resulted in a two-unit increase in solution pH (as they reported) at the end of their 100 h long experiments conducted at 25°C. The increase in solution pH is expected to be even larger at higher temperatures. This lack of water chemistry control during their experiments must have had a profound influence on what they measured and complicates the interpretation of the results, making it more difficult to accept the conclusions. Their PD sweeps showed a continuous increase in the rate of the anodic reaction with increasing NaCl concentration, while a decrease is seen for the cathodic reaction at low temperatures and no response at higher temperatures. Their PD results are in conflict with what Fang *et al.* [5,6] and Liu *et al.* [11] reported and with what will be demonstrated herein.

Zhang *et al.* [14] (2018) investigated the effect of salt concentration on uniform CO_2 corrosion of pipeline grade mild steel at 25°C in a rather narrow range of NaCl concentrations from 0.01 M (~0.1 wt.%) to 0.6 M (~3 wt.%). Their WL measurements showed a rapid increase in the corrosion rate with increasing NaCl from 0 to 0.2 M (~1 wt.%), which then stabilized and did not increase further with the addition of NaCl from 1 wt.% to 3 wt.%. For each experiment that lasted for 50 h, six specimens (4 for WL and 2 for surface analysis) were exposed in a small solution volume of 500 ml. The relatively long experiments with a small solution volume to surface area ratios, must have led to a loss of control of water chemistry, including a significant increase in pH and ferrous ion concentration. In addition, their measured initial pH values are 0.5 pH units higher compared to pH values expected under their experimental conditions [6,9,10], and the lack of compensation for the solution resistance in their potentiodynamic sweeps raises questions about the validity of the experimental results.

In summary, while several studies addressed the effect of salt concentration on uniform corrosion of steel in CO_2 aqueous solutions, there is still a lack of clarity, with contradicting results being presented, mostly due to questionable experimental methods and procedures used. Most of the studies mentioned above did not include adequate control of water chemistry, which would have led to significant changes in the solution composition over the course of rather long experiments, with detrimental effects on the quality of obtained results. In most of the studies the effect of solution conductivity on electrochemical measurements was not compensated for, making the results at low salt concentrations questionable. In some studies, conducted at higher temperatures, the complicating effects of salt concentration on formation of protective iron carbonate layers were not properly separated from the effects salt has on anodic and cathodic reactions underlying the CO_2 corrosion process. Finally, the mechanisms behind CO_2 corrosion were often misstated, for example by arguing that the cathodic limiting current density is diffusion controlled when in reality it is a combination of diffusion and the slow homogenous chemical CO_2 hydration reaction.

Therefore, there is a need to address the effect of salt concentration on the CO_2 corrosion process in a more systematic and mechanistically correct way and extend that to strong acid and H_2S corrosion. Studying the effect of salt concentration in strong acid solutions provides a baseline for a better understanding of salt effects on CO_2 and H_2S corrosion, as the main electrochemical reactions underlying the three types of corrosion are the same. Also, it is important to consider the shortcomings listed above when planning and executing experimentations.

The present study covers a wide range of salt concentrations and a variety of methods used to mechanistically investigate the effect of salt concentration on uniform strong acid, CO_2, and H_2S corrosion of carbon steel. The effect of NaCl concentration on corrosion behavior of an X65 carbon steel was studied by performing WL and/or electrochemical measurements (LPR and PD sweeps) in N_2-, CO_2-, and H_2S-saturated aqueous solutions at different NaCl concentrations, ranging from 0 wt.% to 20 wt.%.

The experimental results are used to quantify the effect of salt concentration on kinetic parameters needed for the development of an electrochemical model. In addition to that, models are reproduced or developed for the two key parameters that are influenced by changing salt concentration: transport phenomena and solution chemistry. Ultimately, the electrochemical model is coupled with the models for transport phenomena and solution chemistry to build a corrosion rate prediction model valid for different operational conditions and wide range of NaCl concentrations.

Chapter 2: How Does Salt Concentration Influence CO_2/H_2S Corrosion Processes?

The Required Information

Salt concentration influences the aqueous CO_2/H_2S corrosion processes by altering the transport properties in the solution, the solution chemistry, and the mechanisms and the rate of reactions involved in the corrosion process. Each factor can be further evolved as shown in Figure 2-1. To improve our understanding of the effect of salt concentration on the CO_2/H_2S corrosion process as well as development of an accurate corrosion rate prediction model it is necessary to study the effect of salt concentration on each these factors in some detail. In the following text, the effect of salt concentration on each of these factors will be comprehensively reviewed and the available models in the literature for each case will be discussed and compared with experimental data.

Figure 2-1

The factors that are influenced by salt concentration in the CO_2/H_2S *corrosion process*

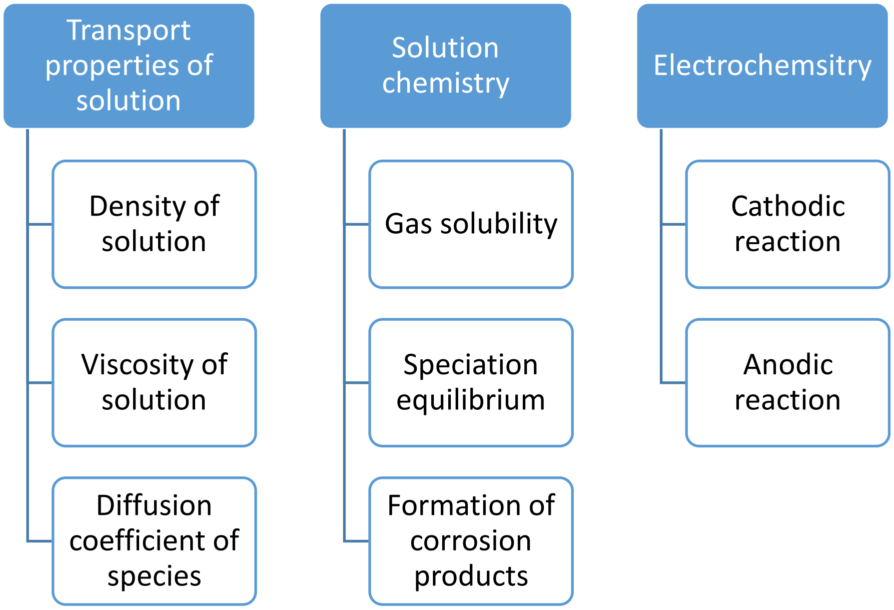

Consider a metal (*e.g.,* carbon steel) is corroding in a solution. The corrosion process involves anodic metal dissolution (oxidation) reaction at anodic areas and reduction reaction at cathodic areas [15]. This explanation is based on the mixed-potential theory presented formally for the first time by Wagner and Traud [16]. According to the mixed-potential theory the anodic and cathodic areas are internally short-circuited. In another words, the total potential difference (iR drop) across an anodic site adjacent to a cathodic site on the metal surface is virtually zero. This postulate requires that the distance between adjacent anodic and cathodic sites on the metal surface be negligible (of the order of few Angstroms), the solution be sufficiently conductive, and the metal surface be homogenous (*e.g.*, no high-resistance corrosion product layers on the surface) [15]. The amount of metal dissolution (also called metal weight loss or metal corrosion) can be expressed in terms of a corrosion current by using the Faraday's law given below:

$$\Delta W = \frac{M}{nF} \cdot t \cdot I_{Corr} \tag{2-1}$$

where, ΔW is the amount of weight loss due to corrosion in kg, M is the metal atomic weight in kg/mol, n is the number of electrons exchanged within the dissolution reaction, F is Faraday's constant (= 96485.33 C/mol), t is the length of time in sec that the metal surface is exposed to the solution, and I_{corr} is the corrosion current in A [17]. If both sides of Equation (2-1) are divided by t, then the left-hand side will be equal to the rate of corrosion (CR) in kg/s; hence, CR and I_{Corr} are directly related.

$$CR = \frac{M}{nF} I_{Corr} \tag{2-2}$$

According to the mixed-potential theory, there cannot be an accumulation of electric charge during an electrochemical reaction. This means that during the corrosion of electrically isolated metal sample, the total current (an indication of the rate) of anodic metal dissolution (oxidation), I_a and the total current (an indication of the rate) of reduction, I_c must be equal in magnitude, but opposite in sign [18]:

$$I_a = -I_c \tag{2-3}$$

Since the metal dissolution current, I_a is equal to I_{corr}, therefore:

$$I_{corr} = I_a = -I_c \tag{2-4}$$

The currents introduced in Equation (2-4) are equal to the product of the corresponding current density times the corresponding surface area:

$$I_{corr} = I_a = i_a A_a \tag{2-5}$$

$$I_{corr} = I_c = i_c A_c \tag{2-6}$$

where i_a is the total dissolution current density or total anodic current density in A/m^2, A_a is the total surface area of the anodic sites in m^2, i_c is the total reduction current density in A/m^2, and A_c is the total surface area of the cathodic sites in m^2. According to the mixed-potential theory, the metal surface is assumed to be uniform, and the anodic and cathodic sites are tiny and uniformly scattered all over the metal surface. Moreover, the anodic and cathodic sites are shifting around the metal surface with time [15]. Therefore, it is correct to assume that A_a is equal to A_c and both are equal to the total corroding metal surface area (A):

$$A = A_a = A_c \tag{2-7}$$

Finally, the corrosion current can be expressed in terms of corrosion current density (i_{corr}) in A/m^2 as follows:

$$I_{corr} = i_{corr} A \tag{2-8}$$

Using i_{corr} instead of I_{corr} in corrosion rate calculations makes them easier as the surface area will be kept out of the equations.

The aqueous CO_2 or H_2S corrosion processes (which can be classified as corrosion in weak acids) can be considered to consist of the following simultaneous steps: (1) electrochemical metal dissolution, (2) electron flow in metal, (3) transport of products away from the surface (4) electrochemical reduction, (5) transport of reactants in the solution to the surface, (6) chemical reaction in the bulk solution. The consecutive reaction reaches a steady state, when the overall current is equal to the current associated with the slowest step which is called the rate determining step (rds) [15,19]. The aqueous strong acid corrosion process does not have step 6.

The rds in aqueous CO_2 or H_2S corrosion processes can be any of the above six steps listed above. When corrosion occurs spontaneously (zero overpotential) in the absence of a passive layer (for example carbon steel does not have a passive layer on its surface), the dissolution step (step 1) cannot be the controlling step. Since the electric conductivity of the metal is sufficiently high, the electron flow in the metal (step 2) is usually not the rds. When there is no compact corrosion product layer on the surface that hinders the transport of metal ions produced from the dissolution step in the solution, transport of products (metal ions) away from the surface (step 3) cannot be a rds. Thus, three rds possibilities remain: electrochemical reduction control (step 4) transport of reactants in the solution to the surface (step 5) or chemical reaction in the bulk solution (step 6). It is important to identify the type of control over the corrosion current or in other words the rds step in the corrosion process. This allows ignoring the non-rds steps and focus on parameters that influences the rds step for a better understanding of the corrosion process [15]. In the case of aqueous CO_2 and H_2S corrosion, which is the focus of this study, the rds is often identified to be a combination of step 5- reactant transport in the solution (*i.e.*, mass transfer) and step 6- chemical reaction controls. However, in some situations, the electrochemical reduction step (step 4) is the rds. In some other situations, it is possible that none of the three steps is much slower than the other(s) and the corrosion process is labeled to be under “mixed control”. Examples of each case will be presented in Chapters 9, 10, and 11, where experimental results are reported.

The rate of aqueous CO_2 and H_2S corrosion processes is often controlled by a combination of the rate of mass transfer of reactants (corrosive species) from the bulk solution to the surface and the rate of chemical reactions. For strong acid corrosion, it will be just mass transfer of reactants. The scenario where the corrosion process is controlled by the mass transfer rate is described in the following. For the mixed mass transfer and chemical reaction scenario, the reader is referred to Appendix V and W. The charge-transfer control scenario is comprehensively explained in Chapter 5.

The rate of mass transfer of a species from the bulk solution to the surface is usually stated as flux density, N in mol/m^2/s. N is a vector quantity that indicates the direction in which the species is moving and the number of moles of that species passing per sec across a plane of 1 m^2 normal to the species flow direction. For a solution consisting of a nonionized solvent, ionized electrolytes[4], and uncharged minor components, the flux density of each dissolved species such as i is given by:

$$N_i = -u_i c_i \nabla \mu_i + c_i v \tag{2-9}$$

where, u_i is the mobility of species i in m^2 mol/J/s and represents the average velocity of species i in the solution when a force of 1 N/mol is applied to it, c_i is the concentration of species i in mol/m^3, μ_i is the electrochemical potential of species i in J/mol, and v is the average velocity of the bulk fluid in m/s. The first term on the right-hand side of Equation (2-9) is associated with the gradient of the electrochemical potential, which is used as the driving force for the *mass transfer* of species to the surface. The second term on the right-

---

[4] Electrolyte is used in electrochemistry to refer not only to the ionically conducting medium through which electricity is passed, but also the substances that when dissolved (or melted), give rise to a conducting medium [20].

hand side of Equation (2-9) is related to *convection* due to the bulk motion of the solution. The electrochemical potential, μ_i can be expressed in terms of “chemical” and “electrostatic potential” parts:

$$\mu_i = \mu_i^0 + RTln(\gamma_i^c c_i) + Fz_i\Phi \tag{2-10}$$

where, μ_i^0 is the standard chemical potential of species i in j/mol, R is the gas constant equal to 8.3145 J/mol/K, T is the solution temperature in K, γ_i^c is the molar activity coefficient of species i, z_i is the charge number of species i, and Φ is the electric potential in V [20]. Considering the Nernst-Einstein relationship which is applicable only at infinite dilution ($D_i = RTu_i$), combining Equations (2-9) and (2-10) gives:

$$N_i = -D_i \nabla c_i - D_i c_i \nabla ln\gamma_i^c - \frac{Fz_iD_i}{RT} c_i \nabla\Phi + c_i v \tag{2-11}$$

where, the del operator (∇) is taken in x, y, and z directions.

Each term in Equation (2-11) represents a mechanism of mass transfer. The first two terms are related to molecular “diffusion” due to a concentration gradient (chemical driving force). The third term is associated with the “migration” of a charged species in an electric field (electrostatic potential driving force). The last term is “convection” due to bulk motion of the solution [21]. In many practical applications, the term related to migration in Equation (2-11) can be neglected. Migration becomes important in ionic systems in which there is no supporting electrolyte[5]. For transport of neutral species in

---

[5] According to an IUPAC definition, a supporting electrolyte, is an electrolyte containing chemical species that are not electroactive (within the range of potentials used) and has an ionic strength and conductivity much larger than those due to the addition of electroactive species to the electrolyte [22]. Supporting electrolyte is also sometimes referred to as inert electrolyte or inactive electrolyte. The main role of a supporting electrolyte is to reduce the ohmic drop (*iR* voltage) in the cell to a minimum and to effectively eliminate the contribution of the electroactive species (analyte) to the migration current [23].

any environments or for transport of charged species in environments that contain considerable amounts of supporting electrolyte (*e.g.* NaCl) migration can be neglected [19]. Therefore, Equation (2-11) can be simplified to:

$$N_i = -D_i \nabla c_i - D_i c_i \nabla ln\gamma_i^c + c_i v \tag{2-12}$$

The flux density is usually converted to the current density as it is much easier to measure or monitor in a process such as aqueous CO_2/H_2S corrosion. The total current density (i) in an electrolytic solution due to mass transfer of all electroactive species involved in the corrosion process from the bulk to the surface can be expressed by the equation below [21]:

$$i = F \sum_i z_i N_i \tag{2-13}$$

where, F is the Faraday's constant and z_i is the charge number of species i.

If the rate of mass transfer of electroactive species i (step 5) is slower that the rate of reduction reaction of species i at the surface (step 4), the concentration of species i at the surface, $c_{s,i}$ is different from that in the bulk, $c_{b,i}$ and a gradient of concentration is established. This concentration gradient occurs in the very thin region next to the surface. This region is called Nernst diffusion layer or mass transfer boundary layer. The mass transfer rate presented by Equation (2-12) can be simply explained by the concept of the Nernst diffusion layer. According to this concept, the solution near the corroding surface can be divided into two regions. In the inner region (Nernst diffusion layer), the effect of flow or convection is negligible, and diffusion is the only mechanism of transport. In the outer region, due to convective mixing, concentrations are considered to be uniform and equal to those in the bulk solution. The thickness of Nernst diffusion boundary layer (δ_m)

for species i is defined where the concentration of species i, c_i is 0.99 of its concentration in the bulk, $c_{b,i}$. $\delta_{m,i}$ depends on diffusion coefficient of species i (D_i), in addition to the solution properties (density, and viscosity) and fluid dynamics (velocity and flow regime). For example, for a higher diffusion coefficient and a higher fluid velocity δ_m will be smaller. Various δ_m equations for different experimental apparatus (rotating disk, rotating cylinder, pipe, and duct channel) are listed in Appendix X.

From Equation (2-12), it is obvious that the net flux of species i which is an indication of the rate of mass transfer of species i to the surface, depends on diffusion coefficient of species i (D_i), concentration of species i in the bulk ($c_{b,i}$), and average velocity of fluid (v). The velocity of fluid can be theoretically computed by Navier-Stokes and continuity equations. For Newtonian fluids which include most of the electrolytic solutions, like the one used in this study, the fluid velocity depends on density and viscosity of solution [21]. For the chemical reaction step (step 6), the rate depends on the concentration of dissolved corresponding reactants and products in the bulk.

The rate of reduction electrochemical reaction at metal surface (step 4) depends on the concentration of electroactive species at the metal surface and the mechanism of electron transfer throughout the overall electrochemical reaction. The former as explained by the concept of the Nernst diffusion layer is directly related to the bulk concentration of those electroactive species. For the dissolution step (step 1), assuming that there is no saturation of dissolution products (metal ion) at the surface, the rate depends on the surface concentration of catalytic species involved in the dissolution reaction (*e.g.*, OH^-)

as well as the mechanism of the electron transfer during the course of the overall dissolution rection.

Therefore, to understand better the effect of salt concentration on the corrosion process, the changes in solution chemistry (*e.g.*, bulk concentrations), density and viscosity of solution, diffusion coefficient of dissolved species, and electrochemistry of surface reactions involved in the corrosion need to be addressed. The effect of salt concentration on each the abovementioned parameters will be discussed in detail in the next chapters.

Chapter 3: The Effect of Salt Concentration on Transport Properties of Solution

In this section, the effect of salt concentration on solution density, solution viscosity, and diffusion coefficient of dissolved species in the solution will be reviewed.

3.1 The Effect of Salt Concentration on Solution Density

When a salt such as NaCl is added to a solution, the salt crystal dissolves in water and ions become surrounded by water molecules (Figure 3-1). The ions interact strongly with water molecules; this is known as aquation. The solution volume increases by small factor when salt is added to water. However, the mass of solution increases by a larger factor comparing to the volume because salt is much denser that water. Therefore, the density of solution increases with increasing salt concentration.

Figure 3-1

The schematics of dissolved NaCl in water (Adapted from Prof. P. Shapley webpage at University of Illinois, 2011, http://butane.chem.uiuc.edu/pshapley/genchem1/l21/1.html)

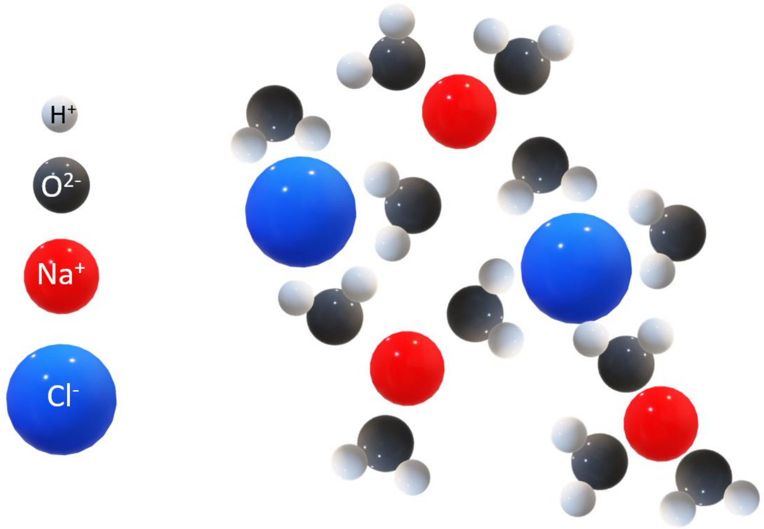

Figure 3-2 shows the changes in the aqueous NaCl solution with NaCl concentration at 30°C and 1 bar. The calculated solution density by two reproduced models is compared with the experimental data obtained from Perry's Handbook [24] . Both models could capture the experimental data almost perfectly. The Rogers and Pitzer [25] model is a semi-empirical with a validity range of 0-300°C, 1-1000 bar and 0-5 molal (0-22.6 wt.%) NaCl. The Batzle and Wang [26] model is an empirical model with a validity range of 0-350°C, 0.1-981 bar and 0-5.4 molal (0-24 wt.%) NaCl. The Batzle and Wang [26] model will be used in development of the corrosion rate prediction model for this study because it cover a wide range of operational conditions in addition to being simple to reproduce. The equations related to the Batzle and Wang [26] are given below:

$$\begin{aligned}\rho_w = 1 + 1\times10^{-6}(&-80T_c - 3.3T_c^2 + 0.00175T_c^3 + 489P - 2T_cP \\ &+ 0.016T_c^2P - 1.3\times10^{-5}T_c^3P - 0.333P^2 \\ &- 0.002T_cP^2)\end{aligned} \tag{3-1}$$

$$\begin{aligned}\rho_{sol} = \rho_w + S\Big(&0.668 + 0.44S \\ &+ 10^{-6}\big(300P - 2400PS \\ &+ T_c(80 + 3T_c - 3300S - 13P + 47PS)\big)\Big)\end{aligned} \tag{3-2}$$

where ρ_w and ρ_{sol} are pure water and solution (brine) densities in g/cm^3, respectively, T_c is the solution temperature in °C, P is the total pressure in MPa, and S is salt weight fraction as follows:

$$S = \frac{mass\ of\ salt}{mass\ of\ water + mass\ of\ salt} \tag{3-3}$$

Figure 3-2

Variation in aqueous NaCl solution density vs. NaCl concentration at 30ºC and 1 bar. The dots are experimental data and solid lines are calculated values.

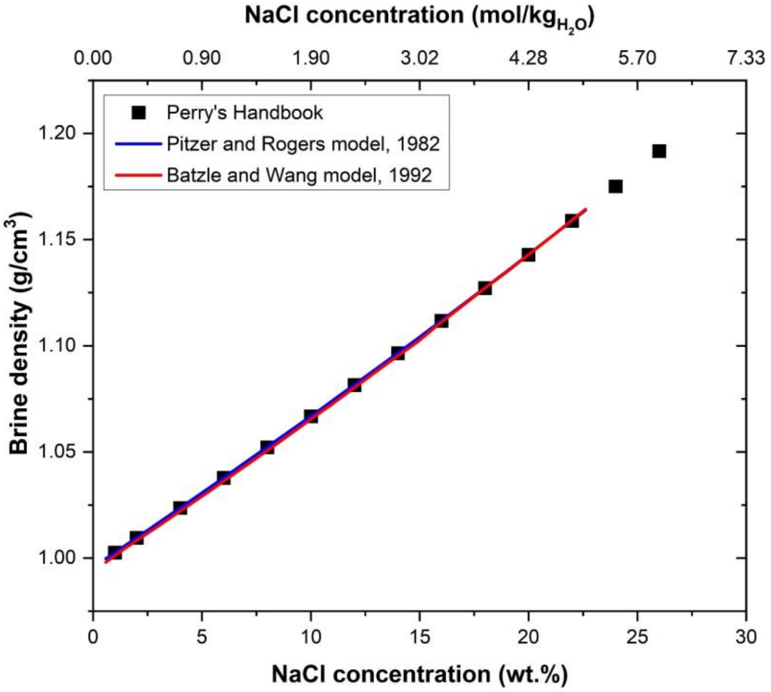

Dissolution of gases (CO_2 and H_2S) in the solution can also change the solution density. However, the change in the solution density becomes significant at very high partial pressures of gas, *e.g.*, above 100 bar. These high pressures are usually encountered in sequestration and geochemical processes. In the oil and gas industry where the maximum operational pressure is usually around 70 bar, the solubility of gas in the solution has a negligible effect on the solution density [27–29]. It is shown that in H_2O-NaCl-CO_2 system, the effect of CO_2 solubility on the density of the solution was less than that of temperature and pressure [29]. Figure 3-3 shows clearly that CO_2 solubility has a minor effect on the density of seawater solution. For example, at 65 bar of pure CO_2 gas and solution temperature of 1°C, the solubility of CO_2 is around 1.67 mol/kgH_2O [30]. This is equal to a CO_2 mass fraction of ~0.06, which according to Figure 3-3 results in the density to be 1.016 of that for seawater without CO_2. Considering that the solubility of gas decreases with increasing salt concentration (see Section 4.1), the effect of dissolved gas on solubility becomes even less at higher salt concentration. Therefore, the effect of dissolved gas on the density of solution will be ignored in this study.

Figure 3-3

The ratio of CO_2-bearing seawater solution density to seawater solution density at different concentration of dissolved CO_2 at pressures above 50 bar and temperatures between 1°C to 7°C. CO_2 mass fraction is equal to the mass of dissolved CO_2 divided by the mass of solution. The graph is reproduced from Duan et al. [28]

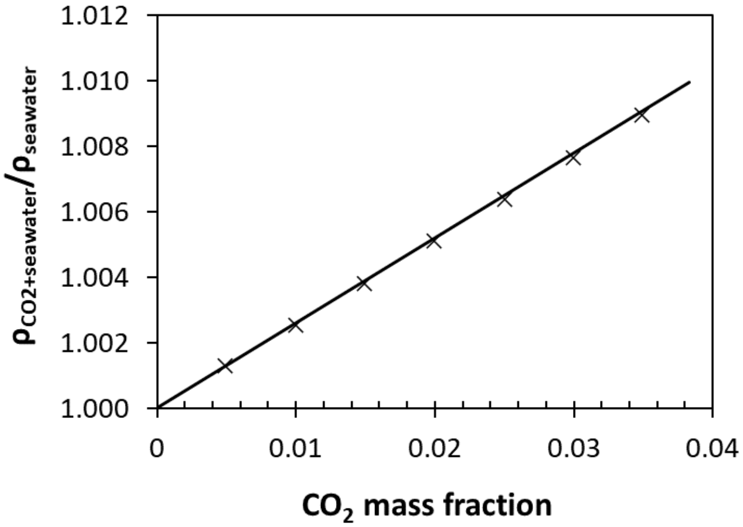

3.2 The effect of Salt Concentration on Solution Viscosity

The solution viscosity is a key factor in fluid flow wherever electrolyte solutions must be stirred, pumped, or moved through pipelines and other equipment. Variations in viscosity can have a significant effect on the flow pattern and consequently on the mass transfer of species in the solution [31]. Consequently, the effect of salt concentration on solution viscosity which in turn has a significant role in mass transfer processes involved in CO_2/H_2S corrosion, needs to be addressed carefully.

Poiseuille [32] was the pioneer in research on the effect of salt on water viscosity. Ever since, much research has studied this subject. Detailed historical reviews are reported elsewhere [33,34]. Generally, when salts such as NaCl are added to a solution, the solution viscosity increases. However, there are a few salts such as KCl that are exceptions and cause the solution viscosity to decrease at higher concentrations. The relationship between solution viscosity and salinity can be described by the contribution of three factors: Brownian motion, Debye-Huckel electrostatic ionic interaction [35], and structural temperature effect. Brownian motion relates to the random movement of momentum by fluid particles in a solution from one location to another. The Debye-Huckel contribution associates with resistance to shear due to the electrostatic forces between dissolved ions. The contribution of Brownian motion and the Debye-Huckel interaction to the viscosity of any ionic solution is always positive. However, the structural temperature effect depending on the type of dissolved salts, can alter the viscosity of brines either positively or negatively [36]. The structural temperature effect is related to changes in the structure of water molecules with the addition of ions. This phenomenon becomes important in dilute solutions of alkali halide salts. For example, solutions of potassium fluoride (KF) in water are more viscous than pure water, while solutions of potassium iodide (KI) in water are less viscous than pure water. The F^- ion strengthens the structure of water, an analogy to the effect created by lowering the temperature, whereas the I^- ion weakens the structure, as if the temperature was raised. The temperature analogy was the reason for choosing the term structural temperature for this effect. Therefore, ions such as F^- are called ‘structure making’ ions or *osmotropes,* and ions such as I^- are called ‘structure breaking’ ions or *chaotropes* [36,37]. More on how the variation in concentration of different ions influences the solution viscosity can be found a paper published by Kwak *et al.* [38]. For the case of NaCl which is the focus of this study, the solution viscosity increases with increasing NaCl concentration.

The viscosities of electrolyte solutions are usually expressed by the Jones-Dole equation [34] as follows:

$$\frac{\eta_s}{\eta_w} = 1 + Ac^{\frac{1}{2}} + Bc \tag{3-4}$$

where η_w and η_s are the viscosities of pure water and salt solution, respectively, c is the molar concentration of solute (salt), and A and B are constants specific to the solute. A is an electrostatic term that can be neglected at moderate concentrations, and B is a measure of ion-water interactions and can be treated as the structural temperature effect [38]. Coefficient A is a function of solvent properties and limiting conductivities of dissolved ions and can be calculated by an expression proposed by Falkenhagen and Dole [39,40]. Equation (3-4) is valid for dilute solutions (not more than 0.2 M to 0.3 M) [34,41]. For applications in higher solute concentrations, extended Jones-Dole equations have been reported by Kaminsky and others [41,42].

For the H_2O-NaCl system, several models have been described for solution viscosity of solution in over large ranges of temperature, pressure and NaCl concentrations [26,43,44,31,45]. From these, the Kestin and Khalifa [43], the Batzle and Wang [26], the Mao and Duan [31], and the Islam and Carlson [45] models have been reproduced and compared with each other as well as with experimental data, to find the most suitable model for this study. Figure 3-4 shows the comparison at two different conditions. All four models confirm the increase in solution viscosity with increasing NaCl concentration. The Islam and Carlson [45] model for the viscosity of aqueous NaCl solutions is the same as the Mao and Duan [31] model, except that a simpler equation is used for calculating the density of water, instead of the IAPWS 1997 [46] equation used in the Mao and Duan model [31]. Thus, these two models predict almost the same values for the viscosity as shown by the examples in Figure 3-4. The Islam and Carlson [45] and the Mao and Duan [31] models are identified as the suitable models because they are more recent and cover a wider range of conditions. The validity range of these models is $1^oC < T < 350^oC$, 1 bar < P < 1000 bar, and 0 m < NaCl < 6 m [31,45].

Figure 3-4

Comparison of four viscosity models [26,31,43,45] *for the H_2O-NaCl system at (A) 30°C and 1 bar total pressure, and (B) 50°C and 20 bar total pressure. Solid lines are calculated viscosities. Solid squares are experimental data obtained from* [47,48].

(A)

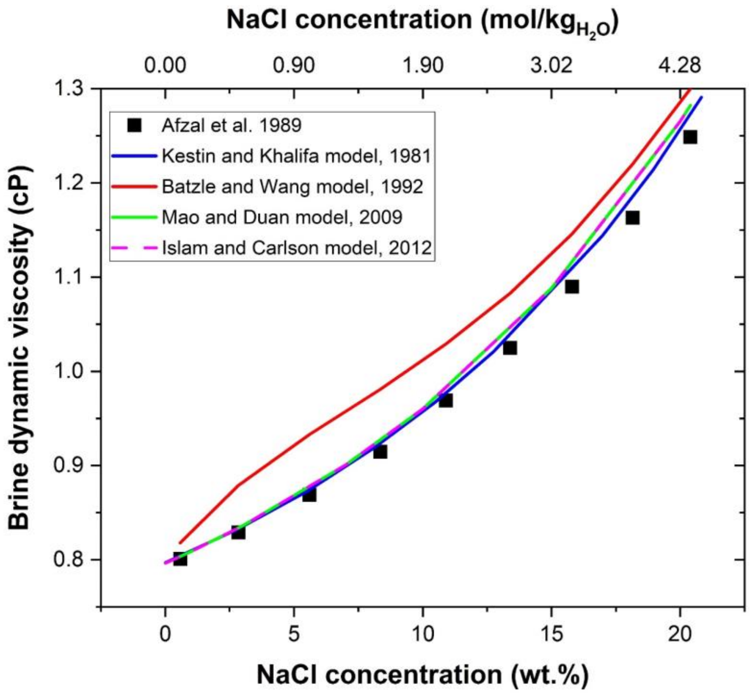

(B)

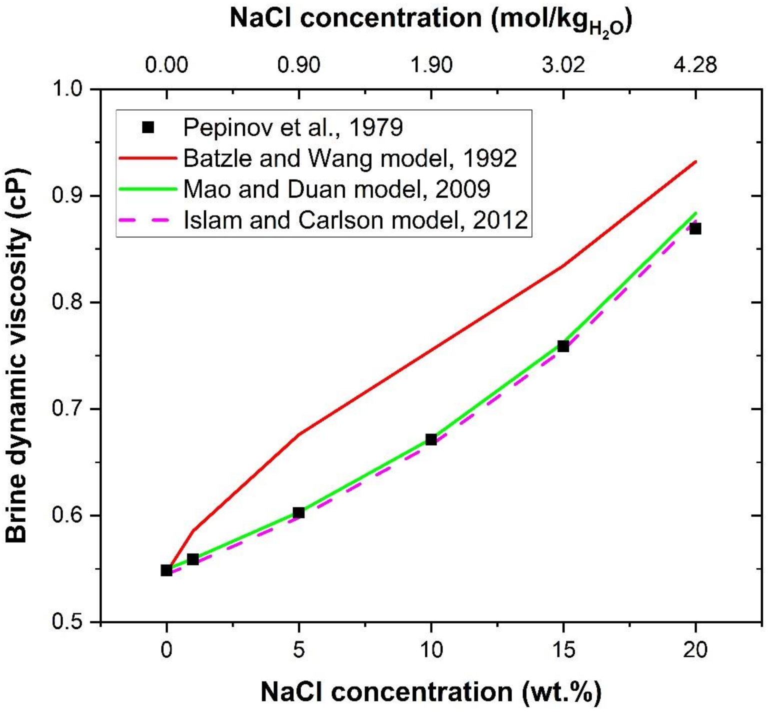

In corrosion prediction studies done so far, to the best of the author's knowledge, when gases such as CO_2 or H_2S are dissolved in aqueous NaCl solutions, the solution viscosity is often assumed to be as unchanged and the same as that for a pure aqueous NaCl solution [19,49–51]. This might be true at low partial pressures of gas (below 10 bar) when solubility of gas in the solution is small. However, at high partial pressures, neglecting the presence of dissolved gas in the solution will introduce an error in the viscosity predictions. Figure 3-5 shows two examples for the effect of dissolved CO_2 on the viscosity of aqueous NaCl solution. When CO_2 is not present, the viscosity at both total pressures of 10 bar and 50 bar are almost the same, showing that the dependency of viscosity of on pressure is insignificant. However, dissolution of CO_2 in the solution increases its viscosity and this rise in the viscosity becomes larger at higher CO_2 partial pressures (10 bar *vs.* 50 bar in Figure 3-5). In the presence of CO_2, the increase in solution viscosity becomes less at higher NaCl concentrations due to salting out of CO_2, which is explained in Section 7.1. The increase in the solution viscosity with dissolution of H_2S gas will be the same as that for CO_2. However, since the partial pressures of H_2S encountered in oil and gas production are usually much lower than 1 bar, the amount of dissolved H_2S in the solution is small, and thereby, the effect of dissolved H_2S on the brine viscosity is ignored in this study.

Figure 3-5

The effect of dissolved CO_2 on the viscosity of aqueous NaCl solution at different NaCl concentrations. The solution viscosity is calculated with Mao and Duan [31] *and Islam and Carlson models* [45].

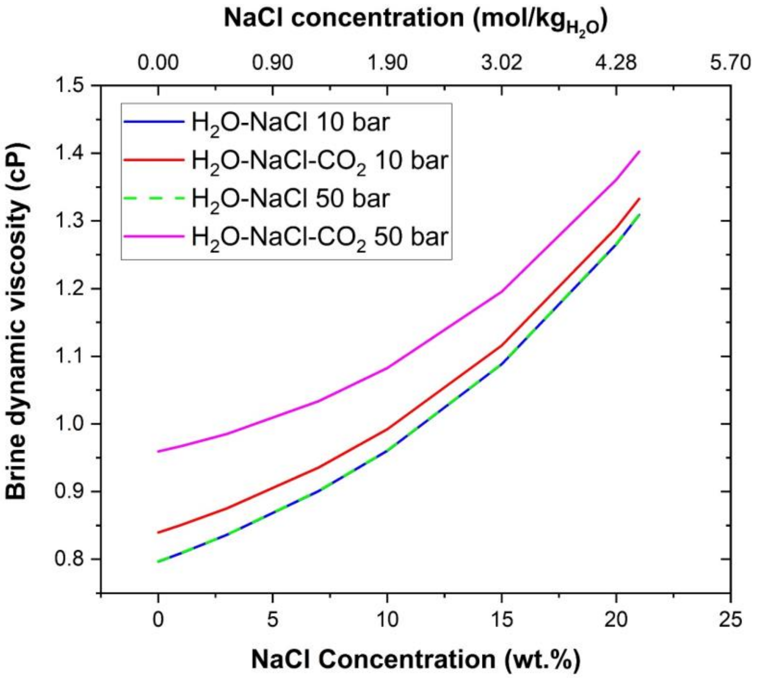

A combination of Mao and Duan [31] and Islam and Carlson [45] models is used in this study to capture the effects of both NaCl concentration and dissolved CO_2 on the viscosity of brine. The equations related to this model will be listed in the following text.

The first step to calculate the viscosity of CO_2 bearing aqueous NaCl solutions is to calculate the water viscosity [31]:

$$\mu_w = \exp\left(\sum_{i=1}^{5} a_i T^{i-3} + \sum_{i=6}^{10} a_i \rho_w T^{i-8}\right) \tag{3-5}$$

where μ_w is dynamic viscosity of pure water in Pa·s, a_i are coefficients listed in Table 3-1, T is solution temperature in K, and ρ_w is density of pure water in g/cm^3. ρ_w is given by the following equation [45]:

$$\rho_w = b_0 + \sum_{i=1}^{3} c_i 10^{d_i T} + \sum_{i=1}^{2} e_i P^i \tag{3-6}$$

where the coefficients b_0, c_i, d_i, and e_i are reported in Table 3-1, P is the total pressure in MPa. Then, the viscosity of the aqueous NaCl solution will be calculated by using the equation below:

$$\mu_{sol} = \mu_w \exp(Fm + Gm^2 + Hm^3) \tag{3-7}$$

where μ_{sol} is the viscosity of brine (H_2O-NaCl) in Pa·s, m is the concentration of NaCl in molality (mol/kgH_2O), and F, G, and H are polynomial functions of absolute temperature (T in K) given below:

$$F = f_0 + f_1 T + f_2 T^2 \tag{3-8}$$

$$G = g_0 + g_1 T + g_2 T^2 \tag{3-9}$$

$$H = h_0 + h_1 T \tag{3-10}$$

The coefficients used in Equations (3-8)-(3-10) are shown in Table 3-1.

Finally, the viscosity of the CO_2 bearing aqueous NaCl solution can be calculated as follows:

$$\mu_{sol} = \mu_b\left(1 + 4.65 x_{CO_2}^{1.0134}\right) \tag{3-11}$$

where, μ_{sol} is viscosity of solution for H_2O-NaCl-CO_2 system in Pa·s and x_{CO_2} is the mass fraction of dissolved CO_2 in the solution which is equal to:

$$x_{CO_2} = \frac{m_{CO_2} \times M_{CO_2}}{1000 + m_{CO_2} \times M_{CO_2} + m_{NaCl} \times M_{NaCl}} \quad (3\text{-}12)$$

Table 3-1

Coefficients used in Equations (3-5) and (3-6) for calculating the solution viscosity in H_2O*-NaCl-*CO_2 *system. These coefficients are taken from* [30,44].

i	a_i	b_i	c_i	d_i	e_i	f_i	g_i	h_i
0		1.34136579e-1	-	-	-	-0.21319213	0.69161945e-1	-0.2598855e-2
1	0.28853170e7	-	-4.07743800e0	-5.56126409e-3	4.45861703e-4	0.13651589e-2	-0.27292263e-3	0.77989227e-5
2	-0.11072577e5	-	1.63192756e1	-1.07149234e-2	-4.51029739e-7	-0.12191756e-5	0.20852448e-6	-
3	-0.90834095e1	-	1.37091355e0	-5.46294495e-4	-	-	-	-
4	0.30925651e-1	-	-	-	-	-	-	-
5	-0.27407100e-4	-	-	-	-	-	-	-
6	-0.19283851e7	-	-	-	-	-	-	-
7	0.56216046e4	-	-	-	-	-	-	-
8	0.13827250e2	-	-	-	-	-	-	-
9	-0.47609523e-1	-	-	-	-	-	-	-
10	0.35545041e-4	-	-	-	-	-	-	-

where m_{CO_2} and m_{NaCl} are the molality concentrations of dissolved CO_2 and NaCl, and M_{CO_2} and M_{NaCl} are the molecular weights of CO_2 and NaCl, respectively. In this study, m_{CO_2} is calculated by the Mao *et al.* [30] model, which is discussed in detail in Section 7.1.4.

3.3 The Effect of Salt Concentration on Diffusion Coefficient of Dissolved Species

As explained earlier and shown by Equation (2-12), diffusion coefficients of electroactive species are needed to determine the rate of mass transfer governing the corrosion process. The concentration dependence of diffusion coefficient and therefore its effect on the mass transfer rate can be understood better by expanding the first term of Equation (2-9), assuming that mass transfer occurs only due to the gradients of chemical potential and convection is negligible:

$$N_i = -u_i c_i \nabla \mu_i \tag{3-13}$$

Since corrosion occurs uniformly across the metal surface, the gradient (∇) of chemical potential for two directions (assume y and z) parallel to the metal surface will be zero. Thus, Equation (3-13) can be written in one dimensional domain in x direction, normal to the metal surface.

$$N_i = -u_i c_i \frac{d\mu_i}{dx} \tag{3-14}$$

Using thermodynamic transformations gives [20]:

$$N_i = -u_i c_i \frac{d}{dx}\left(\mu_i^o + RTln(\gamma_i^c c_i)\right) \tag{3-15}$$

$$= -u_i c_i \frac{RT}{\gamma_i^c c_i}\frac{d}{dx}(\gamma_i^c c_i)$$

$$= -u_i RT\frac{dc_i}{dx} - \frac{u_i RT c_i}{\gamma_i^c}\frac{d\gamma_i^c}{dx}$$

$$= -u_i RT\frac{dc_i}{dx} - \frac{u_i RT c_i}{\gamma_i^c}\frac{d\gamma_i^c}{dc_i}\frac{dc_i}{dx}$$

$$= -u_i RT\frac{dc_i}{dx}\left(1 + \frac{c_i}{\gamma_i^c}\frac{d\gamma_i^c}{dc_i}\right)$$

$$= -u_i RT\frac{dc_i}{dx}\left(1 + \frac{dln\gamma_i^c}{dlnc_i}\right)$$

Finally, recalling the Fick's first law of diffusion ($N_i = -D_i \frac{dc_i}{dx}$):

$$D_i = u_i RT\left(1 + \frac{dln\gamma_i^c}{dlnc_i}\right) \tag{3-16}$$

Equation (3-16) implies that at a constant temperature, the diffusion coefficient of species i varies with the variation of the mobility of species i (u_i) along with the variation of the activity coefficient of species i (γ_i^c). Since the activity coefficient of species i is a function of concentrations of all the species in the solution (explained in Section 8.3.1 and Appendix L), the diffusion coefficient of species i depends on the concentrations as well. However, for a uniform concentration distribution of species throughout the solution, such as the case for concentrated aqueous salt solutions, the concentration dependent term , $dln\gamma_i^c / dlnc_i$ << 1, and the diffusion coefficient is equal to $D_i = u_i RT$ [20,52]. This means that for solutions with uniform chemical composition, the diffusion coefficient of dissolved species is only dependent on the mobility of those species in the solution and the effect of salt concentration on diffusion coefficient is equivalent to the effect of salt concentration on the mobility. However, this is often not clearly distinguished in the literature from the case where the chemical composition of solution is not uniform (for example, when two solutions with different chemical compositions are separated by a permeable membrane and diffusion occurs on both sides) and the activity term ($dln\gamma_i^c / dlnc_i$) is considerable. Most studies on the effect of salt concentration on diffusion coefficient have been focused on such a case. This lack of clarity is related to the different definitions for diffusion coefficient.

The term "diffusion coefficient" which is frequently just denoted by D, has been very commonly misunderstood in the scientific literature due to different types of diffusion processes that exist. In general, there are two distinctive diffusion processes: (1) self-diffusion, D^* (also called tracer diffusion, single ion diffusion, ionic diffusion), and (2) mutual diffusion, D (or interdiffusion, concentration diffusion, salt diffusion). Self-diffusion is related to the random motion of individual particles in a solution with equal opportunities of taking up any point in the total space occupied by the liquid [53–55]. Mutual diffusion is when a concentration gradient or in a more precise way, a gradient of chemical potential exists in the solution that results in a bulk movement of particles (*e.g.,* ions) [53,55,56]. The activity term ($dln\gamma_i^c / dlnc_i$) becomes significant when mutual diffusion occurs [55]. However, for the self-diffusion coefficient, which is the type of diffusion process investigated in most electrochemical studies as well as this work, only changes in the mobility of species with salt concentration matter. Self-diffusion coefficient is henceforth shortened to diffusion coefficient in this document for simplicity.

The concentration dependence of diffusion coefficient in electrolyte solutions is a very complex subject, especially at higher temperatures and in multicomponent systems where there is much less experimental data [57]. This dependency has been extensively studied for dilute solutions. The first study was done around the year 1900 by Friedrich Kohlrausch who empirically showed that at very low concentrations (< 10^{-3} M [58]) the molar conductivity of strong electrolytes alters linearly with the square root of the molar concentration:

$$\lambda_i = \lambda_i^0 - K\sqrt{c} \tag{3-17}$$

where λ is the ionic equivalent conductance of species i (such as Na^+, Cl^-, or H^+) in S.cm^2/equiv, λ_i^0 is the ionic equivalent conductance in S.cm^2/equiv at infinite dilution or the “limiting ionic equivalent conductance”, K is an empirical constant, c is the molar concentration of solute (for example NaCl). This equation is known as Kohlrausch’s law [59]. Ionic equivalent conductance is related to the ionic mobility by:

$$\lambda_i = |z_i|F^2 u_i \tag{3-18}$$

where, u_i is the mobility of species i in cm^2·mol/J/s and other parameters have their usual definition. Using the Nernst-Einstein relation ($D_i = RTu_i$), the diffusion coefficient can be obtained from ionic equivalent conductance as follows:

$$\mathrm{D}_i = \frac{RT\lambda_i}{|z_i|F^2} \tag{3-19}$$

where D_i is the diffusion coefficient of species i in cm^2/s. For salts, sometimes their diffusion coefficient (*e.g.*, NaCl) is reported instead of that for its constituent ions (Na^+

and Cl^-). In this case, the diffusion coefficient of salt can be calculated as a function of the equivalent conductance of constituent ions, using the Nernst-Hartley equation [21,60].

Decades later, Noble Prize winner in chemistry, Lars Onsager [61,62] theoretically derived Kohlrausch’s law by using Debye-Huckel [35] distribution functions. Onsager expression which is known as “Onsager limiting law” was adapted to the self-diffusion case by Gosting and Herned [63] in 1951. Their proposed equation for 1:1 electrolytes (such as NaCl, KCl, AgI, *etc.*) at 25°C is:

$$D_i = D_i^0 \left[1 - 0.7816 \left(1 - \sqrt{d(\omega_j)}\right) \sqrt{c}\right] \tag{3-20}$$

where D_i and D_i^0 are the diffusion coefficient of species i at concentration c and infinite dilution in cm^2/s, $d(\omega_j)$ is a function of mobility and valance of species i, and c is the molar concentration of salt [63,64]. Mills and Godbole [64] showed that Equation (3-20) is valid up to ~0.005 M of supporting electrolytes. Bernard et al. [65] later extended the Onsager limiting law to more concentrated solutions (up to ~ 1 M) by using the mean spherical approximation (MSA) theory originated by Enskog and Chapman [66].

In dilute solutions, the change in diffusion coefficient with salt concentration is associated with two long-range (coulombic) ionic interactions known as relaxation and electrophoretic effects [67]. Debye-Huckel identified these two effects for the first time [35,68]. The relaxation effect represents the return to equilibrium (local electroneutrality) after a distortion in the ionic atmosphere (fixed background of solution) due to the movement of diffusing species [67–70]. The electrophoretic effect is related to the decrease in the velocity of the diffusing species because of the counterflow of solvent in the ionic atmosphere [63,67–69]. In the case of self-diffusion which is the focus of this study since there is only one diffusing species (trace component) in a system essentially in equilibrium (*i.e.*, uniform concentrations throughout the whole solution) there are no gradients in activity coefficients or solvent flux, which means there is no net motion of ionic species, and thereby, the electrophoretic effect is negligible [69]. As salt concentration increases, the contribution of interparticle short-range interactions becomes significant in diffusion coefficient behavior. Short-range interactions depend on the crystallographic diameter of diffusing species as well as its solvation structure. Wang and Anderko [71] modeled the contribution of short-range interactions in diffusion coefficient by using a hard-sphere model. However, the self-diffusion coefficients in electrolyte solution is mainly influenced by long-range interactions [72].

Experimental results have shown that generally the diffusion coefficient decreases with increasing salt concentration [57,58]. The degree of decrease depends on the nature of salt and the diffusing species itself. For example, the magnitude of decrease for diffusion coefficient of Cl^- ion in three salt solutions varies in the following order: KCl < NaCl < LiCl [58]. There are some exceptions as well, depending on the nature of salt and its constituent ions. For example, the diffusion coefficient of Cl^- ion in aqueous CsCl solution first decreases and then increases with increasing CsCl concentration [58].

Diffusion coefficient measurement is a tedious, time-consuming, and expensive task. It becomes even more complicated with a higher number of species dissolved in the solution [57,73]. It is therefore desirable to find a reliable method for estimating the diffusion coefficient over wide range of conditions. The estimation procedure has two steps: (1) correct the diffusion coefficient for the effect of temperature, (2) correct the diffusion coefficient for the effect of salt concentration. Each step will be explained below.

3.3.1 Correcting Diffusion Coefficient for the Effect of Temperature

The diffusion coefficients of species at 25°C and infinite dilution (D^o) in water are usually found in the literature. Table 3-2 lists these diffusion coefficients for species involved in CO_2/H_2S corrosion process.

Table 3-2

The diffusion coefficients of some species involved in weak acid corrosion at 25°C, 1 bar total pressure and infinite dilution in water.

Species name	Species formula	$D^{o}_{289.15} \times 10^{9}$(m^2/s)	Ref.
Hydrogen ion	H^+	9.312	[21]
Sodium ion	Na^+	1.334	[21]
Ferrous ion	Fe^{2+}	0.720	[21]
Hydroxyl ion	OH^-	5.260	[21]
Chloride ion	Cl^-	2.032	[21]
Carbon monoxide	CO_2	1.920	[74,75]
Carbonic acid	H_2CO_3	1.465[a]	This study
Bicarbonate ion	HCO_3^-	1.105	[21]
Carbonate ion	CO_3^{2-}	0.804	[76]
Hydrogen sulfide	H_2S	1.910	[77,78]
Bisulfide ion	HS^-	1.731	[79]
Sulfide	S^{2-}	0.842[b]	This study, [80]
Acetic acid	CH_3COOH	1.201	[81]
Acetate ion	CH_3COO^-	1.089	[82]
Formic acid	$HCOOH$	1.460	[83]
Formate ion	$HCOO^-$	1.454	[79]
Oxygen	O_2	2.229	[84–86]
Methane	CH_4	1.907	[87,88]

[a] This value was calculated by using the modified Wilke and Change [89] equation proposed by Bidstrup and Geankoplis [90]. Carbonic acid was assumed to be a carboxylic acid with a Le Bas [91] molar volume of 49 cm^3/mol. The Le Bas molar volume was obtained by adding 7.4 cm^3/mol which is the Le Bas molar volume of oxygen in the -OH structure to the Le Bas molar volume of formic acid, 41.6 cm^3/mol [90]. The calculated diffusion coefficient for carbonic acid agrees well with the reported value by Krieg *et al.* [92].

[b] This is a calculated value. The measured diffusion coefficient was at 18°C, which was converted to that at 25°C by using the Stokes-Einstein equation.

The first step in estimation of the diffusion coefficient is the correction for the effect of temperature. There are several models in the literature that take into account the temperature effect on diffusion coefficient [88,89,93,94]. The simplest relation for the temperature dependence of diffusion coefficient is given by Stokes-Einstein equation [95]:

$$D_i = \frac{k_B T}{6\pi \mu_{sol} R_i} \tag{3-21}$$

where, D_i is the diffusion coefficient of species i in the solution in m^2/s, μ_{sol} is the viscosity of solution in Pa.s, k_B is Boltzmann constant (1.380649e-23 J/K), and R_i is the radius of hydrated species in m, and T is in K. Equation (3-21) can be expressed as below to correct the diffusion coefficient at infinite dilution for the effect of temperature:

$$\frac{D^o_{T,i}}{D^o_{298.15,i}} = \frac{T}{298.15} \times \frac{\mu_{298.15,w}}{\mu_{T,w}} \tag{3-22}$$

where, $D^o_{T,i}$ is the diffusion coefficient of species i at temperature T and infinite dilution in water and $\mu_{T,w}$ is the dynamic viscosity of pure water at temperature T. Expression (3-22) has been used in most of the rate prediction models available in the literature for weak acid corrosion [49,50,96,97] in order to account for the effect of temperature on diffusion coefficient of dissolved species. However, this equation does not produce accurate results, as shown in Figure 3-6. Instead, an equation proposed by Smolyakov [98] which relates the limiting conductance to temperature is used in this work:

$$ln\lambda^0_{T,i} = \frac{A + \frac{B}{T}}{\mu_{T,w}} \tag{3-23}$$

$\lambda^0_{T,i}$ is the conductance of species i at temperature T and infinite dilution in water in S.cm^2/mol, $\mu_{T,w}$ is the dynamic viscosity of pure water in Pa.s at temperature T, and A (dimensionless) and B (in K) are adjustable constants which differ for each species. If both sides of Equation (3-23) are multiplied by RT/F^2 (see Equation (3-19)) and then the resulting equation is divided by itself at T = 298.15 K, the following equation will be obtained that can be used to correct the diffusion coefficient for the effect of temperature:

$$\frac{D^o_{T,i}}{D^o_{298.15,i}} = \frac{T}{298.15} \times \frac{\mu_{298.15,w}}{\mu_{T,w}} \exp\left(\frac{B}{T} - \frac{B}{298.15}\right) \tag{3-24}$$

Equation (3-24) has an extra exponential term compared to Equation (3-22). The exponential term dampens (positive B constant) or accelerates (negative B constant) the temperature dependence of the diffusion coefficient. If B is zero, Equations (3-24) and (3-22) will be the same. The B values for some species are listed in Table 3-3. The B values for more species can be found in [70,98]. For carboxylic acids (*e.g.*, acetic acid) and their dissociated ions (*e.g.*, acetate), it has been reported that the diffusion coefficient has a linear relationship with temperature [89,90,93]. This means that B should be equal to zero for these species as reported in Table 3-3.

Figure 3-6 shows that the diffusion coefficients obtained by the Smolyakov equation match very well with the experimental data found in the literature.

Figure 3-6

Comparison of two models with experimental data for the diffusion coefficient of (A) H^+ ion, (B) $CO_{2(aq)}$, (C) $H_2S_{(aq)}$, (D) Na^+ ion, and (E) OH^- ion at infinite dilution in water. Data are taken from [75,78,77,98–103].

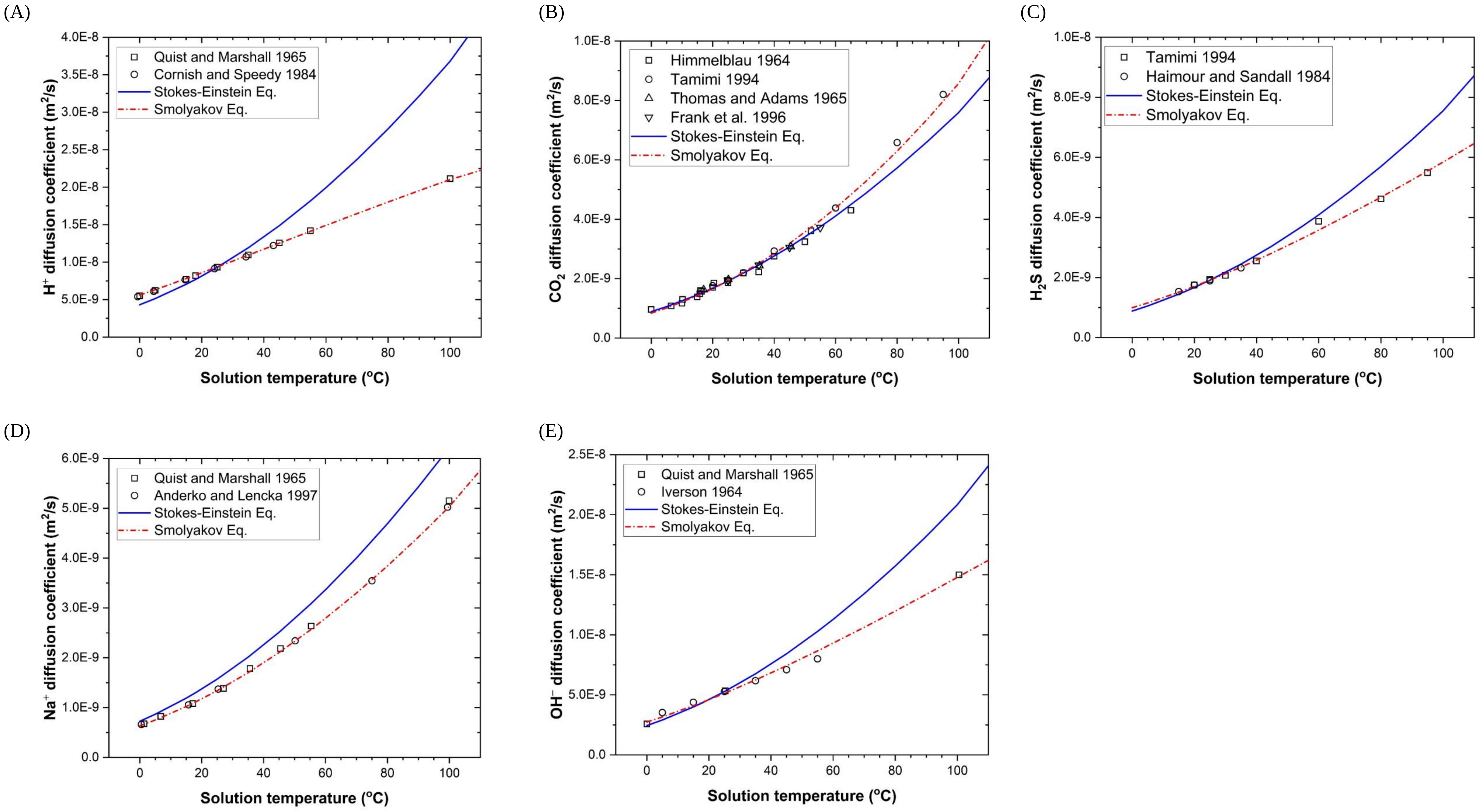

Table 3-3

Values of B used in Equation (3-24) for calculating the temperature dependence of diffusion coefficient for some important species for corrosion studies in the oil and gas industry. For species not listed in this table, B can be considered zero.

Species name	Species formula	B^a	Ref.	Experimental data source
Hydrogen ion	H^+	837.790	[98]	N/A
Sodium ion	Na^+	75.492	[98]	N/A
Hydroxide ion	OH^-	468.130	[98]	N/A
Chloride ion	Cl^-	216.030	[98]	N/A
Carbon dioxide	CO_2	-180.000	This study	[75,78,101,102]
Carbonic acid	H_2CO_3	0	This study	N/A
Bicarbonate ion	HCO_3^-	0	This study	N/A
Carbonate ion	CO_3^{2-}	0	This study	N/A
Hydrogen sulfide	H_2S	379.550	This study	[77,78]
Bisulfide	HS^-	0	This study	N/A
Sulfide	S^{2-}	0	This study	N/A
Acetic acid	CHCOOH	0	This study	N/A
Acetate ion	$CHCOO^-$	0	This study	N/A
Formic acid	HCOOH	0	This study	N/A
Formate ion	$HCOO^-$	0	This study	N/A
Oxygen	O_2	-378.720	This study	[74,75,84–86,104,105]
Methane	CH_4	387.620	This study	[87,88,106]

^{a} It has the unit of temperature, Kelvin.

3.3.2 Correcting Diffusion Coefficient for the Effect of Salt Concentration

Several equations and models have been proposed for correcting the diffusion coefficients in concentrated aqueous salt solutions. Similar to Equation (3-22) for the effect of temperature, the simplest method offered to account for the effect of salt concentration on diffusion coefficient is using the Stokes-Einstein relation [21]:

$$\frac{D_{T,i}}{D^{o}_{298.15,i}} = \frac{T}{298.15} \times \frac{\mu_{298.15,w}}{\mu_{T,sol}} \tag{3-25}$$

$D_{T,i}$ is the diffusion coefficient of species i in a solution with a finite salt concentration, and $\mu_{T,sol}$ is the dynamic viscosity of the solution at temperature T. Due to its simplicity, Equation (3-25) has been used repeatedly in corrosion modeling studies [107–109]. However, as will be shown below, Equation (3-25) estimates the variation in diffusion coefficient with salt concentration quite erroneously. Based on Equation (3-25), when salt concentration is varied in a solution, the only parameter that influences the diffusion coefficient is the solution viscosity.

Another approach frequently used in the literature [110–114] are correlations with a square root dependency of the diffusion coefficient with salt concentration, similar to the Kohlrausch law Equation (3-17). The simplest form of this correlations for univalent salt (*e.g.*, NaCl, KCl, *etc.*) solutions is as follows:

$$\frac{D_{T,i}}{D^{o}_{T,i}} = 1 - k\sqrt{c} \tag{3-26}$$

where, $D_{T,i}$ is the diffusion coefficient of species i at temperature T in the concentrated aqueous salt solution, $D^{o}_{T,i}$ is the diffusion coefficient of species i at temperature T and infinite dilution in water (obtained from Equation (3-24)), c is concentration of salt in the solution (concentration of supporting electrolyte) usually in molarity (M), and k is a constant that depends on the nature of dissolved salt and the diffusing species. Equation (3-26) is known as the *square root* equation. The unit for k is the reciprocal of square root of the concentration unit. Sometimes, for salts with ions higher than univalent or when there is more than one salt dissolved in the solution, concentration is replaced by ionic strength (I):

$$\frac{D_{T,i}}{D_{T,i}^{o}} = 1 - k\sqrt{I} \tag{3-27}$$

I can be calculated by using the following equation:

$$I = \frac{1}{2}\sum_{j} c_j z_j^2 \tag{3-28}$$

where, c_j is the concentration of species j in the solution and z_j is the charge number of species j. The summation is applied to all charged species in the solution. It should be noted that Equation (3-28) is not applicable for dissolved neutral species in the solution such as CH_4, particularly when their concentrations are high and can influence the diffusion process of trace electroactive species.

Stackelberg and Pilgram [110] reported a k value of 0.21 for diffusion coefficient of H^+ ion in KCl aqueous solution. Ciskowska *et al.* [114] assumed a k value of 0.256 for diffusion coefficient of H^+ ion in $LiClO_4$ salt. Equation (3-26) has been found with some modifications as well [115]. For example, Equation (3-20) mentioned earlier or a dependence to the cube root of salt concentration by Stastny and Strafelda [111] for aqueous KCl solutions, $D_{T,i}^{o}(1 - k(c_{KCl}/c_{H^+})^{\frac{1}{3}})$. Stokes *et al.* [112] emphasized that modification of Equation (3-26) would definitely enhance its accuracy and suggested using $\frac{1}{1+\kappa a}$ or $\frac{1}{\left[(1+\kappa a)\left(1+\frac{\kappa a}{\sqrt{2}}\right)\right]}$ instead of constant k. κ is Debye length in 1/m and a is Debye-Huckel ion-size parameter in m. However, they did not implement these substitutions in their work.

At higher salt concentration it is believed that the change in viscosity of the solution becomes an important factor in the estimation of the diffusion coefficient. Given that diffusion and viscous flow processes are analogous, variation in some fundamental properties of solution such as net intermolecular friction forces at higher salt concentrations affects both processes [52,69,113]. Therefore, this idea of multiplying the right-hand side of Equation (3-26) by a viscosity term of μ_T^o/μ_T has been introduced to improve the accuracy of diffusion coefficient estimation for the effect of salt concentration [73,112–114]. This improvement practically means combining Equations (3-25) and (3-26). However, it has been reported that the addition of the viscosity term to Equation (3-26) tends to overcorrect the diffusion coefficient [69,112]. Pinto and Graham [69] claimed that the viscosity term with an exponent of 0.7 instead of 1 usually gives more accurate results. Accordingly, the modified Equation (3-26) will be as follows:

$$\frac{D_{T,i}}{D_{T,i}^o} = (1 - k\sqrt{c})\left(\frac{\mu_T^o}{\mu_T}\right)^{0.7} \tag{3-29}$$

The implementation of Equation (3-29) does not explicitly exist in the literature. This brings the need to investigate whether addition of the viscosity term really improves the diffusion coefficient estimation or Equation (3-26) works just fine by itself. An investigation is done by back-calculating the k values from the experimental diffusion coefficient data, using both Equations (3-26) and (3-29). For each species, a single k

value should result in accurate estimations of the species diffusion coefficient for the whole concentration range. Thus, the equation that induces k values with less deviation is assumed to be more suitable for concentration dependency correction of diffusion coefficient. The "coefficient of deviation"[6] is used as an indication of the degree of deviation in k. Figure 3-7 (A) shows the comparison of two equations. The deviation of k for Equation (3-26) is generally smaller than that for Equation (3-29), implying that there is no need for the addition of the viscosity term and Equation (3-26) is sufficient for concentration dependency of diffusion coefficient. A similar comparison shown in Figure 3-7 (B) between the molality (m) and the molarity (M) concentration units. The coefficient of deviation obtained by for the molality unit is slightly smaller than that for the molarity unit for all three ions. However, the difference is not significant, and therefore, either of the concentration units can be used in Equation (3-26) for correcting the diffusion coefficient of a species with respect to salt concentration, providing that a k value with a matching unit exist for that species. Typically, molality is favored over molarity because, first, it does not depend on the volume (density) of solution, which makes it easier to work with, and second, it is the most used concentration unit in the solution chemistry models available in the literature. Therefore, Equation (3-26) with the molality concentration unit is the suggested form of the square root equation for correcting the diffusion coefficient for the effect of salt concentration. For example, A k value of 0.271 $(\text{mol/l})^{-0.5}$ or 0.263 $(\text{mol/kgH}_2\text{O})^{-0.5}$ is obtained for H^+ diffusion coefficient

---

[6] The coefficient of variation (CV) is defined as the ratio of the standard deviation to the mean. It is often expressed as a percentage.

in NaCl solution, which is close to the values reported earlier. The k value for some other species important in CO_2/H_2S corrosion in aqueous NaCl solutions are listed in Table 3-4.

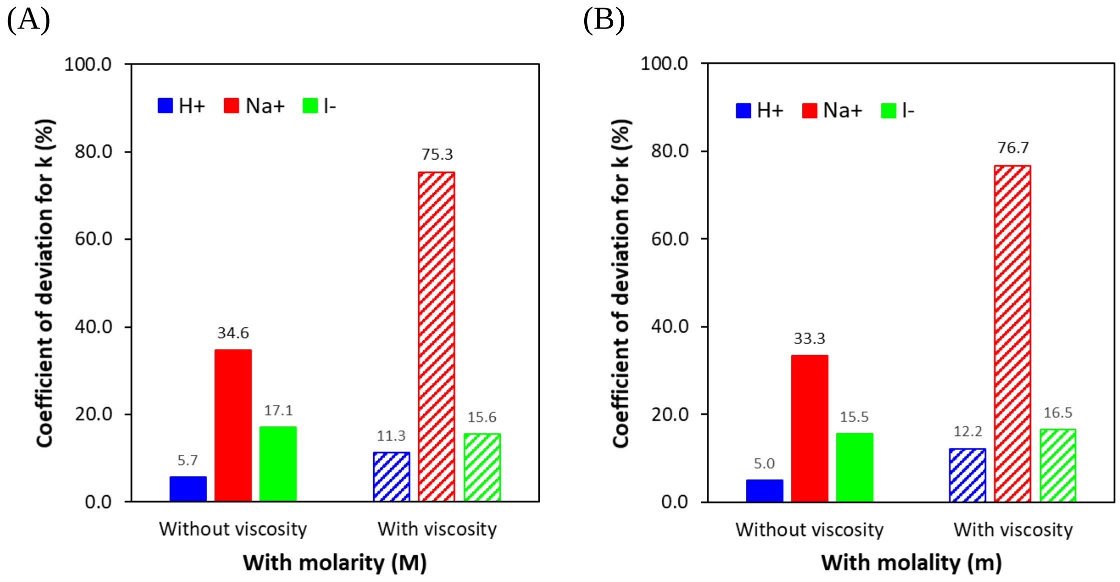

Figure 3-7

Comparison of the accuracy of square root Equations (3-26) and (3-29), without and with the viscosity term, respectively, for the concentration dependency of diffusion coefficients: (A) with molarity unit (M), (B) with molality concentration unit (m). Experimental diffusion coefficient data for H^+ *ion (19 measurements),* Na^+ *ion (5 measurements), and* I^- *ion (12 measurements) at* 25^oC *and atmospheric pressure are taken from* [57,69,112,113].

Table 3-4

The k value used in the square root Equation (3-26*) for correcting the diffusion coefficient of aqueous species for the effect of NaCl concentration.*

Species name	Species formula	k (mol/lit)$^{-0.5}$	k (mol/kgH_2O)$^{-0.5}$	Ref.	Experimental data source
Hydrogen ion	H^+	0.271	0.263	This study	[57,69,113]
Sodium ion	Na^+	0.150	0.152	This study	[57,81]
Iodide ion	I^-	0.154	0.157	This study	[112]
Carbon dioxide	CO_2	0.151	0.144	This study*	[75,116]
Carbonic acid*	H_2CO_3	0.151	0.144	This study	N/A
Hydrogen sulfide	H_2S	0.131	0.129	This study	[117]

*Assume to be the same as CO_2.

Another model for the concentration dependency of diffusion coefficient is proposed by Appelo [118]. The Appelo model seems to be originated from Stokes *et al.* [112]'s suggestion and it is an extension of a simpler model presented by Snyder *et al.* [119]. Similar to Equation (3-26), the concentration dependency equation has the square root of ionic strength (concentration for 1:1 salt); however, it is placed inside and exponential function to dampen the changes in diffusion coefficient with varying salt concentration. There are some concerns with the Appelo model. First, the units for Debye length (κ in m^{-1}), ion-size parameter (a in m), and Debye-Huckel parameter are reported incorrectly, A ($= \frac{3A_\phi}{\ln(10)}$ in (kg/mol)$^{0.5}$). Next, the unit for ionic strength is not mentioned clearly whether it is molality or molarity. Third, the range of validity of the Appelo model for salt concentration is not specified; howbeit, from the Appelo paper [118] graphs it seems to be 2 molal, which is moderately low. Forth, the species covered by Appelo model are limited, which makes it impractical for the case of CO_2 and H_2S corrosion. Finally, the Appelo model does not work for neutral species such as H_2CO_3 and H_2S, which contribute to the mass transfer processes involved in CO_2 and H_2S corrosion. Despite these issues, the Appelo model is reproduced and is compared with other models for its accuracy as shown in Figure 3-8.

A more complex model for the estimation of diffusion coefficient in concentrated solutions is proposed by Pinto and Graham [69]. This model uses an analogy between Stefan-Maxwell flux equation and Fick's law of diffusion and therefore connects the diffusion coefficient to the Stefan-Maxwell phenomenological coefficients. The Pinto and Graham model [69] only considers the relaxation effect and assumes that electrophoretic effect is negligible, which is a good assumption, as explained earlier. Another assumption in the original Pinto and Graham model [69] is that all ions are considered completely unhydrated. Later, they included the hydration number in the diffusion coefficient calculations [73]. This makes the model truly complicated. Additionally, the equations and parameters required to reproduce the model are not clearly described in their latest publication [73]. Thus, it is concluded that the updated Pinto and Graham model [73] is impossible to replicate. Another issue with the Pinto and Graham model is that it is not applicable to neutral species such as H_2CO_3 and H_2S which are important in CO_2 and H_2S corrosion. They only provided a phenomenological coefficient for H^+ ion. Despite this, the original model is reproduced and compared with other models presented in Figure 3-8. Instead of 0.43 and 3.16 reported in the original Pinto and Graham model for the ternary constant of H^+ and Na^+ ions, respectively, 0.62 and 17 were found to be appropriate in the reproduced model.

The most comprehensive model and supposedly the most accurate model available in the literature for accounting for the effect of salt concentration on diffusion coefficient was proposed by Wang and Anderko [71]. They included the effects of both long-range electrostatic forces (relaxation effect) and short-range forces (due to interparticle interactions) in their model. They claimed that without considering the short-range interactions, the model for univalent ions is only valid up to ~1 M of salt concentration. However, with the short-range interactions included the validity range expands to ~ 30 M [70]. Another advantage of the Wang and Anderko model is covering the effect of salt concentration on diffusion coefficients of both ionic and neutral species

[71]. However, this model is much more complicated than the previous models. Additionally, not all the equations and parameters required to replicate the model are clearly provided in the corresponding publications [70,71]. Therefore, the Wang and Anderko model is difficult to reproduce. For comparison, the accuracy of the Wang and Anderko model with other models, the diffusion coefficient is obtained from OLI software in which the Wang and Anderko model is incorporated. Figure 3-8 (A) shows the comparison between the models discussed above for H^+ ion in an aqueous NaCl solution. The experimental data obtained by Roberts and Northey [120] are not comparable with other data, and thereby, are ignored in this study. The Stokes-Einstein Equation has the least accuracy among the models. The accuracy of estimations for the Appelo [118] and the Wang and Anderko [71] (OLI software in Figure 3-8) models are similar, a fairly good accuracy at low NaCl concentrations, but the predictions deviate from experimental data at moderate and high NaCl concentrations. Equation (3-26) (square root Eq. in Figure 3-8) and the Pinto and Graham [69] models shows almost the same accuracy for the estimation of H^+ ion diffusion coefficient, a very good agreement with the experimental data. For the diffusion coefficient of Na^+ ion shown in Figure 3-8 (B), the Appelo model [118] predictions are totally off. The Stokes-Einstein Eq. exaggerates the effect of salt concentration of Na^+ ion diffusion coefficient and this exaggeration increases with increasing NaCl concentration. The Wang and Anderko [71] model (OLI software) behaves similarly to the Stokes-Einstein Eq., except that the degree of exaggeration decreases at higher NaCl concentrations. Equation (3-26) slightly underpredicts Na^+ ion diffusion coefficient for NaCl concentrations below 15 wt.% and

overpredicts for higher NaCl concentrations. Finally, the Pinto and Graham model shows prefect predictions for the entire range of NaCl concentrations.

Taking into consideration the simplicity of the square root equation (Equation (3-26)) and its applicability for neutral species, it will be used in this study for correcting the diffusion coefficient for the effect of salt concentration.

Figure 3-8

Comparison of models for the concentration dependency of diffusion coefficient with experimental data measured in aqueous NaCl solution at 25°C and atmospheric pressure: (A) H^+ ion, (B) Na^+ ion. The points are experimental data and the solid lines are model predictions. The "square root Eq." represents Equation (3-29) *and the "OLI software" represents the Wang and Anderko model* [71]. *Experimental data are taken from* [54,57,69,113].

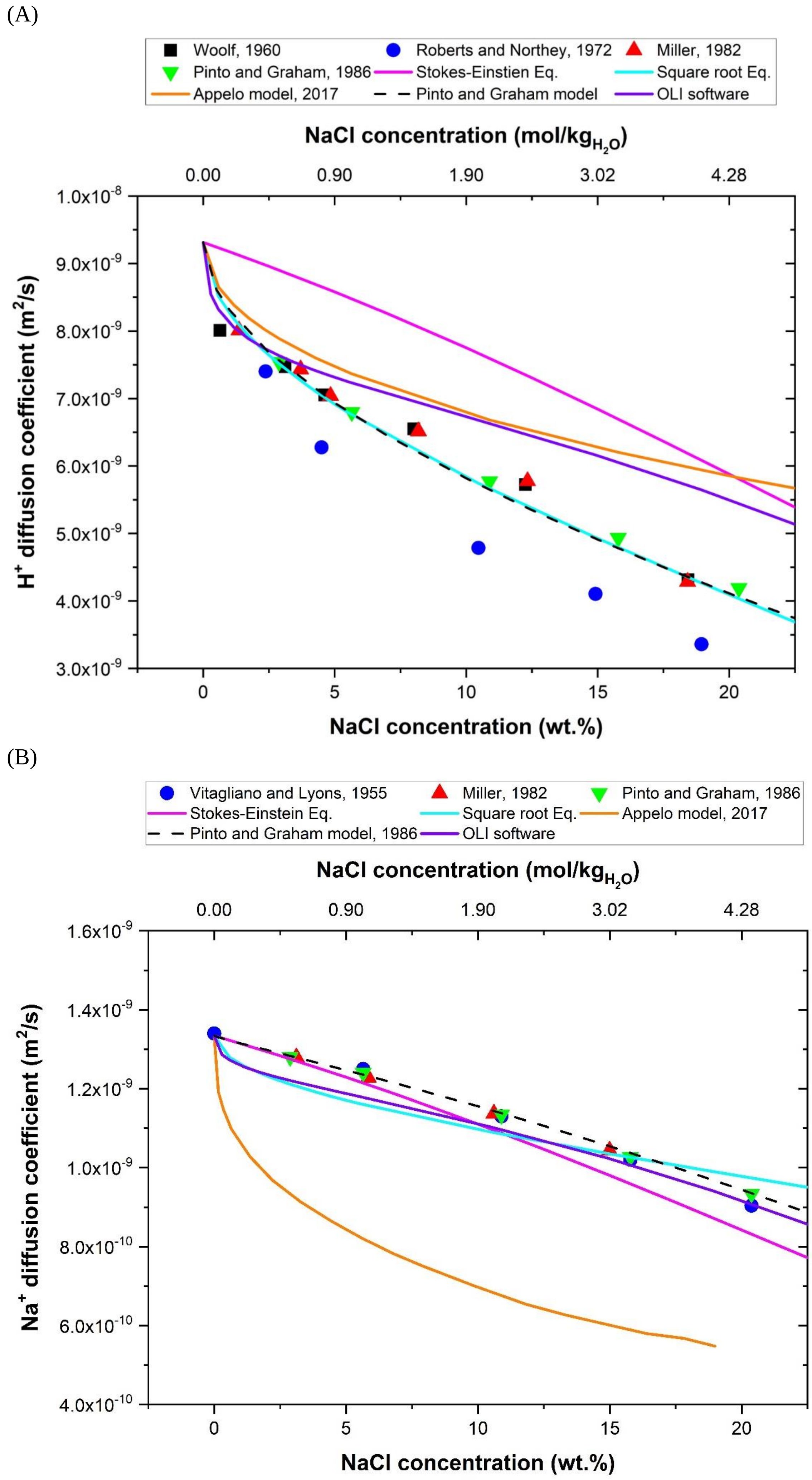

The effect of pressure on diffusion coefficient of dissolved species is negligible [121]. This is probably because the volume of aqueous solutions is almost independent of pressure[7].

---

[7] For pressures above the saturation pressure of the solution.

Chapter 4: The Effect of Salt Concentration on Solution Chemistry

A solution is defined as a condensed homogenous mixture (liquid or solid) containing two or more substances. The main substance of the solution is called solvent and the other constituent substances dissolved in the solvent are solutes. Solutions are classified into ideal solutions and non-ideal solutions [122]. An ideal solution is a solution in which the forces (interactions) among the molecules are the same for all the molecules, independent of species. However, no real solution is truly ideal, although many real solutions are nearly ideal when they contain only molecules that are structurally similar, such as H_2O and D_2O mixture [123]. Therefore, an ideal solution is a hypothetical solution. When a salt (soluble electrolyte) is dissolved in water (solvent), it dissociates into ions and forms an electrolyte solution[8]. It is assumed that salts are strong electrolyte and will dissociate completely in water [125]. The presence of charged ions in the electrolyte solution causes interactions between these ions as well as with water molecules. These interactions can be categorized as follows [124]:

- Solute-solute interaction
    - Long-range coulombic interactions: act over long distances between ions. They are electrostatic interactions and follow Coulomb law.
    - Ion-induced dipole interactions: weak attractions that result when the approach of an ion induces a dipole in a nonpolar molecule.
    - Short-range interactions: act over short distances.
        - Short-range attractions: they can be coulombic or non-coulombic.

---

[8] Electrolyte solutions are solutions with electrical conductivity [124].

        - Short-range repulsions: They become significant when two particles approach very close to each other.
    - Hard spheres: when the ions come into contact and the short-range repulsive interactions become infinite.
- Solute-solvent interactions: they are attractive when the ion and the end of the dipole or induced dipole have opposite charge. They are repulsive when the ion is in close distance to the end of dipole which has the same charge as the ion.
    - Ion-dipole interactions
    - Ion-induced dipole interactions

A theoretical description of interactions between ions and dipoles with each other and with solvent molecules is given by Bockris and Reddy [20]. As a result of these interactions there is shift of electrolyte solution from an ideal condition to a non-ideal condition, changes in chemical potential of all species, and therefore, changes in phase and speciation equilibria. Experimental evidence for departure from ideality in electrolyte solutions is listed by Wright [124].

For the hypothetical ideal condition (noninteracting particles), the chemical potential of an arbitrary dissolved species i (μ_i) can be expressed in the form:

$$\mu_i(ideal) = \mu_i^o + RTlnx_i \tag{4-1}$$

For the real condition (non-ideal condition with interacting particles), the chemical potential is given by:

$$\mu_i(real) = \mu_i^o + RTlnx_i + RTln\gamma_i^x \tag{4-2}$$

where μ_i^o is the chemical potential of species i at standard condition, x_i is the mole fraction of species i in the solution, and γ_i^x is the activity coefficient of species i in mole fraction basis. The difference between Equations (4-1) and (4-2), i.e., $RTln\gamma_i^x$ arises from interactions between dissolved species in the solution or non-ideality. Therefore, the non-ideality in an electrolyte solution can be analyzed by considering the physical significance of the activity coefficient term in Equation (4-2) [20,124].

For the case of aqueous CO_2 and H_2S corrosion of carbon steels, changes in phase equilibria are associated to gas solubility ($CO_{2(g)}$[9] and $H_2S_{(g)}$) [30,126,127] and water evaporation [128] equilibria and changes in speciation equilibria correspond to $H_2CO_{3(aq)}$, $H_2S_{(aq)}$, and $H_2O_{(l)}$ dissociation equilibria. Hence, when the effect of salt concentration on CO_2 and H_2S corrosion is being studied, changes in gas solubility and speciation equilibria have to be taken into consideration.

4.1 The Effect of Salt Concentration on Solubility of Gas

When a soluble electrolyte (*e.g.*, NaCl) is dissolved in a solvent (*e.g.*, water) the solubility of the non-electrolyte (*e.g.*, CO_2 and H_2S) molecularly distributed in the solvent decreases. This phenomenon is called “salting-out effect” [129]. If the solubility of non-electrolyte increases the term “salting-in” is used [130]. Salting-out and salting-in are generally used to denote, respectively, an increase and a decrease in dissolved gas concentration due to a change in the activity coefficient of the nonelectrolyte with increasing concentration of electrolyte [131]. The magnitude of salting-out or salting-in or in other words−the magnitude of the salt effect on the activity coefficient of a nonelectrolyte in aqueous solutions depends strongly on properties of both the nonelectrolyte and the salt [131]. Although several qualitative and quantitative theories

---

[9] The subscript (g) denotes gaseous phase.

have been proposed so far to explain the salting out effect, the exact mechanism is still unknown [129,131,132]. The salting-out effect is mainly due to changes in different interactions between electrolyte, non-electrolyte, and solvent. Put in a simple way, the salting-out effect can be explained through a combination of electrostatic repulsion and enhancement of the hydrophobic effect [130].

Measurement of solubility of a gas in a solution is a challenging and time-consuming task. This has been motivating scientists to develop solubility models for various gases such as O_2, N_2, CO_2, CH_4, H_2S, NH_3, *etc.*, valid for a variety of conditions and applications. CO_2 and H_2S solubility models are mainly developed for applications in geologic sequestration processes, enhanced oil recovery and enhanced geothermal systems [127,133,134]. These models cover a wide range of temperature, pressure, and salt concentration, which make them coincidentally suitable for studying the effect of salt concentration on CO_2/H_2S corrosion process. In Chapter 7, a few CO_2 and H_2S solubility models in aqueous NaCl solutions and the effect of NaCl concentration on CO_2 and H_2S solubility will be discussed and compared.

4.2 The Effect of Salt Concentration on Speciation Equilibria

As mentioned above, adding salt to the solution changes the interaction between dissolved species, and thereby, varies the chemical potentials of these species. For an arbitrary reaction shown below:

$$aA + bB \rightleftharpoons cC + dD \qquad (4\text{-}3)$$

the Gibbs free energy change of reaction ($\Delta_r G$) can be expressed in terms of chemical potentials of reactants and products:

$$\Delta_r G = c\mu_C + d\mu_D - a\mu_A - b\mu_B \tag{4-4}$$

Expanding the chemical potentials using Equation (4-2), gives the following:

$$\begin{aligned}\Delta_r G = c\mu_C^o + RTln(x_C\gamma_C^x)^c + d\mu_D^o + RTln(x_D\gamma_D^x)^d - a\mu_A^o \\ - RTln(x_A\gamma_A^x)^a - b\mu_B^o - RTln(x_B\gamma_B^x)^b\end{aligned} \tag{4-5}$$

At equilibrium, $\Delta_r G = 0$. Upon rearrangement, the above equation becomes:

$$c\mu_C^o + d\mu_D^0 - a\mu_A^o - b\mu_B^o = -RTln\frac{(x_C\gamma_C^x)^c(x_D\gamma_D^x)^d}{(x_A\gamma_A^x)^a(x_B\gamma_B^x)^b} \tag{4-6}$$

Recalling equation $\Delta_r G^o = -RTlnK$, the left-hand side of (4-6) corresponds to the standard Gibbs free energy change of reaction ($\Delta_r G^o$) and the term inside the natural logarithm on the right-hand side of Equation (4-6) is equal to the reaction equilibrium constant (K). Thus, the following expression can be extracted:

$$K(T,P) = \left(\frac{x_C^c x_D^d}{x_A^a x_B^b}\right)\left(\frac{\gamma_C^{x\,c}\gamma_D^{x\,d}}{\gamma_A^{x\,a}\gamma_B^{x\,b}}\right) \tag{4-7}$$

K is only a function of temperature and pressure. In ideal solutions, the activity coefficient quotient is equal to one and K will be equal to the mole fraction quotient. At a constant temperature and pressure, for K to remain constant when activity coefficients deviate from unity (ideal condition) due to addition of salt to the solution, the concentrations must change as well. Therefore, addition of salt concentration to the solution changes equilibrium concentrations, *i.e.*, disrupts the equilibrium, due to variations in the activity coefficients of participating species. This holds for speciation reactions occur in aqueous CO_2/H_2S corrosion processes such as $H_2CO_{3(aq)}$, $H_2S_{(aq)}$, and $H_2O_{(l)}$ dissociation reactions. Therefore, in order to understand the effect of salt concentration on speciation equilibria variations in the activity coefficients of species participating in the (electro)chemical reactions, and consequently changes in the equilibrium concentrations of these species need to be investigated.

The first significant theory for calculating activity coefficient was proposed by Debye-Huckel [35] in 1920s. The Debye-Huckel theory discusses equilibrium properties of electrolyte solutions and allows the calculation of an activity coefficient for individual ions, or equivalently, the mean activity coefficient of salts. Fundamental concepts of the Debye-Huckel theory also form the basis of modern theories describing the non-equilibrium properties of electrolyte solutions such as diffusion and conductance. The Debye-Huckel theory is thus considered central to all theoretical approaches to electrolyte solutions [124]. According to the Debye-Huckel theory, the non-ideality in a solution is due to electrostatic interactions between the ions. Only electrostatic interactions obeying the Coulomb inverse square law are considered in the Debye-Huckel theory [124]. A thorough explanation of the derivation procedure is given by Bockris and Reddy [20] and a complete list of assumptions made in the Debye-Huckel theory is provided by Wright [124]. The Debye-Huckel equation for calculating activity coefficient is given below:

$$log\gamma_i^x = -A_\gamma^x z_i^2 \sqrt{I_x} \tag{4-8}$$

where, A_γ^x is a constant called Debye-Huckel limiting slope (dimensionless), z_i is charge of species i, and I_x is ionic concentration in mole fraction-based ionic strength (dimensionless) [135]. Equation (4-8) can be expressed based on molality [136,137] or molarity [20] units. The Debye-Huckel theory is limited to very low concentrations, up to ~ 0.01 M for 1:1 electrolytes in aqueous solutions, and because of this, Equation (4-8) is named “Debye-Huckel limiting law” [20]. To increase the range of applicability of the Debye-Huckel equation extensions to this equation have been proposed that are listed in Table 4-1. These formulas are expressed as a function of the ionic strength rather than any individual ionic concentrations. The interactions between species (ions and neutrals) are not considered in these formulas and the only thermodynamic property of species included is charge of species. In 1948, Robinson and Stokes [138] suggested that the concept of ion-solvent interaction or ionic hydration could explain the limitation of the Debye-Huckel equation at high electrolyte concentrations. They proposed the following equation to modify the Debye-Huckel equation:

$$log\gamma_i^{m'} = log\gamma_i^m - \frac{h_i}{\nu_i} lna_w - \ln(1 - 0.018(h_i - \nu_i)m) \tag{4-9}$$

where, γ_i^m is the activity coefficient obtained from the Debye-Huckel equation in Table 4-1, h_i is hydration number of ion i, ν_i is the stoichiometric number of ion in the salt, a_w is the activity of water, and m is the molality concentration of the solution. Equation (4-9) is valid for temperatures up to 50^{o}C and ionic strengths of 4 m [138].

In 1973, Pitzer [139] proposed a semiempirical model that accounts for the binary and ternary short range interactions in calculating the activity coefficients of ionic species in aqueous electrolytes. At very low ionic strengths (*i.e.*, salt concentrations), the Pitzer model will approach to a modified form of the Debye-Huckel equation [140,141]. Later in 1984, Harvie *et al.* [142] added the activity coefficient terms and equation for neutral species. In 1986, Felmy and Weare [143] added the triple ion interaction terms to the Harvie *et al.* [142] equations. Since then, there have been several extensions to the Pitzer interaction model [144,145]; however, the original form of Pitzer equations and the important contributing terms have remained unchanged. Instead, efforts have been put into improving the Pitzer interaction parameters to enhance the accuracy of estimations as well as to cover more species [146–150]. Other models have been proposed for the calculation of activity coefficient such as the specific ion interaction theory (SIT) [151–153], the ion association model [140,154,155], the three-characteristic-parameter correlation (TCPC) model [156,157], the UNIQUAC (universal quasichemical) model [158,159], the mixed-solvent electrolyte (MSE) model [135]. Among these activity coefficient models, the Pitzer interaction model is the most popular model. On the other hand, the MSE model is the most comprehensive model as it can cover conditions with more than one solvent in addition to accounting for the nonideality in the vapor phase. Therefore, in this study, a modified Pitzer interaction model and an updated version of the MSE model will be employed separately into two different speciation equilibrium models to investigate the effect of salt concentration on speciation equilibrium in CO_2 and H_2S corrosion processes.

Table 4-1

The Debye-Huckel equation and its extensions for calculating the activity coefficient.

Equation name	Equation	Applicability range	Ref.
Debye-Huckel limiting law	$log\gamma_i^m = -A_{\gamma,10}^m z_i^2\sqrt{I_m}$	< 0.01 M, only ions	[20]
Debye-Huckel	$log\gamma_i^m = -A_{\gamma,10}^m z_i^2\frac{\sqrt{I_m}}{1+B_\gamma^m å\sqrt{I_m}}$	< 0.01 M, only ions	[20,138]
Extended Debye-Huckel	$log\gamma_i^m = A_{\gamma,10}^m z_i^2\frac{\sqrt{I_m}}{1+B_\gamma^m å\sqrt{I_m}} + b_\gamma^m I_m$	0.006-6.0 m, 25°C-100°C, only ions	[138,160]
Davies	$log\gamma_i^m = -A_{\gamma,10}^m z_i^2\frac{\sqrt{I_m}}{1+\sqrt{I_m}} + 0.3I_m$	0.5 M, temperature close to 25°C, only ions	[161]
Modified Davies	$log\gamma_i^m = -A_{\gamma,10}^m z_i^2\frac{\sqrt{I_M}}{1+\sqrt{I_M}} + 0.2I_m$	0.5 M, temperatures close to 25°C, only ions	[162]
B-dot	$log\gamma_i^m = -A_{\gamma,10}^m z_i^2\frac{\sqrt{I_m}}{1+B_\gamma^m å\sqrt{I_m}} + \dot{B}I_m$	0-3 m, up to 300°C, ions and neutral species	[163]
Bromley	$log\gamma_i^m = -A_{\gamma,10}^m z_i^2\frac{\sqrt{I_m}}{1+B_\gamma^m å\sqrt{I_m}} + \frac{z_i^2\left(0.06+0.6b_\gamma^m\right)I_m}{\left(1+\frac{1.5}{z_i^2}I_m\right)^2} + b_\gamma^m I_m$	Up to 6 m, up to 100°C, only ions	[164]
Pitzer-Debye-Huckel	$log\gamma_i^x = -A_x\left(\frac{2z_i^2}{\rho}\ln\left(1+\rho I_x^{\frac{1}{2}}\right) + \frac{I_x^{\frac{1}{2}}(z_i^2-2I_x)}{1+\rho I_x^{\frac{1}{2}}}\right)$	Pure water to fused salt, up to 120°C, only ions	[141]

γ_i^m is molality-based activity coefficient, A_γ^m is molality based Debye-Huckel limiting slope in $(kgH_2O)^{0.5}/mol^{0.5}$, $A_{\gamma,10}^m = \frac{A_\gamma^m}{ln10}$, z_i is the charge of species i, I_m is the molality based ionic strength of solution, å is ion size parameter in cm, B_γ^m is a constant related to the radius of ionic cloud in kg /mol$^{0.5}$/cm [20,165]. If B_γ^må is considered to be equal to 1, then the Extended Debye-Huckel equation is reduced to Guggenheim equation [166]. $\dot{B}$ is called the “deviation function” in kgH_2O/mol and describes the deviation of activity coefficient from Debye-Huckel equation [163]. I_x is the mole-fraction based ionic strength of solution and ρ is called the closest approach parameter [141].

A_γ^m and B_γ^m has a value of 1.17 and 0.3281 at 25°C in water, respectively. The equation for B_γ^m is given in Helgeson and Kirkham [165]. If B_γ^må in the “Extended Debye-Huckel” equation is set equal to 1, the Guntelberg equation is obtained [167]. If 1.5 is used, the Scatchard equation will be obtained [168]. To calculate the mean activity coefficient of salts $|z_+z_-|$ needs to be used in above equations instead of z_i^2 (z_+ and z_- are the charge of cation an anion of the salt, respectively).

Two groups of models exist for calculating equilibrium concentrations in concentrated solutions. In the first group, the equilibrium constants are a function of salt concentration (to be more accurate−ionic strength) in addition to temperature and pressure. For the arbitrary Reaction (4-3), this type of models relates the equilibrium constant to the equilibrium concentrations as follows:

$$K^*(T,P,I_x) = \left(\frac{x_C^c x_D^d}{x_A^a x_B^b}\right) \tag{4-10}$$

K^* is called "stoichiometric equilibrium constant" [169]. The Equation (4-10) can be expressed in molality- and molarity-based forms as well. The equilibrium concentrations can be calculated by solving a system of equations for all participating reactions in addition to an equation for charge neutrality (if electrochemical reactions are involved). The equilibrium activity coefficients are calculated subsequently, if needed, by using the equilibrium concentrations.

The second group of models uses equations identical to Equation (4-7). This equation is repeated here for the reader's convenience:

$$K(T,P) = \frac{{a_C^x}^c {a_D^x}^d}{{a_A^x}^a {a_B^x}^b} = \frac{\left(x_C^c {\gamma_C^x}^c\right)\left(x_D^d {\gamma_D^x}^d\right)}{\left(x_A^a {\gamma_A^x}^a\right)\left(x_B^b {\gamma_B^x}^b\right)} = \left(\frac{x_C^c x_D^d}{x_A^a x_B^b}\right)\left(\frac{{\gamma_C^x}^c {\gamma_D^x}^d}{{\gamma_A^x}^a {\gamma_B^x}^b}\right) \tag{4-11}$$

where, a_i^x is the activity[10] of species i in mole fraction basis, which is equal to $x_i \gamma_i^x$. The molality form of Equation (4-7) is also frequently used in the literature. K is called

---

[10] Activity is literally an "effective concentration" defined for the first time by Lewis to be able to treat nonideal solutions with the same chemical potential equation as that for ideal solutions, i.e., $\mu_i - \mu_i^o = RTlnx_i$ for ideal solution and $\mu_i - \mu_i^o = RTlna_i$ for non-ideal solutions. More about the origin of activity and it definition can be found elsewhere [20,58].

"thermodynamic equilibrium constant [169]." Comparing Equations (4-10) and (4-11) shows that K^* and K are connected via the following relation:

$$K = K^* \left(\frac{{\gamma_C^x}^c {\gamma_D^x}^d}{{\gamma_A^x}^a {\gamma_B^x}^b} \right) \tag{4-12}$$

Equation (4-12) indicates that since K^* is a function of salt concentration and K is not, therefore, the activity coefficients, which are functions of salt concentration counteract changes in K^* due to variations in salt concentration and keep K constant.

In the second group of equilibrium speciation models, the equilibrium concentrations and the equilibrium activity coefficients need to be calculated simultaneously in a loop. The calculations are more intricate for the second group of models as it involves a system of non-linear equations that need to be solved in an iterative procedure. However, the second group of models are generally more accurate than the first group and cover a wider range of operating conditions. Examples of models from both groups and the relevant calculations will be discussed in Chapter 8.

Chapter 5: The Effect of Salt Concentration on Electrochemistry of a Corrosion Process

Aqueous metallic corrosion is an electrochemical process occurring at the interface between the metal and its electrolytic environment [15]. The kinetics of governing electrochemical reactions in a corrosion process determine the overall corrosion rate.

For an electrochemical electrode reaction in the general form of:

$$CR = 3.1536 \times 10^{10} \frac{W}{DAt} \tag{5-1}$$

a series of steps exists that leads to the conversion of the dissolved oxidized species (O) to the reduced species (R). In general, the rate of an electrochemical electrode reaction (usually expressed as a current density) is governed by the rates of one or more of the following processes [170][11]:

1. Mass transfer (*e.g.*, of H^+ ions from the bulk solution to the metal surface);
2. Charge (electron) transfer at the electrode surface, such as H^+ ion reduction reaction or active dissolution of iron;
3. Chemical reactions preceding or following the electron transfer. These might be homogeneous processes (e.g., protonation or dimerization) or heterogeneous ones (e.g., catalytic decomposition) on the electrode surface. For example, the

---

[11] These steps are valid when there is no surface layer (*e.g.*, corrosion products) on the electrode surface. If layers exist on the electrode surface, then diffusion of electroactive species through the layer to the electrode surface and/or diffusion of species produced by the oxidation reaction at the surface through the layer toward the electrolyte might become the controlling step.

preceding homogenous reaction of $CO_{2(aq)}$ hydration and production of $H_2CO_{3(aq)}$ in the case of CO_2 corrosion;

4. Other surface reactions, such as adsorption, desorption, or crystallization (electrodeposition).

Figure 5-1 shows the schematic of a typical electrode reaction that goes through all the steps mentioned above. In an unsteady state, the rate of these steps differs from each other. However, when a steady-state current is obtained, the rates of all reaction steps in a sequence will be the same. The magnitude of this steady-state current is determined by the slowest one or more steps called the rate determining step(s) (rds). When the corrosion process is controlled by the mass transfer of electroactive species to the electrode surface, the corrosion process is called *mass transfer controlled*. This scenario has been explained in Chapter 2 already. When a chemical reaction is the rds step, the corrosion process is said to be *chemical reaction controlled*. If the corrosion process is limited by the rate of charge transfer at the electrode surface the corrosion process is considered as *charge transfer controlled*. In the case of metallic corrosion in aqoues NaCl solutions, adosrtion of Cl^- ions on the surface influences the cathodic and anodic charge transfer reactions [171–174]. However, the adsortion process itself is usually not a controling step. Thus, a slow adsoption step is not reviewed in this study. If more than one rds step affect the rate of the corrosion process, it is called *mixed control*.

The controlling steps discussed above are valid for the case of aqueous uniform corrosion as it is the focus of this study. In the case of aqueous localized corrosion, other controlling steps might be involved.

Figure 5-1

The pathway of typical heterogenous electrochemical electrode reaction. The schematic is reproduced from Bard and Faulkner [170].

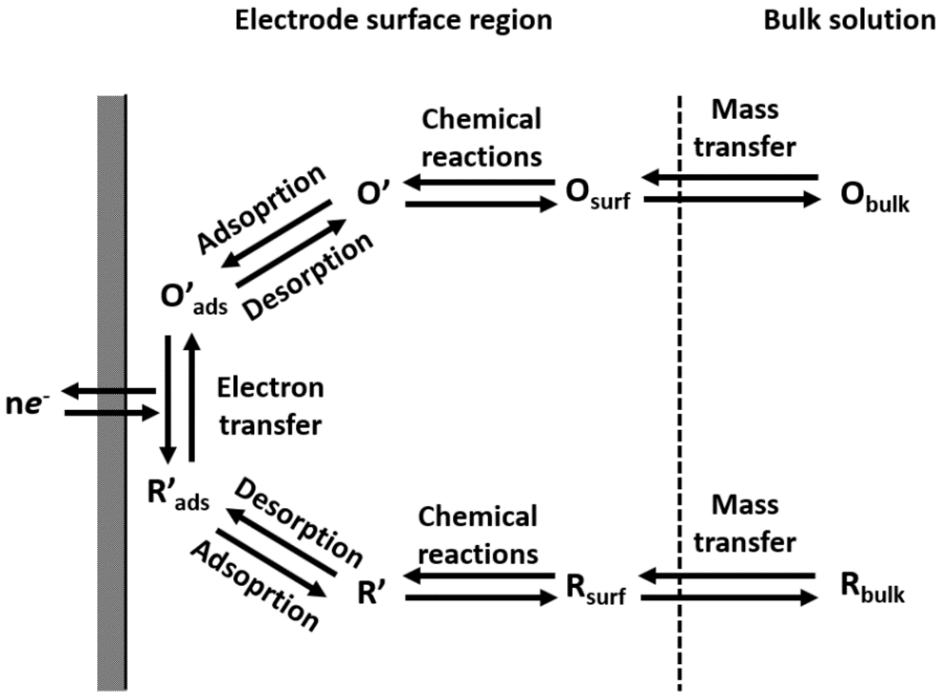

Which step is controlling the rate of an electrochemical depends on the solution chemistry, temperature, pressure, flow conditions, surface potential, *etc*. The rds does not always remain the same. A change in one or more of the above parameters can change the rds. For a mass transfer controlled electrochemical reaction, its rate depends on solution density and viscosity, and diffusion coefficient and activity (concentration) of electroactive species. The effect of salt concentration on all these parameters has been described above. Quantification the effect of salt concentration on the overall rate of mass transfer, which is usually expressed as a limiting current density (i_{Lim}) is discussed in

Section 12.2 and Appendix U. It is also possible that the rate of the reaction is controlled by a combination of a (relatively) slow chemical reaction step and a slow mass transfer step. This scenario, which is very common in weak acid corrosion, including CO_2 and H_2S corrosion, is explained comprehensibly in Section 12.2 and Appendices V and W. The charge transfer rate as the slowest step and the effect of salt concentration on this step will be presented below. The three common rate controlling scenarios in aqueous uniform strong acid, CO_2, and H_2S corrosion are depicted in Figure 5-2 by Evans diagrams. The charge transfer control scenario (Figure 5-2 A) usually occurs at temperatures below ~ 20^{o}C and solution pH values below ~ 4. In this case, salt effects on electrochemistry and solution chemistry become important in the corrosion process. On the other hand, the mass transfer control scenario (Figure 5-2 B) is dominant at temperatures above ~ 60^{o}C and solution pH values above ~ 5.5. Under these conditions, the effects of salt concentration on solution density, solution viscosity, diffusion coefficient of aqueous species, and solution chemistry become important in the corrosion process. The mixed control scenario (Figure 5-2 C) happens in conditions in between the ranges mentioned for the charge transfer control and the mass transfer control. In the mixed control conditions, salt effects on all parameters listed in Figure 2-1 can influence the corrosion process.

Figure 5-2

The Evans diagrams for the three common scenarios in aqueous corrosion of carbon steel: (A) charge transfer control, (B) mass transfer control or combination of mass transfer and a preceding chemical reaction control, (C) mixed control. i_{Lim} *and* i_{Corr} *represents the limiting current and the corrosion current densities, respectively.*

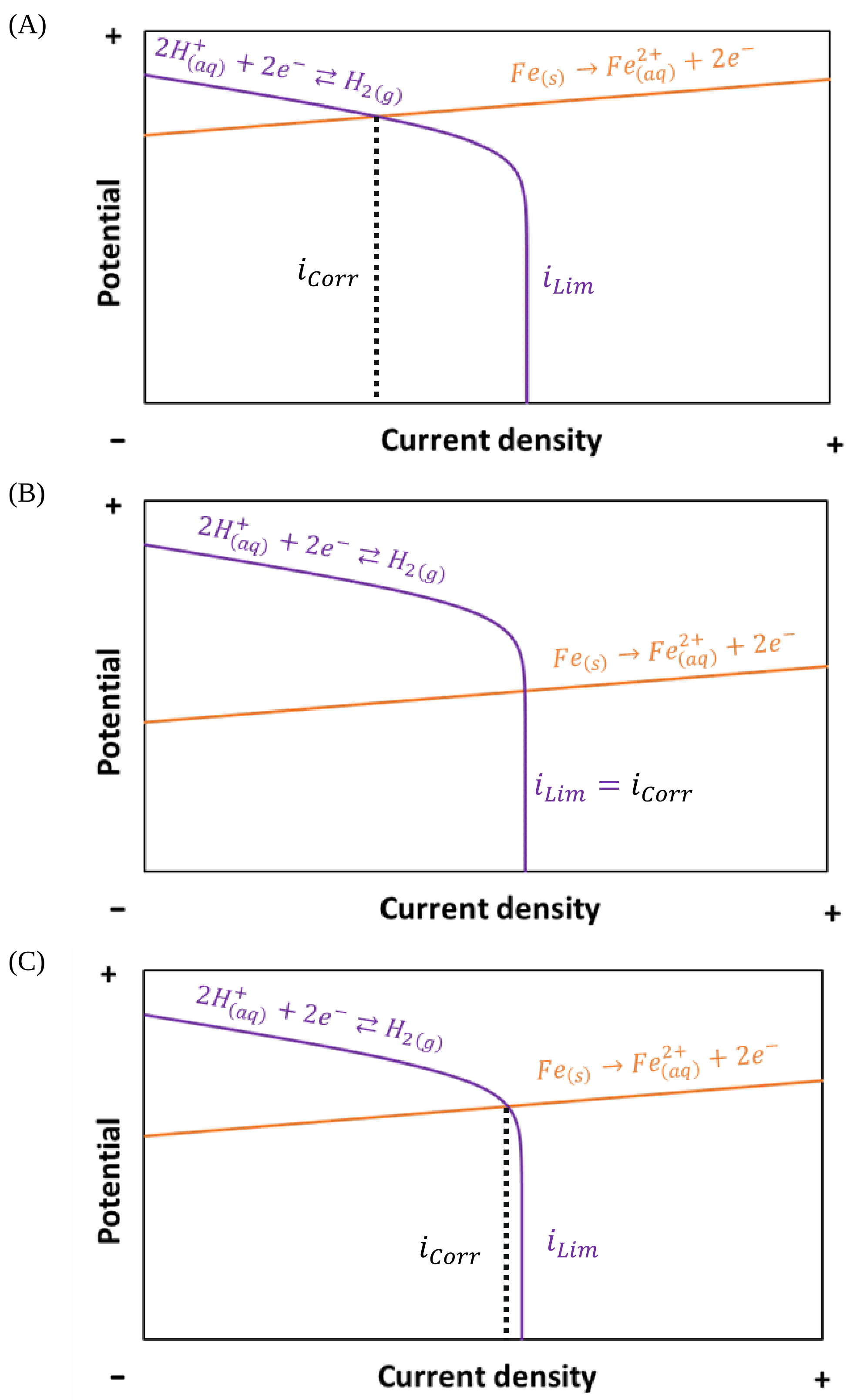

The theory of charge-transfer controlled reactions is well-understood and has been reviewed thoroughly by several authors including Vetter [175], Bard and Faulkner [170], Bockris and Khan [176] and Gileadi [177]. The key equations for calculating the rate of charge transfer are summarized as follows.

For an electrochemical electrode reaction in the general form of:

$$R \underset{v_c}{\overset{v_a}{\rightleftarrows}} Ox + ne^- \tag{5-2}$$

the current density associated with it, according to Faraday's law, is proportional to the difference between the rates of the anodic direction (v_a) and the cathodic direction (v_c):

$$i = nF(v_a - v_c) \tag{5-3}$$

where, i the net rate of reaction in terms of current density in A/m^2, n is the stoichiometric number of electrons involved in the electrode reaction, F is the Faraday's constant (= 96485.33 C/mol), and v is the heterogenous reaction rate in mol/m^2/s. The rates of the anodic ($R \rightarrow O + ne^-$) and cathodic ($O + ne^- \rightarrow R$) reactions at the electrode/electrolyte interface is related to the electrode potential and surface concentrations of reacting species as follows:

$$i_a = nFv_a = nFk_a a_{R,s}^{n_R} \exp\left(\frac{\alpha_a FE}{RT}\right) \tag{5-4}$$

$$i_c = -nFv_c = -nFk_c a_{O,s}^{n_O} \exp\left(-\frac{\alpha_c FE}{RT}\right) \tag{5-5}$$

where, i_a and i_c are the net anodic and cathodic reaction rates in terms of current densities in A/m^2, k_a and k_c are the anodic and cathodic heterogenous rate constants at the reversible potential[12] (E_{rev}) in mol/m^2/s, α_a and α_c are electrochemical transfer coefficients, $a_{R,s}$ and $a_{O,s}$ are the activities of the reduced and oxidized species at the surface[13], respectively, n_R and n_O are the reaction orders with respect to the reduced and oxidized species, correspondingly, E is the potential at electrode/electrolyte interface with respect to a reference electrode in V, R is the gas constant (= 8.3145 J/mol/K), and T is the electrolyte temperature in K. For electrolytes near ideal conditions, activities are usually replaced by concentrations for making the calculations simpler. The negative sign for i_c is due to the consumption of electrons by the reduction reaction at the electrode surface. The net charge transfer rate for Reaction (5-2) is equal to:

$$\begin{aligned} i &= i_a + i_c \\ &= nFk_a a_{R,s}^{n_R} \exp\left(\frac{\alpha_a FE}{RT}\right) - nFk_c a_{O,s}^{n_O} \exp\left(-\frac{\alpha_c FE}{RT}\right) \end{aligned} \tag{5-6}$$

At the equilibrium potential or reversible potential, E_{rev}, the net charge transfer reaction rate (current density) is equal to zero. In the absence of a net current, the activities of species at the surface are equal to their bulk activities (*i.e.*, $a_{R,s} = a_{R,b}$ and $a_{O,s} = a_{O,b}$). Moreover, the current density of the anodic direction is equal to that of cathodic direction. The current density at equilibrium is called the exchange current density (i_0) and is equal to:

$$i_0 = nFk_a a_{R,b}^{n_R} \exp\left(\frac{\alpha_a FE_{rev}}{RT}\right) = nFk_c a_{O,b}^{n_O} \exp\left(-\frac{\alpha_c FE_{rev}}{RT}\right) \tag{5-7}$$

---

[12] Potential at equilibrium

[13] Activities in Equation (5-4) and (5-5) need to be divided by reference activities to make the activity terms dimensionless: $(a_s/a_{ref,s})^n$. However, for a simpler presentation, the reference activities are commonly ignored from the equations. Usually, the molarity unit is used in charge transfer rate equations.

where, $a_{R,b}$ and $a_{R,b}$ are the activities of reduced and oxidized species in the bulk electrolyte, respectively, E_{rev} is in V. Combining Equations (5-6) and (5-7), i can be expressed in terms of i_0:

$$\begin{aligned} i = i_0 \left(\frac{a_{R,s}}{a_{R,b}}\right)^{n_R} \exp\left(\frac{\alpha_a F(E - E_{rev})}{RT}\right) \\ - i_0 \left(\frac{a_{O,s}}{a_{O,b}}\right)^{n_O} \exp\left(-\frac{\alpha_c F(E - E_{rev})}{RT}\right) \end{aligned} \tag{5-8}$$

$E - E_{rev}$ is called the activation overpotential[14] or the charge-transfer overpotential and commonly presented by η.

The two ratios of $a_{R,s}/a_{R,b}$ and $a_{O,s}/a_{O,b}$ depend on the rates of transport of reactants toward to and products away from the electrode/electrolyte interface. If the mass transfer processes are slow compared to the charge transfer steps, the surface activities become different from those in the bulk. On the contrary, if the charge transfer steps are sluggish relative to the mass transfer processes, the reaction is under charge transfer control and the two ratios are equal to one for all electrode potentials. In such a case, Equation (5-8) converts to a simpler form, which is usually referred to as the *Butler–Volmer* equation for charge-transfer control reactions:

$$i = i_o \left[\exp\left(\frac{\alpha_a F(E - E_{rev})}{RT}\right) - \exp\left(-\frac{\alpha_c F(E - E_{rev})}{RT}\right)\right] \tag{5-9}$$

Equations (5-8) and (5-9) include both the cathodic and anodic partial reactions for a particular redox couple[15]. However, in modeling aqueous metallic corrosion,

---

[14] Overvoltage

[15] For a particular redox couple $\alpha_a + \alpha_c = 1$.

usually, it is only the cathodic or the anodic partial current that is important. In other words, the cathodic partial process can be neglected for a metal ion/metal redox reaction because the deposition of metal ions (*i.e.*, the reverse of metal dissolution) is not of practical significance at the corrosion potential. Likewise, in aqueous metallic corrosion, the anodic partial process can be usually neglected for oxidizing agents (H^+ ion in strong acid, CO_2, and H_2S aqueous corrosion) because only their reduction partial reaction is of significance magnitude at the corrosion potential. Therefore, using Equation (5-9), for the case of carbon steel corrosion in aqueous solutions, the anodic ($i_{a,ct}$) and cathodic ($i_{c,ct}$) charge-transfer control current densities are equal to:

$$i_{Fe,ct} = i_{0,Fe} \exp\left(\frac{\alpha_{Fe} F\left(E - E_{rev,Fe}\right)}{RT}\right) \tag{5-10}$$

$$i_{H^+,ct} = -i_{0,H^+} \exp\left(-\frac{\alpha_{H^+} F\left(E - E_{rev,H^+}\right)}{RT}\right) \tag{5-11}$$

$i_{a,ct}$ and $i_{c,ct}$ can be expressed in terms of reaction rate constants as well [177]:

$$i_{Fe,ct} = n_{Fe} F k_{o,Fe} a_{Fe,b}^{n_{Fe}} \exp\left(\frac{\alpha_{Fe} F(E - E_{rev,Fe})}{RT}\right) \tag{5-12}$$

$$i_{H^+,ct} = -n_{H^+} F k_{o,H^+} a_{H^+,b}^{n_{H^+}} \exp\left(-\frac{\alpha_{H^+} F(E - E_{rev,H^+})}{RT}\right) \tag{5-13}$$

where,

$$k_{Fe} = k_{o,Fe} \exp\left(-\frac{\alpha_{Fe} F E_{rev,Fe}}{RT}\right) \tag{5-14}$$

$$k_{H^+} = k_{o,H^+} \exp\left(\frac{\alpha_{H^+} F E_{rev,H^+}}{RT}\right) \tag{5-15}$$

and,

$$k_{o,Fe} = k_{Fe}^{*} \exp\left(\frac{-\Delta E_{a,Fe}}{RT}\right) \tag{5-16}$$

$$k_{o,H^+} = k_{H^+}^{*} \exp\left(\frac{-\Delta E_{a,H^+}}{RT}\right) \tag{5-17}$$

where, $k_{o,Fe}$ and k_{o,H^+} are the heterogenous rate constants at $E = 0$ *vs.* a reference electrode for the active dissolution of Fe and H^+ reduction reactions, respectively, in mol/m^2/s, k_{Fe}^{*} and $k_{H^+}^{*}$ are two constants in mol/m^2/s, and $\Delta E_{a,Fe}$ and $\Delta E_{a,H^+}$ are the activation energies for the active dissolution of Fe and H^+ ion reduction reactions, respectively, in J/mol [177]. Plugging Equations (5-14) and (5-15) into Equations (5-12) and (5-13), respectively, results in the following equations:

$$i_{Fe,ct} = n_{Fe} F k_{Fe} a_{Fe,b}^{n_{Fe}} \exp\left(\frac{\alpha_{Fe} F E}{RT}\right) \tag{5-18}$$

$$i_{H^+,ct} = -n_{H^+} F k_{H^+} a_{H^+,b}^{n_{H^+}} \exp\left(-\frac{\alpha_{H^+} F E}{RT}\right) \tag{5-19}$$

Therefore, it can be seen that $i_{Fe,ct}$ and $i_{H^+,ct}$ does not depend on E_{rev} and any arbitrary potential can be used for calculating the charge transfer current densities.

Comparing Equations (5-10) and (5-11) with Equations (5-12) and (5-13) gives correlations for $i_{0,Fe}$ and i_{0,H^+}:

$$i_{0,Fe} = n_{Fe} F k_{o,Fe} a_{Fe,b}^{n_{Fe}} \tag{5-20}$$

$$i_{0,H^+} = n_{H^+} F k_{o,H^+} a_{H^+,b}^{n_{H^+}} \tag{5-21}$$

Knowing the exchange current density, called the reference current density (i_o^{ref}) at a reference temperature (T_{ref}) and a reference activity (a^{ref}), i_o can be calculated at temperature T and activity of a, using the equations below:

$$i_{0,Fe} = i_{o,Fe}^{ref}\left(\frac{a_{Fe,b}}{a_{Fe,b}^{ref}}\right)^{n_{Fe}} \exp\left(\frac{-\Delta E_{a,Fe}}{R}\left(\frac{1}{T}-\frac{1}{T_{ref}}\right)\right) \tag{5-22}$$

$$i_{0,H^+} = i_{o,H^+}^{ref}\left(\frac{a_{H^+,b}}{a_{H^+,b}^{ref}}\right)^{n_{H^+}} \exp\left(\frac{-\Delta E_{a,H^+}}{R}\left(\frac{1}{T}-\frac{1}{T_{ref}}\right)\right) \tag{5-23}$$

Equations (5-20) and (5-21) and Equations (5-24) and (5-25) are theoretical equations. In some conditions, $i_{0,Fe}$ and i_{0,H^+} might a function of activity of more than one species. For example, as will be shown below, $i_{0,Fe}$ depends more on activity of OH^- and Cl^- ions rather than activity of Fe.

In equations (5-10) and (5-11) two parameters that can influence the rate of charge transfer reactions are the exchange current density (i_o) and the electrochemical transfer coefficient (α). The former is directly related to the rate of charge transfer reaction as it is a function of the reaction rate constant. The latter is related to the mechanism of charge transfer reaction, and thereby, indirectly influences the charge transfer rate. The Tafel slope (β)[16], equal to $2.3RT/\alpha F$ is commonly used instead of α when talking about the charge transfer mechanisms of processes. Both i_o (*i.e.*, reaction orders with respect influential species) and α need to be determined empirically. However, sometimes α can deduced from mechanistic studies [19].

The electrochemical electrode reactions are often not as simple as Reaction (5-2). They can occur in various multistep reactions. Therefore, a simple electrochemical electrode reaction in the form of Reaction (5-2) might happen according to a different pathways depending on the electrode type and the electrolyte conditions [178]. These

---

[16] With a unit of V/decade or mV/decade

different pathways for an electrochemical electrode reaction define its mechanism, and therefore its rate. Moreover, due to the multistep nature of the electrochemical electrode reactions the charge transfer rate might be dependent on activities of intermediate species as well. H^+ reduction and Fe oxidation pathways and their activity dependencies will be elucidated in detail in the forthcoming text.

Salt concentration can affect both i_o and α, which in turn can alter the rate of charge transfer processes. Halide ions (*e.g.*, Cl^-) can be adsorbed on the electrode surface and blocking the available area required for charge transfer reactions (either cathodic or anodic) to occur or modifying the charge transfer activation energy (ΔE_a) and in this way changes i_o [171,179]. Additionally, halide ions at certain concentrations might participate directly in the multistep electrode reaction and change the mechanism (and consequently α) of an electrode reaction [173,178]. In the following, a review of the literature on the effect of salt concentration on electrochemistry of strong acid corrosion, CO_2 corrosion and H_2S corrosion will be presented.

5.1 The Effect of Salt Concentration on Electrochemistry of Strong Acid Corrosion

In this section the effect of salt concentration on the electrochemistry of corrosion of carbon steel in aqueous strong acid solutions is described. Aqueous strong acid corrosion is defined as the exposure of carbon steel to aqueous electrolytes in which no weak acid[17] such as carboxylic acids (*e.g.*, acetic acid and formic acid), $H_2CO_{3(aq)}$, $H_2S_{(aq)}$, *etc.*, are dissolved. In the case of carbon steel corrosion, the “strong acid” term

---

[17] A weak acid is an acid that partially dissociates into its constituent ions in an aqueous solution. On the other hand, a strong acid fully dissociates into its constituent ions when it dissolves in an aqueous solution. Even water is considered as a weak acid. However, the contribution of water in providing H^+ ions for the cathodic reaction in corrosion of carbon steels is negligible.

does not imply very low pH values, and in fact, it covers pH values typically in mildly acidic to near neutral ranges (*e.g.*, pH 3−pH 7). Aqueous strong acid corrosion can be considered as the simplest type of carbon steel corrosion, because only the H^+ ion reduction reaction is involved in the cathodic reaction of the corrosion process without any preceding chemical reactions such as the buffering effect imposed by the presence of weak acids.

5.1.1 Salt Concentration Effects on the Anodic Reaction(s) in Strong Acid Corrosion

5.1.1.1 Active Dissolution of Iron in the Absence of Halides

Generally, the anodic dissolution of carbon steels in aqueous solutions is shown be the following half-reaction:

$$Fe_{(s)} \rightarrow Fe^{2+}_{(aq)} + 2e^- \tag{5-24}$$

In the active dissolution region (potentials close to the corrosion potential[18]), Reaction (5-24) is always under charge-tranfer control. Reaction (5-24) might proceed through different pathways depending on the nature of the solution and the steel surface microstructure [178]. The active dissolution of iron in acidic media, free of oxygen, has been the subject of a very large number of scientific articles for the last 50 years. All the reaction mechanisms are based on the generally agreed-upon experimental evidence that the dissolution rate increases with the solution pH at potentials well below the passivity region. The non-obvious participation of hydroxyl ions (OH^-) in this reaction can be related to the multistep nature of the reaction mechanism and the strong dissociative power of transition metals with respect to water [180,181].

---

[18] Or, open circuit potential (OCP)

Two mechanisms are frequently mentioned for dissolution of iron in the active region in the acidic solutions: *catalytic mechanism* and *consecutive mechanism*[19]. According to the catalytic mechanism by Bonhoeffer and Heusler group [172,182], $(FeOH)_{ads}$ enters in a catalytic sequence of dissolution at the end of which $(FeOH)_{ads}$ is regenerated and Fe dissolved as $FeOH^+$:

$$Fe + H_2O \rightleftarrows (FeOH)_{ads} + H^+ + e^- \qquad (5\text{-}25)$$

$$Fe + (FeOH)_{ads} \rightleftarrows [Fe(FeOH)]_{ads} \qquad (5\text{-}26)$$

$$[Fe(FeOH)]_{ads} + OH^- \xrightarrow{rds} FeOH^+ + (FeOH)_{ads} + 2e^- \qquad (5\text{-}27)$$

$$(FeOH)_{ads} + e^- \rightleftarrows Fe + OH^- \qquad (5\text{-}28)$$

$$FeOH^+ + H^+ \rightleftarrows Fe^{2+}_{(aq)} + H_2O \qquad (5\text{-}29)$$

Reaction (5-26) is the formation of a catalytic active surface compound ($[Fe(FeOH)]_{ads}$), which is dependent on the surface activity of metal [183]. The rate determining charge transfer controlled step (Reaction (5-27)) was assumed to take place at active surface sites. In this step, $Fe^{2+}_{(aq)}$ ions pass the double layer and form $FeOH^+$ complexes with OH^- ions. A steady-state anodic Tafel slope of 30 mV/decade and a steady-state electrochemical reaction order of 2 with respect to OH^- ion have reported by Heusler and Bonhoeffer [184].

Bockris *et al.* [185,186] proposed the so-called consecutive mechanism as follows:

$$Fe + H_2O \rightleftarrows Fe + (FeOH)_{ads} + H^+ + e^- \qquad (5\text{-}30)$$

---

[19] Also, called non-catalyzed mechanism

$$(FeOH)_{ads} \xrightarrow{rds} FeOH^{+} + e^{-} \tag{5-31}$$

$$FeOH^{+} + H^{+} \rightleftarrows Fe_{sol}^{2+} + H_2O \tag{5-32}$$

They obtained a steady-state anodic Tafel slope of 40 mV and an electrochemical reaction order with respect to OH^- of 1 [184]. This mechanism was modified later by Kelly [187]. In this mechanism, after the formation of $(FeOH)_{ads}$ on the surface, it needs to pass the electrochemical double layer for Fe_{sol}^{2+} to be produced [183].

Lorenz *et al.* [173,174,183,188] showed that either mechanism can be followed, depending on the surface microstructure. They demonstrated that the iron dissolution mechanism is changed from the catalytic mechanism to the consecutive mechanism and *vice versa* by changing the substructure of the iron bulk material and consequently the dissolution density at the iron surface. A low density of grain boundaries and other imperfections favored the consecutive mechanism, while a high density of imperfections yielded the catalytic mechanism [178].

Hilbert and Miyoshi [183] believed that the catalytic mechanism is possible under certain conditions: (1) a high density of crystal imperfections, and therefore a high catalytic activity of the metal, and (2) dissolution within a limited range of the anodic polarization. The consecutive mechanism is energetically favored. Only at more positive anodic potentials and at highly active surfaces the catalytic mechanism will be predominant. Table 5-1 compares the kinetic data for iron dissolution based on the two mechanisms. The commonality between the two models is that the concentration of ferrous ions in the electrolyte does not influence the dissolution kinetics of iron. The electrochemical reaction order with respect to Fe^{2+} is zero [179].

Table 5-1

Experimental kinetic data for iron dissolution with steady-state and nonsteady-state methods at 25^{o}C. Table is reproduced from [183].

Kinetic parameters	Catalytic mechanism		Consecutive mechanism	
	Steady-state	Nonsteady-state	Steady-state	Nonsteady-state
Tafel slope ($\beta_{a,Fe}$)	30 ± 2 mV	60 ± 7 mV	40 ± 2 mV	60 ± 7 mV
n_{pH}	2 ± 0.3	1 ± 0.1	1 ± 0.1	0.5 ± 0.1
$n_{Fe^{2+}}$	0	0	0	0

Tafel slope is the anodic Tafel slope for the iron dissolution reaction. n_{pH} and $n_{Fe^{2+}}$ are reaction orders for iron dissolution reaction with respect to pH and Fe^{2+} ion concentrations, respectively.

Burstein and Davies [189] stated that the first step in dissolution of iron is adsorption of water molecules on the fresh metal surface:

$$Fe + H_2O \rightleftarrows Fe.H_2O_{ads} \tag{5-33}$$

Then, Reaction (5-33) is followed by one of the two mechanisms as follows:

For pH < 7,

$$Fe.H_2O_{ads} \xrightarrow{rds} FeOH_{ads} + H^+ + e^- \tag{5-34}$$

For pH > 7

$$Fe.H_2O_{ads} \rightleftharpoons Fe.OH^-_{ads} + H^+ \tag{5-35}$$

$$Fe.OH^-_{ads} \xrightarrow{rds} FeOH_{ads} + e^- \tag{5-36}$$

and finally, the same as the abovementioned mechanisms, the lasts reactions are:

$$FeOH_{ads} \rightleftharpoons FeOH^+ + e^- \tag{5-37}$$

$$FeOH^{+} + H^{+} \rightleftarrows Fe_{sol}^{2+} + H_2O \tag{5-38}$$

According to Burstein and Davies [189], an adsorbed layer of intermediate $FeOH_{ads}$ forms on the surface during the dissolution of iron.

Smart and Bockris [190] reported that the current density for iron dissolution has been found to depend on the activity of water with a reaction order of 1.6. They stated that the effect of the activity of water on the current density becomes significant for concentrated salt solutions, for which the activity of water is usually significantly lower than 1. McCafferty and Hackerman [178] claimed that the activity of water is virtually constant for concentrated chloride solutions and therefore, does not have a significant effect on the current density. The results of this study are in agreement with Smart and Bockris [190] findings.

5.1.1.2 Active dissolution of iron in the presence of halides

Heusler *et al*. [172] believed that in the presence of the chloride ion, which is more surface active than SO_4^{2-} or ClO_4^{-}, there is a competitive adsorption between chloride and hydroxyl ions. Chloride adsorption will tend to prevail at high chloride activity and low pH; and accordingly, the dissolution mechanism will be different from the catalytic and consecutive mechanisms [178].

Lorenz *et al.* [173,174] proposed one of the first mechanisms for the dissolution of iron in the active range in the presence of specifically adsorbed halide ions (X^{-}), which is named *halide inhibited* mechanism. The steps in this mechanism are as follows:

$$Fe + H_2O \rightleftarrows (FeOH^{-})_{ads} + H^{+} \tag{5-39}$$

$$Fe + X^{-} \rightleftarrows Fe(X^{-})_{ads} \tag{5-40}$$

$$(FeOH^-)_{ads} + Fe(X^-)_{ads} \overset{rds}{\longrightarrow} FeOH^+ + X^- + 2e^- \tag{5-41}$$

$$FeOH^+ + H^+ \rightleftarrows Fe^{2+}_{aq} + H_2O \tag{5-42}$$

This mechanism is called halide inhibited mechanism because theoretically (surface coverage of 1 by halide ions and Langmuir-type isotherm) the reaction order with respect to halide ions should be -1 and Lorenz *et al.* [173,191] experiments in solutions of pH 0.3-1 and Cl^- concentrations between 0.01-2 M showed -0.7 ± 0.1.

Darwish *et al.* [192] mentioned that in the halide inhibited mechanism, the anodic dissolution reaction will proceed mainly at active sites of the surface (kink sites, lattice steps, ad-atoms, crystal dislocations, and so on). This is a similar assumption to that for the pathway of Fe dissolution reaction without the presence of halide ions. This means that halides inhibit the iron dissolution by blocking the active surface sites required for OH^- adsorption and the reaction to proceed.

Arvia and Podesta [193] proposed a mechanism involving two successive one-electron transfer for dissolution of iron in the presence of halides:

$$Fe + X^- \rightleftarrows (FeX^-)_{ads} \tag{5-43}$$

$$(FeX^-)_{ads} + H_2O \rightleftarrows (FeOH^-)_{ads} + H^+ + X^- \tag{5-44}$$

$$(FeOH^-)_{ads} \rightleftarrows (FeOH)_{ads} + e^- \tag{5-45}$$

$$(FeOH)_{ads} \overset{rds}{\longrightarrow} Fe(OH)^+ + e^- \tag{5-46}$$

$$Fe(OH)^+ \rightleftarrows Fe^{2+}_{aq} + OH^- \tag{5-47}$$

$$OH^- + H^+ \rightleftarrows H_2O \tag{5-48}$$

The rate expression suggested by Arvia and Podesta [193] yields a Tafel slope of 40 mV/dec and an electrochemical reaction order of zero with respect to halide ion concentration. However, the obtained Tafel slope contradicts their own experimental data of 54 mV/dec for pH 1.78 and chloride concentration of 2 M. Moreover, the 40 mV/dec Tafel slop is different from the experimental data of 60 mV/dec for solution pH values below pH 1.5-2 reported by other scientists [178]. Additionally, the zero-reaction order contrasts with the general observation that halide ions inhibit acid dissolution of iron, which corresponds to a negative reaction order [178].

Darwish *et al.* [192] argued that the dissolution mechanism of iron changes, if the concentrations of hydrogen ions and chloride ions are higher than certain levels. They proposed a new mechanism for dissolution of iron in highly concentrated halide and hydrogen solution ($[H^+] > 1$ M):

$$Fe + Cl^- \rightleftarrows Fe(Cl)_{ads} + e^- \tag{5-49}$$

$$Fe(Cl)_{ads} + H^+ \xrightarrow{rds} Fe(ClH^+)_{ads} \tag{5-50}$$

$$Fe(ClH^+)_{ads} \rightleftarrows FeCl^+_{aq} + H^+ + e^- \tag{5-51}$$

The rds step is a chemical adsorption step. Darwish *et al.* [192] stated that in highly concentrated halide ion solutions, all the active sites on the surface are blocked by adsorbed halide ions. Therefore, the formation of $Fe(OH^-)_{ads}$ is no longer possible (related to the mechanism in the absence of halide ions) and because of that the dissolution reaction must change its pathway. In this case, the dissolution will proceed at the less active parts of the surface, where the formation of ion pairs corresponding to the above rds step is favored. Darwish *et al.* [192] proved that iron with a lower purity gives practically the same results as pure iron.

McCafferty and Hackerman [178] proposed that for highly concentrated chloride solutions (*e.g.* 6 N) at sufficiently low pH, iron dissolution is promoted by H^+ ions rather than by OH^- ions, as is the case for 1 N chloride solutions reported by Lorenz *et al.* [174]. At very high H^+ activities, there is a synergistic effect between halide anions chemisorbed at the iron surface and hydrogen ions in solution. Hydrogen ions are electrostatically attracted toward the iron surface covered with Cl^- anions and catalyze the dissolution reaction, as indicated by the positive reaction order of 1.84 with respect to H^+ ion. McCafferty and Hackerman [178] suggested the following mechanism of active iron dissolution at high concentrations of halides and very high H^+ activities:

$$Fe + H_2O \rightleftharpoons Fe.H_2O_{ads} \tag{5-52}$$

$$Fe.H_2O_{ads} + X^- \rightleftharpoons FeX^-{}_{ads} + H_2O \tag{5-53}$$

$$FeX^-{}_{ads} + H^+ \rightleftharpoons FeX^-.H^+ \tag{5-54}$$

$$FeX^-.H^+ + \ H^+ \xrightarrow{rds} FeX^+ + 2H^+ + 2e^- \tag{5-55}$$

$$FeX^+ \rightleftharpoons Fe_{aq}^{2+} + X^- \tag{5-56}$$

The theoretical reaction order with respect to Cl^- was calculated to be above zero. The data reported by McCafferty and Hackerman [178] in 6N chloride solutions with $[H^+]$ = 3N at 25°C showed values between 0.62-0.91 for the reaction order with respect to Cl^- ion concentration. However, in 1 N chloride solution with 0.2 N < $[H^+]$ < 3 N they reported -0.85, which is similar to the reported value by Lorenz *et al.* [174] mechanism.

The chance for simultaneous tunneling of two electrons between the metal and an ion is low enough to be prohibitive[20]. Therefore, from a theoretical point of view, the statistical probability of a mechanism with two consecutive one-electron transfer steps is normally, several orders of magnitude higher than that of a two-electron transfer step [192], suggesting that the mechanism proposed by McCafferty and Hackerman [178] in unlikely to occur.

Chin and Nobe [194] claimed that chloride ion accelerates iron dissolution in deoxygenated acidic concentrated chloride media. They proposed the following mechanism which is named the chloride-accelerated mechanism:

$$Fe + Cl^- + H_2O \rightleftarrows [FeClOH]^-_{ads} + H^+ + e^- \qquad (5\text{-}57)$$

$$[FeClOH]^-_{ads} \xrightarrow{rds} FeClOH + H^+ + e^- \qquad (5\text{-}58)$$

$$FeClOH + H^+ \rightarrow Fe^{2+} + Cl^- + H_2O \qquad (5\text{-}59)$$

The kinetic parameters predicted by this mechanism are dependent on the adsorption behavior of the intermediate, $[FeClOH]^-_{ads}$. By considering Temkin adsorption, the proposed mechanism predicts values of 60 mV, 0.5, and 0.5 for the anodic Tafel slope, the reaction order with respect to the Cl^- concentration, and the reaction order with respect to OH^- concentration, respectively. Kuo and Nobe [195] stated that iron dissolution in acidic concentrated chloride solutions proceed through coupled parallel reactions as represented by Cl^--accelerated and OH^--accelerated mechanisms. The OH^--accelerated mechanism (*i.e.*, mechanisms explained for the absence of halides) is

---

[20] The two-electron transfer step has in fact been shown to be possible for Ti(I)-Ti(III) exchange in aqueous solutions.

dominant for highly acidic and very dilute chloride solutions. Similarly, Kolotyrkin *et al.* [182,196] found that both sulfate and chloride ions accelerated iron dissolution.

Burstein and Davies [197] hypothesized chloride ion accelerates iron dissolution by directly reacting with the bare iron surface, in parallel with the Bockris-Kelly mechanism (Reactions (5-30)-(5-32)), as follows:

$$Fe + Cl^- \xrightarrow{rds} FeCl_{ads} + e^- \tag{5-60}$$

$$FeCl_{ads} \rightleftarrows FeCl^+ + e^- \tag{5-61}$$

$$FeCl^+ \rightleftarrows Fe^{2+}_{sol} + Cl^- \tag{5-62}$$

Smart *et al.* [198] proposed the following mechanism for iron dissolution in high chloride concentration media:

$$Fe + H_2O \rightleftharpoons FeOH + H^+ + e^- \tag{5-63}$$

$$FeOH + Cl^-_{ads} \xrightarrow{rds} FeCl + OH^- \tag{5-64}$$

$$FeCl \rightleftharpoons Fe^{2+} + Cl^- + e^- \tag{5-65}$$

Their mechanism involves the adsorption of Cl$^-$, which agrees with the experimental results. They suggested that the rate of dissolution is controlled by a chemical step in which the Cl$^-$ reacts with $FeOH$ to form $FeCl$ species on an interface saturated with adsorbed Cl$^-$. Consequently, corrosion rates may be enhanced at the sites where Cl$^-$ is adsorbed. According to Smart *et al.* [198] mechanism, the order with respect to Cl$^-$ concentration should be +1. However, experiments showed a value of -0.7. The authors explained that by considering water activity this seemingly contradiction can be justified.

In summary, there is no decisive opinion on the role of chloride ion on iron dissolution. Some studies state that it inhibits iron dissolution reaction and some believe it accelerates the dissolution reaction of iron. One common belief in all the proposed mechanisms is that the iron dissolution reaction in the active region involves several chloro-iron complexes in the form of adsorbed reaction intermediates. Table 5-1 summarizes the experimental kinetic data available in the literature regarding iron dissolution reaction in different electrolyte conditions.

Table 5-2

A summary of experimental kinetic data for the iron dissolution reaction in different solution conditions.

#	Conditions	Tafel slope (mV/dec)	n_{H^+}	n_{OH^-}	n_{Cl^-}	Ref.
1	1 N HCl, O_2-free solution	58	N/A	N/A	N/A	[191]
2	0.5 N H_2SO_4 + xKCl, 0.3 < pH < 1, 25°C, x < 0.1 N	30	N/A	N/A	0	[174]
3	0.5 N H_2SO_4 + xKCl, 0.3 < pH < 1, 25°C, 0.1 N < x < 2 N	60 ± 5	N/A	1 ± 0.1	-0.7 ± 0.1	[174]
4	0.2 M NaCl, 50°C, 2.12 < pH < 3.69	37-61	N/A	N/A	N/A	[193]
5	2 M NaCl, 25°C, 1.78 < pH < 2.73	32-54	N/A	N/A	N/A	[193]
6	1 N chloride solution, 0.2 N < $[H^+]$ < 3 N, 25°C	65-75	-0.66 to -0.7	N/A	-0.85	[178]
7	6 N chloride solution, 0.12 N < $[H^+]$ < 0.24 N, 25°C	60-85	-0.9	N/A	0.62-0.91	[178]
8	6 N chloride solution, 0.24 N < $[H^+]$ < 1.2 N, 25°C	60-85	0	N/A	0.62-0.91	[178]
9	6 N chloride solution, 2.4 N < $[H^+]$ < 6 N, 25°C	60-85	1.84	N/A	0.62-0.91	[178]
10	xNaCl + yHCl (x + y = 1 N), 0 < pH < 1.8	70	N/A	0.6	0.5	[194]
11	unbuffered weakly acid deaerated solution, T = 298.15, pH ≥ 5	60 ± 5	N/A	N/A	N/A	[199]
12	xNaCl + yHCl (x + y = 5 M), O_2-free solution, 25°C, a_{H^+} < 1 M	60	N/A	0.6	N/A	[192]
13	xNaCl + yHCl (x + y = 5 M), O_2-free solution, 25°C, a_{H^+} > 2 M	100	N/A	-1 ± 0.1	N/A	[192]
14	4.9 M NaCl + 0.1 M $HClO_4$, O_2-free solution, 25°C	64	N/A	N/A	N/A	[192]
15	2 M $HClO_4$ + $xNaClO_4$ + yNaCl, x + y = 3, 0.5 M < y < 3 M, O_2-free solution, 25°C	N/A	N/A	N/A	0.6 ± 0.1	[192]
16	xNaCl + yHCl, x + y = 4.5 M, 23°C, $[H^+]$ < 0.1 M, low polarization	75	N/A	0.6	N/A	[195]
17	xNaCl + yHCl, x + y = 4.5 M, 23°C, $[H^+]$ < 0.1 M, high polarization	40	N/A	1.1	N/A	[195]
18	0.01 M $HClO_4$ + xNaCl + $yNaClO_4$, x + y = 4.49 M, 23°C, pH = 1.1, 0.2 M < $[Cl^-]$ < 4 M, low polarization	75	N/A	N/A	0.4	[195]

n_{H^+}, n_{OH^-}, and n_{Cl^-} are the reaction orders for iron dissolution in the active region with respect to concentrations of H^+, OH^-, and Cl^-, respectively.
N is concentration unit in normality and M is concentration unit in molarity.

5.1.2 Salt Concentration Effects on the Cathodic Reaction in Strong Acid Corrosion

The main cathodic reaction in strong acid aqueous corrosion is H^+ ion reduction (or hydrogen evolution reaction[21]). The H_2O reduction reaction can become influential in strong acid corrosion only at pH > 5 [200]. These two reactions are presented below:

$$2H^+_{(aq)} + 2e^- \rightleftarrows H_{2(g)} \tag{5-66}$$

$$2H_2O_{(l)} + 2e^- \rightleftarrows H_{2(g)} + 2OH^-_{(aq)} \tag{5-67}$$

A commonly accepted mechanism for H^+ ion reduction reaction in acidic solution is as follows [15,171][22]:

$$H^+_{(aq)} + H_2O_{(l)} \rightleftarrows H_3O^+_{(aq)} \tag{5-68}$$

$$H_3O^+_{(aq)} + e^- \xrightarrow{rds} H_{ads} + H_2O_{(l)} \tag{5-69}$$

$$H_{ads} + H_{ads} \rightleftarrows H_{2(g)} \tag{5-70}$$

Reaction (5-68) is just the hydronium ion formation step. Reaction (5-69) is the electronation of hydrated protons and formation of neutral hydrogen atoms on the metal surface and is also called the adsorption step. Reaction (5-70) is the desorption step, which does not involve charge transfer and is called the *chemical-desorption* step. A simpler representation of the above mechanism can be obtained by summing Reactions (5-68) and (5-69):

---

[21] The abbreviation for hydrogen evolution reaction is HER.

[22] Since H+ ion reduction is an heterogenous reaction and occurs on the surface, the scientific way of showing the mechanism reactions is to include M as the metal surface in the reactions. For example, for Reaction (5-69), it will be:

$$H_3O^+_{(aq)} + M(e^-) \xrightarrow{rds} MH_{ads} + H_2O_{(l)}$$

$$H^+_{(aq)} + e^- \xrightarrow{rds} H_{ads} \tag{5-71}$$

$$H^+_{(aq)} + H_{ads} + e^- \rightleftarrows H_{2(g)} \tag{5-72}$$

Another desorption reaction has been also proposed, which results in the second mechanism for H^+ ion reduction as follows:

$$H^+_{(aq)} + H_2O_{(l)} \rightleftarrows H_3O^+_{(aq)} \tag{5-73}$$

$$H_3O^+_{(aq)} + e^- \xrightarrow{rds} H_{ads} + H_2O_{(l)} \tag{5-74}$$

$$H_{ads} + H_3O^+_{(aq)} + e^- \rightleftarrows H_{2(g)} + H_2O_{(l)} \tag{5-75}$$

This desorption step, Reaction (5-75), is called the *electrochemical-desorption* step. The two chemical-desorption and the electrochemical-desorption reactions can occur simultaneously. In both mechanisms, the rds step is specified as the adsorption step. However, it is reported that the desorption step can be the rds step instead or even both the adsorption and the desorption steps be the rds step at the same time. This later is called a *dual mechanism* and happens in a certain range of potentials [15]. A comprehensive review of H+ ion reduction mechanism is given by Bockris sand Reddy [15]. If H^+ ion reduction rate is controlled by the rate of charge transfer, the reaction rate is usually related to H^+ ion activity (concentration). Different Tafel slopes and reaction orders with respect to H^+ ion activity (concentration) have been reported for H^+ ion reduction reaction in the literature. Table 5-3 summarized some of these values in solutions with different Cl^- ion concentrations.

The only piece of information that could be found about the effect of Cl^- ion (salt concentration) on H^+ ion reduction was a work done by Vracar and Drazic [171]. They reported that Cl^- ions had an inhibition effect on H^+ ion reduction reaction due to the adsorption of Cl^- ion on the surface and blocking the surface areas required for H^+ ion adsorption and reduction reactions. Their experiments on the surface of an Armco iron electrode in 0.5 mol/lit H_2SO_4 solution showed that the corrosion current density decreased from ~ 2.5e-5 A/cm^2 to ~1.5e-5 A/cm^2 when Cl^- ion concentration was increased from 0.05 M to 0.5 M [171].

No information could be found in the literature on the effect of salt concentration on the H_2O reduction reaction. This effect is investigated in detail in Section 12.1. However, it is worth noting that the contribution of the H_2O reduction reaction in the overall rate of carbon steel corrosion in aqueous solutions is usually negligible.

Table 5-3

A summary of experimental kinetic data for the H^+ reduction reaction in different solutions with different Cl^- concentrations.

#	Conditions	Tafel slope (mV/dec)	n_{H^+}	Ref.
1	xNaCl + yHCl (x + y = 1 N), $0 < pH < 1.8$	N/A	-1	[194]
2	1 N chloride solution, 0.2 N < $[H^+]$ < 3 N, 25°C	110-130	1	[178]
3	6 N chloride solution, 0.14 N < $[H^+]$ < 6.84 N, 25°C	115-140	N/A	[178]
4	xNaCl + yHCl (x + y = 5 M), 10^{-2} M < y < 5 M	115	1.1 ± 0.07	[192]
5	4.9 M NaCl+ 0.1 M $HClO_4$	116	N/A	[192]
6	0.1-3 M $ZnCl_2$ + 0-5 M $CaCl_2$ + 0.01M $FeCl_2$, pH < 2, 0.2 M < $[Cl^-]$ <16 M	90-150, average: 114 ± 11	N/A	[198]

5.2 The Effect of Salt Concentration on Electrochemistry of CO_2 Corrosion

CO_2 is not corrosive itself when it comes to metals. For example, in $CO_{2(g)}$ capture facilities, when metals are exposed to liquid $CO_{2(l)}$, if no water is involved, then corrosion will not occur. However, in the presence of water, CO_2 reacts with water and produces carbonic acid ($H_2CO_{3(aq)}$), which then dissociates and aggravates corrosion. CO_2 aqueous corrosion occurs when a metal (*e.g.,* carbon steel) is exposed to an aqueous solution saturated with CO_2 gas. The overall CO_2 corrosion reaction is given by Reaction (5-76) or Reaction (5-77). The appropriate form of reaction depends on whether iron carbonate saturation (S) is exceeded one or not. Since the scope of this study is only uniform bare steel corrosion, conditions with S above one will not be the focus here. However, the effect of salt concentration on $FeCO_3$ solubility and protectiveness of this layer has been studies elsewhere [201].

$$Fe_{(s)} + CO_{2(g)} + H_2O_{(l)} \rightarrow Fe^{2+}{}_{(aq)} + CO_3^{2-}{}_{(aq)} + H_{2(g)} \tag{5-76}$$

$$Fe_{(s)} + CO_{2(g)} + H_2O_{(l)} \rightarrow FeCO_{3_{(s)}} + H_{2(g)} \tag{5-77}$$

The above reactions consist of two simultaneous electrochemical reactions: anodic (oxidation) and cathodic (reduction). The effect of salt concentration on each will be discussed in the following text.

5.2.1 Salt Concentration Effects on the Anodic Reaction(s) in CO_2 Corrosion

It is reported that the anodic dissolution on iron in CO_2-saturated solutions is the same as that in the strong acid corrosion and is not altered by the presence of $CO_{2(aq)}$ species in the solution [202,203]. In a recent study by Almedia *et al.* [204] at the atmospheric pressure in the presence and absence of CO_2, they demonstrated by electrochemical impedance spectroscopy (EIS) experiments that CO_2 does not act directly in the anodic dissolution of iron. However, they speculated that this conclusion will be different at high CO_2 pressure (*e.g.*, 30 bar) [204]. On the other hand, Nesic *et al.* [205] believed that the anodic dissolution of iron is influenced by the presence of CO_2. They proposed a new set of reactions for the anodic dissolution of iron in CO_2-satuarated aqueous solutions for a pH range of 2.5 to 6.5. They stated that an intermediate species of $FeCO_{2ads}$ forms on the metal surface, similar to $FeOH_{ads}$ mentioned for strong acid corrosion mechanism, and catalyzes the anodic dissolution of iron [205]. However, Wiekowski *et al.* [206] showed with radiotracer analysis that no adsorption of labeled CO_2 was detected on the metal surface in CO_2-containing solutions, contradicting the Nesic *et al.* [205] proposed mechanism. Kahyarian *et al.* [207,208] in a series of experiments on X65 carbon steel in 0.1 M NaCl solutions at 10^{o}C and 30^{o}C, pH 4 and 5, and CO_2 partial pressure pressures of 0 bar, 1 bar, and 5 bars reported that the slight increase in the corrosion rate when pCO_2 was increased from 0 bar to 5 bars was due to the influence of CO_2 on the anodic reaction in the active range. Kahyarian *et al.* [207,208] potentiodynamic sweeps also show accelerations in the anodic Fe dissolution reaction in the active region at both solution pH values of 4 and 5 and both temperatures.

Based on the literature review, some studies stated that CO_2 influences the anodic dissolution reaction of iron, while others claimed that the anodic dissolution of iron is not affected by the presence of CO_2. Since, there is no information on the effect of salt concentration on the anodic dissolution of iron in CO_2 corrosion, it is assumed here that the effect will be the same as that for strong acid corrosion discussed earlier. However, this subject will be investigated more when strong acid corrosion and CO_2 corrosion are compared in Section 10.1.4.

5.2.2 Salt Concentration Effects on the Cathodic Reaction in CO_2 Corrosion

Three reactions have been considered in the literature [96] as the cathodic reactions for CO_2 aqueous corrosion:

$$2H^{+}_{(aq)} + 2e^{-} \rightleftarrows H_{2(g)} \tag{5-78}$$

$$2H_2CO_{3(aq)} + 2e^{-} \rightleftarrows H_{2(g)} + 2HCO^{-}_{3(aq)} \tag{5-79}$$

$$2H_2O_{(l)} + 2e^{-} \rightleftarrows H_{2(g)} + 2OH^{-}_{(aq)} \tag{5-80}$$

Reactions (5-78) and (5-80) are the same as those for strong acid corrosion. Reaction (5-79), called *direct direction of carbonic acid,* was proposed to justify the larger limiting current density, and therefore, the higher corrosion rates seen in CO_2 corrosion compared to those in strong acid corrosion under similar conditions [209–212]. However, recent studies [208,213–215] have shown that the direct reduction of carbonic acid (Reaction (5-79)) does not happen and that the main contribution of carbonic acid to the overall CO_2 corrosion process is by being a source of H^+ ions, for H^+ ion reduction reaction (Reaction (5-78)). This is called the *buffering effect*. Hence, similar to strong acid corrosion the main cathodic reaction in CO_2-saturated solutions is H^+ ion reduction reaction. This implies that the effect of salt concentration on the cathodic reaction in CO_2 corrosion should be analogous to that in strong acid corrosion, which is expected to be a retardation due to the adsorption of Cl^- ions on the metal surface.

In the CO_2 corrosion process, the water reduction (Reaction (5-80)) becomes practically important only at $P_{CO_2} << 1$ bar and pH > 5 [200]. This indicates that water reduction is not prominent at $P_{CO_2} \approx 1$ bar, what is usually seen in real field conditions.

5.3 The Effect of Salt Concentration on Electrochemistry of H_2S Corrosion

The overall reaction for aqueous H_2S corrosion is given by Reactions (5-81) or (5-82). Theoretically, depending on the iron sulfide saturation level, for $S_{FeS} > 1$, Reaction (5-81) is more probable, whereas for $S_{FeS} < 1$, Reaction (5-82) is more likely to occur. However, the corrosion rate data have shown that the corrosion rate decreases as soon as the metal surface is exposed to $H_2S_{(aq)}$ and the reason for that is believed to be the formation of an FeS layer in an order of milliseconds (usually mackinawite) on the metal surface [49,216–218]. This means that considering Reaction (5-82) as the overall reaction for aqueous H_2S corrosion is more sensible.

$$Fe_{(s)} + H_2S_{(aq)} \rightleftarrows Fe^{2+}_{(aq)} + H_{2(g)} + S^{2-}_{(aq)} \tag{5-81}$$

$$Fe_{(s)} + H_2S_{(aq)} \rightleftarrows FeS_{(s)} + H_{2(g)} \tag{5-82}$$

Resembling CO_2 corrosion, two simultaneous electrochemical reactions: anodic (oxidation) and cathodic (reduction) result in the above overall reactions. The effect of salt concentration on each will be reviewed in the following text.

5.3.1 Salt Concentration Effects on the Anodic Reaction(s) in H_2S Corrosion

In analogy to CO_2 corrosion, the anodic dissolution of iron in H2S corrosion can be assumed the same as that in strong acid corrosion with the overall anodic reaction to be Reaction (5-24). Strong evidence for this assumption is given in a work done by Morris et al. at 25°C, pH 4, 0.2 M NaCl solution, using an iron RDE setup in a range of partial pressure of H2S from 10-4 atm to 1 atm. They showed in their potentiodynamic sweeps that increasing partial pressure of H2S did not change the iron exchange current density as well the Tafel slope. Another research by Zheng [49] at 30oC, pH values of 4 an 5, with X65 carbon steel RCE specimens in a range of H2S partial pressure of 0% to 10%23 showed almost no change in the anodic sweep with respect to partial pressure of H2S. These pieces of evidence support the assumption that the presence of H2S does not change the iron dissolution mechanism [219]. However, other pathways than those mentioned in Section 3.1.1 have been proposed for anodic dissolution of iron in H2S-bearing solutions. These pathways can be categorized into two general groups: electrochemical and non-electrochemical reaction mechanisms. The electrochemical mechanisms involve electron transfer, while the non-electrochemical reaction mechanisms are ordinary chemical reactions.

Ogundele and White [220] suggested an alternative pathway for the dissolution of iron in aqueous solutions containing H_2S by the following reactions:

$$Fe + HS^- \rightleftarrows (FeHS^-)_{ads} \tag{5-83}$$

$$(FeHS^-)_{ads} \xrightarrow{rds} FeHS^+ + 2e^- \tag{5-84}$$

$$FeHS^+ \rightleftarrows Fe^{2+} + HS^- \tag{5-85}$$

The second step was considered as the rds. $(FeHS^-)_{ads}$ is an intermediate species which acts as a catalyst in the H_2S iron dissolution mechanism.

---

[23] The percent is in the gas phase. Five partial pressures of 0%, 10^{-4}%, 10^{-3}%, 10^{-2}%, 10% were tested.

Another electrochemical mechanism supported by several research [221–224] is as follows:

$$Fe + H_2S + H_2O \rightleftarrows (FeHS^-)_{ads} + H_3O^+ \tag{5-86}$$

$$(FeHS^-)_{ads} \xrightarrow{rds} Fe(SH)_{ads} + e^- \tag{5-87}$$

$$Fe(SH)_{ads} \rightleftarrows FeSH^+{}_{ads} + e^- \tag{5-88}$$

Reaction (5-86) is a chemisorption process and $(FeHS^-)_{ads}$ is considered as a catalyst adsopbed on the iron surface, which then transforms to $FeSH^+{}_{ads}$. Reactions (5-87) and (5-88) correspond to the anodic discharge process (desorption). The product, $FeSH^+{}_{ads}$, may be incorporated directly into a growing layer of mackinawite (Reaction (5-89)) or it may be hydrolyzed to yield ferrous iron (Reaction (5-90)).

$$FeSH^+{}_{ads} \rightleftarrows FeS_{1-x} + xHS^- + \ (1-x)H^+ \tag{5-89}$$

$$FeSH^+{}_{ads} + H_3O^+ \rightleftarrows Fe^{2+} + H_2S + H_2O \tag{5-90}$$

Based on both mechanisms, the anodic dissolution of iron accelerates in the presence of $H_2S_{(aq)}$.

The non-electrochemical reaction mechanism, also called *direct reaction* or *solid-state reaction*, was proposed by Shoesmith *et al.* [225]. In this mechanism, H_2S can directly adsorb on the iron surface exposed to aqueous H_2S solution to form an iron sulfide (mackinawite) layer on the surface, as shown in Reaction (5-82). However, Zheng [49] argued that the experimental evidence increasingly points to the electrochemical nature of H_2S corrosion.

To the best knowledge of author, there is no information in the open literature on the effect of salt concentration on the anodic dissolution of iron in H_2S-containing solutions. Based on the discussion presented above, the mechanism of iron dissolution is considerd to be similar to that presented for strong acid corrosion.

5.3.2 Salt Concentration Effects on the Cathodic Reaction in H_2S Corrosion

Three reactions have been considered in the literature [226,219,225,227,49] as the cathodic reactions for H_2S aqueous corrosion:

$$2H^+_{(aq)} + 2e^- \rightleftarrows H_{2(g)} \tag{5-91}$$

$$2H_2S_{(aq)} + 2e^- \rightleftarrows H_{2(g)} + 2HS^-_{(aq)} \tag{5-92}$$

$$2H_2O_{(l)} + 2e^- \rightleftarrows H_{2(g)} + 2OH^-_{(aq)} \tag{5-93}$$

Reactions (5-91) has been already discussed in Section 5.1.2 and it is assumed that the mechanism of H^+ ion reduction in H_2S-containing solutions remains the same as that in strong acid solutions. Similar to CO_2 corrosion, water reduction reaction (Reaction (5-93)) comes into effect in the overall cathodic reaction rate at p_{H_2S} << 1 bar and pH > 5. For Reaction (5-92), which is called the *direct reduction of H_2S*, there is an ongoing debate about the occurrence of this reaction in aqueous H_2S corrosion. Over the last five decades, the direct reduction of H_2S has been considered as one of the cathodic reactions in aqueous H_2S corrosion of iron (or carbon steel). Bolmer [226] was the first who introduced the idea of another cathodic reaction in aqueous H_2S corrosion based on the observed increase in the cathodic current density in the presence of $H_2S_{(aq)}$. Bolmer [226] potentiodynamic results shows that at higher partial pressures of H_2S, both the charge-transfer controlled, and the mass transfer controlled limiting current densities becomes larger[24]. Since then several research have been published all in the support of direct

---

[24] At a constant pressure.

reduction of H_2S [225,227–229]. Morris *et al.* [219] reported a higher limiting current density by a factor of ~ 1.3 at pH 2.1 and p_{H_2S} of 0.19 atm compared to that in H_2S-free system. They attributed this to the direct reduction of H_2S. They also observed an acceleration in the charge-transfer portion of their sweep with higher partial pressure of H_2S [219]. However, they related that the fluctuations due to the electrode hydrogen preconditioning [219]. Kittel *et al.* [227] in a systematic study showed that both rates of charge-transfer and mass transfer (limiting current density) portions of the potentiodynamic sweeps on stainless steel electrodes at pH 6 increased with increasing partial pressure of H_2S. They claimed that without the direct reduction of H_2S the acceleration in the cathodic current density cannot be explained [227]. Recently, Kahyarian and Nesic [230] argued the direct reduction of H_2S is not significant in aqueous H_2S corrosion and H^+ ion reduction reaction is the only dominant cathodic reaction. They stated that similar to the role H_2CO_3 in CO_2 corrosion, $H_2S_{(aq)}$ has a buffering effect and plays as an extra source of H^+ ion for the H^+ ion reduction reaction. Thus, the cathodic reaction rate in the presence of H_2S is larger than that in strong acid corrosion under identical conditions. They reasoned that the second hump (wave), which is observed in potentiodynamic sweeps in the limiting current density region at low solution pH values (pH < 3) in aqueous H_2S corrosion is when the H_2S buffering effect kicks in, rather than to be the limiting current density for direct reduction of $H_2S_{(aq)}$. However, they did not support their argument with any experimental measurements, nor justified the accelerations measured by Bolmer [226], Morris *et al.* [219], and Kittel et al.

[227] in the charge transfer portion of the potentiodynamic sweep due to the presence of $H_2S_{(aq)}$.

In this study, the direct reduction of H_2S is considered insignificant in aqueous H_2S corrosion. Therefore, the H^+ ion reduction reaction is the only dominant cathodic reaction in aqueous H_2S corrosion. As far as this author knows, there is no information available in the literature on the effect of salt concentration on the cathodic reactions in H_2S corrosion.

Chapter 6: Motivation, Hypotheses, and Objectives

6.1 Motivations

The literature review presented above shows that the effect of salt concentration on uniform strong acid, CO_2 and H_2S corrosion is a very broad and complex subject that requires information from transport phenomena, thermodynamics of speciation equilibria and electrochemistry. Additionally, it shows that there is little information about the role of salt concentration on mechanisms and rates of uniform strong acid and CO_2 corrosion, while there is no information about that for uniform H_2S corrosion. The existing information is sometimes unreliable, often even contradictory, and insufficient for practical applications such as corrosion rate prediction. Finally, the existing corrosion rate prediction models are mostly applicable to very low salt concentrations, <3 wt.%, and those supposedly intended for high salt concentrations are either empirical models or they have only included the effect of salt concentration on density, viscosity, gas solubility, and solution chemistry in a very rudimentary form.

6.2 Hypotheses

It is anticipated that salt concentration influences the aqueous uniform strong acid, CO_2 and H_2S corrosion processes by changing:

- Solution density
- Solution viscosity
- Diffusion coefficients of dissolved species
- Solubility of CO_2 and H_2S in the solution

- The equilibrium activity coefficients and concentrations of corrosive species such as H^+ ion, $H_2CO_{3(aq)}$, and $H_2S_{(aq)}$.
- The rates and mechanisms of the H^+ ion reduction and the Fe dissolution reactions.

6.3 Objectives

The following research objectives are defined for this study:

- Based on the hypotheses, gather all required information for studying the effect of salt concentration on uniform strong acid, CO_2, and H_2S corrosion.
- Compile all segments of information, understand how each parameter influences the uniform strong acid, CO_2, and H_2S corrosion process, and finally try to connect them theoretically in a coherent manner.
- Understand the role of salt concentration on the mechanisms of electrochemical reactions underlying strong acid, CO_2 and H_2S corrosion by performing corrosion rate and electrochemical experiments.
- Reproduce or develop models valid for a wide range of salt concentrations for each parameter listed in the hypotheses.
- Develop a comprehensive corrosion rate prediction model for concentrated salt solutions by assembling all the models produced in the previous objective.
- Compare the final corrosion rate model predictions with the obtained experimental data.

Chapter 7: Thermodynamic Models for $CO_{2(g)}$ and $H_2S_{(g)}$ Solubility in Aqueous NaCl Solutions

In this chapter, the focus is the thermodynamic models which have been adopted in this study for calculating CO_2 and H_2S solubility in aqueous NaCl solutions. With the help of these models the effect of salt concentration on CO_2 and H_2S solubility (salting out effect) can be quantified.

7.1 The Effect of Salt Concentration on Solubility of CO_2 Gas

There are numerous models available in the open literature for calculating CO_2 solubility in aqueous NaCl solutions. The first group of models are simple models that correlate the CO_2 Henry's law constant to ionic strength [231–236] without considering the interactions between $CO_{2(aq)}$ molecules and salt ions. The second group of CO_2 solubility models are more advanced than the first group due to the consideration of the interactions between CO_2 molecules with salt ions. Some of these models are listed in the open literature [30,134,237]. The difference among these advanced models is mostly related to their range of validity, in their underlying approach, or their ability to calculate H_2O solubility in the CO_2-rich phase. Two approaches are usually used for the vapor-liquid equilibrium calculations in the second group models: gamma-phi (γ-φ) and phi-phi () [123,238]). The equilibrium condition in approach is $x^g_{CO_2}\varphi^g_{CO_2}P = x^l_{CO_2}\gamma^l_{CO_2}f^o_{CO_2}$ and in approach is $x^l_{CO_2}\varphi^l_{CO_2}P = x^g_{CO_2}\varphi^g_{CO_2}P$. Each parameter is defined in the footnote[25][123]. The γ-φ approach is the traditional method for solving low-pressure

---

[25] x is the mole fraction, g and l denote gas and liquid phases, φ is fugacity coefficient, γ is activity coefficient, $f^o_{CO_2}$ is the fugacity (unit of pressure) of pure CO_2 in standard-state, P is total pressure. At low pressures, the standard-state fugacity can be ignored.

vapor-liquid equilibria. In this approach, an equation of state (EOS) is used to describe the non-ideality of the gas-rich phase and the Henry's law or an excess Gibbs free energy (G^E) is used to determine the non-ideality of the H_2O-rich phase [239]. The γ-φ approach is more flexible to integration with the speciation and chemical equilibrium calculations [240]. The φ- φ approach is more general because it can handle the transition from subcritical to supercritical condition and it is applicable to high pressure, but it is computationally more complicated. The φ- φ approach works well when an accurate PvTx EOS be available for all phases [123,240]. Therefore, for corrosion studies in aqueous solutions for which the working pressure does not go more than 100 bar, the solubility models based on the γ-φ approach should be sufficient.

Three CO_2 solubility models from the first group: the Oddo and Tomson model [232], the Battistelli model [235], and the Dubessy *et al.* model [236], and two CO_2 solubility models from the second group: the Mao *et al.* model [30] and the Springer *et al.* model [241] are reproduced in this work. The Springer *et al.* model [241] is a comprehensive solution chemistry model that allows the calculation of equilibrium concentrations and activity coefficients of all dissolved species, including $CO_{2(aq)}$ and $H_2S_{(aq)}$. The first four models will be explained in this section and the Springer *et al.* [241] model will be explained in Section 8.3.1.

7.1.1 The Oddo and Tomson CO_2 Solubility Model

The Oddo and Tomson model [232] is an empirical model originally developed for the calculation of $CaCO_3$ saturation and scaling tendency in concentrated salt solutions. The required inputs for this model are temperature, total pressure, and NaCl concentration. The validity range of the Oddo and Tomson model [232] is reported to be for temperatures between 25°C to 250°C, pressures between 1 to 1200 bar, ionic strengths between and 0 to 4 M. An equation for the CO_2 Henry's law constant is proposed in the Oddo and Tomson model [232] as a function of temperature and ionic strength as follows:

$$H^{cp}\left(T_f, I_M\right) = \frac{14.5}{1.00258} \times 10^{-\left(2.27+5.65e-3T_f-8.06e-6T_f^2+0.075I_M\right)} \tag{7-1}$$

where, H^{cp} is the CO_2 Henry's law solubility constant[26] in salt solution in M/bar, T_f is the solution temperature in °F, and I_M is the solution ionic strength in M. The constant in the form of a fraction in Equation (7-1) is for unit conversion from psi to bar as well as excluding free $H_2CO_{3(aq)}$ from the total amount of dissolved $CO_{2(aq)}$. The CO_2 solubility ($c_{CO_{2(aq)}}$) can be obtained using H^{cp}:

$$p_{CO_2} = y_{CO_2} \cdot P \tag{7-2}$$

$$f_{CO_2} = \varphi_{CO_2}^{Pure} \cdot p_{CO_2} \tag{7-3}$$

$$c_{CO_{2(aq)}} = H^{cp} \cdot f_{CO_2} \tag{7-4}$$

where, f_{CO_2} is the $CO_{2(g)}$ fugacity in bar, p_{CO_2} is the partial pressure of $CO_{2(g)}$ in bar, $y_{CO_{2(g)}}$ is the mole fraction of $CO_{2(g)}$ in the gas phase, $\varphi_{CO_2}^{Pure}$ is the fugacity coefficient[27] of pure $CO_{2(g)}$ in the gas phase, and P is total pressure in bar. y_{CO_2} can be calculated using equation below:

---

[26] The naming and unit conversion for the Henry's law solubility (H) and volatility (K) constants are taken from Sander's publication [242].

[27] The fugacity coefficient of gas takes into account the non-ideality in the gas phase. The deviation of fugacity coefficient from unity is significant at high pressures.

$$y_{CO_2} = \frac{P - p_{H_2O}}{P} \tag{7-5}$$

p_{H_2O} is water vapor ($H_2O_{(g)}$) pressure in bar and can be obtained from a model by Atkinson [128] mentioned in Appendix H. The Atkinson model [128] is advantageous over other water vapor calculation models because it considers the effect of NaCl concentration on p_{H_2O}. $\varphi_{CO_2}^{Pure}$ is calculated by using an equation of state proposed by Duan *et al.* [243]. The calculation procedure for $\varphi_{CO_2}^{Pure}$ is explained in Appendix J. The original Oddo and Tomson model [232] uses p_{CO_2} instead of f_{CO_2} in Equation (7-4). In this study, the fugacity coefficient is added to the model to improve the accuracy of the Oddo and Tomson model [232] at high pressures.

7.1.2 The Battistelli et al. CO_2 Solubility Model

The Battistelli *et al.* model [235] is an empirical model for H_2O-NaCl-CO_2 mixtures that considers the effect salt on CO_2 solubility by modifying the $CO_{2(g)}$ Henry's law constant in pure water with a coefficient called "salting-out" coefficient. The modified Henry's law constant is calculated as:

$$K_H^{px,b}(T, m_{NaCl}) = K_H^{px,w}(T) \times 10^{m_{NaCl} k_b(T)} \tag{7-6}$$

where, $K_H^{px,w}$ and $K_H^{px,b}$ are Henry's law volatility constants for pure water and NaCl aqueous solutions, respectively, in Pa, k_b is the salting-out coefficient in kgH_2O/mol, T is the solution temperature in K, m_{NaCl} is the molality concentration of NaCl in the solution. In the literature, the form of Equation (7-6) is the famous Setschenow equation [244,245]. K_H^w and k_b are obtained by using the following equations:

$$K_H^{px,w}(T) = \sum_{i=1}^{6} B(i)T^{i-1} \tag{7-7}$$

$$k_b(T) = \sum_{i=1}^{5} C(i)T^{i-1} \tag{7-8}$$

where, B and C coefficients are listed in Table 7-1. To calculate CO_2 solubility, $K_H^{px,b}$ is divided by the partial pressure of CO_2 in the gas phase (p_{CO_2})[28]:

$$x_{CO_{2(aq)}} = \frac{K_H^{px,b}}{p_{CO_2}} \tag{7-9}$$

p_{CO_2} can be calculated using equation (7-5). The mole fraction of CO_2 in the liquid phase ($x_{CO_{2(aq)}}$) can be converted to the molality concentration of CO_2 in the liquid phase ($x_{CO_{2(aq)}}$), using the following equation:

$$m_{CO_{2(aq)}} = \frac{x_{CO_{2(aq)}}}{1 - x_{CO_{2(aq)}}}\left(m_{NaCl} + \frac{1000}{M_w}\right) \tag{7-10}$$

M_w is the molecular weight of water in g/mol. Battistelli *et al.* [235] claimed that their model is valid from 0°C to 300°C and NaCl concentrations up to 4.87 m.

---

[28] p_{CO_2} is usually reported in atm or bar. Therefore, $K_h^{px,b}$ needs to be converted from Pa to the appropriate unit before calculating $x_{CO_{2(aq)}}$.

Table 7-1

Coefficients used in Equations (7-7) and (7-8) for calculating the $CO_{2(g)}$ Henry's law volatility constant for pure water and the salting-out coefficient.

i	B	C
1	7.83666e7	1.19784e-1
2	1.96025e6	-7.17823e-4
3	8.20574e4	4.93854e-6
4	-7.40674e2	-1.03826e-8
5	2.18380	1.08233e-11
6	-2.20999e-3	N/A

7.1.3 The Dubessy et al. CO_2 Solubility Model

The Dubessy *et al.* solubility model [236] is an empirical vapor-liquid equilibrium model for aqueous NaCl solutions valid in the temperature range of 50°C to 270°C and NaCl concentrations up to 6 m. The dependency of CO_2 solubility on NaCl concentration is modeled in the Dubessy *et al.* model [236] by correlating the CO_2 Henry's law constant in aqueous NaCl solution and in pure water with polynomial terms as functions of temperature and NaCl concentration. Their proposed equation is given below:

$$\begin{aligned} log K_H^{px,b}(T, m_{NaCl}) \\ &= log K_H^{px,w}(T) + \beta_1(T) m_{NaCl} + \beta_2(T) m_{NaCl}^2 \\ &+ \beta_3(T) m_{NaCl}^3 \end{aligned} \quad (7\text{-}11)$$

where $K_H^{px,w}$ and $K_H^{px,b}$ are in bar, T is in K, and β_i are fit coefficients expressed in the following form:

$$\beta_i(T) = \sum_{j=1}^{5} a_{ij} \times T^{j-1} \tag{7-12}$$

The a_{ij} coefficients are listed in Table 7-2. Dubessy *et al.* [236] used the equation proposed by Harvey [246] for calculating $K_H^{px,w}$. This equation is presented below:

$$lnK_H^{px,w} = lnp_w - \frac{9.4234}{T_r} + \frac{4.0087(1-T_r)^{0.355}}{T_r} + 10.3199{T_r}^{-0.41}\exp(1-T_r) \tag{7-13}$$

where, p_w is the water vapor pressure in bar and T_r is the reduced temperature for water ($T_r = \frac{T}{T_c}$ and $T_c = 647.14$ K) [246]. p_w can be estimated using the Atkinson model [128] described in Appendix H. When $K_H^{px,b}$ is calculated, the CO_2 solubility in molality can be obtained following Equations (7-9) and (7-10).

Table 7-2

The a_{ij} coefficients used in Equation (7-12) for calculating the effect of NaCl concentration on Henry's law volatility constant in H_2O-NaCl-CO_2 mixtures [236].

j	a_{1j}	a_{2j}	a_{3j}
1	3.114712456	-2.05637458	0.253424331
2	-2.7655585e-2	2.081980200e-2	-0.26047432e-2
3	0.9176713976e-4	-0.765857702e-4	0.0972580216e-4

4	-12.78795941e-8	12.011325315e-8	-1.551654794e-8
5	6.2704268351e-11	-6.790343083e-11	0.8948557284e-11

7.1.4 The Mao et al. CO_2 Solubility Model

Now that three models from the first group for CO_2 solubility in aqueous salt solutions have been explained, a model from the second group will be describe here. The Mao *et al.* model [30] is an updated version of the Li and Duan model [126], which is one of most eminent CO_2 solubility model in the literature. The Mao *et al.* model [30] is an empirical $\gamma - \varphi$ vapor-liquid equilibrium model, which relies on exhaustive set of experimental data from the literature. Zhao *et al.* [237] reported that the Mao *et al.* model [30] is in excellent agreement with the experimental CO_2 solubility in aqueous NaCl solution with an average absolute deviation of 2.09% from experimental data. The Mao *et al.* model [30] is valid from 0°C to 500°C, from 1 bar to 1000 bar, and from 0 to 4.5 mol/kgH_2O (~ 21 wt.%) of NaCl. The equation and parameters required to reproduce the Mao *et al.* model [30] will be presented below.

The basis of the Mao *et al.* model [30] is the balance between the chemical potential of CO_2 in the gas phase ($\mu^{g}_{CO_2}$) and that in the liquid phase ($\mu^{l}_{CO_2}$). The chemical potential can be expressed in terms of fugacity for the gas phase and activity for the liquid phase as follows:

$$\mu^{g}_{CO}(T, P, y_{CO}) = \mu^{g(o)}_{CO}(T) + RT ln f_{CO}(T, P, y_{CO}) \tag{7-14}$$

$$= \mu_{CO_2}^{g(o)}(T) + RTlny_{CO_2}P + RTln\varphi_{CO_2}^{Pure}(T,P)$$

$$+ RTln\gamma_{CO_2}^{g}\left(T,P,y_{CO_2}\right)$$

$$\mu_{CO_2}^{l}(T,P,m_{NaCl}) = \mu_{CO_2}^{l(o)}(T,P) + RTlna_{CO_2}(T,P,m_{NaCl}) \qquad (7\text{-}15)$$

$$= \mu_{CO_2}^{l(o)}(T,P) + RTlnm_{CO_2}$$

$$+ RTln\gamma_{CO_2}^{l}(T,P,m_{NaCl})$$

where, $\mu_{CO_2}^{g(o)}$ is the standard chemical potential of $CO_{2(g)}$ in the gas phase in J/mol and defined as the hypothetical ideal gas chemical potential at total pressure of 1 bar [30], and $\mu_{CO_2}^{l(o)}$ is the standard chemical potential of $CO_{2(aq)}$ in the liquid phase in J/mol and defined as the chemical potential in a hypothetically ideal solution of unit molality. f_{CO_2} is the fugacity of $CO_{2(g)}$ in the gas phase, y_{CO_2} is the mole fraction of $CO_{2(g)}$ in the gas phase, φ_{CO_2} is the fugacity coefficient of $CO_{2(g)}$ in the gas phase (mixture of $CO_{2(g)}$ and $H_2O_{(g)}$), $\varphi_{CO_2}^{Pure}$ is the fugacity coefficient of pure $CO_{2(g)}$ (assuming only $CO_{2(g)}$ in the gas phase), and $\gamma_{CO_2}^{g}$ is the activity coefficient of $CO_{2(g)}$ in the gas phase. In the liquid phase, a_{CO_2} is the activity of $CO_{2(aq)}$ and $\gamma_{CO_2}^{l}$ is the activity coefficient of $CO_{2(aq)}$. T is solution temperature in K, P is total pressure above the solution in bar, and m_{NaCl} is the concentration of NaCl in the solution in mol/kgH_2O.

The vapor-liquid equilibrium is reached when $\mu_{CO_2}^{g} = \mu_{CO_2}^{l}$. Therefore, Equations (7-14) and (7-15) are set equal and after some simplifications the following equation is obtained:

$$ln\frac{y_{CO_2}P}{m_{CO_2}} = \frac{\mu_{CO_2}^{l(o)}(T,P) - \mu_{CO_2}^{g(o)}(T)}{RT} - ln\gamma_{CO_2}^{g}\left(T,P,y_{CO_2}\right) - ln\varphi_{CO_2}^{Pure}(T,P) + ln\gamma_{CO_2}^{l}(T,P,m_{NaCl}) \tag{7-16}$$

$\mu_{CO_2}^{g(o)}$ is considered zero in the Mao *et al.* model for simplifying the parametrization of variables needed to calculate CO_2 solubility. This assumption does not influence the results as the difference between $\mu_{CO_2}^{l(o)}$ and $\mu_{CO_2}^{g(o)}$ is important.

In the Mao *et al.* model [30], the interaction between CO_2 and H_2O molecules in the gas phase is accounted for in terms of $\gamma_{CO_2}^{g}$. However, $\gamma_{CO_2}^{g}$ is not calculated separately in this model, rather it is grouped with the chemical potential difference term in Equation (7-16), which is then obtained by fitting it to the experimental results. In contrast, this interaction between gas molecules in a gas mixture is often accounted for in the literature by employing different mixing rules such as the ideal mixing rule [243,247] or the quadratic mixing rule [248]. The quadratic mixing rule will be used in the Springer *et al.* [241] speciation model discussed in Section 8.3.1.

$\gamma_{CO_2}^{l}$ in Equation (7-16) can be calculated using a virial expansion of the excess Gibbs free energy [143]:

$$ln\gamma_{CO_2}^{l} = \sum_{c} 2\lambda_{CO_2-c}m_c + \sum_{a} 2\lambda_{CO_2-a}m_a + \sum_{c}\sum_{a} \xi_{CO_2-c-a}\, m_c m_a \tag{7-17}$$

where, m_c and m_a are the molality concentrations of cation c and anion a, respectively; λ and ξ are the second-order and third-order virial coefficients, respectively, representing the interactions between ions ($Na^+_{(aq)}$ and $Cl^-_{(aq)}$) themselves, and with and neutral species ($CO_{2(aq)}$). The summations are over all the species dissolved in the solution. In the Mao *et al.* model [30], the dissociation of $CO_{2(aq)}$ in water and dissociation of water are considered to be negligible, which are acceptable assumptions because the first and the second dissociation equilibrium constants for $CO_{2(aq)}$ and the dissociation equilibrium constant for $H_2O_{(l)}$ are very small (of the order of 10^{-7} and 10^{-11} for $CO_{2(aq)}$ and 10^{-14} for water at 25^{o}C and 1 bar). Therefore, the interactions between $HCO_3{}^-{}_{(aq)}$, $CO_3{}^{2-}{}_{(aq)}$, $H^+_{(aq)}$, $OH^-_{(aq)}$ with $CO_{2(aq)}$ are ignored in the Mao *et al.* model [30]. Therefore, Equation (7-17) can be reduced to:

$$ln\gamma^l_{CO_2} = 2\lambda_{CO_2-Na}m_{Na} + 2\lambda_{CO_2-cl}m_{cl} + \xi_{CO_2-Na-Cl}m_{Na}m_{Cl} \qquad (7\text{-}18)$$

The activity coefficient of $CO_{2(aq)}$ can be calculated by using Equation (7-18). It should be noted that the interaction between CO_2 molecules with each other ($\lambda_{CO_2-CO_2}$) is neglected by Mao *et al.* [30] in Equation (7-18). However, this type of interaction is considered in the Li and Duan speciation model [136,249], which is explained in Section 8.1.3. The molality-based activity coefficient of $CO_{2(aq)}$ ($\gamma^m_{CO_2}$) at 25^{o}C, 1 bar total pressure, and 4.28 m (20 wt.%) NaCl is 2.2703 when the interactions between $CO_{2(aq)}$ molecules are not considered in the calculations. However, at the same conditions, $\gamma^m_{CO_2}$ is 2.32 when the interactions between $CO_{2(aq)}$ molecules are included in the calculations.

For the H_2O-NaCl-CO_2 system, considering that NaCl is a 1:1 salt, m_{Na}= m_{Cl} = m_{NaCl}. Plugging Equation (7-18) into Equation (7-16) gives:

$$ln\frac{y_{CO_2}P}{m_{CO_2}} = \frac{\mu_{CO_2}^{l(0)}(T,P)}{RT} - ln\gamma_{CO_2}^{g}(T,P,y_{CO_2}) - ln\varphi_{CO_2}^{Pure}(T,P) + 2\lambda_{CO_2-Na}m_{Na} + 2\lambda_{CO_2-cl}m_{cl} + \xi_{CO_2-Na-Cl}m_{Na}m_{Cl} \qquad (7\text{-}19)$$

To satisfy the electroneutrality law in the solution, Duan *et al.* [126,250] concluded that one of the variables ($\frac{\mu_{CO_2}^{l(0)}}{RT} - ln\gamma_{CO_2}^{g}\lambda_{CO_2-Na}$, λ_{CO_2-cl}, or $\xi_{CO_2-Na-Cl}$) in Equation (7-19) must be set to zero. That variable is λ_{CO_2-Cl} [126,250]. The remaining variables are obtained by fitting the experimental results with an equation proposed by Mao *et al.* [30] as below:

$$Par(T,P) = c_1 + c_2T + \frac{c_3}{T} + c_4T^2 + \frac{c_5}{T^2} + c_6P + c_7PT + \frac{c_8P}{T} + c_9PT^2 + c_{10}P^2T + c_{11}P^3 \qquad (7\text{-}20)$$

$\frac{\mu_{CO_2}^{l(0)}}{RT} - ln\gamma_{CO_2}^{g}$s parameterized by fitting Equation (7-20) with experimental solubility data of CO_2 in pure water. λ_{CO_2-Na} and $\xi_{CO_2-Na-Cl}$ are obtained simultaneously by matching the experimental CO_2 solubility data in aqueous NaCl solutions. The c coefficients in Equation (7-20) are listed in Table 7-3. It should be noted that all the variables on the right-hand side of Equation (7-20) are a function of T and P, except $\gamma_{CO_2}^{g}$, which is a function of y_{CO_2} in addition to T and P. This dependency of $\gamma_{CO_2}^{g}$ on the composition of the gas mixture in the gas phase has been ignored in the Mao et al. model, which is an acceptable assumption at temperatures below 100°C [251].

After all, by introducing the calculated variables from Equation (7-20) and $\varphi_{CO_2}^{Pure}$ into Equation (7-19), the CO_2 solubility in molality units can be obtained.

Table 7-3

Coefficients used in Equation (7-20) for calculating the parameters required for CO_2 solubility estimation in aqueous NaCl solutions. The coefficients are valid for a temperature range of $273.15 \leq T \leq 503^{*}$.

Coefficients	$\frac{\mu^{l(0)}_{CO_2}}{RT} - ln\gamma^{g}_{CO_2}$	$\lambda_{CO_2-Na}{}^{\dagger}$	$\xi_{CO_2-Na-Cl}{}^{\dagger}$
c_1	0.23018254e2	-0.31312239	0.34096802e-2
c_2	-0.36540569e-1	0.55326470e-3	-0.27671084e-4
c_3	-0.18366895e4	0.75844401e2	0
c_4	0.20330876e-4	0	0
c_5	-0.39072384e6	0	0
c_6	-0.58269326e-1	-0.18950519e-3	0
c_7	0.15061716e-3	0.71628762e-6	-0.83847525e-7
c_8	0.78086969e1	0	0
c_9	-0.13013307e-6	0	0
c_{10}	0.11145375e-8	-0.14585720e-9	0.34225403e-10
c_{11}	-0.13073985e-9	0	0

[*] For temperatures greater than 503 K, readers can refer to the original publication [30].
[†] The units for λ and ξ are kgH_2O/mol and $(kgH_2O/mol)^2$, respectively.

7.1.5 Quantification of Salting Out of CO_2 and Comparison of CO_2 Solubility Models

Figure 7-1 compares CO_2 solubility models at different temperatures and atmospheric, moderate, and high pressures. All the models are reproduced for this work except the Zhao *et al.* model [237]. The data for the Zhao *et al.* model [237] are taken from their publication and an online version of the model which is currently unavailable. The salting out effect is captured by all six models. The Mao *et al.* [30], the Zhao *et al.* [237], and the Springer *et al.* [241] models in which interspecies interactions are included behave almost the same for all three conditions over the entire range of NaCl concentrations. The Oddo and Tomson model [232] overpredicts considerably in all three cases, and thereby, it is not recommended. The Dubessy *et al.* model [236] shows acceptable predictions at low and moderate pressures. However, it overpredicts CO_2 solubility at high pressures. The Battistelli *et al.* model [235] slightly underpredicts CO_2 solubility at low and moderate pressures. The Battistelli *et al.* model [235] performs better than the Dubessy *et al.* model [236] at high pressures. In summary, the interspecies interaction-based models are more accurate that the ionic strength-based models. However, they are more complex to reproduce. In case simplicity is more important than the accuracy, the Dubessy *et al.* model [236] is suggested to be used for pressures below 70 bar and the Battistelli *et al.* model [235] for pressures above 70 bar.

Figure 7-1

Comparison of CO_2 solubility models in aqueous NaCl solutions at (A) 25°C and 1 bar and (B) 50°C and 150 bar. Pressures are total pressure. The Dubessy et al. model [236] *is not supposed to be used for temperatures below 50°C. The measurements are taken from* [237,252]

(A)

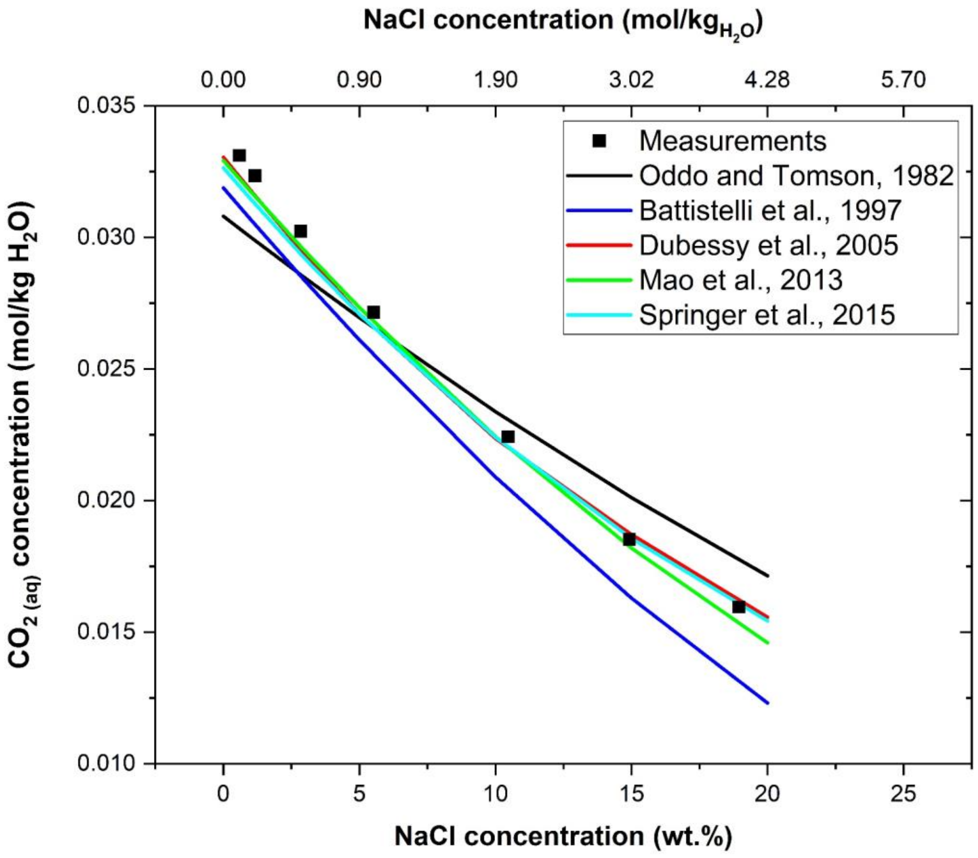

(B)

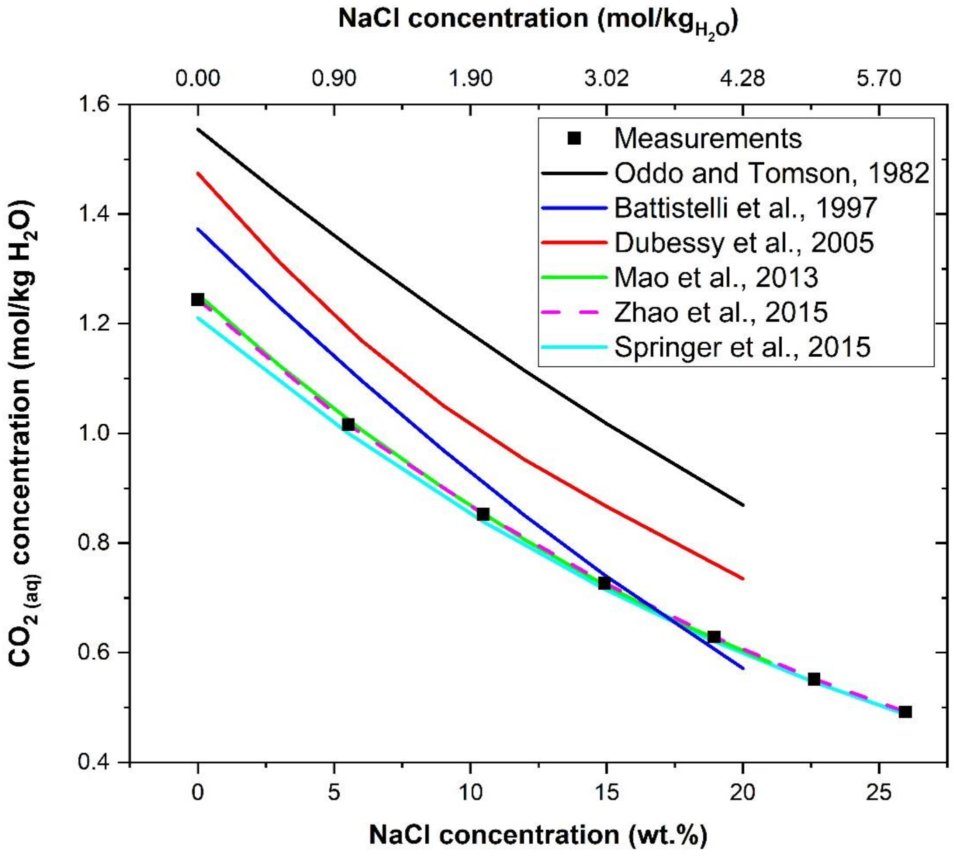

7.2 The Effect of Salt Concentration on Solubility of H_2S Gas

The number of models available in the literature for H_2S solubility in water and NaCl aqueous solutions is limited compared to that for CO_2 solubility due to the hazardous nature of H_2S gas and difficulties related to operating experiments with this gas, particularly at high pressures and temperatures. Similar to CO_2, two group of models can be found in the literature for solubility of H_2S gas in aqueous NaCl solutions. The first group relates the Henry's law constant to the solution ionic strength without taking into account the interactions between H_2S molecules and other dissolved species in the solution [236,245,155,253–255]. The second group of models considers interspecies interactions in the liquid phase [127,256–258] and in some cases even in the gas phase [241]. The Millero and Harshey [254] and the Dubessy *et al.* [236] models from the first group and the Duan *et al.* [127] and the Springer *et al.* [241] models from the second group will be explained in the following text. The Springer *et al.* model [241] is presented in Section 8.3.1. Similar to the CO_2 solubility models, the effect of pressure on solubility of $H_2S_{(g)}$ is not considered in the first group of models, which makes them applicable only for pressures lower than 5 bar [127]. However, in this study the fugacity coefficient is added to these models (Equation (7-26)) to make them appropriate for higher pressures.

7.2.1 The Millero and Harshey H_2S Solubility Model

The Millero and Harshey model [254] is an empirical model in the form of Setschenow equation:

$$ln\frac{m_{H_2S}^{w}}{m_{H_2S}^{b}} = k_b I_m \tag{7-21}$$

where, $m_{H_2S}^{w}$ and $m_{H_2S}^{b}$ are molality concentrations of $H_2S_{(aq)}$ in pure water and salt solution, respectively, k_b is the salting out coefficient in kgH_2O/mol and I_m is molality based ionic strength of solution. k_b is given as a function of temperature (in ^{o}C) as follows:

$$k_b(T_c) = 8.743 \times 10^{-4} - 2.5317 \times 10^{-3} T_c + 3.1982 \times 10^{-5} T_c^2 \tag{7-22}$$

The H_2S Henry's law volatility constant equation proposed by Clark and Glew [259] is used to calculate $x_{H_2S}^{w}$:

$$K_H^{pm,w} = 10^{103.70 - \frac{4455.94}{T} - 37.1874 \times \log(T) + 0.01426 \times T} \tag{7-23}$$

$$m_{H_2S}^{w} = \frac{K_H^{pm,w}}{f_{H_2S}} \tag{7-24}$$

where, $K_H^{pm,w}$ is the H_2S Henry's law volatility constant in atm·kgH_2O/mol and f_{H_2S} is the fugacity of $H_2S_{(g)}$ in atm, and T is the solution temperature in K. Equation ((7-23) is valid from 25^{o}C to 260^{o}C. f_{H_2S} can be calculated using equations below:

$$p_{H_2S} = y_{H_2S} \cdot P \tag{7-25}$$

$$f_{H_2S} = \varphi_{H_2S}^{Pure} \cdot p_{H_2S} \tag{7-26}$$

where, P and p_{H_2S} are the total pressure and the partial pressure of $H_2S_{(g)}$ and have the same unit as that of f_{H_2S}. y_{H_2S} is the mole fraction of $H_2S_{(g)}$ in the gas phase and can be calculated by:

$$y_{H_2S} = \frac{P - p_{H_2O}}{P} \tag{7-27}$$

where, p_{H_2O} is water vapor ($H_2O_{(g)}$) pressure in bar and can be obtained from a model by Atkinson [128] mentioned in Appendix H. The fugacity coefficient of pure $H_2S_{(g)}$, $\varphi_{H_2S}^{Pure}$ can be obtained by Duan *et al.* [256] EOS presented in Appendix J. The validity range for the Millero and Harshey model [254] is not explicitly reported. However, from their publications [253,254], it can be speculated that the model is valid for temperatures below 50°C and ionic strengths up to 1 m.

7.2.2 The Dubessy et al. H$_2$S Solubility Model

The Dubessy *et al.* solubility model [236] is an empirical vapor-liquid equilibrium model for aqueous NaCl solutions valid in the temperature range of 50°C to 250°C and NaCl concentrations up to 6 m. The dependency of H_2S solubility on NaCl concentration is modeled in the Dubessy *et al.* model [236] by correlating the H_2S Henry's law constant in aqueous NaCl solution ($K_H^{px,b}$) and that in pure water ($K_H^{px,w}$) with polynomial terms as functions of temperature and NaCl concentration. Their proposed equation is given below:

$$\begin{aligned} log K_H^{px,b}(T, m_{NaCl}) \\ &= log K_H^{px,w}(T) + \beta_1(T) m_{NaCl} + \beta_2(T) m_{NaCl}^2 \\ &+ \beta_3(T) m_{NaCl}^3 \end{aligned} \tag{7-28}$$

where $K_H^{px,w}$ and $K_H^{px,b}$ are in bar, T is in K, and β_i are fit coefficients expressed in the following form:

$$\beta_i(T) = \sum_{j=1}^{5} a_{ij} \times T^{j-1} \tag{7-29}$$

The a_{ij} coefficients are listed in Table 7-4. Dubessy *et al.* [236] used the equation proposed by Harvey [246] for calculating $K_H^{px,w}$. This equation is presented below:

$$lnK_H^{px,w} = lnp_{H_2O} - \frac{-5.7131}{T_r} + \frac{5.3727(1-T_r)^{0.355}}{T_r} + 5.4227{T_r}^{-0.41}\exp(1-T_r) \tag{7-30}$$

The concentration of dissolved H_2S in aqueous NaCl solutions ($m_{H_2S_{(aq)}}$) can be calculated by using the following equations:

$$x_{H_2S_{(aq)}} = \frac{K_H^{px,b}}{p_{H_2S}} \tag{7-31}$$

$$m_{H_2S_{(aq)}} = \frac{x_{H_2S_{(aq)}}}{1-x_{H_2S_{(aq)}}}\left(m_{NaCl} + \frac{1000}{M_w}\right) \tag{7-32}$$

where, $m_{H_2S_{(aq)}}$ is in molality (mol/kgH_2O), p_{H_2S} is partial pressure of H_2S in the gas phase in bar, $x_{H_2S_{(aq)}}$ is the mole fraction of dissolved H_2S in the aqueous NaCl solution, m_{NaCl} is the molality concentration of NaCl in the solution in mol/kgH_2O, and M_w is the molecular weight of water in g/mol.

Table 7-4

The a_{ij} coefficients used in Equation (7-29) for calculating the effect of NaCl concentration on Henry's law volatility constant in H_2O-NaCl-H_2S mixtures [236].

j	a_{1j}	a_{2j}	a_{3j}
1	-12.4617636	5.327383011	-0.75715275
2	12.69373100e-2	-5.82779828e-2	0.831927411e-2
3	-4.791540697e-4	2.3650333285e-4	-0.338668040e-4
4	7.9817223650e-7	-4.207913036e-8	0.6037602785e-8
5	-4.931093145e-11	2.7628521914e-11	-0.397049836e-11

7.2.3 The Duan et al. H_2S Solubility Model

The Duan *et al.* [127] H_2S solubility model is an empirical vapor-liquid equilibrium model for calculating H_2S solubility in pure water as well as aqueous NaCl solutions. The Duan *et al.* [127] model considers the interspecies interactions between H_2S molecules and salt ions in the liquid phase and uses an accurate EOS for the vapor phase. The Duan et al. H_2S solubility model [127] is almost the same as the Sun and Duan [126] and Mao *et al.* [30] CO_2 solubility models mentioned earlier. Only the final equation required to calculate H_2S solubility in aqueous NaCl solutions is presented here to avoid repetition:

$$ln\frac{y_{H_2S}P}{m_{H_2S}} = \frac{\mu_{H_2S}^{l(0)}(T,P)}{RT} - ln\varphi_{H_2S}^{Pure}(T,P) + 2\lambda_{H_2S-Na}m_{Na} + 2\lambda_{H_2S-cl}m_{cl} + \xi_{H_2S-Na-Cl}m_{Na}m_{Cl} \quad (7\text{-}33)$$

The activity coefficient of H_2S in the gas phase, $\gamma_{H_2S}^{g}$ is considered to be one in the Duan *et al.* H_2S solubility model [127]. λ_{H_2S-cl} is set to zero similar to the Mao *et al.* model [30] for CO_2 solubility. $\varphi_{H_2S}^{Pure}$ can be obtained from Duan *et al.* [256] et al. presented in Appendix J. $\frac{\mu_{H_2S}^{l(0)}}{RT}$, λ_{H_2S-Na}, and $\xi_{H_2S-Na-Cl}$ are calculated using the following equation:

$$Par(T,P) = c_1 + c_2T + \frac{c_3}{T} + c_4T^2 + \frac{c_5}{680-T} + c_6P + \frac{c_7P}{680-T} + \frac{c_8P^2}{T} \tag{7-34}$$

where T is the solution temperature in K, and P is total pressure in bar. The c_i coefficients are itemized in Table 7-5. The accuracy of the Duan *et al.* [127] H_2S solubility model is claimed to be within the 7% of the experimental data. The Duan *et al.* [127] H_2S solubility model is valid for 0° to 227°C solution temperature, 0 to 200 bar total pressure, and NaCl concentrations up to 6 M.

Table 7-5

Coefficients used in Equation (7-20) for calculating parameters needed for estimation of H_2S solubility in aqueous NaCl solutions [127].

Coefficients	$\frac{\mu_{H_2S}^{l(0)}}{RT}$	λ_{H_2S-Na} [†]	$\xi_{H_2S-Na-Cl}$ [†]
c_1	42.564957	8.5004999e-2	-1.0832589e-2
c_2	-8.6260377e-2	3.5330378e-5	0
c_3	-6084.3775	-1.5882605	0
c_4	6.8714437e-5	0	0
c_5	-102.76849	0	0
c_6	8.4482895e-4	1.1894926e-5	0
c_7	-1.0590768	0	0
c_8	3.5665902e-3	0	0

[†] The units for λ and ξ are kgH_2O/mol and $(kgH_2O/mol)^2$, respectively.

7.2.4 Quantification of Salting out of H_2S and Comparison of H_2S Solubility Models

Figure 7-2 shows the H_2S solubility values in aqueous NaCl solutions calculated with five models at various combinations of temperatures and pressures. According to all five models, increasing NaCl concentration results in a decrease in H_2S solubility. The Millero and Harshey model [254] overpredicts H_2S solubility for all three conditions. The other models predict similar values for all three examples indicating that all of them can be used for the estimation of dissolved H_2S in aqueous NaCl solutions. The Duan *et al.* [127] and the Springer *et al.* [241] model are used in this study.

Figure 7-2

Comparison of H_2S solubility models in aqueous NaCl solutions at (A) 25°C and 1 bar, (B) 80°C and 1 bar. Pressures are total pressure. H_2S solubility values are calculated at 25°C for Dubessy et al. model and up to 25 wt.% NaCl for the Millero and Harshey model regardless of their validity range. Measurements are taken from [260].

(A)

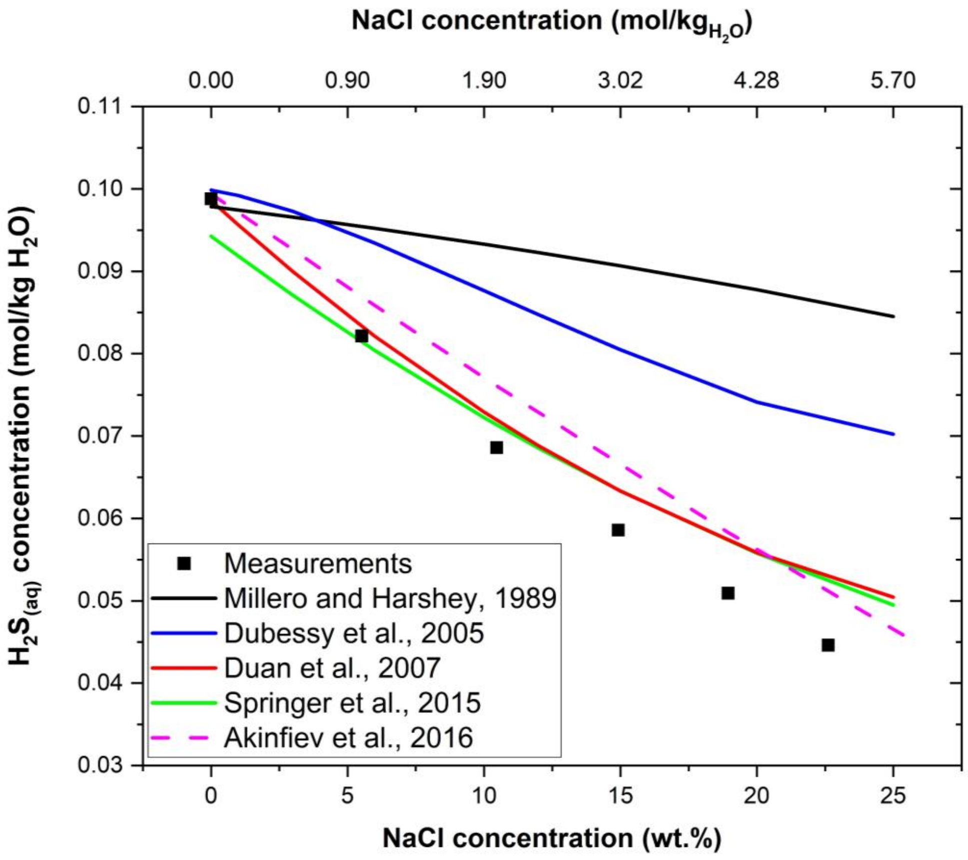

(B)

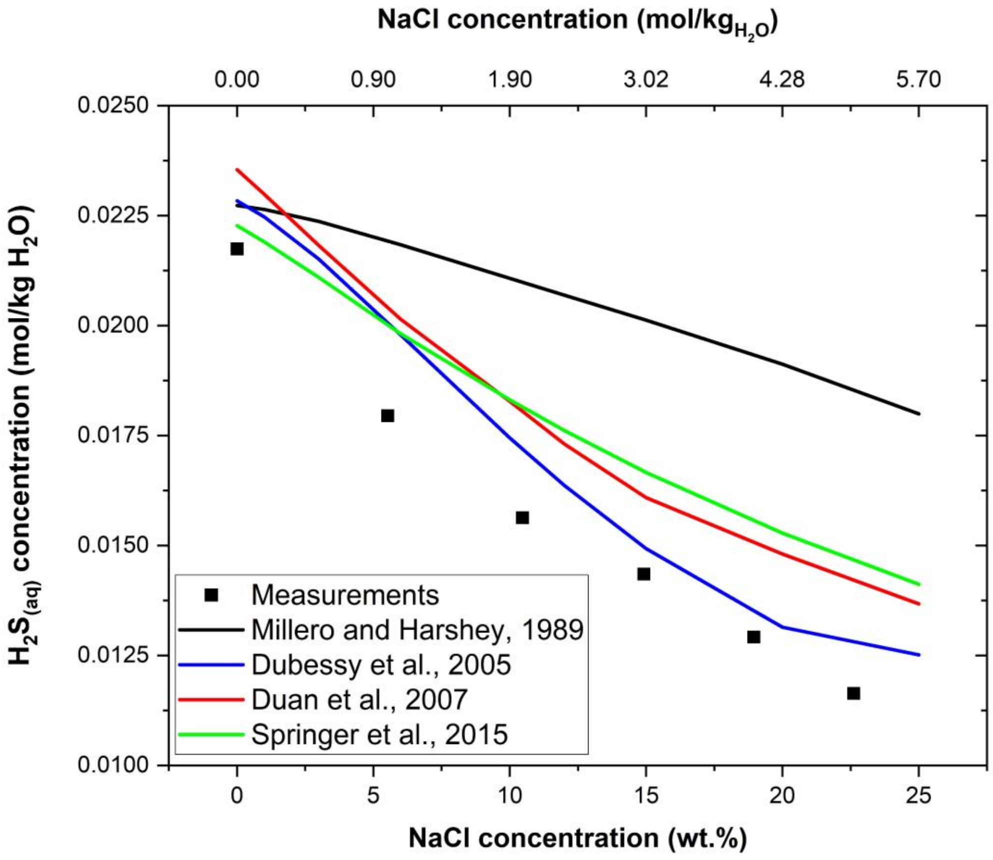

7.2.5 The Effect of Electrolyte Type and Ionic Strength on H_2S Solubility

Figure 7-3 shows measured H_2S solubility values [261] vs. ionic strength in aqueous solutions containing different HCl/NaCl ratios. Following the yellow triangles on the H_2S concentration line shows that increasing NaCl concentration decreased H_2S solubility. However, following the pink squares on the H_2S concentration line shows that addition of HCl did not have any effect on H_2S solubility. This indicates that HCl acid did not cause salting out of H_2S gas. Another interesting conclusion which can be made from Figure 7-3 is that the interaction between H_2S molecules and Cl^- ions is negligible compared to that between H_2S molecules and Na^+ ions. This conclusion agrees surprisingly with the assumption observed in the Duan *et al.* [127] H_2S solubility model for $\lambda_{H_2S-Cl} = 0$.

Figure 7-3

Variation in H_2S solubility (solid line) with respect to ionic strength in aqueous solutions containing NaCl-HCl mixtures at 25°C and ~1 atm H_2S partial pressure. The bars show NaCl or HCl concentration in M. Data are processed from [261].

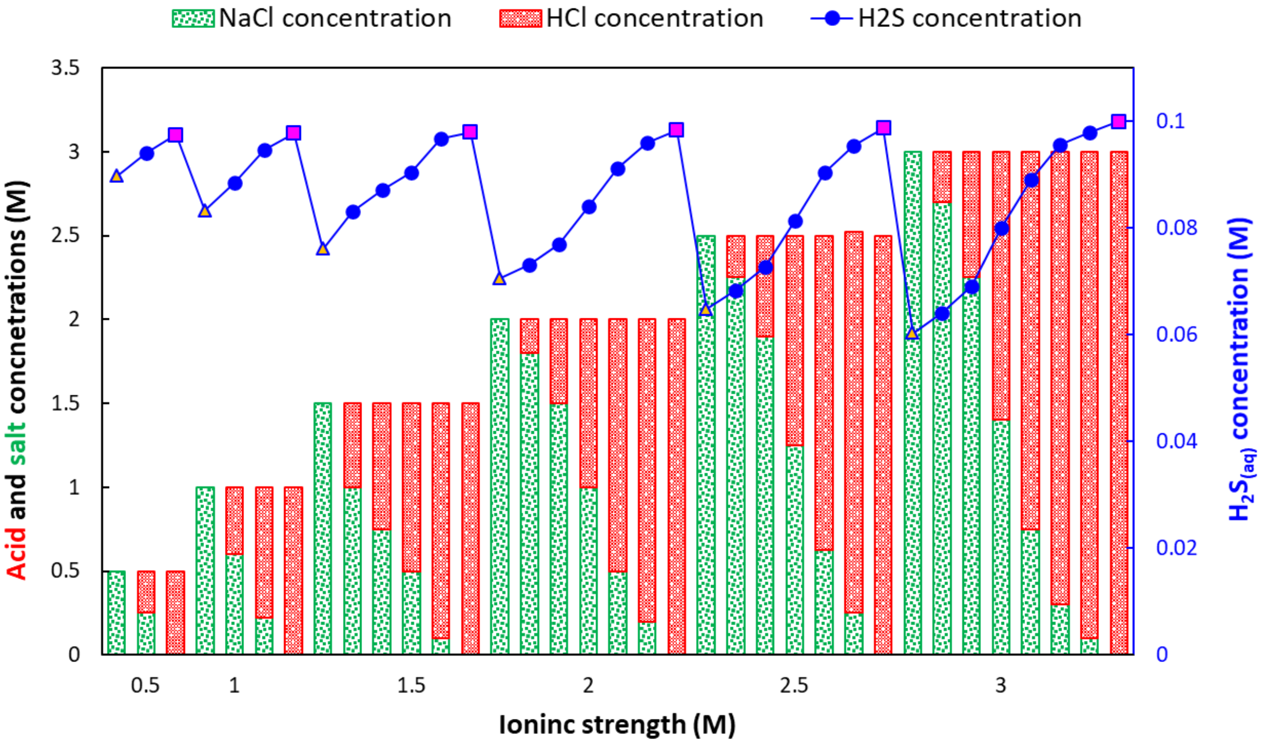

Figure 7-4 shows H_2S solubility measurements as a function of ionic strength in aqueous solutions with different electrolytes. For both salts (NaCl and $NaClO_4$) H_2S solubility decreased at higher ionic strengths. For HCl and $HClO_4$ solutions with ionic strengths lower than 5 M, change in the ionic strength did not vary H_2S solubility. However, for HI acid, the amount of dissolved H_2S in the solution increased with increasing ionic strength. Therefore, it can be concluded that salting out or salting in depends on the nature of dissolved electrolytes.

Figure 7-4

Variation in H_2S solubility vs. ionic strength in aqueous solutions with different electrolytes at 25°C and ~ 1 atm H_2S partial pressure. Data are borrowed from [261–264]

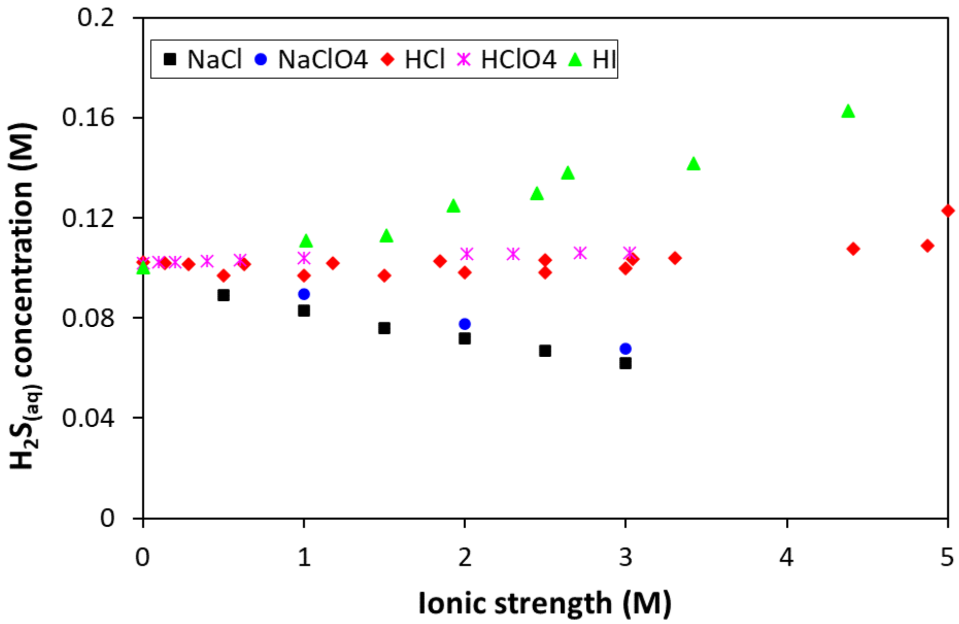

7.3 Comparison of Salting Out of CO_2 and H_2S in Aqueous NaCl Solutions

Figure 7-5 compares CO_2 solubility with H_2S solubility in aqueous NaCl solutions. At a constant NaCl concentration, $H_2S_{(g)}$ solubility in the solution is almost three times of CO_2 solubility. This holds for the entire range of NaCl concentrations. This difference in solubility is important when comparing the rate of corrosion under CO_2 and H_2S gases and will be used when analyzing the experimental results.

Figure 7-5

Comparison of CO_2 solubility with H_2S solubility in aqueous NaCl solutions at 60^oC and ~10 bar $CO_{2(g)}$ or $H_2S_{(g)}$ partial pressures. Solubility values are obtained with Mao et al. [30] *and Duan et al.* [127] *models.*

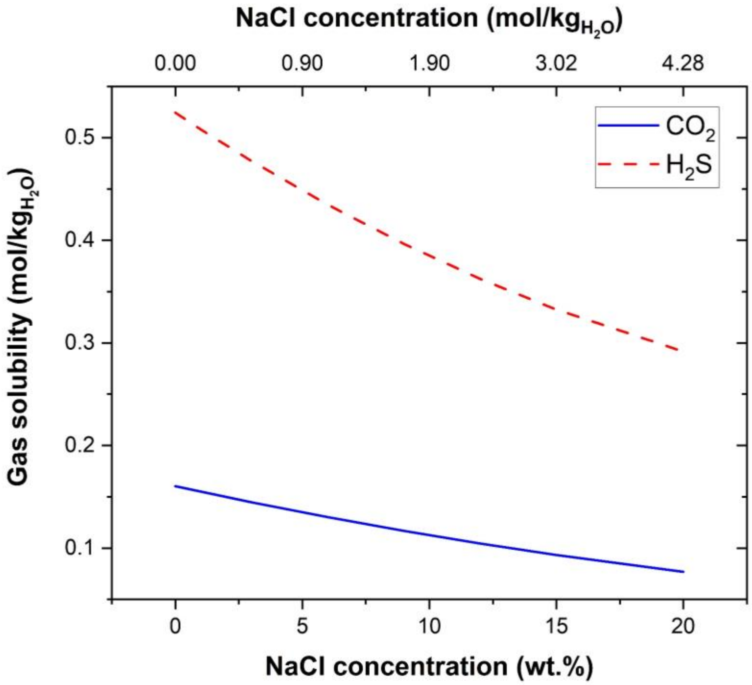

Chapter 8: Thermodynamic Models for Speciation Equilibria in H_2O-NaCl-CO_2-H_2S systems

In this chapter three speciation equilibrium models for the H_2O-NaCl-CO_2 system, one model for the H_2O-NaCl-H_2S system, and one model for the H_2O-NaCl-CO_2-H_2S system is presented. At the end of this chapter, the effect of salt concentration on solution chemistry is investigated with the help of these models. Finally, the speciation equilibrium models are compared with experimental measurements and with each other.

8.1 The Effect of Salt Concentration on Speciation Equilibria in Solutions Saturated with $CO_{2(g)}$

Several models exist in the literature for calculating equilibrium concentrations in CO_2-saturated aqueous NaCl solutions. Examples for models based on *stoichiometric* equilibrium constants are [232,255,169,265,266,201] and for models based on *thermodynamic* equilibrium constants are [127,240,241,249]. Out of these, four models have been reproduced in this study and will be explained in the following text: the Oddo and Tomson model [232], the Millero *et al.* model [266], the Li and Duan model [136], and the MSE model [241]. The MSE model which covers the H_2O-NaCl-CO_2 and the H_2O-NaCl-H_2S systems as well as their combination, the H_2O-NaCl-CO_2-H_2S will be described in Section 8.3.

Before explaining the speciation equilibrium models, it is necessary to review the speciation equilibria reactions occur in aqueous NaCl solutions saturated with CO_2 gas. When $CO_{2(g)}$ dissolves in water, it will react with water molecules and the following reactions take place:

1) $CO_{2(g)}$ dissolution

$$CO_{2(aq)} + H_2O_{(l)} \overset{K_{sol}}{\longleftrightarrow} H_2CO_{3(aq)} \tag{8-1}$$

2) The hydration reaction

$$CO_{2(aq)} + H_2O_{(l)} \overset{K_{hyd}}{\longleftrightarrow} H_2CO_{3(aq)} \tag{8-2}$$

3) The dissociation of carbonic acid

$$H_2CO_{3(aq)} \overset{K_{ca}}{\leftrightarrow} HCO_{3(aq)}^{-} + H_{(aq)}^{+} \tag{8-3}$$

4) The dissociation of carbonate ion

$$HCO_{3(aq)}^{-} \overset{K_2}{\leftrightarrow} CO_{3(aq)}^{2-} + H_{(aq)}^{+} \tag{8-4}$$

where, K_{sol} is CO_2 solubility equilibrium constant and can be obtained from one of the models presented in Section 7.1. In CO_2 equilibrium speciation models, Reactions (8-2) and (8-3) are consistently lumped together as follows:

$$CO_{2(aq)} + H_2O_{(l)} \overset{K_1}{\leftrightarrow} HCO_{3(aq)}^{-} + H_{(aq)}^{+} \tag{8-5}$$

The reason is that the stoichiometric equilibrium constant (K_{hyd}^{*}) for Reaction (8-2) is negligible (~ 2.58×10^{-3} at 25°C) [267]. This means that more than 99% of $CO_{2(g)}$ dissolved in water exists as $CO_{2(aq)}$ and less than 1% is in the form of true of free $H_2CO_{3(aq)}$ [268]. Thus, $H_2CO_{3(aq)}$ is ignored in speciation equilibrium calculations. It is worth mentioning that $K_1 = K_{hyd} \times K_{ca}$. In addition to above reactions, water molecules go through a dissociation reaction as follows:

$$H_2O_{(l)} \overset{K_w}{\leftrightarrow} OH_{(aq)}^{-} + H_{(aq)}^{+} \tag{8-6}$$

Now that the possible reactions in the liquid phase in H_2O-NaCl-CO_2 mixtures are mentioned, the speciation equilibrium models will be discussed.

8.1.1 An Ionic Strength-Based Speciation Equilibrium Model for H_2O-NaCl-CO_2 Systems Based on Oddo and Tomson Equations

The Oddo and Tomson model [232] was introduced previously in Section 7.1.1. The required inputs for the Oddo and Tomson model is temperature, total pressure, and NaCl concentration (ionic strength). In this part, only the equations related to the stoichiometric equilibrium constants, K_1^* and K_2^* for Reactions (8-5) and (8-4), respectively, will be added:

$$K_1^* = 10^{6.41-1.594\times10^{-3}T_f+3.52\times10^{-6}T_f^2-3.07\times10^{-5}P-0.4772I_M^{0.5}+0.118I_M} \tag{8-7}$$

$$K_2^* = 10^{10.61-4.97\times10^{-3}T_f+1.33\times10^{-5}T_f^2-2.624\times10^{-5}P-1.166I_M^{0.5}+0.3466I_M} \tag{8-8}$$

where, K_1^* and K_2^* are in Molar, T_f is solution temperature in ^{o}F, P is total pressure in psi, and I_M is the molarity based ionic strength. For the stoichiometric equilibrium constant (K_{wa}^*) for water dissociation Reaction (8-6), the empirical equation developed by Marshall and Franck [269] can be used (Appendix G). The effect of salt concentration on dissociation reaction of water is ignored in the calculations as this effect is shown to be minor (< 5% at 25^{o}C and 1 atm) in a range of NaCl concentrations from 0 to 5 M [270]. Therefore, the activity of water, a_{H_2O} (dimensionless) can be assumed to be equal to unity, *i.e.*, $K_w^* = K_w$.

The stochiometric equilibrium constants are given below in terms of molarity concentrations (c_i):

$$K_1^* = \frac{c_{H^+_{(aq)}} c_{HCO^-_{3(aq)}}}{c_{CO_{2(aq)}}} \tag{8-9}$$

$$K_2^* = \frac{c_{H^+_{(aq)}} c_{CO^{2-}_{3(aq)}}}{c_{HCO^-_{3(aq)}}} \tag{8-10}$$

$$K_w^* = c_{H^+_{(aq)}} c_{OH^-_{(aq)}} \tag{8-11}$$

Since Equations (8-7) and (8-8) are in molarity unit, the concentration unit in the above equations needs to be in molarity.

The main species produced due to dissociation Reactions (8-5), (8-4), and (8-6) in H_2O-NaCl-CO_2 systems are $H^+_{(aq)}$, $HCO^-_{3(aq)}$, $CO^{2-}_{3(aq)}$, and $OH^-_{(aq)}$. To calculate the equilibrium concentrations of these four species, four equations are required. Three equations come from Equations (8-9), (8-10), and (8-11). The fourth equation is the charge neutrality equation[29]:

$$c_{H^+_{(aq)}} = c_{HCO^-_{3(aq)}} + 2c_{CO^{2-}_{3(aq)}} + c_{OH^-_{(aq)}} \tag{8-12}$$

For the same reason just mentioned above, molarity unit is used in Equation (8-12). Nevertheless, the charge neutrality equation holds valid with any concentration unit.

If concentrations of $HCO^-_{3(aq)}$, $CO^{2-}_{3(aq)}$, and $OH^-_{(aq)}$ in Equation (8-12) are written in term of $H^+_{(aq)}$ concentration, using Equations (8-9), (8-10), and (8-11), the following cubic equations will be obtained:

$$Ac^3_{H^+_{(aq)}} + Bc^2_{H^+_{(aq)}} + Cc_{H^+_{(aq)}} + D = 0 \tag{8-13}$$

$$A = 1$$

---

[29] Charge neutrality or charge balance or electroneutrality is observed in all solutions except in a thin double layer near electrodes and other boundaries. The general charge neutrality is $\sum_i z_i c_i = 0$ [21].

$$B = 0$$

$$C = -\left(K_w^* + K_1^* \cdot c_{CO_{2(aq)}}\right)$$

$$D = -2 \cdot K_1^* \cdot K_2^* \cdot c_{CO_{2(aq)}}$$

where, $c_{CO_{2(aq)}}$ is the concentration of dissolved CO_2 in the solution in molarity, which has been already shown how to calculate using Equation (7-1). The equilibrium concentrations of all four species can be obtained by solving Equation (8-13) [271]. The validity range for the Oddo and Tomson model [232] is from 25°C to 250°C, 1 to 1200 bars, and 0 to 4 M.

The autogenous pH of solution can be obtained by using the following equation:

$$pH = -\log\left(m_{H^+}\gamma_{H^+}^m\right) \tag{8-14}$$

where, m_{H^+} is molality concentration of $H_{(aq)}^+$, and $\gamma_{H^+}^m$ is the molality-based activity coefficient of $H_{(aq)}^+$. The equilibrium concentration of $H_{(aq)}^+$ obtained by the Oddo and Tomson [232] model is in molarity. Therefore, it needs to be converted to molality before being used in Equation (8-14):

$$m_{H^+} = \frac{10^5 c_{H^+}}{(100 - wt)\rho_b} \tag{8-15}$$

where, wt is salt concentration in weight percent and ρ_b is the solution density in kg/m^3. For instant, for a 20 wt.% NaCl aqueous solution, $wt = 20$. $\gamma_{H^+}^m$ can be obtained by the simplified Pitzer's equation presented in Section 5.1.2.

8.1.2 An Ionic Strength-Based Speciation Equilibrium Model for H_2O-NaCl-CO_2 Systems Based on Millero et al. Equations

The Millero *et al.* model [266] is an empirical speciation equilibrium model that expresses the dissociation equilibrium constants for Reactions (8-5) and (8-4) as a function of temperature and NaCl concentration. The inputs needed for the Millero *et al.* model are temperature, total pressure, NaCl concentration. According to the Millero *et al.* model [266], the stoichiometric equilibrium constants, K_1^* and K_2^* are in the following form:

$$pK_i^* - pK_i = A_i + \frac{B_i}{T} + C_i lnT \tag{8-16}$$

where, K_i^* is in molality, K_i is the equilibrium constant for Reactions (8-5) and (8-4) in pure water in molality, T is temperature in K, and A_i, B_i, and C_i are adjustable coefficients as a function of NaCl molality listed Table 8-1.

Millero *et al.* [266] suggested using the following equations for the determination of K_1 and K_2:

$$pK_1 = -402.56788 + \frac{11656.46}{T} + 72.173 lnT - 0.161325T + 7.5526 \times 10^{-5} T^2 \tag{8-17}$$

$$pK_2 = -122.4994 + \frac{5811.18}{T} + 20.5263 lnT - 0.0120897T \tag{8-18}$$

The equilibrium concentrations of aqueous species can be obtained using a similar procedure to one explained above for the Oddo and Tomson model [232]. For computing the molality of dissolved CO_2 in the solution ($m_{CO_{2(aq)}}$), any CO_2 solubility model applicable to aqueous NaCl solutions can be used. In this study, the Mao *et al.* [30] CO_2 solubility model is used (Equation (7-19)). The Millero *et al.* [198] equations are claimed to be valid between 0°C to 250°C and NaCl concentration from 0 to 6 molality.

Additionally, the Millero et al. model [198] includes equations for determining activity coefficients of $CO_{2(aq)}$, $H^{+}_{(aq)}$, $HCO^{-}_{3(aq)}$, and $CO^{2-}_{3(aq)}$ as well as activity of water, using the simplified Pitzer equations:

$$\begin{aligned} ln\gamma^{m}_{H^{+}} = F &+ 2m_{Cl}\,(B_{H-Cl} + m_{Cl}C_{H-Cl}) \\ &+ m_{Na}m_{Cl}\,(B'_{Na-Cl} + C_{Na-Cl}\,) \\ &+ m_{Na}\,(2\theta_{Na-H} + m_{Cl}\,\psi_{H-Na-Cl}) \end{aligned} \tag{8-19}$$

$$\begin{aligned} ln\gamma^{m}_{HCO_3^-} = F &+ 2m_{Na}\left(B_{Na-HCO_3} + m_{Cl}C_{Na-HCO_3}\right) \\ &+ m_{Na}m_{Cl}(B'_{Na-Cl} + C_{Na-Cl}) \\ &+ m_{Cl}\left(2\theta_{Cl-HCO_3} + m_{Na}\psi_{Cl-HCO_3-Na}\right) \end{aligned} \tag{8-20}$$

$$\begin{aligned} ln\gamma^{m}_{CO_3^{2-}} = 4F &+ 2m_{Na}\left(B_{Na-CO_3} + m_{Cl}C_{Na-CO_3}\right) \\ &+ 4m_{Na}m_{Cl}B'_{Na-Cl} + 2m_{Na}m_{Cl}C_{Na-Cl} \\ &+ m_{Cl}\left(2\theta_{Cl-CO_3} + 2\theta^{E}_{Cl-CO_3}m_{Na}\psi_{Cl-CO_3-Na}\right) \end{aligned} \tag{8-21}$$

$$ln\gamma^{m}_{CO_2} = 2m_{Na}\left(\lambda_{Na-CO_2} + \lambda_{Cl-CO_2}\right) + m_{Na}m_{Cl}\xi_{Na-Cl-CO_2} \tag{8-22}$$

$$lna_{H_2O} = \frac{-2m_{NaCl}}{55.51\emptyset} \tag{8-23}$$

The reader is referred to the original publication [1] for the interactions parameters and coefficients used in the above equations. A more comprehensive version of these equations with details about each parameter and coefficient will be presented when the Li and Duan [1,2] model is explained. The autogenous pH solution can be obtained by using Equation (8-15).

Table 8-1

Coefficients used in Equation (8-16) for calculating the stoichiometric equilibrium constants for carbonic acid dissociation in aqueous NaCl solutions.

i	Coefficients
1	$A_1 = 31.3616m^{0.5} + 0.86644m - 0.33611m^{1.5} + 0.05888m^2$
1	$B_1 = -1422.25317m^{0.5}$
1	$C_1 = -4.84141m^{0.5}$
2	$A_2 = 36.88545m^{0.5} + 1.66599m - 0.68730m^{1.5} + 0.12070m^2$
2	$B_2 = -1669.55918m^{0.5}$
2	$C_2 = -5.83555m^{0.5}$

m is the molality concentration of NaCl.

8.1.3 Li and Duan Speciation Equilibrium Model for H_2O-NaCl-CO_2 Systems Based on Modified Pitzer Equations

The Li and Duan model [136,249] is a semi-empirical speciation equilibrium model for H_2O-NaCl-CO_2 systems that allows calculating the equilibrium concentrations and activity coefficients simultaneously for all involved species. The Li and Duan model [136,249] is from the second group of models discussed earlier. In the Li and Duan model [136,249], the equilibrium constants are only a function of temperature and pressure and the effect of salt concentration on speciation equilibria is considered by calculating the activity coefficients, using modified Pitzer equations [142,143]. The required inputs for the Li and Duan model [136,249] are temperature, total pressure[30], and NaCl concentration. Concentrations and activity coefficients are based on molality in the Li and Duan model [136,249].

A relatively complex algorithm is used in the original Li and Duan model to calculate the equilibrium concentrations and the equilibrium activity coefficients [136]. Moreover, this algorithm is for a closed system, which means that the mass of carbon in that system should be constant. In this study, a simpler algorithm is used[31]. Additionally, since in corrosion studies, open systems are usually being encountered, the algorithm used to reproduce the Li and Duan model is modified for an open system. Moreover, unlike the original publications all the steps to compute the equilibrium concentrations and activity coefficients are explained in detail in this study. There are few mistakes in the original publication[32]. These mistakes to some extend have been repeated elsewhere [277] as well as in the reproductions of the Li and Duan model such as [208,107]. These mistakes are explained in Appendices where the Pitzer equations and parameters are introduced.

The Li and Duan model [249] suggests using the following empirical equations for calculating the thermodynamic equilibrium constants, K_1 and K_2 for Reactions (8-5) and (8-4), respectively:

---

[30] In this study, it is assumed that only $CO_{2(g)}$ and $H_2O_{(g)}$ are present in the gas phase. Therefore, the partial pressure of CO_2 is equal to the water vapor pressure subtracted from the total pressure.

[31] There are several algorithms and software packages available for calculating speciation equilibrium and phase equilibrium [272–276].

[32] Parameters in Table 3, equation 21 for the osmotic coefficient of water, c_5 parameter for $\beta^{(0)}$ and $\beta^{(1)}$ for $HCl_{(aq)}$ in Table 6, c_6 parameter for C^{φ} of $NaCl_{(aq)}$ in Table 7, and c_2 parameter for $\beta^{(0)}$ of $NaOH_{(aq)}$ in Table 8, and the unit for saturation pressure of water which is MPa and not bar in Appendix B of Li and Duan [136].

$$lnK_i = a_1 + a_2T + a_3T^{-1} + a_4T^{-2} + a_5lnT + (a_6T^{-1} + a_7T^{-2} + a_8T^{-1}lnT)(P - P_s) + (a_9T^{-1} + a_{10}T^{-2} + a_{11}T^{-1}lnT)(P - P_s)^2 \tag{8-24}$$

where, K_i are in molality, T is the solution temperature in K, P is total pressure in bar, P_s is considered to be 1 bar at temperature below 100°C or the saturation pressure of pure water at temperature above 100°C (Appendix H), and a_j are fit parameters listed in Table 8-2. Equation (G-1) in Appendix G is suggested for the equilibrium dissociation constant of water (K_w) in Reaction (8-6).

The thermodynamic equilibrium constants corresponded to Reactions (8-5), (8-4), and (8-6), respectively, are equal to:

$$K_1 = \frac{\left(m_{H^+_{(aq)}}\gamma^m_{H^+_{(aq)}}\right)\cdot\left(m_{HCO^-_{3(aq)}}\gamma^m_{HCO^-_{3(aq)}}\right)}{\left(m_{CO_{2(aq)}}\gamma^m_{CO_{2(aq)}}\right)\cdot a_{H_2O_{(l)}}} \tag{8-25}$$

$$K_2 = \frac{\left(m_{H^+_{(aq)}}\gamma^m_{H^+_{(aq)}}\right)\cdot\left(m_{CO^{2-}_{3(aq)}}\gamma^m_{CO^{2-}_{3(aq)}}\right)}{m_{HCO^-_{3(aq)}}\gamma^m_{HCO^-_{3(aq)}}} \tag{8-26}$$

$$K_w = \frac{\left(m_{H^+_{(aq)}}\gamma^m_{H^+_{(aq)}}\right)\cdot\left(m_{OH^-_{(aq)}}\gamma^m_{OH^-_{(aq)}}\right)}{a_{H_2O_{(l)}}} \tag{8-27}$$

Since the units for K_1, K_2, and K_w are in molality, the above equations are expressed in molality.

Table 8-2

The fit parameters used in Equation (8-24) for the calculation of dissociation equilibrium constants for Reactions (8-5) and (8-4) [249].

i	K_1	K_2
1	233.5159304	-151.1815202
2	0	-0.088695577
3	-11974.38348	-1362.259146
4	0	0
5	-36.50633536	27.79798156
6	-45.08004597	-29.51448102
7	2131.318848	1389.015354
8	6.714256299	4.419625804
9	0.008393915212	0.003219993525
10	-0.4015441404	-0.1644471261
11	-0.00124018735	-0.0004736672395

In the Li and Duan model [136,249], the activity coefficients of dissolved species in addition to the osmotic coefficient[33] and activity of water are calculated using modified Pitzer equations [143]. The general form of the Pitzer equations for activity coefficients is given below:

---

[33] Characterizes the deviation of a solvent from ideal behavior [140].

$$ln\gamma_i = ln\gamma_i^{DH} + \sum_j B_{ij}(I)m_j + higher\ terms \tag{8-28}$$

where, γ_i is the activity coefficient of species i, m is the molality concentration, and B_{ij} are virial coefficients related to interactions between anions and cations and are a function of ionic strength. γ_i^{DH} is essentially an extended Debye-Huckel activity coefficient and it is only a function of ionic strength. γ_i^{DH} is a more complex version of the extended Debye-Huckel equation shown in Table 4-1 [137,139,143]. Higher terms have been added to the equation to include more variety of interactions and make the activity coefficient calculations more accurate at high concentrations. A detailed description of all the equations and the relevant parameters and coefficients is given in Appendix L.

The modified Pitzer equations for the activity coefficients and the osmotic coefficient are concentration dependent. On the other hand, the equilibrium equations, Equations (8-25) to (8-27), are functions of concentrations, activity coefficients, and osmotic coefficient. Therefore, all these equations need to be solved simultaneously in a loop to obtain the equilibrium concentrations, the equilibrium activity coefficients, and the equilibrium osmotic coefficient. The algorithm used in the present stduy for this purpose is illustrated in Figure 8-1. This algorithm is proposed for an open system, what is seen in most corrosion scenarios, including internal corrosion of oil and gas pipelines, which is the subject of the present study. In an open system, at a constant temperature and total pressure, the mole fraction of gaseous species in the gas phase is constant. This means that the partial pressure of gaseous species is constant as well. For the H_2O-NaCl-

CO_2 mixture, the only gaseous species are water vapor and $CO_{2(g)}$. The steps to the algorithm are discussed below:

1) Calculate the water vapor pressure. In the original Li and Duan model [136] a simplified version of the IAPWS-IF97 proposed by Wagner et al. [46] is recommended. However, in this study, a model by Atkinson [128] is used because it considers the effect of salt concentration on water vapor pressure. Both models are shown in Appendix H.
2) Calculate the CO_2 partial pressure using Equations (7-2) and (7-5).
3) Compute the fugacity coefficient of pure CO_2, using Duan *et al.* [243] fugacity model. The interactions between $CO_{2(g)}$ and water vapor molecules are not considered in the Li and Duan model [136].
4) Calculate CO_2 solubility ($m_{CO_{2(aq)}}$). In the original Li and Duan model [136], a CO_2 solubility model by Duan and Sun [126] is suggested. However, in this study, the Mao *et al.* [30] model in Section 7.1.4, which is an updated version of the Duan and Sun model [126] is employed.
5) Calculate the thermodynamic equilibrium constants, using Equations (8-24) and (G-1) in Appendix G.
6) Find initial concentrations for initiating the iteration loop. The best choice are the equilibrium concentrations at ideal conditions. The procedure is exactly the same as that used in the Oddo and Tomson [232] model in Section 8.1.1. Four equations are needed to calculate the equilibrium concentrations of $H^{+}_{(aq)}$, $HCO^{-}_{3(aq)}$, $CO^{2-}_{3(aq)}$, and $OH^{-}_{(aq)}$. Three of them are supplied by

equations for the thermodynamic equilibrium constants at ideal conditions ($\gamma_i = 1$):

$$K_1 = \frac{m_{H^+_{(aq)}} m_{HCO^-_{3(aq)}}}{m_{CO_{2(aq)}}} \tag{8-29}$$

$$K_2 = \frac{m_{H^+_{(aq)}} m_{CO^{2-}_{3(aq)}}}{m_{HCO^-_{3(aq)}}} \tag{8-30}$$

$$K_w = m_{H^+_{(aq)}} m_{OH^-_{(aq)}} \tag{8-31}$$

The fourth equation is the charge balance equation:

$$m_{H^+_{(aq)}} = m_{HCO^-_{3(aq)}} + 2m_{CO^{2-}_{3(aq)}} + m_{OH^-_{(aq)}} \tag{8-32}$$

Finally, the following cubic equation can be solved to acquire the initial equilibrium molality concentrations:

$$Am^3_{H^+_{(aq)}} + Bm^2_{H^+_{(aq)}} + Cm_{H^+_{(aq)}} + D = 0 \tag{8-33}$$

$$A = 1$$

$$B = 0$$

$$C = -\left(K_w + K_1 m_{CO_{2(aq)}}\right)$$

$$D = -2K_1K_2 m_{CO_{2(aq)}}$$

7) Calculate the initial ionic strength of solution, using the following equation:

$$I_m = \frac{1}{2}\sum_{i=1}^{6} m_i z_i^2 \tag{8-34}$$

$$= \frac{1}{2}(m_{Na^+} + m_{Cl^-} + m_{H^+} + m_{OH^-} + m_{HCO_3^-} + 4m_{CO_3^{2-}})$$

where, I_m is the molality-based ionic strength, m_i is the molality concentration of species i, and z_i is the charge number of species i.

8) Initiate a *while* loop with its "criterion" being the variation in the ionic strength which needs to be less than a desired value. In this study, the desired value set to be 10^{-12}.
9) Calculate the activity coefficients and the osmotic coefficient (activity of water), using the modified Pitzer Equations (L-1) to (L-5) in Appendix L.
10) Calculate new concentrations by solving the following system of nonlinear equations for autogenous pH conditions:

$$K_1\left(m_{CO_{2(aq)}}\gamma^m_{CO_{2(aq)}}\right)\cdot a_{H_2O_{(l)}} - \left(m_{H^+_{(aq)}}\gamma^m_{H^+_{(aq)}}\right)\cdot\left(m_{HCO^-_{3(aq)}}\gamma^m_{HCO^-_{3(aq)}}\right) = 0 \tag{8-35}$$

$$K_2\left(m_{HCO^-_{3(aq)}}\gamma^m_{HCO^-_{3(aq)}}\right) - \left(m_{H^+_{(aq)}}\gamma^m_{H^+_{(aq)}}\right)\cdot\left(m_{CO^{2-}_{3(aq)}}\gamma^m_{CO^{2-}_{3(aq)}}\right) = 0 \tag{8-36}$$

$$K_w a_{H_2O_{(l)}} - \left(m_{H^+_{(aq)}}\gamma^m_{H^+_{(aq)}}\right)\cdot\left(m_{OH^-_{(aq)}}\gamma^m_{OH^-_{(aq)}}\right) = 0 \tag{8-37}$$

$$m_{H^+_{(aq)}} = m_{HCO^-_{3(aq)}} + 2m_{CO^{2-}_{3(aq)}} + m_{OH^-_{(aq)}} \tag{8-38}$$

The first three equations correspond to equilibrium Reactions (8-5), (8-4), and (8-6), respectively, and the fourth equation is the charge neutrality equation. The *fsolve* solver in MATLAB with *Levenberg-Marquardt* algorithm is used to solve the above system of equations for concentrations of $H^+_{(aq)}$, $HCO^-_{3(aq)}$, $CO^{2-}_{3(aq)}$, and $OH^-_{(aq)}$. The initial conditions for the *fsolve* solver can be those obtained in Step 6. For constant pH conditions, one more equation representing the pH constrain needs to be added to the system of equations.

11) Recalculate the ionic strength of solution using the concentrations obtained in Step 10.
12) Subtract the ionic strength in Step 11 from the initial ionic strength computed in Step 7. Calculate the absolute value of their difference.
13) If the absolute value of the difference is smaller than the desired value defined in Step 8, then the calculated concentrations, activity coefficients, and osmotic coefficient are the equilibrium values. Otherwise, return to Step 9 and calculate the activity coefficients and the osmotic coefficient with new concentrations obtained in Step 10 and iterate the steps until the condition defined in Step 8 is satisfied.

Figure 8-1

The flow diagram of the algorithm used to calculate the speciation equilibrium with the Li and Duan model in the H_2O-NaCl-CO_2 system.

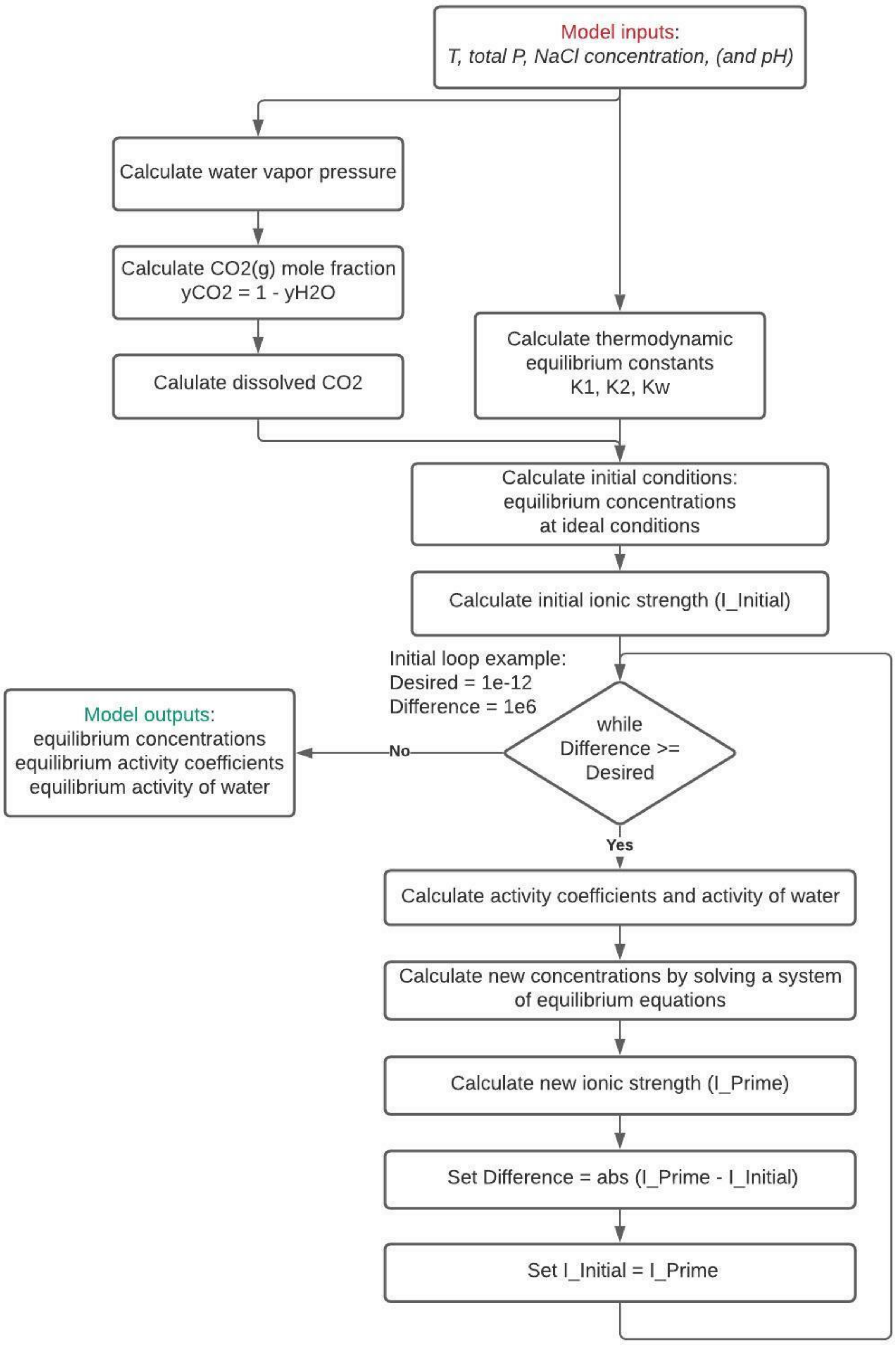

8.2 The Effect of Salt Concentration on Speciation Equilibria in Solutions Saturated with $H_2S_{(g)}$

Other than the mixed solvent electrolyte model, which is explained in Section 8.3.1 no other complete speciation equilibrium model could be found in the literature that is specifically developed for salt solutions saturated with $H_2S_{(g)}$. In the present study, for the first time, the H_2S solubility and dissociation constants from different publications in the open literature are put together to develop a simple ionic-strength based speciation equilibrium model for the H_2O-NaCl-H_2S system.

8.2.1 An Ionic Strength-Based Speciation Equilibrium Model for H_2O-NaCl-H_2S Systems

It is beneficial to review the speciation equilibria reactions that occur in aqueous (NaCl) solutions saturated with H_2S gas, before introducing the speciation equilibrium models. When $H_2S_{(g)}$ dissolves in water, , the following reactions take place:

1) Dissolution of $H_2S_{(g)}$

$$H_2S_{(g)} \overset{K_{sol}^*}{\longleftrightarrow} H_2S_{(aq)} \tag{8-39}$$

2) dissociation of dissolved $H_2S_{(aq)}$

$$H_2S_{(aq)} \overset{K_1^*}{\leftrightarrow} HS_{(aq)}^- + H_{(aq)}^+ \tag{8-40}$$

3) Dissociation of bisulfide ion

$$HS_{(aq)}^- \overset{K_2^*}{\leftrightarrow} S_{(aq)}^{2-} + H_{(aq)}^+ \tag{8-41}$$

Moreover, the water dissociation reaction always occurs in aqueous systems:

$$H_2O_{(l)} \overset{K_w^*}{\leftrightarrow} H^+_{(aq)} + OH^-_{(aq)} \qquad (8\text{-}42)$$

The speciation equilibrium model presented in this section is considered a simple ionic-based model, which consists of empirical equations extracted from different publications [236,278]. The model inputs are temperature, total pressure, and NaCl concentration.

The Dubessy *et al.* model [236] explained in Section 4.2.2 is used for H_2S solubility calculation. Assuming an open system, the water vapor pressure and H_2S partial pressure need to be calculated first. Then, the fugacity coefficient of H_2S is determined and from there, the concentration of dissolved $H_2S_{(aq)}$ can be obtained.

For K_1^*, an equation offered by Millero *et al.* [279] is adopted with a minor modification to fit better with the experimental pH data. The modified equation is given below:

$$K_1^* = 10^{98.080 - \frac{5765.4}{T} - 15.0455 lnT + 0.4737 wt^{0.5} - 0.114 wt} \qquad (8\text{-}43)$$

where, K_1^* is in mol/kgH_2O, T is temperature in K, and wt is NaCl concentration in wt.% [34]. For example, for 3 wt.% NaCl solution, $wt = 3$. The validity range reported by Millero *et al.* [279] for their proposed equation is from 0°C to 300°C [281] and from 0.5 wt.% to 4 wt.%. However, in this study, Equation (8-43) is used for a wider range of NaCl concentrations from 0 wt.% to 20 wt.% NaCl.

The equation implemented in the model for K_2^* is taken from Kharaka *et al.* [278]:

---

[34] In the original publication by Millero *et al.* [279], salinity, S(‰) with a unit of g/kg is used instead of wt. According to Millero and Leung [280], S is defined as weight of salt in one kilogram of solution. This indicates that $wt = 0.1S$. wt.% = 100 × salt mass/(salt mass + water mass)

$$K_2^* = \frac{(100 - wt)\rho_b}{10^5} \cdot 10^{-23.93+0.030446T-2.4831\times10^{-5}T^2} \tag{8-44}$$

where, K_2^* is in mol/kgH$_2$O and ρ_b is the density of solution in kg/m^3. The term contains ρ_b and wt is for conversion from molarity to molality concentration unit. K_2^* values are very small (~10^{-19} mol/kgH$_2$O at 25°C and pure water). Therefore, Reaction (8-41) has a minor effect on the equilibrium concentrations.

For K_{wa}^*, the empirical equation developed by Marshall and Franck [269] can be used (Appendix G). The effect of salt concentration on dissociation reaction of water is ignored in the calculations as this effect is shown to be minor (< 5% at 25°C and 1 atm) in a range of NaCl concentrations from 0 to 5 M [270]. Therefore, the activity of water, a_{H_2O} (dimensionless) can be assumed to be equal to unity, *i.e.*, $K_w^* = K_w$.

The stochiometric equilibrium constants are given below in terms of molality concentrations (m_i):

$$K_1^* = \frac{m_{H^+_{(aq)}} m_{HS^-_{(aq)}}}{m_{H_2S_{(aq)}}} \tag{8-45}$$

$$K_2^* = \frac{m_{H^+_{(aq)}} m_{S^{2-}_{(aq)}}}{m_{HS^-_{(aq)}}} \tag{8-46}$$

$$K_w^* = m_{H^+_{(aq)}} m_{OH^-_{(aq)}} \tag{8-47}$$

The main species produced due to dissociation Reactions (8-5), (8-4), and (8-6) in H$_2$O-NaCl-H$_2$S systems are $H^+_{(aq)}$, $HS^-_{(aq)}$, $S^{2-}_{(aq)}$, and $OH^-_{(aq)}$. To calculate the equilibrium concentrations of these four species, four equations are required. Three equations are: Equations (8-45), (8-46), and (8-47). The fourth equation is the charge neutrality equation[35]:

$$m_{H^+_{(aq)}} = m_{HS^-_{(aq)}} + 2m_{S^{2-}_{(aq)}} + m_{OH^-_{(aq)}} \tag{8-48}$$

If $HS^-_{(aq)}$, $S^{2-}_{(aq)}$, and $OH^-_{(aq)}$ concentrations in Equation (8-48) are derived with respect to $H^+_{(aq)}$ concentration, using Equations (8-45), (8-46), and (8-47), the following cubic equation can be established:

$$Am^3_{H^+_{(aq)}} + Bm^2_{H^+_{(aq)}} + Cm_{H^+_{(aq)}} + D = 0 \tag{8-49}$$

$$A = 1$$

$$B = 0$$

$$C = -\left(K^*_w + K^*_1 \cdot m_{H_2S_{(aq)}}\right)$$

$$D = -2 \cdot K^*_1 \cdot K^*_2 \cdot m_{H_2S_{(aq)}}$$

where, $m_{H_2S_{(aq)}}$ is the concentration of dissolved H_2S in the solution in molality, calculated from Dubessy *et al.* model [236] (Section 7.2.2). The equilibrium concentrations of all four species can be determined by solving Equation (8-49) [271].

The autogenous pH of solution can be obtained by using Equation (8-14). $\gamma^m_{H^+}$ can be obtained by using the simplified Pitzer's equations presented in Section 8.1.2.

---

[35] The charge neutrality equation holds valid with any concentration unit.

8.3 The Effect of Salt Concentration on Speciation Equilibria in Solutions Saturated with $CO_{2(g)}$ and $H_2S(g)$ Mixture

To the best of the author knowledge, the only available speciation equilibrium model in the open literature for the H_2O-NaCl-CO_2-H_2S system is the mixed solvent electrolyte model proposed by Springer *et al*. [240]. This model works for both H_2O-NaCl-CO_2 and H_2O-NaCl-H_2S systems as well.

8.3.1 The Mixed-Solvent Electrolyte (MSE) Speciation Equilibrium Model for H_2O-NaCl-CO_2-H_2S Systems

The mixed-solvent electrolyte (MSE) model is a comprehensive semi-empirical model that can predict the phase and chemical equilibria as well as thermal and volumetric properties of water, nonaqueous, or mixed solvents containing electrolytes and non-electrolytes with concentrations ranging from dilute solutions to highly concentrated solutions (such as saturation levels or fused salts) [135]. The MSE model thermodynamic framework was derived by Wang *et al.* [135]. Springer *et al.* adopted the MSE model for calculating phase and chemical equilibria in CO_2 containing aqueous and NaCl aqueous solutions (sometime called sweet systems[36]). Later, Springer *et al.* [241] updated the coefficients used in the MSE model in addition to extending it to the H_2O-NaCl-CO_2-H_2S system (sometime called sour system[37]). The MSE model is the foundation of the thermodynamic model implemented in the Stream Analyzer platform of

---

[36] In the oil and gas industry, any aqueous system that does not have $H_2S_{(aq)}$ such as H_2O-NaCl-CO_2 system is sometimes called sweet system.

[37] In the oil and gas industry, any aqueous system that has $H_2S_{(aq)}$ such as H_2O-NaCl-CO_2-H_2S system is sometimes called sour system.

the OLI Systems software. The MSE model[38] reproduced in this study for the H_2O-NaCl-CO_2-H_2S system is based on the latest release of the OLI Systems software, V11. The interaction parameters used in this study are provided by the OLI Systems through private communications. However, for proprietary reasons, they could not be listed in this document and only parameters provided in the Springer *et al.* publication [241] are reported here. In spite of this, it is expected that by using parameters included in Springer *et al.* [241] satisfactory results still can be obtained.

Since the MSE model works for both H_2O-NaCl-CO_2 and H_2O-NaCl-H_2S systems as well as their combination, *i.e.*, the H_2O-NaCl-CO_2-H_2S system, to avoid any repetition, the later system will be explained in this section. For any subsystem[39], such as the H_2O-NaCl-CO_2 and the H_2O-NaCl-H_2S systems, the equations and parameters related to unconcerned species need to be eliminated from the model.

The MSE model for the H_2O-NaCl-CO_2-H_2S system is stated to be valid for 0-300°C, 0-3500 bar, and 0-6 molal of NaCl. The required inputs for the MSE model in an open system are temperature (T), total pressure (P), NaCl concentration[40], $CO_{2(g)}$ mole fraction in the gas phase, and $H_2S_{(g)}$ mole fraction in the gas phase. The mole fraction of water can be calculated by using a water vapor pressure model. In this study, the Atkinson [128] water chemistry model is employed (Appendix H). Additionally, the

---

[38] The MSE model in this study corresponds to the MSE-SRK thermodynamic model in the OLI Systems software, as Soave-Redlich-Kwong (SRK) equation of state is used for the thermodynamic calculations in the gas phase.

[39] For the H_2O-NaCl-CO_2-H_2S system, the subsystems can be H_2O, H_2O-NaCl, H_2O-CO_2, H_2O-H_2S, H_2O-NaCl-CO_2, H_2O-NaCl-H_2S, and H_2O-CO_2-H_2S.

[40] In the MSE model the concentration unit for all species is mole fraction. However, conversion of input from other concentration units to mole fraction or conversion of outputs from mole fraction to other concentration units are feasible.

MSE model can be implemented in autogenous pH or in constant pH modes. Therefore, if the constant pH mode is chosen, then pH will be another required input.

There is a major difference between the MSE model and common speciation equilibrium models found in the literature such as the Li and Duan [136,249] model discussed in Section 8.1.3. In the MSE model, hydrogen or proton ion, H^+, is replaced with hydronium ion, H_3O^+. According to the OLI Systems webpage[41], the purpose of this replacement was to improve the predictions of properties (*e.g.*, pH) for strong acid solutions such as HCl aqueous solutions. The influence of having H_3O^+ ion instead of H^+ ion in the model on the equilibrium concentrations and the equilibrium activity coefficients is negligible that can be ignored. However, the equilibrium reactions for $CO_{2(aq)}$, $H_2S_{(aq)}$, and $H_2O_{(l)}$ dissociation will be different as H_3O^+ ion is composed of a water molecule and an H^+ ion:

$$H_3O^+_{(aq)} \leftrightarrow H^+_{(aq)} + H_2O_{(l)} \tag{8-50}$$

In the reproduced MSE model, five dissociation reactions are considered for the H_2O-NaCl-CO_2-H_2S open system in the liquid phase: two for $CO_{2(aq)}$ dissociation, two for $H_2S_{(aq)}$ dissociation and one for $H_2O_{(l)}$ dissociation. These reactions are given below:

$$CO_{2(aq)} + 2H_2O_{(l)} \leftrightarrow H_3O^+_{(aq)} + HCO^-_{3(aq)} \tag{8-51}$$

$$HCO^-_{3(aq)} + H_2O_{(l)} \leftrightarrow H_3O^+_{(aq)} + CO^{2-}_{3(aq)} \tag{8-52}$$

$$H_2S_{(aq)} + H_2O_{(l)} \leftrightarrow H_3O^+_{(aq)} + HS^-_{(aq)} \tag{8-53}$$

$$HS^-_{(aq)} + H_2O_{(l)} \leftrightarrow H_3O^+_{(aq)} + S^{2-}_{(aq)} \tag{8-54}$$

---

[41] https://wiki.olisystems.com/wiki/Development_of_the_Hydronium_Ion_for_MSE

$$2H_2O_{(l)} \leftrightarrow H_3O^+_{(aq)} + OH^-_{(aq)} \tag{8-55}$$

Reactions (8-51), (8-52), and (8-55) for CO_2 and H_2O dissociation have an extra $H_2O_{(l)}$ molecule on their reactant side compared to Reactions (8-5), (8-4), and (8-6), respectively. This is true for the H_2S dissociation reactions, when Reactions (8-53) and (8-54) are compared with Reactions (8-40) and (8-41), correspondingly.

Two reactions are considered for the vapor/liquid equilibria in the reproduced MSE model for the H_2O-NaCl-CO_2-H_2S open system:

$$CO_{2(g)} \leftrightarrow CO_{2(aq)} \tag{8-56}$$

$$H_2S_{(g)} \leftrightarrow H_2S_{(aq)} \tag{8-57}$$

Totally, there are three species in the gas phase ($H_2O_{(g)}$, $CO_{2(g)}$, and $H_2S_{(g)}$) and nine species in the liquid phase including water ($H_3O^+_{(aq)}$, $Na^+_{(aq)}$, $OH^-_{(aq)}$, $Cl^-_{(aq)}$, $HCO^-_{3(aq)}$, $CO^{2-}_{3(aq)}$, $HS^-_{(aq)}$, $S^{2-}_{(aq)}$, and $H_2O_{(l)}$). In this study, gas-rich phases and the formation of solids in the liquid phase are not considered.

The approach used in the MSE model to solve the dissociation and the vapor /liquid equilibria is equality of chemical potential of both side of reactions. For the dissociation equilibria in the liquid phase the equality of chemical potential is expressed as follows:

$$\sum \nu_i \, \mu_i^l = 0 \tag{8-58}$$

where[42], μ_i^l is the chemical potential of species i in the liquid phase in J/mol and ν_i is the stoichiometric coefficient of species i. For the liquid/vapor equilibria the chemical potential equality is given as below:

$$\mu_i^g = \mu_i^l \tag{8-59}$$

where, μ_i^g is the chemical potential of species i in the gas phase. In following text, the equations required to calculate both μ_i^l and μ_i^g will be explained from top to bottom.

According to the MSE model [241], μ_i^l can be calculated using:

$$\mu_i^l(T,P,x_i) = \mu_i^{l(o),m}(T,P) + RTln\frac{1000}{M_w} + RTlnx_i\gamma_i^{x,*}(T,P,x) \tag{8-60}$$

where, $\mu_i^{l(o),m}$ is the molality based standard-state chemical potential of species i in J/mol, T is temperature in K, P is total pressure, R is the gas constant in J/mol/K, M_w is the molecular weight of water in g/mol, x_i is the mole fraction of species i, and $\gamma_i^{x,*}$ is the unsymmetrical normalized mole fraction-based activity coefficient of species i [241][43]. The term $ln(1000/M_w)$ is for converting the unsymmetrical mole fraction-based standard-state chemical potential of species i ($\mu_i^{l(o),*}$) to the molality based standard-state chemical potential of species i ($\mu_i^{l(o),m}$):

$$\mu_i^{l(o),*} = \mu_i^{l(o),m} + RTln\frac{1000}{M_w} \tag{8-61}$$

The thermodynamic calculations related to this conversion is explained in detail in Appendix P. The reason for this conversion is that the chemical potential of electrolyte

---

[42] Equivalent to $\underset{Reactants}{\sum \nu_i \mu_i^l} = \underset{Products}{\sum \nu_i \mu_i^l}$

[43] More about the definition of each parameter can be found in Appendices M, N, and O.

species are often reported in molality basis in the literature [125], such as tables of standard state properties [282]. For water, since the mole-fraction standard-state based chemical potential (μ_w^o) is identical to that in molality basis ($\mu_w^{o,m}$), the above conversion is not required (Appendix N).

$\mu_i^{l(o),m}$ can be calculated as a function of temperature and pressure using Helgeson-Kirkham-Flowers (HKF) equation of state. A detailed description of HKF equations and $\mu_i^{l(o),m}$ calculation procedure is given in Appendix M. The standard-state chemical potential of water (μ_w^o) can be calculated according to Appendix N.

The chemical potential of species i in the gas phase (μ_i^g) is defined by:

$$\mu_i^g(T,P,y_i) = \mu_i^{g(o)}(T) + RTln\frac{Py_i\varphi_i(T,P)}{P_o} \tag{8-62}$$

where, $\mu_i^{g(o)}$ is the chemical potential of pure component i in the ideal gas state in J/mol, y_i is the mole fraction of species i in the gas phase (dimensionless), φ_i is the fugacity coefficient of pure gas species i (dimensionless), P is total pressure, and $P_o = 1$ bar is to make the term inside the natural logarithm dimensionless[44]. Calculation of $\mu_i^{g(o)}$ is explained in Appendix Q.

For a generic dissociation reaction in the form:

$$aA_{(aq)} + bB_{(aq)} \overset{K_{eq}}{\longleftrightarrow} cC_{(aq)} + dD_{(aq)} \tag{8-63}$$

The equality of chemical potentials for aqueous species mentioned in Equation (8-58) means:

---

[44] The choice of pressure unit is arbitrary. The fugacity coefficient (φ) does not depend on the pressure unit.

$$a\mu_A^l + b\mu_B^l - c\mu_C^L - d\mu_D^L = 0 \tag{8-64}$$

Expanding Equation (8-64) gives[45]:

$$\begin{aligned} &a\mu_A^{l(o),m} + aRTln\frac{1000}{M_w} + aRTlnx_A\gamma_A^{x,*} \\ &+ b\mu_B^{l(o),m} + bRTln\frac{1000}{M_w} + bRTlnx_B\gamma_B^{x,*} \\ &\qquad - \left(c\mu_C^{l(o),m} + cRTln\frac{1000}{M_w} + cRTlnx_C\gamma_C^{x,*}\right) \\ &\qquad - \left(d\mu_D^{l(o),m} + dRTln\frac{1000}{M_w} + dRTlnx_D\gamma_D^{x,*}\right) = 0 \end{aligned} \tag{8-65}$$

$$\begin{aligned} &c\mu_C^{l(o),m} + d\mu_D^{l(o),m} - a\mu_A^{l(o),m} - b\mu_B^{l(o),m} \\ &\qquad = -RTln\left(\frac{(x_C\gamma_C^{x,*})^c\cdot(x_D\gamma_D^{x,*})^d}{\left(x_A\gamma_A^{x,*}\right)^a\cdot\left(x_B\gamma_B^{x,*}\right)^b}\cdot\left(\frac{1000}{M_w}\right)^{c+d-a-b}\right) \end{aligned} \tag{8-66}$$

The left-hand side of Equation (8-66) is equal to the molar standard-state Gibbs free energy of dissociation reaction ($\Delta_r\bar{G}^o$) in J/mol. The term inside the natural logarithm on the right-hand side of Equation (8-66) is equal to the equilibrium constant of Reaction (8-63) in the molality basis (K_{eq})[46]. This resembles the well-known relation in thermodynamic for a system at equilibrium:

$$\Delta_r\bar{G}^o = -RTlnK_{ep} \tag{8-67}$$

Therefore, K_{ep} can be determined according to the following equation:

---

[45] This is only valid when neither reactants nor products is water. If water is involved in the reaction, no conversion term ($1000/M_w$) is required for water as $\mu_w^{l(o),*} = \mu_w^{l(o),m}$. In other words, the corresponding exponent of water for the conversion factor in the equation should be equal to zero (see Appendix Q).

[46] According to Appendix P, $x_i\gamma_i^{x,*}\cdot\frac{1000}{M_w} = \left(\frac{m_iM_wx_w}{1000}\right)\gamma_i^{x,*}\cdot\frac{1000}{M_w} = m_i\cdot\left(x_w\gamma_i^{x,*}\right) = m_i\gamma_i^m$

$$K_{ep} = \exp\left(\frac{a\mu_A^{l(o),m} + b\mu_B^{l(o),m} - c\mu_C^{l(o),m} - d\mu_D^{l(o),m}}{RT}\right) \tag{8-68}$$

Using $\mu_i^{l(o),m}$ values obtained with the HKF equation of state and following the above thermodynamic calculation, the equilibrium constants for the dissociation Reactions (8-51) to (8-55) can be obtained. These equations are given in Appendix R.

Similar to the aqueous species, applying the chemical potential equality Equation (8-59) to a symbolic liquid/vapor equilibrium in the following form:

$$A_{(g)} \overset{K_{sol}}{\longleftrightarrow} A_{(aq)} \tag{8-69}$$

results in:

$$\mu_A^{g(o)} + RTln\frac{Py_A\varphi_A}{P_o} = \mu_A^{l(o),m} + RTln\frac{1000}{M_w} + RTlnx_A\gamma_A^{x,*} \tag{8-70}$$

$$\mu_A^{g(o)} - \mu_A^{l(o),m} = RTln\frac{1000}{M_w} + RTln\frac{x_A\gamma_A^{x,*}}{\frac{Py_A\varphi_A}{P_o}} \tag{8-71}$$

$$\mu_A^{l(o),m} - \mu_A^{g(o)} = -RTln\frac{m_A\gamma_A^m}{f_A} \tag{8-72}$$

where, f_A is the fugacity of species A in the gas phase[47] and γ_A^m is the unsymmetrical molality-based activity coefficient of species A in infinitely dilute reference state. The left-hand side of Equation (8-72) is the molar standard-state Gibbs free energy of dissolution reaction ($\Delta_r\bar{G}^o$) in J/mol. The natural logarithm expression on the left-hand side of Equation 5-58) is equivalent to the solubility equilibrium constant[48] (K_{sol}). Therefore, considering Equation (8-67), K_{sol} can be obtained by:

---

[47] $f_i = Py_i\varphi_i/P_o$

[48] Regularly called the Henry's law constant.

$$K_{sol} = \exp\left(\frac{\mu_A^{g(o)} - \mu_A^{l(o),m}}{RT}\right) \qquad (8\text{-}73)$$

Following the above procedure for the vapor/liquid equilibria in Reactions (8-56) and (8-57), using $\mu_i^{l(o),m}$ and $\mu_A^{g(o)}$ values obtained with the HKF equation of state and the heat capacity integrations, respectively, the equilibrium constants for CO_2 and H_2S dissolution reactions can be determined. The equations for both equilibrium constants are provided in Appendix R.

The next step in the MSE model is to calculate the aqueous species activity coefficients (γ_i^x) in Equation (8-60) and gaseous species fugacity coefficients (φ_i) in Equation (8-62). The latter is computed by using the Soave-Redlich-Kwong (SRK) equation of state [248]. A detailed description of the calculation procedure for fugacity coefficients is presented in Appendix K.

The activity coefficient of an aqueous species (γ) is related to its excess Gibbs free energy (G^E). The excess Gibbs free energy of species i is the difference between the Gibbs free energy of species i in the real solution with that in a hypothetical ideal solution [283]. The relation between γ and G^E will be derived next. Starting with the conventional expression for the chemical potential of the arbitrary aqueous species i and expanding it gives:

$$\mu_i^l(T,P,x_i) = \mu_i^{l(o)}(T,P) + RTlnx_i + RTln\gamma_i^x(T,P,x) \qquad (8\text{-}74)$$

where, $\mu_i^{l(o)}$ is defined as the standard-state chemical potential of species i, x_i is the mole fraction of species i, γ_i^x is the (symmetrical) mole-fraction based activity coefficient in pure water reference state, and other parameters have their usual meaning. It should be noted that Equation (8-74) is equivalent to Equation (8-60), which is used in the MSE model to calculate the chemical potential of aqueous species.[49]

The sum of the first two terms on the right-hand side of Equation (8-74) is equal to the chemical potential of species i in an ideal solution ($\mu_i^{l,id}$) [125]:

$$\mu_i^{l,id}(T,P,x_i) = \mu_i^{l(o)}(T,P) + RTlnx_i \tag{8-75}$$

and, the last term on the right-hand side of Equation 5-60) is the molar excess chemical potential of species i (μ_i^E) [284]:

$$\mu_i^E(T,P,x) = RTln\gamma_i^x(T,P,x) \tag{8-76}$$

where, μ_i^E is in J/mol. μ_i^E is identical to the partial molar excess Gibbs free energy of species i ($\bar{G}_i^E$):

$$\mu_i^E = \bar{G}_i^E = \left(\frac{\partial G_i^E}{\partial n_i}\right)_{T,P.n_{j\neq i}} \tag{8-77}$$

where, G_i^E is excess Gibbs free energy for any amount of species i in J and n_i is the number of moles of species i in the solution. Therefore, γ_i^x can be related to G_i^E as follows:

$$ln\gamma_i^x = \left(\frac{\partial G_i^E/RT}{\partial n_i}\right)_{T,P.n_{j\neq i}} \tag{8-78}$$

In the MSE model, the excess Gibbs free energy is divided into three different contributions [135,240,241]:[50]

---

[49] More details in Appendix P.

[50] The approach used in the MSE model by Springer *et al.* [135,240,241] follows the UNIQUAC model originally proposed by Abrams and Prausnitz [158] and Maurer and Prausnitz and the extended UNIQUAC model advanced by Sander *et al.* [285–287] and Thomsen [288].

$$\frac{G_i^E}{RT} = \frac{G_{i,LR}^E}{RT} + \frac{G_{i,II}^E}{RT} + \frac{G_{i,SR}^E}{RT} \tag{8-79}$$

where, $G_{i,LR}^E$ is the contribution of long-range electrostatic interactions, $G_{i,II}^E$ accounts for specific ionic interactions (ion-ion and ion/molecule) that are not included in the long-range contribution, and $G_{i,SR}^E$ represents the short-range intermolecular interactions (molecule/molecule, ion/ion, and ion/molecule) [135,240,241]. Similarly, applying Equation (8-78) to Equation (8-79) results in an equation for the activity coefficient with three contributions:

$$ln\gamma_i^x = ln\gamma_i^{x,LR} + ln\gamma_i^{x,II} + ln\gamma_i^{SR} \tag{8-80}$$

The long-range activity coefficient contribution ($\gamma_i^{x,LR}$) can be derived based on the extended Pitzer–Debye–Huckel excess Gibbs free energy equation [135,141,241].[51] The derivation procedure is shown in Appendix S. The final equation is given below [135]:

$$\begin{aligned} ln\gamma_i^{x,LR} = {} & -A_x \left\{ \frac{2z_i^2}{\rho} \ln\left(\frac{1+\rho I_x^{\frac{1}{2}}}{\sum_k x_k \left[1+\rho\left(I_{x,k}^0\right)^{\frac{1}{2}}\right]} \right) + \frac{I_x^{\frac{1}{2}}\left(z_i^2 - 2I_x\right)}{1+\rho I_x^{\frac{1}{2}}} \right\} \\ & - \frac{4A_x I_x}{\rho} \left\{ 1 - \frac{1+\rho\left(I_{x,i}^o\right)^{\frac{1}{2}}}{\sum_k x_k \left[1+\rho\left(I_{x,k}^o\right)^{\frac{1}{2}}\right]} \right\} \end{aligned} \tag{8-81}$$

---

[51] The equation proposed by Pizer is based on unsymmetrical infinite dilution reference state ($\gamma_i^{x,*}$ = 1 when x_i → 0). However, the equation used in this study is in the symmetrical pure liquid reference state (γ_i^x = 1 when x_i → 1). The conversion to the unsymmetrical infinite dilution reference state is done when all three contributions to the activity coefficients are put together.

where, A_x is the Debye-Huckel limiting slope parameter in mole fraction basis (dimensionless) provided in Appendix I, z_i is the charge number of species i, x_i is the mole fraction of species i, ρ is an empirical parameter called the "closest approach" and is related to the hard-core collision diameter or distance of closest approach of ions in the solution [289]. A value of 14 is used for ρ in this study [135]. I_x is the ionic strength in mole fraction basis, and $I_{x,i}^{o}$ is the mole-fraction based ionic strength when the system composition reduces to pure component i, *i.e.*, $x_i = 1$. The summation is over all aqueous species (charged and neutral species) as well as solvent (water) [135,241]. I_x and $I_{x,i}^{o}$ equations are given below [135]:

$$I_x = \frac{1}{2}\sum_i x_i z_i^2 \tag{8-82}$$

$$I_{x,i}^{o} = \frac{1}{2} z_i^2 \tag{8-83}$$

The specific ionic interaction activity coefficient contribution ($\gamma_i^{x,II}$) term can be calculated from an expression given below [135]:

$$ln\gamma_i^{x,II} = \sum_i \sum_j x_i x_j\, B_{ij} - \sum_i \sum_j x_i x_j \frac{\partial B_{ij}}{\partial x_k} - 2\sum_i x_i B_{ik} \tag{8-84}$$

where, x_i is the mole fraction of species i, and B_{ij} is a function of I_x as below [135,241]:

$$B_{ij} = b_{ij} + c_{ij} \cdot exp\left(-\sqrt{I_x + a_1}\right) \tag{8-85}$$

where, a_1 is a constant equal to 0.01, and b_{ij} and c_{ij} are binary interaction parameters obtained by the two equations below[241]:

$$b_{ij} = b_{0,ij} + b_{1,ij}T + \frac{b_{2,ij}}{T} + b_{3,ij}T^2 + b_{5,ij}\exp\left(b_{6,ij}T\right) + b_{7,ij}TlnT + \frac{b_{8,ij}}{\exp\left(b_{9,ij}T\right)} + b_{P0,ij}P + b_{P1,ij}PT + \frac{b_{P2,ij}P}{T} \tag{8-86}$$

$$c_{ij} = c_{0,ij} + c_{1,ij}T + \frac{c_{2,ij}}{T} + c_{3,ij}T^2 + c_{5,ij}\exp\left(c_{6,ij}T\right) + c_{7,ij}TlnT + \frac{c_{8,ij}}{\exp\left(c_{9,ij}T\right)} \tag{8-87}$$

where, T is temperature in K, and P is pressure in atm, and $b_{\#,ij}$ and $c_{\#,ij}$ coefficients are listed in Table 8-3 [241]. It is assumed that $b_{\#,ij}$ and $c_{\#,ij}$ matrices are symmetrical, which means $b_{ij} = b_{ji}$ and $c_{ij} = c_{ji}$, and therefore, $B_{ij} = B_{ji}$ [241].

The derivative of B_{ij} with respect to x_k is given below:

$$\frac{\partial B_{ij}}{\partial x_k} = -\frac{c_{ij} \cdot exp\left(-\sqrt{I_x + a_1}\right) \cdot (z_k^2 - 2I_x)}{4\sqrt{I_x + a_1}} \tag{8-88}$$

Table 8-3

$b_{\#,ij}$ *binary interaction parameters for contribution of the specific ionic interactions to activity coefficient in the MSE model for* H_2O*-NaCl-*CO_2*-*H_2S *system* [241].

Species i	Species j	$b_{0,ij}$	$b_{1,ij}$	$b_{2,ij}$	$b_{3,ij}$	$b_{5,ij}$	$b_{6,ij}$	$b_{7,ij}$	$b_{8,ij}$	$b_{9,ij}$	$b_{P0,ij}$	$b_{P1,ij}$	$b_{P2,ij}$
Na^+	Cl^-	-213.999	1.86323	16036.8	0	-3.1279e-5	0.0221142	-0.244873	-4963540	0.0519778	0.00689898	0	-2.156
Na^+	CO_2	-10.9006	0	0	0	0	0	0	0	0	0	0	0
Na^+	H_2S	-8.8532	0	0	0	0	0	0	0	0	0	0	0
Cl^-	H_3O^+	75.511	-0.0858707	-21132.3	0	0	0	0	0	0	0	0	0
Cl^-	H_2S	-0.40445	0	0	0	0	0	0	0	0	0	0	0
H_2O	CO_2	-10.2134	0.0102376	783.548	0	0	0	0	0	0	0	0	0
H_2O	H_2S	-0.632123	0	0	0	0	0	0	0	0	0	0	0

$b_{\#,ij}$ for pairs that are not listed in the table are zero.

In this study a different set of parameters is used. An updated set of parameters based on V11 of OLI software is provided by OLI Systems and is used in this study. However, for proprietary reasons, it could not be included in this document. Despite of these, the current parameters listed in this table produce satisfactory results.

Table 8-4

$c_{\#,ij}$ *binary interaction parameters for the contribution of specific ionic interactions contribution to activity coefficient in the MSE model for* H_2O*-NaCl-*CO_2*-*H_2S *system* [241].

Species i	Species j	$c_{0,ij}$	$c_{1,ij}$	$c_{2,ij}$	$c_{3,ij}$	$c_{5,ij}$	$c_{6,ij}$	$c_{7,ij}$	$c_{8,ij}$	$c_{9,ij}$
Na^+	Cl^-	202.887	-2.15391	-9832.11	0	5.616e-5	0.0221142	0.293881	8004790	0.0519778
Cl^-	H_3O^+	-167.683	0.228176	35827.5	0	0	0	0	0	0

$c_{\#,ij}$ for pairs that are not listed in the table are zero.

In this study a different set of parameters is used. An updated set of parameters based on V11 of OLI software is provided by OLI Systems and is used in this study. However, for proprietary reasons, it could not be included in this document. Despite of these, the current parameters listed in this table produce satisfactory results.

The short-range activity coefficient contribution ($\gamma_i^{x,SR}$) is calculated by using the following equation [158]:

$$ln\gamma_i^{x,SR} = \ln\left(\frac{\Phi_i}{x_i}\right) + \left(\frac{z}{2}\right) q_i \ln\left(\frac{\theta_i}{\Phi_i}\right) + l_i - \frac{\Phi_i}{x_i}\left(\sum_j x_j l_j\right) - q_i \ln\left(\sum_j \theta_j \tau_{ji}\right) + q_i - q_i\left(\sum_j \frac{\theta_j \tau_{ij}}{\sum_k \theta_k \tau_{kj}}\right) \tag{8-89}$$

where, z is a constant called the lattice coordination number and is equal to 10, Φ_i and θ_i are defined as the average segment fraction and the average area fraction of molecule i, respectively:

$$\Phi_i \equiv \frac{r_i x_i}{\sum_j r_j x_j} \tag{8-90}$$

$$\theta_i \equiv \frac{q_i x_i}{\sum_j q_j x_j} \tag{8-91}$$

where, the structural parameters, q_i and r_i, are originally defined as the van der Waals area and volume of molecules i, respectively, relative to those of a standard segment [158]. However, this definition gave unsatisfactory results when used for multi-component electrolyte solutions. Therefore, in the extended UNIQUAC model, the structural area (q_i) and volume (r_i) parameters are considered as adjustable parameters [125]. In this study, q_i is 1.40 and r_i is 0.94 for all the species. l_i is defined by the following equation [158]:

$$l_i \equiv \left(\frac{z}{2}\right)(r_i - q_i) - (r_i - 1) \tag{8-92}$$

τ_{ij} definition is given by [158]:

$$\tau_{ij} \equiv \exp\left(-\frac{a_{ij}}{RT}\right) \tag{8-93}$$

where, a_{ij} is the binary interaction parameter between neutral molecules i and j and $a_{ij} \neq a_{ji}$, R is the gas constant in J/mol/K, and T is temperature in K. a_{ij} interaction parameters can be calculated by:

$$a_{ij} = a_{ij}^{(0)} + a_{ij}^{(1)}T + a_{ij}^{(2)}T^2 + \left[a_{ij}^{(P0)} + a_{ij}^{(P1)}T + a_{ij}^{(P2)}T^2\right]P \tag{8-94}$$

where, $a_{ij}^{(\#)}$ coefficients are given in Table 8-5. In this study, a slightly different set of parameters that those reported in Table 8-5 are used. The updated parameters are provided by OLI Systems and could not be included in this document. Inspite of this, the current parameters listed in Table 8-5 produce satisfactory results. It is evident from Table 8-5 that the short-range interaction parameters are established only for neutral molecules [241].

Table 8-5

Binary interaction parameters for the contribution of short-range interactions to activity coefficient in the MSE model for the H_2O-NaCl-CO_2-H_2S system [241].

Species i	Species j	$a_{ij}^{(0)}$	$a_{ij}^{(1)}$	$a_{ij}^{(2)}$	$a_{ij}^{(P0)}$	$a_{ij}^{(P1)}$	$a_{ij}^{(P2)}$
$H_2O_{(l)}$	$CO_{2(aq)}$	6809.06	-28.4899	0	-0.852074	0.00250429	0
$H_2O_{(l)}$	$H_2S_{(aq)}$	-2159.65	13.7874[§]	0	-0.2733197	0	0
$CO_{2(aq)}$	$H_2O_{(l)}$	-3387.02	-0.570569	0	-0.0085503	-0.000666502	0
$CO_{2(aq)}$	$H_2S_{(aq)}$	-25.1807	-25.1807	0	0	0	0
$H_2S_{(aq)}$	$H_2O_{(l)}$	13062.3	-28.1389	0	-0.905971	0	0
$H_2S_{(aq)}$	$CO_{2(aq)}$	-6906.15	31.6201	0	0	0	0

[§] It is reported incorrectly in the Springer *et al.* publication.

The $a_{ij}^{(\#)}$ parameters for $H_2O_{(l)}$ and $H_2S_{(aq)}$ are incorrectly switched in the Springer *et al.* publication.

In this study a different set of parameters is used. An updated set of parameters based on V11 of OLI software is provided by OLI Systems and is used in this study. However, for proprietary reasons, it could not be included in this document. Despite of these, the current parameters listed in this table produce satisfactory results.

As discussed at the beginning of this section, the computation of chemical equilibria requires the simultaneous use of standard-state chemical potential and activity coefficients of all species involved in the chemical reactions (Equations (8-60) and (8-61)). Since the standard-state chemical potentials from the available thermodynamic databases are defined for unsymmetrical, infinitely dilute reference state, an appropriate conversion must be performed on activity coefficients calculated in symmetrically pure liquid reference state to have consistent reference states. For this purpose, the mole fraction-based activity coefficient of species i in the symmetrical pure liquid reference state, γ_i^x, is converted to that based on the unsymmetrical, infinitely dilute reference state ($\gamma_i^{x,*}$) via[52]:

$$ln\gamma_i^{x,*} = ln\gamma_i^x - \lim_{\substack{x_i \to 0 \\ x_w \to 1}} ln\gamma_i^x \tag{8-95}$$

or a different presentation:

$$ln\gamma_{i,LR}^{x,*} = ln\gamma_{i,LR}^x - \lim_{\substack{x_i \to 0 \\ x_w \to 1}} ln\gamma_{i,LR}^x \tag{8-96}$$

$$ln\gamma_{i,II}^{x,*} = ln\gamma_{i,II}^x - \lim_{\substack{x_i \to 0 \\ x_w \to 1}} ln\gamma_{i,II}^x \tag{8-97}$$

$$ln\gamma_{i,SR}^{x,*} = ln\gamma_{i,SR}^x - \lim_{\substack{x_i \to 0 \\ x_w \to 1}} ln\gamma_{i,SR}^x \tag{8-98}$$

$$ln\gamma_i^{x,*} = ln\gamma_{i,LR}^{x,*} + ln\gamma_{i,II}^{x,*} + ln\gamma_{i,SR}^{x,*} \tag{8-99}$$

where, $\gamma_{i,LR}^{x,*}$, $\gamma_{i,II}^{x,*}$, and $\gamma_{i,SR}^{x,*}$ are the three contributions of mole-fraction based activity coefficient in the unsymmetrical, infinitely dilute reference state.

---

[52] Another form of Equation (8-95) is: $\gamma_i^{x,*} = \frac{\gamma_i^x}{\gamma_i^{x,\infty}}$, where $\gamma_i^{x,\infty} = \lim_{\substack{x_i \to 0 \\ x_w \to 1}} ln\gamma_i^x$ [125].

Figure 8-2

The flow diagram of the algorithm used to calculate the speciation equilibrium with the MSE model in the H_2O*-NaCl-*CO_2*-*H_2S *system.* H_2S *mole percent is taken as the model input. However,* CO_2 *can be the model input as well, instead of* H_2S*.*

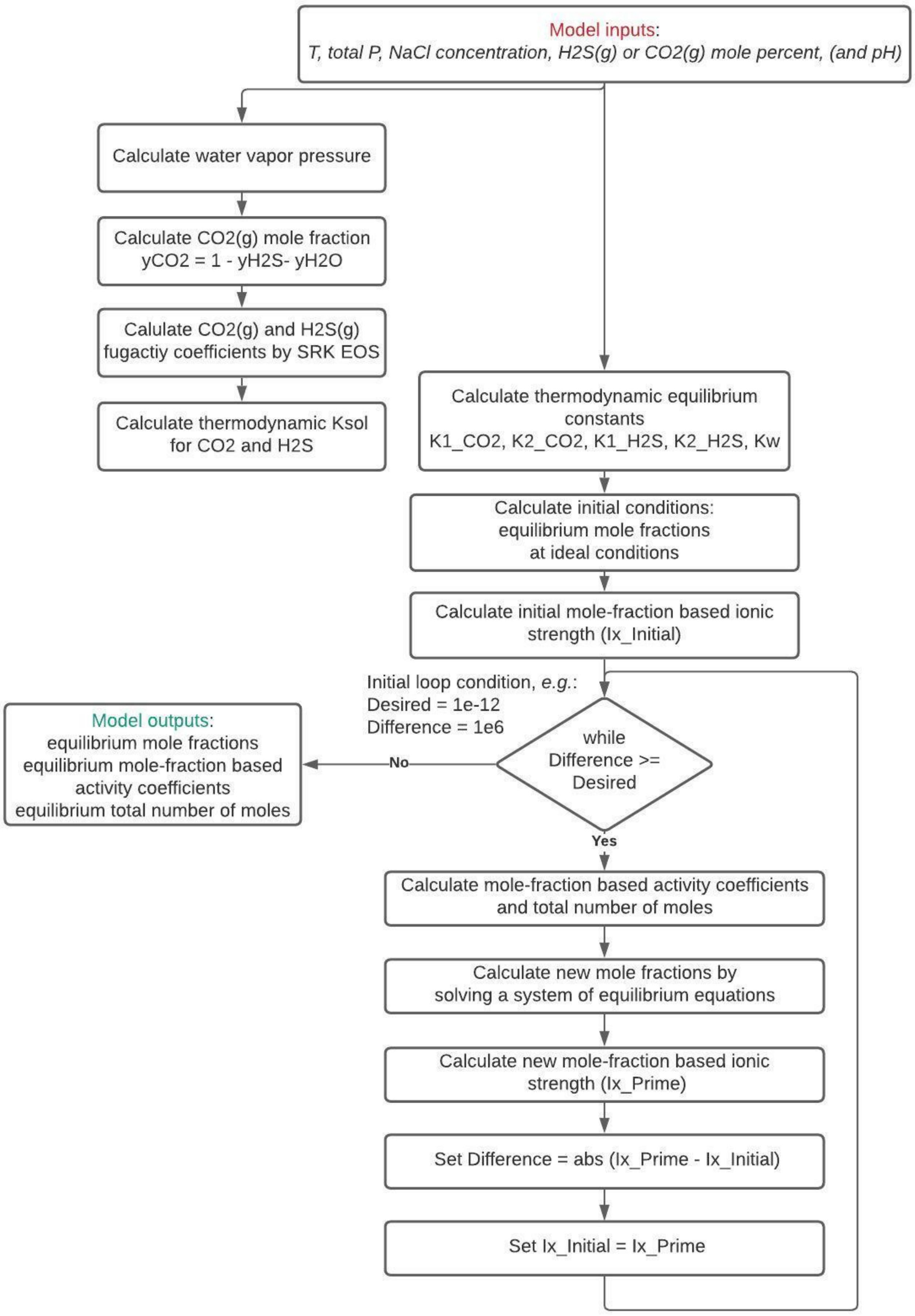

The equations for calculating the three activity coefficient contributions, Equations (8-81), (8-84), and (8-89), are all mole fraction dependent. On the other hand, the equilibrium equations, Equations (R-3), (R-4), and (R-10) to (R-14) in Appendix R, are all functions of mole fractions and activity coefficients. Therefore, all these equations need to be solved simultaneously in a loop by an iterative procedure to obtain the equilibrium concentrations and the equilibrium activity coefficients. The algorithm used in this study for computing the equilibrium concentrations and activity coefficients is illustrated in Figure 8-1. This algorithm is designed for an open system[53], what is seen in most corrosion scenarios, including internal corrosion of oil and gas pipelines. In an open system, at a constant temperature and total pressure, the mole fraction of gaseous species in the gas phase is constant. This means that the partial pressure of gaseous species is constant as well in the gas phase. For the H_2O-NaCl-CO_2-H_2S mixture, the gaseous species are water vapor, $CO_{2(g)}$ and $H_2S_{(g)}$.

The required model inputs for an open H_2O-NaCl-CO_2-H_2S system are temperature, total pressure, NaCl concentration, and the mole fraction (mole percent or partial pressure) of either $CO_{2(g)}$ or $H_2S_{(g)}$.

The steps to the algorithm are discussed below:

1) Calculate the water vapor pressure. In this study, a model by Atkinson [128] is used because it considers the effect of salt concentration on water vapor pressure. Appendix H describes the Atkinson model [128].

---

[53] Contrary to this study, the OLI software is mainly designed for closed systems: constant initial moles.

2) Calculate $CO_{2(g)}$ and $H_2S_{(g)}$ fugacity (f) based on the SRK equation of state given in Appendix K and the following equations[54]:

$$f_i = P y_i \varphi_i \tag{8-100}$$

3) Calculate the thermodynamic equilibrium constant (K_{sol}^{i}) for CO_2 and H_2S solubility, Reactions (8-56) and (8-57), using Equations (R-3) and (R-4) in Appendix R.

   Calculate molality-based activity (a_i^m) of $CO_{2(aq)}$ and $H_2S_{(aq)}$ by:

$$a_i^m = K_{sol}^{i} \times f_i \tag{8-101}$$

4) Calculate the thermodynamic equilibrium constants (K_1^i, K_2^i, and K_w) for CO_2, H_2S, and water dissociation, Reactions (8-51) to (8-55), with the help of Equations (R-10) to (R-14) in Appendix R.

5) Find initial concentrations for initiating the iteration loop. The best choice are the equilibrium concentrations at ideal conditions. Six equations are needed to calculate the equilibrium concentrations of $H^+_{(aq)}$, $HCO^-_{3(aq)}$, $CO^{2-}_{3(aq)}$, $HS^-_{(aq)}$, $S^{2-}_{(aq)}$, and $OH^-_{(aq)}$. Five of them come from the equations for the thermodynamic dissociation equilibrium constants, assuming ideal conditions ($\gamma_i^m = 1$ and $a_{H_2O_{(l)}} = 1$):

$$K_1^{CO_2} = \frac{m_{H_3O^+_{(aq)}} m_{HCO^-_{3(aq)}}}{m_{CO_{2(aq)}}} \tag{8-102}$$

$$K_2^{CO_2} = \frac{m_{H_3O^+_{(aq)}} m_{CO^{2-}_{3(aq)}}}{m_{HCO^-_{3(aq)}}} \tag{8-103}$$

---

[54] All the parameters are defined earlier.

$$K_1^{H_2S} = \frac{m_{H_3O^+_{(aq)}} m_{HS^-_{(aq)}}}{m_{H_2S_{(aq)}}} \tag{8-104}$$

$$K_2^{H_2S} = \frac{m_{H_3O^+_{(aq)}} m_{S^{2-}_{(aq)}}}{m_{HS^-_{(aq)}}} \tag{8-105}$$

$$K_w = m_{H_3O^+_{(aq)}} m_{OH^-_{(aq)}} \tag{8-106}$$

The sixth equation is the solution charge neutrality constrain:

$$m_{H_3O^+_{(aq)}} = m_{HCO^-_{3(aq)}} + 2m_{CO^{2-}_{3(aq)}} + m_{HS^-_{(aq)}} + 2m_{S^{2-}_{(aq)}} + m_{OH^-_{(aq)}} \tag{8-107}$$

Finally, the following cubic equation can be solved to acquire the initial equilibrium molality concentrations:

$$Am^3_{H_3O^+_{(aq)}} + Bm^2_{H_3O^+_{(aq)}} + Cm_{H_3O^+_{(aq)}} + D = 0 \tag{8-108}$$

$$A = 1$$

$$B = 0$$

$$C = -\left(K_w + K_1^{CO_2} m_{CO_{2(aq)}} + K_1^{H_2S} m_{H_2S_{(aq)}}\right)$$

$$D = -2(K_1^{CO_2} K_2^{CO_2} m_{CO_{2(aq)}} + K_1^{H_2S} K_2^{H_2S} m_{H_2S_{(aq)}})$$

6) Calculate the initial mole fraction based ionic strength of solution, using Equation (8-82):

$$I_x = \frac{1}{2}(x_{Na^+} + x_{Cl^-} + x_{H_3O^+} + x_{OH^-} + x_{HCO_3^-} + 4x_{CO_3^{2-}} + x_{HS^-} + 4x_{S^{2-}}) \tag{8-109}$$

where, x_i is the mole fraction of species i. For example, $x_{H_3O^+}$ is equal to the number of moles of $H_3O^+_{(aq)}$ ($n_{H_3O^+}$) divided by the initial total number of moles in the solution (n_T^o):

$$x_{H_3O^+} = \frac{n_{H_3O^+}}{n_T^o}$$
$$= \frac{m_{H_3O^+}}{m_{Na^+} + m_{Cl^-} + m_{H_3O^+} + m_{OH^-} + m_{HCO_3^-} + m_{CO_3^{2-}} + m_{HS^-} + m_{S^{2-}} + 1000/M_w} \quad (8\text{-}110)$$

Here, it is assumed that the solution contains only 1000 g of water as the solvent. This means that the numbers of moles of species will be equal to their molality concentrations. Thus:

$$n_{H_3O^+} \equiv m_{H_3O^+} \quad (8\text{-}111)$$

$$n_T^o = m_{Na^+_{(aq)}} + m_{Cl^-_{(aq)}} + m_{H_3O^+_{(aq)}} + m_{OH^-_{(aq)}} + m_{HCO^-_{3(aq)}}$$
$$+ m_{CO^{2-}_{3(aq)}} + m_{HS^-_{(aq)}} + m_{S^{2-}} + m_{CO_{2(aq)}} + m_{H_2S_{(aq)}} \quad (8\text{-}112)$$
$$+ 1000/M_w$$

where, m_i are the molality concentrations obtained in Step 6 and M_w is the molecular weight of water in g/mol. Equations (8-110) to (8-112) are valid for other aqueous species as well. The mole fraction of water (x_w) can be calculated from the following equation:

$$x_w = \frac{n_w}{n_T^o} = \frac{1000/M_w}{n_T^o} \quad (8\text{-}113)$$

where, n_w is number of moles of water.

7) Initiate a *while* loop with its "criterion" defined as the variation in the ionic strength which needs to become less than a desired value. In this study, the desired value set to be 10^{-12}.

8) Calculate the three contributions (γ_{LR}^{x}, γ_{II}^{x}, and γ_{SR}^{x}) of the symmetrical mole-fraction based activity coefficient for all species including water, using Equations (8-81), (8-84), and (8-89) and the mole fractions obtained in Step 7.
9) Convert the symmetrical mole-fraction based activity coefficients to the unsymmetrical mole-fraction based activity coefficients at infinitely dilute for all species including water, using Equation (8-96) to (8-99).
10) Calculate new mole fractions by solving the following system of nonlinear equations for the autogenous pH conditions:

$$K_1^{CO_2} \cdot a_{CO_{2(aq)}}^{x} \cdot (x_w \gamma_w^{x,*})^2 - \left(x_{H_3O^+_{(aq)}} \gamma_{H_3O^+_{(aq)}}^{x,*}\right) \cdot \left(x_{HCO^-_{3(aq)}} \gamma_{HCO^-_{3(aq)}}^{x,*}\right) \cdot \left(\frac{1000}{M_w}\right) = 0 \tag{8-114}$$

$$K_2^{CO_2} \left(x_{HCO^-_{3(aq)}} \gamma_{HCO^-_{3(aq)}}^{x,*}\right) \cdot (x_w \gamma_w^{x,*}) - \left(x_{H_3O^+_{(aq)}} \gamma_{H_3O^+_{(aq)}}^{x,*}\right) \cdot \left(x_{CO^{2-}_{3(aq)}} \gamma_{CO^{2-}_{3(aq)}}^{x,*}\right) \cdot \left(\frac{1000}{M_w}\right) = 0 \tag{8-115}$$

$$K_1^{H_2S} \cdot a_{H_2S_{(aq)}}^{x} \cdot (x_w \gamma_w^{x,*}) - \left(x_{H_3O^+_{(aq)}} \gamma_{H_3O^+_{(aq)}}^{x,*}\right) \cdot \left(x_{HS^-_{(aq)}} \gamma_{HS^-_{(aq)}}^{x,*}\right) \cdot \left(\frac{1000}{M_w}\right) = 0 \tag{8-116}$$

$$K_2^{H_2S} \left(x_{HS^-_{(aq)}} \gamma_{HS^-_{(aq)}}^{x,*}\right) \cdot (x_w \gamma_w^{x,*}) - \left(x_{H_3O^+_{(aq)}} \gamma_{H_3O^+_{(aq)}}^{x,*}\right) \cdot \left(x_{S^{2-}_{(aq)}} \gamma_{S^{2-}_{(aq)}}^{x,*}\right) \cdot \left(\frac{1000}{M_w}\right) = 0 \tag{8-117}$$

$$K_w (x_w \gamma_w^{x,*})^2 - \left(x_{H_3O^+_{(aq)}} \gamma_{H_3O^+_{(aq)}}^{x,*}\right) \cdot \left(x_{OH^-_{(aq)}} \gamma_{OH^-_{(aq)}}^{x,*}\right) \cdot \left(\frac{1000}{M_w}\right)^2 = 0 \tag{8-118}$$

$$x_{H_3O^+_{(aq)}} + x_{Na^+_{(aq)}} - \left(x_{Cl^-_{(aq)}} + x_{OH^-_{(aq)}} + x_{HCO^-_{3(aq)}} + 2x_{CO^{2-}_{3(aq)}} + x_{HS^-_{(aq)}} + 2x_{S^{2-}_{(aq)}}\right) = 0 \tag{8-119}$$

$$1 - \left(x_{Na^+_{(aq)}} + x_{Cl^-_{(aq)}} + x_{H_3O^+_{(aq)}} + x_{OH^-_{(aq)}} + x_{HCO^-_{3(aq)}} + x_{CO^{2-}_{3(aq)}} + x_{HS^-_{(aq)}} + x_{S^{2-}_{(aq)}} + x_{CO_{2(aq)}} + x_{H_2S_{(aq)}} + x_w\right) = 0 \tag{8-120}$$

where, the first five equations correspond to dissociation equilibria, Reactions (8-51) to (8-55), the sixth equation is the charge neutrality equation, and the seventh equation indicates that the sum of all the mole fractions is equal to unity. For the constant pH conditions, one more equation representing the pH constrain needs to be added to the system of equation.

The activities of dissolved $CO_{2(aq)}$ and $H_2S_{(aq)}$ in mole fraction basis in Equations (8-114) and (8-116), respectively, are equal to:

$$a^x_{CO_{2(aq)}} = \frac{a^m_{CO_{2(aq)}} M_w}{1000} \tag{8-121}$$

$$a^x_{H_2S_{(aq)}} = \frac{a^m_{H_2S_{(aq)}} M_w}{1000} \tag{8-122}$$

where, $a^m_{CO_{2(aq)}}$ and $a^m_{H_2S_{(aq)}}$ are obtained from Step 4.

The mole fraction of $H_2O_{(l)}$ (x_w) in Equations (8-114) to (8-120) is defined as:

$$x_w = \frac{1000}{M_w n_T} \tag{8-123}$$

and, the mole fractions of $Na^+_{(aq)}$, $Cl^-_{(aq)}$, $CO_{2(aq)}$, and $H_2S_{(aq)}$ in Equation (8-120) are defined as:

$$x_{Na^+_{(aq)}} = \frac{n_{Na^+_{(aq)}}}{n_T} \equiv \frac{m_{Na^+_{(aq)}}}{n_T} \tag{8-124}$$

$$x_{Cl^-_{(aq)}} = \frac{n_{Cl^-_{(aq)}}}{n_T} \equiv \frac{m_{Cl^-_{(aq)}}}{n_T} \tag{8-125}$$

$$x_{CO_{2(aq)}} = \frac{a^x_{CO_{2(aq)}}}{\gamma^{x,*}_{CO_{2(aq)}}} \tag{8-126}$$

$$x_{H_2S_{(aq)}} = \frac{a^x_{H_2S_{(aq)}}}{\gamma^{x,*}_{H_2S_{(aq)}}} \tag{8-127}$$

where, n_T is total number of moles in the solution at equilibrium[55], and $m_{Na^+_{(aq)}}$ and $m_{Cl^-_{(aq)}}$ are equal to the initial moles of $Na^+_{(aq)}$ and $Cl^-_{(aq)}$. Since the amount of water as the solvent is assumed constant (1000 g), the initial moles of $Na^+_{(aq)}$ and $Cl^-_{(aq)}$ are equivalent to their molality concentrations given as model inputs. Additionally, $Na^+_{(aq)}$ and $Cl^-_{(aq)}$ are presumed to be non-reacting species. Hence, their number of moles remains constant throughout the iteration process.

Equations (8-121) to (8-127) need to be implemented into Equations (8-114) to (8-120). Finally, there are seven independent equations: Equations (8-114) to (8-120) and seven unknows: $x_{H_3O^+_{(aq)}}$, $x_{OH^-_{(aq)}}$, $x_{HCO^-_{3(aq)}}$, $x_{CO^{2-}_{3(aq)}}$, $x_{HS^-_{(aq)}}$, $x_{S^{2-}_{(aq)}}$, and n_T. Therefore, the system of equations can be solved for the unknowns. The *fsolve* solver in MATLAB with *Levenberg-Marquardt* algorithm is used to solve the system of equations. The initial conditions for the *fsolve* solver can be the initial mole fractions and n_T^o acquired in Steps 6 and 7.

---

[55] n_T is different from n_T^o as the system of study is an open system, in which there is a continuous supply of $CO_{2(aq)}$ and $H_2S_{(aq)}$

11) Recalculate the mole-fraction based ionic strength of solution using the mole fractions and n_T obtained in Step 11.
12) Subtract the ionic strength in Step 12 from the initial ionic strength computed in Step 7. Calculate the absolute value of their difference.
13) If the absolute value of the difference is smaller than the desired value defined in Step 8, then the calculated mole fractions, n_T, and activity coefficients are the equilibrium values. Otherwise, return to Step 9 and calculate the activity coefficients with new mole fractions obtained in Step 11 and iterate the steps until the condition defined in Step 8 is satisfied.
14) Convert the calculated equilibrium mole fractions (x_i) and equilibrium unsymmetrical mole-fraction based activity coefficients ($\gamma_i^{x,*}$) to molality concentrations (m_i) and unsymmetrical molality-based activity coefficients (γ_i^m), respectively, by using the following equations:

$$m_i \equiv x_i n_T \tag{8-128}$$

$$\gamma_i^m \equiv x_w \gamma_i^{x,*} \tag{8-129}$$

As noted earlier, one the most applicable outputs of any speciation equilibrium model is the equilibrium pH of the solution. In the MSE model, since $H^+_{(aq)}$ does not exist, the pH needs to be calculated based on $H_3O^+_{(aq)}$, with a different equation than Equation (8-14) used in Li and Duan model:

$$pH = -log_{10}\left(\frac{x_{H_3O^+_{(aq)}}\gamma^{x,*}_{H_3O^+_{(aq)}}}{x_w\gamma_w^{x,*}}\right) - log_{10}(\frac{1000}{M_w}) \tag{8-130}$$

The derivation of Equation (8-130) is given in Appendix T.

8.4 Quantification of the Effect of Salt Concentration on Speciation Equilibria in Solutions Saturated with $CO_{2(g)}$ or $H_2S(g)$

As mentioned in Chapter 4, when salt concentration is varied in an aqueous solution, the equilibrium activity coefficients of all species present in the solution change due to alternation of interspecies interactions. Because of that, the equilibrium concentrations of reacting species need to vary as the thermodynamic equilibrium constants do not change with salt concentration. These changes in the equilibrium activity coefficients and equilibrium concentrations can be quantified with the help of thermodynamic speciation models explained in previous section. Two examples obtained by using the MSE model will be presented below for aqueous NaCl solutions saturated with CO_2 and H_2S gases.

Figure 8-3 shows the equilibrium concentration, the equilibrium activity coefficient, and the equilibrium activity of five aqueous species in addition to activity of water for aqueous NaCl solutions saturated with CO_2 at 25°C and 1 bar total pressure.

In Figure 8-3 A, with increasing NaCl concentration, the activity coefficient of $H_3O^+_{(aq)}$ ion decreases from 1.0 at 0 wt.% NaCl to about 0.8 at ~ 1 wt.% NaCl. With further increase in NaCl concentration, the activity coefficient of $H_3O^+_{(aq)}$ ion reverses the trend and increases to ~ 4.0 at 25 wt.% NaCl. On the other hand, the concentration of $H_3O^+_{(aq)}$ ion shows an increasing trend between 0 wt.% to ~ 3 wt.% and a decreasing trend for NaCl concentrations greater then ~ 3 wt.%. The activity of $H_3O^+_{(aq)}$ ion, which is the product of concentration and activity coefficient monotonously increases with higher NaCl concentrations.

For $CO_{2(aq)}$ in Figure 8-3 C, its concentration decreases, while its activity coefficient increases with increasing NaCl concentration. The activity of $CO_{2(aq)}$ is almost[56] constant over the entire range of NaCl concentrations as fugacity of $CO_{2(g)}$ is almost constant in an open system. According to Figure 8-3 B and D, the trends for concentration, activity coefficient, and activity of $OH^-_{(aq)}$ and HCO_3^- ions with NaCl concentration are similar. The concentration for both shows a maximum at ~ 3 wt.% NaCl. Their activity coefficients decrease monotonously when NaCl concentration is increased. However, the slope of changes becomes smaller at high NaCl concentrations. The activity of $OH^-_{(aq)}$ and HCO_3^- ions sharply decrease with increasing NaCl concentration.

The activity coefficient of $Cl^-_{(aq)}$ ion shows a minimum at ~ 6 wt.% NaCl, whereas its concentration and activity monotonously increase with a rise in NaCl concentration (Figure 8-3 E). In Figure 8-3 F, the activity of water decreases from 1 at 0 wt.% NaCl to around 0.77 at 25 wt.% NaCl.

The reason for the observed trends in the activity coefficients of aqueous dissolved species with NaCl concentration can be understood by considering the changes in the three contributions of activity coefficient with NaCl concentration. Figure 8-4 illustrates the variations in the long-range, specific ionic interaction, and short-range contributions of the activity coefficient with NaCl concentration for $H_3O^+_{(aq)}$, $\mathrm{CO}_{2(\mathrm{aq})}$, $HCO^-_{3(aq)}$, and $Cl^-_{(aq)}$ ions. For example Figure 8-4 C, for $H_3O^+_{(aq)}$ ion, the long-range

---

[56] Water vapor pressure decreases slightly with increasing NaCl concentration. Thus, there will be a very small increase in the activity of $CO_{2(aq)}$ with higher NaCl concentration.

($\gamma_{H_3O^+_{(aq)}}^{m,LR}$) and the short-range ($\gamma_{H_3O^+_{(aq)}}^{m,SR}$) contributions of the activity coefficient decreases with increasing NaCl concentration, while the specific ionic interaction ($\gamma_{H_3O^+_{(aq)}}^{m,II}$) contribution increases. The slope of changes for $\gamma_{H_3O^+_{(aq)}}^{m,II}$ is greater than that for $\gamma_{H_3O^+_{(aq)}}^{m,LR}$ and $\gamma_{H_3O^+_{(aq)}}^{m,SR}$. Therefore, the activity coefficient of $H_3O^+_{(aq)}$ ion shows a minimum at low NaCl concentrations.

Figure 8-3

Bulk concentration, activity coefficient, and activity of (A) $H_3O^+_{(aq)}$ ion, (B) $OH^-_{(aq)}$ ion, (C) $CO_{2(aq)}$, (D) $HCO^-_{3(aq)}$ ion, (E) $Cl^-_{(aq)}$ ion, and (F) $H_2O_{(l)}$ calculated by the mixed solvent electrolyte speciation model for CO_2 saturated aqueous NaCl solutions at 25°C, and 1 bar total pressure (~ 0.98 bar pCO_2). 25 wt.% NaCl is equivalent to 5.7 molal NaCl.

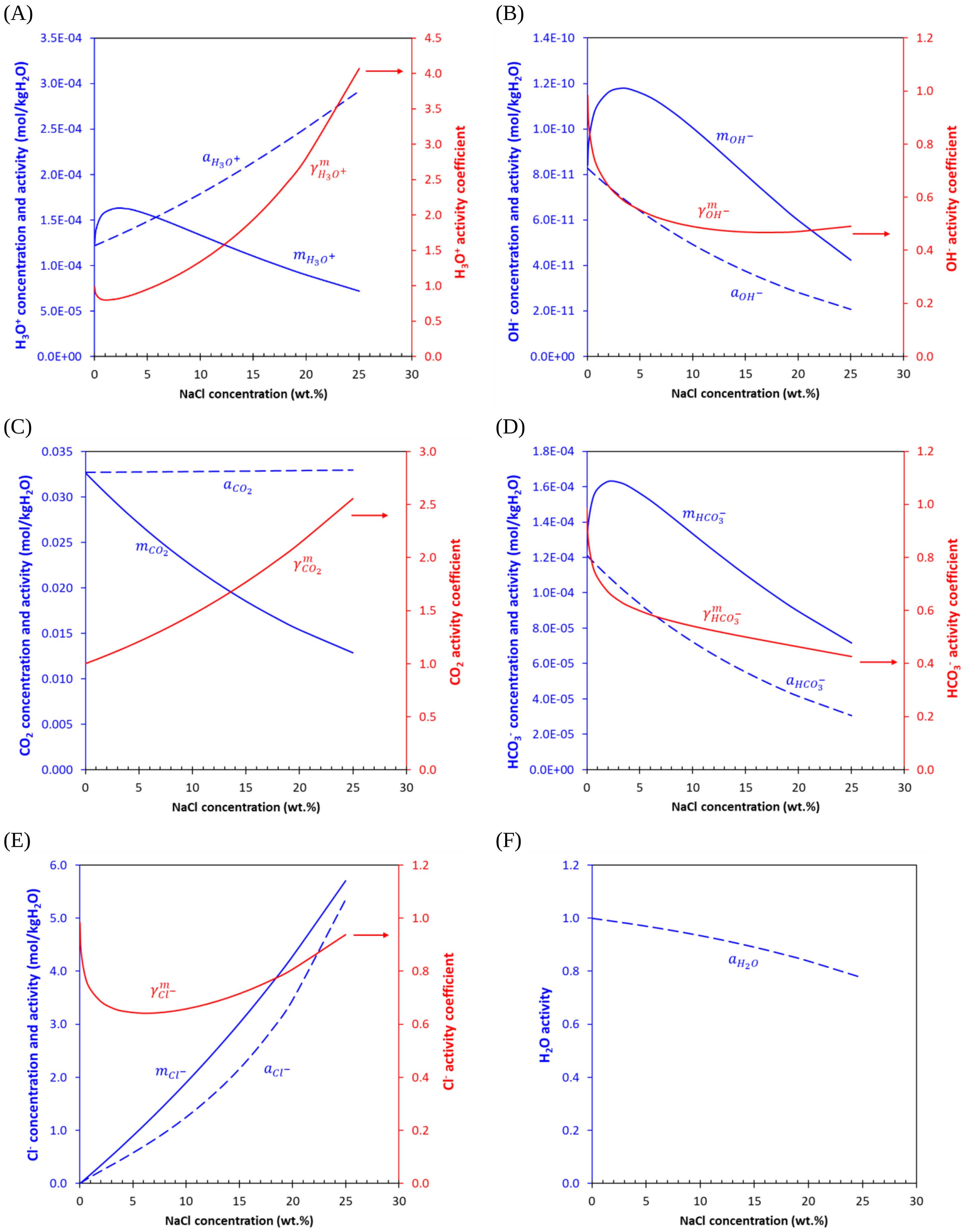

Figure 8-4

The variations in the long-range ($\gamma^{m,LR}$), the specific ionic interaction ($\gamma^{m,II}$), and the short-range ($\gamma^{m,SR}$) contributions of molality-based activity coefficient (γ^{m}) with respect to salt concentration at 25°C and 1 bar total pressure for: (A) $H_3O^+_{(aq)}$ ion, (B) $CO_{2(aq)}$, (C) $HCO^-_{3(aq)}$ ion, (D) $Cl^-_{(aq)}$.

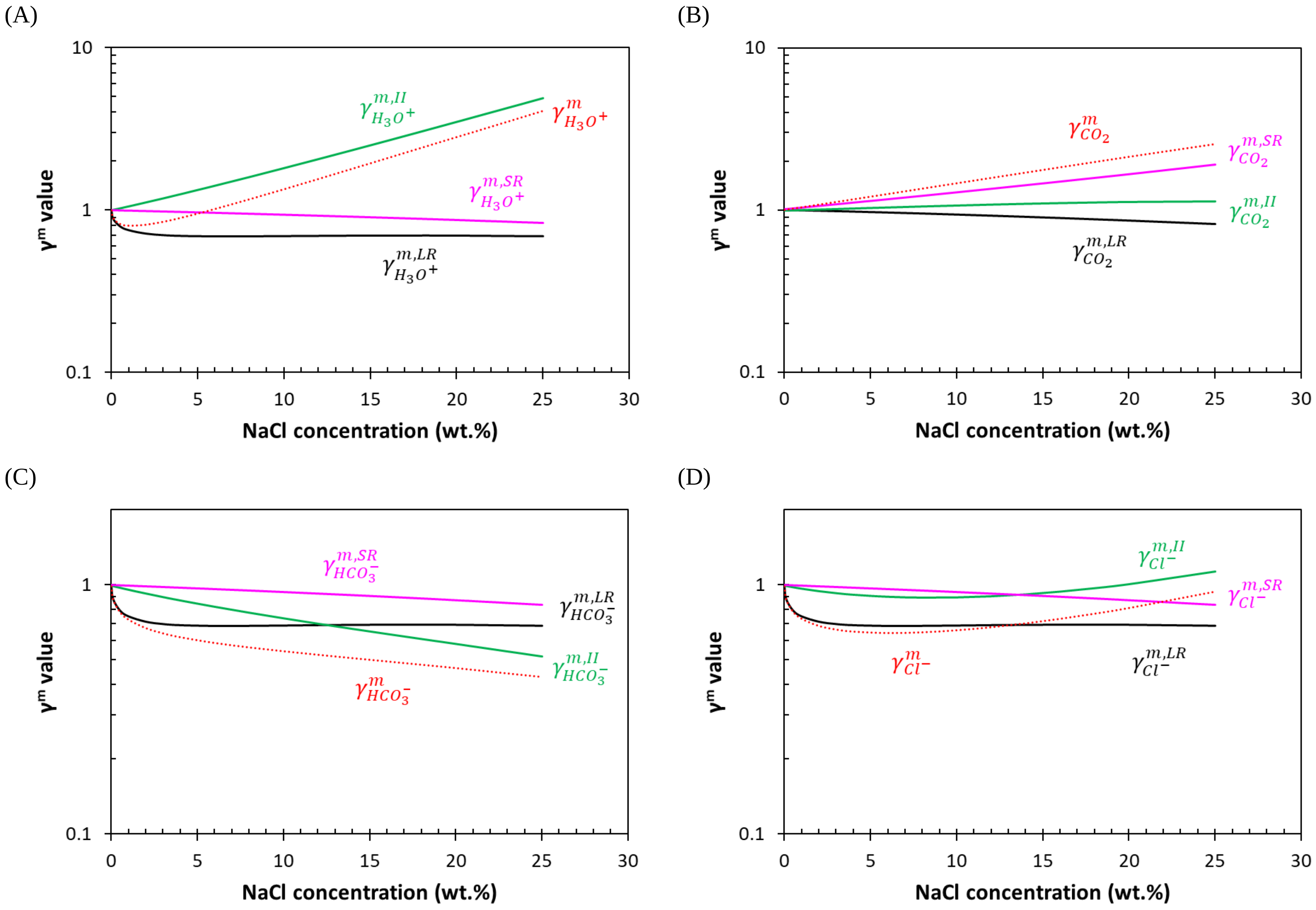

Figure 8-5 illustrates the equilibrium concentration, the equilibrium activity coefficient, and the equilibrium activity of five aqueous species in addition to activity of water for aqueous NaCl solutions saturated with H_2S at 25^{o}C and 1 bar total pressure.

In Figure 8-5 A, when NaCl concentration is increased, the activity coefficient of $H_3O^+_{(aq)}$ ion decreases from 1.0 at 0 wt.% NaCl to about 0.8 at ~ 1 wt.% NaCl. At higher NaCl concentration, the activity coefficient of $H_3O^+_{(aq)}$ ion switches the trend and increases to ~ 4.0 at 25 wt.% NaCl. On the other hand, the concentration of $H_3O^+_{(aq)}$ ion shows an increasing trend between 0 wt.% to ~ 3 wt.% and a declining trend for NaCl concentrations larger then ~ 3 wt.%. The activity of $H_3O^+_{(aq)}$ ion, which is the product of concentration and activity coefficient, monotonously increases when NaCl concentration is increased. In Figure 8-5 B, the activity coefficient of $OH^-_{(aq)}$ ion reveals a minimum at ~ 16 wt.%, whereas the concentration of $OH^-_{(aq)}$ ion has a maximum at around 6 wt.% NaCl. The activity of $OH^-_{(aq)}$ ion decreases monotonously with increasing NaCl concentration.

With increasing NaCl concentration in Figure 8-5 C, the concentration of $H_2S_{(aq)}$ decreases, while its activity coefficient increases. The activity of $H_2S_{(aq)}$ almost[57] does not vary over the entire range of NaCl concentrations as fugacity of $H_2S_{(g)}$ is almost constant in an open system. The activity coefficient of $HS^-_{(aq)}$ ion has a minimum at around 2 wt.% NaCl, while its concentration shows a maximum at this NaCl concentration (Figure 8-5 D).

---

[57] Water vapor pressure decreases slightly with increasing NaCl concentration. Thus, there will be a very small increase in the activity of $CO_{2(aq)}$ with higher NaCl concentration.

The activity coefficient of $Cl^-_{(aq)}$ ion shows a minimum at ~ 6 wt.% NaCl, whilst its concentration and activity monotonously increase with a rise in NaCl concentration (Figure 8-5 E). The activity of water decreases from 1 at 0 wt.% NaCl to around 0.77 at 25 wt.% NaCl (Figure 8-5 F).

The reason for the observed trends in the activity coefficients of aqueous dissolved species with NaCl concentration can be understood by considering the changes in the three contributions of activity coefficient with NaCl concentration. Figure 8-6 presents the variations in the long-range, specific ionic interaction, and short-range contributions of the activity coefficient with NaCl concentration for $H_3O^+_{(aq)}$, $H_sS_{(aq)}$, $HS^-_{(aq)}$, and $Cl^-_{(aq)}$ ions. For example in Figure 8-6 C, for $HS^-_{(aq)}$ ion, the long-range ($\gamma^{m,LR}_{HS^-_{(aq)}}$) and the short-range ($\gamma^{m,SR}_{HS^-_{(aq)}}$) contributions of the activity coefficient decreases with increasing NaCl concentration, while the specific ionic interaction ($\gamma^{m,II}_{HS^-_{(aq)}}$) contribution increases. The slope of changes for $\gamma^{m,II}_{HS^-_{(aq)}}$ is larger than that for $\gamma^{m,LR}_{HS^-_{(aq)}}$ and $\gamma^{m,SR}_{HS^-_{(aq)}}$. Therefore, the activity coefficient of $HS^-_{(aq)}$ ion shows a minimum at low NaCl concentrations.

Figure 8-5

Bulk concentration, activity coefficient, and activity of (A) $H_3O^+_{(aq)}$ ion, (B) $OH^-_{(aq)}$ ion, (C) $H_2S_{(aq)}$, (D) $HS^-_{(aq)}$ ion, (E) $Cl^-_{(aq)}$ ion, and (F) $H_2O_{(l)}$ calculated by the mixed solvent electrolyte speciation model for H_2S saturated aqueous NaCl solutions at 25°C, and 1 bar total pressure (~ 0.98 bar pH_2S). 25 wt.% NaCl is equivalent to 5.7 molal NaCl.

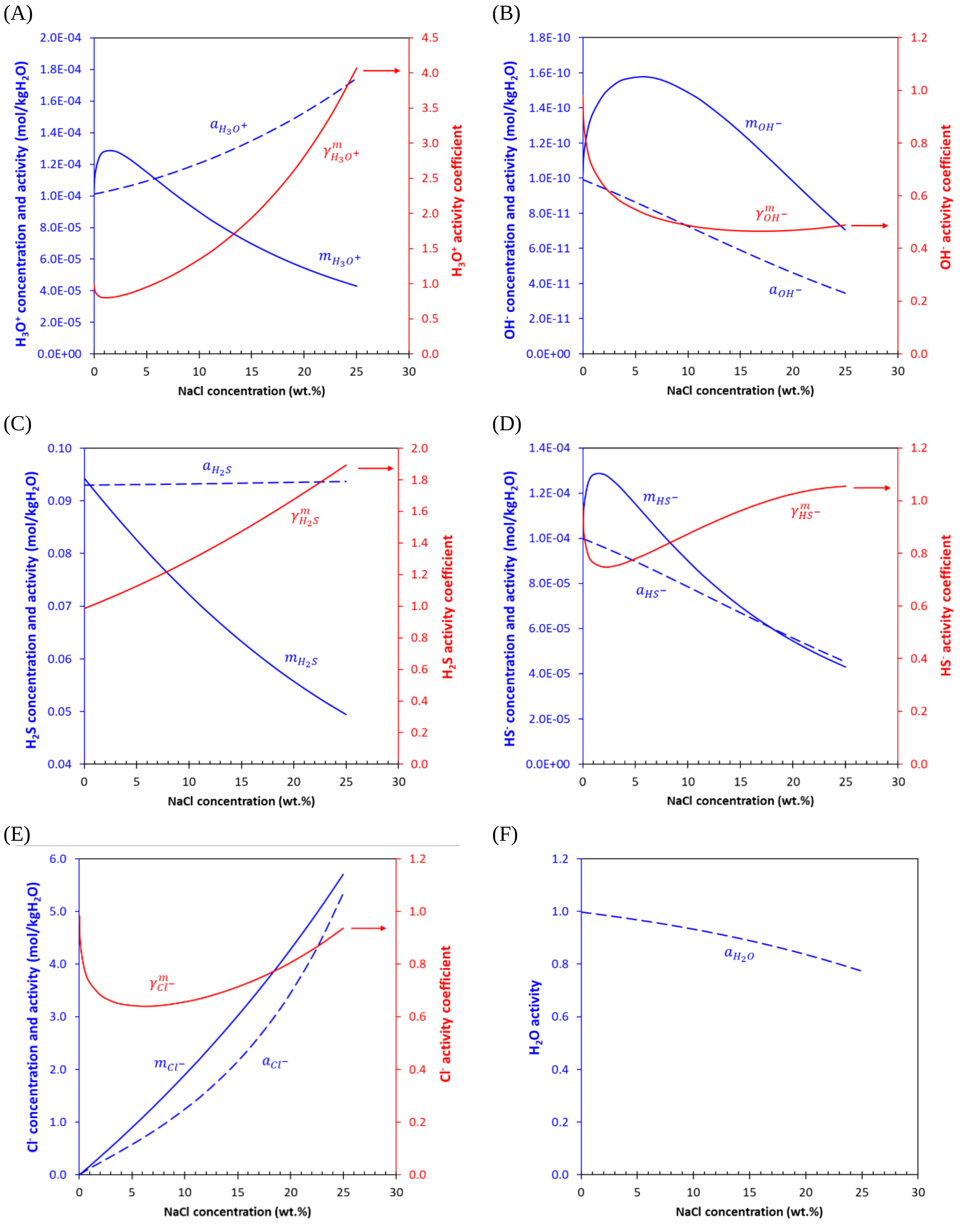

Figure 8-6

The variations in the long-range ($\gamma^{m,LR}$), the specific ionic interaction ($\gamma^{m,II}$), and the short-range ($\gamma^{m,SR}$) contributions of molality-based activity coefficient (γ^{m}) with respect to salt concentration at 25°C and 1 bar total pressure for: (A) $H_3O^+_{(aq)}$ ion, (B) $H_2S_{(aq)}$, (C) $HS^-_{(aq)}$ ion, and (D) $Cl^-_{(aq)}$.

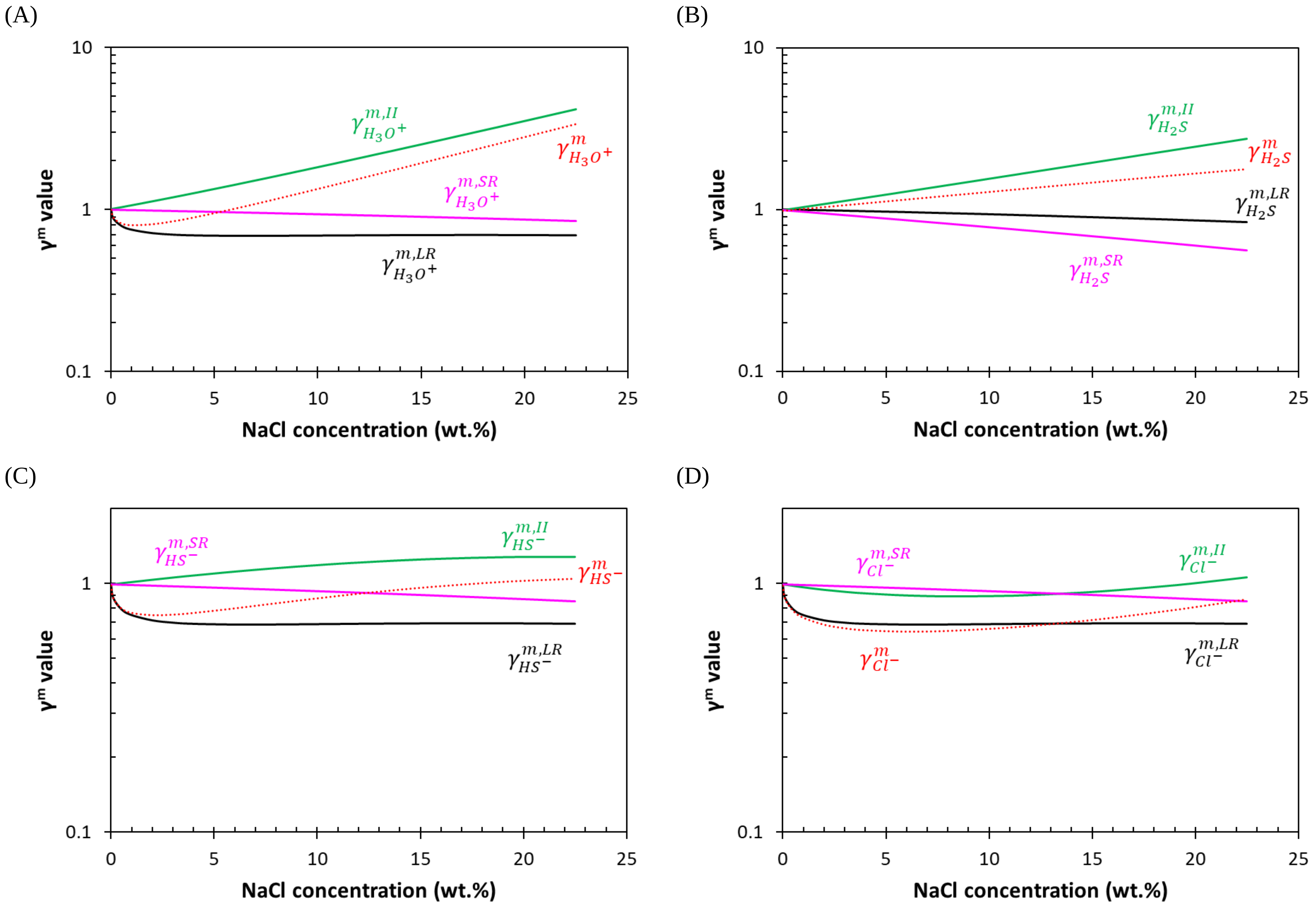

8.5 Comparison of Speciation Equilibrium Models for Solutions Saturated with $CO_{2(g)}$

Since pH can be easily measured, it is the most convenient property of a solution for assessing the accuracy of the speciation equilibrium models. Therefore, in the present study, the accuracy of speciation equilibrium models is investigated by comparing the experimental pH values with those estimated by the models.

Figure 8-7 compares the experimental autogenous pH of aqueous NaCl solutions at 1 bar CO_2 and 25°C extracted from the literature with predicted pH values obtained by different speciation equilibrium models introduced in this chapter. The Oddo and Tomson [232] model overpredicts pH between 0 wt.% to ~10 wt.% and underpredicts at higher NaCl concentrations. The Millero *et al.* [266] and the Li and Duan [136,249] models overpredict pH over the entire range of NaCl concentrations. The overprediction by Millero *et al.* [266] model amplifies at higher NaCl concentrations. However, the accuracy of Li and Duan [136,249] model remains almost unchanged over the whole NaCl concentration range with a maximum overprediction of 0.15 pH unit at ~10 wt.%. The MSE model [135,241] predicts pH satisfactorily for the entire range of NaCl concentrations. The maximum error by the MSE model occurs at middle concentrations, for example at 10 wt.% the error is about + 0.1 pH unit. A common problem with all the equilibrium speciation models is that they foresee a linear relation between pH and NaCl concentration, while the experimental pH values show a logarithmic trend with respect to NaCl concentration.

Figure 8-7

Comparison of speciation equilibrium models with experimental data for the autogenous pH of aqueous NaCl solution saturated with $CO_{2(g)}$ at 25^{o}C and 1 bar total pressure. Data are taken from [7,9,10]. *The models are reproduced based on* [232,266,136,249,135,241].

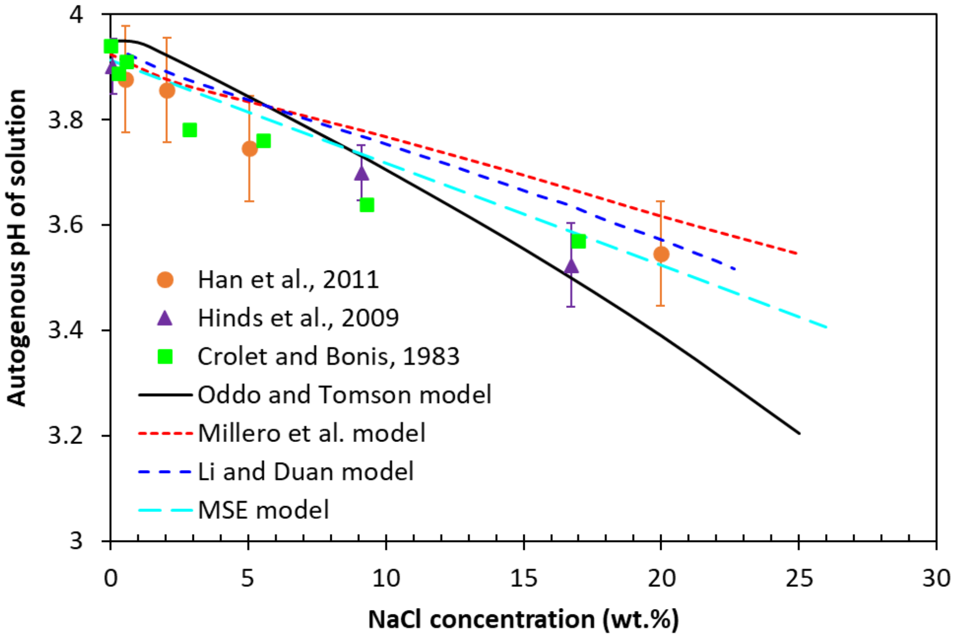

Figure 8-8 shows comparisons between the experimental autogenous pH data in an aqueous ~ 3 wt.% NaCl solution saturated with $CO_{2(g)}$ at three different temperatures and a total pressure range of 1 to 40 bar with pH values predicted by the speciation equilibrium models mentioned earlier. The Oddo and Tomson [232] model in Figure 8-8 A practically underpredicts pH for all temperatures and pressures. The Millero *et al.* [266] model predicts reasonably at 74^{o}C for the entire range of pressure, whilst it overpredicts at 26^{o}C and 50^{o}C (Figure 8-8 B). The Li and Duan [136,249] model in

Figure 8-8 C shows acceptable predictions for all three temperature and for pressures blow 25 bar. However, at higher pressures, it marginally underpredicts pH with a maximum error of around – 0.1 pH unit at 26^{o}C. The MSE model [135,241] predictions are in very good agreement with the experimental data for all three temperatures and in the entire range of pressure. There are only slight underpredictions at 74^{o}C and pressures larger than 30 bar.

Overall, the MSE model [135,241] reveals a better accuracy comparing to the other models. The Li and Duan model [136,249] comes next followed by the Millero *et al.* model[266]. The Oddo and Tomson [232] model has the least accuracy among the studied models. This conclusion implies that the CO_2 speciation models which consider the interspecies interactions are more accurate compared to ionic strength-based CO_2 speciation models.

Figure 8-8

Comparison of the experimental autogenous pH of ~ 3 wt.% NaCl solution saturated with $CO_{2(g)}$ at different temperatures and pressures with the predicted pH values obtained by (A) Oddo and Tomson model [232], *(B) Millero et al. model* [266], *(C) Li and Duan model* [136,249], *and (D) MSE model* [135,241]. *The experimental data are borrowed from* [9].

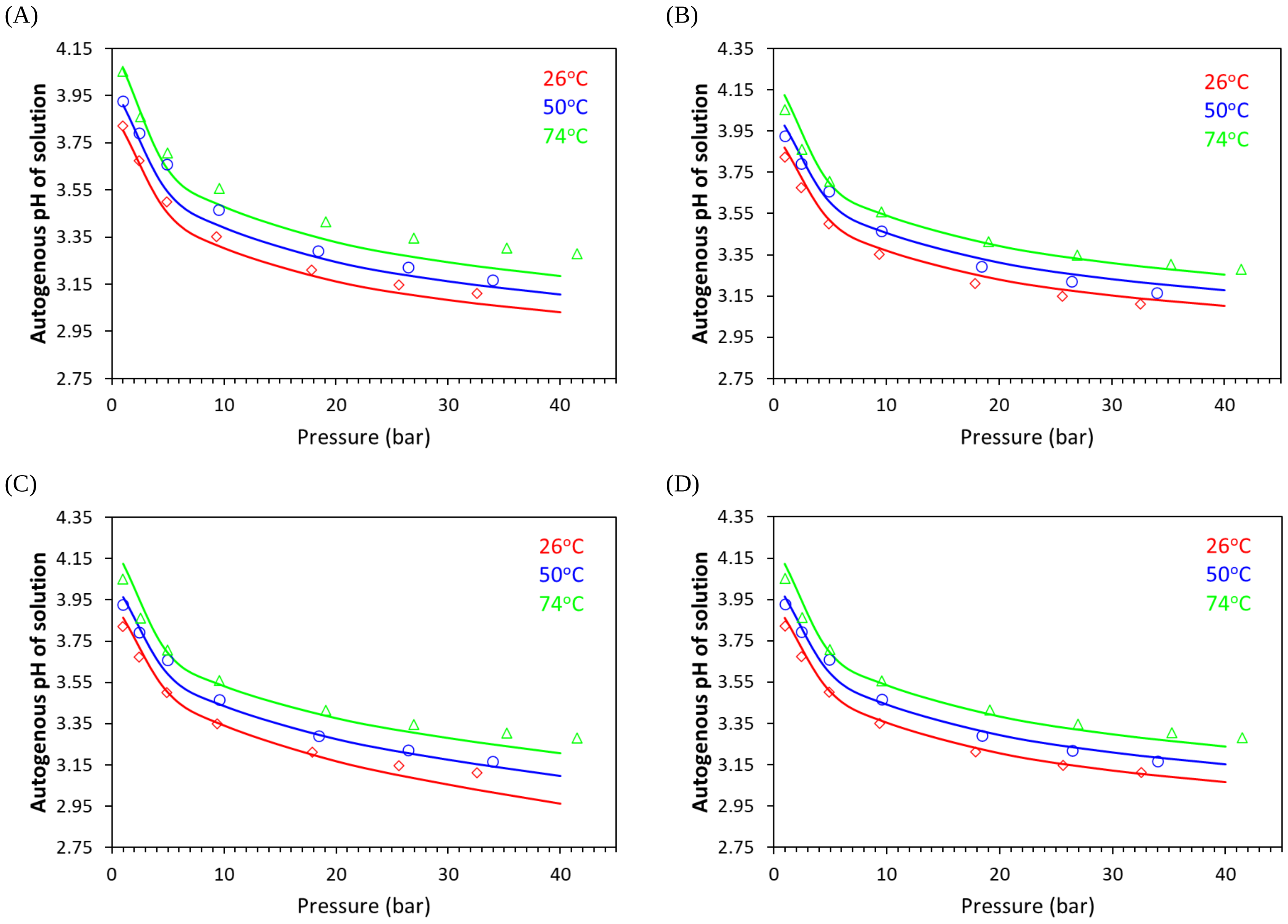

8.6 Comparison of Speciation Equilibrium Models for Solutions Saturated with $H_2S_{(g)}$

Figure 8-9 compares the predicted pH values obtained by two speciation equilibrium models with the experimental pH measurements at 20°C and 1 bar H_2S and different NaCl concentrations. A double-junction pH probe resistant to Na+ ion interference was used for pH measurements. The ionic strength-based model, which is implemented for pH estimation for the first time in this study, predicts pH very well over the entire range of NaCl concentrations. The maximum prediction error is approximately -0.05 pH unit at 3 wt.% NaCl. For the MSE model, the pH predictions match well with the experimental pH values at low and high NaCl concentration. However, the accuracy is less for the middle range NaCl concentration. The max error is about + 0.14 pH unit at 10 wt.% NaCl. The logarithmic relation between the experimental pH and NaCl concentration is reasonably captured by the ionic strength-based speciation model, whereas the MSE model shows a linear trend for pH with varying NaCl concentration. Although the MSE model is expected to be more accurate, the ionic strength-based speciation model reveals a better accuracy. However, more conditions need to be examined to strengthen this conclusion.

Figure 8-9

Comparison of the experimental autogenous pH of aqueous NaCl solutions saturated with $H_2S_{(g)}$ *at 20°C, 1 bar total pressure, and different NaCl concentrations with the predicted pH values obtained by two speciation models. The dots are experimental measurements.*

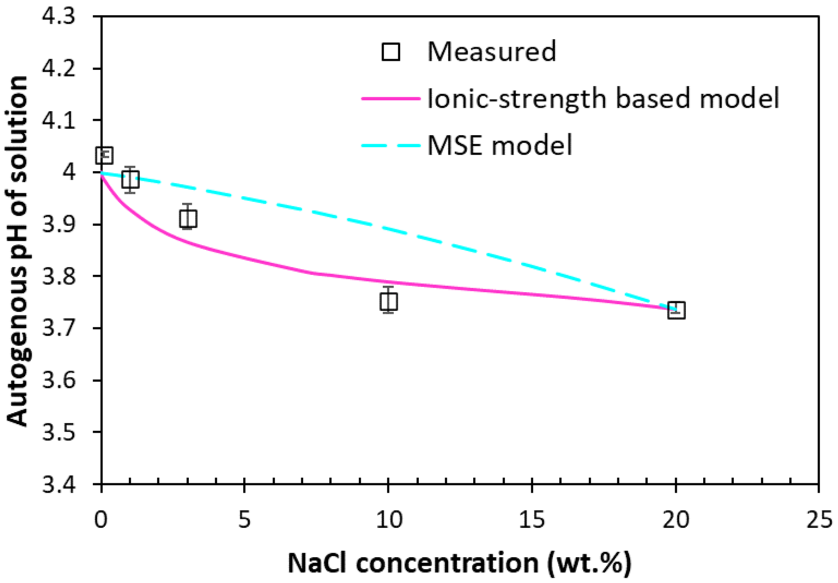

Chapter 9: Experimentation to Investigate the Effect of Salt Concentration on Strong Acid Corrosion

Aqueous strong acid corrosion can be considered as the simplest type of carbon steel corrosion because the extra source of H^+ ions produced by dissociation of weak acids such as $H_2CO_{3(aq)}$ and $H_2S_{(aq)}$ or in other words the buffering effect does not occur in the strong acid solutions. Additionally, since $CO_{2(aq)}$ and $H_2S_{(aq)}$ and their derivatives are not present in strong acid solutions, the possible effects of these species on the anodic iron dissolution do not interfere with the effect of salt concentration on this reaction, if at all. Therefore, corrosion studies in strong acid solutions provides a base understanding of the effect of salt concentration on the H^+ ion reduction and the Fe dissolution reaction without the influence of weak acids. In this chapter, the effect of salt concentration is experimentally investigated on the rate and the mechanism of aqueous corrosion of carbon steel in strong acid solutions in the absence of CO_2 or H_2S.

9.1 The Effect of Salt Concentration on Strong Acid Corrosion at pH 3 Using a Rotating Disk Electrode (RDE)

9.1.1 Experimental Materials and Methodology for RDE Strong Acid Corrosion Experiments

Experiments were carried out in a custom-made glass cell with an outer jacket for temperature control. Figure 9-1 shows the apparatus used in this set of experiments. An industrial chiller (not visible in Figure 9-1) was used to circulate glycol as the coolant (the green liquid) through the outer jacket for controlling the solution temperature during the experiments. Glycol did not have any contact with the experimental solution

Figure 9-1

The apparatus used in the RDE strong acid experiments: (1) glass cell, (2) motor, (3) rotation speed controller, (4) pH probe, (5) pH meter, (6) Ag/AgCl reference electrode, (7) thermometer, (8) gas out bubbler, (9) potentiostat for data acquisition, (10) laptop for data collection, (11) hot plate stirrer.

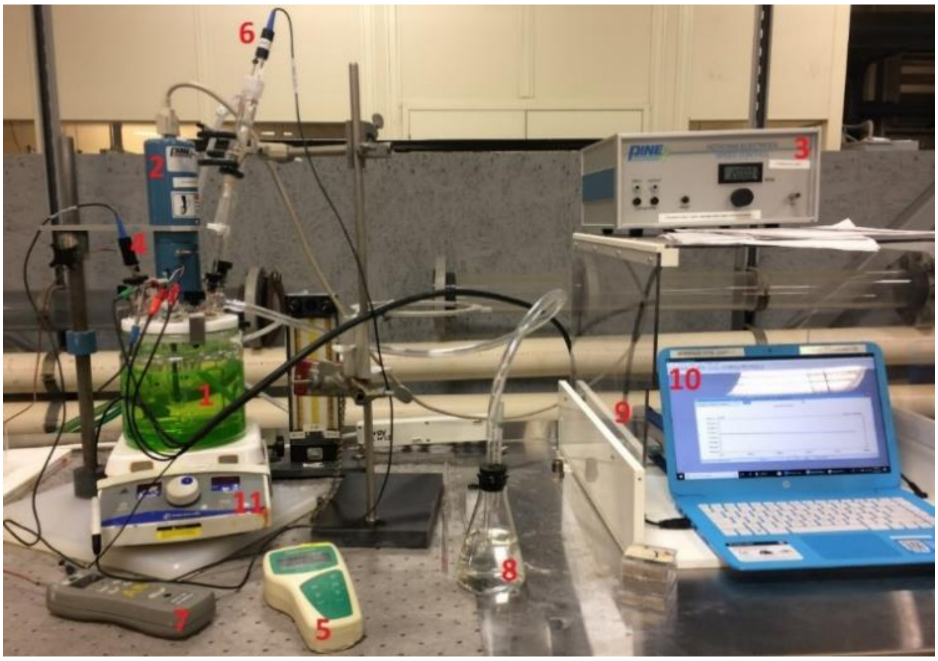

Figure 9-2 shows a close-up view of the glass cell. A conventional three-electrode setup was used for performing the electrochemical experiments, which consisted of a rotating disk electrode (RDE) assembly as the working electrode, a graphite bar as the counter electrode and an Ag/AgCl electrode as the reference electrode. The counter electrode was mounted in a glass tube with a porous tip to avoid interference of gaseous species with the main working solution, such as $H_{2(g)}$ and $O_{2(g)}$ which may form on the counter electrode during the negative and positive potential sweeps (*vs.* OCP). The porous tip provides ionic conductivity between the counter electrode and the solution. The external reference electrode was connected via a Luggin capillary tube, which was filled with 1M KCl. The capillary tip was adjusted close to the RDE almost at the same level to diminish the effect of solution resistance on the electrochemical measurements, but, not too close to disturb the RDE laminar flow (approximately 3 mm from the Teflon RDE holder). The immersion depth for the RDE was approximately somewhere in the middle of the glass cell. It is reported that the electrode immersion depth does not influence the electrochemical measurements [290].

Figure 9-2

A picture of the custom-made glass cell and its components used in the RDE strong acid experiments: (1) glass cell, (2) outer jacket, (3) Teflon lid, (4) clamp, (5) coolant (glycol) in, (6) coolant out, (7) RDE and its holder, (8) pH probe, (9) Luggin capillary for the Ref. electrode, (10) counter electrode, (11) thermocouple, and (12) magnetic stirring bar.

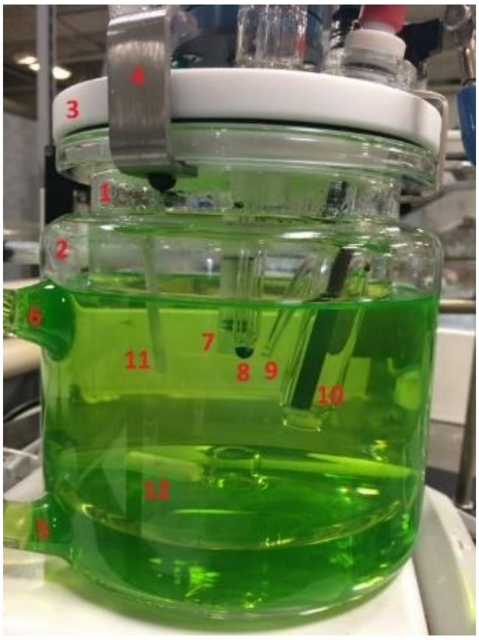

The RDE specimen was a carbon steel cylinder with a diameter of 5 mm and a height of 4 mm. The specimen was flush mounted in a Teflon holder as shown in Figure 9-3. The assembly was polished before each experiment. The two red O-rings were used to seal the connection between the specimen holder and the RDE shaft.

Figure 9-3

The RDE specimen and its Teflon holder used in the RDE strong acid experiments: (A) the bottom view and (B) the side view of the specimen holder.

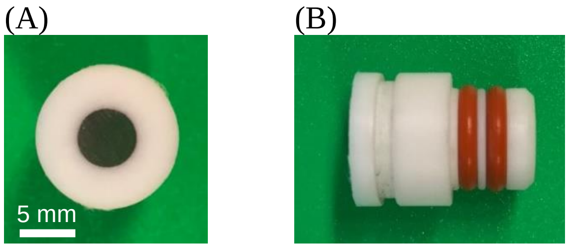

The carbon steel grade used for the experiments was API 5L X65, a common steel grade for manufacturing oil and gas transmission pipelines [291]. Table 9-1 shows the chemical composition of tested X65 carbon steel. The microstructure of the experimental X65 carbon steel (Figure 9-4) was a uniform, fine structure of pearlite in a ferrite matrix.

Table 9-1

Chemical composition of the experimental API 5L X65 (type 48) carbon steel (in wt.%).

Al	As	C	Co	Cr	Cu	Mn	Mo	Nb	Ni
0.028	0.008	0.05	<0.001	0.252	0.173	1.51	0.092	0.034	0.291
P	S	Sb	Si	Sn	Ti	V	Zr	Fe	
0.004	<0.001	<0.001	0.167	0.002	0.012	0.04	<0.001	balance	

Figure 9-4

Microstructure of the experimental API 5L X65 (type 48) carbon steel (in wt.%): (A) magnification 1, (B) magnification 2.

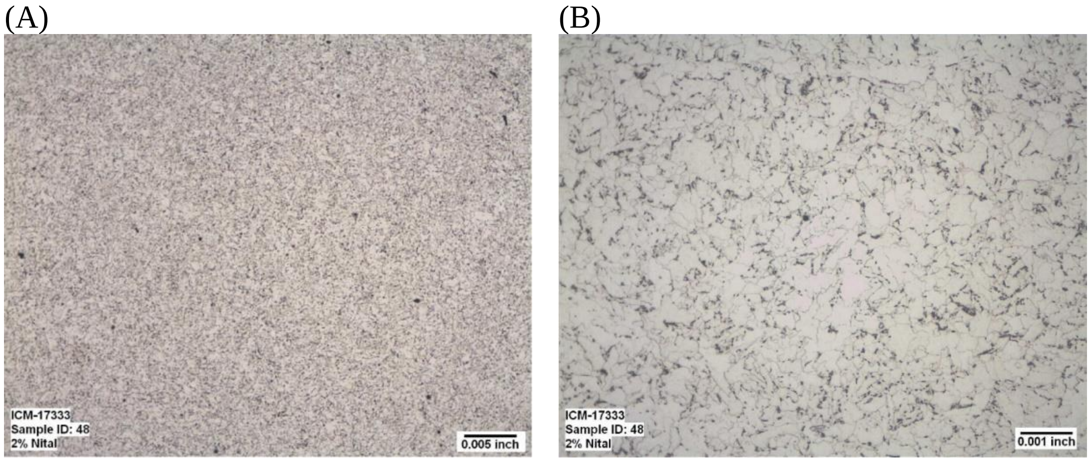
(A) (B)

Experiments were conducted in N_2-saturated aqueous solutions with different NaCl concentrations to investigate the effect of salt concentration on uniform strong acid corrosion. NaCl is the major salt present in water produced from conventional hydrocarbon reservoirs [4,25]; thereby, it was chosen for the experiments. A low solution temperature of 10°C was chosen for the experiments. Lower temperatures slow down the kinetics of the charge transfer reactions at the metal surface more than the rate of diffusion of electroactive species to the metal surface. This results in more separation between the charge transfer and the mass transfer-controlled regions of the cathodic potentiodynamic sweeps and facilitates evaluation of the effect of salt concentration in each potential range.

For each experiment, NaCl was dissolved in one liter of deionized water (18 MΩ.cm) in the glass cell. The solution was then sparged with $N_{2(g)}$ for at least 2 h, while being stirred. After about 1.5 h of sparging, pH of solution reached a stable value (Figure 9-5)[58]. At this point, pH was adjusted to 3.0 by adding 0.1 M HCl to the solution. More HCl was required for higher NaCl concentrations.

---

[58] The equilibrium speciation models are not able to predict the increasing trend seen in the autogenous pH of N_2 saturated aqueous solutions with respect to NaCl concentration. They predict a decreasing trend.

Figure 9-5

Autogenous pH of N_2 saturated solutions measured at 10°C, and 1 bar total pressure (~ 0.98 bar pN_2) before pH adjustment. The error bars represent the minimum and maximum values obtained in repeated experiments (with at least 2 repeats).

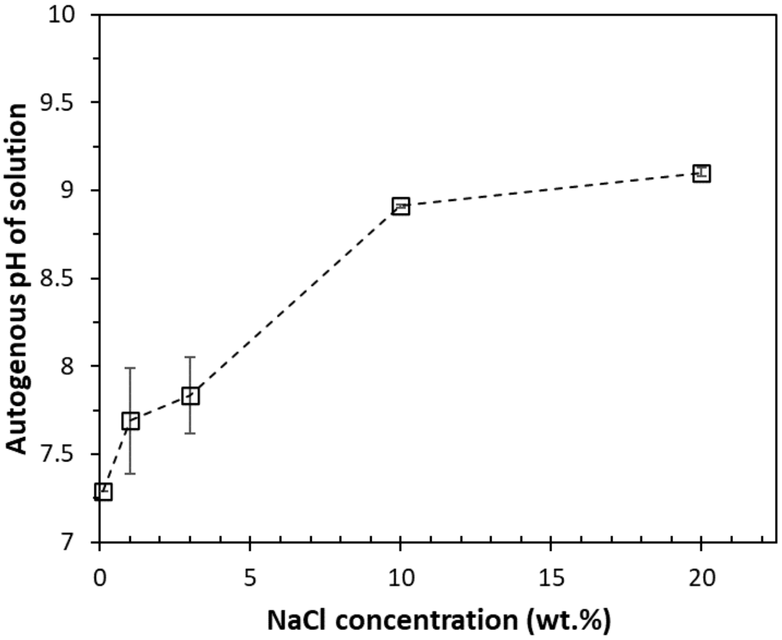

The specimen assembly (shown in Figure 9-3) was sequentially wet polished with 240-, 400- and 600-grit abrasive papers. Subsequently, the assembly was ultrasonically degreased with isopropanol for 3 min and dried in cool N_2 gas prior to immersion in the test solution.

After introducing the RDE assembly to the solution and prior to each electrochemical test, the open circuit potential (OCP) was monitored until a stable potential value (ΔE_{OCP}< 2 mV/min) was achieved. The linear polarization resistance (LPR) technique was performed in a potential range of -5.0 mV to 5 mV vs. OCP at a scan rate of 0.125 mV/s to measure the corrosion rate. Then, EIS was carried out in a frequency range of 10,000 Hz to 0.1 Hz at OCP with a 10 mV AC peak to peak amplitude and a sampling rate of 8 points/dec to determine the solution resistance (iR drop). Finally, the potentiodynamic (PD) polarization sweeps were conducted according to the following steps: (1) a cathodic sweep starting from the OCP toward more negative potentials up to -1.00 V vs OCP; (2) wait for the OCP to return close to its initial value—within a few mV (this took about 1 h); (3) an anodic sweep starting from the OCP to more positive potentials up to 0.35 V vs OCP. The PD sweeps were done with a scan rate of 0.5 mV/s. A Gamry Reference 600 potentiostat was used for all the electrochemical measurements.

Table 9-2 summarizes the conditions used in the experiments. For each NaCl concentration, at least two separate tests were conducted to assure the reproducibility of results.

Table 9-2

The experimental conditions used in the RDE strong acid experiments.

Parameter	Description
Specimen material	API 5L X65 carbon steel
RDE diameter (mm)	5.00 ± 0.05
Temperature (°C)	10.0 ± 0.5
Total pressure (bar)	1
N_2 partial pressure (bar)	~ 0.98
NaCl concentration (wt.%)[59]	0.1, 1, 3, 10, 20
pH	3.00 ± 0.02
RDE rotational speed (rpm)[60]	2000 ± 2

The following experimental considerations were followed during the experiments:

1. To make sure that the concentration of dissolved oxygen in the experimental solution was less than 10 ppb during the experiments the oxygen level was monitored by an Orbisphere 410 oxygen meter at the gas outlet.
2. Temperature could not be kept constant by just circulating coolant in the glass cell jacket. Therefore, a hot plate was used continuously to balance the temperature. A constant temperature of 10 ± 0.5°C was achieved by an equilibrium between coolant circulation and the hot plate.

---

[59] wt.% = 100 × mass of salt / (mass of salt + mass of water)

[60] revolutions per minute

3. Measuring pH correctly in solutions with high salinity is challenging [10]. The pH measurements were done with a double-junction pH probe, which was resistant to Na^+ ion interference.

9.1.2 Results and Discussion for RDE Strong Acid Corrosion Experiments

Figure 9-6 shows the PD sweeps at different NaCl concentrations. The potential values are corrected for the solution resistance (iR drop) in all the sweeps shown. At least, two sets of PD sweeps were obtained for each NaCl concentration to verify the reproducibility of results. Increasing NaCl concentration altered both anodic and cathodic branches. The most obvious effect in the PD sweeps with increasing NaCl concentration is the change in the cathodic limiting current density (i_{Lim}).

Figure 9-6

Potentiodynamic polarization sweeps of X65 carbon steel rotating disk specimen (2000 rpm) exposed to N_2*-saturated aqueous solutions with different NaCl concentrations at* 10^oC*, 1 bar total pressure, and pH 3.*

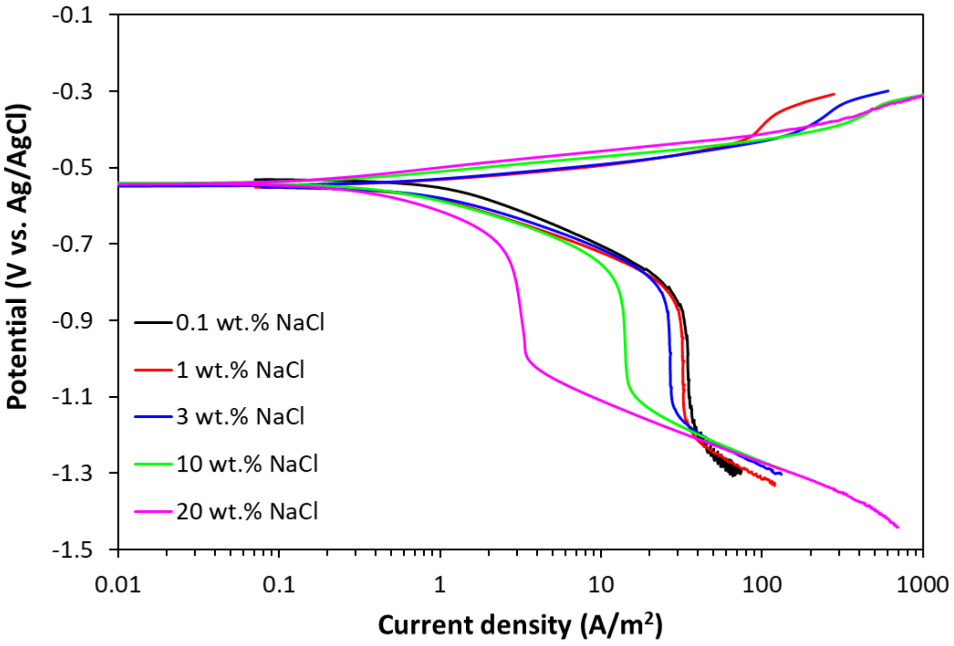

For a precise analysis of the effect of NaCl concentration on the mechanisms of the corrosion process, electrochemical features of the experimental sweeps were determined by overlaying the experimental sweeps for the best fit with those calculated by an electrochemical model [96][61]. The fitted sweeps for two NaCl concentrations are shown in Figure 9-7 as a demonstration of fitting exercise accuracy.

---

[61] Activation energies of 59860 J/mol for H^+ ion, 24809 J/mol H_2O reduction and 25398 J/mol for Fe oxidation reactions. A reversible potential of -0.685 V vs. Ag/AgCl was used for all three reactions. The reference temperature was 20^oC.

Figure 9-7

Comparison of the experimental sweeps at 1 wt.% (A) and 20 wt.% (B) NaCl concentrations measured in the RDE strong acid experiments with those obtained by a simple electrochemical model [96].

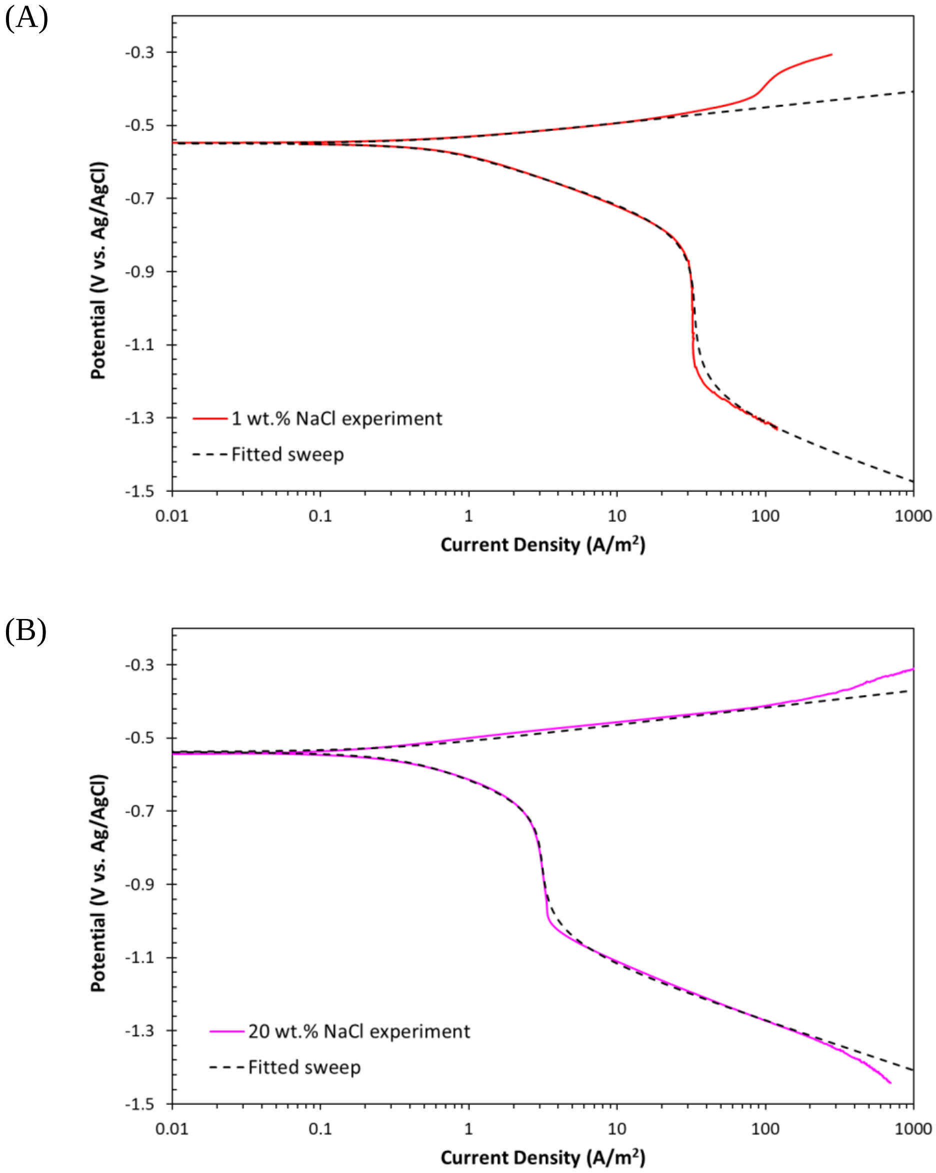

The electron transfer coefficients for the H^+ ion reduction reaction (α_{H^+}) and the Fe oxidation reaction in the active region (α_{Fe}) at different NaCl concentrations are listed in Table 9-3. α_{H^+} values are somewhat smaller than the theoretical value of

0.5, commonly considered for the hydrogen evolution on an iron surface [185]. Such deviations have been reported in the literature between the experimental α_{H^+} and the theoretical value of 0.5 [185,292,198,207]. The difference between the α_{H^+} values found experimentally and the theoretical value of 0.5 can arise because of a different underlying mechanism for the cathodic H^+ ion reduction reaction. However, it can also be due to inherent errors in the fitting exercise. If the fitting exercise is assumed to be accurate, then α_{H^+} values slightly increased with increasing NaCl concentration. This implies that the rise in NaCl concentration might have an influence on the mechanism of cathodic H^+ ion reduction reaction. This subject will be investigated in some more detail in the next sections.

Table 9-3

The electron transfer coefficients for H^+ reduction reaction (α_{H^+}) and Fe oxidation (α_{Fe}) for the RDE (2000 rpm) strong acid experiments at 10°C, ~1 bar N_2 and pH 3. Each data is an average of two measurements.

NaCl (wt.%)	0.1	1	3	10	20
α_{H^+}	0.40±0.01	0.45±0.02	0.46±0.01	0.50±0.00	0.52±0.00
β_c[62]	-141±3	-124±4	-122±3	-112±0	-108±0
α_{Fe}	1.30±0.00	1.20±0.00	1.20±0.00	1.20±0.00	1.20±0.00
β_a[63]	43±0	47±0	47±0	47±0	47±0

---

[62] β_c is the H^+ ion reduction cathodic Tafel slope in mV/dec and equal to $1000RT/nF\alpha_{H^+}$.

[63] β_a is the Fe oxidation anodic Tafel slope in mV/dec and equal to $1000RT/nF\alpha_{Fe}$.

α_{Fe} was close to 1.20 for most NaCl concentrations. Bockris *et al.* [185] proposed 1.5 for iron dissolution in acidic media without the presence of halides. Chin and Nobe [194] reported 1.18 for dissolution of iron in acidic chloride media, which is very close to the results of the present study. Since α_{Fe} almost did not change with increasing NaCl concentration, it can be concluded that the mechanism of anodic dissolution of iron in the active region remained unchanged at different salt concentrations. The mechanisms of iron dissolution in the presence of chlorides have been comprehensively explained in Chapter 5.

The variations in the exchange current density for H^+ reduction (i_{o,H^+}) is presented in Figure 9-8 A. i_{o,H^+} sharply decreases with increasing NaCl concentration from 0.1 wt.% to 1 wt.% and then shows a gradual decrease with further increase in NaCl concentration. This indicates that the rate of H^+ ion reduction decreased with increasing NaCl concentration, which is likely due to the adsorption of Cl^- ions on the steel surface and blocking the required sites for H^+ ions to adsorb and be reduced [171]. It seems that the surface becomes saturated with adsorbed Cl^- ion at ~ 3 wt.% NaCl concentration. The trend observed for i_{o,H^+} in Figure 9-8 A can be modeled by using a correlation similar to Equation (5-23):

$$i_{o,H^+} = i_{o,H^+}^{ref} \left(\frac{a_{H^+,b}}{a_{H^+,b}^{ref}}\right)^{n_{H^+}^{H^+}} \left(\frac{a_{Cl^-,b}}{a_{Cl^-,b}^{ref}}\right)^{n_{Cl^-}^{H^+}} e^{-\frac{E_{a,H^+}}{R}\left(\frac{1}{T}-\frac{1}{T_{ref}}\right)} \qquad 9\text{-}1)$$

where, i_{o,H^+}^{ref} is the reference current density at T_{ref} (293.15 K) and potential of -685 mV *vs.* Ag/AgCl in A/m^2, $a_{H^+,b}$ is the bulk activity of H^+ ion in molarity concentration, $a_{H^+,b}^{ref}$ is the reference bulk activity of H^+ ion (= 10^{-4} M), $n_{H^+}^{H^+}$ is the reaction order of the H^+ ion reduction reaction with respect to H^+ ion activity, $a_{Cl^-,b}$ is the bulk activity of Cl^- ion in molarity concentration, $a_{Cl^-,b}^{ref}$ is the reference bulk activity of Cl^- ion (= 1 M), $n_{Cl^-}^{H^+}$ is the reaction order of the H^+ ion reduction reaction with respect to Cl^- ion activity, $\Delta E_{a,H^+}$ is the activation energy for the H^+ ion reduction reaction (= 59860 J/mol), T is solution temperature in K, and R is the gas constant in J/mol/K. Since the solution pH was constant in the experiments, the activity of H^+ ion was constant as well[64]. This means that $n_{H^+}^{H^+}$ cannot be determined from this set of data points. Experiments at different pH values are required to obtain $n_{H^+}^{H^+}$. However, an empirical value of 0.5 previously reported in the literature is chosen for $n_{H^+}^{H^+}$ [200,215]. By a simple curve fitting using the bulk activities calculated with the MSE model, $n_{Cl^-}^{H^+}$was determined to be ~ -0.09 and i_{o,H^+}^{ref} term was 8.55 A/m^2. The negative sign found for $n_{Cl^-}^{H^+}$ confirms the inhibition effect of Cl^- ion concentration on the charge transfer rate for H^+ ion reduction reaction.

---

[64] The changes in molarity-based activity due to changes in density with NaCl concentration is ignored.

Figure 9-8

Variations in (A) the cathodic limiting current density (i_{Lim}) and the H^+ reduction exchange current density (i_{o,H^+}) and (B) the Fe oxidation exchange current density ($i_{o,Fe}$) with NaCl concentration. The current densities were extracted from the PD sweeps of X65 RDE (2000 rpm) exposed to N_2-saturated aqueous solutions at 10°C, 1 bar total pressure, and pH 3. The error bars represent the minimum and maximum values obtained in two repeated experiments. The reference temperature was 20°C.

(A
)

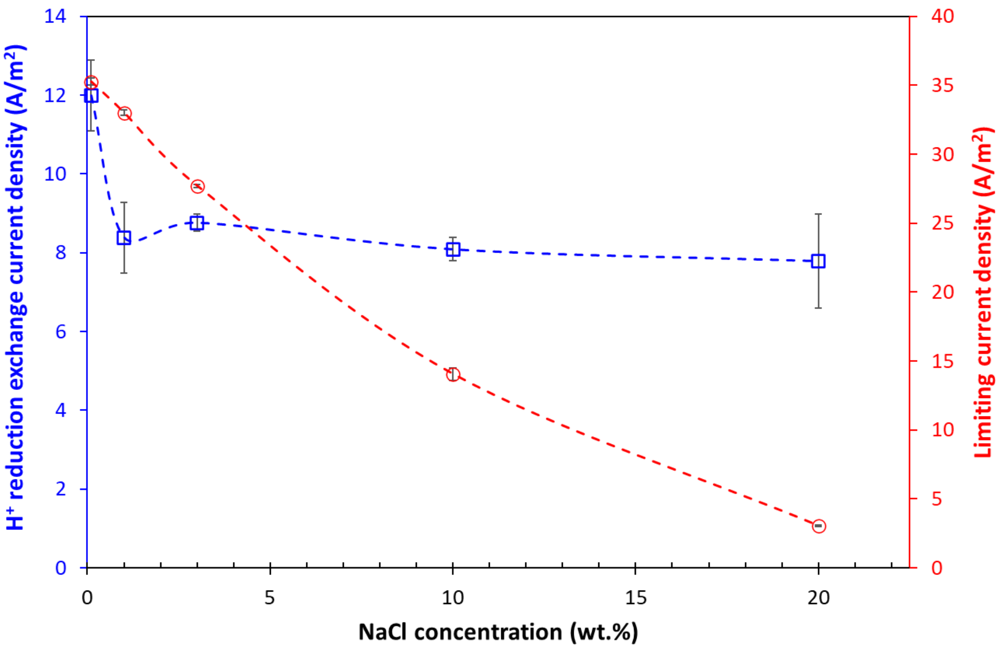

(B)

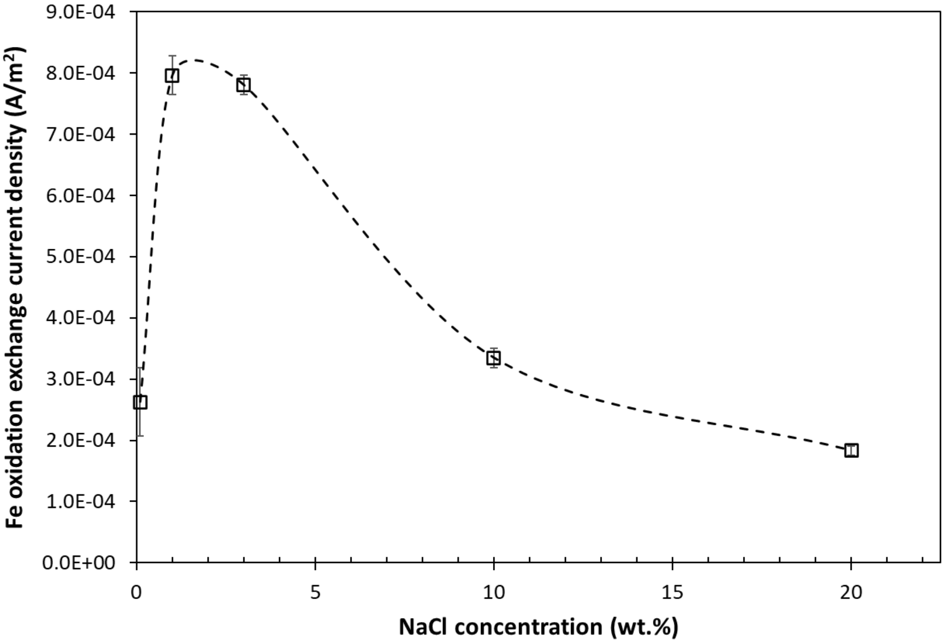
Fe oxidation exchange current density (A/m^2)
9.0E-04
8.0E-04
7.0E-04
6.0E-04
5.0E-04
4.0E-04
3.0E-04
2.0E-04
1.0E-04
0.0E+00
0
5
10
15
20
NaCl concentration (wt.%)

Figure 9-8 B show the variation in the Fe oxidation exchange current density ($i_{o,Fe}$) with NaCl concentration. $i_{o,Fe}$ increased at lower NaCl concentrations and it reversed trend at an NaCl concentration between 1 wt.% to 3 wt.% and decreased at higher NaCl concentrations. This behavior of $i_{o,Fe}$ can be justified by considering the changes in the bulk activities of OH$^-$ ion, Cl$^-$ ion, and H_2O with NaCl concentration. $i_{o,Fe}$ can be related to the activities of OH$^-$ and Cl$^-$ ions, and H_2O with the following correlation:

$$i_{o,Fe} = i_{o,Fe}^{ref}\left(\frac{a_{OH^-,b}}{a_{OH^-,b}^{ref}}\right)^{n_{OH}^{Fe}}\left(\frac{a_{Cl^-,b}}{a_{Cl^-,b}^{ref}}\right)^{n_{Cl^-}^{Fe}}\left(\frac{a_{H_2O,b}}{a_{H_2O,b}^{ref}}\right)^{n_{H_2O}^{Fe}} e^{-\frac{E_{a,Fe}}{R}\left(\frac{1}{T}-\frac{1}{T_{ref}}\right)} \tag{9-2}$$

where, $i_{o,Fe}^{ref}$ is the reference current density at T_{ref} (293.15 K) and potential of -685 mV *vs.* Ag/AgCl in A/m^2, $a_{OH^-,b}$ is the bulk activity of OH$^-$ ion in molarity concentration, $a_{OH^-,b}^{ref}$ is the reference bulk activity of OH$^-$ ion (= 10^{-10} M), n_{OH}^{Fe} is the reaction order of the Fe oxidation reaction with respect to OH$^-$ ion activity, $a_{Cl^-,b}$ is the bulk activity of Cl$^-$ ion in molarity concentration, $a_{Cl^-,b}^{ref}$ is the reference bulk activity of Cl$^-$ ion (= 1 M), $n_{Cl^-}^{Fe}$ is the reaction order of the Fe oxidation reaction with respect to Cl$^-$ ion activity, $a_{H_2O,b}$ is the bulk activity of liquid water in molarity unit, $a_{H_2O,b}^{ref}$ is the reference bulk activity of liquid water (= 55.4 M), $n_{H_2O}^{Fe}$ is the reaction order of the Fe oxidation reaction with respect to H_2O, and $\Delta E_{a,Fe}$ is the activation energy for the Fe oxidation reaction in the active region (= 25398 J/mol), T is solution temperature in K, and R is the gas constant in J/mol/K.

Lorenz [174] and McCafferty and Hackerman [178], reported different $n_{Cl^-}^{Fe}$ values at different range of Cl$^-$ activities (concentrations), as summarized in Table

5-2. This implies that the iron dissolution reaction might proceed through different pathways depending on the Cl$^-$ activity in the solution. From the $i_{o,Fe}$ trend in Figure 9-8 B, it can be postulated that at low NaCl concentrations below 1 wt.%, Cl$^-$ ions accelerates the anodic dissolution reaction by playing a catalytic role in iron dissolution, similar to that of OH^- ions [172,194,195]. However, at high NaCl concentrations above 1 wt.%, Cl$^-$ ions inhibits the Fe dissolution reaction by being adsorbed on the surface and blocking the active sites (kinks and dislocations) required for the iron dissolution reaction to occur [173,174,178,192]. Therefore, the $i_{o,Fe}$ curve is divided into two sections: below and above 1 wt.%. Equation (9-2) with the bulk activity values calculated with the MSE was fitted to the experimental $i_{o,Fe}$ values to determine the reaction orders and $i_{o,Fe}^{ref}$ for the two regions. To obtain n_{OH}^{Fe} value experiments at different solution pH are needed. This means that n_{OH}^{Fe} cannot be found from the data presented here. Therefore, a value of 1 was chosen for n_{OH}^{Fe} for the whole range of NaCl concentration according to the Bockris *et al.* [185,186] consecutive mechanism and reports by other scientists [174,195] (see Table 5-2). For NaCl $\leq$ 1 wt.%, $n_{Cl^-}^{Fe}$= 0.48, $n_{H_2O}^{Fe}$ = 0, and $i_{o,Fe}^{ref}$ = 0.51 and for NaCl $>$ 1, $n_{Cl^-}^{Fe}$= -0.25, $n_{H_2O}^{Fe}$ = 2, and $i_{o,Fe}^{ref}$ = 0.117. A reaction order of zero for H_2O at NaCl $\leq$ 1 means that the Fe dissolution reaction process is independent of H_2O activity in this NaCl concentration range. For $n_{H_2O}^{Fe}$ at high NaCl concentrations, the value found in this study is similar to the values (a range of 1.6-1.9) reported by Smart *et al.* [190,198].

The key change in the PD sweeps in Figure 9-6 with the addition of NaCl concentration is the decrease in the cathodic limiting current density (i_{Lim}).

Figure 9-8 A shows the experimental i_{Lim} obtained from the PD sweeps. i_{Lim} which represents the rate of mass transfer of electroactive species to the metal surface, depends on bulk activity (concentration in strong acid condition) and diffusivity of electroactive species (H^+ ion in the case of strong acid corrosion) in the bulk solution, density, and viscosity of solution. The effect of NaCl concentration on all these parameters have been discussed above and models introduced for each. With increasing NaCl concentration, the density and viscosity of solution increases, whereas the diffusion coefficient of H^+ ion and its concentration decrease. Table 9-4 lists the values of these parameters at the experimental NaCl concentrations calculated by the models introduced in previous chapters. Particularly, for H^+ concentration, the MSE model is used.

Table 9-4

Variation in solution density, solution viscosity, H^+ ion diffusion coefficient and H^+ ion concentration with NaCl concentration in N_2-saturated aqueous solutions at 10^oC, 1 bar total pressure, and pH 3.

NaCl (wt.%)	Density (kg/m^3)	Viscosity (kg/m/s)	H^+ diffusion coefficient (m^2/s)	H^+ concentration (mol/lit)
0	998.90	1.30e-3	7.01e-9	1.04e-3
0.1	999.57	1.30e-3	6.78e-9	1.13e-3
1	1005.63	1.32e-3	6.26e-9	1.23e-3
3	1019.34	1.36e-3	5.66e-9	1.14e-3
10	1069.88	1.55e-3	4.39e-9	0.657e-3
20	1149.00	2.04e-3	3.10e-9	0.260e-3

i_{Lim} in A/m^2 can be calculated by using Levich equation [290,293]:

$$i_{Lim} = 620 \cdot n \cdot F \cdot \omega_{RDE}^{0.5} \cdot \rho^{1/6} \cdot \mu^{-1/6} \cdot D_{H^+}^{2/3} \cdot c_{b,H^+} \qquad (9\text{-}3)$$

where, n is the number of electrons involved in the electrode reaction (1 for H$^+$ ion reduction); F is the Faraday's constant (= 96485.3 C/mol); ω is the RDE angular velocity (rad/s); ρ is the density of the solution (kg/m^3); μ is the dynamic viscosity of the solution (kg/m-s); D is the diffusion coefficient of H$^+$ ion (m^2/s); and c_{b,H^+} is concentration of H$^+$ ion in the bulk solution (mol/lit).

To investigate which of the four parameters mentioned above has a greater impact on the variation in i_{Lim} with increasing NaCl concentration, i_{Lim} is calculated at the experimental NaCl concentration for five scenarios, using the data provided in Table 9-4. Figure 9-9 shows the calculated i_{Lim}values for the five scenarios and compares them with the experimental i_{Lim}. The "ideal condition" scenario indicates i_{Lim} is calculated for all NaCl concentration with density, viscosity, H$^+$ diffusion coefficient and H$^+$ concentration for pure water. This scenario means that the effect of salt concentration is not considered for any of the four parameters. Therefore, i_{Lim} is constant for all NaCl concentrations. The "Rho" scenario is when in calculations only density of solution is allowed to change with NaCl concentration, and the other three parameters are kept constant as those for pure water. This scenario reveals the effect of density on i_{Lim} variation, when NaCl concentration is increased. Similarly, the other scenarios can be described as below:

- "Rho+Mu": density and viscosity of solution change with NaCl concentration and the other two parameters are kept constant as those for pure water. This scenario reveals the effect of viscosity on i_{Lim} variation, when NaCl concentration is increased.

- "Rho+Mu+D": density and viscosity of solution and diffusion coefficient of H^+ ion change with NaCl concentration and H^+ concentration is kept constant as that for pure water. This scenario reveals the effect of H^+ ion diffusion coefficient on i_{Lim} variation, when NaCl concentration is increased.
- "Rho+Mu+D+[H^+]": the effect of NaCl concentration on all the four parameters is considered in i_{Lim} calculations. This scenario reveals the effect of solution chemistry (H^+ ion concentration) on i_{Lim} variation, when NaCl concentration is increased.

Figure 9-9 elucidates that the changes in solution density and solution viscosity with NaCl concentration had a minor effect on the i_{Lim} variation. In contrast, changes in H^+ diffusion coefficient and H^+ ion bulk concentration showed substantial contributions on the i_{Lim} variation. The contribution of changes in H^+ ion bulk concentration seems to be greater than that for changes in H^+ diffusion coefficient. Therefore, the decreasing trend seen for i_{Lim} with increasing NaCl concentration was mainly due to the change in H^+ ion bulk concentration and then the H^+ diffusion coefficient.

The comparison between the calculated i_{Lim} (solid black line) and the experimental i_{Lim} (square dots) shows that there is a very good agreement between the estimations and the experimental measurements. This means that the models reproduced and used in this study are reliably accurate models. The peak seen at low NaCl concentrations in the calculated i_{Lim} is due to the H^+ concentration trend with NaCl concentration (Table 9-4). The reason why this peak was not detected in the experimental i_{Lim} might be related to the insufficient resolution chosen for NaCl concentration in the experiments. Coincidentally, this peak was observed for CO_2 experiments (presented in Chapter 10).

Figure 9-9

The cumulative changes in H^+ *limiting current density in the RDE strong acid corrosion experiments calculated with Levich equation when the effect of NaCl concentration is applied to solution density (Rho), solution viscosity (Mu),* H^+ *diffusion coefficient (D), and* H^+ *concentration (*$[H^+]$*).*

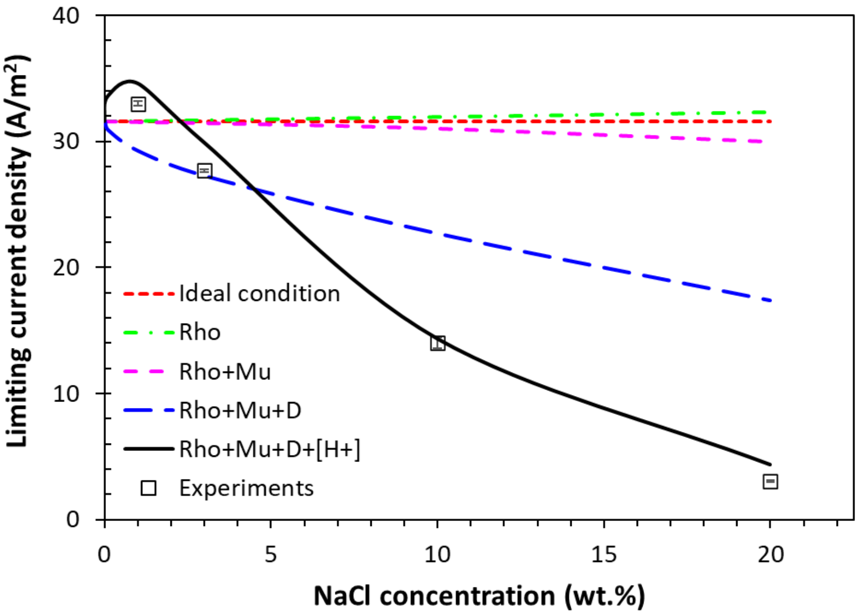

Figure 9-10 shows the RDE strong acid corrosion rate obtained from LPR measurements and PD sweeps at different NaCl concentrations. An average B value[65] of 14.45 mV/dec obtained from PD sweeps was used for converting the measured polarization resistance (Rp) to the corrosion rate. The PD corrosion rates were

---

[65] In the Stern-Geary equation ($B = \frac{\beta_c \times \beta_a}{2.3(\beta_c + \beta_a)}$), where β_c is the cathodic Tafel slope and β_a is the anodic Tafel slope. In this study, β_c at the corrosion current density is used in the Stern-Geary equation.

extracted from the sweep fitting practice explained earlier. A similar trend and a similar magnitude of corrosion rates were obtained with both techniques, indicating the reliability of results.

Figure 9-10

Variation in the corrosion rate with NaCl concentration for X65 carbon steel RDE (2000 rpm) exposed to N_2*-saturated aqueous NaCl solutions at 10°C, 1 bar total pressure, and pH 3. The corrosion rates were measured using LPR and PD sweep techniques. The error bars represent the minimum and maximum values obtained in two repeated experiments.*

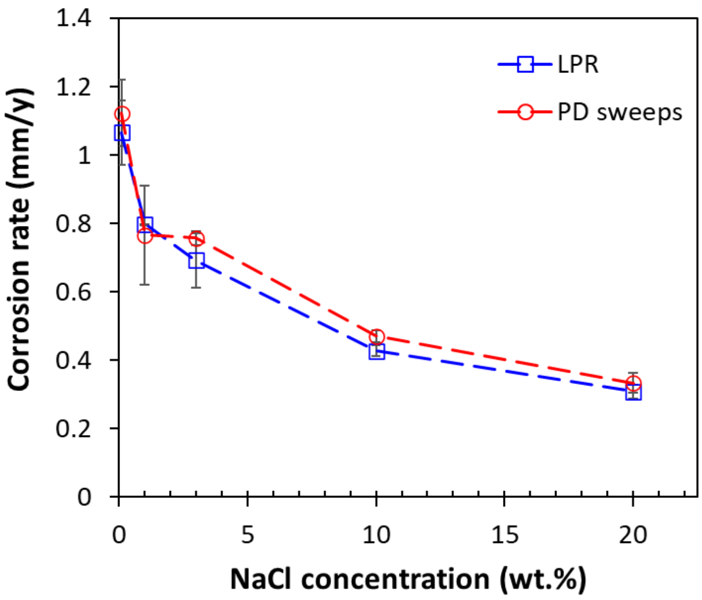

Both LPR and PD sweep techniques show that the corrosion rates decreased with increasing NaCl concentration. The decrease in the corrosion rate with the addition of NaCl concentration from 1 wt.% to 20 wt.% can be attributed to deceleration in both anodic and cathodic charge transfer reactions as well as reduction of i_{Lim}. To understand which of these three parameters under the experimental conditions is more influential on the corrosion rate, the Evans diagram is prepared (Figure 9-11). The Evans diagram is obtained by fitting the experimental PD sweeps with those obtained by an electrochemical model [96].

Figure 9-11

The Evans diagram for the effect of NaCl concentration on uniform strong acid corrosion of X65 RDE at 10°C, ~1 bar N_2, pH 3, and 2000 rpm rotational speed. E_{corr} is the corrosion potential (OPC), i_{corr} is the corrosion current density, and i_{Lim} is the H^+ ion reduction reaction limiting current density (Blue: 1 wt.% NaCl and red: 20 wt.% NaCl).

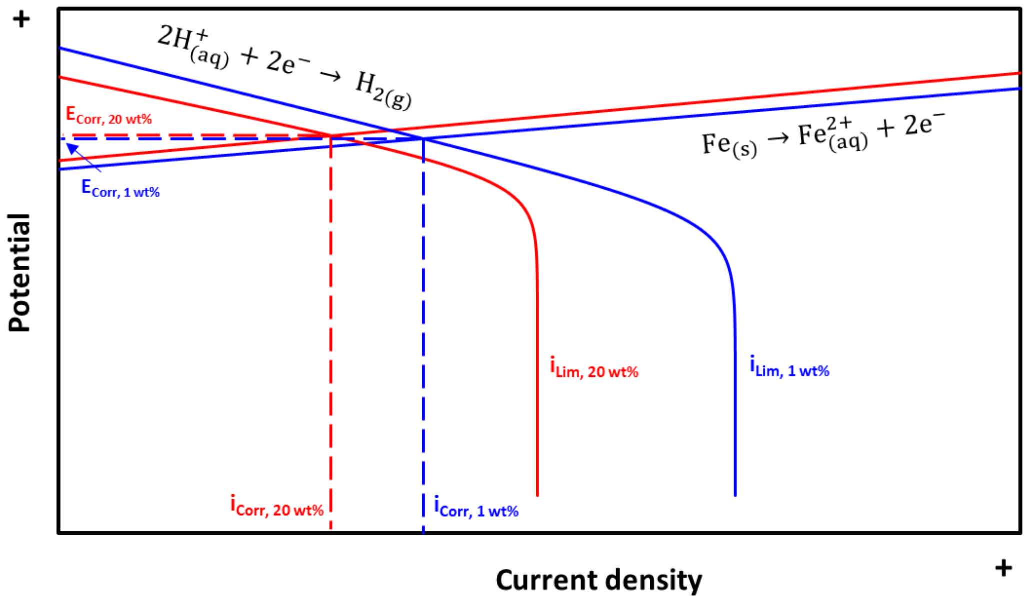

When NaCl concentration is increased from 1 wt.% to 20 wt.%, the corrosion potential (OCP) remains almost unchanged, while the corrosion current density decreases, due to retardation of both anodic and cathodic charge transfer reactions.

Increasing NaCl concentration also decreases i_{Lim} due to a decrease in the rate of mass transfer of H^+ ions to the electrode surface. However, the decrease in i_{Lim} has no effect on the corrosion rate. Therefore, the uniform strong acid corrosion process under the studied experimental conditions was controlled by the rates of charge transfer of H^+ ion reduction and Fe oxidation reactions at the steel surface.

An additional conclusion is that NaCl concentration influenced i_{Lim} more than the rates of charge transfer processes, because i_{Lim} decreased more than the corrosion current density (i_{Corr}) when NaCl concentration was increased from 1 wt.% to 20 wt.%.

9.1.3 Summary and Conclusions of RDE Strong Acid Corrosion Experiments

The effect of salt concentration was investigated on uniform corrosion of X65 carbon steel by carrying out electrochemical experiments with an RDE setup at a rotational rate of 2000 rpm in N_2-saturated solutions at 10°C, 1 bar total pressure, and pH 3. The following are major conclusions found in this set of experiments, when NaCl concentration was increased from 0.1 wt.% to 20 wt.%:

1. The uniform strong acid corrosion rate decreased steadily with increasing NaCl concentration.
2. The analysis of the PD sweeps showed that both cathodic (H^+ reduction) and anodic (iron dissolution) charge transfer reactions were retarded.
3. The limiting current density (i_{Lim}) for H^+ ion reduction decreased due to a reduction in the rate of mass transfer of H^+ ions to the steel surface.
4. The decreasing trend seen for i_{Lim} is mainly due to changes in H^+ ion bulk concentration and H^+ diffusion coefficient.

5. The mechanism of active dissolution of iron did not change. However, the mechanism of H^+ ion reduction at the steel surface seemed to be somewhat affected.
6. The strong acid corrosion process was under charge transfer control and the variation in the mass transfer rate of H^+ ions to the surface did not have an impact on the corrosion rate.

9.2 The Effect of Salt Concentration on Strong Acid Corrosion at 20ºC and pH 3 Obtained Using a Rotating Cylinder Electrode (RCE)

9.2.1 Experimental Materials and Methodology for RCE Strong Acid Corrosion Experiments

Experiments were carried out in 2-liter glass cell shown by a schematic in Figure 9-12. In this set of experiments, a combination of a conventional portable cooler and a hot plate was used to adjust the temperature. Electrochemical experiments were conducted in N_2-saturated aqueous solutions with different NaCl concentrations to investigate the effect of salt concentration on uniform strong acid corrosion.

A three-electrode setup was used for performing the electrochemical experiments. The reference electrode was a silver/silver chloride (Ag/AgCl) electrode. The counter electrode was a platinized titanium mesh with dimensions 20×30 mm^2. The working electrode (specimen) was a rotating cylinder electrode (RCE) with an exposed surface area of 5.4 cm^2 made from API 5L X65 carbon steel with a chemical composition listed in Table 9-1. The schematic of the working electrode is shown in Figure 9-12.

Figure 9-12

The schematic of the experimental setup (A) and specimen (B) used in the RCE strong acid corrosion experiments.

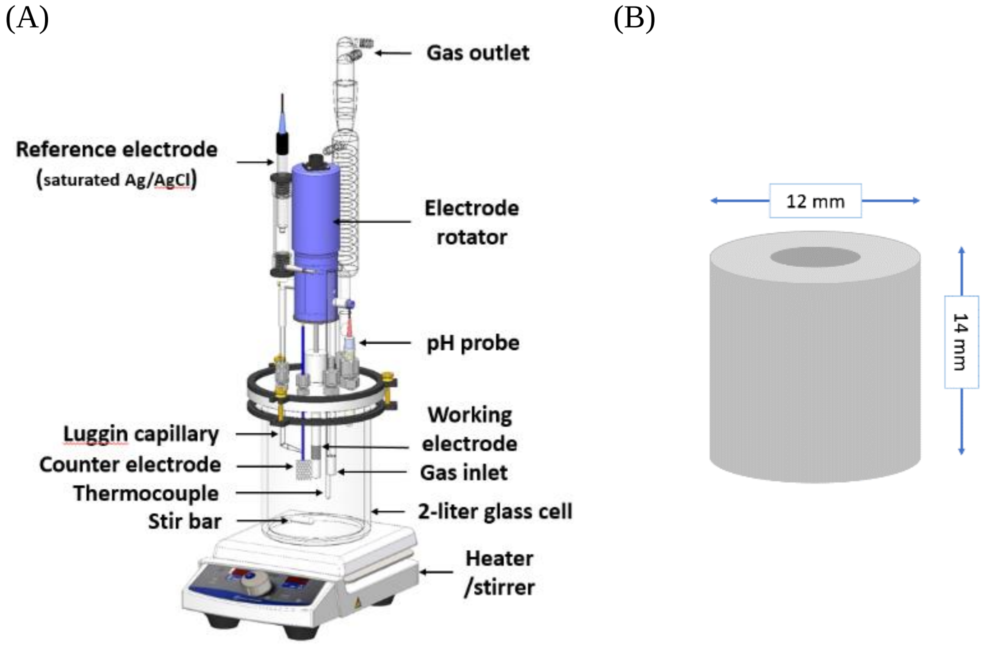

The specimen was sequentially wet polished with 80-, 240-, 400- and 600-grit abrasive papers. Subsequently, it was ultrasonically degreased with isopropanol for 3 min and dried in cool N_2 gas prior to immersion in the test solution.

For each experiment, a specified amount of NaCl was added to two liter of double-distilled deionized water (conductivity $< 1\ \mu$S/cm) in a glass cell. The solution was then sparged with N_2 for at least 2 h while being stirred. After about 1.5 h of sparging, the pH of solution became stable. Figure 9-13 shows the autogenous pH of solution before pH adjustment at different NaCl concentration. Similar to the RDE strong acid experiments, the autogenous pH of solution increased with increasing NaCl concentration. This trend cannot be justified by the speciation models discussed in this study and needs further investigation. The solution pH was then adjusted to 3.0

by adding 0.1 M HCl to the solution. More HCl was required for higher NaCl concentrations. The pH measurements were done with a double-junction pH probe, resistant to Na^+ ion interference, as measuring pH correctly in high ionic strength solutions is challenging [10].

Figure 9-13

Autogenous pH of N_2 saturated solutions measured at 20°C, and 1 bar total pressure (~ 0.98 bar pN_2) before pH adjustment. The error bars represent the minimum and maximum values obtained in repeated experiments (with at least 2 repeats).

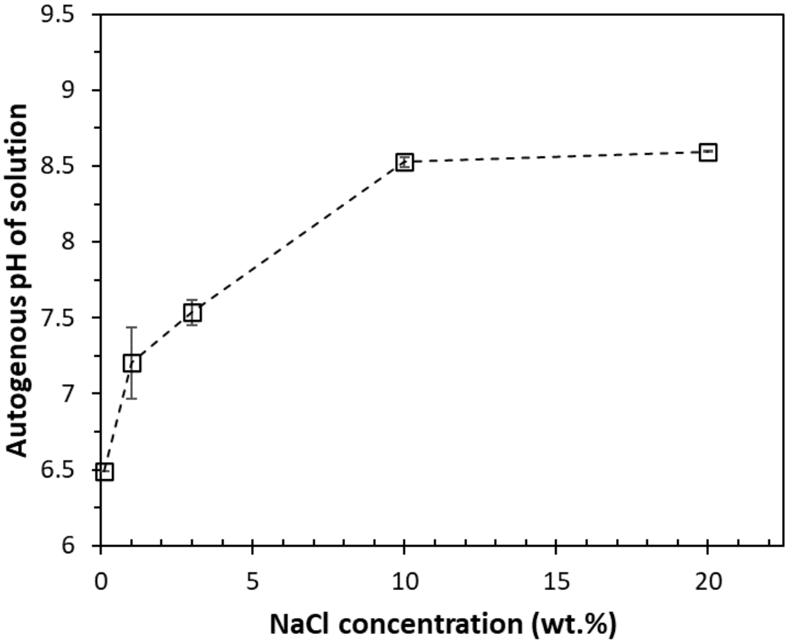

After at least 30 min from pH adjustment, the RCE specimen was inserted into the solution. Prior to each electrochemical test, the open circuit potential (OCP) was monitored until a stable potential value (ΔE_{OCP}< 2 mV/min) was achieved. The LPR technique was performed in a potential range of -5.0 mV to 5 mV vs. OCP at a scan rate of 0.125 mV/s to measure the corrosion rate. Then, EIS was carried out in a frequency range of 10,000 Hz to 0.1 Hz at OCP with a 10 mV AC peak to peak amplitude and a sampling rate of 8 points/dec to determine the solution resistance (iR drop). Finally, the PD sweeps were conducted according to the following steps: (1) a cathodic sweep starting from the OCP toward more negative potentials up to -1.00 V vs OCP; (2) wait for the OCP to return close to its initial value—within a few mV (this took about 1 h); (3) an anodic sweep starting from the OCP to more positive potentials up to 0.35 V vs OCP. The PD sweeps were done with a scan rate of 0.5 mV/s. A Gamry Reference 600 potentiostat was used for all the electrochemical measurements. For each NaCl concentration at least two separate tests were conducted to assure about the reproducibility of results.

Table 9-5

The experimental conditions used in the RDE strong acid experiments.

Parameter	Description
Specimen material	API 5L X65 carbon steel
RCE surface area (cm^2)	5.4 ± 0.1
Temperature (°C)	20.0 ± 1
Total pressure (bar)	1
N_2 partial pressure (bar)	~ 0.98
NaCl concentration (wt.%)[66]	0.1, 1, 3, 10, 20
pH	3.00 ± 0.02
RCE rotational speed (rpm)[67]	1000 ± 2

9.2.2 Results and Discussion for RCE Strong Acid Corrosion Experiments

Figure 9-14 shows the PD sweeps at different NaCl concentrations. In all the sweeps, the potential values are corrected for the solution resistance (iR drop). At least, two sets of PD sweeps were obtained for each NaCl concentration to verify the reproducibility of results. Both anodic and cathodic portions of the PD sweeps were affected when NaCl concentration was increased. The key change in the PD sweeps with increasing NaCl concentration is the decrease in i_{Lim}.

---

[66] wt.% = 100 × mass of salt / (mass of salt + mass of water)

[67] revolutions per minute

Figure 9-14

Potentiodynamic polarization sweeps of X65 carbon steel RCE with a rotational speed of 1000 rpm exposed to N_2*-saturated aqueous solutions with different NaCl concentrations at 20°C, 1 bar total pressure, and pH 3.*

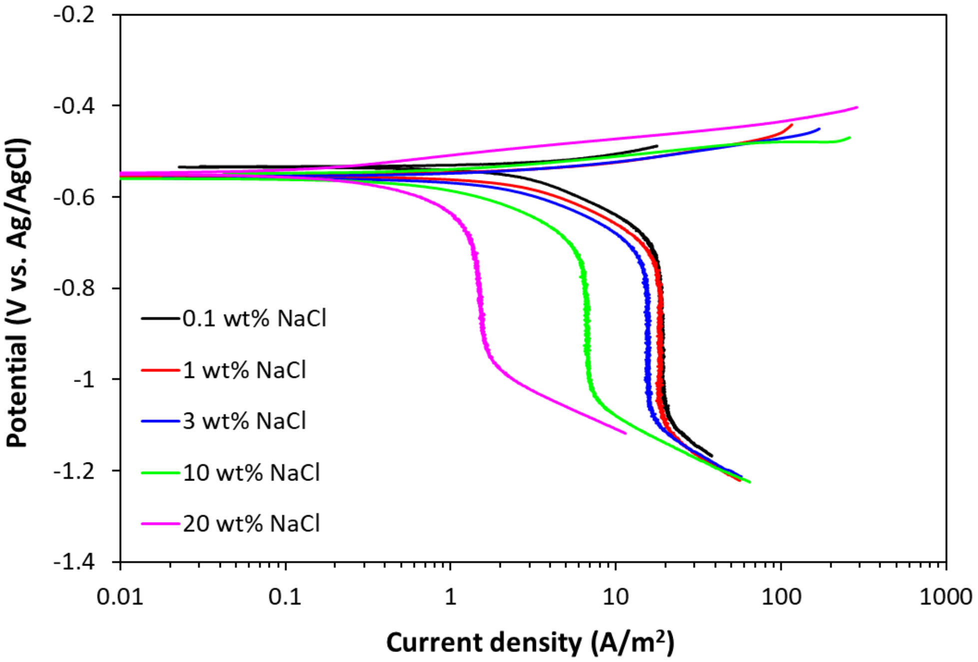

For a detailed analysis of the effect of NaCl concentration on the mechanism of strong acid corrosion, the electrochemical features of the sweeps were obtained by overlaying them with the best fit calculated by an electrochemical model [96][68]. The fitted sweeps for two NaCl concentrations are shown in Figure 9-15 as a demonstration of fitting exercise accuracy.

---

[68] Activation energies of 59860 J/mol for H^+ ion, 24809 J/mol H_2O reduction and 25398 J/mol for Fe oxidation reactions. A reversible potential of -0.685 V vs. Ag/AgCl was used for all three reactions. The reference temperature was 20°C.

Figure 9-15

Comparison of the experimental sweeps at 1 wt.% (A) and 20 wt.% (B) NaCl concentrations measured in the RCE strong acid experiments with those obtained by a simple electrochemical model [96].

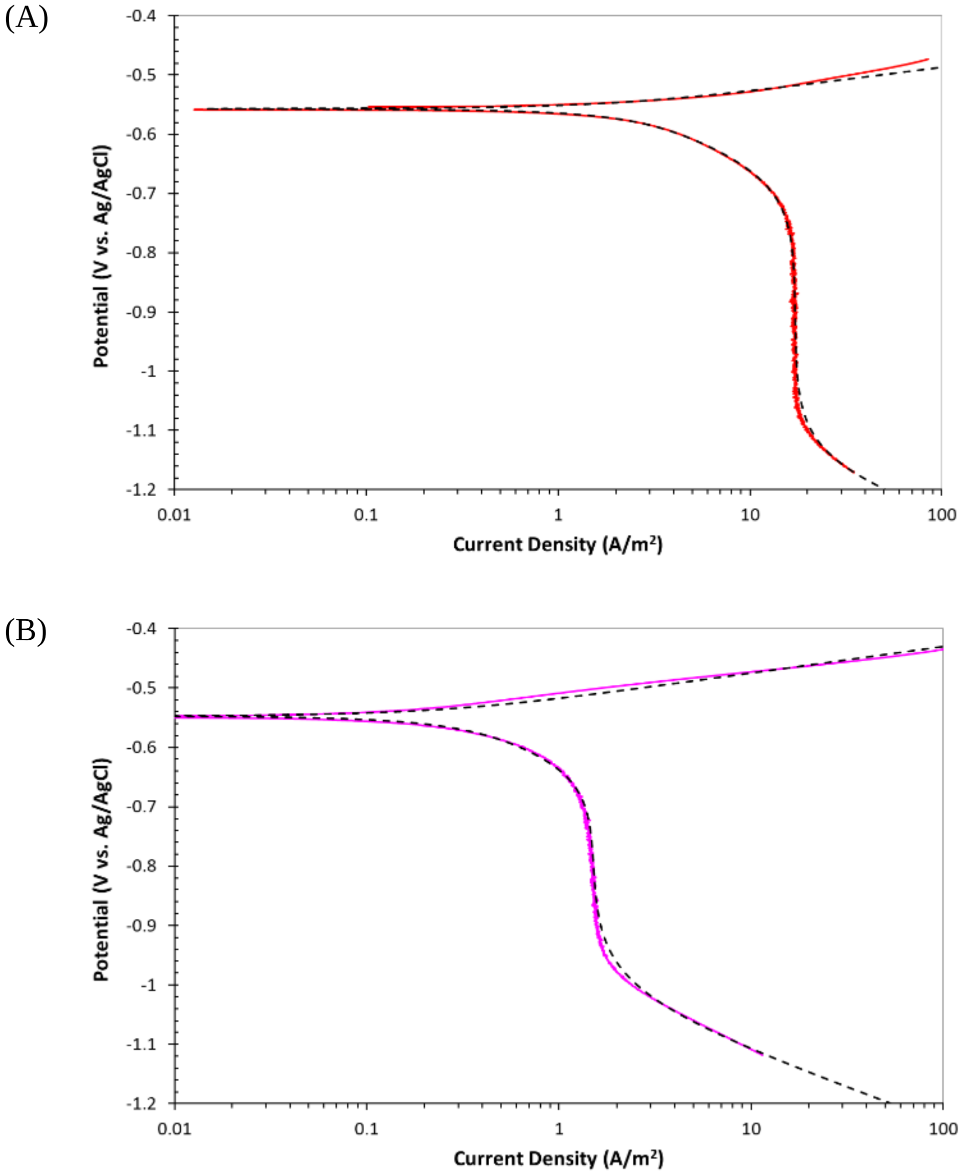

The electron transfer coefficients for H$^+$ reduction reaction (α_{H^+}) and Fe oxidation in the active region (α_{Fe}) at different NaCl concentrations are listed in Table 9-6. The α_{H^+} values are larger than the theoretical value of 0.5, commonly suggested for the hydrogen evolution on an iron surface [185]. Such differences have been reported in the literature between the experimental α_{H^+} and the theoretical value of 0.5 [185,198,207,292]. As mentioned earlier, in Section 9.1.2, the difference between the experimental α_{H^+} values and the theoretical value of 0.5 can be because of a different underlying mechanism for the cathodic H^+ ion reduction reaction or because of errors in the fitting exercise. However, since these deviations have been repeated in two separate sets of experiments with different specimen types, a different underlying mechanism is more likely.

Table 9-6

The electron transfer coefficients for H^+ reduction reaction (α_{H^+}) and Fe oxidation (α_{Fe}) for the RCE strong acid experiments at 20°C, ~1 bar N_2 and pH 3. Each data is an average of two measurements.

NaCl (wt.%)	0.1	1	3	10	20
α_{H^+}	0.55±0.00	0.56±0.01	0.58±0.00	0.66±0.00	0.66±0.01
β_c	-106±0	-103±0	-100±0	-89±0	-89±0
α_{Fe}	1.40±0.00	1.40±0.00	1.40±0.00	1.30±0.00	1.30±0.00
β_a	41±0	41±0	41±0	45±0	45±0

It appears that α_{H^+} increased slightly with increasing NaCl concentration. This increasing trend for α_{H^+} was observed in the RDE strong acid experiments reported in Section 9.1 as well. Therefore, it can be concluded that increasing NaCl concentration alters to some extent the mechanism of the cathodic H^+ ion reduction reaction in acid aqueous NaCl solutions saturated with N_2 gas.

The measured α_{H^+} values with the RCE setup at 20°C (Table 9-6) are larger than those measured with the RDE setup at 10°C (Table 9-3). The 10 degrees temperature difference is not expected to cause any significant change in the mechanism of the H^+ ion reduction reaction. Another difference between the two cases, is the type of specimens and their corresponding flow regimes. The RCE setup under the experimental conditions experiences urbulent flow, while the RDE setup produced a laminar flow; however this should not affect the kinetics of the charge transfer reactions. The third difference is the polishing procedures used for preparing the specimens. The RDE specimen, it was polished on a metallographic polishing machine commonly found in metallography labs. For the RCE specimen, standard floor drilling machine was used to polish rotating the RCE specimen. The RCE specimen was being rotated, while the sandpaper in a stationary position was in contact with the RCE surface. A different surface finish might lead to a slightly different charge transfer mechanism, given that the charge transfer reactions are strongly affected by the nature of the surface. However, the exact reason behind the different α_{H^+} values for the two electrode setups cannot be pinpoint with current results. Further investigations are required on this subject. Studying systematically the mechanism of charge transfer processes necessitates applications of electrochemical transient techniques such as electrochemical impedance spectroscopy, which is out of the scope of this study.

The α_{Fe} was ~ 1.35 for all NaCl concentrations. Bockris *et al.* [185] proposed a theoretical value of 1.5 for iron dissolution in acidic media without the presence of halides. For dissolution of iron in acidic chloride media, the measured α_{Fe} is very close values reported in the literature [193–195] and only slightly higher than what was obtained using the RDE experiments described in Section 9.1. Since α_{Fe} did not really change with increasing NaCl concentration, it can be concluded that the mechanism of anodic dissolution of iron in the active region remained unaffected by the presence of salt. The mechanisms of iron dissolution in the presence of chloride have been comprehensively explained in Section 5.1.1.

The variations in the exchange current densities for H^+ reduction (i_{o,H^+}) is plotted in Figure 9-16 A. The i_{o,H^+} dramatically decreased with increasing NaCl concentration from 0.1 wt.% to 3 wt.% and flattened out with further increase in NaCl concentration. This trend is the same as that observed in the RDE strong acid experiments, raising confidence in these results. The declining trend of i_{o,H^+} shows that the rate of H^+ ion reduction decreased with increasing NaCl concentration, which is most probable because of the adsorption of Cl^- ions on the steel surface blocking the areas required for H^+ ions to adsorb on and be reduced [171].

The i_{o,H^+} trend seen in Figure 9-16 A can be modeled by using a correlation similar to Equation (5-23):

$$i_{o,H^+} = i_{o,H^+}^{ref} \left(\frac{a_{H^+,b}}{a_{H^+,b}^{ref}}\right)^{n_{H^+}^{H^+}} \left(\frac{a_{Cl^-,b}}{a_{Cl^-,b}^{ref}}\right)^{n_{Cl^-}^{H^+}} e^{-\frac{E_{a,H^+}}{R}\left(\frac{1}{T}-\frac{1}{T_{ref}}\right)} \tag{9-4}$$

where, i_{o,H^+}^{ref} is the reference current density in A/m^2 at T_{ref} (293.15 K) and potential of -685 mV *vs.* Ag/AgCl, $a_{H^+,b}$ is the bulk activity of H^+ ion in molarity concentration, $a_{H^+,b}^{ref}$ is the reference bulk activity of H^+ ion (= 10^{-4} M), $n_{H^+}^{H^+}$ is the reaction order of the H^+ ion reduction reaction with respect to H^+ ion activity, $a_{Cl^-,b}$ is the bulk activity of Cl^- ion in molarity concentration, $a_{Cl^-,b}^{ref}$ is the reference bulk activity of Cl^- ion (= 1 M), $n_{Cl^-}^{H^+}$ is the reaction order of the H^+ ion reduction reaction with respect to Cl^- ion activity, E_{a,H^+} is the activation energy for the H^+ ion reduction reaction (= 59860 J/mol), T is solution temperature in K, and R is the gas constant in J/mol/K. Equation (9-4) with the bulk activities calculated with the MSE model was fitted to the experimental i_{o,H^+} values in Figure 9-16 A to extract the reaction orders and i_{o,H^+}^{ref}. Since the solution pH was constant in the experiments, the activity of H^+ ion was constant as well[69]. This means that $n_{H^+}^{H^+}$ cannot be determined from the fitting exercise. To be able to obtain $n_{H^+}^{H^+}$ experiments at different pH values are required. Therefore, an empirical value of 0.5 previously reported in the literature was chosen for $n_{H^+}^{H^+}$ [200,215]. $n_{Cl^-}^{H^+}$ was determined to be ~ -0.31 and i_{o,H^+}^{ref} term was 6.9 A/m^2. The negative sign found for $n_{Cl^-}^{H^+}$ proves that Cl^- ion had a retardation effect on the rate of the H^+ ion reduction reaction in the charge transfer region.

---

[69] The changes in molarity-based activity due to changes in density with NaCl concentration is ignored.

Figure 9-16

Variations in (A) the cathodic limiting current density (i_{Lim}) and the H^+ reduction exchange current density (i_{o,H^+}) and (B) the Fe oxidation exchange current density ($i_{o,Fe}$) with NaCl concentration. The current densities were extracted from the PD sweeps of X65 carbon steel RCE specimen with a rotational speed of 1000 rpm exposed to N_2-saturated aqueous solutions at 20°C, 1 bar total pressure, and pH 3. The error bars represent the minimum and maximum values obtained in two repeated experiments. The reference temperature was 20°C.

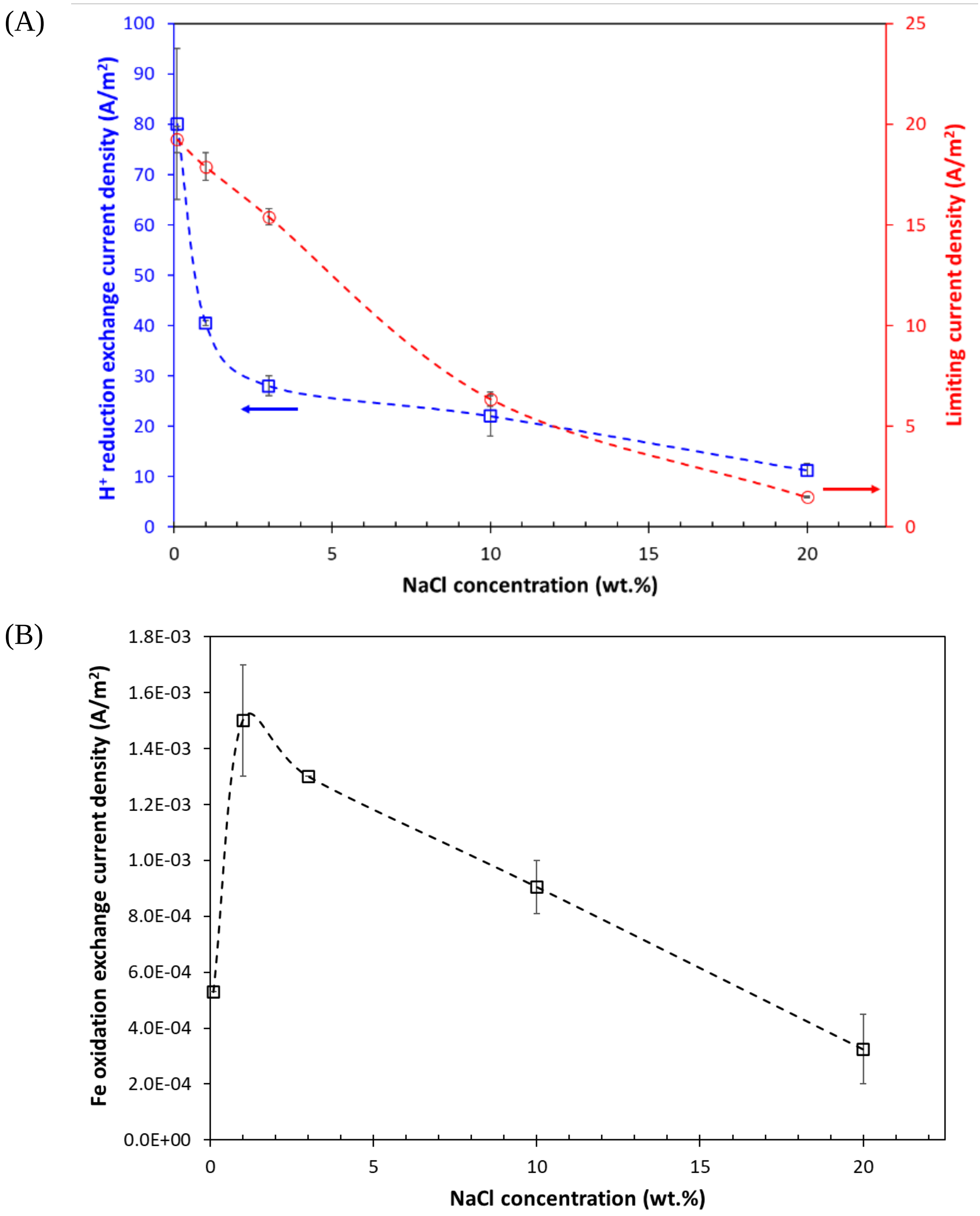

Figure 9-16 B shows the variation in the Fe oxidation exchange current density ($i_{o,Fe}$) with NaCl concentration. At low NaCl concentrations, $i_{o,Fe}$ increased with increasing NaCl concentration. $i_{o,Fe}$ reversed trend and decreased at higher NaCl concentrations. The observed trend for $i_{o,Fe}$ is identical to that measured in the RDE strong acid experiments (Figure 9-8 B). This indicates that the obtained trends are accurate and consistent. The $i_{o,Fe}$ trend can be justified by considering the changes in the bulk activities of OH$^-$ and Cl$^-$ ions, and H_2O with NaCl concentration. The $i_{o,Fe}$ can be related to the activities of OH$^-$ and Cl$^-$ ions, and H_2O with the following correlation:

$$i_{o,Fe} = i_{o,Fe}^{ref}\left(\frac{a_{OH^-,b}}{a_{OH^-,b}^{ref}}\right)^{n_{OH}^{Fe}}\left(\frac{a_{Cl^-,b}}{a_{Cl^-,b}^{ref}}\right)^{n_{Cl^-}^{Fe}}\left(\frac{a_{H_2O,b}}{a_{H_2O,b}^{ref}}\right)^{n_{H_2O}^{Fe}} e^{-\frac{E_{a,Fe}}{R}\left(\frac{1}{T}-\frac{1}{T_{ref}}\right)} \quad (9\text{-}5)$$

where, $i_{o,Fe}^{ref}$ is the reference current density in A/m^2 at T_{ref} (293.15 K) and -685 mV *vs.* Ag/AgCl, $a_{OH^-,b}$ is the bulk activity of OH$^-$ ion in molarity concentration, $a_{OH^-,b}^{ref}$ is the reference bulk activity of OH$^-$ ion (= 10^{-10} M), n_{OH}^{Fe} is the reaction order of the Fe oxidation reaction with respect to OH$^-$ ion activity, $a_{Cl^-,b}$ is the bulk activity of Cl$^-$ ion in molarity concentration, $a_{Cl^-,b}^{ref}$ is the reference bulk activity of Cl$^-$ ion (= 1 M), $n_{Cl^-}^{Fe}$ is the reaction order of the Fe oxidation reaction with respect to Cl$^-$ ion activity, $a_{H_2O,b}$ is the bulk activity of liquid water in molarity unit, $a_{H_2O,b}^{ref}$ is the reference bulk activity of liquid water (= 55.4 M), $n_{H_2O}^{Fe}$ is the reaction order of the Fe oxidation reaction with respect to H_2O, and $E_{a,Fe}$ is the activation energy for the Fe oxidation reaction in the active region (= 25398 J/mol), T is solution temperature in K, and R is the gas constant in J/mol/K.

Lorenz [174] and McCafferty and Hackerman [178], reported different $n_{Cl^-}^{Fe}$ values at different range of Cl$^-$ activities (concentrations), as summarized in Table 5-2. This indicates that the iron dissolution reaction may possibly advance through different pathways depending on the Cl$^-$ activity in the solution. From the $i_{o,Fe}$ trend presented in Figure 9-8 B, it can be assumed that at low NaCl concentrations below 1 wt.%[70], Cl$^-$ ions accelerates the anodic dissolution reaction by playing a catalytic role in iron dissolution, similar to that of OH^- ions [172,194,195]. However, at high NaCl concentrations above 1 wt.%, Cl$^-$ ions inhibits the Fe dissolution reaction by being adsorbed on the surface and blocking the active sites (surface imperfections) required for the Fe dissolution reaction to occur [173,174,178,192]. Therefore, the $i_{o,Fe}$ curve is divided into two sections: below and above 1 wt.%. Equation (9-5) with the bulk activity values calculated with the MSE was fitted to the experimental $i_{o,Fe}$ values to determine the reaction orders and $i_{o,Fe}^{ref}$ for the two sections. To obtain n_{OH}^{Fe} value experiments at different solution pH are needed. This means that n_{OH}^{Fe} cannot be found from the data presented here. Therefore, a value of 1 was chosen for n_{OH}^{Fe} for the whole range of NaCl concentration according to the Bockris *et al.* [185,186] consecutive mechanism and reports by other scientists [174,195] (see Table 5-2). For NaCl $\leq$ 1 wt.%, $n_{Cl^-}^{Fe}$= 0.49, $n_{H_2O}^{Fe}$ = 0, and $i_{o,Fe}^{ref}$ = 0.061 and for NaCl $>$ 1, $n_{Cl^-}^{Fe}$= -0.24, $n_{H_2O}^{Fe}$ = 2, and $i_{o,Fe}^{ref}$ = 0.0143. A reaction order of zero for H_2O at NaCl $\leq$ 1 means that the Fe dissolution reaction process is independent of H_2O activity in this NaCl concentration range. For $n_{H_2O}^{Fe}$ at high NaCl concentrations, the value found in

---

[70] It can be any NaCl concentration between 1 wt.% and 3 wt.%, as the experimental NaCl resolution was not small enough to determine the exact maximum.

this study is similar to the values (a range of 1.6-1.9) reported by Smart *et al.* [190,198].

The most obvious change in the PD sweeps in Figure 9-14 with the addition of NaCl concentration is the decrease in the cathodic limiting current density (i_{Lim}). The experimental i_{Lim} extracted from the PD sweeps is presented in Figure 9-16 A. As mentioned earlier, i_{Lim} depends on bulk activity (concentration in strong acid condition) and diffusivity of electroactive species (H^+ ion in the case of strong acid corrosion), density, and viscosity of solution. The effect of NaCl concentration on all these parameters have been addressed earlier and models presented for each. With increasing NaCl concentration, the density and viscosity of solution increases, whereas the diffusion coefficient of H^+ ion and its concentration decrease. Table 9-7 lists the values of these parameters at the experimental NaCl concentrations calculated by the models introduced in previous chapters. For H^+ concentration, the MSE model is used.

Table 9-7

Variation in solution density, solution viscosity, H^+ ion diffusion coefficient and H^+ ion concentration with NaCl concentration in N_2-saturated aqueous solutions at 10°C, 1 bar total pressure, and pH 3.

NaCl (wt.%)	Density (kg/m^3)	Viscosity (kg/m/s)	H^+ diffusion coefficient (m^2/s)	H^+ concentration (mol/lit)
0	997.10	1.00e-3	8.53e-9	1.04e-3
0.1	997.77	1.00e-3	8.26e-9	1.13e-3
1	1003.84	1.01e-3	7.61e-9	1.23e-3
3	1017.56	1.04e-3	6.88e-9	1.14e-3
10	1067.92	1.20e-3	5.34e-9	0.665e-3
20	1146.22	1.58e-3	3.77e-9	0.268e-3

The i_{Lim} in A/m^2 can be calculated by using Eisenberg *et al.* equation [294]:

$$i_{Lim} = \frac{79.1 \cdot n \cdot F \cdot V^{0.7}}{d_{RCE}^{0.3}} \rho^{0.344} \cdot \mu^{-0.344} \cdot D_{H^+}^{0.644} \cdot c_{b,H^+} \tag{9-6}$$

where, n is the number of electrons involved in the electrode reaction (= 1 for H^+ ion reduction); F is the Faraday's constant (= 96485 C/mol); V is the RCE linear velocity (m/s); ρ is the density of the solution (kg/m^3); μ is the dynamic viscosity of the solution (kg/m-s); D is the diffusion coefficient of H^+ ion (m^2/s); and c_{b,H^+} is concentration of H^+ ion in the bulk solution (mol/m^3).

To find out which of the four parameters mentioned above has a greater effect on the variation in i_{Lim} with increasing NaCl concentration, i_{Lim} is calculated at the experimental NaCl concentration for five scenarios, using the data provided in Table 9-7.

Figure 9-17 shows the calculated i_{Lim}values for the five scenarios and compares them with the experimental i_{Lim}. The “ideal condition” scenario indicates i_{Lim} is calculated for all NaCl concentration with density, viscosity, H^+ diffusion coefficient and H^+ concentration for pure water. This scenario means that the effect of salt concentration is not considered for any of the four parameters. Therefore, i_{Lim} is constant for all NaCl concentrations. The “Rho” scenario is when in calculations only density of solution is allowed to change with NaCl concentration, and the other three parameters are kept constant as those for pure water. This scenario reveals the effect of density on i_{Lim} variation, when NaCl concentration is increased. Similarly, the other scenarios can be described as below:

- “Rho+Mu”: density and viscosity of solution change with NaCl concentration and the other two parameters are kept constant as those for pure water. This scenario reveals the effect of viscosity on i_{Lim} variation, when NaCl concentration is increased.
- “Rho+Mu+D”: density and viscosity of solution and diffusion coefficient of H^+ ion change with NaCl concentration and H^+ concentration is kept constant as that for pure water. This scenario reveals the effect of H^+ ion diffusion coefficient on i_{Lim} variation, when NaCl concentration is increased.
- “Rho+Mu+D+[H^+]”: the effect of NaCl concentration on all the four parameters is considered in i_{Lim} calculations. This scenario reveals the effect of solution chemistry (H^+ ion concentration) on i_{Lim} variation, when NaCl concentration is increased.

Figure 9-17

The cumulative changes in H^+ limiting current density in the RCE strong acid corrosion experiments calculated with Eisenberg et al. [294] *equation when the effect of NaCl concentration is applied to solution density (Rho), solution viscosity (Mu), H^+ diffusion coefficient (D), and H^+ concentration ($[H^+]$).*

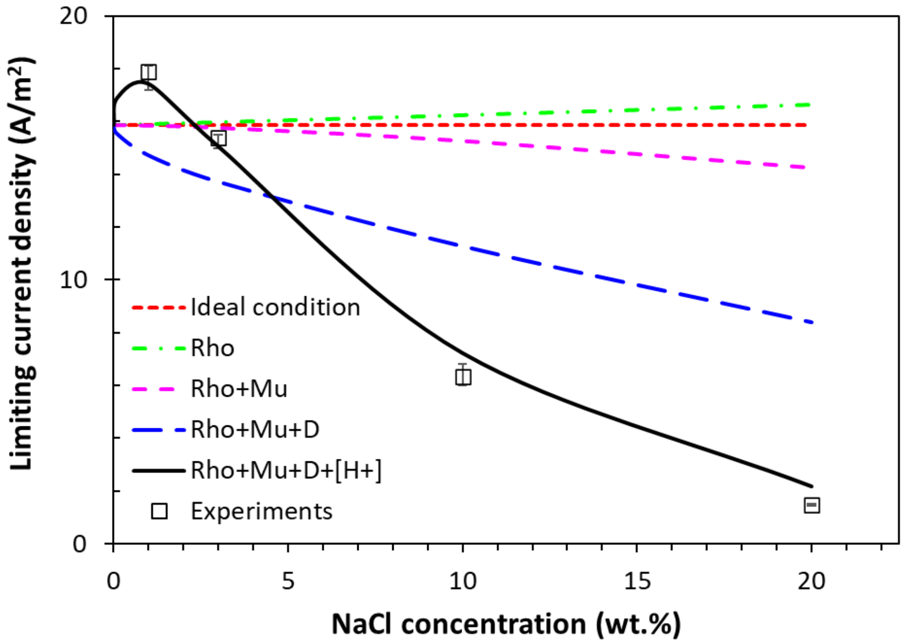

Figure 9-17 clarifies that the changes in solution density and solution viscosity with NaCl concentration had a minor effect on the i_{Lim} variation. On the other hand, changes in H^+ diffusion coefficient and H^+ ion bulk concentration showed substantial contributions to the i_{Lim}variation. The contribution of H^+ ion bulk concentration seems to be greater than that for changes in H^+ diffusion coefficient. Therefore, the decreasing trend seen for i_{Lim} with increasing NaCl concentration is mainly due to changes in H^+ ion bulk concentration and then the H^+ diffusion coefficient.

The comparison between the calculated i_{Lim} (solid black line) and the experimental i_{Lim} (square dots) shows that there is a very good agreement between the estimations and the experimental measurements. This means that the models reproduced and used in this study are reasonably accurate models. The peak seen at low NaCl concentrations in the calculated i_{Lim} is due to the H^+ concentration trend with NaCl concentration (Table 9-7). The reason why this peak was not detected in the experimental i_{Lim} islikely related to the insufficient resolution chosen for NaCl concentration variation in the experiments. Coincidentally, this peak was observed for CO_2 experiments (presented in Chapter 10).

The RCE strong acid corrosion rates obtained from LPR measurements and PD sweeps at different NaCl concentrations are shown Figure 9-18. An average B value of 13.38 mV/dec obtained from PD sweeps was used for converting the measured polarization resistance (Rp) to the corrosion rate. This B value is close to 14.45 mV/dec reported in the previous section for the RDE strong acid corrosion experiments. The PD corrosion rates were extracted from the sweeps using the curve fitting practice explained earlier. Almost identical corrosion rate values were obtained with both techniques, indicating the consistency of results.

Figure 9-18

Variation in the corrosion rate with NaCl concentration for X65 carbon steel RCE with a rotational speed of 1000 rpm exposed to N_2-saturated aqueous NaCl solutions at 20°C, 1 bar total pressure, and pH 3. The corrosion rates were measured using LPR and PD sweep techniques. The error bars represent the minimum and maximum values obtained in two repeated experiments.

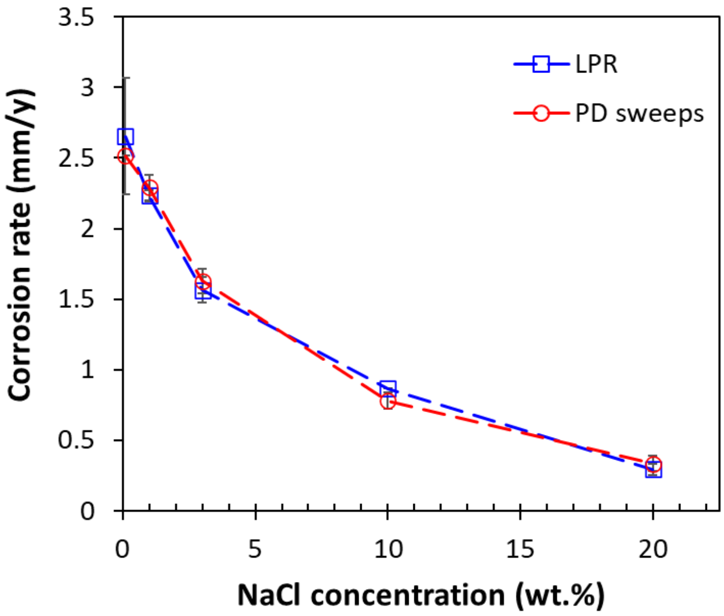

Both LPR and PD sweep techniques show that the corrosion rates decreased with increasing NaCl concentration. The decrease in the corrosion rate with the addition of NaCl concentration from 1 wt.% to 20 wt.% can be attributed to deceleration in both anodic and cathodic charge transfer reactions as well as reduction of i_{Lim}. To understand which of these three parameters under the experimental conditions plays a more influential role in the declining trend for the corrosion rate, the Evans diagram is prepared (Figure 9-19). The Evans diagram is obtained by fitting the experimental PD sweeps with those obtained by an electrochemical model [96].

Figure 9-19

The Evans diagram for the effect of NaCl concentration on uniform strong acid corrosion of X65 carbon steel RCE specimen with a rotational speed of 1000 rpm at 20^{o}*C, ~1 bar* N_2*, pH 3, and 1000 rpm rotational speed.* E_{corr} *is the corrosion potential (OPC),* i_{corr} *is the corrosion current density, and* i_{Lim} *is the* H^+ *ion reduction reaction limiting current density (Blue: 1 wt.% NaCl and red: 20 wt.% NaCl).*

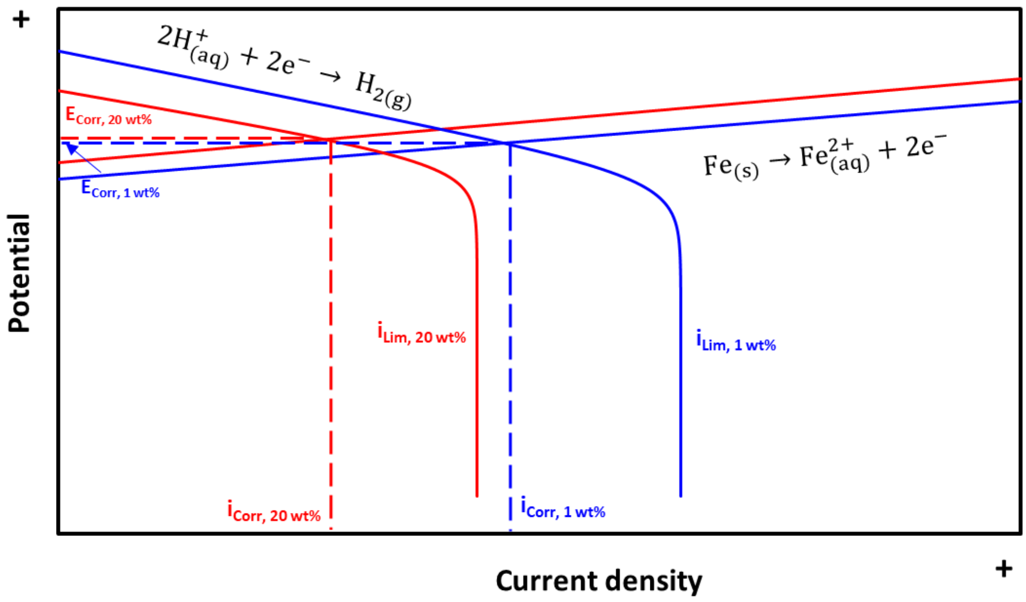

When NaCl concentration is increased from 1 wt.% to 20 wt.%, the corrosion potential (OCP) remains almost unchanged, whereas the corrosion current density decreases, due to retardation of both anodic and cathodic charge transfer reactions. Increasing NaCl concentration also decreases i_{Lim} due to a decrease in the rate of mass transfer of H^+ ions to the electrode surface. However, the decrease in i_{Lim} has no effect on the corrosion rate. Therefore, the uniform corrosion process in strong acid solutions under the studied experimental conditions was controlled by the rates of charge transfer of H^+ ion reduction and Fe oxidation reactions at the steel surface.

Another important conclusion is that i_{Lim} was affected more by NaCl concentration compared to the rates of charge transfer processes, because i_{Lim} decreased more than the corrosion current density (i_{Corr}) when NaCl concentration was increased from 1 wt.% to 20 wt.%.

9.2.3 Summary and Conclusions of RCE Strong Acid Corrosion Experiments

The effect of salt concentration was investigated on uniform corrosion of X65 carbon steel by carrying out electrochemical experiments with an RCE setup at a rotational rate of 1000 rpm in N_2-saturated solutions at 20°C, 1 bar total pressure, and pH 3. The following are major conclusions found in this set of experiments, when NaCl concentration was increased from 0.1 wt.% to 20 wt.%:

1. The uniform strong acid corrosion rate decreased steadily with increasing NaCl concentration.
2. The analysis of the PD sweeps showed that both cathodic (H^+ reduction) and anodic (iron dissolution) charge transfer reactions were retarded.
3. The limiting current density (i_{Lim}) for H^+ ion reduction decreased due to a reduction in the rate of mass transfer of H^+ ions to the steel surface.
4. The decreasing trend seen for i_{Lim} is mainly due to changes in H^+ ion bulk concentration and H^+ diffusion coefficient.
5. The mechanism of active dissolution of iron did not change. However, the mechanism of H^+ ion reduction at the steel surface seemed to be affected.

6. The strong acid corrosion process was under charge transfer control and the variation in the mass transfer rate of H^+ ions to the surface did not have an impact on the corrosion rate.
7. The results obtained in this set of experiments are identical to the results shown for the RDE strong acid corrosion, indicating the consistency of measurements and results.

Chapter 10: Experimentation to Investigate the Effect of Salt Concentration on CO_2 Corrosion

CO_2 is always present in production streams extracted from hydrocarbon reservoirs. When CO_2 dissolves in water, it produces carbonic acid, which subsequently dissociates and accelerates corrosion of carbon steel structures and facilities exposed to this corrosive medium. Corrosion of metals (mostly carbon steels) due to their exposure to aqueous CO_2-containing solutions is called CO_2 corrosion. In this chapter, the effect of salt concentration on CO_2 corrosion of carbon steel is experimentally investigated.

10.1 The Effect of Salt Concentration on CO_2 Corrosion at 10ºC, 1 bar CO_2, and pH 3 Using a Rotating Disk Electrode (RDE)

Even though it has been shown that the contribution of CO_2 in the overall corrosion process is insignificant at atmospheric pressures and pH lower than pH 4 [96], experiments were conducted in an acidic medium of pH 3 at pCO_2 of 1 bar to broaden the range of data required for developing a CO_2 corrosion prediction model in concentrated salt solutions. This part of the present study has been partially published elsewhere [295].

10.1.1 Experimental Materials and Methodology for RCE CO_2 Corrosion Experiments at 10ºC and pH 3

The experimental materials, apparatus, and methodology used in this part of experiments were the same as those utilized for the RDE strong corrosion experiment in Section 9.1, except that $CO_{2(g)}$ was sparged into the solution instead of $N_{2(g)}$. Therefore, to avoid repetition, readers are referred to Section 9.1 for details about the experimental procedure. Only the summary of the experimental conditions is presented here as Table 10-1. Four NaCl concentrations from 1 wt.% to 20 wt.% were used in this set of experiments.

Table 10-1

The experimental conditions used in the RDE CO_2 experiments at pH 3.

Parameter	Description
Specimen material	API 5L X65 carbon steel
RDE diameter (mm)	5.00 ± 0.05
Temperature (°C)	10.0 ± 0.5
Total pressure (bar)	1
CO_2 partial pressure (bar)	~ 0.98
NaCl concentration (wt.%)[71]	1, 3, 10, 20
pH	3.00 ± 0.02
RDE rotational speed (rpm)[72]	2000 ± 2

Figure 10-1 shows the autogenous pH of solution measured after at least 1.5 hr of CO_2 being sparged in the solution. Contrary to N_2-saturated solutions, the autogenous pH of solution decreased with increasing NaCl concentration. This means that less HCl was needed to adjust pH at 3 for higher NaCl concentrations.

---

[71] wt.% = 100 × mass of salt / (mass of salt + mass of water)

[72] revolutions per minute

Figure 10-1

Autogenous pH of CO_2 saturated solutions measured at 10°C, and 1 bar total pressure (~ 0.98 bar pCO_2) before pH adjustment. The error bars represent the minimum and maximum values obtained in repeated experiments (with at least 2 repeats).

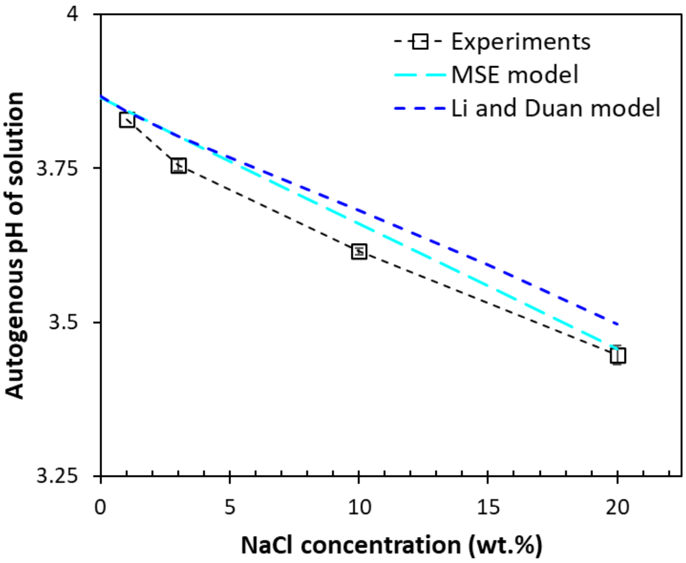

The experimental pH values are compared in Figure 10-1 with two activity coefficient-based speciation models discussed in Chapter 8. Both models predict the experimental results well, with a better accuracy for the MSE model. For example, the maximum pH difference between the measured pH and the predicted pH by the MSE model is 0.05 pH unit at 10 wt.% NaCl. This difference is ~ 0.07 pH unit for the Li and Duan model. The good agreement between the experimental data and the models validates the accuracy of the MSE model [135,241] and the Li and Duan [127,249] model introduced in this study.

To decide about the appropriate scan rate for the PD sweep experiments, two scan rates of 0.125 mV/s and 0.5 mV/s were tested at the same experimental condition (20 wt.% NaCl was chosen). Figure 10-2 shows the measured PD sweeps at these two scan rates. Since there was no significant difference in the PD sweeps for the two scan rates, 0.5 mV/s was chosen as the experimental scan rate to shorten the duration of each experiment and save resources.

Figure 10-2

The cathodic sweeps for X65 carbon steel RDE specimen (2000 rpm) obtained at two scan rates of 0.125 and 0.5 mV/s in 20 wt.% NaCl aqueous solution at 1 bar CO_2*, 10°C, and pH 3.*

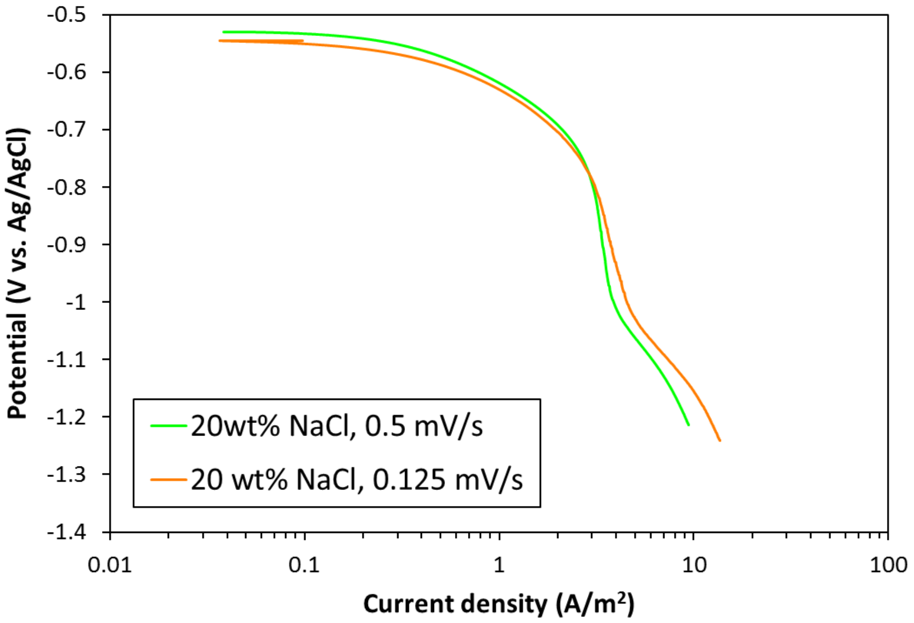

At the end of each experiment, scanning electron microscopy couple with X-ray diffraction spectroscopy (SEM/EDS) was performed on the corroded surface to study the surface morphology and the surface chemical composition. Before, mounting the specimen into the SEM/EDS chamber, the surface was rinsed for at least one minute with DI water to remove salt, followed by rinsing with isopropanol alcohol and drying in a cool $N_{2(g)}$ stream. The surface morphology was also inspected by using a surface profilometry technique.

10.1.2 Results and Discussion for RDE CO_2 Corrosion Experiments at 10°C and pH3

Figure 10-3 shows the CO_2 corrosion rate variation with NaCl concentration. Similar corrosion rates were measured by the two techniques: LPR and PD sweeps. The similarities between the trend and the magnitude of the CO_2 corrosion rate indicate that the results can be trusted. The CO_2 corrosion rate generally decreased with increasing NaCl concentration. However, LPR corrosion rates show a maximum at 3 wt.% NaCl. The actual maximum in the CO_2 corrosion rate could be at any NaCl concentration between 1 wt.% and 3 wt.%, as the experimental NaCl concentration resolution was not adequate to capture the exact location of the maximum. A similar behavior in the corrosion rate as a function of salt concentration is reported in Sections 10.2.2 and 10.3.2 and also by other researchers [8,11,296,297]. The observed trend in the corrosion rate can be explained by looking at the variations in the PD sweeps and the solution chemistry with respect to NaCl concentration.

Figure 10-3

Variation in the corrosion rate with NaCl concentration for X65 carbon steel RDE (2000 rpm) exposed to aqueous NaCl solutions at 10°C, ~1 bar $CO_{2(g)}$*, and pH 3. The corrosion rates were measured using LPR and PD sweep techniques. The error bars represent the minimum and maximum values obtained in two repeated experiments.*

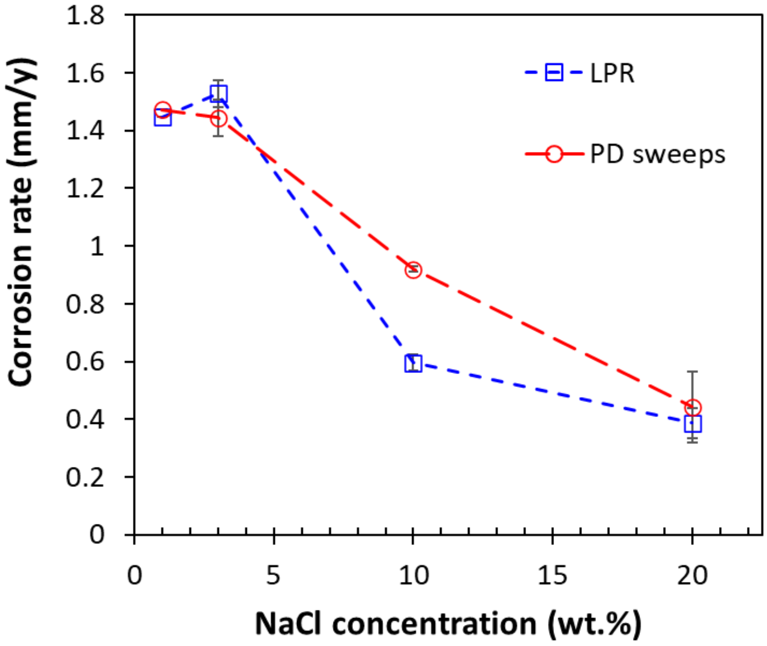

Figure 10-4 shows the PD sweeps at different NaCl concentrations. The potential values are corrected for the solution resistance (iR drop) in all the sweeps. At least, two sets of PD sweeps were obtained for each NaCl concentration to verify the reproducibility of results. The spikes in the more negative potential range for 1 wt.% was due to the formation of $H_{2(g)}$ bubbles on the RDE surface. Increasing NaCl concentration altered both the anodic and the cathodic branches. The most significant change in the PD sweeps with increasing NaCl concentration was the decrease in i_{Lim}.

Figure 10-4

Potentiodynamic polarization sweeps of X65 carbon steel rotating disk specimen (2000 rpm) exposed to CO_2-saturated aqueous solutions with different NaCl concentrations at 10°C, 1 bar total pressure, and pH 3.

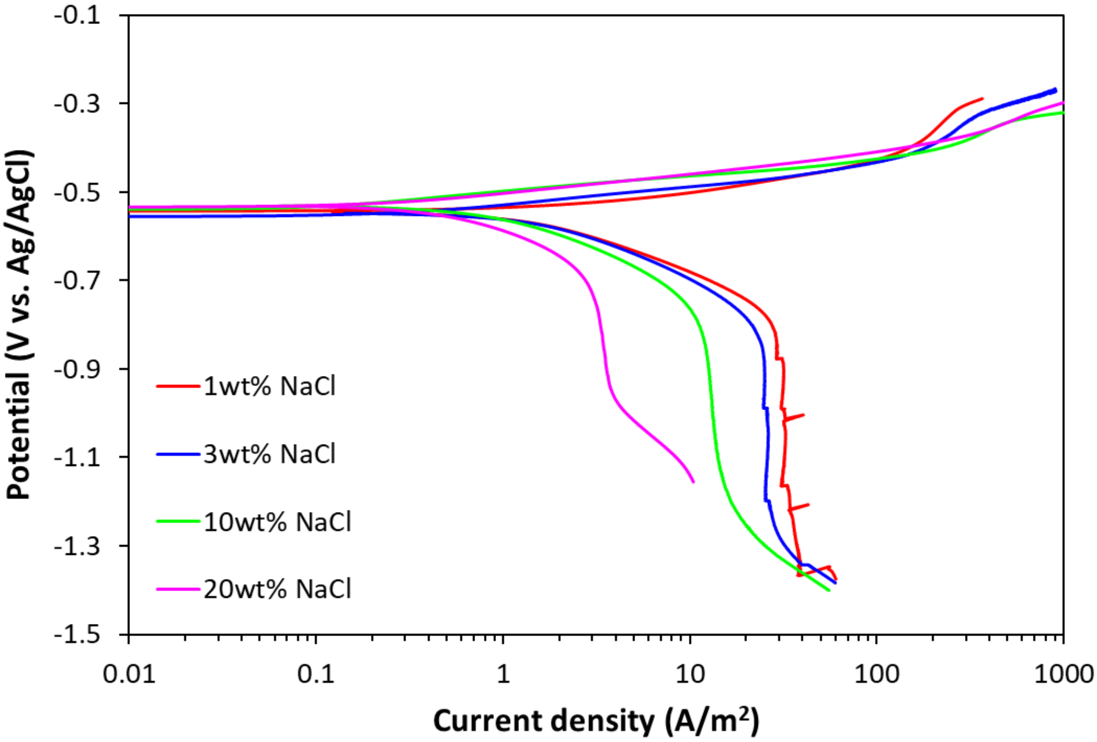

In Figure 10-4, the changes in the cathodic branch are obvious; however, the anodic sweeps are overlapped, and their variations with NaCl concentration is not distinguishable easily. Thus, similar to the strong acid experiments, the kinetic features of the PD sweeps were obtained by fitting the sweeps for the best fit with a simple electrochemical model [96][73]. The fitted sweeps for two NaCl concentrations are shown in Figure 10-5 as a demonstration of the accuracy of the fitting exercise.

---

[73] Activation energies of 59860 J/mol for H^+ ion, 24809 J/mol H_2O reduction and 25398 J/mol for Fe oxidation reactions. A reversible potential of -0.685 V vs. Ag/AgCl was used for all three reactions. The reference temperature was 20°C.

Figure 10-5

Comparison of the experimental sweeps at 1 wt.% (A) and 20 wt.% (B) NaCl concentrations measured in the RDE CO_2 experiments with those obtained by a simple electrochemical model [96].

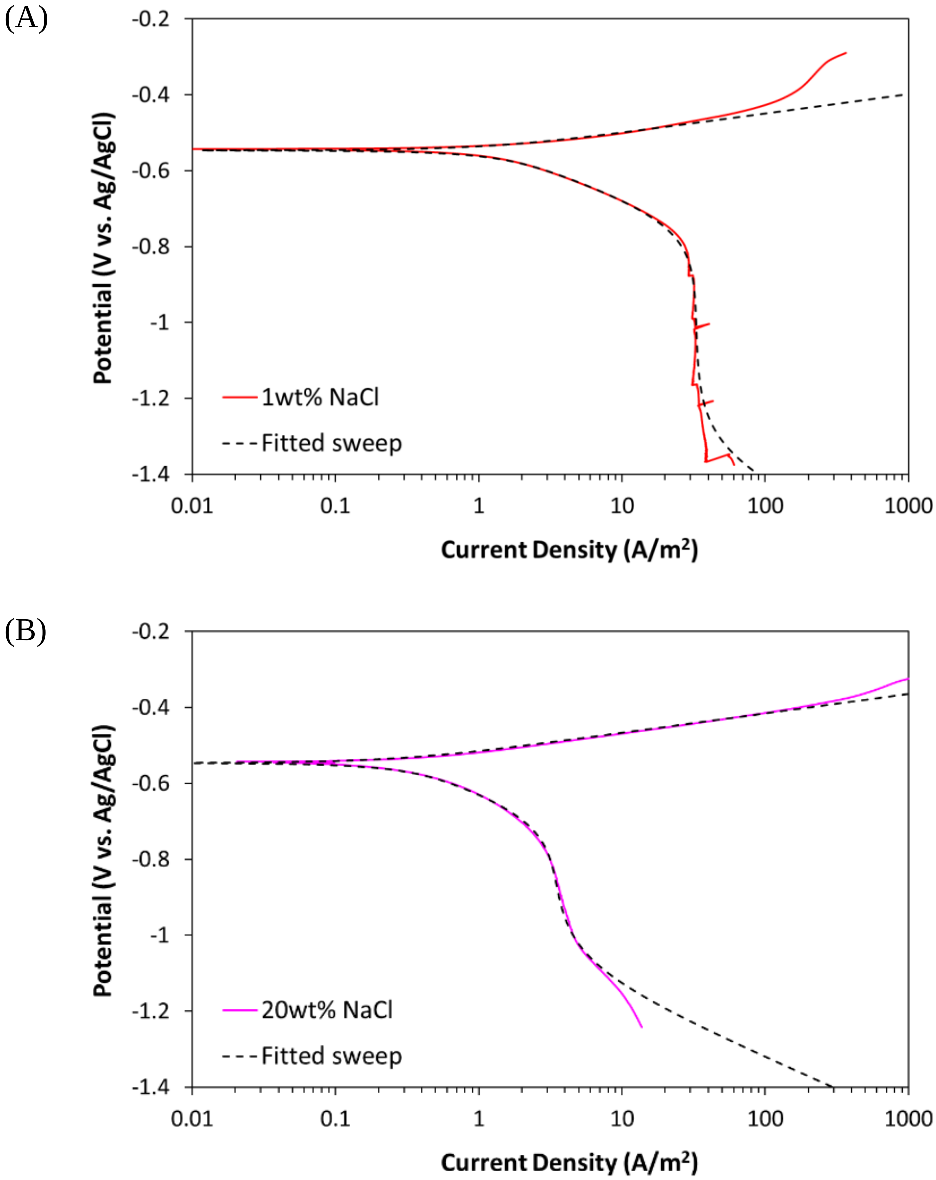

The results of the fitting exercise are presented in Table 10-2. The electron transfer coefficient for H^+ reduction reaction (α_{H^+}) deviated slightly from the theoretical value of 0.5, commonly considered for the hydrogen evolution on an iron surface [185]. Similar deviations have been reported in the literature [207,292]. The slight changes in the electron transfer coefficient (or Tafel slope) with respect to NaCl concentration imply that NaCl concentration did not influence the mechanism of cathodic H^+ reduction reaction.

Table 10-2

The electron transfer coefficients for H^+ reduction reaction (α_{H^+}) and Fe oxidation (α_{Fe}) for the RDE (2000 rpm) strong acid experiments at 10°C, ~1 bar CO_2 and pH 3. Each data is an average of two measurements.

NaCl (wt.%)	1	3	10	20
α_{H^+}	0.44±0.00	0.43±0.01	0.42±0.00	0.44±0.01
β_c	-128±0	-131±2	-134±0	-128±3
α_{Fe}	1.2±0.1	1.1±0.0	1.1±0.0	1.1±0.0
β_a	47±5	51±0	51±0	51±0

The electron transfer coefficient for active anodic dissolution of iron (α_{Fe}) was almost 1.10 for all NaCl concentrations. Bockris *et al.* [185] proposed 1.5 for iron dissolution in acidic media without the presence of halides. Chin and Nobe [194] reported 1.18 for dissolution of iron in acidic chloride media, which is very close to the results of this study. Since α_{Fe} (*i.e.,* the anodic Tafel slope) did not change with increasing NaCl concentration, it can be concluded that the mechanism of anodic dissolution of iron in the active region remained unchanged. The mechanisms of iron dissolution in the presence of chloride have been comprehensively explained in Section 5.1.1.

Figure 10-6 A shows the variation in the H^+ ion reduction exchange current density (i_{o,H^+}) as a function of NaCl concentration. As stated in Chapter 5, the exchange current density indicates the charge transfer rate for an electrochemical reaction. i_{o,H^+} decreased when NaCl concentration was increased from 1 wt.% to 20 wt.%. This means that the H^+ ion reduction rate in the charge transfer region decreased with increasing NaCl concentration. The reason for this decrease can be linked to the adsorption of Cl^- ions on the surface and blocking the surface areas needed for H^+ ions to be adsorbed and reduced on [171]. Therefore, the decrease in i_{o,H^+} can be listed as one of the reasons for the decreasing trend of the corrosion rate shown in Figure 10-3. The trend observed for i_{o,H^+} in Figure 10-6 A can be modeled by using a correlation similar to Equation (5-23):

$$i_{o,H^+} = i_{o,H^+}^{ref} \left(\frac{a_{H^+,b}}{a_{H^+,b}^{ref}}\right)^{n_{H^+}^{H^+}} \left(\frac{a_{Cl^-,b}}{a_{Cl^-,b}^{ref}}\right)^{n_{Cl^-}^{H^+}} e^{-\frac{E_{a,H^+}}{R}\left(\frac{1}{T}-\frac{1}{T_{ref}}\right)} \tag{10-1}$$

where, i_{o,H^+}^{ref} is the reference current density in A/m^2 at T_{ref} (293.15 K) and -685 mV *vs.* Ag/AgCl, $a_{H^+,b}$ is the bulk activity of H^+ ion in molarity concentration, $a_{H^+,b}^{ref}$ is the reference bulk activity of H^+ ion (= 10^{-4} M), $n_{H^+}^{H^+}$ is the reaction order of the H^+ ion reduction reaction with respect to H^+ ion activity, $a_{Cl^-,b}$ is the bulk activity of Cl^- ion in molarity concentration, $a_{Cl^-,b}^{ref}$ is the reference bulk activity of Cl^- ion (= 1 M), $n_{Cl^-}^{H^+}$ is the reaction order of the H^+ ion reduction reaction with respect to Cl^- ion activity, E_{a,H^+} is the activation energy for the H^+ ion reduction reaction (= 59860 J/mol), T is solution temperature in K, and R is the gas constant in J/mol/K. Equation (10-1) with the bulk activities calculated with the MSE model was fitted to the experimental i_{o,H^+} values in Figure 10-6 A to obtain the reaction orders and i_{o,H^+}^{ref}.

Since the solution pH was constant in the experiments, the activity of H^+ ion was constant as well[74]. This means that $n_{H^+}^{H^+}$ cannot be determined from the fitting exercise. To be able to obtain $n_{H^+}^{H^+}$ experiments at different pH values are required. Therefore, an empirical value of 0.5 previously reported in the literature was chosen for $n_{H^+}^{H^+}$ [200,215]. The fitting exercise gave $n_{Cl^-}^{H^+}$ = -0.23 and i_{o,H^+}^{ref} = 11.9 A/m^2. The negative sign found for $n_{Cl^-}^{H^+}$ proves that Cl^- ion had a retardation effect on the rate of the H^+ ion reduction reaction in the charge transfer region. i_{o,H^+}^{ref} reported here is slightly higher than that reported for strong acid corrosion under similar conditions in Section 9.1.2. This can be taken as evidence of the influence of CO_2 on the charge transfer rate in H^+ ion reduction reaction. However, since both numbers are in the same order of magnitude, the slight difference could be just related to the experimental and/or fitting exercise error. This subject will be further investigated in Section 10.1.4.

---

[74] The changes in molarity-based activity due to changes in density with NaCl concentration is ignored.

Figure 10-6

Variations in (A) the cathodic limiting current density (i_{Lim}) *and the* H^+ *reduction exchange current density* (i_{o,H^+}) *and (B) the Fe oxidation exchange current density* ($i_{o,Fe}$) *with NaCl concentration. The current densities were extracted from the PD sweeps of X65 RDE (2000 rpm) exposed to* CO_2*-saturated aqueous solutions at 10°C, 1 bar total pressure, and pH 3. The error bars represent the minimum and maximum values obtained in two repeated experiments. The reference temperature was 20°C.*

(A)

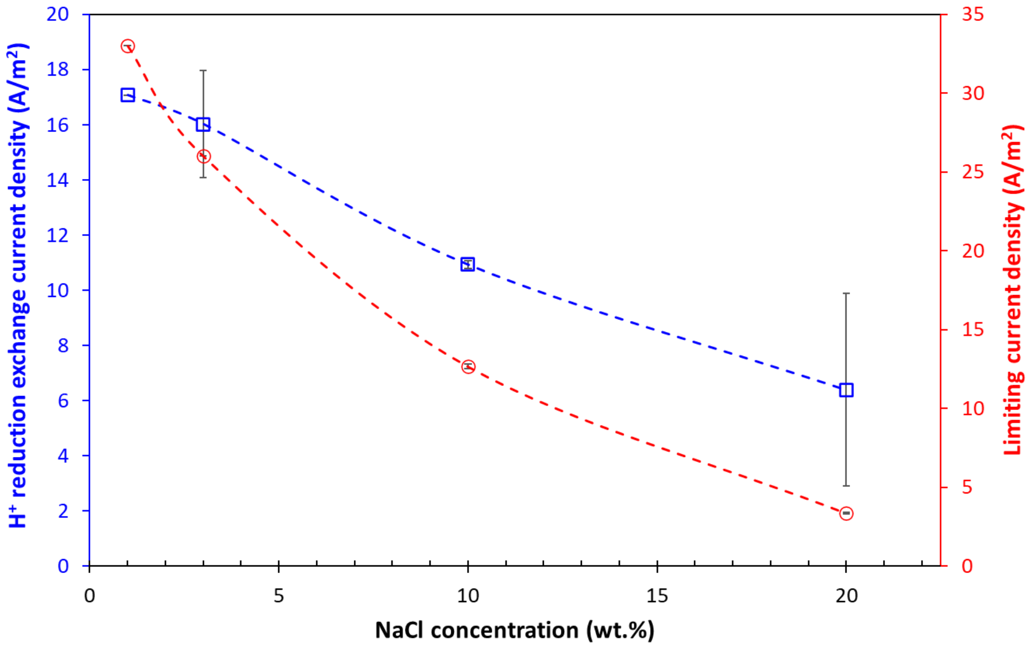

(B)

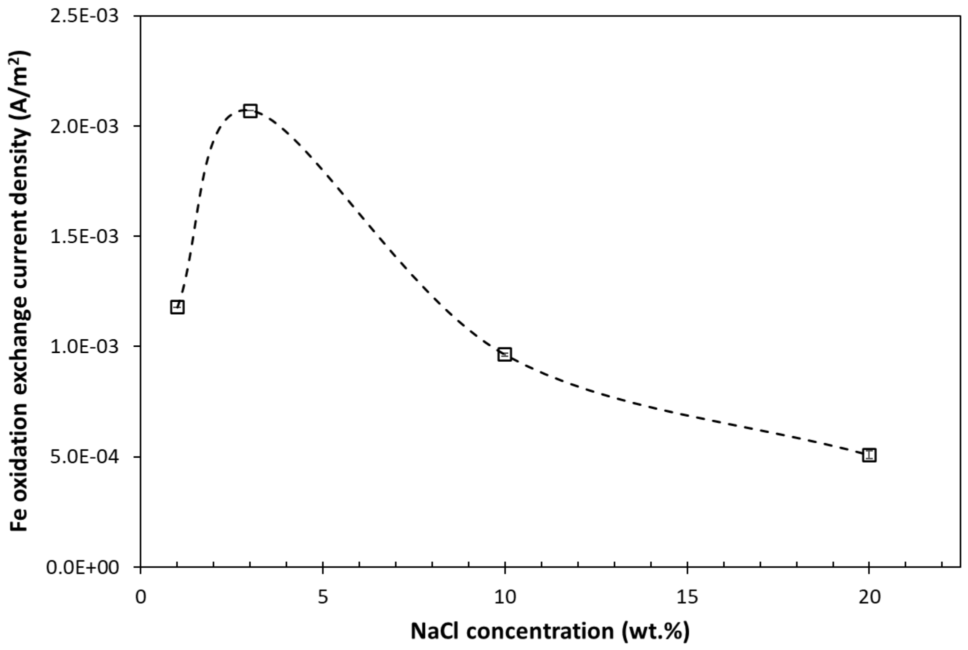

$i_{o,Fe}$ variation with NaCl concentration is shown in B. $i_{o,Fe}$ denotes the rate of anodic dissolution of Fe in the active region. $i_{o,Fe}$ increased at lower NaCl concentrations and then overturned trend and decreased at higher NaCl concentrations. This trend is somehow similar to that reported for the CO_2 corrosion rate in Figure 10-3. Therefore, variation in $i_{o,Fe}$ with NaCl concentration is possibly another reason for the small increase followed by the decrease in the CO_2 corrosion rate when NaCl concentration was increased from 1 wt.% to 20 wt.%.

The observed trend for $i_{o,Fe}$ can be justified by considering the changes in the activities of OH^- ion, Cl^- ion, and H_2O. Similar to Equation (5-22), $i_{o,Fe}$ can be expressed in terms of activities of OH^- ion, Cl^- ion, and H_2O as follows:

$$i_{o,Fe} = i_{o,Fe}^{ref}\left(\frac{a_{OH^-,b}}{a_{OH^-,b}^{ref}}\right)^{n_{OH}^{Fe}}\left(\frac{a_{Cl^-,b}}{a_{Cl^-,b}^{ref}}\right)^{n_{Cl^-}^{Fe}}\left(\frac{a_{H_2O,b}}{a_{H_2O,b}^{ref}}\right)^{n_{H_2O}^{Fe}} e^{-\frac{E_{a,Fe}}{R}\left(\frac{1}{T}-\frac{1}{T_{ref}}\right)} \tag{10-2}$$

where, $i_{o,Fe}^{ref}$ is the reference current density in A/m^2 at T_{ref} (293.15 K) and -685 mV *vs.* Ag/AgCl, $a_{OH^-,b}$ is the bulk activity of OH^- ion in molarity concentration, $a_{OH^-,b}^{ref}$ is the reference bulk activity of OH^- ion (= 10^{-10} M), n_{OH}^{Fe} is the reaction order of the Fe oxidation reaction with respect to OH^- ion activity, $a_{Cl^-,b}$ is the bulk activity of Cl^- ion in molarity concentration, $a_{Cl^-,b}^{ref}$ is the reference bulk activity of Cl^- ion (= 1 M), $n_{Cl^-}^{Fe}$ is the reaction order of the Fe oxidation reaction with respect to Cl^- ion activity, $a_{H_2O,b}$ is the bulk activity of liquid water in molarity unit, $a_{H_2O,b}^{ref}$ is the reference bulk activity of liquid water (= 55.4 M), $n_{H_2O}^{Fe}$ is the reaction order of the Fe oxidation reaction with respect to H_2O, and $E_{a,Fe}$ is the activation energy for the Fe oxidation reaction in the active region (= 25398 J/mol), T is solution temperature in K, and R is the gas constant in J/mol/K.

Lorenz [174] and McCafferty and Hackerman [178], reported different $n_{Cl^-}^{Fe}$ values at different range of Cl^- activities (concentrations), as reviewed in Table 5-2. This suggests that the iron dissolution reaction might proceed through different pathways depending on the Cl^- activity in the solution. From the $i_{o,Fe}$ trend presented in Figure 10-6 B, it can be assumed that at low NaCl concentrations below 3 wt.%[75], Cl^- ions accelerates the anodic dissolution reaction by playing a catalytic role in iron dissolution, similar to that of OH^- ions [172,194,195]. However, at high NaCl concentrations above 3 wt.%, Cl^- ions inhibits the Fe dissolution reaction by being adsorbed on the surface and blocking the active sites (surface imperfections) required for the Fe dissolution reaction to occur [173,174,178,192]. Therefore, the $i_{o,Fe}$ curve is divided into two sections: below and above 3 wt.%. Equation (10-2) with the bulk activity values calculated with the MSE was fitted to the experimental $i_{o,Fe}$ values to determine the reaction orders and $i_{o,Fe}^{ref}$ for the two regions. To obtain n_{OH}^{Fe} value experiments at different solution pH are needed. This means that n_{OH}^{Fe} cannot be found from the data presented here. Therefore, a value of 1 was chosen for n_{OH}^{Fe} for the whole range of NaCl concentration according to the Bockris *et al.* [185,186] consecutive mechanism and reports by other scientists [174,195] (see Table 5-2). For NaCl $\leq$ 3 wt.%, $n_{Cl^-}^{Fe}$= 0.57, $n_{H_2O}^{Fe}$ = 0, and $i_{o,Fe}^{ref}$ = 0.82 and for NaCl $>$ 3, $n_{Cl^-}^{Fe}$= -0.40, $n_{H_2O}^{Fe}$ = 2, and $i_{o,Fe}^{ref}$ = 0.3. A reaction order of zero for H_2O at NaCl $\leq$ 3 means that the Fe dissolution reaction process is independent of H_2O activity in this NaCl

---

[75] It can be any NaCl concentration between 1 wt.% and 3 wt.%, as the experimental NaCl resolution was not small enough to determine the exact maximum.

concentration range. For $n_{H_2O}^{Fe}$ at high NaCl concentrations, the value found in this study is similar to the values (a range of 1.6-1.9) reported by Smart *et al.* [190,198]. A similar comparison to i_{o,H^+}^{ref} can be made here between the $i_{o,Fe}^{ref}$ values found in this set of experiments and those obtained for strong acid corrosion experiments done at similar conditions in Section 9.1.2. The $i_{o,Fe}^{ref}$ values for both NaCl regions were slightly larger than those found in strong acid corrosion experiments. This indicates that the presence of CO_2 accelerated the rate of anodic Fe dissolution. However, since the difference between the $i_{o,Fe}^{ref}$ values in the two cases are within the experimental and fitting procedure errors, no conclusive conclusion can be made here. This topic is investigated in more detail in Section 10.1.4.

The next kinetic parameter in the PD sweeps that changed with NaCl concentration was i_{Lim}. For the case of CO_2 corrosion, i_{Lim} is determined by a combination of the slow hydration rate of $CO_{2(aq)}$ and the slow rate of diffusion of H^+ ions from the bulk solution to the metal surface. Figure 10-6 A shows that i_{Lim} decreased monotonously when NaCl concentration was increased from 1 wt.% to 20 wt.%.

i_{Lim} in CO_2 corrosion depends mainly on bulk activities of $CO_{2(aq)}$ (a_{CO_2}) and H^+ ion (a_{H^+}). This is explained in detail in Chapter 12. a_{CO_2} was constant[76] because experiments were conducted in an open system (Figure 10-7 A). a_{H^+} was also constant for all NaCl concentrations because pH of solution was adjusted at a constant

---

[76] In this argument, the effect of NaCl concentration on water vapor pressure, and therefore, on a_{CO_2} is neglected.

value of 3 in all the experiments (Figure 10-7 B). Therefore, a_{H^+} and a_{CO_2} cannot be the reason for the changes in i_{Lim} with NaCl concentration.

Figure 10-7

Bulk concentration, molality-based activity coefficient, and activity of (A) dissolved $CO_{2(aq)}$ and (B) H_3O^+ ion calculated by the Li and Duan model for CO_2 saturated aqueous NaCl solutions at 20°C, and 1 bar total pressure (~ 0.98 bar pCO_2).

(A)

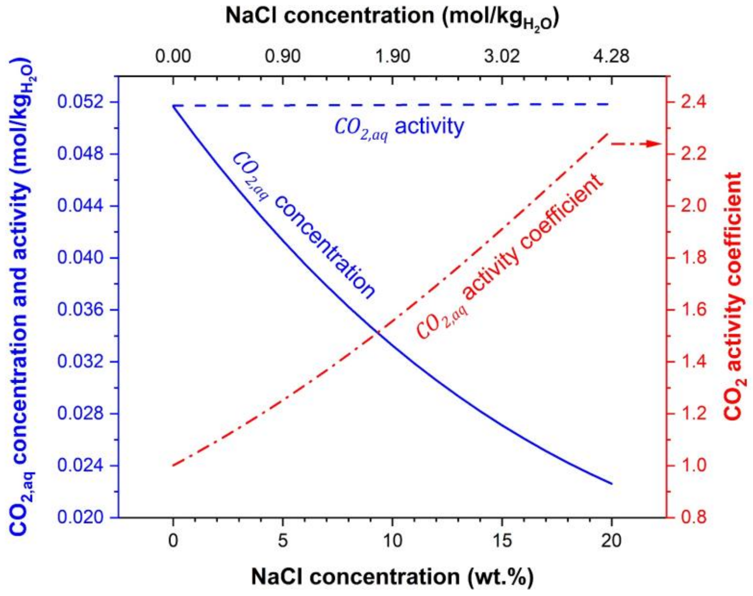

(B)

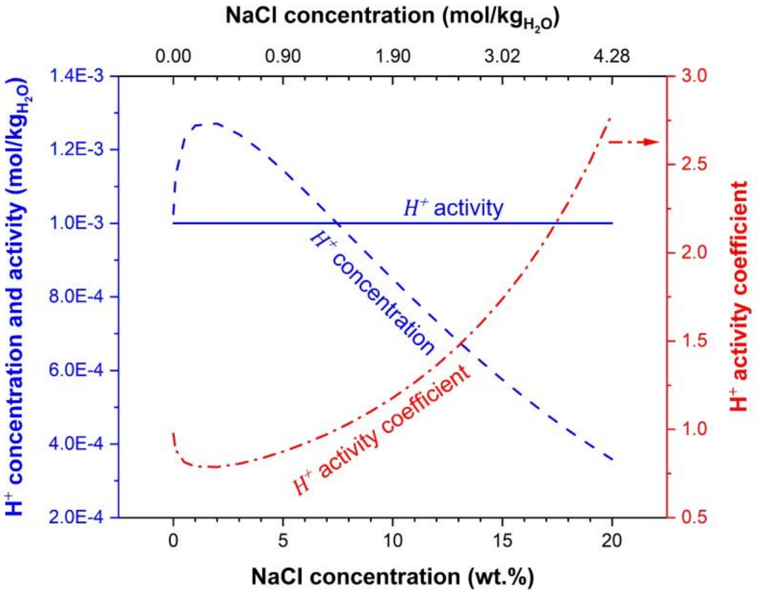

To justify the changes in i_{Lim} with NaCl concentration, a simplification can be made here. pH was constant at 3 in all the experiments; therefore, a_{H^+} was equal to 10^{-3} mol/kgH$_2$O (Figure 10-7 B). At 10^{o}C, the bulk activity of $H_2CO_{3(aq)}$ ($a_{H_2CO_3}$) was about 6 × 10^{-5} mol/kgH$_2$O [298]. since $a_{H_2CO_3}$ is much smaller than a_{H^+}, the CO$_2$ buffering effect is insignificant. Consequently, i_{Lim} values in this set of experiments must be very close to those obtained in the RDE strong acid experiments in Section 9.1.2. Comparing i_{Lim} values in Figure 10-6 A with those in Figure 9-8 A confirms the above argument. Therefore, the same reasons mentioned in Section 9.1 for the decrease in i_{Lim} in the strong acid corrosion experiments with NaCl concentration are valid here as well. The decreasing trend seen for i_{Lim} with increasing NaCl concentration was mainly due to the changes in H$^+$ ion bulk concentration and the H$^+$ diffusion coefficient. It was explained in Section 9.1.2, that at low NaCl concentrations below ~ 2 wt.%, since c_{H^+} is increasing with NaCl concentration, it is expected to have a rising trend for i_{Lim} with respect to NaCl concentration. However, this was not seen in the experimental i_{Lim} values presented in Figure 10-6 A most likely due to an insufficient resolution chosen for NaCl concentration in the experiments.

If the CO$_2$ buffering effect is not neglected from the beginning, i_{Lim} in CO$_2$ corrosion in addition to dependencies on a_{CO_2} and a_{H^+} mentioned above, depends on an effective diffusion coefficient (D_{eff}), which is equal to:

$$D_{eff} = \frac{D_{H^+}}{\gamma_{H^+}} + \frac{a_{H_2CO_3}}{a_{H^+}} \frac{D_{H_2CO_3}}{\gamma_{H_2CO_3}} \tag{10-3}$$

where, D_{H^+} and $D_{H_2CO_3}$ are the diffusion coefficients of H$^+$ ion and H$_2$CO$_3$ in the solution, γ_{H^+} and $\gamma_{H_2CO_3}$ are the activity coefficients of H$^+$ ion. a_{H^+} was equal to 10^{-3}

mol/kgH$_2$O. At 10^{o}C, $a_{H_2CO_3}$ was about 6 × 10^{-5} mol/kgH$_2$O [298]. This mean that the ratio of $a_{H_2CO_3}$ to a_{H^+} is negligible, and D_{eff} is practically equal to the first term on the right-hand side of Equation (10-5. Therefore, i_{Lim} under the experimental conditions of this part of study only depends on D_{H^+} and γ_{H^+}. D_{H^+} continually decreases with increasing NaCl concentration (Section 3.3.2). As shown in Figure 10-7 B, for NaCl concentrations below ~ 2 wt.%, γ_{H^+} decreases with increasing NaCl concentration. For higher NaCl concentrations, γ_{H^+} has a rising trend with respect to NaCl concentration. Considering that the slope of changes for γ_{H^+} with NaCl concentration is greater than that for D_{H^+}, it is expected that with increasing NaCl concentration, i_{Lim} increases at NaCl concentrations lower than ~ 2 wt.% and decreases at NaCl concentrations above ~ 2 wt.%. This matches very well with the argument mentioned above using the c_{H^+} trend with respect to NaCl concentration. Therefore, the variation in i_{Lim} could be justified by both the change in c_{H^+} and the change in γ_{H^+} with NaCl concentration. Finally, the i_{Lim} variation with NaCl concentration can be a reason for the observed trend in the CO$_2$ corrosion rate in Figure 10-3.

Three possible reasons have been discussed for the effect of NaCl concentration on the CO$_2$ corrosion rate: changes in i_{o,H^+}, $i_{o,Fe}$, and i_{Lim} with NaCl concentration. To characterize which of these three parameters controlled the rate of CO$_2$ corrosion in this set of experiment, the Evans diagram is utilized.

Figure 10-8 shows the Evans diagrams for 1 wt.% and 20 wt.% NaCl concentrations at the experimental conditions used in this set of experiments. The corrosion process was under pure charge transfer control for the entire range of experimental concentrations. This means that decrease in the CO$_2$ corrosion rate at

10^{o}C, pH3 and ~1 bar CO_2, was due to decrease in the rates of Fe dissolution reaction ($i_{o,Fe}$) and H^+ ion reduction reaction (i_{o,H^+}) in the charge transfer region. The decrease in i_{Lim} with NaCl concentration did not have any influence on the CO_2 corrosion rate variation.

The LPR results in Figure 10-3 showed a maximum in the CO_2 corrosion rate at 3 wt.%. However, the PD sweeps did not explicitly show that maximum. Therefore, this maximum cannot be justified by using the Evans diagram. However, as will be discussed in Sections 10.2.2 and 10.3.2, it is speculated that the possible maximum in the CO_2 corrosion rate at low NaCl concentration is due to increase in rate of anodic dissolution of Fe.

Another interesting conclusion is that i_{Lim} was influenced more by NaCl concentration compared to the rates of charge transfer processes, because i_{Lim} decreased more than the corrosion current density (i_{Corr}) when NaCl concentration was increased from 1 wt.% to 20 wt.%. This has been seen in strong acid corrosion experiments as well.

Figure 10-8

The Evans diagram for the effect of NaCl concentration on uniform strong acid corrosion of X65 RDE at 10°C, ~1 bar CO_2, pH 3, and 2000 rpm rotational speed. E_{corr} *is the corrosion potential (OPC),* i_{corr} *is the corrosion current density, and* i_{Lim} *is the* H^+ *ion reduction reaction limiting current density (Blue: 1 wt.% NaCl and red: 20 wt.% NaCl).*

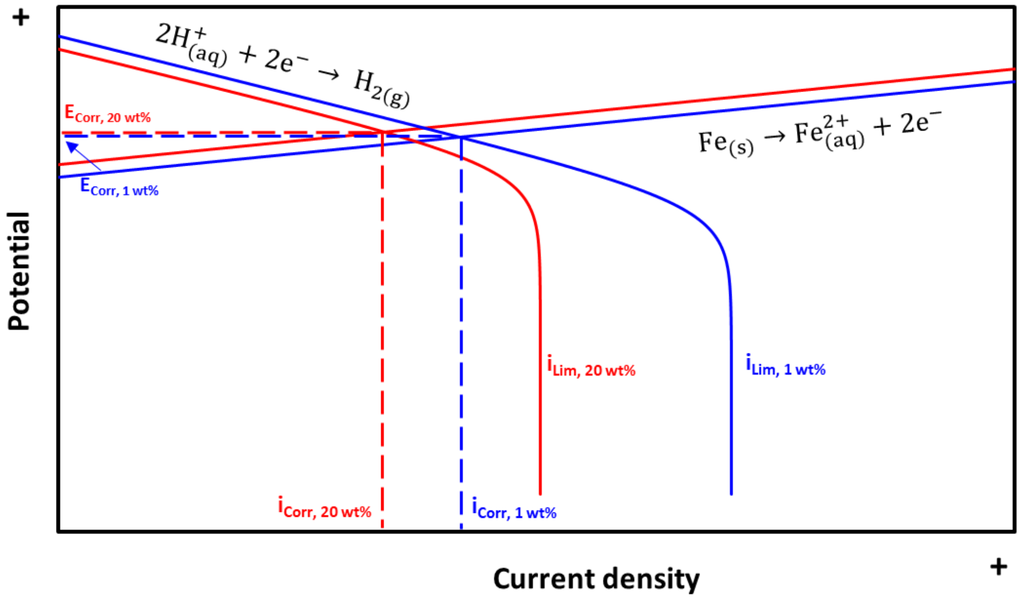

10.1.3 Surface Analysis of the Corroded Surface in RDE CO_2 Corrosion Experiments at pH 3

Figure 10-9 shows SEM/EDS results for a freshly polished steel surface and the corroded steel surface in 1 and 20 wt.% NaCl solutions. The morphology of the corroded surface was similar for both NaCl concentrations. The EDS elemental analysis of the steel surface detected a similar composition for all three cases, which means that no corrosion layer formed on the surface when carbon steel specimens exposed to the experimental solution. Oxygen in the EDS spectrum for 1 wt.% NaCl was most likely due to the exposure of the specimen to air prior to conducting the EDS analysis.

Figure 10-9

SEM/EDS results for (A) freshly polished steel surface, (B) corroded surface in 1 wt.% NaCl solution, and (C) corroded surface in 20 wt.% NaCl solution (C) in the RDE CO_2 *experiments at* 10^oC*, pH 3, and ~1 bar* CO_2*.*

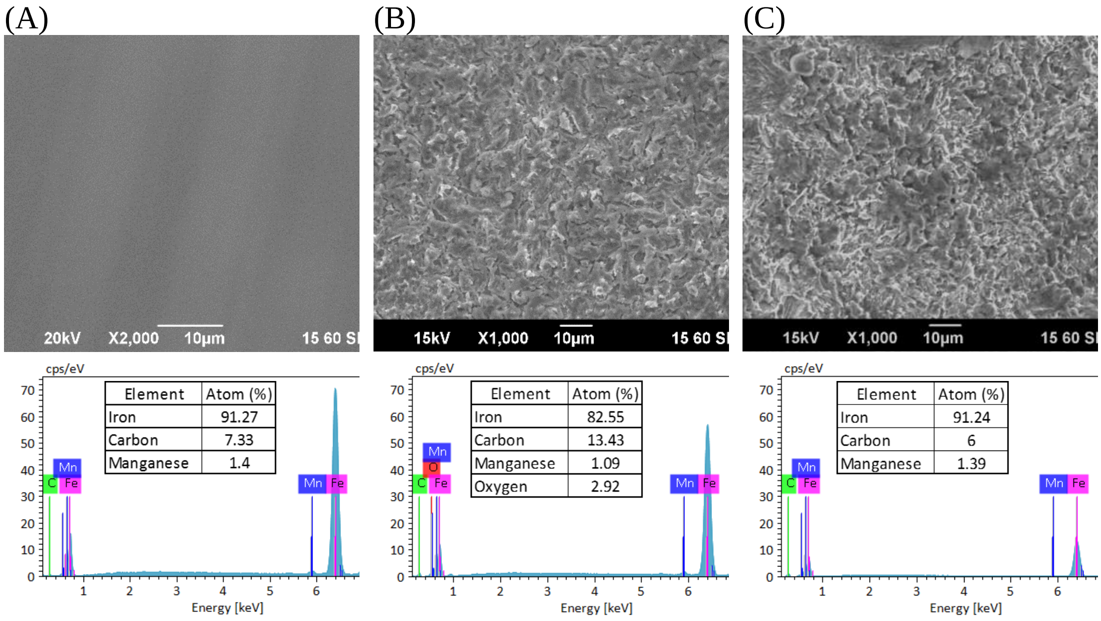

(A)

Element	Atom (%)
Iron	91.27
Carbon	7.33
Manganese	1.4

(B)

Element	Atom (%)
Iron	82.55
Carbon	13.43
Manganese	1.09
Oxygen	2.92

(C)

Element	Atom (%)
Iron	91.24
Carbon	6
Manganese	1.39

Figure 10-10 shows the surface profilometry of the corroded steel specimens in 1 and 20 wt.% NaCl solutions obtained with an Alicona optical profilometer. The 1D profiles show changes in the surface roughness along the vertical red lines drawn on the 2D profiles. No indication of localized corrosion was detected over the entire surface of the corroded steel specimens from tests in both solutions. Therefore, it can be concluded that the specimens were corroded uniformly in both NaCl solutions under the experimental conditions. Surface analysis indicated that carbon steel surface was corroded uniformly, and no corrosion layer formed on the steel surface under the experimental conditions.

Figure 10-10

2D (above) and 1D (below) surface profilometry of the corroded steel surface in (A) 1 wt.% and (B) 20 wt.% NaCl solutions in the RDE CO_2 corrosion experiments at 10oC, pH 3, and ~ 1 bar CO_2.

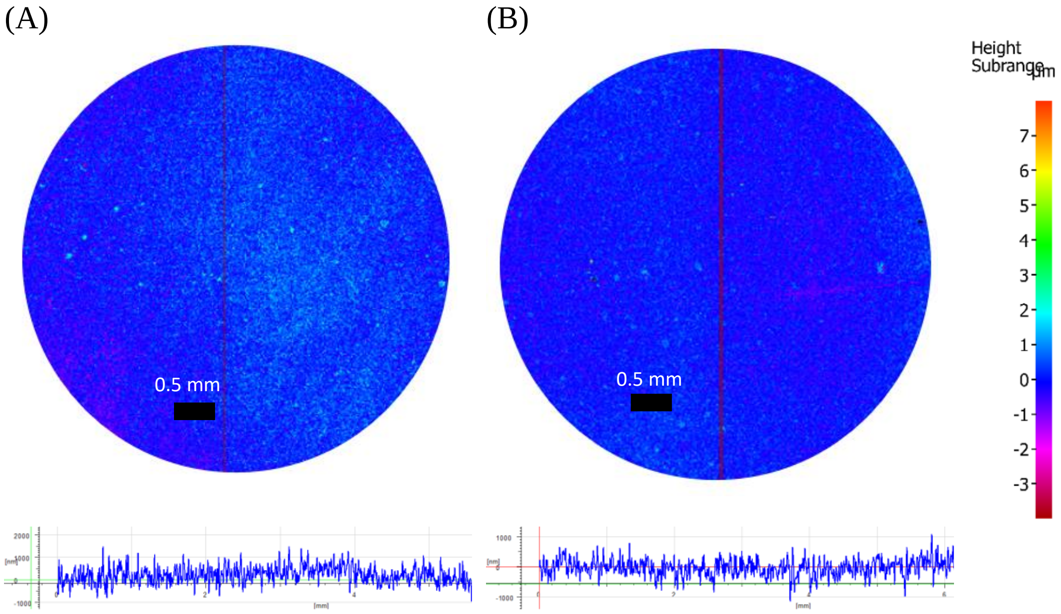

10.1.4 *Comparison between RDE Strong Acid Corrosion and RDE CO_2 Corrosion at 10°C and pH 3*

In this part, the results presented in Section 9.1 for the RDE strong acid corrosion experiments are compared with those reported in Section 10.1 for the RDE CO_2 corrosion experiments. All the experimental conditions were the same except the gases used for saturating the solutions with. Since N_2 is considered as a neutral gas, it can be assumed that two CO_2 partial pressures (pCO_2) of 0 bar and ~1 bar are being compared. Therefore, this part essentially studies the effect of CO_2 gas on corrosion of carbon steel in aqueous NaCl solutions.

Figure 10-11 compares the corrosion rates measured in the RDE strong acid experiments with those obtained in the RDE CO_2 corrosion experiments. The corrosion rates reported by both techniques were higher for CO_2 corrosion. This means that the presence of CO_2 accelerates the corrosion process[77]. It is mentioned throughout this document that $CO_{2(g)}$ dissolves in the solution and produces $H_2CO_{3(aq)}$ in a slow heterogenous chemical reaction. $H_2CO_{3(aq)}$ subsequently dissociates and provides more H^+ ions for the cathodic H^+ ion reduction and in this way, it speeds up the corrosion process. This effect is called CO_2 buffering effect. $H_2CO_{3(aq)}$ acts as a source of H^+ ion for the main cathodic reaction in the corrosion process, which is H^+ ion reduction reaction.

However, at 10°C and pH 3 the CO_2 buffering effect is negligible because $a_{H_2CO_{3(aq)}}= 6 \times 10^{-5}$ mol/kgH_2O [298] is considerably smaller than $a_{H^+}= 10^{-3}$ mol/kgH_2O (~ 6%). This means that at pH 3, the activity of H^+ ions is sufficiently large than the extra H^+ ions provided by the $H_2CO_{3(aq)}$ dissociation reaction does not change the rate of the corrosion process. Therefore, other parameters must have changed in the presence of CO_2 that caused higher corrosion rates in the CO_2 corrosion experiments. This will be further investigated by comparing the PD sweeps and the extracted kinetic parameters from these sweeps.

All the PD sweep repeats (at last two) measured in the strong acid corrosion experiments at different NaCl concentrations are overlapped in Figure 10-12 with

---

[77] In this section, when it is said that the presence of CO_2 influences a process, CO_2 might be any species such as $H_2CO_{3(aq)}$ or CO_2-containing complexes.

their corresponding PD sweeps obtained in the CO_2 acid experiments for a comparison. For each graph and each gas at least two sets of PD sweeps are presented for a precise analysis.

Figure 10-11

Comparison of corrosion rates measured by LPR and PD sweeps for X65 carbon steel RDE (2000 rpm) specimen exposed to aqueous NaCl solutions at 10°C and pH 3 saturated with N_2 *gas* ($pCO_2 = 0$ *bar) with those under the same conditions except saturated with* CO_2 *gas (pCO2 ≅ 1 bar).*

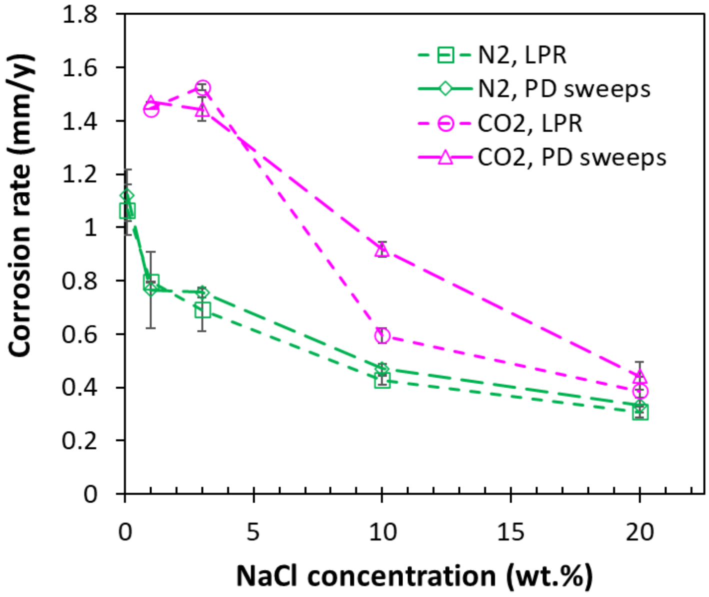

Figure 10-12

Comparison of PD sweeps for X65 carbon steel RDE (2000 rpm) specimen exposed to aqueous NaCl solutions at 10ºC and pH 3 saturated with N_2 gas (pCO_2 = 0 bar) with those under the same conditions except saturated with CO_2 gas (pCO2 ≅ 1 bar).

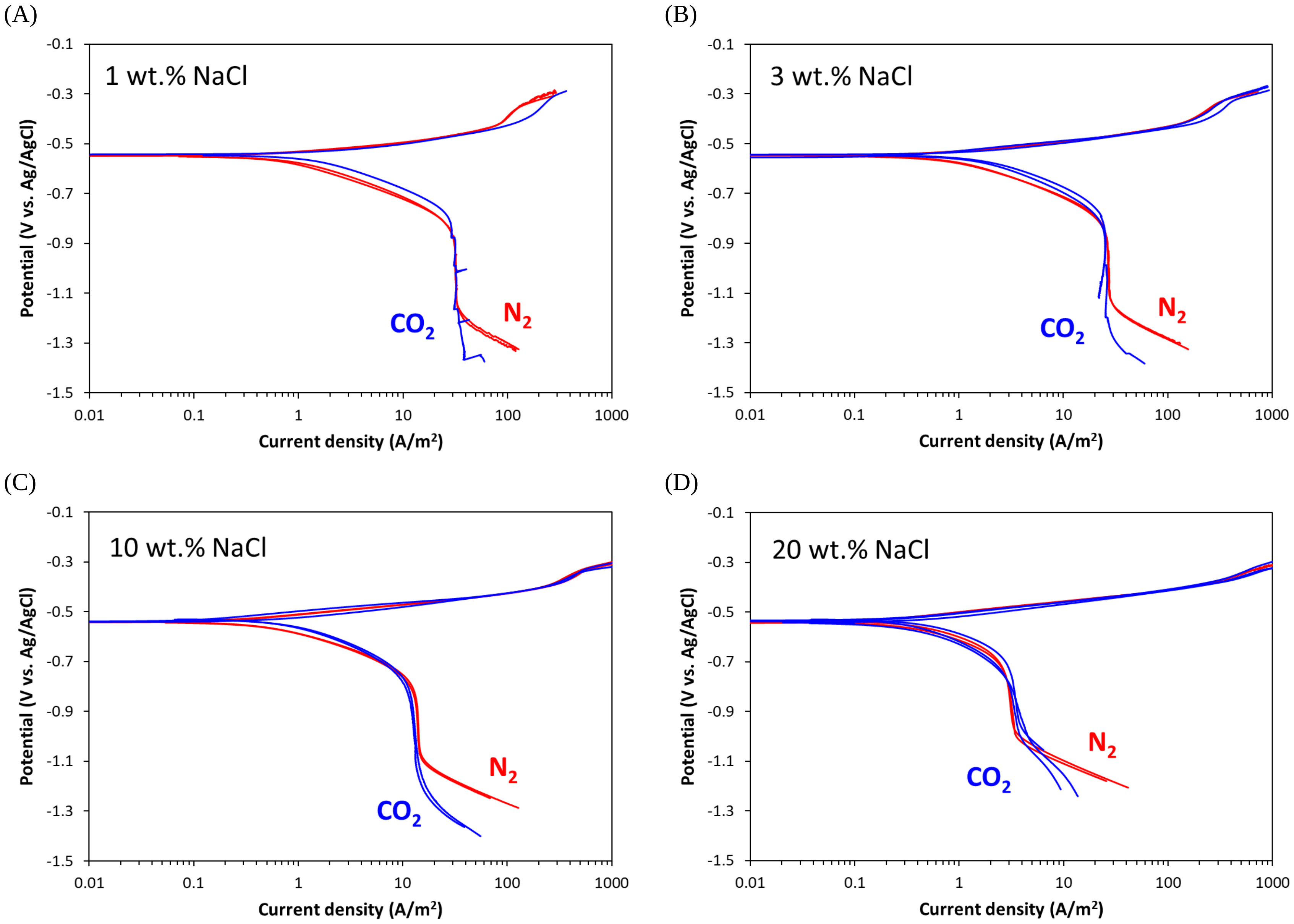

The most obvious difference in the PD sweeps between the strong acid corrosion and CO_2 corrosion is water reduction reaction. The water reduction reaction was slower in the CO_2-satuared solutions for all NaCl concentration. Additionally, the Tafel slope for the water reduction reaction in CO_2 corrosion was larger than that for strong acid corrosion. This suggests that the mechanism of the water reduction reaction differed in the presence of CO_2. However, the water reduction reaction had almost no effect in the overall corrosion rate for both strong acid and CO_2 corrosion. Therefore, it cannot be the reason for different corrosion rates reported for the two types of corrosion.

i_{Lim} values were almost identical in both strong acid and CO_2 corrosion experiments for all NaCl concentrations. For a better comparison the measured i_{Lim} values in both cases are plotted in Figure 10-13 A. This comparison confirms the argument given above about the negligible CO_2 buffering effect at 10°C and pH 3.

Figure 10-13

Comparison of (A) H^+ ion limiting current density (i_{Lim}), (B) H^+ ion reduction exchange current density (i_{o,H^+}), and (C) Fe oxidation exchange current density ($i_{o,Fe}$) for strong acid corrosion with those for CO_2 corrosion. The data are extracted from the PD sweeps for X65 carbon steel RDE (2000 rpm) specimen exposed to aqueous NaCl solutions at 10°C and pH 3 saturated with N_2 gas (pCO_2 = 0 bar) and CO_2 gas (pCO2 ≅ 1 bar).

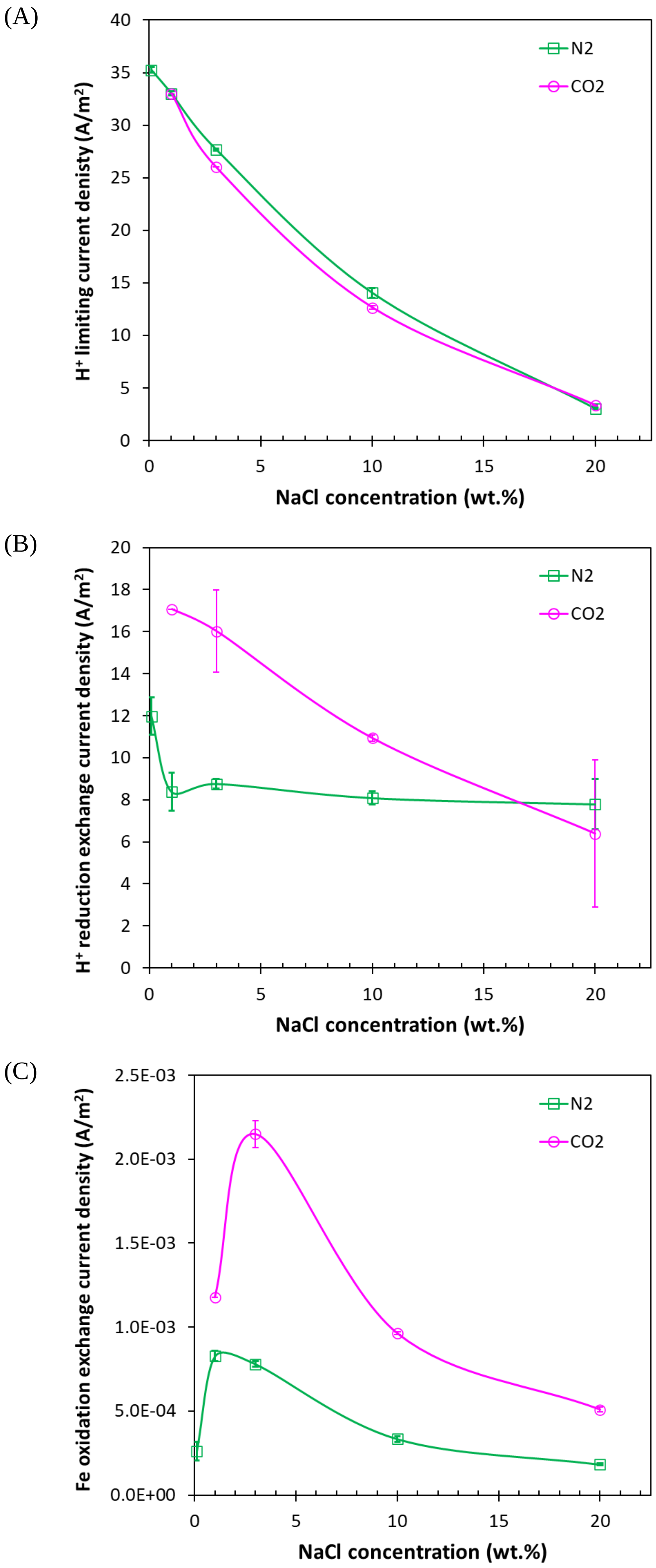

The charge transfer regions of the cathodic PD sweeps for CO_2 corrosion in Figure 10-12 seem to be slightly different than those for strong acid corrosion in all NaCl concentration. The difference could originate from the mechanism of H^+ ion reduction reaction (α_{H^+}) or the rate of H^+ ion reduction reaction (i_{o,H^+}) or both. Comparing α_{H^+} in strong acid corrosion (Table 9-3) with those for CO_2 corrosion (Table 10-2) shows that salt concentration changed the former from 0.4 to 0.52, while the latter was almost constant at 0.43 for all NaCl concentrations. At 1 wt.% and 3 wt.% NaCl, α_{H^+} was almost the same for strong acid and CO_2 corrosion; however, at 10 wt.% and 20 wt.% NaCl, α_{H^+} for strong acid corrosion was greater than that for CO_2 corrosion. Based on these difference in the values and the trends with NaCl concentration, it is tempting to conclude that the presence of CO_2 influenced the mechanism of the H^+ ion reduction reaction. However, since the magnitude of differences in α_{H^+} between the two types of corrosion are within the experimental and the fitting procedure errors, no definitive conclusion can be drawn in this case.

To compare the rate of H^+ ion reduction reaction, i_{o,H^+} values for the two type of corrosion are plotted in Figure 10-13 B. i_{o,H^+} values were larger for CO_2 corrosion for almost the entire range of NaCl concentrations. This implies that the presence of CO_2 increased the rate of H^+ ion reduction reaction in the charge transfer region. Kahyarian [207] carried out a series of experiments on 316L SS, pure iron, and X65 carbon steel at 30°C, pH 4, 0.1 M NaCl solution and three partial pressure of 0 bar, 1 bar, and 5 bars. Kahyarian's [207] data show no change in the charge transfer controlled cathodic current on 316L SS, but slight increases for pure iron and X65 carbon steel when pCO_2 goes from 0 bar to 5 bars [207]. The increase in the charge transfer controlled cathodic current for X65 carbon steel agrees with the results obtained in this study. However, Kahyarian [207] stated that the changes in the charge transfer controlled cathodic current are within the experimental errors, and therefore concluded that the presence of CO_2 had no significant effect on the charge transfer controlled cathodic current. Thus, a systematic investigation is required on this subject to understand better the effect of $CO_{2(g)}$ on H^+ ion reduction reaction in the charge transfer region.

The anodic PD sweeps for strong acid corrosion and CO_2 corrosion in Figure 10-12 appear to be identical. However, reviewing the extracted kinetic parameters for the Fe dissolution reaction reported earlier for both types of corrosion indicates that the sweeps are actually not identical. α_{Fe} for strong acid corrosion in Table 9-3 was around 1.2 for all NaCl concentrations, whilst α_{Fe} for CO_2 corrosion reported in Table 10-2 was almost 1.1 for all NaCl concentrations. Although the presence of CO_2 caused a 0.1 difference in α_{Fe}; however, since the magnitude of difference was within the experimental and the fitting procedure errors, it cannot be concluded for sure that CO_2 altered the mechanism of anodic Fe dissolution reaction in the active region.

$i_{o,Fe}$ values for strong acid and CO_2 corrosion at different NaCl concentrations are presented in Figure 10-13 C for comparison. $i_{o,Fe}$ for CO_2 corrosion was higher than that for strong acid corrosion in all NaCl concentrations. This comparison suggests that the presence of CO_2 accelerated the Fe dissolution reaction in the active region. The literature review done in Section 5.2.1 includes some studies that reported an effect of CO_2 on the anodic Fe dissolution reaction as well as studies that were against this ideal and claimed that the anodic Fe dissolution reaction is not affected by the presence of CO_2. The most recent ones and the closest to this study in terms of the experimental conditions are those done by Kahyarian *et al.* [207,208]. They reported in a series of experiments on X65 carbon steel in 0.1 M NaCl solutions at 10°C and 30°C, pH 4 and 5, and CO_2 partial pressure pressures of 0 bar, 1 bar, and 5 bars that the slight increase in the corrosion rate, when pCO_2 was increased from 0 bar to 5 bars, was due to the influence of CO_2 on the anodic reaction in the active range. Kahyarian *et al.* [207,208] potentiodynamic sweeps also show small accelerations in the anodic Fe dissolution reaction in the active region at both solution pH values of 4 and 5 and both temperatures. Therefore, Kahyarian *et al.* [207,208] results support the conclusion made here about the effect of CO_2 on the anodic dissolution of iron the active range.

At the end, the higher corrosion rates for CO_2 corrosion compared to those for strong acid corrosion for all tested NaCl concentrations up to 20 wt.% can be attributed to the increase in the rates of the H^+ ion reduction reaction in the charge transfer region and the anodic iron dissolution reaction in the active region. However, since the focus of this study was not the effect of CO_2 on the cathodic and anodic reactions, the results of this part need to be confirmed by further systematic and targeted investigations.

10.1.5 Summary and Conclusions of RDE CO_2 Corrosion Experiments at 10°C and pH 3

This set of experiments was done to understand the effect of salt concentration on aqueous uniform CO_2 corrosion of carbon steel at low pH values. Experiments were carried out using X65 carbon steel specimens exposed to aqueous NaCl solutions, at 10°C and pH 3, and 1 bar $CO_{2(g)}$. A comparison was made at the end between this set of experiments and that presented in Section 9.1. The major conclusions found in this part are as follows:

1. With increasing NaCl concentration, the uniform CO_2 corrosion rate first increased between 1 wt.% and 3 wt.% and then switched trend and decreased steadily between 3 wt.% and 20 wt.%.
2. The analysis of PD sweeps showed that the mechanisms of H^+ ion reduction and the active dissolution of iron at the steel surface did not change with increasing NaCl concentration.
3. With increasing NaCl concentration the rate of the H^+ ion reduction reaction in the charge transfer region decreased continually, while the rate of active dissolution of showed a maximum at 3 wt.% NsCl.
4. The H^+ ion limiting current density (i_{Lim}) decreased with increasing NaCl due to a decrease in H^+ ion concentration (*i.e.*, increase in the H^+ ion activity coefficient) and H^+ ion diffusion coefficient.
5. The decreasing trend seen for i_{Lim} is mainly due to changes in H^+ ion bulk concentration and H^+ diffusion coefficient.
6. The CO_2 corrosion process was under pure charge transfer control.
7. The comparison between strong acid and CO_2 corrosion under similar experimental conditions showed higher corrosion rates in CO_2 corrosion, which were attributed to increases in the rates of the cathodic H^+ ion reduction reaction in the charge transfer region and the anodic dissolution of iron in the active region in the presence of CO_2.

10.2 The Effect of Salt Concentration on CO_2 Corrosion at 30°C, 1 bar CO_2, and Autogenous pH Using a Rotating Cylinder Electrode (RCE)

The difference between this set of experiments with other sets for CO_2 corrosion was that the solution pH was not adjusted to a constant value and experiments were done at autogenous (natural) pH of solution. It means that the decrease in solution pH with increasing NaCl concentration was not compensated by a pH adjuster (HCl or NaOH). This part of study has been already published elsewhere [299].

10.2.1 Experimental Materials and Methodology for RCE CO_2 Corrosion Experiments at Autogenous pH and 1 bar CO_2

In this part of study, two separate sets of experiments were conducted in CO_2 saturated aqueous solutions at different NaCl concentrations: corrosion rate measurements and PD sweep experiments. Experiments were carried out in a 2-liter glass cell at 30°C, 1 bar total pressure (~ 0.97 bar pCO_2), autogenous pH, and five NaCl concentrations of 0, 0.1, 1, 3, 10, and 20 wt.% (or, 0, 0.017, 0.17, 0.53, 1.90, and 4.28 m). The experimental setup used in this set of experiments is shown in Figure 10-14. For each experiment, the specified amount of NaCl was dissolved in deionized water (conductivity < 1 mS/cm). The solution was then continuously sparged for at least 2 h with CO_2 gas, while being stirred by a magnetic stirrer to remove the dissolved oxygen and saturate the solution with CO_2 gas. An oxygen probe connected to the gas outlet was used to monitor the dissolved oxygen level in the solution and ensure that it remained below 10 ppb during the experiments. All the experiments were done at an autogenous pH under continuous sparging with CO_2 gas. The pH measurements were conducted with double-junction pH probes, which were resistant to Na^+ ion interference. The solution pH was continuously monitored during the experiments.

Figure 10-14

(A) Schematic; (B) picture of the experimental apparatus and a zoomed-in view of the experimental glass cell.

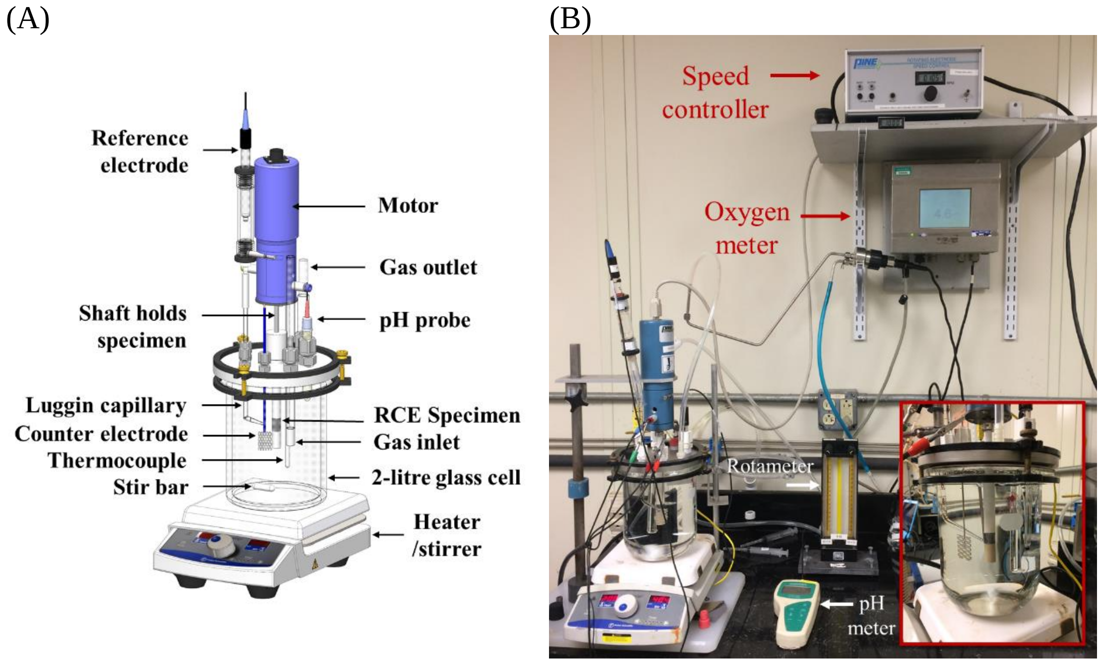

API 5L X65 carbon steel was used in the experiments, as it is a common pipeline-grade steel in the oil and gas industry. The chemical composition of the experimental X65 steel is listed in Table 9-1. Specimens were in the shape of an annulus (RCE) with an outer diameter of 12 mm, a length of 14 mm, and an exposed surface area of 5.4 cm^2. This resulted in a cell volume to specimen surface area ratio of approximately 400 cm^3/cm^2, which is reasonably high for the relatively short experiments conducted in the study, so that there was no significant accumulation of corrosion products and deviation of the water chemistry [300]. Before insertion into the glass cell, the specimen was sequentially wet polished with 80-, 240-, 400- and 600-grit abrasive papers. Subsequently, it was ultrasonically cleaned with isopropanol alcohol for 3 min and dried in cool N_2 gas. Prior to immersion in the test solution, the specimen was weighed with a 0.01 mg high-precision analytical balance. Then, the specimen was flush mounted onto an RCE shaft and inserted into the solution. The shaft was rotated at 1000 rpm by a motor throughout the experiments, while the magnetic stirrer was stopped, to have a controlled flow condition. The RCE rotational speed was chosen so that it corresponded to the flow conditions encountered in oil and gas pipelines by creating equivalent mass transfer conditions. The 1000 rpm rotational speed in our RCE system is approximately equivalent to an average flow velocity of 1 m/s in a 10 cm ID pipe [301]. For the electrochemical tests (LPR, PD sweeps, and EIS), the RCE acted as the working electrode in the electrochemical experiments. In conjunction with the RCE, a saturated silver/silver chloride (Ag/AgCl) reference electrode connected to a Luggin capillary served as the reference electrode and a platinized titanium mesh (20 mm × 30 mm) was used as the counter electrode to complete the three-electrode setup needed for the electrochemical measurements. The three-electrode setup can be seen in Figure 10-14.

In the first set of experiments, WL and LPR techniques were performed in the same experiment, using the same specimen, to identify the overall effect of salt concentration on the CO_2 corrosion rate. Each WL experiment lasted 24 h, which was the time required for obtaining sufficiently accurate WL measurements. The LPR corrosion rate was measured on average every 6 h during the 24 h period (totally five times), by sweeping the potential in a range from -5 mV to $+5$ mV *vs.* OCP with a scan rate of 0.125 mV/s. The Stern-Geary constant (B) used for converting the polarization resistance into the corrosion rate was taken to be 23.6 mV/dec as determined by fitting the PD sweeps with an electrochemical model [96]. The measured polarization resistance values were corrected for the solution resistance measured with EIS. The corresponding increase of pH after 24 h was less than 0.7 pH units, at any NaCl concentration. The pH drift did not have a marked effect on the corrosion rate measurements, as there was no statistically significant change in the measured LPR corrosion rates from the beginning to the end of each experiment, as shown in Figure 10-15.

Figure 10-15

Variation in the LPR corrosion rate with time in 24 h long weight loss experiments conducted with X65 carbon steel RCE with a rotational speed of 1000 rpm in CO_2 *saturated aqueous NaCl solutions at 30°C, 1 bar total pressure, and autogenous pH.*

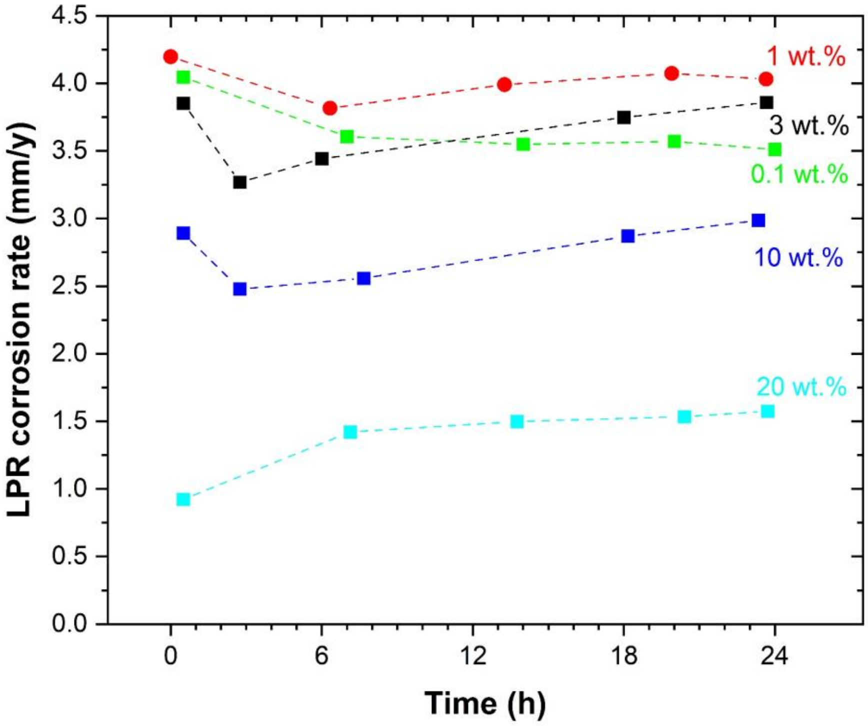

After 24 h, the specimen was retrieved from the solution; thoroughly rinsed with distilled water for at least one minute to remove the salt, followed by rinsing with isopropanol alcohol and drying in a cool N_2 gas stream. The specimen then was weighed again to determine the WL corrosion rate. At the end of each experiment, the concentration of Fe^{2+} ion in the solution was measured by spectrophotometry. If it is assumed that all Fe corroded from the steel matrix ends up as dissolved Fe^{2+} ion in the solution, the measured Fe^{2+} ion concentration can be used to calculate the time averaged corrosion rate. This method often called “iron counts” (IC) [302,303] was used to cross-validate the corrosion rates obtained by WL and LPR techniques. The average corrosion rate from the WL experiments was determined using the following equation [18]:

$$CR = 3.1536 \times 10^{10} \frac{W}{DAt} \tag{10-4}$$

where, CR is corrosion rate in mm/y, W is mass loss in kg, D is density of metal in kg/m^3, A is specimen surface area in m^2, and t is exposure time in seconds. The density of the experimental material was 7870 kg/m^3. The time averaged LPR corrosion rate was determined by the cumulative trapezoidal integration of the instantaneous LPR corrosion rates taken on average every 6 h over the 24 h experiments.

In the second set of experiments, EIS followed by PD sweep measurements were done to determine the effect of NaCl concentration on individual reaction mechanisms underlying CO_2 corrosion. EIS was done at three DC voltages of -50 mV, 0 mV, and +50 mV vs. OCP in a frequency range of 10000 – 0.1 Hz with a peak-to-peak AC voltage amplitude of 10 mV. Prior to changing the potential in PD sweep experiments, the OCP was monitored to ensure having a stable potential value (drift <

2 mV/min). The PD sweep experiments were conducted according to the following steps: (1) a cathodic sweep starting from the OCP toward more negative potentials up to −1.00 V *vs.* OCP; (2) wait for the OCP to return close to its initial value—within a few mV (this took about 0.5–1 h); (3) an anodic sweep starting from the OCP to more positive potentials up to 0.35 V *vs.* OCP. The PD scan rate was chosen to be 0.5 mV/s to shorten the duration of the polarization. A slower scan rate of 0.125 mV/s was also used at one salt concentration and resulted in identical sweeps to those obtained at 0.5 mV/s. All electrochemical measurements were conducted using a Gamry potentiostat Reference 600. In the PD sweep measurements lasted about 4 h, the increase in pH over the course of each experiment was less than 0.2 pH units, for any NaCl concentration. The solution resistance measured with EIS was used to correct potentials for the PD sweeps as well as the LPR measurements.

10.2.2 Results and Discussion for RCE CO_2 Corrosion Experiments at autogenous pH and 1 bar CO_2

Figure 10-16 shows the variation in autogenous pH of the CO_2 saturated solution with respect to NaCl concentration. The solution pH decreased from about pH 4.0 at 0 wt.% NaCl to about pH 3.5 at 20 wt.% NaCl. The results are comparable to those reported previously under similar conditions [6,9,10]. The reason behind such behavior is explained below. Both solution chemistry models predict a linear trend for the solution pH with NaCl respect to NaCl concentration, while the experimental results show a logarithmic trend. The MSE model predicts slightly more accurately compared to the Li and Duan Model. The maximum error in the models occurs at NaCl concentrations of about 10 wt.%.

Figure 10-16

Autogenous pH of CO_2 saturated solutions measured at 30°C, and 1 bar total pressure (~ 0.97 bar pCO_2). The error bars represent the minimum and maximum values obtained in repeated experiments (with at least 5 repeats). The experimental data are compared with two speciation models.

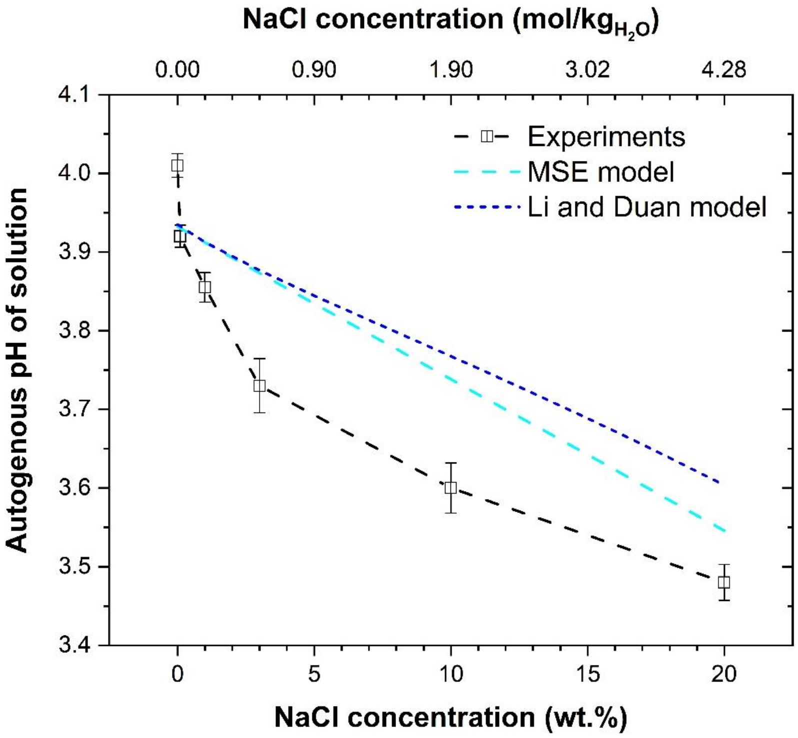

When CO_2 gas is dissolved in water according to

$$CO_{2(g)} \rightleftarrows CO_{2(aq)} \quad (10\text{-}5)$$

it is partially hydrated to form carbonic acid:

$$CO_{2(aq)} + H_2O_{(l)} \rightleftarrows H_2CO_{3(aq)} \quad (10\text{-}6)$$

and then carbonic acid (a weak acid) dissociates in two steps:

$$H_2CO_{3(aq)} \rightleftarrows H^+_{(aq)} + HCO^-_{3(aq)} \quad (10\text{-}7)$$

$$HCO^-_{3(aq)} \rightleftarrows H^+_{(aq)} + CO^{2-}_{3(aq)} \quad (10\text{-}8)$$

Due to the salting out effect explained in Sections 4.1 and 7.1, Reactions (10-5) and (10-6) move from right to left. The consequence is that Reactions (10-7) and (10-8) will also shift from right to left in order to establish equilibria, and that leads to a lower activity of H^+ ions and an increase in pH. However, pH measurements presented in Figure 10-16 show exactly the opposite trend, where the solution pH decreased with increasing NaCl concentration; thus, the salting out effect cannot be used to explain these experimental observations. The only possible explanation for the pH variation with the addition of NaCl is the change in the activity coefficient of H^+ ion.

Figure 10-17 shows the changes in activity coefficient, concentration, and activity of dissolved CO_2, H^+ ion, HCO_3^- ion, OH^-, Cl^- ion, and water with NaCl concentration calculated by the Li and Duan speciation equilibrium model described in Section 8.1.3. At 20 wt.% NaCl, the amount of dissolved CO_2 is less than half of the amount dissolved in pure water (salting out of CO_2) (Figure 10-17 A). According to Figure 10-17 B, the activity coefficient for bicarbonate ion ($\gamma_{HCO_3^-}$) monotonously decreases with salt concentration, while the bicarbonate concentration ($c_{HCO_3^-}$) has a peak somewhere at around 4 wt.% NaCl. Figure 10-17 C shows that γ_{H^+} decreases from unity by about 20% between 0 wt.% and 2 wt.% NaCl and then increases beyond that, so that at 20 wt.% NaCl, it is 2.4. c_{H^+} has the opposite trend and reaches a peak at around 4 wt.% NaCl. a_{H^+} monotonously increases with higher NaCl concentrations; when pH is calculated ($pH = -\,log\ a_{H^+}$), this results in a continuous downward trend for pH, just as obtained in the experiments. Therefore, the observed decreasing trend in pH with the addition of NaCl is solely a result of the change in the activity coefficient and the concentration of H^+ ion and is not related to the salting out effect. This becomes obvious if one recalls that $a_{CO_{2(aq)}}$ only depends on the partial pressure of gaseous CO_2 and does not depend on NaCl concentration. So, $a_{CO_{2(aq)}}$ remains constant[78] even as $c_{CO_{2(aq)}}$ decreases significantly with increasing NaCl concentration. It is $a_{CO_{2(aq)}}$and not $c_{CO_{2(aq)}}$ that is linked to the activities of other dissolved species such as that for H^+ ions and the resulting pH. Since $a_{CO_{2(aq)}}$does not change with NaCl concentration, it could not be the reason for the observed trend in pH.

---

[78] In this argument, the effect of NaCl concentration on water vapor pressure, and therefore, on a_{CO_2} is neglected.

Figure 10-17

Bulk concentration, molality-based activity coefficient, and activity of (A) dissolved CO_2, (B) bicarbonate ion, (C) H^+ ion, (D) OH^- ion, (E) Cl^- ion, and (F) H_2O calculated by the Li and Duan speciation model for CO_2 saturated aqueous NaCl solutions at 30°C, and 1 bar total pressure (~ 0.97 bar pCO_2).

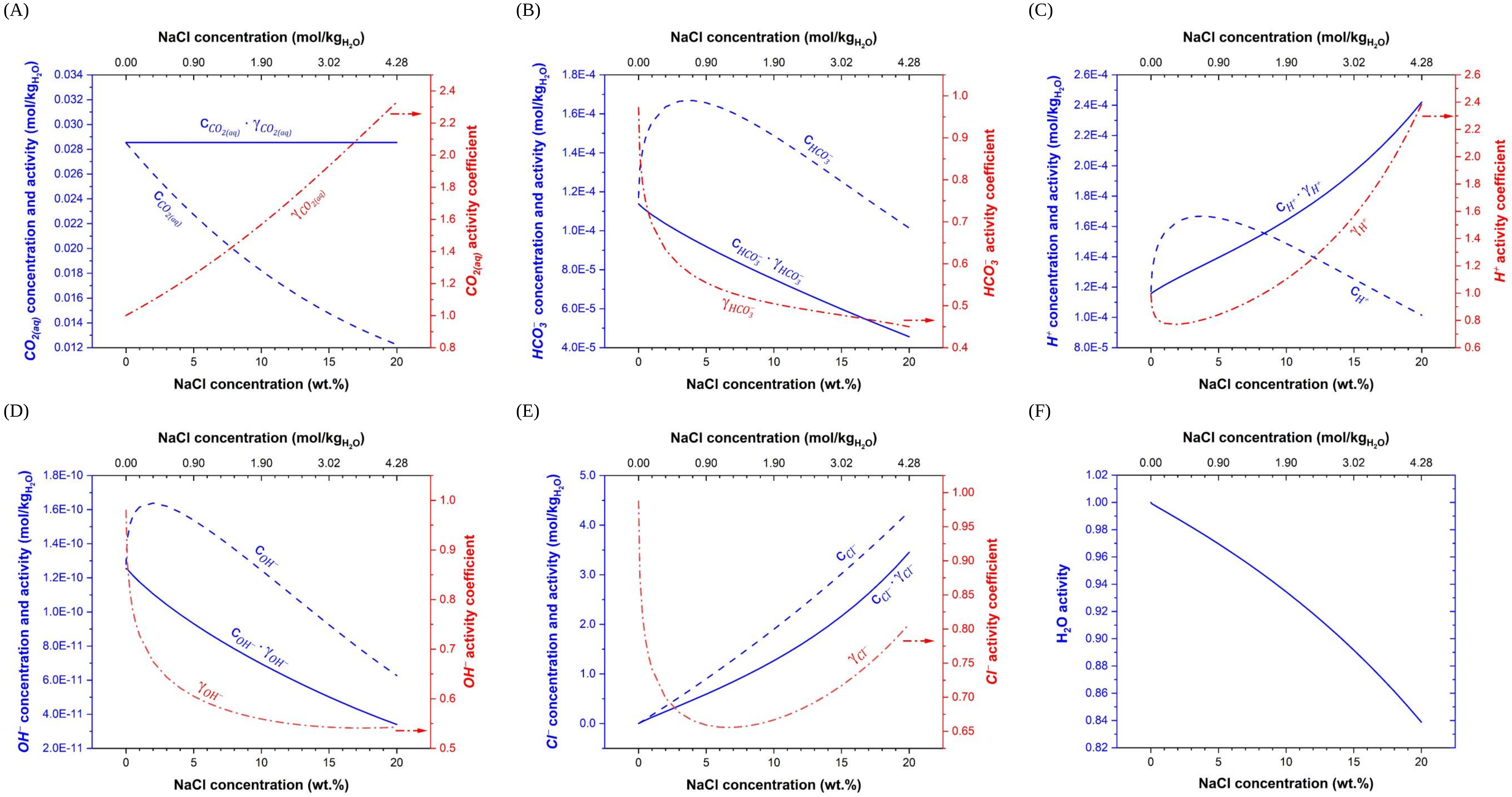

Figure 10-18 shows the variation in the corrosion rate as a function of NaCl concentration, as measured by three independent methods: WL, LPR and IC. The experimental error obtained from multiple measurements show the minimum and maximum values. The error bars for WL and IC are not visible since they are smaller than the symbols. The agreement between the results obtained by these three independent techniques is reasonably good, thereby increasing the reliability of the conclusions.

Figure 10-18

Variation in the corrosion rate with NaCl concentration for X65 carbon steel RCE with a rotational speed of 1000 rpm exposed to CO_2 *saturated aqueous NaCl solutions for 24 h at 30*^{o}*C, 1 bar total pressure, and autogenous pH. The corrosion rates were measured using weight loss, LPR, and iron counts techniques. The error bars represent the minimum and maximum values obtained in repeated experiments (two repeats).*

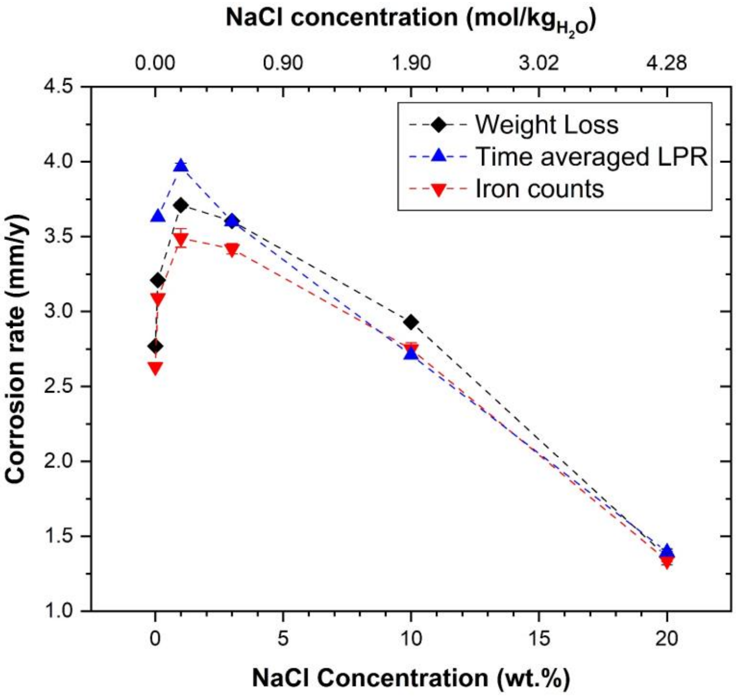

The corrosion rate increases sharply with increasing NaCl concentration and reaches its maximum value at about 1 wt.% NaCl. The maximum could actually be anywhere between 0.1 wt.% and 3 wt.% NaCl, as the resolution in this concentration range is not sufficient to precisely determine the location of the maximum. The corrosion rate then decreases with further increase in NaCl concentration up to 4.28 m (20 wt.%) NaCl. A similar trend was reported by other researchers in oxygen-saturated, aerated and deaerated solutions [8,11,296,297]. It is tempting to explain the increase in the corrosion rate at low NaCl concentrations by the corresponding increase in c_{H^+}, as shown in Figure 10-17 C, which appears to have the same trend. In addition, as discussed earlier in Section 5.1.1, several studies have reported that Cl^- ions increase the rate of anodic iron dissolution in acidic media by taking part directly in the dissolution reaction, which happens in parallel with the other well understood pathway involving OH^- ions [178,182,192–195,197]. The acceleration of the anodic reaction could lead to higher corrosion rates; however, caution needs to be taken as most of the referenced studies have been done at very low pH values (< pH 2.0) [178,182,192,194,195,197] conditions, which differ significantly from those in our study. Contrarily, there are other studies conducted at low pH values, postulating that Cl^- ions inhibit iron dissolution reaction by adsorbing on the steel surface and blocking the active surface sites required for OH^- adsorption, which governs iron dissolution reaction [178,179,188,198]. Yet another explanation was put forward by Foley [304], suggesting that the increase in the corrosion rate at low NaCl concentrations is mainly related to the large decrease in the solution resistance when NaCl is added. The EIS results showed that the solution resistance between the WE and RE decreased from 4320 $\Omega\cdot cm^2$ at 0 wt.% NaCl to 108 $\Omega\cdot cm^2$ at 0.1 wt.% NaCl. However, there is no evidence that the change in the solution resistance directly influenced the corrosion rate. The solution resistance becomes important in situations where there is a large separation between anodes and cathodes, which is not the case for uniform aqueous CO_2 corrosion studied here.

There are a few possible explanations for the observed decrease in the corrosion rate seen in Figure 10-18 with further addition of NaCl. The blocking of the active surface sites by adsorbed Cl^- ions that inhibit iron dissolution reaction is one possibility [174,178,188]. This explanation can be valid for the H^+ ion cathodic reaction as well. The deceleration of the H^+ ion reduction reaction due to the blocking of the active cathodic sites on the steel surface by adsorbed Cl^- ions could be used as another reason for the decrease in the corrosion rate [171]. However, the cathodic reaction rate is usually limited by the slow rate of CO_2 hydration to form $H_2CO_{3(aq)}$ followed by the slow rate of diffusion of H^+ ions from the bulk solution to the metal surface; hence the effect of NaCl concentration on the cathodic limiting current density needs to be considered. On top of all these possibilities, it is not clear at this point which reaction (anodic or cathodic) controls the corrosion rate, or whether it is under mixed control.

To pinpoint the main reason for the changes in the corrosion rate with increasing NaCl concentration a more in-depth analysis of the underlying electrochemical reactions and how they are affected by the presence of NaCl is required. This was done by performing PD sweeps and EIS, for which the results are presented below.

PD sweep measurements were done to elucidate the core electrochemical mechanisms behind the CO_2 corrosion process. Cathodic and anodic PD sweeps were done at various NaCl concentrations and are summarized in . The potential values are corrected for the solution resistance (iR drop) in all the presented sweeps. For each NaCl concentration, at least two sets of PD sweeps were conducted. The magnitude of the scatter is reasonably small for all NaCl concentrations. Therefore, the PD sweeps can be considered as being reproducible and can be relied on when analyzing the effect of NaCl concentration on CO_2 corrosion mechanisms. The PD results will be discussed in terms of the effect of NaCl concentration on the cathodic reaction mechanisms, followed by the anodic reaction mechanisms, and then the overall corrosion process.

Figure 10-19

Potentiodynamic sweeps for X65 carbon steel RCE with a rotational speed of 1000 rpm exposed to CO_2 *saturated solutions with different NaCl concentrations at 30°C, 1 bar total pressure, and autogenous pH.*

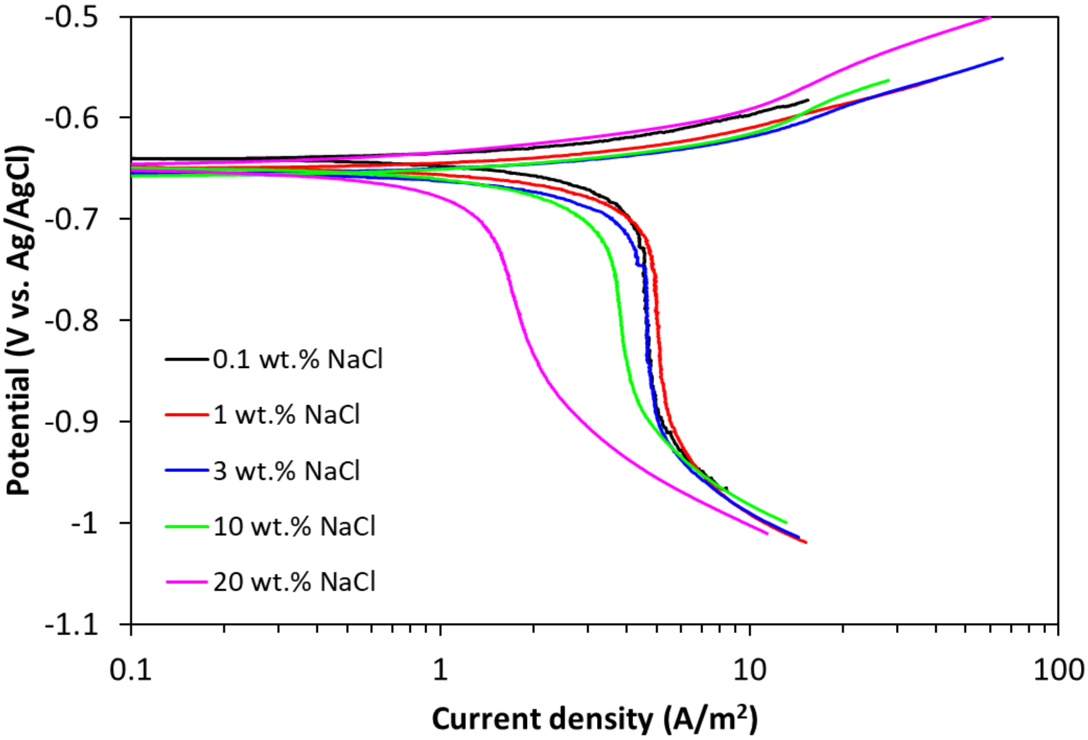

The most obvious effect in the PD sweeps with increasing NaCl concentration is the change in the cathodic limiting current density (i_{Lim}). To enable a more precise analysis, the magnitude of i_{Lim} at different NaCl concentrations is extracted from the raw data by overlaying the PD sweeps for the best fit with those generated by a simple electrochemical model [96][79].

---

[79] Activation energies of 59860 J/mol for H^+ ion, 24809 J/mol H_2O reduction and 25398 J/mol for Fe oxidation reactions. A reversible potential of -0.685 V vs. Ag/AgCl was used for all three reactions. The reference temperature was 20°C.

The variation in i_{Lim} with NaCl concentration is shown in Figure 10-20 A. Clearly there is a small increase in the magnitude of i_{Lim} at low NaCl concentrations, followed by a decrease by approximately a factor of 3, when NaCl concentration is further increased. The local maximum is somewhere between 0.1 wt.% (0.017 m) and 3 wt.% (0.53 m) NaCl, which is qualitatively similar to what was seen for c_{H^+} presented in Figure 10-17 C. This is no coincidence, as the main cathodic reaction in aqueous CO_2 solutions is the reduction of H^+ ions, Reaction (5-78). The H^+ ions reduction reaction is limited by the slow hydration rate of CO_2 and the slow rate of diffusion of H^+ ions from the bulk solution to the metal surface; hence, one would expect that the change in the diffusional flux of H^+ ions will resemble the change in c_{H^+} with NaCl concentration. However, at 15 wt.% NaCl, c_{H^+} is approximately the same as that for 0.1 wt.% NaCl, while i_{Lim} decreases approximately by a factor of 2 in the same range of NaCl concentrations. Thus, the variation in c_{H^+} alone cannot explain the change seen in i_{Lim}.

i_{Lim} in CO_2 corrosion in addition to a dependency on c_{H^+} (a_{H^+} and γ_{H^+} to be more precise) depends on the H^+ diffusion coefficient (D_{H^+}). It was shown in Figure (3-8) A that D_{H^+} decreases with increasing NaCl concentration, which is another reason for the decrease in i_{Lim}. It is explained in Chapter 12 that i_{Lim} in CO_2 corrosion also depends on activity and activity coefficient of H_2CO_3 and HCO_3^- as well as their diffusion coefficients.

The variations in the charge transfer portions of the PD sweeps with NaCl concentration are not obvious by visual inspection. By fitting the measured PD sweeps with those generated by a simple electrochemical model [96], the exchange current densities (i_o) and the electron transfer coefficients (Tafel slopes) for both cathodic and anodic reactions were obtained.

For all NaCl concentrations, the best fit for the H^+ ion reduction reaction was obtained with a cathodic transfer coefficient of 0.5 (equivalent to a cathodic Tafel slope of approximately 120 mV at 30°C). This value is a commonly accepted value for the H^+ ion reduction reaction in acidic solutions [185], suggesting that there is no change in mechanisms for this reaction with the addition of NaCl. However, the extracted values for i_{o,H^+}, shown in Figure 10-20 A, decrease with increasing NaCl concentration. This indicates that the rate of H^+ ion reduction reaction slows down with increasing NaCl concentration, due to a change in the surface coverage [171]. Therefore, the decrease in i_{o,H^+} can be listed as one of the reasons for the decreasing trend of the corrosion rate shown in Figure 10-18.

The trend observed for i_{o,H^+} in Figure 10-20 A can be modeled by using a correlation similar to Equation (5-23):

$$i_{o,H^+} = i_{o,H^+}^{ref} \left(\frac{a_{H^+,b}}{a_{H^+,b}^{ref}}\right)^{n_{H^+}^{H^+}} \left(\frac{a_{Cl^-,b}}{a_{Cl^-,b}^{ref}}\right)^{n_{Cl^-}^{H^+}} e^{-\frac{E_{a,H^+}}{R}\left(\frac{1}{T}-\frac{1}{T_{ref}}\right)} \tag{10-9}$$

where, i_{o,H^+}^{ref} is the reference current density in A/m^2 at T_{ref} (293.15 K) and -685 mV *vs.* Ag/AgCl, $a_{H^+,b}$ is the bulk activity of H^+ ion in molarity concentration, $a_{H^+,b}^{ref}$ is the reference bulk activity of H^+ ion (= 10^{-4} M), $n_{H^+}^{H^+}$ is the reaction order of the H^+ ion reduction reaction with respect to H^+ ion activity, $a_{Cl^-,b}$ is the bulk activity of Cl^- ion in molarity concentration, $a_{Cl^-,b}^{ref}$ is the reference bulk activity of Cl^- ion (= 1 M), $n_{Cl^-}^{H^+}$ is the reaction order of the H^+ ion reduction reaction with respect to Cl^- ion activity, E_{a,H^+} is the activation energy for the H^+ ion reduction reaction (= 59860 J/mol), T is solution temperature in K, and R is the gas constant in J/mol/K.

Equation (10-9) with the bulk activities calculated with the MSE model was fitted to the experimental i_{o,H^+} values in Figure 10-20 A to obtain the reaction orders and i_{o,H^+}^{ref}. Since the solution pH was constant in the experiments, the activity of H^+ ion was constant as well[80]. This means that $n_{H^+}^{H^+}$ cannot be determined from the fitting exercise. To be able to obtain $n_{H^+}^{H^+}$ experiments at different pH values are required. Therefore, an empirical value of 0.5 previously reported in the literature was chosen for $n_{H^+}^{H^+}$ [200,215]. The fitting exercise gave $n_{Cl^-}^{H^+}$ = -0.30 and i_{o,H^+}^{ref} = 7.4 A/m^2. The negative sign found for $n_{Cl^-}^{H^+}$ proves that Cl^- ion had a retardation effect on the rate of the H^+ ion reduction reaction in the charge transfer region.

The anodic electron transfer coefficient for the iron dissolution reaction in the active range was found to be approximately 1 (equivalent to an anodic Tafel slope of 60 mV at 30°C) for all NaCl concentrations, indicating that iron dissolution occurred with the same or a similar mechanism when NaCl concentration was increased [181].

---

[80] The changes in molarity-based activity due to changes in density with NaCl concentration is ignored.

Figure 10-20

Variations in (A) the cathodic limiting current density (i_{Lim}) and the H^+ reduction exchange current density (i_{o,H^+}) and (B) the Fe oxidation exchange current density ($i_{o,Fe}$) with NaCl concentration. The current densities were extracted from the PD sweeps of X65 carbon steel RCE specimen with a rotational speed of 1000 rpm exposed to CO_2-saturated aqueous solutions at 30°C, 1 bar total pressure, and autogenous pH. The error bars are the minimum/maximum values obtained in two repeated experiments. The reference temperature was 20°C.

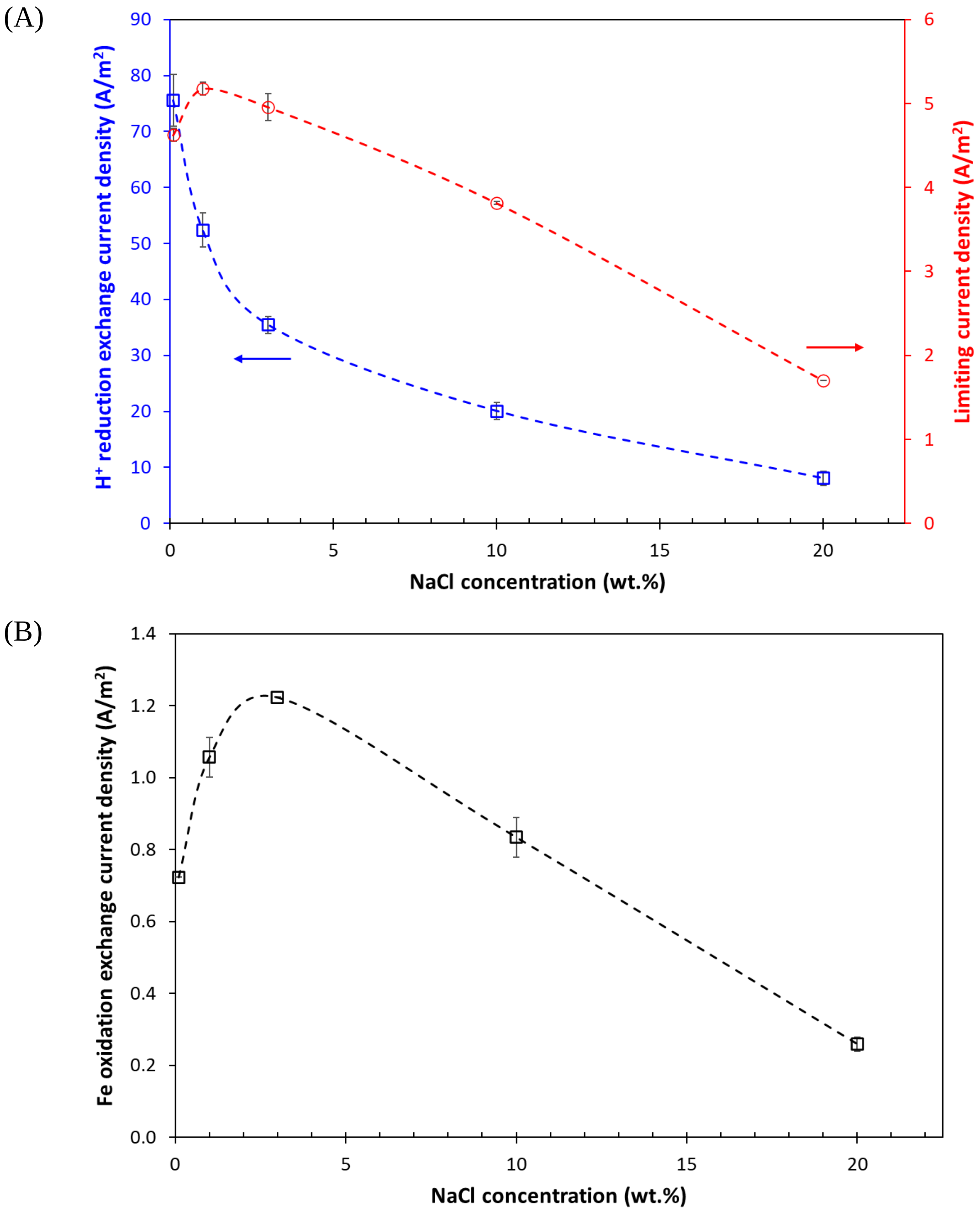

$i_{o,Fe}$ as shown in Figure 10-20 B, increases at lower NaCl concentrations and then reverses trend and decreases at higher NaCl concentrations. The observed trend for $i_{o,Fe}$ is the same as that measured in the RDE CO_2 experiments (Figure 10-6 B) as well as those reported for the strong acid experiments in Chapter 9. This shows the accuracy and consistency of the results. The $i_{o,Fe}$ trend in Figure 10-20 B is similar to that reported for the CO_2 corrosion rate in Figure 10-18. Thus, variation in $i_{o,Fe}$ with NaCl concentration is possibly another reason for the small increase followed by the monotonous decrease in the CO_2 corrosion rate when NaCl concentration was increased from 0.1 wt.% to 20 wt.%.

The $i_{o,Fe}$ trend can be justified by considering the changes in the bulk activities of OH^- and Cl^- ions, and H_2O with NaCl concentration. $i_{o,Fe}$ can be related to the activities of OH^- and Cl^- ions, and H_2O with the following equation:

$$i_{o,Fe} = i_{o,Fe}^{ref}\left(\frac{a_{OH^-,b}}{a_{OH^-,b}^{ref}}\right)^{n_{OH}^{Fe}}\left(\frac{a_{Cl^-,b}}{a_{Cl^-,b}^{ref}}\right)^{n_{Cl^-}^{Fe}}\left(\frac{a_{H_2O,b}}{a_{H_2O,b}^{ref}}\right)^{n_{H_2O}^{Fe}} e^{-\frac{E_{a,Fe}}{R}\left(\frac{1}{T}-\frac{1}{T_{ref}}\right)} \qquad (10\text{-}10)$$

where, $i_{o,Fe}^{ref}$ is the reference current density in A/m^2 at T_{ref} (293.15 K) and -685 mV *vs.* Ag/AgCl, $a_{OH^-,b}$ is the bulk activity of OH^- ion in molarity concentration, $a_{OH^-,b}^{ref}$ is the reference bulk activity of OH^- ion (= 10^{-10} M), n_{OH}^{Fe} is the reaction order of the Fe oxidation reaction with respect to OH^- ion activity, $a_{Cl^-,b}$ is the bulk activity of Cl^- ion in molarity concentration, $a_{Cl^-,b}^{ref}$ is the reference bulk activity of Cl^- ion (= 1 M), $n_{Cl^-}^{Fe}$ is the reaction order of the Fe oxidation reaction with respect to Cl^- ion activity, $a_{H_2O,b}$ is the bulk activity of liquid water in molarity unit, $a_{H_2O,b}^{ref}$ is the reference bulk activity of liquid water (= 55.4 M), $n_{H_2O}^{Fe}$ is the reaction order of the Fe oxidation reaction with respect to H_2O, and $E_{a,Fe}$ is the activation energy for the Fe oxidation reaction in the active region (= 25398 J/mol), T is solution temperature in K, and R is the gas constant in J/mol/K.

Lorenz [174] and McCafferty and Hackerman [178] reported different $n_{Cl^-}^{Fe}$ values for different range of Cl^- activities (concentrations), as mentioned in Table 5-2. This indicates that the Fe dissolution reaction might proceed through different pathways depending on the activity of Cl^- ion in the solution. From the $i_{o,Fe}$ trend presented in Figure 10-20 B, it can be assumed that at low NaCl concentrations below 3 wt.%[81], Cl^- ions speeds up the anodic dissolution reaction by playing a catalytic role in iron dissolution, similar to that of OH^- ions [172,194,195]. However, at NaCl concentrations above 3 wt.%, Cl^- ions impedes the Fe dissolution reaction by being adsorbed on the surface and blocking the active sites (surface imperfections) required for the Fe dissolution reaction to happen [173,174,178,192]. Therefore, the $i_{o,Fe}$ curve is divided into two sections: below and above 3 wt.%. The reaction orders and $i_{o,Fe}^{ref}$ values for each region can be obtained by fitting Equation (10-10) using the bulk activity values calculated with the MSE model to the experimental $i_{o,Fe}$ values. Obtaining n_{OH}^{Fe} value needs experimentation at different solution pH. This means that n_{OH}^{Fe} cannot be found from the data presented in Figure 10-20 B. Therefore, a value of 1 was chosen for n_{OH}^{Fe}

---

[81] It can be any NaCl concentration between 1 wt.% and 3 wt.%, as the experimental NaCl resolution was not small enough to determine the exact maximum.

for the whole range of NaCl concentration according to the Bockris *et al.* [185,186] consecutive mechanism and reports by other scientists [174,195] (see Table 5-2). For NaCl ≤ 3 wt.%, $n_{Cl^-}^{Fe}$= 0.19, $n_{H_2O}^{Fe}$ = 0, and $i_{o,Fe}^{ref}$ = 0.91 and for NaCl > 3, $n_{Cl^-}^{Fe}$= -0.24, $n_{H_2O}^{Fe}$ = 2, and $i_{o,Fe}^{ref}$ = 0.61. A reaction order of zero for H_2O at NaCl ≤ 3 means that the Fe dissolution reaction process is independent of H_2O activity in this NaCl concentration range. For $n_{H_2O}^{Fe}$ at high NaCl concentrations, the value found in this study is similar to the values (a range of 1.6-1.9) reported by Smart *et al.* [190,198].

Figure 10-21 shows the Evans diagrams for 0.1 wt.%, 1 wt.%, and 20 wt.% NaCl concentrations produced by a simple electrochemical model [96] at the experimental conditions of this part of study. The comparison between 0.1 wt.% and 1 wt.% NaCl in Figure 10-21 A demonstrates that the corrosion process at low NaCl concentrations below ~ 1 wt.% was controlled by charge transfer processes. The Evans diagrams show the rate of cathodic reaction for both 0.1 wt.% and 1 wt.% NaCl concentrations was the same. However, the rate of anodic dissolution of iron increased with increasing NaCl concentration from 0.1 wt.% to 1 wt.%. Consequently, the net effect was a slight increase in the corrosion rate[82]. This indicates that at low NaCl concentration, the increase in the CO_2 corrosion rate was due to the increase in the rate of anodic dissolution of Fe as shown in Figure 10-20 B.

For NaCl concentrations higher than ~ 1 wt.%, the corrosion process was under mixed control. This means that the corrosion process was controlled by both charge

---

[82] The increase in the corrosion rate for the weight loss experiments was greater than the PD sweep measurements; however, the PD sweeps show an identical trend for the corrosion rate with respect to NaCl concentration.

transfer processes as well as i_{Lim}. The reason for the decrease in the CO_2 corrosion rate in this NaCl concentration range was due to the decrease in the rates of both iron dissolution reaction and charge transfer controlled H^+ ion reduction reaction as well as the decrease in i_{Lim}.

A further important conclusion is that the rates of charge transfer processes were impacted more by increasing NaCl concentration compared to i_{Lim} because when NaCl concentration was increased from 1 wt.% to 20 wt.%, the corrosion current density decreased more than i_{Lim}.

Figure 10-21

The Evans diagram for the effect of NaCl concentration on uniform strong acid corrosion of X65 carbon steel RCE specimen with a rotational speed of 1000 rpm at 30°C, ~1 bar CO_2*, autogenous pH, and 1000 rpm rotational speed.* E_{corr} *is the corrosion potential (OPC),* i_{corr} *is the corrosion current density (Green: 0.1 wt.% NaCl, Blue: 1 wt.% NaCl, and red: 20 wt.% NaCl). A and B do not have the same axis scale.*

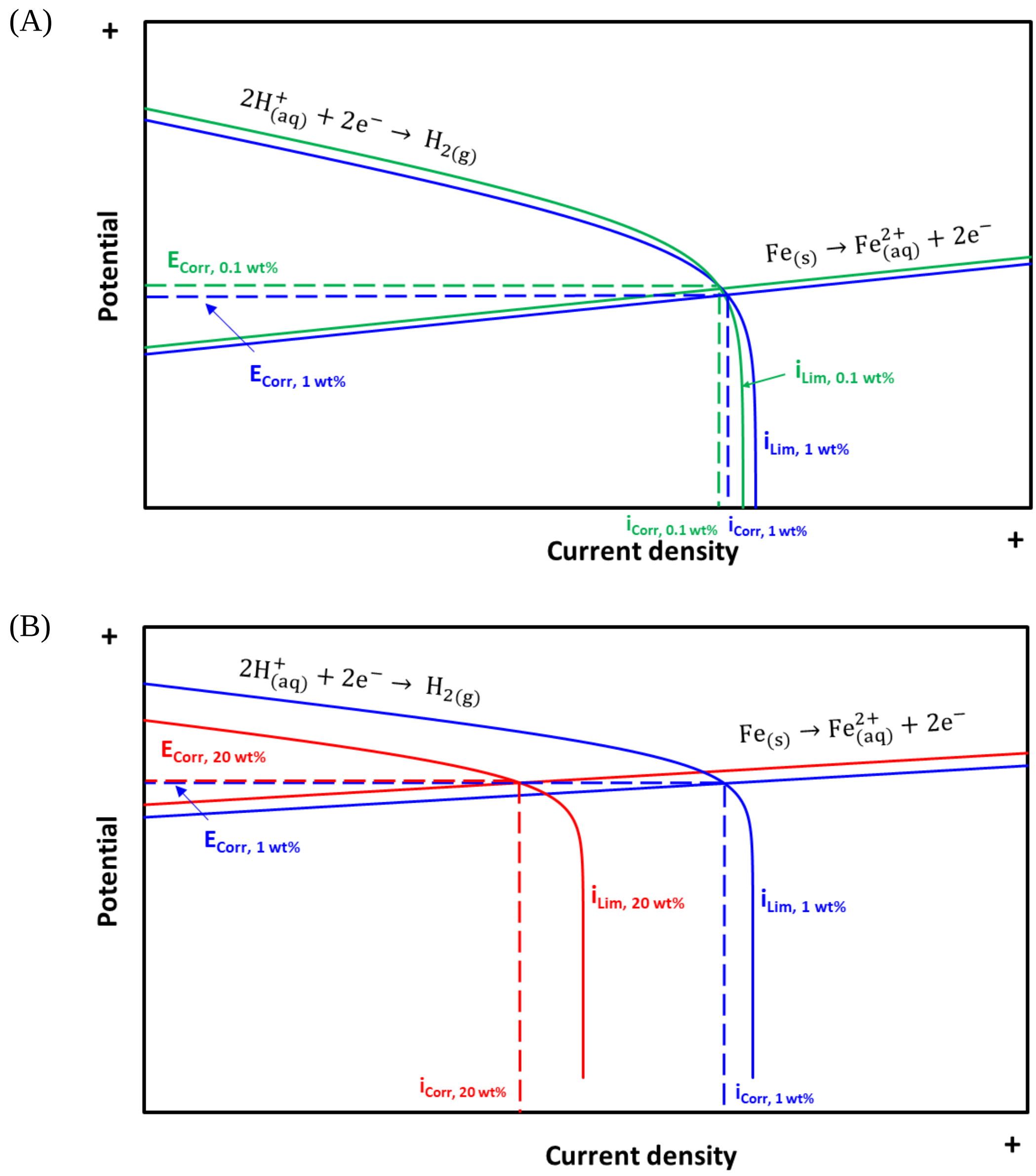

EIS measurements at different DC potentials were used to identify the reactions that are reflected by measurements. In Figure 10-22, the EIS spectrum was recorded at OCP and at 50 mV above and below OCP. For both 0.1 and 20 wt.% NaCl, the shape of the curves in the Nyquist plot does not change at these three potentials. Similar results were obtained for all the intermediate salt concentrations (not shown here). This indicates that the same or very similar reaction(s) are detected at these three potentials. The question then becomes which reaction(s) are behind the EIS spectra shown in Figure 10-22. If the magnitude of the impedance increases (*i.e.*, the reaction happens slower) when moving to more negative DC potentials, the anodic reaction is dominant in the measured impedance and if the impedance decreases the cathodic reaction is prevailing [305]. Since in Figure 10-22, the magnitude of the impedance increased when the DC potential was varied from +50 mV vs. OCP to -50 mV vs. OCP, the EIS measurements captured the anodic impedance mainly. Therefore, even if measurements were made at OCP where the magnitudes of the anodic and cathodic current densities are the same, the impedance data carry information predominantly about the anodic reaction.

Figure 10-22

EIS Nyquist plots at three DC potentials for X65 carbon steel RCE with a rotational speed of 1000 rpm exposed to CO_2 saturated solutions at 30°C, 1 bar total pressure, and autogenous pH: (A) 0.1 wt.%, (B) 20 wt.% NaCl.

(A)

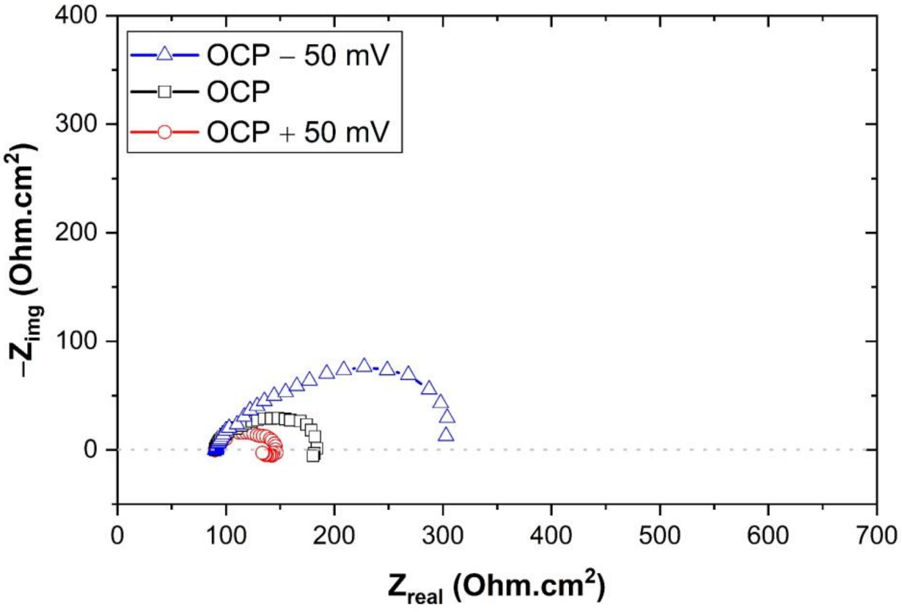

(B)

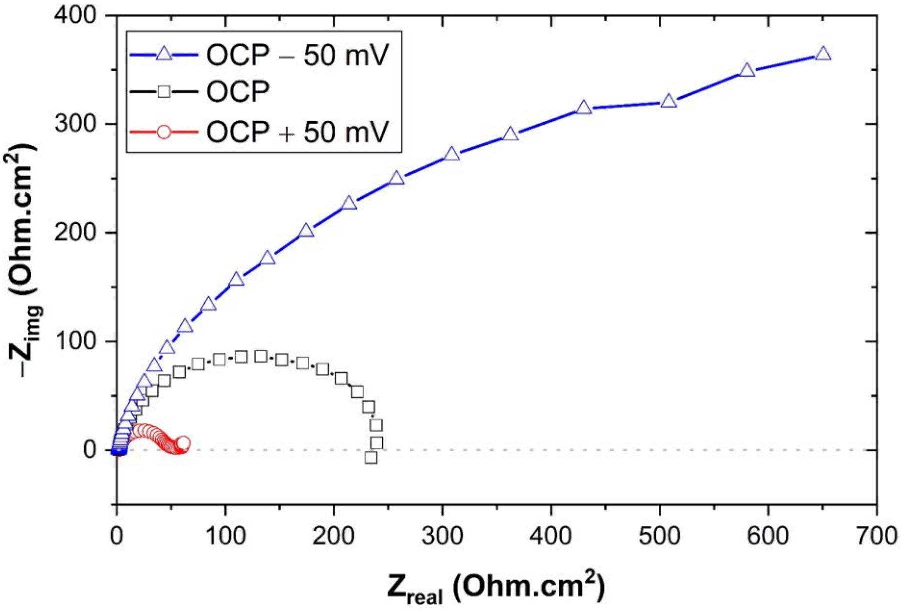

Figure 10-23 shows the impedance spectra at OCP for different NaCl concentrations. The solid data points in EIS spectra represent the characteristic frequencies ($f = 1/2\pi RC$), *i.e.*, the frequency at the maximum of $|Z_{img}|$. A depressed capacitive semicircle in the high-to-medium frequency range and an inductive loop in the low frequency range can be observed in the Nyquist plots. The diameter of the depressed capacitive semicircle estimates the resistance to charge-transfer controlled reaction, which is inversely proportional to the anodic reaction rate—in this case dissolution of iron.

Figure 10-23

EIS Nyquist spectra at OCP for X65 carbon steel RCE with a rotational speed of 1000 rpm exposed to CO_2 saturated solutions in different NaCl concentrations at 30°C, 1 bar total pressure, and autogenous pH. The solution resistance is subtracted from all spectra for a better comparison. The characteristic frequencies (solid data symbols) are 1.77 Hz, 3.16 Hz, 4.26 Hz, 2.37 Hz, and 1.34 Hz for 0.1, 1, 3, 10, and 20 wt.% NaCl, respectively.

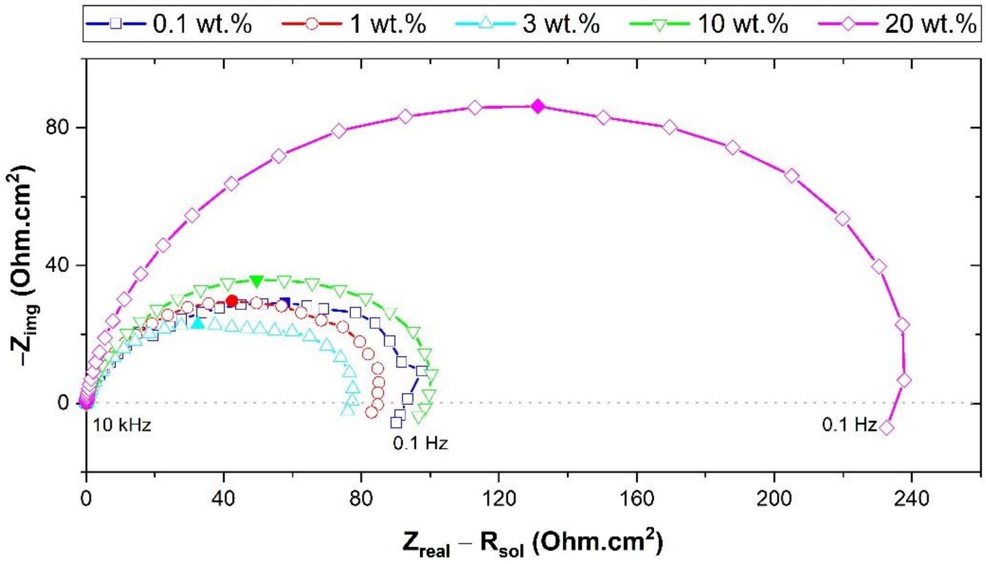

The magnitude of the impedance initially decreased with salt concentrations, meaning that the rate of the anodic reaction increased between 0.1 and 3 wt.% NaCl. At even higher salt concentrations, the trend was reversed. The observed trend here with respect to NaCl concentration is the same as that seen in Figure 10-20 B for i_o^{Fe}. The presence of an inductive loop is usually associated with the relaxation (the delay in the response of a system after an external perturbation [306]) of adsorbed water-iron intermediate species on the surface [307]. This means that the inductive loop is related to the Fe dissolution mechanism and is not associated to the presence of CO_2. However, Zeng *et al.* [12] reported that this type of inductive loop was not observed when the solution was sparged with air. The results of das Chagas Almeida [204] in N_2-containing solution seems to not have the inductive loop at high frequencies. This implies that the inductive loop is somehow related to the presence of dissolved CO_2 in the solution.

Figure 10-24 compares the EIS charge transfer resistance (R_{ct}) and the LPR polarization resistance (R_p). The R_p is here directly comparable to the R_{ct} because the frequency corresponding to the LPR measurements (0.0125 Hz) is almost the same as the one used for determining the R_{ct} from the Nyquist diagrams. The calculated R_{ct} is slightly higher than the R_p in the whole range of salt concentrations, most likely because LPR cannot distinguish between the faradaic and non-faradaic processes. The measured R_p includes a combination of effects from all processes that affect the charge transfer including double layer charging, adsorption of intermediate species on the surface, etc. EIS has this advantage over LPR and other DC techniques that the resistance related to the charge transfer reactions can be separated from that related to other processes [308]. The R_{ct} obtained with EIS decreased with increasing NaCl concentration from 0.1 to 3 wt.%, and then increased continuously with higher NaCl concentrations. In similar studies, Eliyan *et al.* [8,309] reported a decrease in the R_{ct} with increasing NaCl concentration up to ~ 7 wt.% (80 g/l). However, NaCl concentrations higher than 7 wt.% were not examined in their study.

Figure 10-24

Comparison of EIS charge transfer resistance (R_{ct}) with LPR polarization resistance (R_P) at different NaCl concentrations. R_{ct} and R_P are obtained in the same experiment with an X65 carbon steel RCE with a rotational speed of 1000 rpm in a CO_2 saturated solution at 30°C, 1 bar total pressure, and autogenous pH.

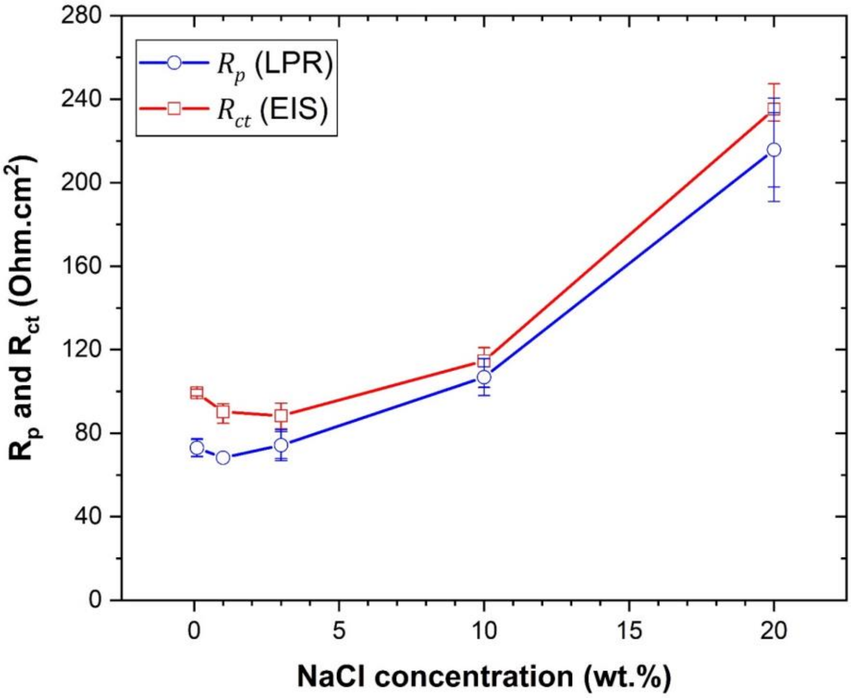

10.2.3 Summary and Conclusions of RCE CO_2 Corrosion Experiments at Autogenous pH and 1 bar CO_2

The effect of salt concentration was investigated on uniform corrosion of X65 carbon steel by carrying out wight loss and electrochemical experiments with an RCE setup at a rotational speed of 1000 rpm in CO_2-saturated solutions at 30°C, 1 bar total pressure, and autogenous pH. The following are major conclusions found in this set of experiments, when NaCl concentration was increased from 0.1 wt.% to 20 wt.%:

1. The decrease in autogenous pH of solution is due to the variations in the activity coefficients of dissolved species, particularly H^+ ion, and is not related to the decrease in CO_2 solubility.
2. The corrosion rate increased sharply and reached its maximum value at about 1 wt.% NaCl and then decreased monotonously with further increase in NaCl concentration.
3. Analysis of PD sweeps indicated that the variation in the corrosion rate with increasing NaCl concentration was primarily attributed to the change in the cathodic limiting current density, which was the predominant factor controlling the rate of the overall corrosion process. The additional factor was the rate of the anodic reaction, which had a similar trend to the corrosion rate when NaCl concentration was increased.
4. The variation in the cathodic limiting current density with respect to NaCl concentration is mainly attributed to the changes in activity and activity coefficient of H^+ ion as well as H^+ diffusion coefficient.

10.3 The Effect of Salt Concentration on CO_2 Corrosion at 20°C, 1 bar CO_2, and pH 5 Using a Rotating Cylinder Electrode (RCE)

This set of experiments was done at pH 5 to amplify the CO_2 buffering effect contribution in the CO_2 corrosion process. Moreover, contrary to the previous set of experiments that pH of solution was allowed to change with NaCl concentration, pH was kept constant at 5.0 for all salt concentrations, so that the only parameter changed in the experiments was NaCl concentration. The combination of these two granted a better understanding of the effect of salt concentration on the CO_2 corrosion process.

10.3.1 Experimental Materials and Methodology for RCE CO_2 Corrosion Experiments at 20°C and pH 5

This set of experiments were carried out at 20°C and 1 bar total pressure ($pCO_2 \cong 0.98$ bar) in a 2-liter glass cell as shown in Figure 10-25. A coil with cooling fluid (glycol) being circulated through it by an industrial chiller was used around the glass cell to cool down the solution temperature. Glycol did not have any contact with the experimental solution. In combination with the cooling coil, a hot plate was used continuously to balance the temperature at 20 ± 0.5°C.

Figure 10-25

(A) Schematic; (B) picture of the experimental apparatus and a zoomed-in view of the experimental glass cell used in the RCE CO_2 corrosion experiments at 20^oC, ~1 bar CO_2 and pH 5.

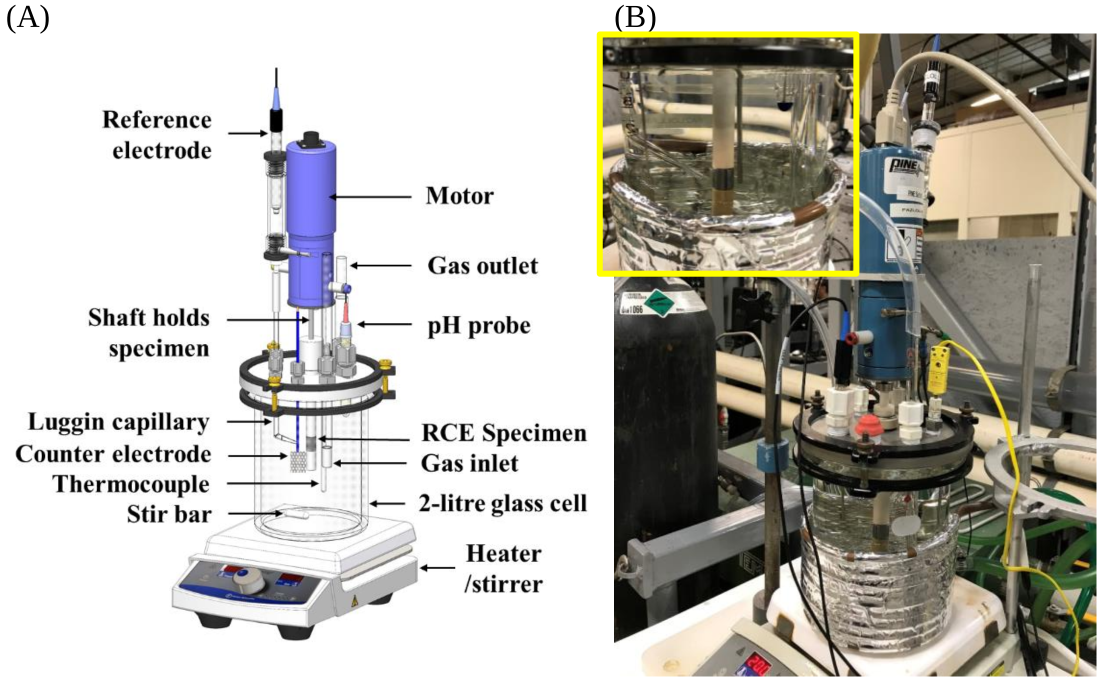

Five NaCl concentrations of 0.1 wt.% (0.017 m), 1 wt.%, 3 wt.%, 10 wt.%, and 20 wt.% (4.28 m) were tested in this set of experiments to study the effect of salt concentration on CO_2 corrosion. For each experiment, the desired amount of NaCl was dissolved in deionized water (conductivity < 1 μS/cm) in the glass cell. Then, the solution was sparged with pure CO_2 gas for at least 2 h, while being stirred by a magnetic stirrer. A rotameter was used to adjust CO_2 gas volumetric flow rate into the glass cell. 2 h was identified experimentally as the least amount of time needed to drop the concentration of dissolved oxygen in the solution to less than 10 ppb and saturate the solution with the experimental gas. The dissolved oxygen was measured during the experiments with an Orbisphere 410 oxygen meter connected to the gas outlet (Figure 10-26) to make sure that oxygen level in the solution was less than 10 ppb. The solution pH was continuously monitored during the experiments. A steady solution pH value for at least 15 min was used as an indication of the solution being saturated with the experimental gas. Double-junction pH probes were used for the pH measurements, as they are suitable for applications in high salinity due to their resistance to Na^+ ion interference [10].

Figure 10-26

A picture of the experimental apparatus used in the RCE CO_2 experiments at 20^oC, ~1 bar CO_2, and pH 5.

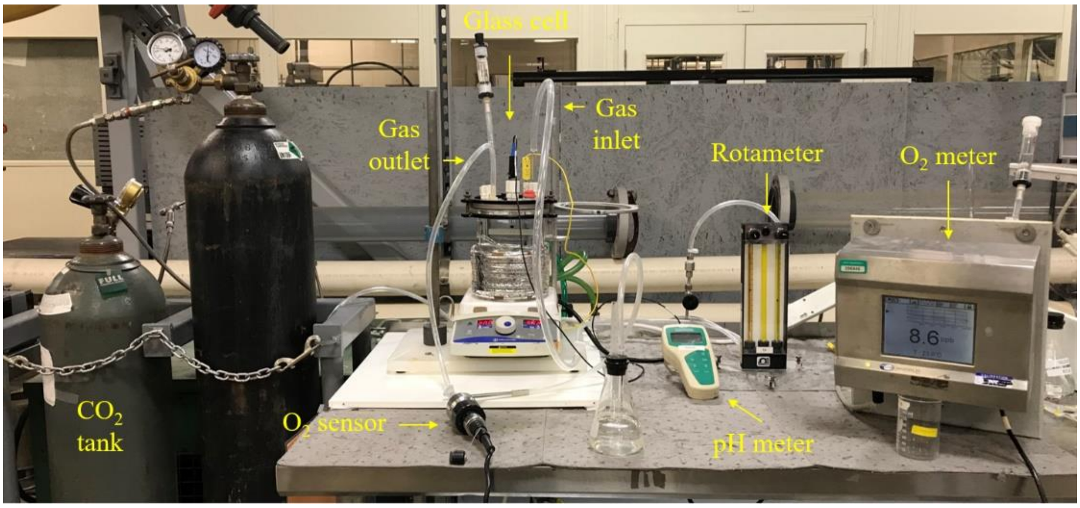

The solution pH was adjusted to pH 5.00 by injecting deaerated NaOH 0.1 M to the solution, after reaching a stable solution pH. The solution was sparged with $CO_{2(g)}$ for another 0.5 h prior to insertion of the specimen(s) in the solution and before beginning the corrosion rate or electrochemical measurements to ensure that solution pH was fixed at 5.00. The magnetic stirrer was stopped throughout the measurements.

The specimen material was API 5L X65 carbon steel. The chemical composition of X65 steel is listed in Table 9-1. Two types of specimens were used for the experiments: annulus specimens with an outer diameter of 12 mm, a length of 14 mm, and an outer surface area of 5.4 cm^2 (Figure 9-12 B), and square specimens with dimensions of 12.5 × 12.5 × 2.5 mm and a total surface area of 4.375 cm^2. A very small hole was drilled in a corner of the square specimen for passing a nylon thread through it. Prior to each experiment, the specimens were sequentially wet polished with 80-, 240-, 400- and 600-grit abrasive papers. Later, they were ultrasonically cleaned with isopropanol alcohol for 3 min and dried in a cool N_2 gas stream. The annulus specimen was flush mounted onto a shaft to be used as a rotating cylinder electrode (RCE) in the experiments. The square specimen was submerged into the experimental solution by hanging it with the nylon thread from the glass cell's lid.

Two separate sets of experiments were conducted: corrosion rate measurements to identify the overall effect of salt concentration on the CO_2 corrosion rate and PD sweeps to investigate how individual reaction mechanisms underlying CO_2 corrosion are affected by salt concentration.

For each corrosion rate measurement experiment, in addition to the RCE as the main specimen, three hanging square specimens were used to produce more results, and therefore have a more reliable analysis. The cell volume to specimen surface area ratio in the corrosion rate measurements was approximately 110 cm^3/cm^2, which was greater than the average minimum ratio of 30 cm^3/cm^2 suggested by ASTM G31 [15]. The RCE assembly was rotated at 1000 rpm, which simulates the mass transfer conditions in a 10 cm ID pipe with an average flow velocity of 1 m/s [301]. On the other hand, the square specimens were in a stationary condition and experienced less flow velocity compared to the RCE, and thus expected to corrode less compared to the RCE specimen. This implies that the effect of flow velocity on the corrosion rate was implicitly investigated in this study.

Corrosion rates were measured using weight loss (WL) and linear polarization resistance (LPR) techniques. The duration of each corrosion rate experiment was 24 h, which started from the moment specimens inserted into the solution and ended when they were retrieved from the solution. 24 h was identified to be an optimum time for obtaining sufficiently accurate WL measurements. Prior to immersion the specimens into the test solution, the specimens were weighed with a precise balance of 0.1 mg precision. The LPR corrosion rate measurement was performed concurrently with the WL corrosion rate measurement in the same experiment and by using the same specimen —on average every 6 h during the 24 h period (totally five times). The LPR technique was implemented using a three-electrode setup (shown in Figure 10-25) and by sweeping the potential in a range from -5 mV to +5 mV vs. OCP with a scan rate of 0.125 mV/s. Each LPR measurement lasted for 80 sec. The RCE acted as the working electrode in the LPR technique. A saturated Ag/AgCl reference electrode connected to a Luggin capillary served as the reference electrode and a platinized titanium mesh (20 mm × 30 mm) was used as the counter electrode to complete the three-electrode setup. The average Stern-Geary constant (B) for converting the measured polarization resistance into the corrosion rate was determined to be around 18.0 mV/dec. This was done by fitting the PD sweeps via an electrochemical model . The measured polarization resistance values were corrected for the solution resistance, which was measured by EIS. EIS was done prior to each LPR measurement with the same electrode setup at OCP in a frequency range of 10000-0.1

Hz with a peak-to-peak AC voltage amplitude of 10 mV. The LPR corrosion rates were determined by the cumulative trapezoidal integration of the five instantaneous LPR corrosion rates taken over the 24 h experiment. The increase in solution pH (due to increase in Fe^{2+} concentration in the solution because of corrosion) after 24 h was less than 0.08 pH units, at any NaCl concentration, which implies that there was no significant deviation of the water chemistry and accumulation of corrosion products in the experiments.

After 24 h, the RCE and square specimens were retrieved from the solution; thoroughly rinsed with distilled water for at least one minute to remove the salt, followed by rinsing with isopropanol alcohol and drying in a cool N_2 gas stream. Later, the specimens were weighed again to determine the WL corrosion rates. Immediately after the final weighing to analyze the morphology and chemical composition of the corroded surface, one square specimen was used for scanning electron microscopy/energy dispersive spectroscopy (SEM/EDS) (Figure 10-27 A), one was mounted in epoxy with its smallest surface upward for the cross-section analysis (Figure 10-27 B), and one was used for the surface profilometry (Figure 10-27 C).

Figure 10-27

Surface analysis specimens: (A) a picture of a square specimen and SEM/EDS specimen holder and a schematic of specimen orientation with respect to SEM/EDS beam, (B) a picture of a square specimen mounted in epoxy for SEM/EDS cross section analysis and a schematic of specimen orientation with respect to SEM/EDS beam, and (C) a schematic of the specimen orientation with respect to Infinite Focus Microscope beam for surface profilometry

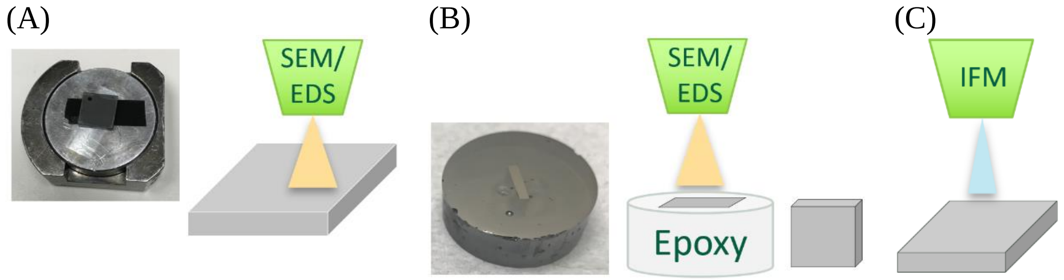

For the PD sweeps only the RCE specimen was used. The cell volume to specimen surface area was approximately 400 cm^3/cm^2 in this case. Before starting to sweep the potential, the open circuit potential (OCP) was monitored to ensure having a stable OCP value (Δ_{OCP} < 2 mV/min). The PD sweep experiments were performed according to the following steps: (1) a cathodic sweep starting from the OCP toward more negative potentials up to -1 V vs. OCP; (2) wait for the OCP to return near its initial value—within a few mV (this took about 1 h); (3) an anodic sweep starting from the OCP to more positive potentials up to 0.35 V vs. OCP. The PD sweep scan rate was 0.125 mV/s. All the PD sweeps were corrected for the solution resistance obtained by EIS. A Gamry potentiostat Reference 600 was used for all the electrochemical measurements. The increase in solution pH for the PD sweep experiments, each lasted about 4 h, was less than 0.05 pH units, for any NaCl concentration.

10.3.2 Results and Discussion for RCE CO_2 Corrosion Experiments at 20°C and pH5

10.3.2.1 pH Measurements and Solution Chemistry

Figure 10-28 shows the variation in autogenous pH of the CO_2 saturated solution with respect to NaCl concentration at 1 bar CO_2 and 20°C. The solution pH decreased from 3.88 at 0.1 wt.% NaCl to 3.48 at 20 wt.% NaCl. The reason behind such behavior is explained in detail in Section 10.2.2.

Figure 10-28

Autogenous pH of CO_2 saturated solutions measured at 20°C, and 1 bar total pressure (~ 0.98 bar pCO_2) before pH adjustment. The error bars represent the minimum and maximum values obtained in repeated experiments (with at least 4 repeats). The experimental data are compared with two speciation models.

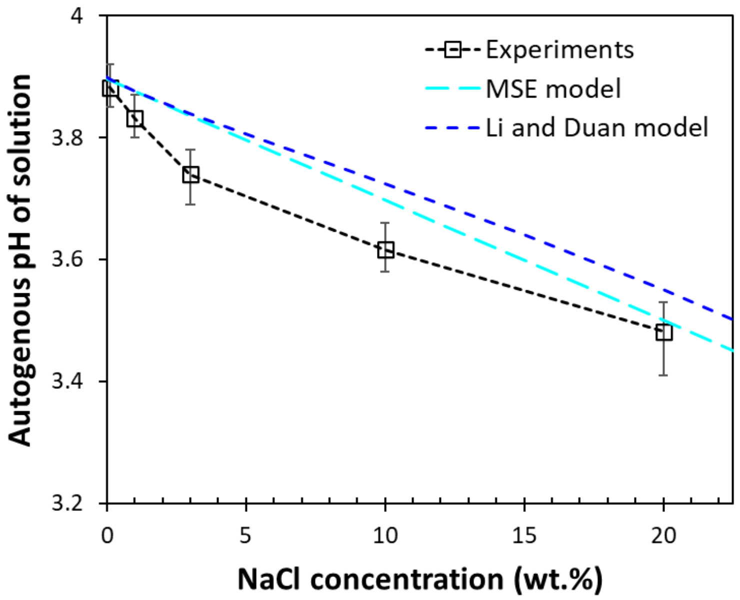

The predicted pH values obtained with the MSE model and the Li and Duan model are compared with the experimental pH values in Figure 10-28. Both models show a linear trend for pH with increasing NaCl concentration, while the experimental pH values have a concave upward trend with respect to NaCl concentration. The MSE model shows more accurate predictions compared to the Li and Duan model, specifically, at high NaCl concentrations.

Figure 10-29 shows the activity coefficient, the concentration, and the activity profiles of $CO_{2(aq)}$, $HCO_{3(aq)}^-$ ion, $H_{(aq)}^+$ ion, $OH_{(aq)}^-$ ion, $Cl_{(aq)}^-$, and $H_2O_{(l)}$ at 20°C, ~ 1 bar CO_2, and pH 5 calculated with the Li and Duan model. Since the partial pressure of CO_2 was almost constant[83] in the open system experiments, $CO_{2(aq)}$ activity is a horizontal line with respect to NaCl concentration (Figure 10-29 A). The solution pH was 5.00 for all NaCl concentration; therefore, $H_{(aq)}^+$ activity is constant for all NaCl concentrations (Figure 10-29 C). However, $H_{(aq)}^+$ concentration profile shows a maximum at 2 wt.% NaCl, whereas $H_{(aq)}^+$ activity coefficient decreases from 1.00 at 0 wt.% NaCl to 0.78 at 2 wt.% NaCl and then continually increases to 2.57 at 20 wt.% NaCl. The reason why $H_{(aq)}^+$ ion activity coefficient, and consequently $H_{(aq)}^+$ ion concentration has such trends with respect to NaCl concentration has been illustrated earlier in Figure 8-4.

---

[83] Water vapor pressure decreases slightly with increasing NaCl concentration [128]. Therefore, CO_2 partial pressure increases with increasing NaCl concentration. However, this increase is negligible and can be ignored.

Figure 10-29

Bulk concentration, molality-based activity coefficient, and activity of (A) dissolved CO_2, (B) bicarbonate ion, (C) H^+ ion, (D) OH^- ion, (E) Cl^- ion, and (F) H_2O calculated by the Li and Duan model speciation model for CO_2 saturated solutions at 20°C, 1 bar total pressure (~ 0.98 bar pCO_2), and pH 5.

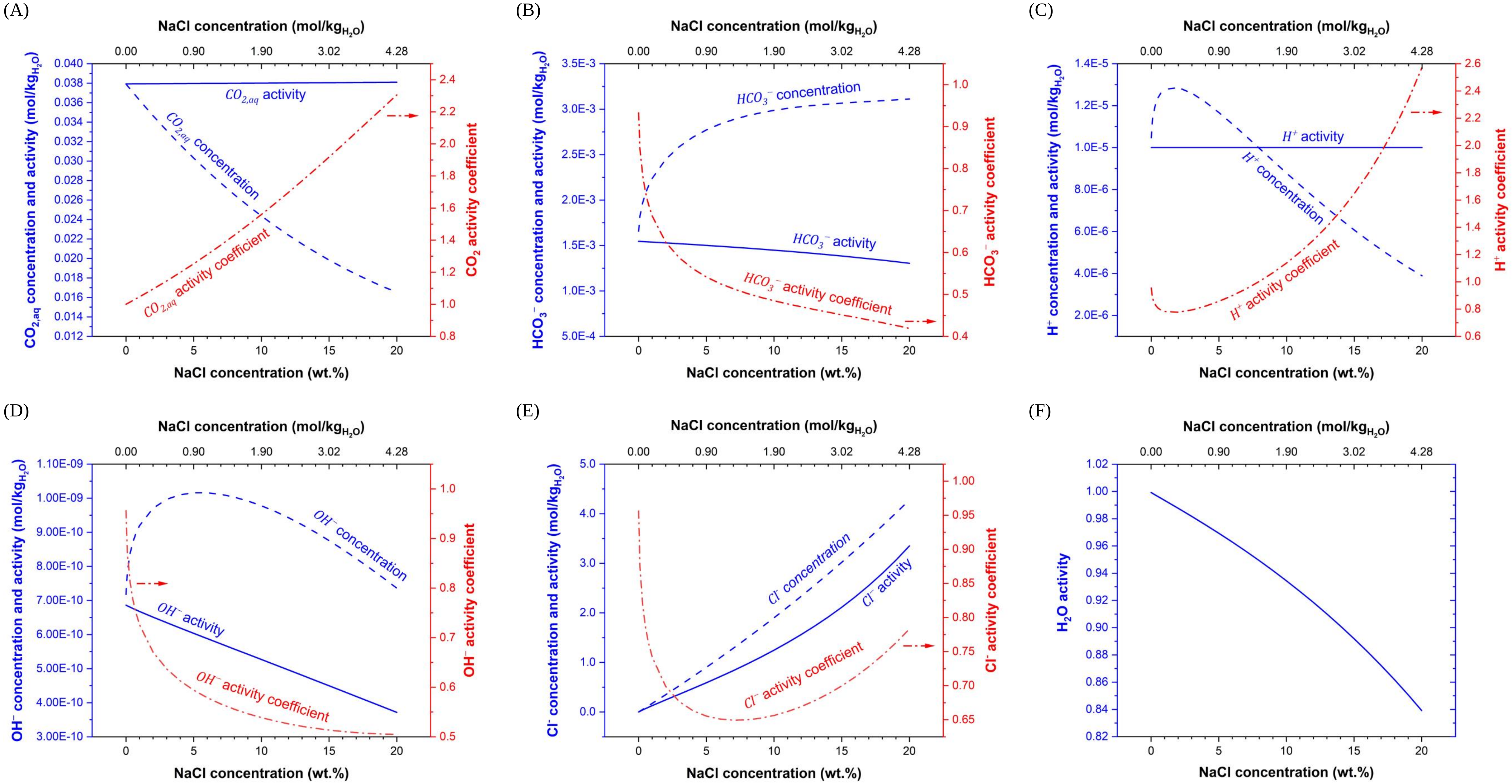

10.3.2.2 Corrosion rate and PD sweep measurements

Figure 10-30 presents the variations in the CO_2 corrosion rate with respect to NaCl concentration. A similar trend was observed for both specimen types. Additionally, similar corrosion rates were measured by two independent techniques: WL and LPR. These similarities between the trend and the magnitude of the corrosion rates promise the reliability of results and conclusions.

Figure 10-30

Variation in the corrosion rate with NaCl concentration for X65 carbon steel RCE with a rotational speed of 1000 rpm and square specimens exposed for 24 h to CO_2 saturated aqueous NaCl solutions at 20°C, 1 bar total pressure, and pH 5. The corrosion rates were measured using weight loss and LPR techniques. The error bars represent the minimum and maximum values obtained in repeated experiments (two repeats).

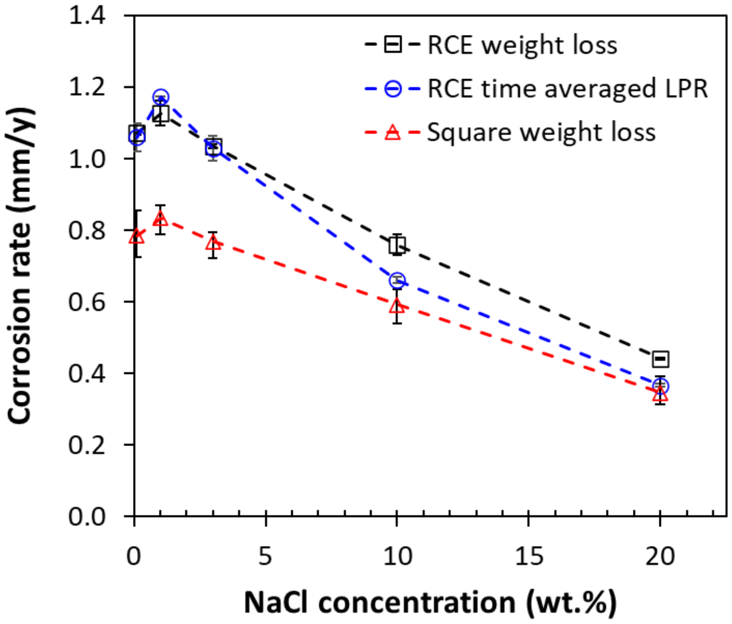

As anticipated, since the square specimens faced less flow velocity compared to the RCE specimen, the corrosion rate for the square specimens were smaller than that for the RCE specimen over the entire range of NaCl concentrations. The small difference observed between the WL and the LPR corrosion rates can be attributed to the fact that even though the LPR corrosion rates were averaged over 24 h, only 6 measurements were conducted in each experiment, which totally covered 8 mins of 24 h period (the duration of each LPR test was 80 s).

Figure 10-30 shows that the corrosion rate increased with increasing NaCl concentration and reached its maximum value at 1 wt.%. The corrosion rate then decreased continually with further increase in NaCl concentration up to 20 wt.% NaCl. The actual maximum in the corrosion rate could be at any NaCl concentration between 0.1 wt.% and 3 wt.%, as the experimental NaCl concentration increments were not adequately small to capture the location of the maximum. A similar behavior in the corrosion rate as a function of salt concentration was reported in Section 10.2.2 and also by other researchers [8,11,296,297]. The reflected trend in the corrosion rate can be explained by a thorough analysis of the variations in the PD sweeps and the solution chemistry with respect to NaCl concentration.

Figure 10-31 displays the PD sweeps at different NaCl concentrations. The potential values are corrected for the solution resistance (iR drop) in all the presented sweeps. For each NaCl concentration, at least two sets of PD sweeps were conducted. The magnitude of the scatter in the sweeps was reasonably small for all NaCl concentrations, as will be shown by the small error bars in the graphs for the kinetic features of the PD sweeps. This indicates the reproducibility of results and the reliability of conclusions. Only one of the sweeps at each NaCl concentration is presented in Figure 10-31 to avoid any overlapping. Varying NaCl concentration influenced both anodic and cathodic branches of the PD sweeps. There seems to be an acceleration and then a retardation in the rate of the anodic reaction with increasing NaCl concentration. The changes in the charge transfer part of the H^+ ion reduction reaction is not easily observable from the PD sweeps in Figure 10-31. However, obviously, there was a considerable change in the H^+ ion reduction reaction limiting current density (i_{Lim}) when NaCl concentration was increased. The water reduction reaction seems to remain untouched with increasing NaCl concentration. For a better understanding of the effect of NaCl concentration on the PD sweeps, kinetic features of the sweeps were extracted by overlaying the experimental sweeps for the best fit with those calculated by a simple electrochemical model [96][84].

---

[84] Activation energies of 59860 J/mol for H^+ ion, 24809 J/mol H_2O reduction and 25398 J/mol for Fe oxidation reactions. A reversible potential of -0.685 V vs. Ag/AgCl was used for all three reactions. The reference temperature was 20°C.

Figure 10-31

Potentiodynamic sweeps for X65 carbon steel RCE with a rotational speed of 1000 rpm exposed to CO_2 *saturated aqueous NaCl solutions at 20°C, 1 bar total pressure, and pH 5.*

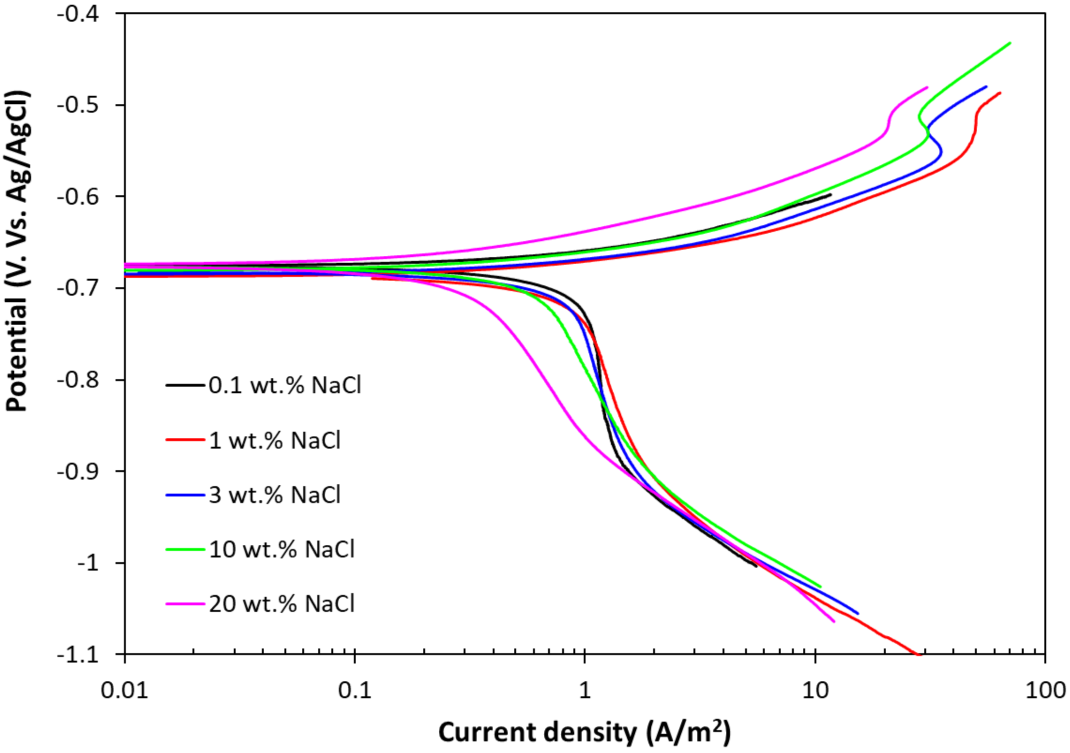

The electron transfer coefficients for H^+ reduction reaction (α_{H^+}) and Fe oxidation in the active region (α_{Fe}) at different NaCl concentrations are presented in Table 10-3. α_{H^+} values are identical to the theoretical value of 0.5, frequently considered for the hydrogen evolution on an iron surface [185]. Since α_{H^+} did not vary with increasing NaCl concentration, it can be concluded that the mechanism of hydrogen evolution under the experimental conditions of this part of study was not affected by the presence of salt.

Table 10-3

The average electron transfer coefficients for H^+ reduction reaction (α_{H^+}) and Fe oxidation (α_{Fe}) for the RCE CO_2 experiments at 20^oC, ~1 bar CO_2, and pH 5. Each data is an average of at least two measurements.

NaCl (wt.%)	0.1	1	3	10	20
α_{H^+}	0.50	0.51	0.50	0.50	0.50
β_c (mV/dec)	-116	-114	-116	-116	-116
α_{Fe}	1.20	1.20	1.25	1.25	1.20
β_a (mV/dec)	48	48	46	46	48

The α_{Fe} was almost 1.20 for all NaCl concentrations. The 0.05 difference for 3 wt.% and 10 wt.% NaCl concentrations are in the range of experimental scatters. Bockris *et al.* [185] proposed 1.5 for iron dissolution in acidic media without the presence of halides. In Section 9.1, an identical value of 1.20 was reported for α_{Fe} in strong acid experiments at pH 3. Additionally, Chin and Nobe [194] reported 1.18 for dissolution of iron in acidic chloride media, which is very close to the results of this set of experiments. Since α_{Fe} was almost constant over the entire range of NaCl concentrations, it leads to the conclusion that the mechanism of anodic dissolution of iron in the active region remained unchanged when NaCl concentration was increased. The mechanisms of iron dissolution in the presence of chloride and $CO_{2(g)}$ have been comprehensively explained in Chapter 5.

Figure 10-32 A shows the changes in the exchange current density (i_{o,H^+}) of the H^+ ion reduction reaction with increasing NaCl concentration. As mentioned in Chapter 5, the exchange current density is an indication of the rate of charge transfer for an electrochemical reaction. The decrease in i_{o,H^+} indicates that the rate of H^+ ion reduction reaction in the charge transfer region decreased when NaCl concentration was increased. The decrease in i_{o,H^+} with increasing NaCl concentration can be attributed to the adsorption of Cl^- ions on the surface and blocking the surface areas required for H^+ ion adsorption and reduction reactions [171]. A reason for the decreasing trend of the corrosion rate in Figure 10-30 at high NaCl concentrations could be the decrease in i_{o,H^+}. The trend observed for i_{o,H^+} in Figure 10-32 A can be modeled by using a correlation similar to Equation (5-23):

$$i_{o,H^+} = i_{o,H^+}^{ref} \left(\frac{a_{H^+,b}}{a_{H^+,b}^{ref}} \right)^{n_{H^+}^{H^+}} \left(\frac{a_{Cl^-,b}}{a_{Cl^-,b}^{ref}} \right)^{n_{Cl^-}^{H^+}} e^{-\frac{E_{a,H^+}}{R}\left(\frac{1}{T}-\frac{1}{T_{ref}}\right)} \tag{10-11}$$

where, i_{o,H^+}^{ref} is the reference current density in A/m^2 at T_{ref} (293.15 K) and -685 mV *vs.* Ag/AgCl, $a_{H^+,b}$ is the bulk activity of H^+ ion in molarity concentration, $a_{H^+,b}^{ref}$ is the reference bulk activity of H^+ ion (= 10^{-4} M), $n_{H^+}^{H^+}$ is the reaction order of the H^+ ion reduction reaction with respect to H^+ ion activity, $a_{Cl^-,b}$ is the bulk activity of Cl^- ion in molarity concentration, $a_{Cl^-,b}^{ref}$ is the reference bulk activity of Cl^- ion (= 1 M), $n_{Cl^-}^{H^+}$ is the reaction order of the H^+ ion reduction reaction with respect to Cl^- ion activity, E_{a,H^+} is the activation energy for the H^+ ion reduction reaction (= 59860 J/mol), T is solution temperature in K, and R is the gas constant in J/mol/K.

Equation (10-11) with the bulk activities calculated with the MSE model was fitted to the experimental i_{o,H^+} values in Figure 10-32 A to obtain the reaction orders and i_{o,H^+}^{ref}. Since the solution pH was constant in the experiments, the activity of H^+

ion was constant as well[85]. This means that $n_{H^+}^{H^+}$ cannot be determined from the fitting exercise. To be able to obtain $n_{H^+}^{H^+}$ experiments at different pH values are required. Therefore, an empirical value of 0.5 previously reported in the literature was chosen for $n_{H^+}^{H^+}$ [200,215]. The fitting exercise gave $n_{Cl^-}^{H^+}$ = -0.23 and i_{o,H^+}^{ref} = 5.1 A/m^2. The negative sign found for $n_{Cl^-}^{H^+}$ proves that Cl^- ion had an inhibition effect on the charge transfer rate for the H^+ ion reduction reaction.

---

[85] The changes in molarity-based activity due to changes in density with NaCl concentration is ignored.

Figure 10-32

Variations in (A) the cathodic limiting current density (i_{Lim}) and the H^+ reduction exchange current density (i_{o,H^+}) and (B) the Fe oxidation exchange current density ($i_{o,Fe}$) with NaCl concentration. The current densities were extracted from the PD sweeps of X65 carbon steel RCE specimen with a rotational speed of 1000 rpm exposed to CO_2-saturated aqueous solutions at 20°C, 1 bar total pressure, and pH 5. The error bars represent the minimum and maximum values obtained in two repeated experiments. The reference temperature was 20°C.

(A)

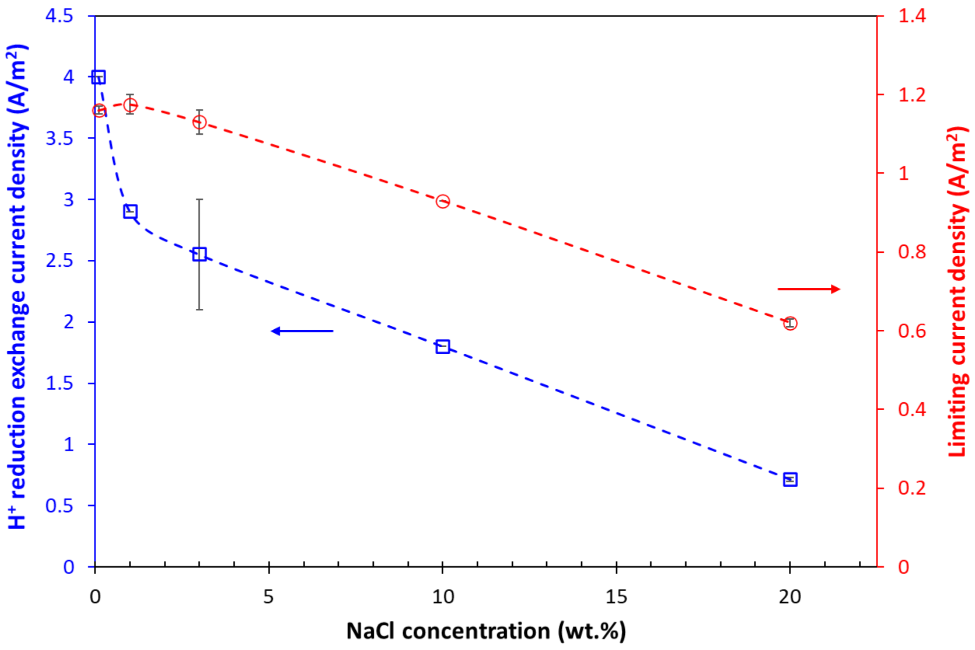

(B)

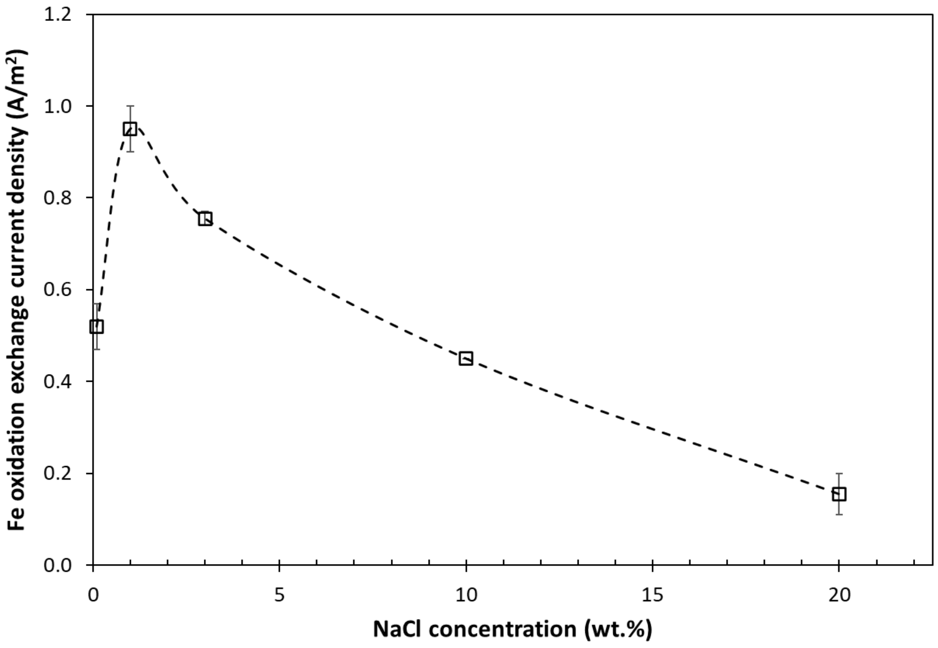

The variation of $i_{o,Fe}$ as a function of NaCl concentration is shown in Figure 10-32 B. $i_{o,Fe}$ indicates the rate of anodic dissolution of Fe in the active region. $i_{o,Fe}$ increased at lower NaCl concentrations and then switched trend and decreased at higher NaCl concentrations. The similarity of the $i_{o,Fe}$ trend to those reported previously in Sections 10.1 and 10.2 as well as to the RDE strong acid experiments shows the accuracy and consistency of the results. The $i_{o,Fe}$ trend in Figure 10-32 B is analogous to that reported for the CO_2 corrosion rate in Figure 10-30. Therefore, changes in $i_{o,Fe}$ with NaCl concentration is possibly another reason for the increase followed by the decrease in the CO_2 corrosion rate when NaCl concentration was increased from 0.1 wt.% to 20 wt.%.

The observed trend for $i_{o,Fe}$ can be justified by considering the changes in the activities of OH^- ion, Cl^- ion, and H_2O. According to Figure 10-29, the activities of OH^- ion and H_2O steadily decreases with increasing NaCl concentration, while the activity of Cl^- ion steadily increases. This results in the maximum seen in Figure 10-32 B for $i_{o,Fe}$. Following Equation (5-22), $i_{o,Fe}$ can be expressed in terms of activities of OH^- ion, Cl^- ion, and H_2O as follows:

$$i_{o,Fe} = i_{o,Fe}^{ref}\left(\frac{a_{OH^-,b}}{a_{OH^-,b}^{ref}}\right)^{n_{OH}^{Fe}}\left(\frac{a_{Cl^-,b}}{a_{Cl^-,b}^{ref}}\right)^{n_{Cl^-}^{Fe}}\left(\frac{a_{H_2O,b}}{a_{H_2O,b}^{ref}}\right)^{n_{H_2O}^{Fe}} e^{-\frac{E_{a,Fe}}{R}\left(\frac{1}{T}-\frac{1}{T_{ref}}\right)} \tag{10-12}$$

where, $i_{o,Fe}^{ref}$ is the reference current density in A/m^2 at T_{ref} (293.15 K) and -685 mV *vs.* Ag/AgCl, $a_{OH^-,b}$ is the bulk activity of OH^- ion in molarity concentration, $a_{OH^-,b}^{ref}$ is the reference bulk activity of OH^- ion (= 10^{-10} M), n_{OH}^{Fe} is the reaction order of the Fe oxidation reaction with respect to OH^- ion activity, $a_{Cl^-,b}$ is the bulk activity of Cl^-

ion in molarity concentration, $a_{Cl^-,b}^{ref}$ is the reference bulk activity of Cl$^-$ ion (= 1 M), $n_{Cl^-}^{Fe}$ is the reaction order of the Fe oxidation reaction with respect to Cl$^-$ ion activity, $a_{H_2O,b}$ is the bulk activity of liquid water in molarity unit, $a_{H_2O,b}^{ref}$ is the reference bulk activity of liquid water (= 55.4 M), $n_{H_2O}^{Fe}$ is the reaction order of the Fe oxidation reaction with respect to H_2O, and $E_{a,Fe}$ is the activation energy for the Fe oxidation reaction in the active region (= 25398 J/mol), T is solution temperature in K, and R is the gas constant in J/mol/K.

Lorenz [174] and McCafferty and Hackerman [178] reported different $n_{Cl^-}^{Fe}$ values for different range of Cl$^-$ activities (concentrations), as mentioned in Table 5-2. This indicates that the Fe dissolution reaction might proceed through different pathways depending on the activity of Cl$^-$ ion in the solution. From the $i_{o,Fe}$ trend presented in Figure 10-32 B, it can be assumed that at low NaCl concentrations below 1 wt.%[86], Cl$^-$ ions speeds up the anodic dissolution reaction by playing a catalytic role in iron dissolution, similar to that of OH$^-$ ions [172,194,195]. However, at NaCl concentrations above 1 wt.%, Cl$^-$ ions impedes the Fe dissolution reaction by being adsorbed on the surface and blocking the active sites (surface imperfections) required for the Fe dissolution reaction to happen [173,174,178,192]. Therefore, the $i_{o,Fe}$ curve is divided into two sections: below and above 1 wt.%. The reaction orders and $i_{o,Fe}^{ref}$ values for each region can be obtained by fitting Equation (10-12), using the bulk activity values calculated with the MSE model, to the experimental $i_{o,Fe}$ values. Obtaining n_{OH}^{Fe} value needs experimentation at different solution pH. This means that

---

[86] It can be any NaCl concentration between 1 wt.% and 3 wt.%, as the experimental NaCl resolution was not small enough to determine the exact maximum.

n_{OH}^{Fe} cannot be found from the data presented in Figure 10-32 B. Therefore, a value of 1 was chosen for n_{OH}^{Fe} for the whole range of NaCl concentration according to the Bockris *et al.* [185,186] consecutive mechanism and reports by other scientists [174,195] (see Table 5-2). For NaCl ≤ 1 wt.%, $n_{Cl^-}^{Fe}$= 0.22, $n_{H_2O}^{Fe}$ = 0, and $i_{o,Fe}^{ref}$ = 0.21 and for NaCl > 1, $n_{Cl^-}^{Fe}$= -0.26, $n_{H_2O}^{Fe}$ = 2, and $i_{o,Fe}^{ref}$ = 0.084. A reaction order of zero for H_2O at NaCl ≤ 1 means that the Fe dissolution reaction process is independent of H_2O activity in this NaCl concentration range. For $n_{H_2O}^{Fe}$ at high NaCl concentrations, the value found in this study is similar to the values (a range of 1.6-1.9) reported by Smart *et al.* [190,198].

The key change in the PD sweeps in Figure 10-31 with NaCl concentration is i_{Lim}. For the case of CO_2 corrosion, i_{Lim} is the rate of the cathodic H^+ ion reduction reaction when mass transfer of species to the metal surface coupled with the preceding homogenous CO_2 hydration chemical reaction is the slowest step.

Figure 10-32 A shows that i_{Lim} slightly increased when NaCl concentration was increased from 0.1 wt.% to 1 wt.%, and then decreased monotonously with further increase in NaCl concentration. The maximum in i_{Lim} could occur at any NaCl concentration between 0.1 wt.% and 3 wt.%. However, the more precise concentration at which i_{Lim} had its maximum cannot be specified as the resolution for the experimental NaCl was not sufficient.

The i_{Lim} in CO_2 corrosion depends principally on $a_{H^+}$and a_{CO_2}. This will be explained in detail in Chapter 12. It was shown in Figure 10-17 that both $a_{H^+}$and a_{CO_2}were constant over the entire range of NaCl concentrations. Therefore, a_{H^+} and a_{CO_2} cannot be the reason for the changes in i_{Lim} with NaCl concentration. i_{Lim} also depends on diffusion coefficients of H^+ ion and H_2CO_3 as well as their activity coefficients. The contributions of H^+ diffusion coefficient and its activity coefficient in the overall i_{Lim} value are dominant comparing to other parameters such as H_2CO_3 diffusion coefficient and its activity coefficient. Therefore, i_{Lim} trend follows changes in H^+ diffusion coefficient and its activity coefficient with NaCl concentration. i_{Lim} is directly related to H^+ ion diffusion coefficient and inversely related to H^+ ion activity coefficient. The slope of changes for H^+ ion activity coefficient with NaCl concentration is greater than that for H^+ ion diffusion coefficient. Therefore, the increase in i_{Lim} at low NaCl concentration is due to the decrease in H^+ activity coefficient as shown in Figure 10-17 C. On the other hand, the decreasing trend for i_{Lim} at NaCl concentrations greater than 3 wt.% is due to the increase in H^+ ion activity coefficients as well as the decrease in the diffusion coefficient of H^+ ion (the effect of salt concentration on the diffusion coefficient is explained in Section 3.3.2).

The observed trend for i_{Lim} with NaCl concentration in Figure 10-32 A is very similar to that reported for the corrosion rate in Figure 10-30. Thus, variation in i_{Lim} with NaCl concentration can be another reason for the measured changes in the corrosion rate with NaCl concentration.

Three possible reasons have been discussed for the effect of NaCl concentration on the CO_2 corrosion rate: changes in the charge transfer controlled H^+ reduction reaction rate (i_{o,H^+}), changes in the anodic dissolution rate of Fe ($i_{o,Fe}$), and changes in i_{Lim} with NaCl concentration. To identify which of these three parameters controlled the rate of CO_2 corrosion at the experimental conditions, the Evans diagram is employed.

Figure 10-33 shows the Evans diagrams for 0.1 wt.%, 1 wt.% and 20 wt.% NaCl concentrations at the experimental conditions used in this set of experiments. The comparison between 0.1 wt.% and 1 wt.% NaCl in Figure 10-33 A demonstrates that the corrosion process in this range of NaCl concentrations was controlled by charge transfer processes as i_{Lim} was almost the same for both NaCl concentrations. The Evans diagrams show that the rate of anodic dissolution of iron increased with increasing NaCl concentration from 0.1 wt.% to 1 wt.%, while the charge transfer H^+ reduction rate decreased. The net effect was a slight increase in the corrosion rate[87]. This indicates that at low NaCl concentration, the increase in the CO_2 corrosion rate was due to the increase in the rate of anodic dissolution of Fe as shown in Figure 10-32 B.

For NaCl concentrations higher than ~ 1 wt.%, the corrosion process was under mixed control. This means that the corrosion process was controlled by both charge transfer processes as well as i_{Lim}. The reason for the decrease in the CO_2 corrosion rate in this NaCl concentration range was due to retardation of both the iron dissolution reaction and the charge transfer controlled H^+ ion reduction reaction as well as the decrease in i_{Lim}.

Another important conclusion is that the rates of charge transfer processes were affected more by increasing NaCl concentration compared to i_{Lim} because the corrosion current density decreased more than i_{Lim}, when NaCl concentration was increased from 1 wt.% to 20 wt.%. These conclusions were also reported for the RCE CO_2 experiments at 30°C and autogenous pH in Section 10.2.

---

[87] The increase in the corrosion rate for the weight loss experiments was greater than the PD sweep measurements; however, the PD sweeps show an identical trend for the corrosion rate with respect to NaCl concentration.

Figure 10-33

The Evans diagrams for the effect of NaCl concentration on uniform CO_2 corrosion of X65 carbon steel RCE specimen with a rotational speed of 1000 rpm at 20°C, ~1 bar CO_2, pH 5, and 1000 rpm rotational speed. E_{corr} *is the corrosion potential (OPC),* i_{corr} *is the corrosion current density (Green: 0.1 wt.% NaCl, Blue: 1 wt.% NaCl, and red: 20 wt.% NaCl). A and B do not have the same axis scale.*

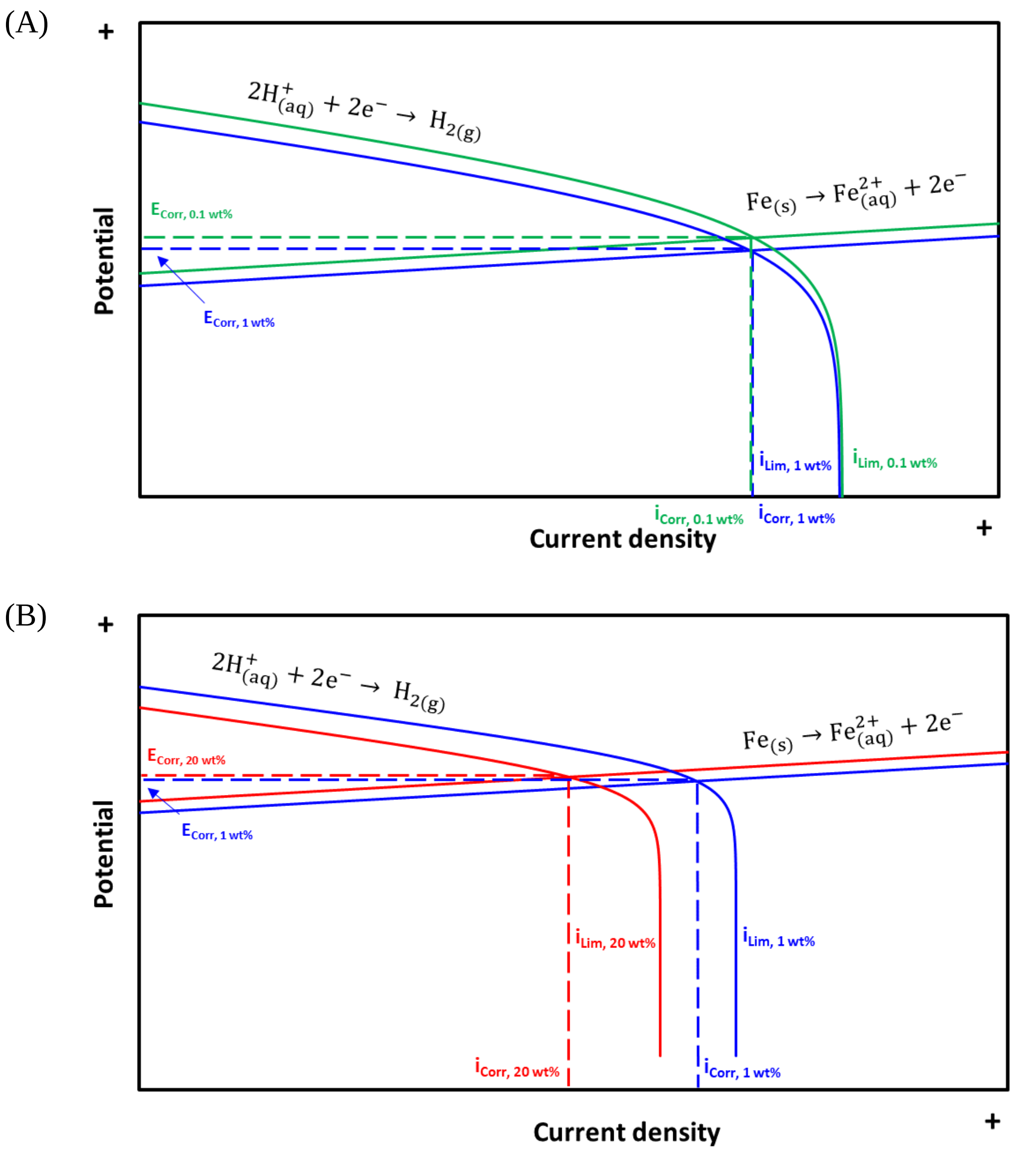

10.3.2.3 Corroded surface analysis

Figure 10-34 illustrates the surface morphology SEM images of the corroded square specimens after exposure to solutions with different NaCl concentrations. The SEM image of a freshly polished specimen is also shown for reference. The surface morphology for all NaCl concentrations is similar. One cannot see any indication of surface layers being formed, except for a small amount of what is assumed to be iron carbide (cementite), which is the uncorroded portion of the steel matrix leftover after the ferrite phase dissolved. There is no visible evidence of localized attack, and it can be concluded that the surface was corroded uniformly.

Figure 10-34

SEM images of the corroded carbon steel X65 square specimens in CO_2-statuarated solutions with different NaCl concentrations at 20°C, 1 bar total pressure, and pH 5. Secondary electron imaging was used to take the images.

Freshly polsihed surface

0.1 wt.% NaCl

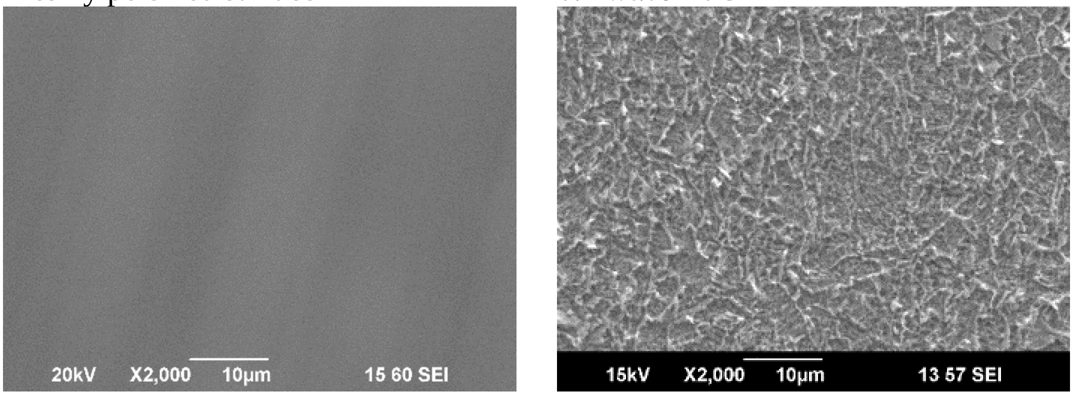

1 wt.% NaCl

3 wt.% NaCl

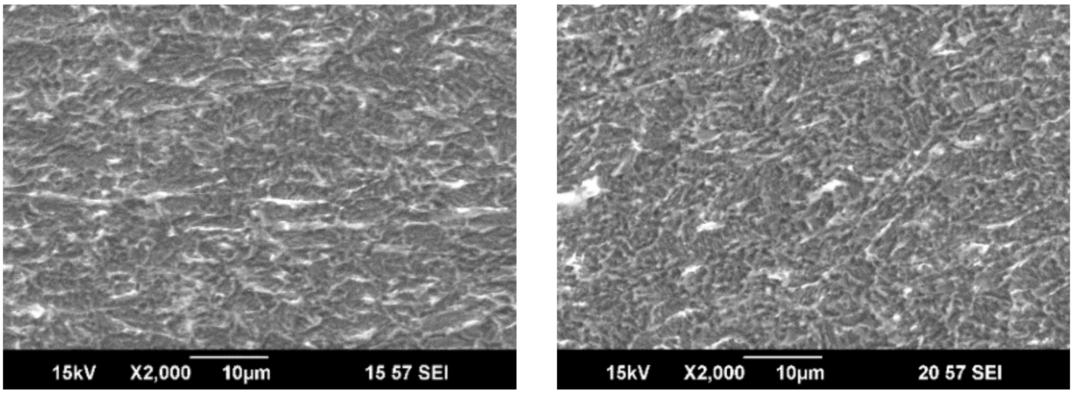

10 wt.% NaCl

20 wt.% NaCl

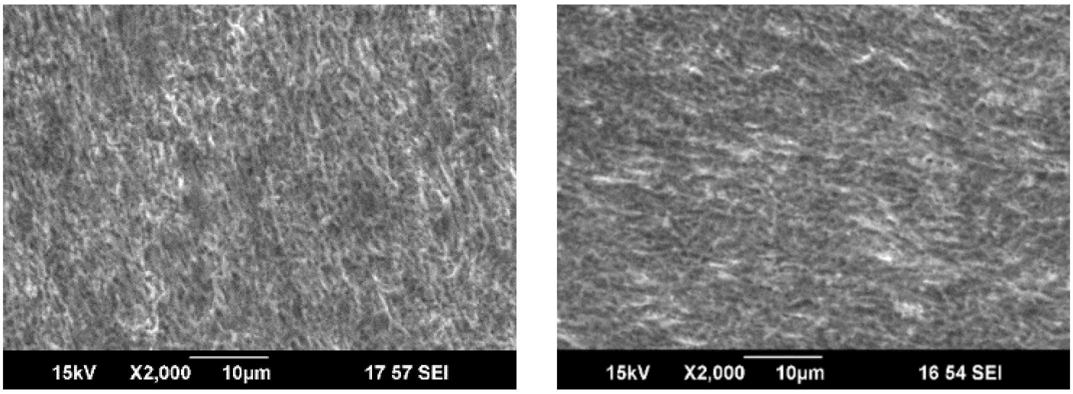

Figure 10-35 presents the EDS analysis of the corroded specimens after exposure to solutions with different NaCl concentrations. The EDS analysis of a freshly polished specimen is included for comparison. The atomic concentrations of elements included in the analysis, Fe, C, Mn, Si, Al, and O, have been normalized to give a total of 100%. The elements P, S, Cl, Ni, Cu, and Mo, which were found to be in trace amounts, are not listed in the elemental composition. Very similar surface composition is detected for all specimens, the only significant difference being the absence of oxygen on the surface of the freshly polished specimen. This suggests that a minute amount of iron carbonate and/or iron oxide might have formed during the experiments or after retrieving the specimens and before they were analyzed by EDS.

Figure 10-35

EDS surface elemental composition analysis of the corroded carbon steel X65 square specimens in CO_2-saturated solutions with different NaCl concentrations at 20°C, 1 bar total pressure, and pH 5. The elemental concentrations are in normalized atomic percentage.

Freshly polsihed surface

0.1 wt.% NaCl

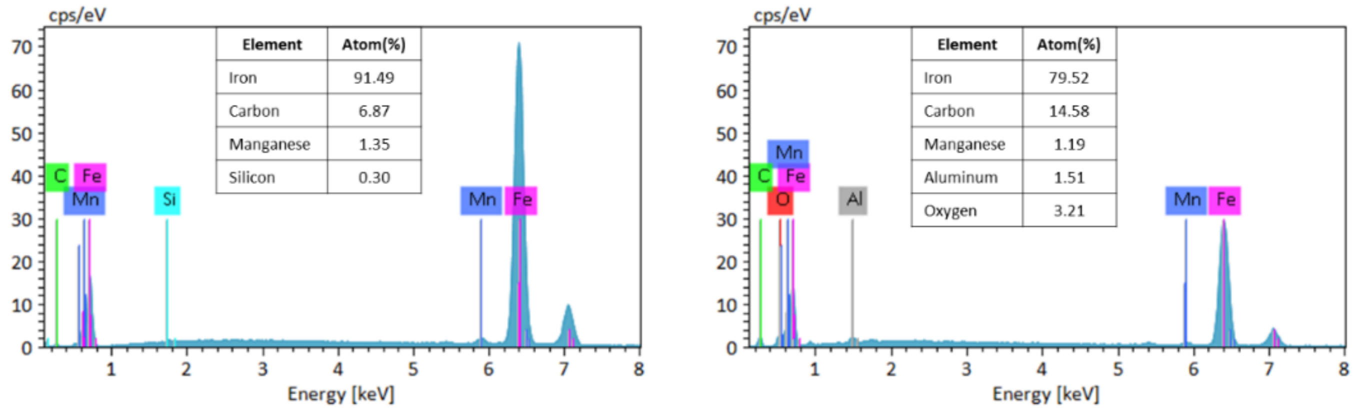

Element	Atom(%)
Iron	91.49
Carbon	6.87
Manganese	1.35
Silicon	0.30

Element	Atom(%)
Iron	79.52
Carbon	14.58
Manganese	1.19
Aluminum	1.51
Oxygen	3.21

1 wt.% NaCl

3 wt.% NaCl

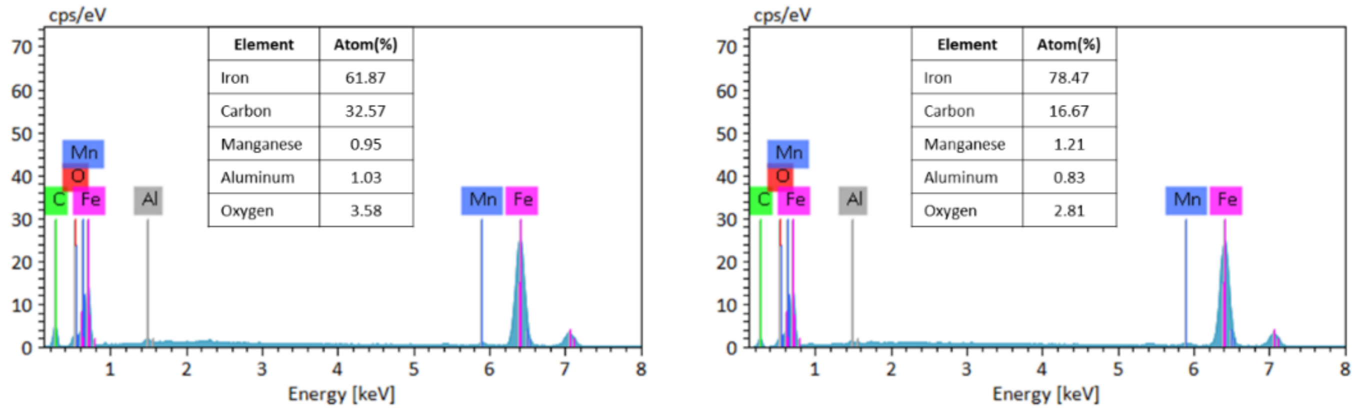

Element	Atom(%)
Iron	61.87
Carbon	32.57
Manganese	0.95
Aluminum	1.03
Oxygen	3.58

Element	Atom(%)
Iron	78.47
Carbon	16.67
Manganese	1.21
Aluminum	0.83
Oxygen	2.81

10 wt.% NaCl

20 wt.% NaCl

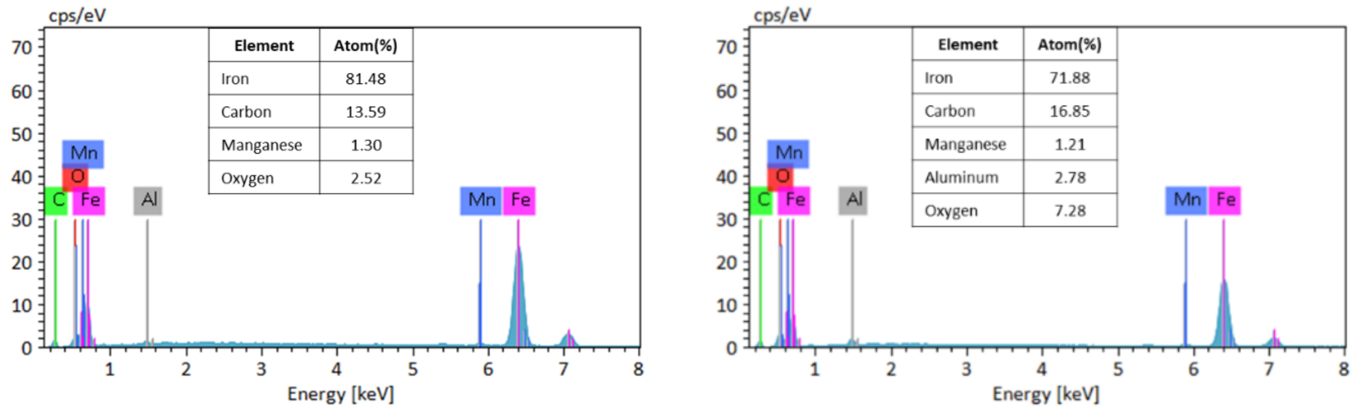

Element	Atom(%)
Iron	81.48
Carbon	13.59
Manganese	1.30
Oxygen	2.52

Element	Atom(%)
Iron	71.88
Carbon	16.85
Manganese	1.21
Aluminum	2.78
Oxygen	7.28

Figure 10-36 shows the cross-section SEM images and their corresponding EDS elemental mapping analysis of the corroded square specimens. The light gray surface in the bottom of the SEM images is the steel matrix as detected Fe by EDS analysis. The black (or dark gray) at the top of the SEM images is the epoxy used for mounting the square specimens. Since the epoxy was polymeric, the EDS analysis detected it as carbon (C). The cross-section SEM images coupled with the EDS elemental maps show that no corrosion layer formed on the surface for any NaCl concentration. These observations prove that the surface was corroded uniformly under the experimental conditions used in this part of study. At 10 wt.% NaCl there seems to be a layer on the steel surface. However, this apparent layer is just a gap between the steel surface and the epoxy that surrounded it.

Figure 10-36

Cross section SEM images and EDS elemental mapping analysis of the corroded carbon steel X65 square specimens in CO_2-saturated NaCl aqueous solutions at 20°C, 1 bar total pressure, and pH 5.

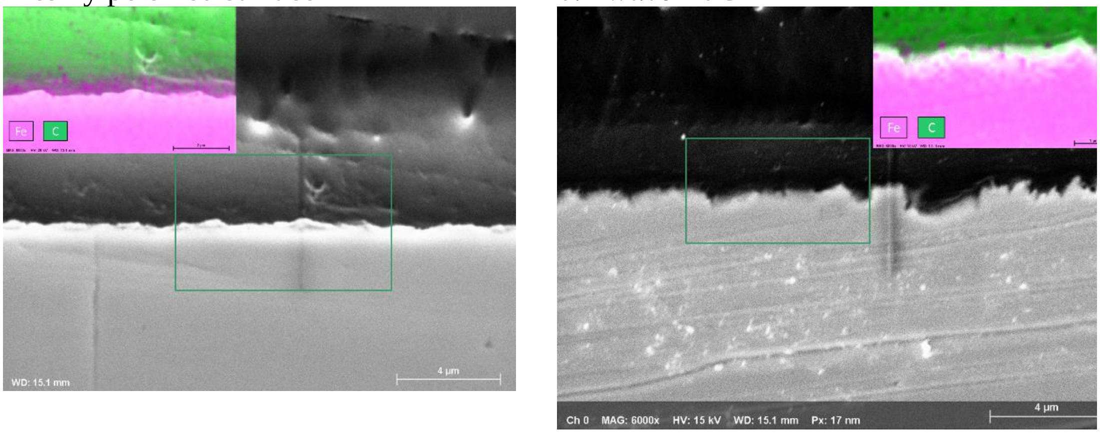

Freshly polsihed surface

0.1 wt.% NaCl

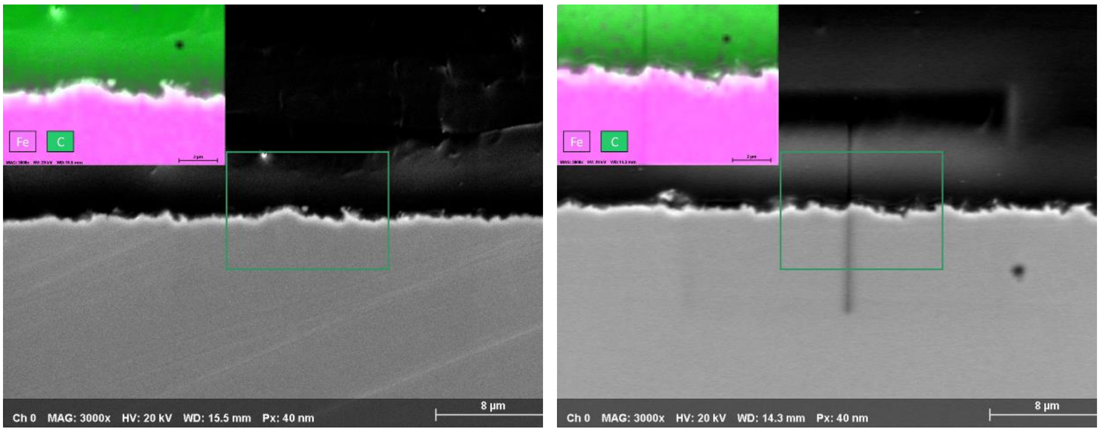

1 wt.% NaCl

3 wt.% NaCl

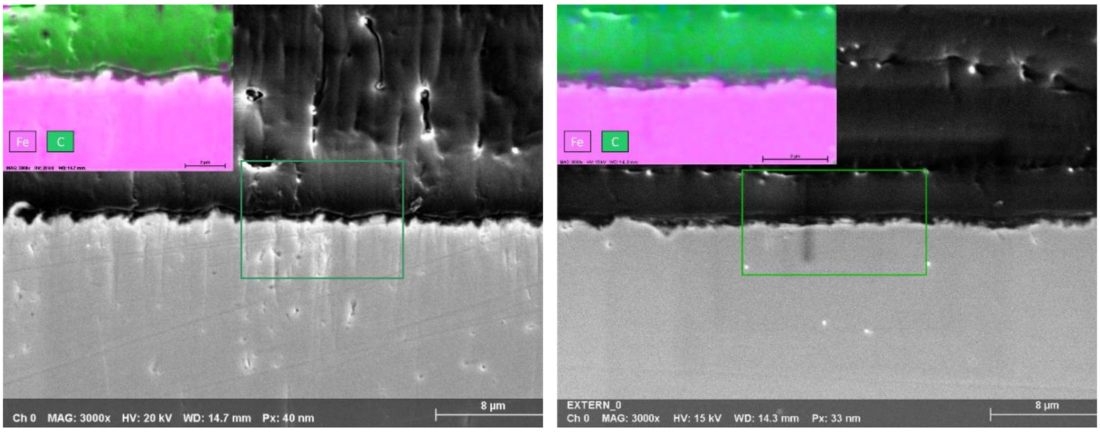

10 wt.% NaCl

20 wt.% NaCl

To make sure that the surface was corroded uniformly at the experimental conditions used in this part of the study, surface profilometry was performed. The advantage of surface profilometry over SEM/EDS analysis is that it can cover a larger surface area, and therefore, it is more a more effective way in identifying localized corrosion (or pits) across the entire surface of a specimen. Figure 10-37 shows the one-dimensional (1D) and two-dimensional (2D) surface roughness profiles of the corroded square specimens exposed to the experimental conditions at different NaCl concentrations. 1D profiles show no sudden change in the surface roughness at any NaCl concentration, which is an indication of uniform corrosion. The uniform blue color on the whole surface of the 2D profiles confirms that CO_2 corrosion occurred uniformly under the experimental conditions for all NaCl concentrations. The purple color (*i.e.*, the presence of hills) seen on surface of some of the 2D profiles (*e.g.*, for 20 wt.%) was due to uneven polishing of the surface during the specimen preparation.

Figure 10-37

1D and 2D surface roughness profilometry of the corroded square specimens in CO_2-satuared solutions with different NaCl concentrations at 20°C, 1 bar total pressure, and pH 5. The length of the black scale bars is equivalent to 0.5 mm.

0.1 wt.% NaCl

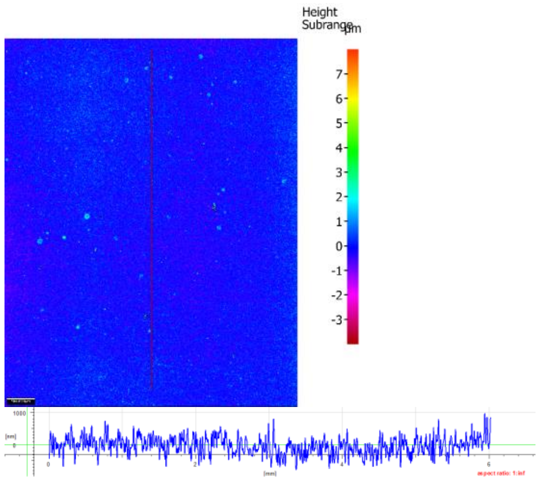

1 wt.% NaCl

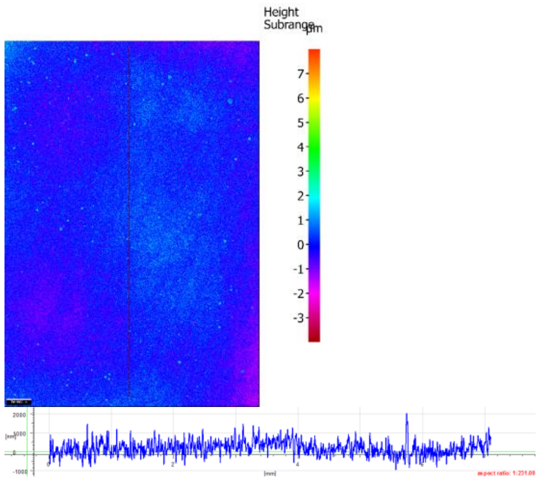

3 wt.% NaCl

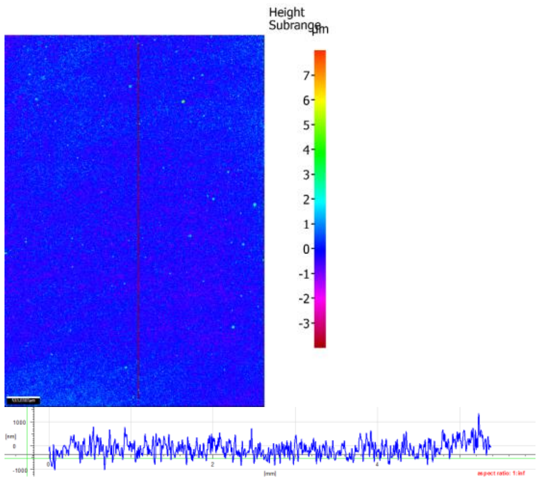

10 wt.% NaCl

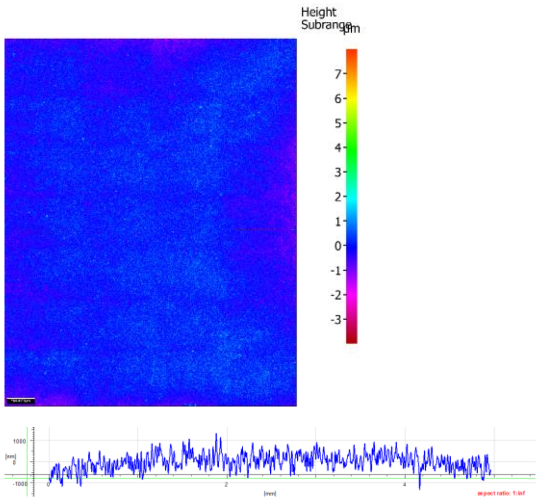

20 wt.% NaCl

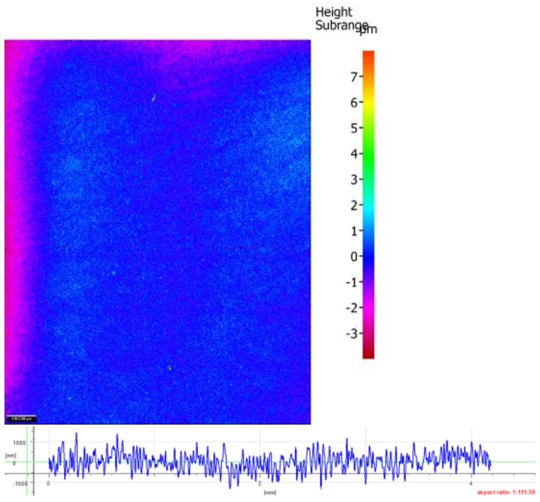

10.3.3 Summary and Conclusions of RCE CO_2 Corrosion Experiments at Autogenous pH and 1 bar CO_2

The effect of salt concentration was studied on uniform CO_2 corrosion of X65 carbon steel by carrying out wight loss and electrochemical experiments with an RCE setup at a rotational speed of 1000 rpm in CO_2-saturated solutions at 20°C, 1 bar total pressure, and pH 5. When NaCl concentration was increased from 0.1 wt.% to 20 wt.%, the major conclusions from this set of experiments are:

1. The autogenous pH of solution deceased. The decrease in pH was related to the variations in the activity coefficients of dissolved species, particularly H^+ ion.
2. The corrosion rate increased and reached its maximum value at about 1 wt.% NaCl and then decreased steadily with further increase in NaCl concentration.
3. Analysis of PD sweeps indicated that the increase in the CO_2 corrosion rate at low NaCl concentrations below ~ 1 wt.% was due to the acceleration of the active dissolution reaction of iron. This means the slope of increase in the rate of the anodic dissolution of iron was greater than the slope of decrease in the rate of the H^+ ion reduction reaction. The decrease in the CO_2 corrosion rate at NaCl concentrations above 1 wt.% was attributed to retardation of both iron dissolution and charge transfer controlled H^+ ion reduction reactions as well as the decrease in i_{Lim}.
4. Evans diagrams showed that increasing NaCl concentration affected more the charge transfer reactions in the CO_2 corrosion process rather than i_{Lim}.

5. Surface analysis showed that CO_2 corrosion occurred uniformly on the steel surface for the entire range of NaCl concentrations under the experimental conditions.

10.4 The Effect of Salt Concentration on CO_2 Corrosion at pH 5, 1 bar CO_2, and 50°C and 80°C Using a Rotating Cylinder Electrode (RCE)

The purpose of this part of study was to understand the effect of salt concentration on the aqueous uniform CO_2 corrosion process at higher temperatures. Similar to the previous set of experiments, the solution pH was adjusted at a somewhat high pH value of 5.00 to strengthen the contribution of CO_2 buffering in the overall CO_2 corrosion process. For all NaCl concentration, the solution pH was 5.00. Therefore, the only parameter that changed in the experiments was NaCl concentration and this allowed to investigate the effect of salt concentration on CO_2 corrosion at relatively high temperature in a systematic way.

10.4.1 Experimental Materials and Methodology for RCE CO_2 Corrosion Experiments at 50°C and 80°C, and pH 5

Experiments for this part of the study were carried out at 1 bar total pressure and two temperatures of $50 \pm 0.5^{o}C$ ($pCO_2 \cong 0.88$ bar) and $80 \pm 0.5^{o}C$ ($pCO_2 \cong 0.52$ bar) in a 5-liter glass cell illustrated in Figure 10-38. An aluminum insulation sheet (not shown in Figure 10-38) was wrapped around the entire glass cell to maintain a stable solution temperature throughout each experiment. A distilling column as shown in Figure 10-38 B was connected to the gas outlet to diminish evaporation of water during the experiments.

Figure 10-38

(A) Schematic; (B) picture of the experimental apparatus and a zoomed-in view of the experimental glass cell.

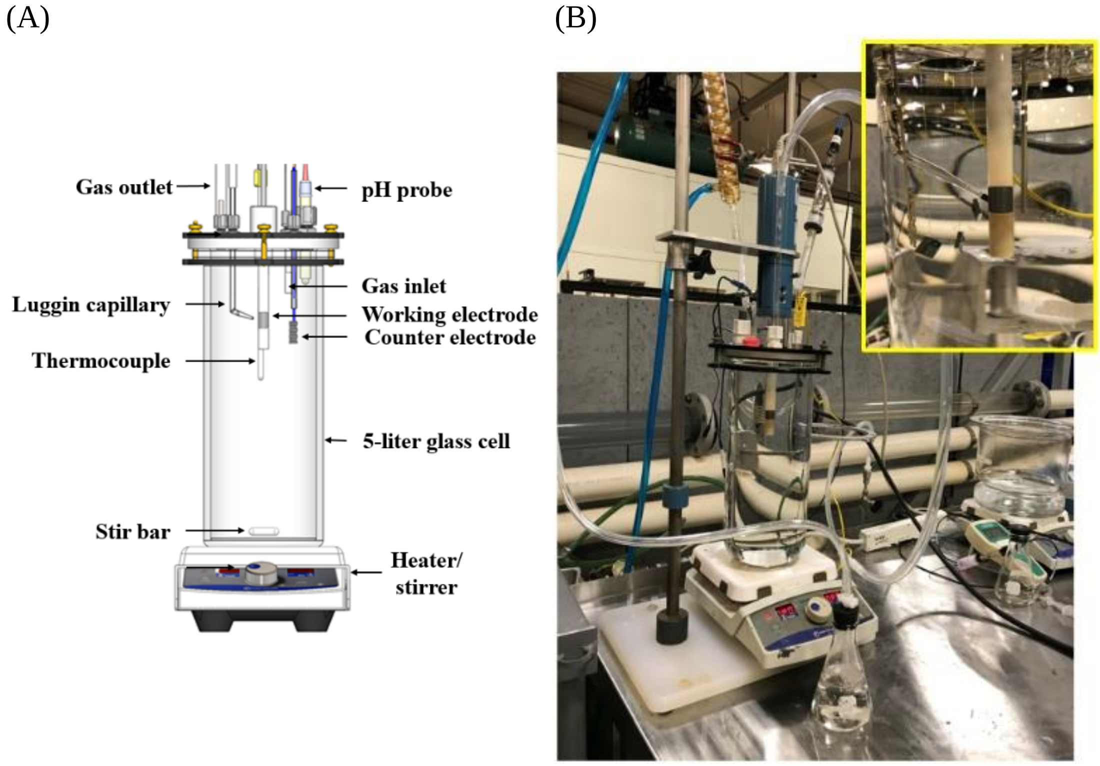

For each temperature, experiments were conducted at two NaCl concentrations of 1 wt.% (0.17 m) and 20 wt.% (4.28 m) to study the effect of salt concentration on uniform CO_2 corrosion. At the beginning of each experiment, the desired amount of NaCl was dissolved in deionized water (conductivity < 1 μS/cm) in the glass cell. Then, the solution was sparged with pure CO_2 gas for at least 3 h, while being stirred by a magnetic stirrer. 3 h was identified experimentally as the least amount of time needed to drop the concentration of dissolved oxygen in the solution (~ 5 liter) to less than 10 ppb and saturate the solution with the experimental gas. The dissolved oxygen was measured during the experiments with an Orbisphere 410 oxygen meter connected to the gas outlet to assure that the oxygen level in the solution was less than

10 ppb. The solution pH was continuously monitored from the beginning to the end of each experiment. The solution was identified saturated with $CO_{2(g)}$ when solution pH remained stable ($\Delta pH < 0.01$) for at least 15 min. Double-junction pH probes suitable for concentrated brines and resistant to temperatures up to 120°C were used for the pH measurements.

Once a stable pH was reached, the solution pH was adjusted to pH 5.00 by injecting deaerated NaOH 0.2 M to the solution. The solution was sparged with $CO_{2(g)}$ for another 0.5 h prior to insertion of the specimen(s) in the solution and before beginning the corrosion rate or electrochemical measurements to make sure that solution pH stayed fixed at 5.00. The magnetic stirrer was stopped throughout the weight loss or electrochemical measurements.

API 5L X65 pipeline grade carbon steel was utilized as the specimen material. The chemical composition of X65 steel has been already mentioned in Table 9-1. Two specimen types were used for the experiments: annulus RCE specimens with an outer diameter of 12 mm, a length of 14 mm, and an outer surface area of 5.4 cm^2 and square specimens with dimensions of 12.5 × 12.5 × 2.5 mm and a total surface area of 4.375 cm^2. Prior to each experiment, the specimens were sequentially wet polished with 80-, 240-, 400- and 600-grit abrasive papers. Later, they were ultrasonically cleaned with isopropanol alcohol for 3 min and dried in a cool N_2 gas stream. The annulus specimen was flush mounted onto a shaft to be used as a rotating cylinder electrode (RCE) in the experiments. The square specimens were submerged into the experimental solution by hanging them with nylon threads from the glass cell's lid (they can be seen in Figure 10-38 B).

Two separate sets of experiments were conducted: corrosion rate measurements to identify the overall effect of salt concentration on the CO_2 corrosion rate and PD sweeps to investigate how individual reaction mechanisms underlying CO_2 corrosion are affected by salt concentration.

For each corrosion rate measurement experiment, in addition to the RCE as the main specimen, three hanging square specimens were used to produce more results, and therefore have a more reliable analysis. Square specimens were exposed to the solution by hanging them with a nylon thread from the glass cell's lid. A very small hole was drilled in one corner of the square specimens for passing the nylon thread. The cell volume to specimen surface area ratio in the corrosion rate measurements was approximately 270 cm^3/cm^2, which was much larger than the average minimum ratio of 30 cm^3/cm^2 suggested by ASTM G31 [15]; however, these experiments were relatively short and no significant contamination of the aqueous solution was expected. The RCE shaft was rotated at 1000 rpm, which simulates the mass transfer conditions in a 10 cm ID pipe with approximately an average flow velocity of 1 m/s [301], determined by using a mass transfer equivalent conditions. The square specimens were in a stationary condition and experienced the flow caused by the RCE assembly, but with a less intensity; thus, expected to have a somewhat smaller corrosion rate compared to the RCE specimen.

Corrosion rates were measured using weight loss (WL) and linear polarization resistance (LPR) techniques. The duration of each corrosion rate experiment was 24 h, which started from the moment specimens inserted into the solution and finished when they were retrieved from the solution. 24 h was identified to be sufficient for obtaining measurable weight loss. Prior to immersion the specimens into the test solution, the specimens were weighed with a precise balance of 0.1 mg precision. The LPR corrosion rate measurement was performed simultaneously with the WL corrosion rate measurement in the same experiment and by using the same specimen —on average every 6 h during the 24 h period (totally five times). The LPR technique was performed using a three-electrode setup (shown in Figure 10-38 A) in a potential range from -5 mV to +5 mV vs. OCP with a scan rate of 0.125 mV/s. The RCE acted as the working electrode in the LPR technique. A saturated Ag/AgCl reference electrode connected to a Luggin capillary served as the reference electrode and a platinized titanium mesh (20 mm × 30 mm) was used as the counter electrode to complete the three-electrode setup. The duration of each LPR measurement was 80 sec. The average Stern-Geary constant (B) for converting the measured polarization resistance into the corrosion rate was determined to be around 24.0 mV/dec for 50^{o}C and 26.3 mV/dec for 80^{o}C. The determination of B value was done by fitting the PD sweeps via a simple electrochemical model [96]. The measured polarization resistance values were corrected for the solution resistance, which was measured by EIS. EIS was done prior to each LPR measurement at OCP with the same electrode setup in a frequency range of 10000-0.1 Hz with a peak-to-peak AC voltage amplitude of 10 mV. The time-averaged LPR corrosion rates were determined by the cumulative trapezoidal integration of the five instantaneous LPR corrosion rates taken over the 24 h experiment. The increase in the solution pH after 24 h was less than 0.2 pH units in all the experiments, indicating that the change in the solution chemistry was small during the corrosion rate measurements.

After 24 h, the RCE and square specimens were retrieved from the solution; carefully rinsed with distilled water for at least one minute to remove the salt, followed by rinsing with isopropanol alcohol and drying in a cool N_2 gas stream. Later, the specimens were weighed again to determine the WL corrosion rates. Immediately after the final weighing to analyze the morphology and chemical composition of the corroded surface, one square specimen was used for scanning electron microscopy/energy dispersive spectroscopy (SEM/EDS) (Figure 10-27 A), one was mounted in epoxy with its smallest surface upward for the cross-section analysis (Figure 10-27 B), and one was used for the surface profilometry (Figure 10-27 C).

For the PD sweeps only the RCE specimen was used in separate experiments. The cell volume to specimen surface area was approximately 925 cm^3/cm^2 in this case. Before starting to sweep the potential, the open circuit potential (OCP) was monitored to ensure having a stable OCP value (Δ_{OCP} < 2 mV/min). The PD sweep experiments were carried out according to the following steps: (1) a cathodic sweep starting from the OCP toward more negative potentials up to -1 V vs. OCP; (2) wait for the OCP to return near its initial value—within a few mV (this took about 1 h); (3) an anodic sweep starting from the OCP to more positive potentials up to 0.35 V vs. OCP. The PD sweep scan rate was 0.125 mV/s. All the PD sweeps were corrected for the solution resistance obtained by EIS. A Gamry potentiostat Reference 600 was used for all the electrochemical measurements. The increase in solution pH for the PD sweep experiments, each lasted about 4 h, was less than 0.05 pH units for all NaCl concentrations.

10.4.2 Results and Discussion for RCE CO_2 Corrosion Experiments at 50^oC and 80^oC, and pH5

10.4.2.1 pH measurements

Figure 10-39 shows the autogenous pH values in CO_2 saturated solutions at 1 bar total pressure, two NaCl concentrations of 1 wt.% and 20 wt.%, and 50^oC and 80^oC. For both temperatures, the autogenous pH of solution decreased when NaCl concentration was increased from 1 wt.% to 20 wt.%. This is consistent with the results reported in previous sets of experiments. The reason for the decrease in the autogenous pH of solution has been already explained comprehensively in Section 10.2.2. Additionally, in Figure 10-39 , the experimental autogenous pH values are compared with those obtained with the MSE model and the Li and Duan model. At 50^oC, the MSE predictions are more accurate compared to those for the Li and Duan model. However, at 80^oC, the Li and Duan model shows a better accuracy. Considering that the MSE model have a better accuracy at temperatures below 50^oC, it is preferred over the Li and Duan model for water chemistry calculations used in the final corrosion rate prediction model.

Figure 10-39

Autogenous pH of CO_2 saturated solutions measured at 1 bar total pressure before pH adjustment: (A) 50°C ($pCO_2 \cong 0.88$ bar) and (B) 80°C ($pCO_2 \cong 0.52$ bar). The error bars represent the minimum and maximum values obtained in repeated experiments (with at least 4 repeats). The experimental data are compared with two speciation models. The experimental data are compared with two speciation models.

(A)

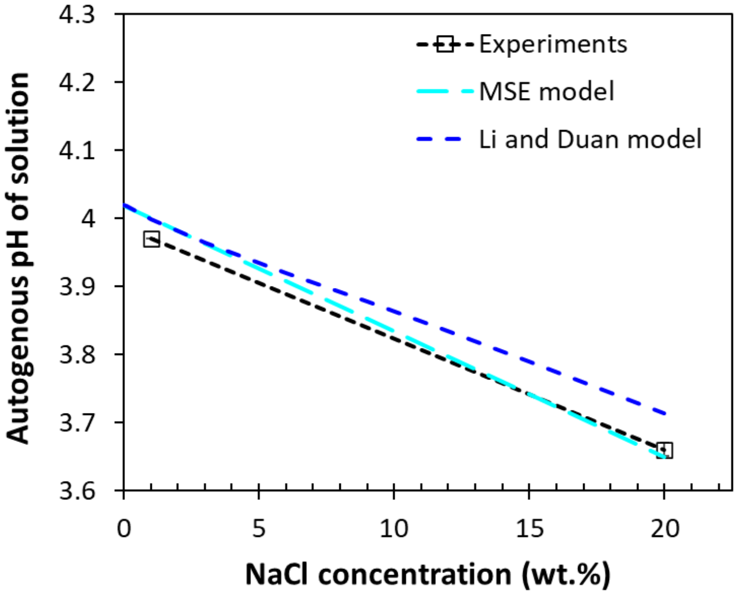

(B)

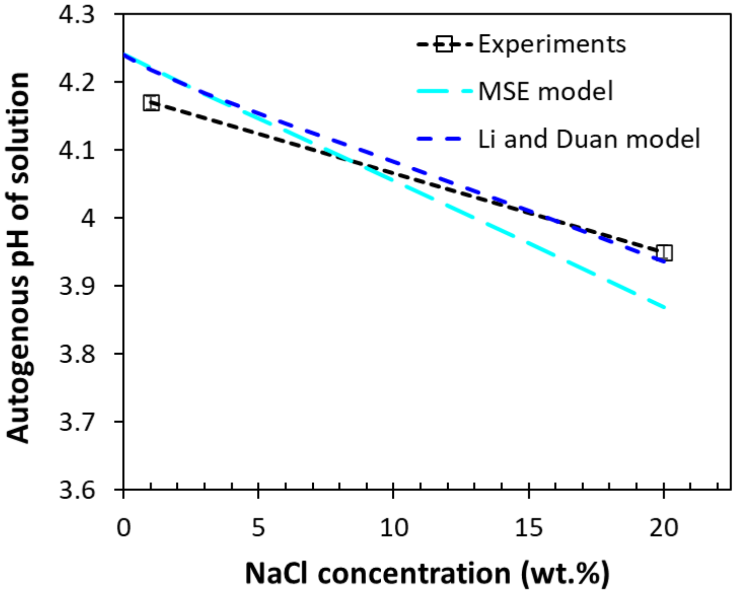

10.4.2.2 Corrosion rate and PD sweep measurements

The variations in the CO_2 corrosion rate with respect to NaCl concentration at 50^{o}C and 80^{o}C are shown in Figure 10-40. A similar trend was observed for both specimen types and both corrosion rate measurement techniques. The corrosion rate for the square specimens was smaller than that for the RCE specimen because the square specimens encountered a smaller flow velocity compared to the RCE specimen. The difference between the WL and the LPR corrosion rates might be due the fact that although the LPR corrosion rates were averaged over 24 h, only 6 measurements were carried out in each experiment, which totally covered 8 mins of 24 h period (the duration of each LPR test was 80 s).

The CO_2 corrosion rate decreased when NaCl concentration was increased from 1 wt.% to 20 wt.%. This agrees very well with the corrosion rate results reported above for lower temperatures. Therefore, it is expected that at CO_2 pressures of the order of 1 bar and for temperatures below 100^{o}C, increasing salt concentration generally decreases the rate of uniform CO_2 corrosion.

Figure 10-40

Variation in the corrosion rate with NaCl concentration for X65 carbon steel RCE with a rotational speed of 1000 rpm and square specimens exposed for 24 h to CO_2 saturated aqueous NaCl solutions at 1 bar total pressure, and pH 5: (A) 50°C (pCO_2 ≅ 0.88 bar) and (B) 80°C (pCO_2 ≅ 0.52 bar). The corrosion rates were measured using weight loss and LPR techniques.

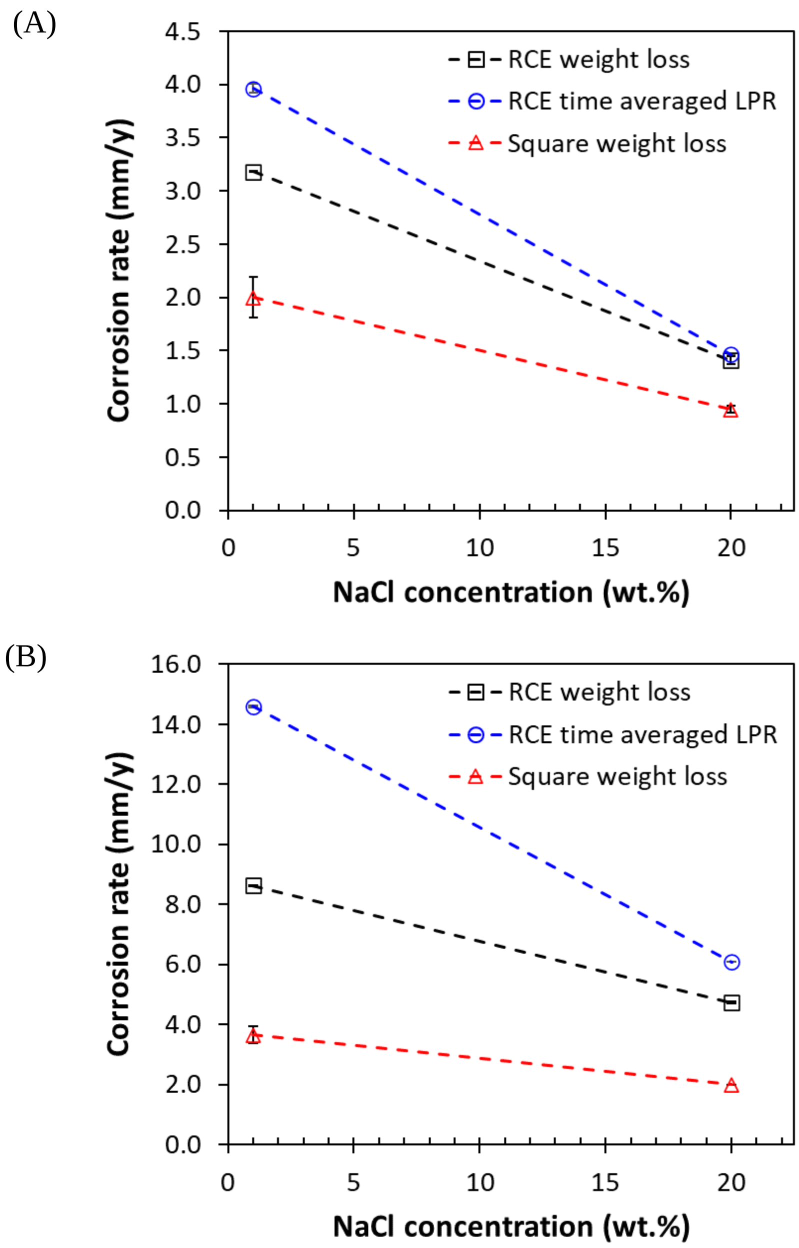

The trend observed for the corrosion rate in Figure 10-40 can be explained by analyzing the measured PD sweeps. Figure 10-41 shows the PD sweeps for 1 wt.% and 20 wt.% NaCl concentrations at 50°C and 80°C. The potential values are corrected for the solution resistance (iR drop) in all the presented sweeps. For each NaCl concentration, only one PD sweep was conducted. For both temperatures, there were changes in the cathodic and anodic branches with increasing NaCl concentration. There was a decrease in the H^+ ion reduction reaction limiting current density (i_{Lim}) when NaCl concentration was increased. The water reduction reaction seems to be accelerated with increasing NaCl concentration. However, the changes in the charge transfer portions of the PD sweeps are not evident from Figure 10-31. Therefore, for a better understanding of the effect of NaCl concentration on the PD sweeps, the kinetic features of the sweeps were extracted by overlapping the experimental sweeps with the best fit created using a simple electrochemical model [96][88].

---

[88] Activation energies of 59860 J/mol for H^+ ion, 24809 J/mol H_2O reduction and 25398 J/mol for Fe oxidation reactions. A reversible potential of -0.685 V vs. Ag/AgCl was used for all three reactions. The reference temperature was 20°C.

Figure 10-41

Potentiodynamic sweeps for X65 carbon steel RCE with a rotational speed of 1000 rpm exposed to CO_2 saturated solutions with different NaCl concentrations at 1 bar total pressure and pH 5:(A) $50^{o}C$ ($pCO_2 \cong 0.88$ bar) and (B) $80^{o}C$ ($pCO_2 \cong 0.52$ bar.

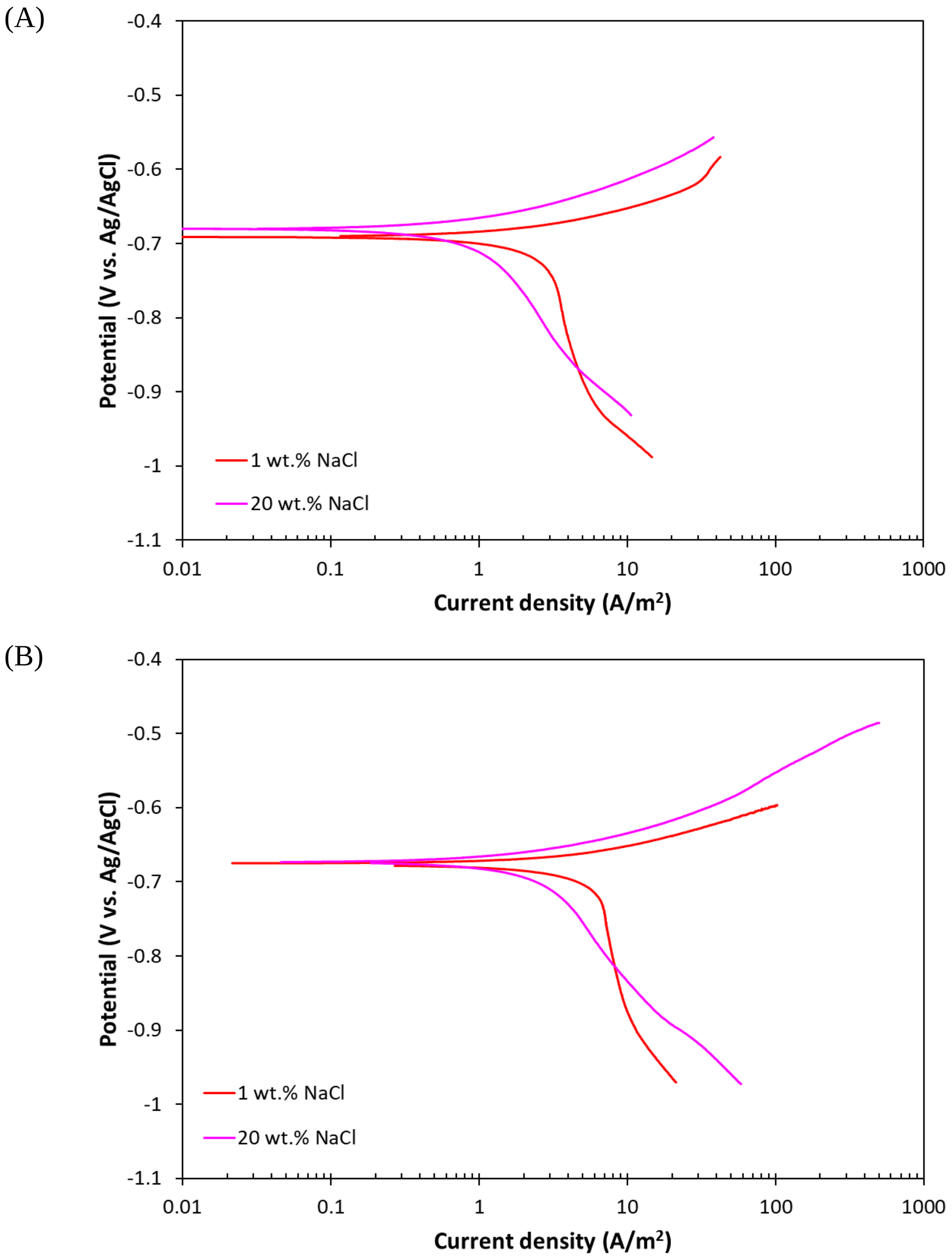

The electron transfer coefficients for the H$^+$ ion reduction reaction (α_{H^+}) and the iron dissolution reaction in the active region (α_{Fe}) at 50°C and 80°C and two NaCl concentrations are presented in Table 10-4. The α_{H^+} values are identical to the theoretical value of 0.5, frequently considered for the hydrogen evolution on an iron surface [185]. At each temperature, since α_{H^+} was identical for both NaCl concentrations, it can be concluded that the mechanism of hydrogen evolution under the experimental conditions in this part of study was not affected by the presence of salt.

Table 10-4

The electron transfer coefficients for H$^+$ reduction reaction (α_{H^+}) and Fe oxidation (α_{Fe}) for the RCE CO$_2$ experiments at 1 bar total pressure, pH 5, and 50°C (pCO$_2$ ≅ 0.88 bar) and 80°C (pCO$_2$ ≅ 0.52 bar).

Temperature (°C)	50		80	
NaCl concentration (wt.%)	1	20	1	20
α_{H^+}	0.5	0.5	0.5	0.5
Cathodic Tafel slope (mV/dec)	128	128	140	140
α_{Fe}	1.00	1.00	1.10	1.10
Anodic Tafel slope (mV/dec)	64	64	70	64

The α_{Fe} did not change with increasing NaCl concentration for both temperatures. This indicates that the mechanism of active dissolution of iron remained unaffected with increasing NaCl concentration. The mechanisms of iron dissolution in the presence of chloride have been comprehensively explained in Chapter 5. The α_{Fe}

values measured at 50°C and 80°C are very similar to the values reported in Section 10.1 for the CO_2 corrosion experiments at 10°C and pH 3 and Section 10.2 for the CO_2 corrosion experiments at 30°C and autogenous pH. As mentioned earlier, Bockris *et al.* [185] proposed 1.5 for iron dissolution in acidic media without the presence of halides. Chin and Nobe [194] reported 1.18 for dissolution of iron in acidic chloride media, which is close to the results of this set of experiments.

Table 10-5 lists the exchange current densities for the H^+ ion reduction reaction (i_{o,H^+}) and the iron dissolution reaction (i_{o,H^+}) in addition to i_{Lim} at 50°C and 80°C for 1 wt.% and 20 wt.% NaCl concentrations. i_{o,H^+} decreased for both temperatures when NaCl concentration was raised from 1 wt.% to 20 wt.%. This agrees well with all the results reported so far in this study for variations in i_{o,H^+} with NaCl concentration. The decrease in i_{o,H^+} with increasing NaCl concentration has been attributed to the adsorption of Cl^- ions on the surface and blocking the surface areas required for H^+ ion adsorption and reduction reactions [171]. A reason for the decreasing trend seen for the corrosion rates in Figure 10-40 could be the decrease in i_{o,H^+}.

Table 10-5

The cathodic limiting current density (i_{Lim}), the H^+ reduction exchange current density (i_{o,H^+}) and the Fe oxidation exchange current density ($i_{o,Fe}$) for the RCE CO_2 experiments at 1 bar total pressure, pH 5, and 50°C ($pCO_2 \cong 0.88$ bar) and 80°C ($pCO_2 \cong 0.52$ bar). The reference temperature was 20°C.

Temperature (°C)	50		80	
NaCl concentration (wt.%)	1	20	1	20
i_{o,H^+} (A/m^2)	19.02	2.38	264	8.25
i_{Lim} (A/m^2)	3.7	1.8	7.3	4.3
$i_{o,Fe}$ (A/m^2)	3.75	1.00	5.52	1.93

As presented in Table 10-5, for both temperatures, $i_{o,Fe}$ decreased with increasing NaCl concentration from 1 wt.% to 20 wt.%, which means that the rate of anodic dissolution of Fe in the active region decreased at higher NaCl concentrations. This is identical to what has been reported previously in this study for changes in $i_{o,Fe}$ with NaCl concentration (for concentrations greater than ~ 1 wt.%). Therefore, changes in $i_{o,Fe}$ with NaCl concentration is another reason for the decrease in the CO_2 corrosion rate when NaCl concentration was increased from 1 wt.% to 20 wt.%.

The next kinetic parameter in the PD sweeps in Figure 10-41 that changed with NaCl concentration was i_{Lim}. In CO_2 corrosion, i_{Lim} indicates the rate of the cathodic H^+ ion reduction reaction is controlled by the rate of mass transfer of species to the metal surface coupled with the preceding homogenous CO_2 hydration chemical reaction. Table 10-5 shows that i_{Lim} decreased with increasing NaCl concentration from 1 wt.% to 20 wt.%.

In CO_2 corrosion, i_{Lim} mainly depends on a_{H^+} and a_{CO_2}. This is explained in detail in Chapter 12. The experiments were conducted in an open system. Thus, a_{CO_2} was constant at each temperature for both NaCl concentrations. At each temperature, the solution pH was adjusted at 5.00 in the experiments; therefore, a_{H^+} was constant for both NaCl concentrations. Consequently, a_{H^+} and a_{CO_2} cannot be the reason for the decrease in i_{Lim} with NaCl concentration. As pointed out earlier, i_{Lim} also depends on diffusion coefficients of H^+ ion and H_2CO_3 as well as their activity coefficients. Compared to parameters such as H_2CO_3 diffusion coefficient and its activity coefficient, the contribution of H^+ diffusion coefficient and its activity coefficient in the overall i_{Lim} value is prevailing. The i_{Lim} is directly related to H^+ ion diffusion coefficient and inversely depends on H^+ ion activity coefficient. The decreasing trend for i_{Lim} when NaCl was increased from 1 wt.% to 20 wt.% is due to the increase in H^+ ion activity coefficients as well as the decrease in the diffusion coefficient of H^+ ion (the effect of salt concentration on the diffusion coefficient is explained in Section 3.3.2). Thus, the decrease in i_{Lim} with NaCl concentration is another reason for the decreasing trend seen for the corrosion rate in Figure 10-40.

Three possible reasons have been listed for the decrease in the CO_2 corrosion rate at 50°C and 80°C when NaCl concentration was increased from 1 wt.% to 20 wt.%: the decreases in i_{o,H^+}, $i_{o,Fe}$, and i_{Lim} with increasing NaCl concentration. To recognize which of these three parameters controlled the rate of CO_2 corrosion at the experimental conditions, the Evans diagram is utilized.

The Evans diagrams for 1 wt.% and 20 wt.% NaCl concentrations at the experimental conditions of this part of the study are illustrated in Figure 10-42. At 50°C, for both NaCl concentrations, the corrosion process was under mixed control.

This means that the rate of the CO_2 corrosion process was controlled by both charge transfer processes as well as i_{Lim}. The reason for the decrease in the CO_2 corrosion rate at 50^{o}C in 1-20 wt.% NaCl concentration range was due to retardation of both the iron dissolution reaction and the charge transfer controlled H^+ ion reduction reaction as well as the decrease in i_{Lim}.

Figure 10-42

The Evans diagrams for the effect of NaCl concentration on uniform strong acid corrosion of X65 carbon steel RCE specimen with a rotational speed of 1000 rpm at 1 bar total pressure, pH 5, and 1000 rpm rotational speed: (A) 50^{o}C ($pCO_2 \cong 0.88$ bar) and (B) 80^{o}C ($pCO_2 \cong 0.52$ bar). E_{corr} is the corrosion potential (OPC), i_{corr} is the corrosion current density (Blue: 1 wt.% NaCl, and red: 20 wt.% NaCl). A and B do not have the same axis scale.

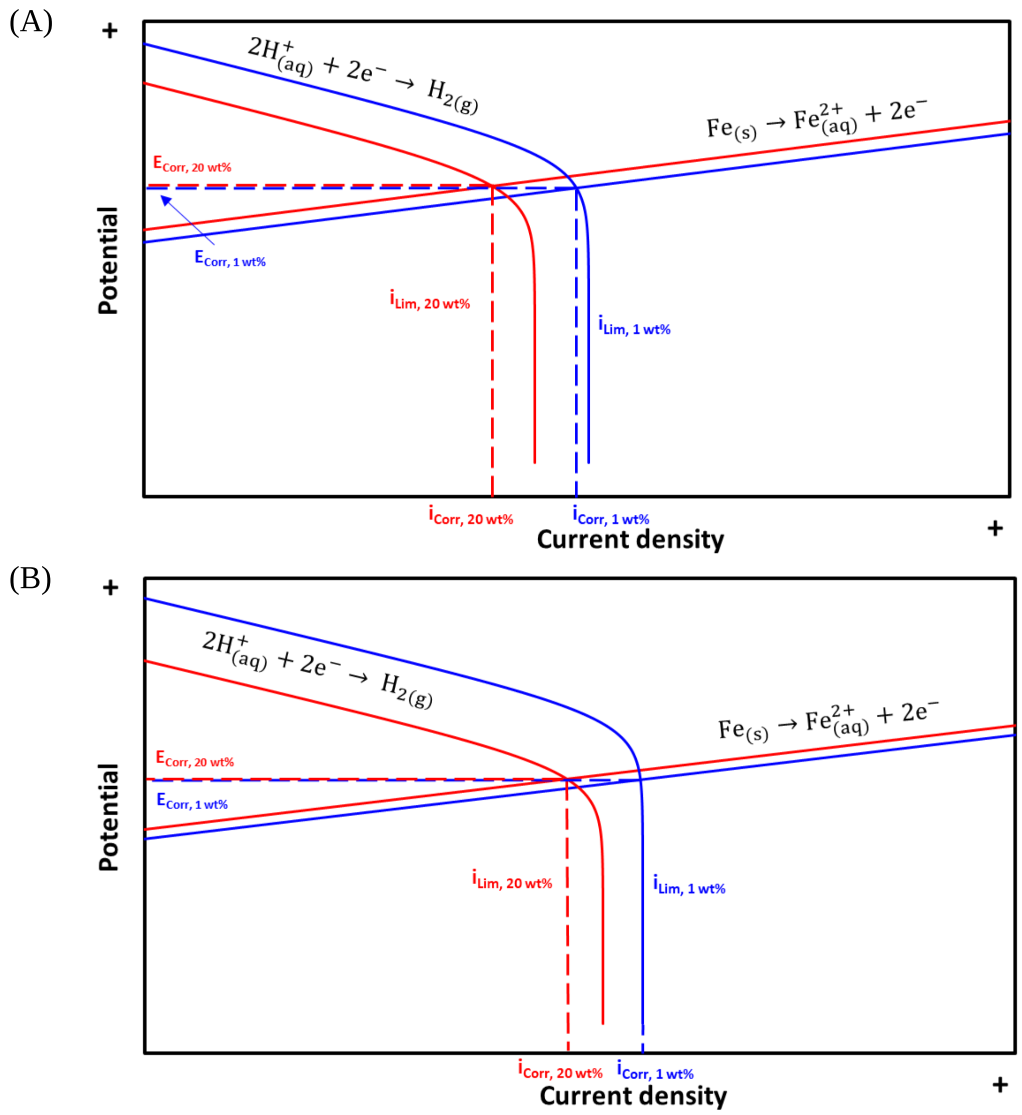

At 80^{o}C and 1 wt.%, the CO_2 corrosion process was purely limiting current density control. However, at 20 wt.%, the CO_2 corrosion process became mixed control. Similar to 50^{o}C, the reason for the decrease in the CO_2 corrosion rate at 80^{o}C in 1-20 wt.% NaCl concentration range was a combination of retardation of both the iron dissolution reaction and the charge transfer controlled H^+ ion reduction reaction as well as the decrease in i_{Lim}. However, at 80^{o}C the contribution of i_{Lim} in controlling the rate of the CO_2 corrosion was greater than the charge transfer processes.

Comparing the Evans diagrams at 50^{o}C and 80^{o}C with that at 20^{o}C presented in Figure 10-33 B shows that at lower temperatures the corrosion process is controlled more by the charge transfer processes (H^+ ion reduction and iron dissolution). On the other hand, increasing temperature causes the rate of the CO_2 corrosion process to be controlled more by i_{Lim}. The reason is that charge transfer processes are more sensitive to temperature and for an identical temperature increase, the rate of the charge transfer processes increases more compared to i_{Lim}. Therefore, at high temperatures, i_{Lim} becomes smaller than the rate of charge transfer processes and controls the overall rate of the CO_2 corrosion process.

A very important and interesting understanding from the Evans diagrams in Figure 10-42 is that the rates of charge transfer processes were affected more by increasing NaCl concentration compared to i_{Lim} because the corrosion current density (i_{Corr}) decreased more than i_{Lim}, when NaCl concentration was increased from 1 wt.% to 20 wt.%. This is particularly obvious in the Evans diagrams for 80^{o}C, as i_{Corr} and i_{Lim} were equal at 1 wt.% NaCl. However, at 20 wt.%, i_{Corr} was smaller than i_{Lim}. The conclusions made here were also reported for the RCE CO_2 experiments at

30°C and autogenous pH in Section 10.2 and the RCE CO_2 experiments at 20°C and pH 5 in Section 10.3. Therefore, since the charge transfer processes occur at the metal surface/electrolyte interface, it can be concluded that salt affects the processes occuring at the metal surface (*e.g.*, H^+ ion adsorption on the surface, H_2 evolution from the surface, and Fe dissolution) more than the processes happen in the bulk solution (*e.g.*, CO_2 hydration reaction, diffusion of participating species to the metal surface).

10.4.2.3 Corroded surface analysis

The SEM images of the corroded square specimens at 50°C and 80°C and two NaCl concentrations are shown in Figure 10-43. The SEM image of a freshly polished specimen is shown in Figure 10-34 for reference. The morphology of the corroded surface was somehow similar under different experimental conditions. A slight difference in the surface morphology was observed for 80°C and 20 wt.%, which will be discussed in the following text. Generally, it can be concluded that salt concentration did not change the morphology of the corroded steel surface. No pitting corrosion was detected in any of the SEM images. However, since these images only covered a very small part of the surface, a conclusion about uniformity of CO_2 corrosion attack cannot be made at this point.

Figure 10-43

SEM images of the corroded carbon steel X65 square specimens in CO_2*-statuarated aqueous NaCl solutions at 1 bar total pressure, pH 5 and 50*^{o}*C and 80*^{o}*C. Secondary electron imaging was used to take the images.*

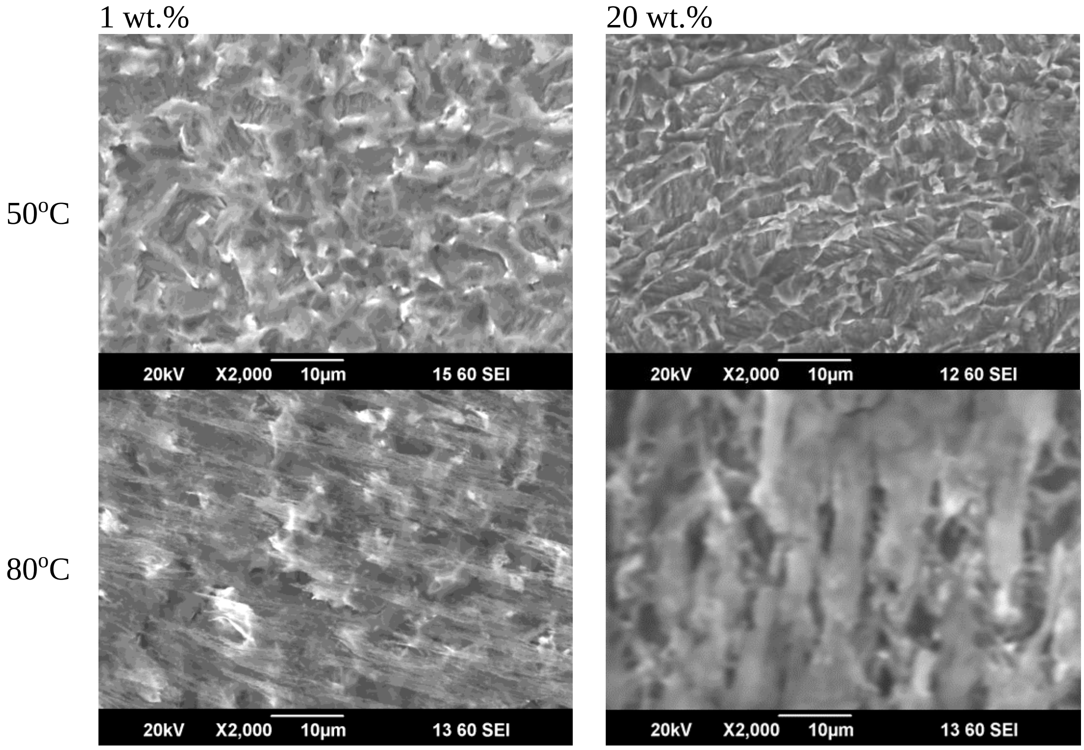

Figure 10-44 shows the EDS elemental composition of the corroded surface at 50^{o}C and 80^{o}C and two NaCl concentrations. The EDS analysis of a freshly polished specimen is shown in Figure 10-35 for comparison. Fe, C, Mn, Si, O, and Cr have been normalized to give a total of 100%. The elements P, S, Cl, Ni, Cu, Mo, and Al which were found to be in trace amounts, are not listed in the elemental composition. For 50^{o}C at 1 wt.% and 20 wt.% NaCl concentrations and for 80^{o}C and 1 wt.% NaCl concentration the elemental compositions of the corroded surface were similar, and iron and carbon were the dominant elements detected. Therefore, it can be concluded that at these three experimental conditions the main phase on the surface was iron and iron carbide. For 80°C and 20 wt.%, since the surface morphology was slightly different from the rest of the conditions, the EDS analysis is presented separately in Figure 10-45.

Figure 10-44

EDS surface elemental composition analysis of the corroded carbon steel X65 square specimens in CO_2-saturated aqueous NaCl solutions at 1 bar total pressure, pH 5 and 50°C and 80°C. The elemental concentrations are in normalized atomic percentage.

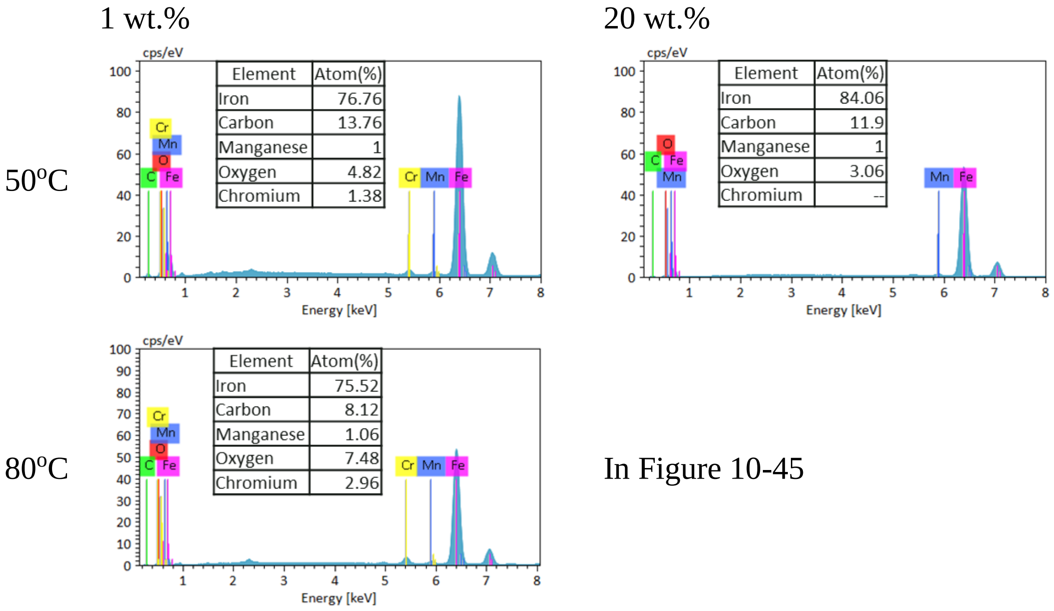

50°C, 1 wt.%:

Element	Atom(%)
Iron	76.76
Carbon	13.76
Manganese	1
Oxygen	4.82
Chromium	1.38

50°C, 20 wt.%:

Element	Atom(%)
Iron	84.06
Carbon	11.9
Manganese	1
Oxygen	3.06
Chromium	--

80°C, 1 wt.%:

Element	Atom(%)
Iron	75.52
Carbon	8.12
Manganese	1.06
Oxygen	7.48
Chromium	2.96

The SEM/EDS analysis was carried out at two spots on the corroded surface of the square specimen exposed to 80°C and 20 wt.% NaCl condition. Figure 10-45 shows the SEM/EDS analysis results. The elemental composition of the light gray spots on the surface (Figure 10-45 left) was similar to those presented above. However, the elemental composition of the dark gray (or black) spots on the surface (Figure 10-45 right) showed higher carbon and oxygen amounts. This might be attributed to the nucleation of iron carbonate phases on the surface at this condition, which was expected because at high temperatures the formation of these phases is likely due to high surface supersaturation [201]. Another possibility is nucleation of magnetite. Gao *et al.* [310] and Chan [311] have reported the formation of magnetite on the surface as a corrosion product in CO_2 containing solutions at high temperatures around 80°C.

Since the light gray phases covered most of the corroded surface it can be concluded that the main phases on the surface at 80°C and 20 wt.% NaCl condition were iron and iron carbide and no surface layer formed on the surface at this condition.

Figure 10-45

SEM images and EDS elemental composition analysis of corroded square specimen in CO2-saturated solution at 1 bar pCO2, pH 5, 80°C, and 20 wt.% NaCl concentration.

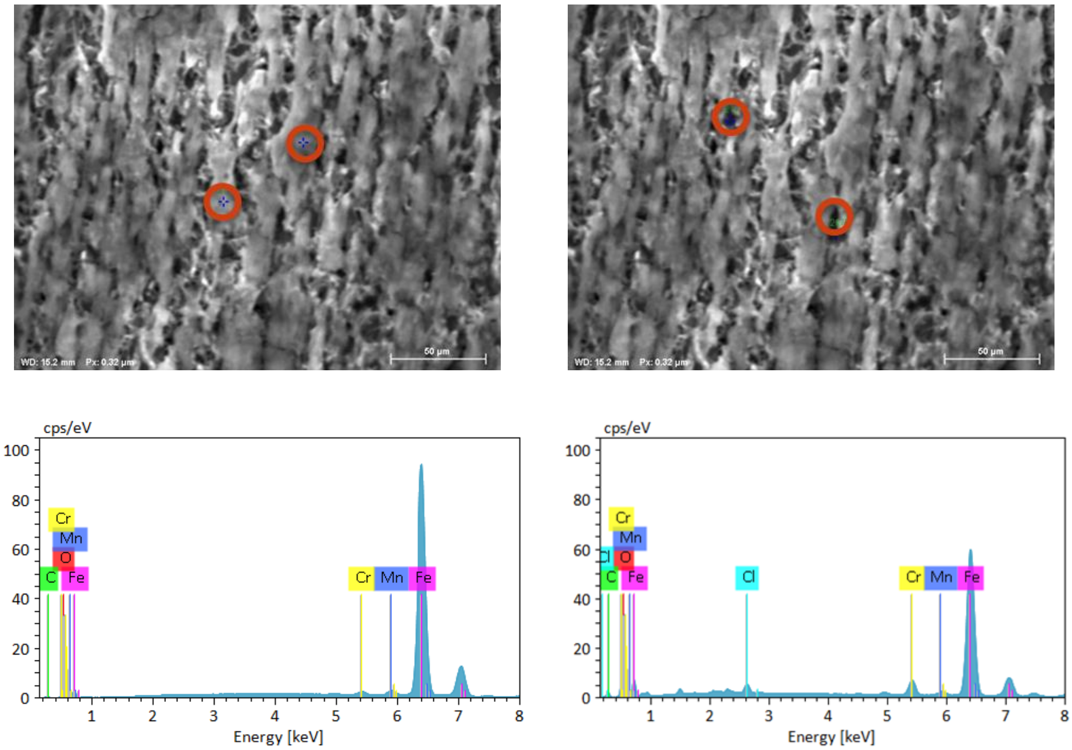

Element	Atom(%)
Iron	92.02
Carbon	3.82
Manganese	1.26
Oxygen	--
Chromium	--
Chloride	--

Element	Atom(%)
Iron	51.35
Carbon	11.41
Manganese	0.61
Oxygen	24.84
Chromium	3.63
Chloride	1.79

Figure 10-46 shows the cross-section SEM images of the corroded square specimen at 50°C and 80°C and two NaCl concentrations. The light gray part in the bottom of the SEM images is the steel matrix. The black (or dark gray) part at the top of the SEM images is the epoxy used for mounting the square specimens. The surface roughness increased with increase in temperature for both NaCl concentrations. This supports the corrosion rate results that showed a higher temperature led to a higher corrosion rate. Additionally, the surface roughness decreased with increasing NaCl concentration from 1 wt.% to 20 wt.% for both temperatures. This proves that an increase in salt concentration decreased the corrosion rate as shown earlier in the corrosion rate results in Figure 10-40. Apparently, a layer formed on the steel surface at 80°C for both NaCl concentrations and at 50°C and 1 wt.% NaCl. To identify this layer, EDS mapping analysis was performed, which will be discussed below.

Figure 10-46

Cross section SEM images of the corroded carbon steel X65 square specimens in CO_2-saturated NaCl aqueous solutions at 1 bar total pressure, pH 5, and 50°C and 80°C.

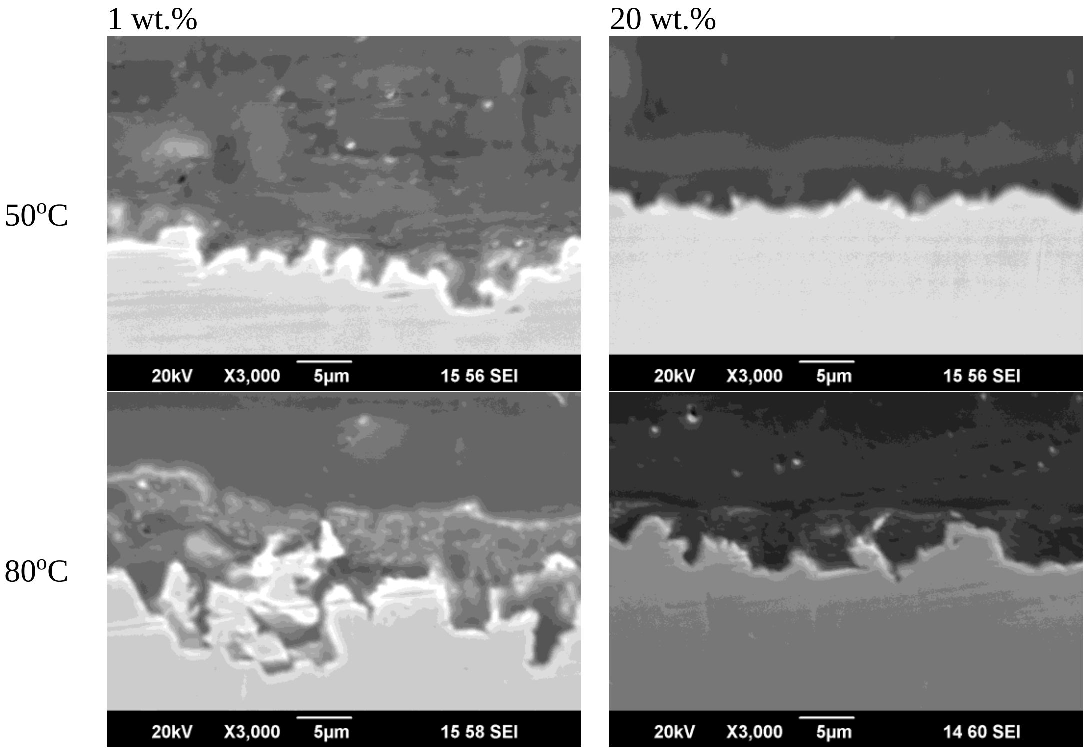

Figure 10-47 shows the elemental composition obtained by EDS mapping analysis over the cross section of the corroded specimen mounted in epoxy. The main elements detected on the surface for both temperatures at 1 wt.% and 20 wt.% NaCl concentrations were iron and carbon. Carbon was dominant in the upper part of the EDS maps because of the presence of epoxy. Therefore, carbon in the steel matrix cannot be distinguished from that in epoxy and this is the reason that the layer seen in the SEM images in Figure 10-46 at 80^{o}C, was not detected as a distinct layer in Figure 10-47. With no other elements in abundance, this means that the layer observed in Figure 10-46 was iron carbide, which is the leftover of the CO_2 corrosion process on the steel surface.

Figure 10-47

EDS elemental mapping analysis of the corroded carbon steel X65 square specimens in CO_2*-saturated NaCl aqueous solutions at 1 bar total pressure, pH 5, and 50°C and 80°C.*

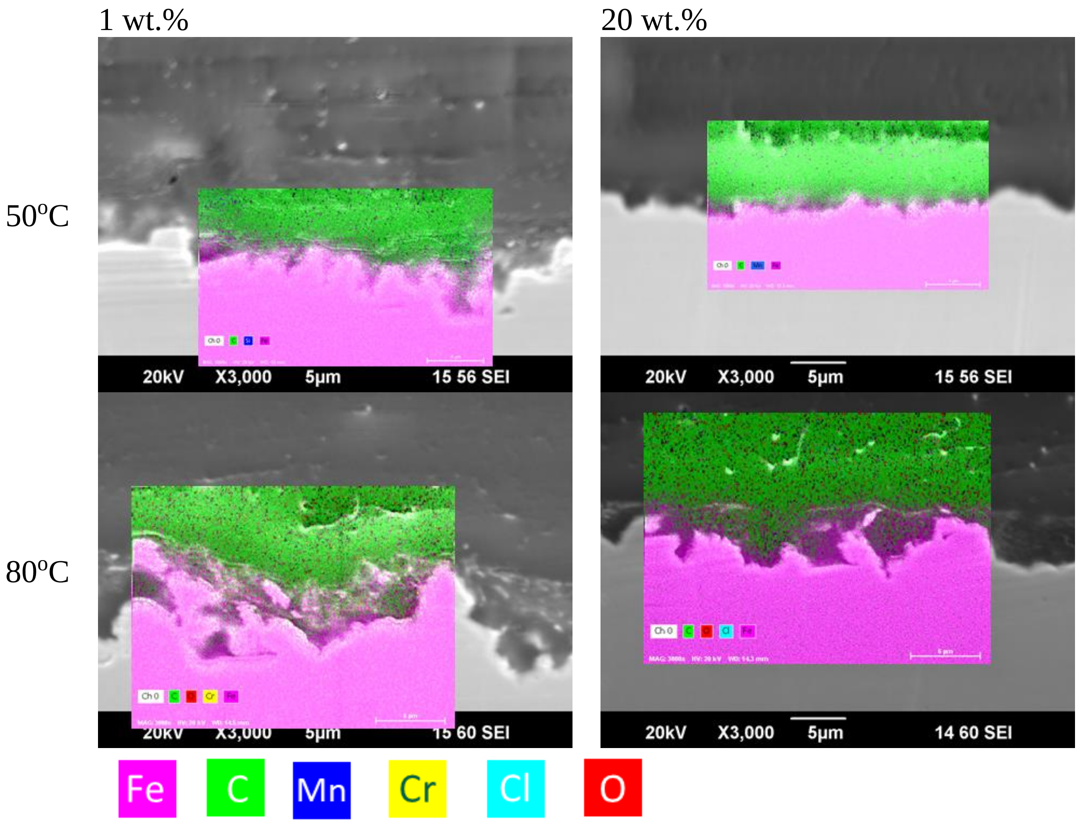

Figure 10-48 shows the one-dimensional (1D) and two-dimensional (2D) surface roughness profiles of the corroded square specimens at 50°C and 80°C for both NaCl concentrations. Surface profilometry was carried out to ensure that the surface was corroded uniformly at the experimental conditions of this part of the study. The advantage of the surface profilometry over the SEM/EDS analyses mentioned above, is that it can cover a larger surface area, and thereby, it is more effective in detecting localized corrosion (or pits) on the entire surface area of a specimen.

1D profiles show no sudden change in the surface roughness at any NaCl concentration, which is an indication of uniform corrosion. The uniform blue color on the whole surface of the 2D profiles confirms that CO_2 corrosion was uniform for both temperatures at 1 wt.% and 20 wt.% NaCl concentrations. The purple color (*i.e.*, the presence of hills) seen on the corners of some of the 2D profiles was due to uneven polishing of the surface during the specimen preparation.

Figure 10-48

1D and 2D surface roughness profilometry of the corroded square specimens in CO_2*-satuared NaCl aqueous solutions at 1 bar total pressure, pH 5, and* 50^{o}*C and* 80^{o}*C.*

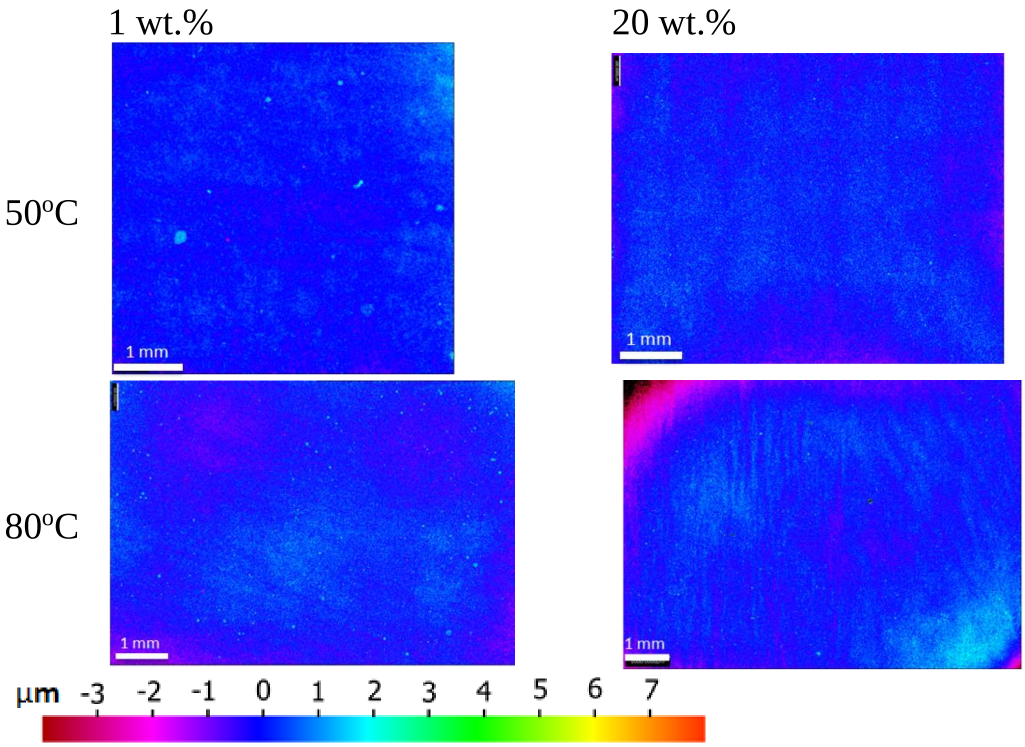

10.4.3 Summary and Conclusions of RCE CO_2 Corrosion Experiments at 1 bar Total Pressure, pH 5, and 50°C and 80°C

The purpose of this part of study was to understand the effect of salt concentration on aqueous uniform CO_2 corrosion of carbon steel at relatively high temperatures. Experiments were carried out using an RCE setup at a rotational speed of 1000 rpm in CO_2-saturated aqueous NaCl solutions at 1 bar total pressure, pH 5, and 50°C and 80°C. The following are the main conclusions found in this set of experiments, when NaCl concentration was increased from 1 wt.% to 20 wt.%:

1. All the results at 50°C and 80°C agreed well with the previous findings at low temperatures.
2. The autogenous pH of solution deceased. The decrease was related to the variations in the activity coefficients of dissolved species, particularly H^+ ion.
3. The uniform CO_2 corrosion rate decreased.
4. Analysis of PD sweeps indicated that the decrease in the CO_2 corrosion rate at NaCl concentrations above 1 wt.% was attributed to retardation of both charge transfer reactions for iron dissolution and H^+ ion reduction as well as the decrease in i_{Lim}.
5. At high temperatures (> 60°C) CO_2 corrosion process is controlled more by i_{Lim} rather than by the charge transfer reactions.
6. Evans diagrams showed that salt concentration influences the charge transfer processes (related to surface effects) more than i_{Lim} (related to bulk solution effects) in the CO_2 corrosion process.
7. Surface analysis showed that CO_2 corrosion occurred uniformly on the steel surface for both temperatures under the experimental conditions.

Chapter 11: Experimentation to Investigate the Effect of Salt Concentration on H_2S Corrosion

H_2S is often present in production streams extracted from hydrocarbon reservoirs. When $H_2S_{(g)}$ dissolves in water, $H_2S_{(aq)}$ is produced, which subsequently dissociates and accelerates corrosion of carbon steel structures and facilities exposed to this corrosive medium. Corrosion of metals (mostly carbon steels) due to their exposure to aqueous H_2S-containing solutions is called H_2S corrosion. In this chapter, the effect of salt concentration on uniform aqueous H_2S corrosion of carbon steel is experimentally investigated. To the best of author's knowledge, no previous study has been done on the effect of salt concentration on uniform H_2S corrosion.

11.1 Safety Related to Working with H_2S Gas

H_2S gas is a hazardous chemical. According to safety standards, exposure to a concentration of greater than 10 ppm is harmful, and is deleterious to human health and may eventually lead to death at concentrations higher than 100 ppm. Therfore, for $H_2S_{(g)}$ concentration up to 100 ppm, the experiments need to be done in a controlled vent hood. For $H_2S_{(g)}$ concentrations greater than 100 ppm, all the experiements must be done in a H_2S safe room.

In this study the following protocol was followed for all the experiments involved $H_2S_{(g)}$ concentrations greater than 100 ppm:

1. Trainning before working with H_2S gas, which included
    a. H_2S certification course
    b. Fit testing for specific self-contained breathing apparatus (SCBA)

2. An SCBA was utilized for working in H_2S safe room with an equally equipped buddy outside the room watching the activities.

11.2 The Effect of Salt Concentration on H_2S Corrosion at pH 5 and 100 ppm $H_2S_{(g)}$ Using a Rotating Cylinder Electrode (RCE)

Two objectives were followed by performing this set of experiments. First and foremost, to study the effect of salt concentration on H_2S corrosion at low H_2S concentrations. Second, to build experience and confidence to safely work with the poisonous H_2S gas for future experiments using pure $H_2S_{(g)}$ at a partial pressure of ~1 bar $H_2S_{(g)}$ (10^6 ppmv). The experiments in this part of study were done at pH 5 to intensify the contribution of the H_2S buffering effect in the H_2S corrosion process. Besides, bulk solution pH was kept constant at 5.0 for all salt concentrations, so that the only parameter changed in the experiments was NaCl concentration. This testing methodology allowed a better understanding of the effect of salt concentration on the H_2S corrosion process.

11.2.1 Experimental Materials and Methodology for RCE H_2S Corrosion Experiments at pH 5 and 100 ppm $H_2S_{(g)}$

This set of experiments were conducted at 20°C, 1 bar total pressure for two NaCl concentrations of 1 and 20 wt.% in a 2-liter glass cell. The schematic of the experimental apparatus used in this part is shown in Figure 11-1.

The gas atmosphere exposed to the solution was an H_2S/N_2 mixture with 100 ppm(v) H_2S gas balanced with N_2 gas. 100 ppm(v) H_2S gas concentration is equivalent to 10^{-4} bar $H_2S_{(g)}$. The H_2S and N_2 gases were mixed, and their ratio was adjusted by using a double-column rotameter. The outlet gas mixture from the glass cell was passed through a saturated NaOH solution followed by an activated carbon-containing flask to scrub H_2S gas from the gas mixture. The scrubbed gas was then sent to a combustion chamber with excess air where any remaining H_2S in the gas stream was converted to sulfur dioxide (SO_2). It is assumed that the combustion process is near 100% conversion and no detectable H_2S remained in the effluent gas.

Figure 11-1

The schematic of the experimental apparatus used for RCE H_2S experiments at pH 5 and 100 ppm $H_2S_{(g)}$. The assigned numbers represent: (1) N_2 gas cylinder, (2) H_2S gas cylinder, (3) double-column rotameter, (4) hot plate, (5) thermocouple, (6) gas inlet, (7) Luggin capillary, (8) pH-electrode, (9) reference electrode, (10) gas outlet from the cell, (11) motor, (12) rotating cylinder electrode, (13) platinum coated counter electrode, (14) stir bar, (15) sodium hydroxide solution, (16) activated carbon scrubber, (17) gas outlet to the combustion chamber.

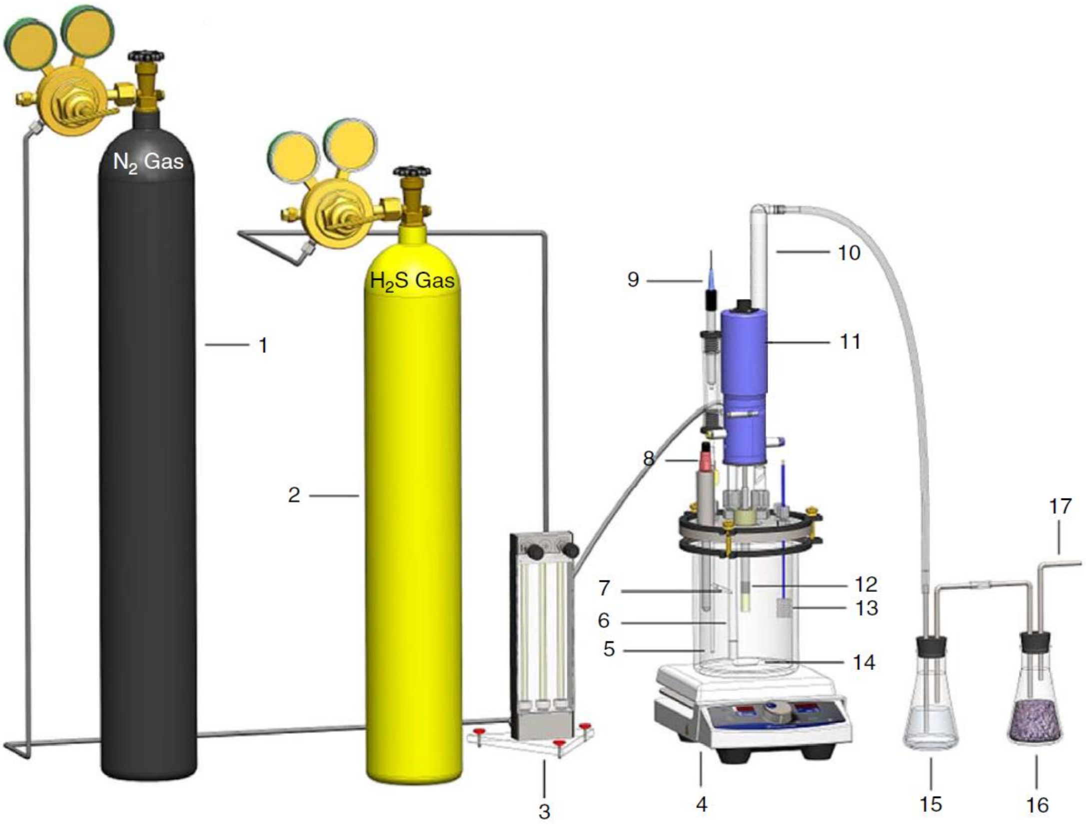

To adjust the solution temperature to 20°C, water was circulated from an industrial chiller through a copper coil around the glass cell to cool down the solution temperature. In combination with the cooling coil and insulation around the cell, a hot plate was used continuously to balance the temperature at 20 ± 0.5°C.

For each experiment, the desired amount of NaCl was mixed with deionized water (conductivity < 1 μS/cm) in the glass cell. Then, the solution was sparged with the H_2S/N_2 gas mixture for at least 3 h, while being stirred by a magnetic stirrer. 3 h was identified experimentally as the least amount of time needed to drop the concentration of dissolved oxygen in the solution (~ 2 liter) to less than 10 ppb and saturate the solution with the gas mixture. The dissolved oxygen was measured during the experiments with an Orbisphere 410 oxygen meter connected to the gas outlet to assure that the oxygen level in the solution was less than 10 ppb. The solution pH was frequently monitored from the beginning to the end of each experiment. The solution was saturated with the gas mixture when solution pH stayed stable (ΔpH < 0.01) for at least 15 min. Double-junction pH probes suitable for concentrated brines and resistant to H_2S were used for the pH measurements.

Once a stable pH was reached, the solution pH was adjusted to pH 5.00 by injecting deaerated HCl 0.01 M to the solution. To make sure that solution pH stayed fixed at 5.00, the solution was sparged with the gas mixture for another 0.5 h prior to inserting the specimen into the solution and before beginning the electrochemical measurements. The magnetic stirrer was stopped throughout the electrochemical measurements.

The specimen material was API 5L X65 pipeline grade carbon steel. The microstructure and chemical composition of X65 steel are presented in Figure 9-4 and

Table 9-1, respectively. The RCE specimen was in the form of an annulus (with an outer diameter of 12 mm, a length of 14 mm, and an outer surface area of 5.4 cm^2. Only the outer surface of the specimen was exposed to the solution. The cell volume to specimen surface area ratio in the experiments was approximately 370 cm^3/cm^2, which was much larger than the average minimum ratio of 30 cm^3/cm^2 suggested by ASTM G31 [15], but again due to relatively short duration of the experiments no significant contamination of the cell was expected. Prior to each experiment, the specimen was sequentially wet polished with 80-, 240-, 400- and 600-grit abrasive papers. Then, the specimen was ultrasonically cleaned in an isopropanol bath for 3 min and dried in a cool N_2 gas stream. The RCE specimen was carefully mounted onto the RCE shaft without touching its surface and the whole assembly was inserted into the solution. The RCE assembly was rotated at 1000 rpm, which simulates the mass transfer conditions in a 10 cm ID pipe with an average flow velocity of 1 m/s [301], using the mass transfer equivalent conditions.

In each experiment, EIS, LPR, and PD sweeps were performed in that order, using the same specimen. First EIS was done to measure the solution resistance. Then LPR was conducted for the corrosion rate measurements to identify the overall effect of salt concentration on the H_2S corrosion rate. Finally, PD sweeps were obtained to investigate how individual reaction mechanisms underlying H_2S corrosion are affected by salt concentration. For each NaCl concentration, the experiments were repeated two times.

The LPR technique was performed using a three-electrode setup as shown in Figure 10-38 A, using a potential range from -5 mV to +5 mV vs. OCP with a scan rate of 0.125 mV/s. The RCE acted as the working electrode in the LPR technique. A saturated Ag/AgCl reference electrode connected to a Luggin capillary served as the reference electrode and a platinized titanium mesh (20 mm × 30 mm) was used as the counter electrode to complete the three-electrode setup. The duration of each LPR measurement was 80 sec. The average Stern-Geary constant (B) for converting the measured polarization resistance into the corrosion rate was determined to be around 18.7 mV/dec. This was done by fitting the PD sweeps via an electrochemical model [96]. The measured polarization resistance values were corrected for the solution resistance, which was measured by EIS. EIS was done prior to each LPR measurement at OCP with the same electrode setup as for LPR in a frequency range of 10000-0.1 Hz with a peak-to-peak AC voltage amplitude of 10 mV.

For the PD sweep measurements, before starting to sweep the potential, the open circuit potential (OCP) was monitored to ensure having a stable OCP value (Δ_{OCP} < 2 mV/min). The PD sweep experiments were carried out according to the following steps: (1) a cathodic sweep starting from the OCP toward more negative potentials up to -1 V vs. OCP; (2) wait for the OCP to return near its initial value—within a few mV (this took about 1 h); (3) an anodic sweep starting from the OCP to more positive potentials up to 0.35 V vs. OCP. The PD sweep scan rate was 0.125 mV/s. All the PD sweeps were corrected for the solution resistance obtained by EIS. A Gamry potentiostat Reference 600 was used for all the electrochemical measurements. Each full set of electrochemical measurements required about 6 h. The increase in the solution pH for each experiment was less than 0.05 pH units for all NaCl concentrations, confirming that no significant contamination of the solution by released corrosion products occurred.

11.2.2 Results and Discussion for RCE H_2S Corrosion Experiments at pH 5 and 100 ppm $H_2S_{(g)}$

11.2.2.1 pH Measurements

Figure 11-2 shows the autogenous pH of solution before pH adjustment for 1 wt.% and 20 wt.% NaCl concentration solutions sparged with an H_2S/N_2 gas mixture at 100 ppm $H_2S_{(g)}$. The purpose of the dashed line is to just show the trend, which is not as expected as the autogenous pH of solution increased with increasing NaCl concentration. The first speculation is that increasing salt concentration decreased H_2S solubility (the salting out effect), and therefore pH increased. However, as explained in Section 10.2.2 for the CO_2-saturated solutions, and it is expected to be same for the H_2S-saturated solutions, it is the activity of dissolved gas and not its concentration (*i.e.*, H_2S solubility) that is linked to pH.

Since the experiments were carried out in an open system at a constant partial pressure of 100 ppm $H_2S_{(g)}$ for both NaCl concentrations, *i.e.*, continuous supply of $H_2S_{(g)}$ throughout the experiments, the fugacity of $H_2S_{(g)}$ ($f_{H_2S_{(g)}}$) was constant and the same for both NaCl concentrations. At a fixed temperature and partial pressure, the H_2S solubility equilibrium constant (K_H in Reaction ((11-1)) is constant. Therefore, activity of $H_2S_{(aq)}$ ($a_{H_2S_{(aq)}}$) was constant and the same for both NaCl concentrations following the equilibrium. On the other hand, the equilibrium Equation (11-4) for the H_2S dissociation Reaction (11-3) shows that $a_{H^+_{(aq)}}$, an indication of solution pH ($-\log_1(a_{H^+_{(aq)}})$), is associated with $a_{H_2S_{(aq)}}$ and not H_2S concentration ($c_{H_2S_{(aq)}}$). Therefore, the $c_{H_2S_{(aq)}}$ decrease with increasing NaCl concentration cannot be the reason for the increase in solution pH.

$$H_2S_{(g)} \overset{K_H}{\leftrightarrow} H_2S_{(aq)} \tag{11-1}$$

$$K_H = \frac{a_{H_2S_{(aq)}}}{f_{H_2S_{(g)}}} \tag{11-2}$$

$$H_2S_{(aq)} \overset{K_1}{\leftrightarrow} HS^-_{(aq)} + H^+_{(aq)} \tag{11-3}$$

$$K_1 = \frac{a_{H^+_{(aq)}} a_{HS^-_{(aq)}}}{a_{H_2S_{(aq)}}} \tag{11-4}$$

Similar to CO_2 saturated solutions, it is speculated that the changes in the autogenous pH of solution with salt concentration in solutions saturated with 100 ppm $H_2S_{(g)}$ mixed with N_2 gas is due to unaccounted variations in the interactions between different species in the solution that alter the H^+ ion activity coefficient.

Figure 11-2

Autogenous pH of aqueous NaCl solutions at 20°C, and 1 bar total pressure saturated with a H_2S/N_2 gas mixture containing 100 ppm $H_2S_{(g)}$. The error bars represent the minimum and maximum values obtained in two repeated experiments.

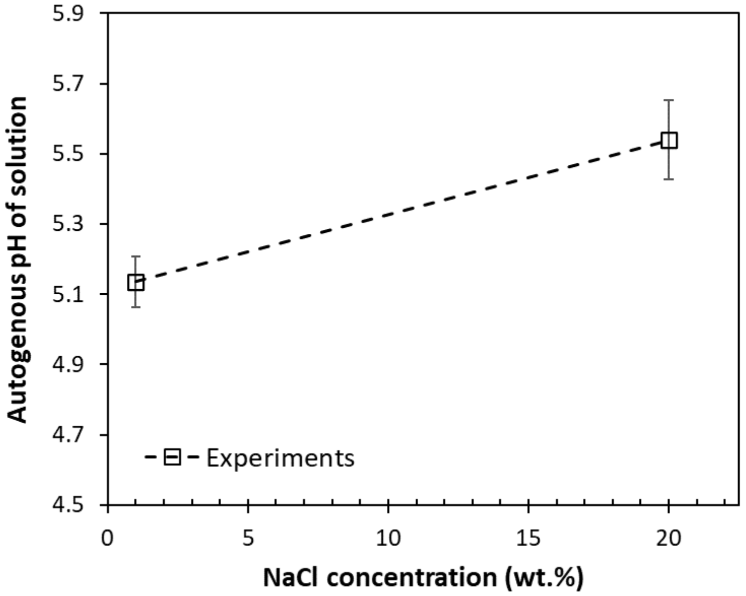

The anomalous trend is in line with the pH measurements in N_2 saturated aqueous NaCl solutions presented in Figure 9-5 and Figure 9-13, while it is opposite to the trend observed for autogenous pH with respect to NaCl concentration in CO_2-saturated (Figure 10-1, Figure 10-16, Figure 10-28, and Figure 10-39) and H_2S-saturated experiments (Figure 11-12). Therefore, it can be speculated that the presence of N_2 gas and its effect on interspecies interactions in the solution caused the increase in pH with increasing NaCl concentration. The speciation equilibrium models discussed in this study for the H_2O-NaCl-H_2S system cannot capture this unexpected trend for autogenous pH at different NaCl concentrations. They predict a declining trend for pH with increasing NaCl concentration. For example, the MSE model predicts 7.14 and 5.73 at 1 and 20 wt.% NaCl concentrations, respectively. Further investigations are required.

11.2.2.2 Corrosion rate and PD sweep and measurements

Figure 11-3 shows the corrosion rate results obtained by LPR and PD sweep measurements at 100 ppm $H_2S_{(g)}$ and two NaCl concentrations. The corrosion rate values measured with both techniques were almost the same, indicating the accuracy of measurements and the reliability of the conclusions. The H_2S corrosion rate decreased when NaCl concentration increased from 1 wt.% to 20 wt.%. This agrees very well with the effect of salt concentration on uniform CO_2 corrosion rate reported in Chapter 10. Similar to CO_2 corrosion, the decrease in H_2S corrosion rate with increasing NaCl concentration can be explained by analyzing the PD sweeps.

Figure 11-3

The variation in the corrosion rate with NaCl concentration for X65 carbon steel RCE specimen with a rotational speed of 1000 rpm exposed to aqueous solutions at 20°C and pH 5 saturated with 100 ppm $H_2S_{(g)}$ *at 1 bar total pressure.*

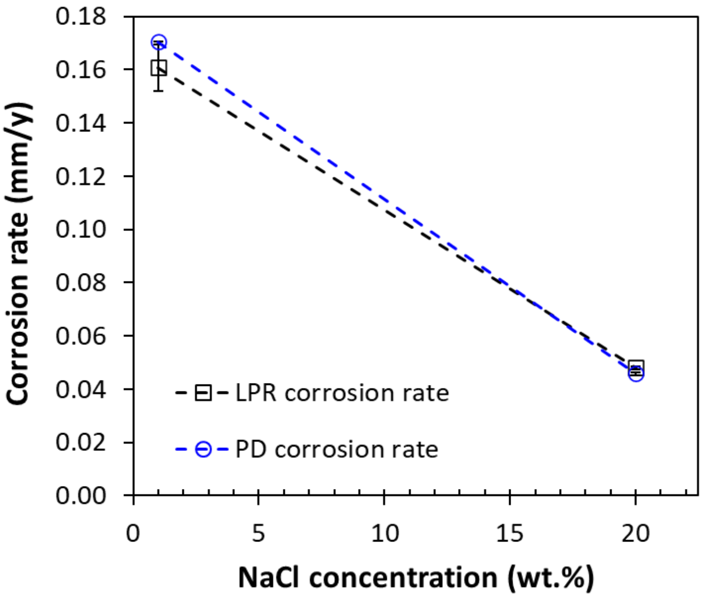

In the following text, the PD sweep results will be presented. The PD sweeps from two separate runs at 20 wt.% NaCl, pH 5 and 100 ppm $H_2S_{(g)}$ are presented in Figure 11-4 as an example to confirm that the PD sweep measurements were repeatable. Therefore, the conclusions arrived at from the PD sweeps can be trusted to be reasonably accurate.

Figure 11-4

Potentiodynamic sweeps from two separate runs for X65 carbon steel RCE specimen with a rotational speed of 1000 rpm exposed to a solution, at 20°C, pH 5, and 20 wt.% NaCl, saturated with 100 ppm $H_2S_{(g)}$ at 1 bar total pressure.

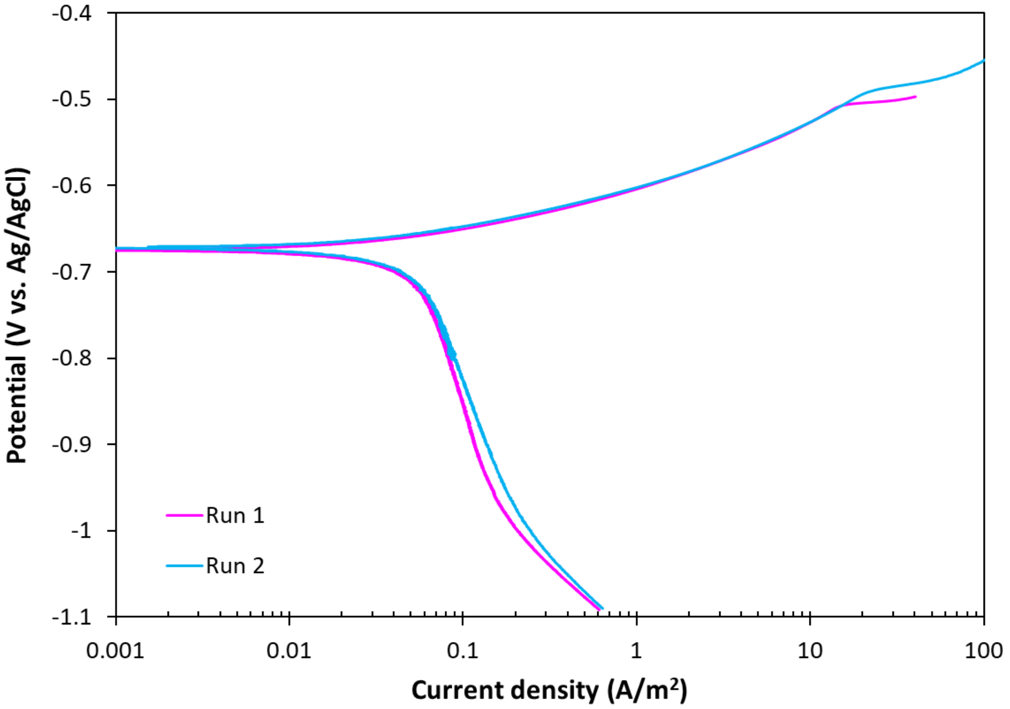

Figure 11-5 shows the PD sweeps for 1 wt.% and 20 wt.% NaCl concentrations at 20°C, pH 5 and 100 ppm $H_2S_{(g)}$. The potential values are corrected for the solution resistance (iR drop) in all the given sweeps. Both anodic and cathodic branches of the sweeps changed with increasing NaCl concentration. The anodic dissolution of iron in the active region and the H^+ ion reduction reaction in the charge transfer region were retarded with increasing NaCl concentration. There was a decrease in the H^+ ion reduction reaction limiting current density (i_{Lim}) when NaCl concentration was increased. The water reduction reaction seems to be unaffected by the higher NaCl concentration.

Figure 11-5

Potentiodynamic sweeps for X65 carbon steel RCE with a rotational speed of 1000 rpm exposed to aqueous NaCl solutions, at 20°C and pH 5, saturated with 100 ppm $H_2S_{(g)}$ *at 1 bar total pressure.*

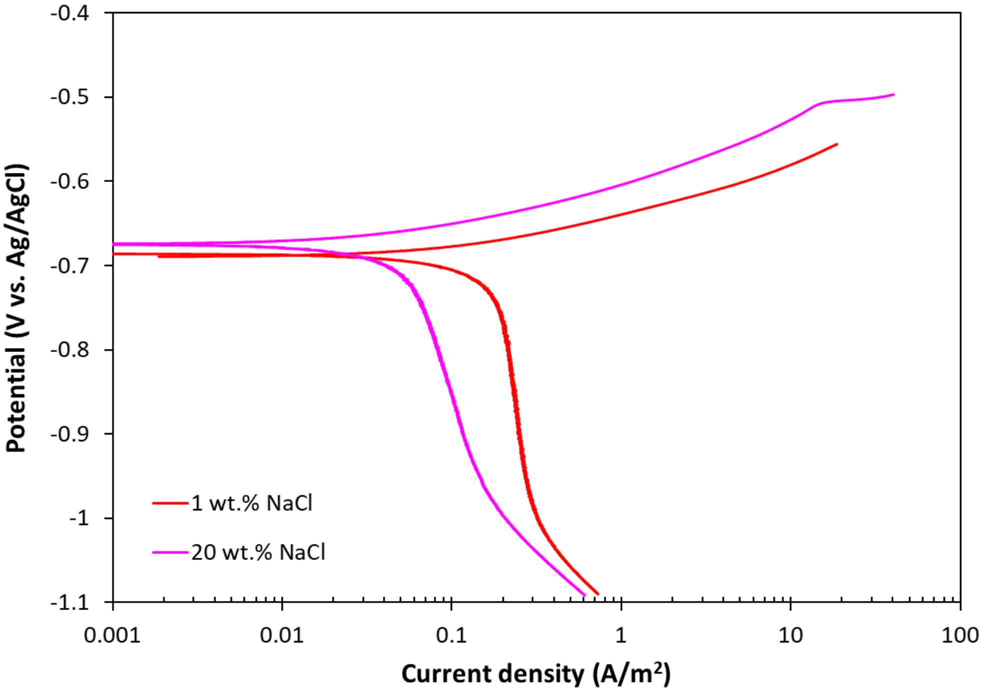

To quantify the effect of NaCl concentration on each of the parameters mentioned above, the kinetic features of the PD sweeps were extracted by overlaying the experimental sweeps for the best fit with those calculated by a simple electrochemical model [96][89].

The electron transfer coefficients for the H^+ ion reduction reaction (α_{H^+}) and the Fe oxidation reaction in the active region (α_{Fe}) at 20°C, pH 5, 100 ppm H2S and NaCl concentrations of 1 wt.% and 20 wt.% are presented in Table 11-1. The α_{H^+} values are the same as the theoretical value of 0.5, commonly considered for the

---

[89] Activation energies of 59860 J/mol for H^+ ion, 24809 J/mol H_2O reduction and 25398 J/mol for Fe oxidation reactions. A reversible potential of -0.685 V vs. Ag/AgCl was used for all three reactions. The reference temperature was 20°C.

hydrogen evolution reaction on an iron surface [185]. Since α_{H^+} did not change with varying NaCl concentration, it can be concluded that the mechanism of hydrogen evolution under the experimental conditions used in this set of experiments was not affected by salt concentration.

Table 11-1

The average electron transfer coefficients for H^+ *reduction reaction (*α_{H^+}*) and Fe oxidation (*α_{Fe}*) for the RCE* H_2S *experiments in aqueous NaCl solutions, at* 20^oC *and pH 5, saturated with 100 ppm* $H_2S_{(g)}$ *at 1 bar total pressure.*

NaCl concentration (wt.%)	1	20
α_{H^+}	0.5	0.5
Cathodic Tafel slope (mV/dec)	116	116
α_{Fe}	1.05	1.2
Anodic Tafel slope (mV/dec)	55	48

The α_{Fe} values are in the same range as those reported for iron dissolution in strong acid corrosion experiments in Chapter 9 and in CO_2 corrosion experiments in Chapter 10. Moreover, Chin and Nobe [194] reported 1.18 for dissolution of iron in acidic chloride media, which is close to the results of this set of experiments. There was a small increase in α_{Fe} with increasing NaCl concentration from 1 wt.% to 20 wt.%. However, this increase is in the range of the experimental error and more different NaCl concentrations need to be experimented to be able to comment with certainty about any possible change in the mechanism for active dissolution of iron. This will be investigated further in Section 11.3. For now, it is expected that similar to

CO_2 corrosion, there was no change with salt concentration in the iron dissolution mechanism in the active region in the presence of 100 ppm $H_2S_{(g)}$

Table 11-2 presents the exchange current densities for the H^+ ion reduction reaction (i_{o,H^+}), the iron dissolution reaction (i_{o,H^+}), and i_{Lim} for 1 wt.% and 20 wt.% NaCl concentrations at 20°C, pH 5 and 100 ppm $H_2S_{(g)}$, as determined by modeling the PD sweeps. The i_{o,H^+} decreased when NaCl concentration was increased from 1 wt.% to 20 wt.%. This is in complete agreement with all the results reported so far for strong acid corrosion in Chapter 9 and for CO_2 corrosion in Chapter 10. The decrease in i_{o,H^+} with increasing NaCl concentration is related to the adsorption of Cl^- ions on the surface, which are an obstruction for the H^+ ion adsorption and reduction reaction [171]. One reason for the decreasing trend seen for the corrosion rates in Figure 11-3 is the decrease in i_{o,H^+}.

Table 11-2

The cathodic limiting current density (i_{Lim}), the H^+ reduction exchange current density (i_{o,H^+}) and the Fe oxidation exchange current density ($i_{o,Fe}$) for the RCE H_2S experiments in aqueous NaCl solutions, at 20°C and pH 5, saturated with 100 ppm $H_2S_{(g)}$ at 1 bar total pressure.

NaCl concentration (wt.%)	1	20
i_{o,H^+} (A/m^2)	0.380	0.0875
i_{Lim} (A/m^2)	0.233	0.087
$i_{o,Fe}$ (A/m^2)	0.160	0.023

The $i_{o,Fe}$ decreased with increasing NaCl concentration from 1 wt.% to 20 wt.%, which means that the rate of anodic dissolution of Fe in the active region decreased at higher NaCl concentrations. This is identical to the results described earlier for changes in $i_{o,Fe}$ with NaCl concentration (for concentrations greater than ~ 1 wt.%) in strong acid corrosion (Chapter 9) and CO_2 corrosion (Chapter 10). Hence, $i_{o,Fe}$ variation with NaCl concentration is another reason for the decrease in the H_2S corrosion rate when NaCl concentration was increased from 1 wt.% to 20 wt.%.

The most noticeable change in the PD sweeps (Figure 11-5) with NaCl concentration was that of i_{Lim}. In H_2S corrosion, i_{Lim} is an indication of the rate of the H^+ ion reduction reaction that is controlled by the relatively slow rate of $H_2S_{(aq)}$ dissociation reaction coupled with the rate of the mass transfer of species to the metal surface. Table 11-2 shows that i_{Lim} decreased with increasing NaCl concentration from 1 wt.% to 20 wt.%.

In H_2S corrosion, i_{Lim} mainly depends on a_{H^+} and a_{H_2S}. This is explained in detail in Chapter 12. The experiments were carried out in an open system. Therefore, a_{H_2S} was constant for both NaCl concentrations. a_{H^+} was constant for both NaCl concentrations because the solution pH was adjusted at 5.00 in the experiments. Consequently, a_{H^+} and a_{H_2S} cannot be the reason for the decrease in i_{Lim} with NaCl concentration. i_{Lim} also depends on diffusion coefficients of H^+ ion and H_2S as well as their activity coefficients. Out of these parameters, the contribution of H^+ diffusion coefficient and its activity coefficient in the total i_{Lim} value is dominant. The i_{Lim} is directly related to H^+ ion diffusion coefficient and inversely depends on H^+ ion activity coefficient. The decreasing trend for i_{Lim} when NaCl increased from 1 wt.% to 20 wt.% is primarily due to the increase in H^+ ion activity coefficients as well as the decrease in the diffusion coefficient of H^+ ion (the effect of salt concentration on the diffusion coefficient is explained in Section 3.3.2). The decrease in i_{Lim} with NaCl concentration is the additional reason for the decreasing trend seen for the H_2S corrosion rate in Figure 11-3.

Three potential reasons have been suggested for the decrease in the H_2S corrosion rate at 20°C, pH 5 and 100 ppm $H_2S_{(g)}$ when NaCl concentration increased from 1 wt.% to 20 wt.%: the decreases in i_{o,H^+}, $i_{o,Fe}$, and i_{Lim} with increasing NaCl concentration. To understand which of these three parameters influences the H_2S corrosion process to a greater extent at the experimental conditions, the Evans diagram is created.

Figure 11-6 illustrates the Evans diagrams for 1 wt.% and 20 wt.% NaCl concentrations at the experimental conditions for this set of experiments. For both NaCl concentrations, the corrosion process was under mixed control. This indicates that the rate of the H_2S corrosion process was controlled by both charge transfer processes as well as i_{Lim}. The reason for the decrease in the H_2S corrosion rate in the NaCl concentration range of 1 wt.% to 20 wt.% was due to retardation of both iron dissolution reaction and H^+ ion reduction reaction in the charge transfer regions as well as the decrease in i_{Lim}. Since the difference between i_{Lim} and i_{Corr} is smaller for 1 wt.% NaCl compared to that for 20 wt.% NaCl, the contribution of i_{Lim} in the overall H_2S corrosion rate was larger at 1 wt.% NaCl. This shows that increasing NaCl concentration slowed down the charge transfer processes more than the rate of parameters controlling i_{Lim}.

Figure 11-6

The Evans diagrams for the effect of NaCl concentration on uniform H_2S corrosion of X65 carbon steel RCE specimen with a rotational speed of 1000 rpm exposed to aqueous NaCl solutions, at 20°C and pH 5, saturated with 100 ppm $H_2S_{(g)}$ at 1 bar total pressure. E_{corr} is the corrosion potential (OPC), i_{corr} is the corrosion current density (Blue: 1 wt.% NaCl, and red: 20 wt.% NaCl).

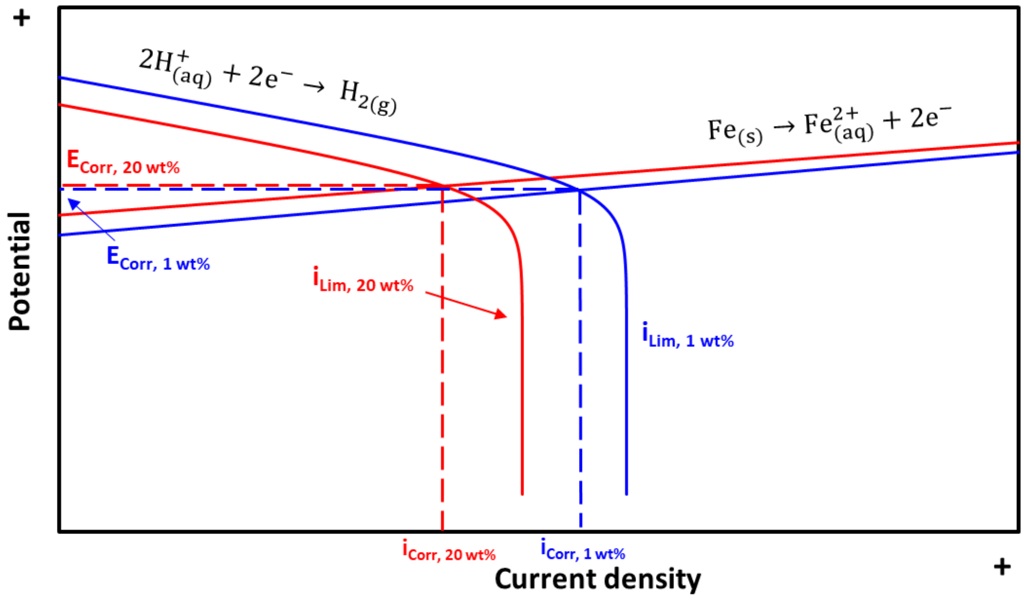

11.2.3 Summary and Conclusions of RCE H_2S Corrosion Experiments at pH 5 and 100 ppm $H_2S_{(g)}$

This set of experiments was done to understand the effect of salt concentration on aqueous uniform H_2S corrosion of carbon steel at low $H_2S_{(g)}$ concentrations. Experiments were carried out using an X65 carbon steel RCE specimen with a rotational speed of 1000 rpm exposed to aqueous NaCl solutions, at 20°C and pH 5, saturated with 100 ppm $H_2S_{(g)}$ at 1 bar total pressure. The main conclusions found in this set of experiments, when NaCl concentration was increased from 1 wt.% to 20 wt.%, are as follows:

1. Similar to the N_2-satuared solutions and unlike the CO_2-saturated solutions, the autogenous pH of solution increased. The increase was attributed to the presence of N_2 gas. Further investigations were recommended on this subject.
2. The uniform H_2S corrosion rate decreased.
3. Analysis of PD sweeps indicated that the decrease in the H_2S corrosion rate was due to retardation of both iron dissolution and H^+ ion reduction reactions in the charge transfer regions as well as the decrease in i_{Lim}. At 1 wt.% NaCl, i_{Lim} and at 20 wt.% charge transfer processes were dominant in the overall H_2S corrosion rate.
4. Evans diagrams showed that salt concentration influences the charge transfer processes more than i_{Lim} in the H_2S corrosion process under the experimental conditions.

11.3 The Effect of Salt Concentration on H_2S Corrosion at pH 5 and 1 bar H_2S Using a Rotating Cylinder Electrode (RCE)

This set of experiments are a very important part of the investigation of the effect of salt concentration on aqueous uniform H_2S corrosion of carbon steel. In this part, a thorough study of the salt effect on uniform H_2S corrosion has been carried out by using weight loss technique, electrochemical techniques, and various surface analysis methods. Experiments were conducted in a pure $H_2S_{(g)}$ atmosphere at a total pressure of 1 bar and an NaCl concentration range of 0.1 wt.% to 20 wt.%. The combination of a high partial pressure of $H_2S_{(g)}$, concentrated brines, and the variety of experimental techniques makes this set of experiments uniquely challenging. No study with such experimental conditions can be found in the literature.

A solution pH of 5 was used in this set of experiments to intensify the contribution of the H_2S buffering effect in the H_2S corrosion process. Furthermore, pH was adjusted to 5.00 for all salt concentrations, in such a way that the only parameter changed in the experiments was NaCl concentration. These two considerations granted an improved understanding of the effect of salt concentration on the H_2S corrosion process.

11.3.1 Experimental Materials and Methodology for RCE H_2S Corrosion Experiments at pH 5 and 1 bar $H_2S_{(g)}$

Experiments were conducted at 20°C and 1 bar total pressure ($pH_2S \cong 0.98$ bar, equivalent to 10^6 ppmv) in a 2-liter glass cell. The experimental apparatus used in this part are shown in Figure 11-7.

The outlet H_2S gas from the glass cell was passed through a saturated NaOH solution followed by an activated carbon-containing flask to scrub H_2S gas from the gas mixture. The scrubbed gas was then sent to a combustion chamber with excess air where the remaining H_2S in the gas stream was converted to sulfur dioxide (SO_2). It is assumed that the combustion process has a near 100% conversion and no detectable H_2S remains in the effluent gas.

To keep the solution temperature at 20°C, water was circulated by an industrial chiller through a copper coil around the glass cell to cool down the solution temperature. In combination with the cooling coil, a hot plate was used continuously to stabilize the temperature at 20 ± 0.5°C.

Figure 11-7

(A) Schematic; (B) picture of the experimental apparatus and (C) a zoomed-in view of the experimental glass cell used in the RCE H_2S corrosion experiments at 20°C, ~1 bar H_2S, and pH 5. The numbers in the schematic represent: (1) N_2 gas cylinder, (2) H_2S gas cylinder, (3) double-column rotameter, (4) hot plate, (5) thermocouple, (6) gas inlet, (7) Luggin capillary, (8) pH-electrode, (9) reference electrode, (10) gas outlet from the cell, (11) motor, (12) rotating cylinder electrode, (13) platinum coated counter electrode, (14) stir bar, (15) sodium hydroxide solution, (16) activated carbon scrubber, (17) gas outlet to the combustion chamber.

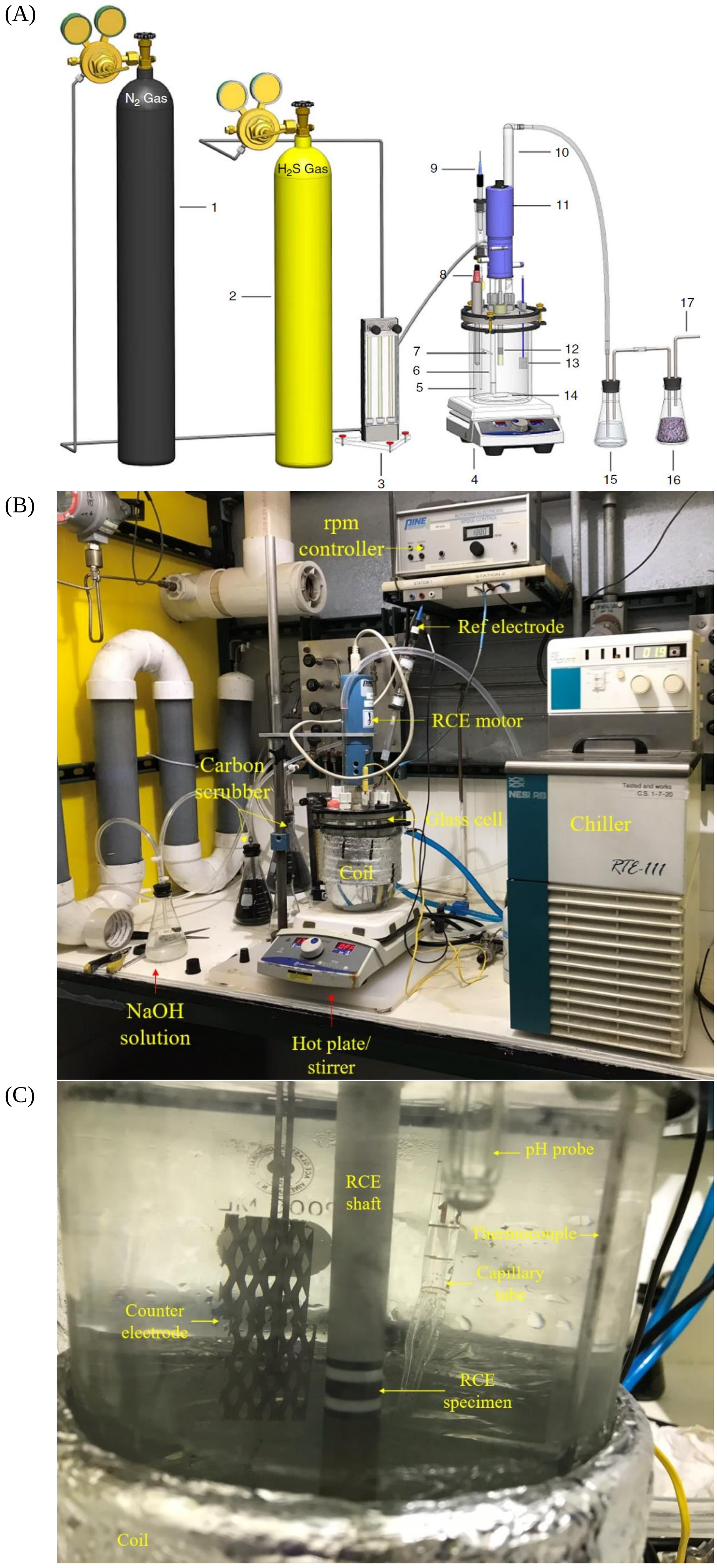

At the beginning of each experiment, the required amount of NaCl was mixed with deionized water (conductivity < 1 μS/cm) in the glass cell. Then, the solution was sparged with pure H_2S gas mixture for at least 3.5 h, while being stirred by a magnetic stirrer. The time of 3.5 h was found experimentally as the least amount of time needed to drop the concentration of dissolved oxygen in the solution (~ 2 liter) to less than 10 ppb and saturate the solution with the H_2S gas. The dissolved oxygen was measured during few experiments with an Orbisphere 410 oxygen meter connected to the gas outlet to assure that the oxygen level in the solution was less than 10 ppb. The solution pH was frequently monitored from the beginning to the end of each experiment. The solution was considered saturated with the H_2S gas when solution pH remained stable (ΔpH < 0.01) for at least 15 min. Double-junction pH probes suitable for concentrated brines and resistant to H_2S gas were used for the pH measurements.

Once a stable pH was reached, the solution pH was adjusted to pH 5.00 by injecting deaerated NaOH 0.2 M to the solution. To make sure that solution pH was stable at 5.00, the solution was sparged with the experimental gas for another 0.5 h prior to inserting the specimen(s) into the solution and before beginning the corrosion rate and the electrochemical measurements. The magnetic stirrer was stopped throughout the measurements.

The specimen material was API 5L X65 pipeline grade carbon steel. The chemical composition of this X65 steel is defined in Table 11-3. The microstructure of the experimental X65 carbon steel is a uniform, fine structure of pearlite in a ferrite matrix (Figure 11-8)[90].

---

[90] The chemical composition of API 5L X65 (type 49) in Table 11-3 is different from that for API 5L X65 (type 48) listed in Table 9-1. However, their microstructures are almost the same. Therefore, it is assumed that they behave similarly in terms of corrosion.

Table 11-3

Chemical composition of the experimental API 5L X65 (type 49) carbon steel (in wt.%).

Al	As	B	C	Ca	Co	Cr	Cu	Mn	Mo
0.032	0.008	0.001	0.13	0.002	0.007	0.14	0.131	1.16	0.16
Nb	Ni	P	Pb	S	Sb	Si	Sn	Ta	Ti
0.017	0.36	0.009	<0.001	<0.009	<0.009	0.26	0.007	0.001	0.001
V	Zr	Fe							
0.047	0.001	Balance							

Figure 11-8

Microstructure of the experimental API 5L X65 (type 49) carbon steel (in wt.%): (A) magnification 1, (B) magnification 2.

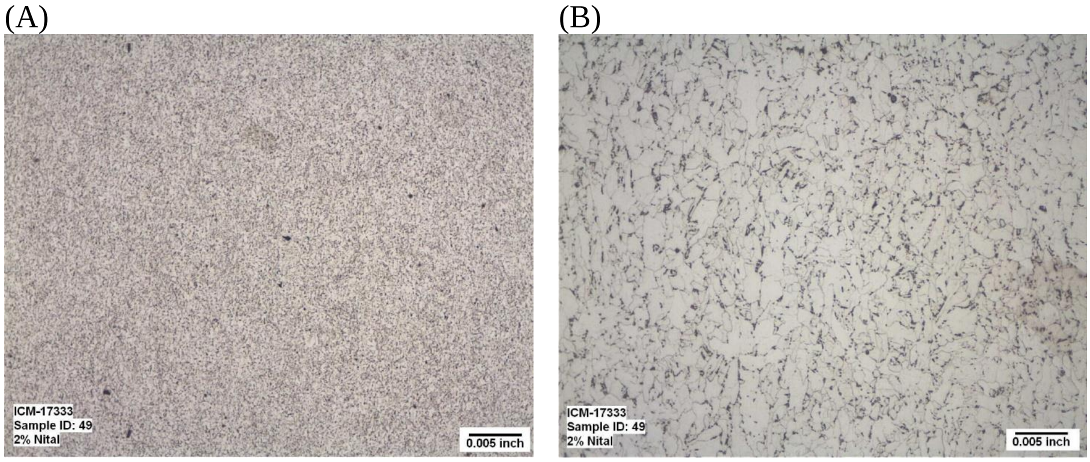

Three types of specimens used in this set of experiments: long RCE annulus specimens (Figure 11-9 A) with an outer diameter of 12.6 mm, a length of 44.3 mm, and an outer surface area of 17.5 cm^2 for corrosion rate measurements, short RCE annulus specimens (Figure 11-9 B) with an outer diameter of 11.9 mm, a length of 4.5

mm, and an outer surface area of 1.7 cm^2 or PD sweep measurements, and, square specimens (Figure 11-9 C) with dimensions of 10 × 10 × 2.5 mm and a total surface area of 4.375 cm^2 for surface analysis.

Figure 11-9

Pictures of X65 specimens used in the RCE H_2S corrosion experiments at 20^{o}C, pH 5 and 1 bar $H_2S_{(g)}$: (A) long annulus specimen for corrosion rate measurements, (B) short annulus specimen for PD sweep measurements[91]*, (C) square specimen for surface analysis. The dimension of squares in the background is 0.5 cm × 0.5 cm.*

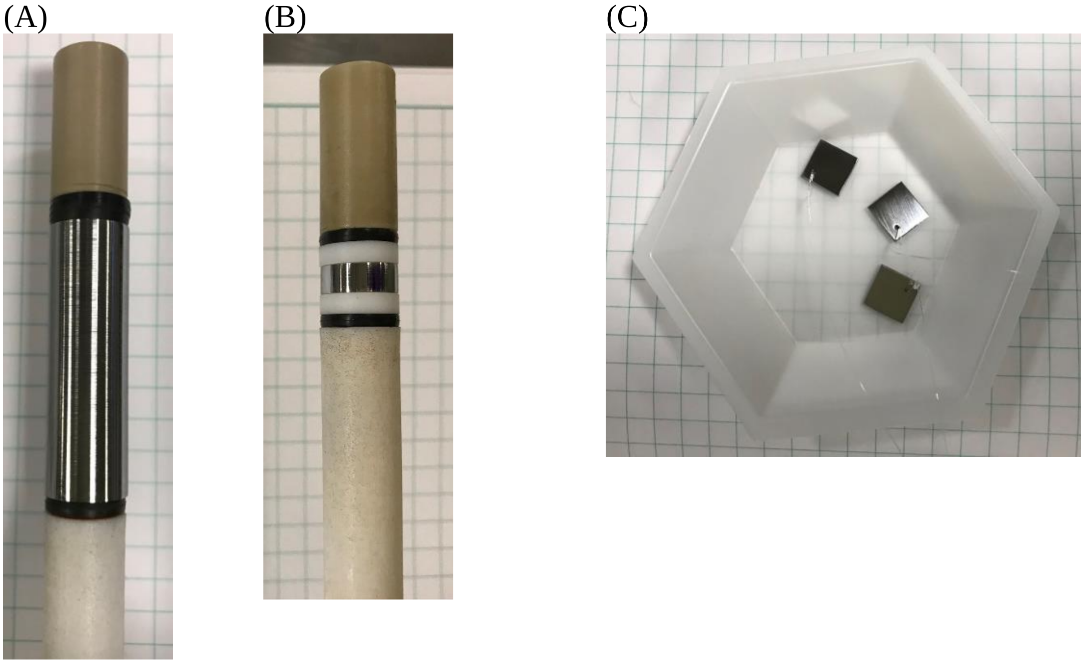

Prior to each experiment, the specimens were sequentially wet polished with 80-, 240-, 400- and 600-grit abrasive papers. Next, the specimens were ultrasonically cleaned with isopropanol alcohol for 3 min and dried in a cool N_2 gas stream. The

---

[91] The RCE shaft was not design for a short RCE specimen. Therefore, two Teflon rings were used on both sides of the RCE specimen to make it long enough for the shaft.

annulus specimen was flush mounted onto a shaft to be used as a rotating cylinder electrode (RCE) in the experiments. The square specimens were submerged into the experimental solution by hanging them with nylon threads from the glass cell's lid. The RCE assembly was rotated at 1000 rpm, which simulates the mass transfer conditions in a 10 cm ID pipe with an average flow velocity of 1 m/s [301]. On the other hand, the square specimens were in a stationary condition and experienced less flow velocity compared to the RCE, and thus were expected to corrode somewhat less compared to the RCE specimen.

Two separate sets of experiments were conducted: corrosion rate measurements at two NaCl concentrations of 1 wt.% (0.17 m) and 20 wt.% (4.28) to characterize the overall effect of salt concentration on the H_2S corrosion rate and PD sweeps at five NaCl concentrations of 0.1 wt.% (0.017 m), 1 wt.%, 3 wt.% (0.53 m), 10 wt.% (1.90 m), and 20 wt.% to investigate how individual reaction mechanisms underlying H_2S corrosion are affected by salt concentration.

For each corrosion rate measurement experiment, the long RCE was used as the specimen. Additionally, three hanging square specimens were used for surface analysis. The cell volume to specimen surface area ratio in the corrosion rate measurements was approximately 65 cm^3/cm^2, which was higher than the average minimum ratio of 30 cm^3/cm^2 suggested by ASTM G31 [15] and again this was not expected to become a problem when it comes to solution contamination by released corrosion products in relatively short experiments.

The H_2S corrosion rates were measured using weight loss (WL) and linear polarization resistance (LPR) techniques. The duration of each corrosion rate experiment was 5 h, which started from the moment the specimen was inserted into the solution and finished when it was retrieved from the solution. All the specimens were introduced to the solution at the same time. The duration of the corrosion rate measurements was chosen to be relatively short to avoid formation of iron sulfides on the steel surface, as the objective of this part of study was to study uninform H_2S corrosion in the absence of protective layers on the surface. Moreover, there was a limitation in the duration of the experiments, which was related to the H_2S safety protocol. Experiments with H_2S concentrations greater than 100 ppm needed to be performed and finished during the regular working hours in a single day, in order to make sure that someone is present in the facility for help in the case of accidents (no unattended overnight exposure could be allowed). The 5 h was identified as the maximum time for a corrosion rate experiment, which could be finished safely during the regular working hours. Prior to immersion the RCE specimen into the test solution, it was weighed with a precise balance of 0.1 mg precision. The LPR corrosion rate measurement was performed concurrently with the WL corrosion rate measurement in the same experiment and by using the same specimen —on average every 0.5 h during the 5 h period (totally eleven times). The LPR technique was implemented using a three-electrode setup (shown in Figure 11-7 C) and by sweeping the potential in a range from -5 mV to +5 mV vs. OCP with a scan rate of 0.125 mV/s. Each LPR measurement lasted for 80 sec. The long RCE acted as the working electrode when using the LPR technique. A saturated Ag/AgCl reference electrode connected to a Luggin capillary served as the reference electrode and two platinized titanium mesh (each 20 mm × 30 mm) were used as the counter electrode to complete the three-electrode setup. The average Stern-Geary constant (B) for converting the measured polarization resistance into the corrosion rate was determined to be around 20.4 mV/dec. This was done by fitting the PD sweeps via an electrochemical model [96]. The measured polarization resistance values were corrected for the solution resistance, which was measured by EIS. EIS was done prior to each LPR measurement with the same electrode setup at OCP in a frequency range of 10000-0.1 Hz with a peak-to-peak AC voltage amplitude of 10 mV. The LPR time-averaged corrosion rates were determined by the cumulative trapezoidal integration of the five instantaneous LPR corrosion rates taken over the 5 h experiment. The increase in solution pH (due to increase in Fe^{2+} concentration in the solution because of corrosion) after 5 h was less than 0.05 pH units, at both NaCl concentration, which confirmed that there was no significant deviation of the water chemistry and accumulation of corrosion products in the experiments.

After 5 h, the specimens were retrieved from the solution and thoroughly rinsed with distilled water for at least one minute to remove the salt. Then, they were rinsed with isopropanol alcohol and dried in a cool N_2 gas stream. One square specimen was immediately used for scanning electron microscopy/energy dispersive spectroscopy (SEM/EDS) (Figure 10-27 A), one was instantly mounted in epoxy with its smallest surface upward for the cross-section analysis (Figure 10-27 B), and one was used later for the surface profilometry (Figure 10-27 C). The long RCE specimen was acid washed in the Clarke solution [312] for 15 sec, followed by cleaning with distilled water. Later, the long RCE specimen was rinsed with isopropanol alcohol and dried in a cool N_2 gas stream. Finally, the RCE specimen was weighed again to determine the WL corrosion rates.

For the PD sweeps the short RCE specimen was used. The reason for using a short RCE specimen was to be able to have a full cathodic sweep up to the water reduction reaction line without surpassing the potentiostat maximum current limitation. At 20°C, pH 5, and 1 bar H_2S, with the typical RCE specimen used in the strong acid corrosion and the CO_2 corrosion experiments (the same diameter, but about three times longer in length compared to the short RCE specimen) the current generated by sweeping the potential in the cathodic region was very high, in the range of 1 A, and this current surpassed the maximum potentiostat limitation as shown in Figure 11-10. The range of currents typically measured in strong acid corrosion and CO_2 corrosion is also marked in Figure 11-10, which is about one to two orders of magnitude smaller than that for H_2S corrosion in pure H_2S atmosphere.

Figure 11-10

A screenshot of the Gamry Framework™ Data Acquisition Software showing the Gamry potentiodynamic measurements in cathodic potential at 1 bar H_2S, 20°C, 3 wt.% NaCl, and pH 5 with an RCE specimen of L=14.2 mm and OD=11.94 mm.

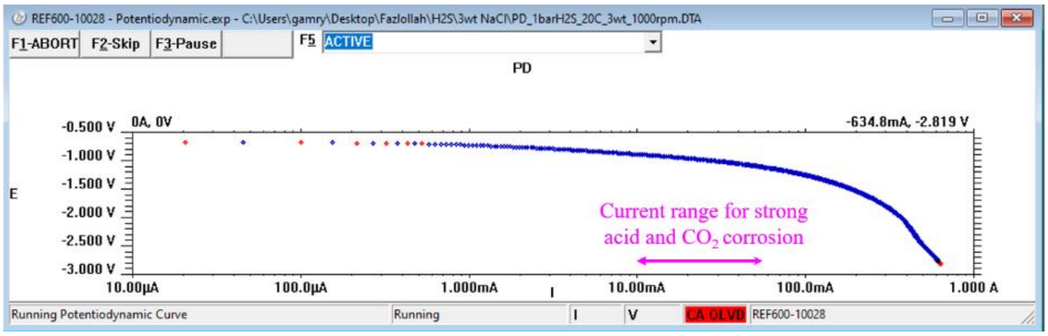

REF600-10028 - Potentiodynamic.exp - C:\Users\gamry\Desktop\Fazlollah\H2S\3wt NaCl\PD_1barH2S_20C_3wt_1000rpm.DTA

F5 ACTIVE

Running Potentiodynamic Curve | Running | I | V | CA OLVD | REF600-10028

The cell volume to specimen surface area was approximately 1176 cm^3/cm^2 in this case, which was much greater than the average minimum ratio of 30 cm^3/cm^2 recommended by ASTM G31 [15]. Before starting the PD sweeps, the open circuit potential (OCP) was monitored to ensure having a stable OCP value ($\Delta_{OCP} < 2$

mV/min). At this time, an LPR corrosion rate measurement in a potential range from -5 mV to +5 mV vs. OCP and using a scan rate of 0.125 mV/s was done. Then, the PD sweep experiments were performed according to the following steps: (1) a cathodic sweep starting from the OCP toward more negative potentials up to -3.5 V vs. OCP; (2) wait for the OCP to return near its initial value—within a few mV (this took about 1 h); (3) an anodic sweep starting from the OCP to more positive potentials up to 0.35 V vs. OCP. The PD sweep scan rate was chosen 5 mV/s. The reason behind that was to be able to reach potentials corresponding to the water reduction region (*e.g.*, around -3 V vs. Ag/Ag/Cl for 1 wt.% NaCl, before correcting for the solution resistance) in a short time to avoid formation of any iron sulfide corrosion products on the steel surface.

Figure 11-11 shows that the cathodic PD sweep for 0.1 wt.% NaCl at two different scan rates. The sweeps overlapped entirely, indicating that the scan rate did not have an influence on the PD sweeps. All the PD sweeps were corrected for the solution resistance obtained by EIS. A Gamry potentiostat Reference 600 was used for all the electrochemical measurements. The increase in solution pH for the PD sweep experiments, each lasted about 2 h, was less than 0.02 pH units, for any NaCl concentration.

Figure 11-11

The cathodic sweeps for X65 carbon steel RCE with a rotational speed of 1000 rpm obtained at two scan rates of 0.5 and 50 mV/s in 0.1 wt.% NaCl aqueous solution at 1 bar H_2S, 20°C, and pH 5.

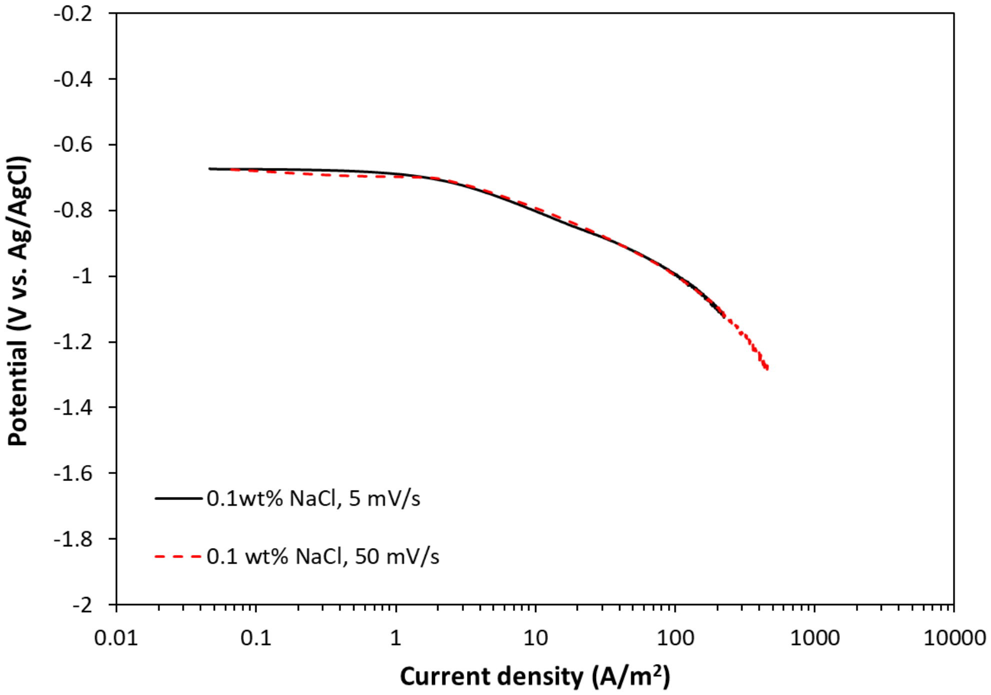

11.3.2 Results and Discussion for RCE H_2S Corrosion Experiments at pH 5 and 100 ppm $H_2S_{(g)}$

11.3.2.1 pH Measurements and Solution Chemistry

The change in autogenous pH of the H_2S saturated solution with respect to NaCl concentration is shown in Figure 11-12. The solution pH decreased from 4.03 at 0.1 wt.% NaCl to 3.73 at 20 wt.% NaCl. The reason behind such behavior is discussed below.

When H_2S gas is dissolved in water according to:

$$H_2S_{(g)} \rightleftarrows H_2S_{(aq)} \tag{11-5}$$

dissolved H_2S forms, which then dissociates in two steps as follows:

$$H_2S_{(aq)} \rightleftarrows H^+_{(aq)} + HS^-_{(aq)} \tag{11-6}$$

$$HS^-_{(aq)} \rightleftarrows H^+_{(aq)} + S^{2-}_{(aq)} \tag{11-7}$$

Figure 11-12

Autogenous pH of H_2S saturated solutions measured at 20°C and 1 bar total pressure (~ 0.98 bar pH_2S) before pH adjustment. The error bars represent the minimum and maximum values obtained in repeated experiments (with at least 3 repeats). The experimental data are compared with two speciation models.

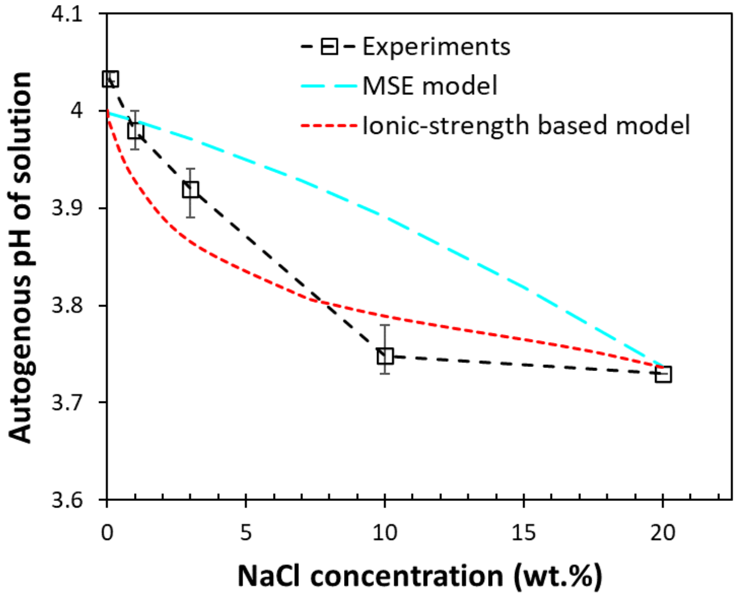

Due to the salting out effect described in Sections 4.1 and 7.2, Reaction (10-5)(11-5) moves from right to left. Because of that, Reactions (11-6) and (11-7) will also shift from right to left in order to establish equilibria, and that leads to a lower activity of H^+ ions and an increase in pH. However, pH measurements reported in Figure 11-12 show exactly the opposite trend, where the solution pH decreased with increasing NaCl concentration. Thus, the salting out effect cannot be used to justify the experimental observations. The only possible explanation for the pH variation with the addition of NaCl is the change in the activity coefficient of H^+ ion.

Figure 11-13 shows the changes in activity coefficient (γ), concentration (m), and activity (a) of dissolved $H_2S_{(aq)}$ and H_3O^+ ion with NaCl concentration in the autogenous pH condition. At 20 wt.% NaCl, the amount of dissolved H_2S is about half of that dissolved in pure water (salting out of H_2S) (Figure 11-13 A). As shown in Figure 11-13 B, $\gamma_{H_3O^+}$ decreases from unity by about 20% between 0 wt.% and ~ 2 wt.% NaCl and then increases beyond that, so that at 20 wt.% NaCl, it is 3.36. $m_{H_3O^+}$ has the opposite trend and reaches a peak at around 2 wt.% NaCl. $a_{H_3O^+}$ monotonously increases with higher NaCl concentrations. Taking into account that $a_{H_3O^+}$ and a_{H^+} have the same trend with NaCl concentration according to Equation (T-2); when pH is calculated ($pH = -\,log\ a_{H^+}$), this results in a continuous downward trend for pH, just as obtained in the experiments. Therefore, the observed decreasing trend in pH with the addition of NaCl is solely a result of the change in the activity coefficient and the concentration of H_3O^+ ion (or equivalently, H^+ ion[92]) and is not related to the salting out effect. This argument can be supported by recalling that $a_{H_2S_{(aq)}}$ only depends on the fugacity of $H_2S_{(g)}$ and does not depend on NaCl concentration. So, $a_{H_2S_{(aq)}}$ remains constant[93] even as $m_{H_2S_{(aq)}}$ decreases significantly with increasing NaCl concentration. It is $a_{H_2S_{(aq)}}$ and not $m_{H_2S_{(aq)}}$ that is associated with the activities of other dissolved species such as that for H_3O^+ ion and the

---

[92] It is an acceptable assumption that concentration, activity coefficient, and activity of H^+ ion are equal to those for H_3O^+ ion.

[93] In this argument, the effect of NaCl concentration on water vapor pressure, and therefore, on a_{H_2S} is neglected.

resulting pH. Since $a_{H_2S_{(aq)}}$ does not change with NaCl concentration, it could not be the reason for the observed trend in pH.

Figure 11-13

Bulk concentration, molality-based activity coefficient, and activity of (A) dissolved $H_2S_{(aq)}$ and (B) H_3O^+ ion calculated by the MSE speciation model for H_2S saturated aqueous NaCl solutions at 20°C, 1 bar total pressure (~ 0.98 bar pH_2S), and autogenous pH.

(A)

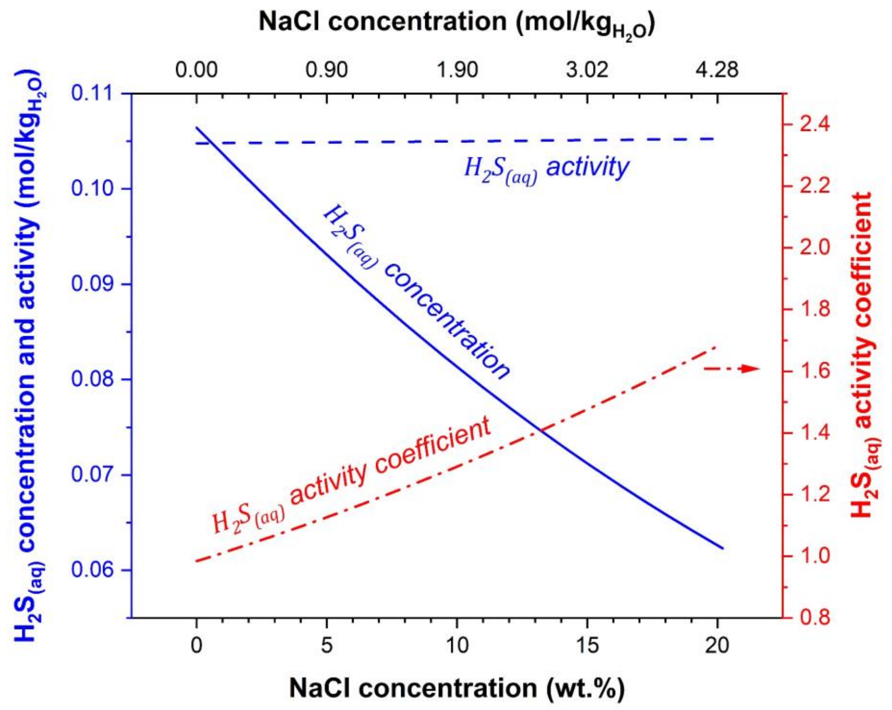

(B)

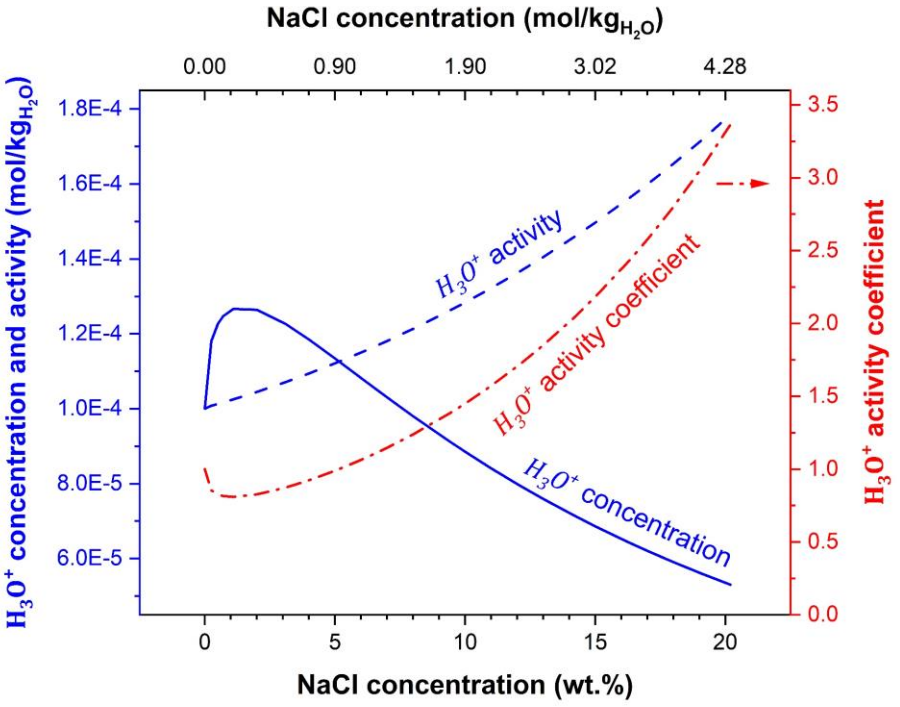

The predicted pH values obtained with the MSE model and the ionic strength-based model are compared with the experimental pH values in. The MSE model results in a linear trend for pH with increasing NaCl concentration, while the experimental pH values have a concave upward trend with respect to NaCl concentration. The MSE model predictions are in good agreement with the experimental pH values at NaCl concentrations below 1 wt.% and at 20 wt.%. However, between 1 wt.% and 20 wt.% NaCl the MSE model predictions deviate from the experimental pH values, with a maximum error of ~ 0.15 pH unit at 10 wt.% NaCl. The ionic strength-based model—introduced in this study for the first time—captures the concave upward trend observed in the experimental pH values in Figure 11-12. The maximum error in the ionic strength-based model is ~ 0.06 pH unit, which occurs at 3 wt.%. The overall accuracy of the ionic strength-based model is better that the MSE model for the experimental conditions used in this set of experiment.

Figure 11-14 shows the changes in concentration, activity coefficient, and activity of $H_2S_{(aq)}$, HS^- ion, H_3O^+ ion, OH^-, Cl^- and activity of water with NaCl concentration at a constant pH value of 5 for all NaCl concentrations. The activity of H_2S is almost constant for all NaCl concentration because the experiments were conducted in an open system[94]. At a constant pH of 5, the activity of H^+ ion is 10^{-5} m for all NaCl concentrations; however, the activity of H_3O^+ ion decreases slightly with increasing salt concentration from 10^{-5} because it is a function of H_2O activity, as mentioned in Appendix T. Another interesting observation is that activity of HS^- ion

---

[94] In this argument, the effect of NaCl concentration on water vapor pressure, and therefore, on a_{H_2S} is neglected

is almost constant because of constant activities of $H_2S_{(aq)}$ and H_3O^+ ion (Reaction (8-53))[95].

---

[95] The changes in $H_2O_{(l)}$ activity with NaCl concentration can be ignored when taking into account the unit conversion from mole fraction to molality.

Figure 11-14

Bulk concentration, molality-based activity coefficient, and activity of (A) dissolved H_2S, (B) HS^- ion, (C) H_3O^+ ion, (D) OH^- ion, (E) Cl^- ion, and (F) H_2O calculated by the MSE model speciation model for H_2S saturated solutions at 20°C, 1 bar total pressure (~ 0.98 bar pH_2S), and pH 5.

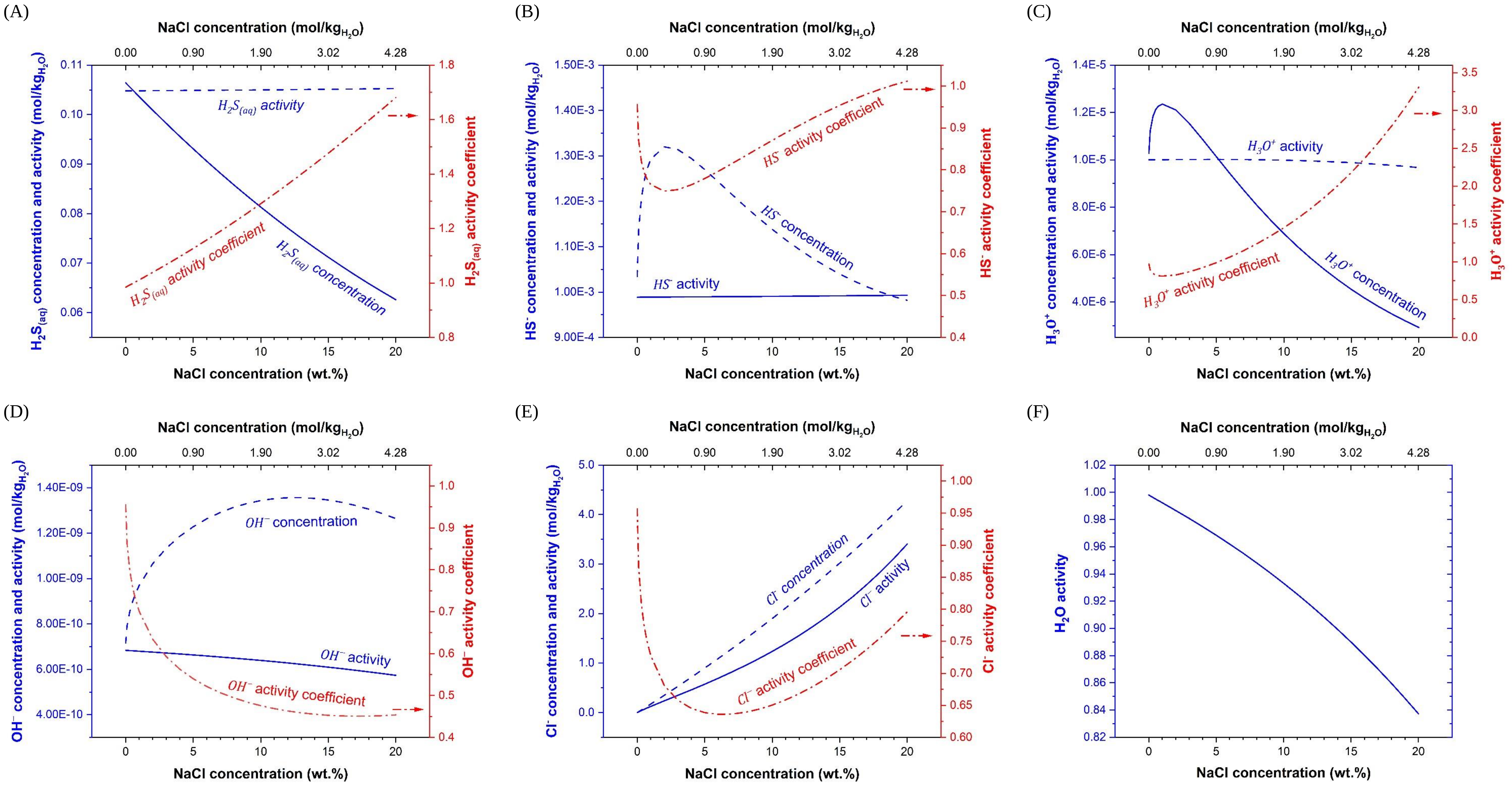

* In the MSE model, the properties for H_3O^+ ion is calculated instead of H^+ ion. At a constant pH of 5, the activity of H^+ ion is 10^{-5} m for all NaCl concentrations; however, the activity of H_3O^+ ion decreases slightly with increasing salt concentration from 10^{-5} because it is a function of H_2O activity, as mentioned in Appendix S.

11.3.2.2 Corrosion rate and PD sweep measurements

Figure 11-15 shows the changes in the LPR corrosion rate with time for 1 wt.% and 20 wt.% NaCl concentrations. An average B-value of 20.3 mV/dec obtained from the potentiodynamic sweeps was used to convert the measured polarization resistance to the corrosion rate. The corrosion rate decreased slightly with time for both salt concentrations, probably due to the ubiquitous formation of iron sulfide films on the steel surface. This will be further discussed in the surface analysis section. However, since the decrease in the corrosion rate was not significant, it can be assumed that the H_2S corrosion process remained almost unchanged throughout the 5 h experiments at both NaCl concentrations. The corrosion rate was higher at 1 wt.% NaCl compared to that at 20 wt.% NaCl during the whole experimental time.

Figure 11-15

Variation in the LPR corrosion rate with time in 5 h long weight loss experiments conducted with X65 carbon steel RCE with a rotational speed of 1000 rpm in aqueous NaCl solutions at 20°C, ~1 bar $H_2S_{(g)}$, and pH 5.

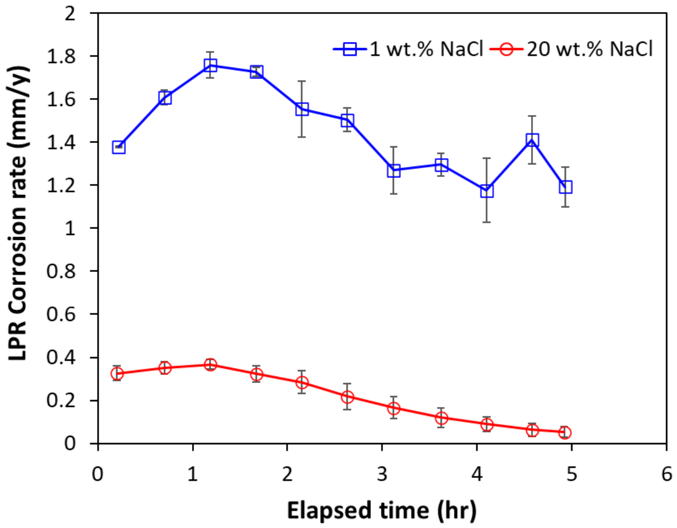

Figure 11-16 presents the variations in the H_2S corrosion rate with respect to NaCl concentration measured in two separate experiments by using two different specimen sizes and four independent techniques. The weight loss and time averaged LPR data were obtained in 5 h experiments. The PD sweeps and LPR data were measured in 2 h experiments. The agreement in the measured trends for the H_2S corrosion rate obtained by the four techniques indicates the reliability results, and therefore, supports the conclusions.

Figure 11-16

Variation in the corrosion rate with NaCl concentration for X65 carbon steel RCE with a rotational speed of 1000 rpm exposed to aqueous NaCl solutions at 20°C, ~1 bar $H_2S_{(g)}$, and pH 5. The corrosion rates were measured using weight loss, time averaged LPR, PD sweep and LPR techniques.

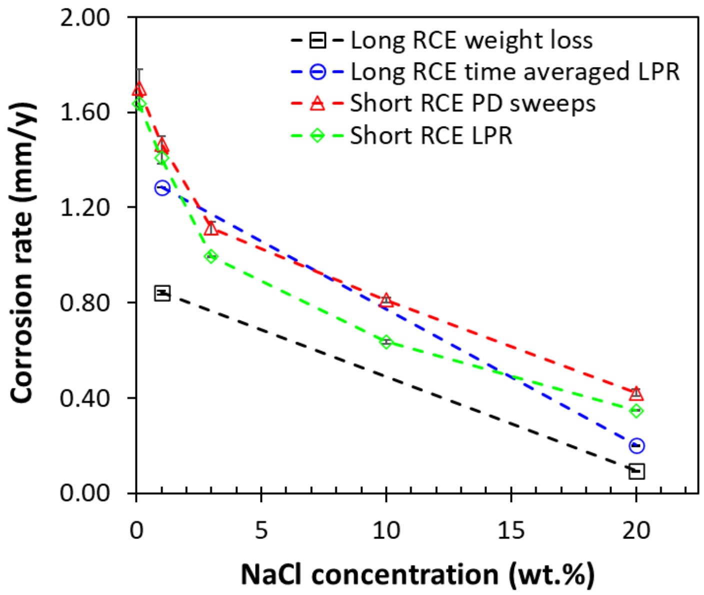

The uniform H_2S corrosion rate decreased with increasing NaCl concentration. The observed trend for the H_2S corrosion rate resembles the results reported in Chapter 10 for changes in the CO_2 corrosion rate with NaCl concentration. For example, for CO_2 experiments at 20^{o}C, 1 bar CO_2, and pH 5 (very similar experimental conditions to those in this section), the corrosion rate shown in Figure 10-30 had an increasing trend between 0.1 wt.% and 1 wt.% NaCl concentrations, while it decreased when NaCl concentration was increased from 1 wt.% NaCl to 20 wt.% NaCl. The decreasing trend for the H_2S corrosion rate between 1 wt.% and 20 wt.% NaCl concentrations is identical to that for the CO_2 corrosion rate. This behavior will be justified by looking at the changes in PD sweeps with NaCl concentration.

For NaCl concentrations below 1 wt.% NaCl, the corrosion rates obtained by the PD sweeps and LPR measurements do not show the increasing trend seen for the weight loss CO_2 corrosion rates in Figure 10-30. The H_2S corrosion rate decreased continually with increasing NaCl concentration from 0.1 wt.% NaCl to 20 wt.%. This declining trend in the H_2S corrosion rate at low NaCl concentrations can be explained by analyzing the PD sweeps (will be presented below). However, since weight loss corrosion rates are always more reliable than the corrosion rates measured by the electrochemical techniques such as PD sweep and LPR, weight loss experiments at NaCl concentrations lower than 1 wt.%. are required to confirm the results obtained by the PD sweeps and LPR measurements.

The corrosion rates obtained by weight loss and time averaged LPR techniques are smaller than those obtained by the PD sweeps and LPR techniques. The reason for this difference can be related to duration of experiments these techniques were applied in. Weight loss and time averaged LPR corrosion rates were obtained in 5 h experiments, while the PD sweep and LPR corrosion rates were measured within the 2 hr from introducing the specimen into the solution. It is shown in the surface analysis section that a layer of iron sulfide(s) formed on the surface in 5 h experiments. However, after 2 h no substantial layer was detected on the surface. The difference in the 5 h and 2 h experiments is evident in Figure 11-15, where the H_2S corrosion rate for both NaCl concentrations starts decreasing after about 2 h.

The two PD sweep repeats for each of the five experimental NaCl concentrations are shown Figure 11-17. For all NaCl concentrations, the repeated PD sweeps matched very well. This indicates the repeatability, and therefore, the reliability of the PD sweep results. The solution resistance measured with EIS is compensated in all the sweeps presented hereafter.

Figure 11-17

The PD sweeps for two separate experiments at each NaCl concentration. The sweeps were obtained with X65 carbon steel RCE with a rotational speed of 1000 rpm exposed to aqueous NaCl solutions at 20°C, ~1 bar H_2S, and pH 5.

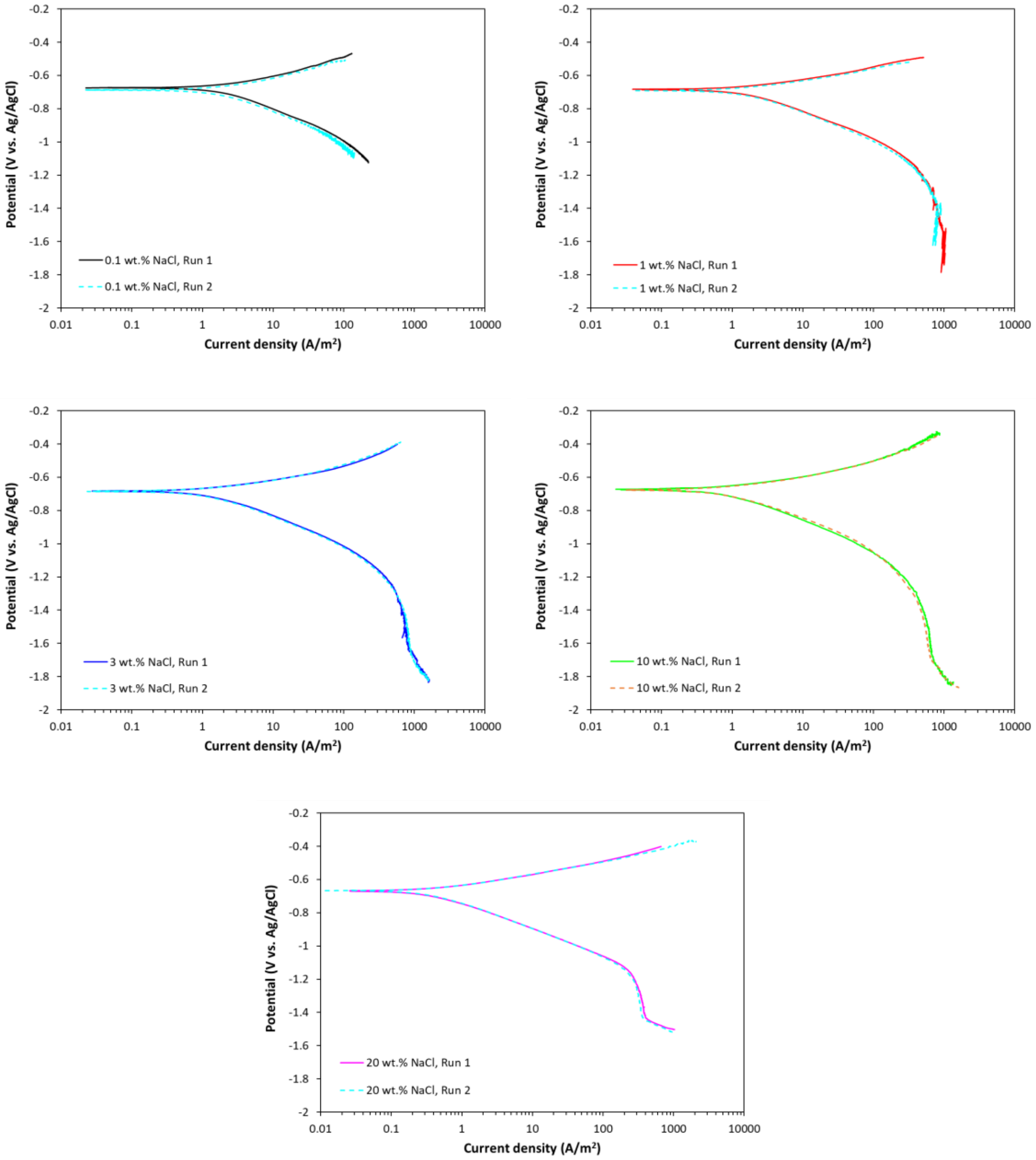

The effect of salt concentration on the PD sweeps is shown in Figure 11-18. The IR corrected cathodic sweep for 0.1 wt.% NaCl concentration could not reach the limiting current density potentials because of the large solution resistance at this NaCl concentration. The spikes appeared in the cathodic branch of the PD sweeps at 1 wt.% and 3 wt.% NaCl concentrations were due to accumulation of $H_{2(g)}$ bubbles on the steel surface at very negative potentials vs. OCP.

Figure 11-18

Potentiodynamic sweeps for X65 carbon steel RCE with a rotational speed of 1000 rpm exposed to aqueous NaCl solutions at 20°C, ~1 bar $H_2S_{(g)}$, and pH 5.

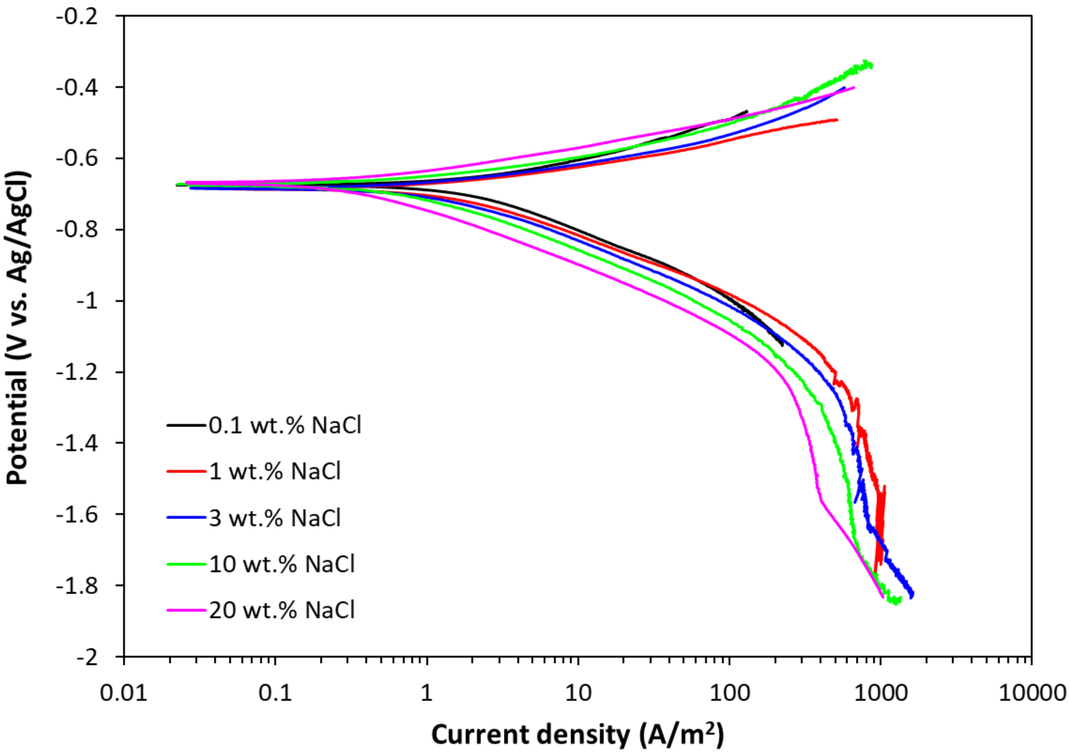

The NaCl concentration altered both anodic and cathodic branches of the PD sweeps. There seems to be an acceleration and then a retardation of the anodic reaction with increasing NaCl concentration, while the charge transfer region of the cathodic H^+ ion reduction reaction appears to be steadily retarded by salt presence.

The H^+ ion reduction reaction limiting current density (i_{Lim}) and the rate of the water reduction reaction seem to decrease at higher NaCl concentrations. To have a clear picture of the effect of NaCl concentration on the PD sweeps, kinetic features of the sweeps were determined by overlaying the experimental sweeps for the best fit with those calculated by a simple electrochemical model [96][96]. The fitted sweeps for two NaCl concentrations are shown in Figure 11-19 as a demonstration of the accuracy of the fitting exercise.

---

[96] An activation energy of 83.2 kJ/mol for H^+ ion and H_2O reduction reactions and an activation energy of 126.8 kJ/mol for Fe oxidation reaction were used [107]. A reversible potential of -0.685 V vs. Ag/AgCl was used for all three reactions. The reference temperature was 20°C.

Figure 11-19

Comparison of the experimental sweeps at 1 wt.% (A) and 20 wt.% (B) NaCl concentrations measured in the RCE H_2S experiments at ~1 bar H_2S with those obtained through a fitting process using a simple electrochemical model [96].

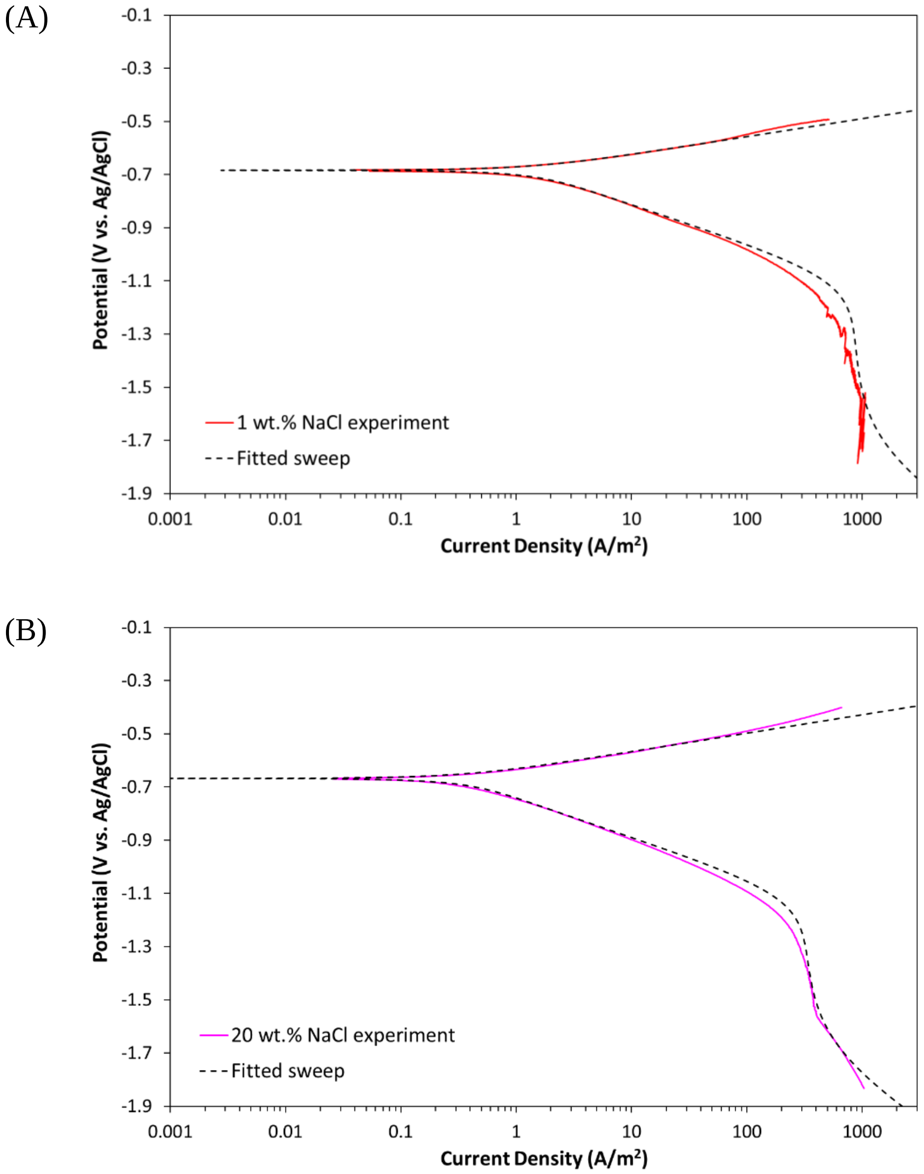

The electron transfer coefficients for H^+ reduction reaction (α_{H^+}) and Fe oxidation in the active region (α_{Fe}) at different NaCl concentrations are presented in Table 11-4. The accuracy of data presented here is expected to be better than those reported for the strong acid corrosion in Chapter 9 and CO_2 corrosion in Chapter 10. This is because the limiting current densities obtained for this set of experiments were much larger than those measured in strong acid and CO_2 corrosion; thus, the straight portions of the PD sweeps related to the charge transfer processes were more distinct and easier to fit with the model. For example, the straight charge transfer portions of the sweeps are clearly visible in Figure 11-19.

Table 11-4

The average electron transfer coefficients for H^+ *reduction reaction (*α_{H^+}*) and Fe oxidation (*α_{Fe}*) for the RCE* H_2S *experiments at 20°C, ~1 bar* H_2S*, and pH 5. Each data is an average of two measurements.*

NaCl (wt.%)	0.1	1	3	10	20
α_{H^+}	0.38±0.00	0.41±0.00	0.40±0.01	0.39±0.01	0.40±0.01
β_c (mV/dec)	-153±0	-141±0	-144±2	-149±3	-144±2
α_{Fe}	0.84±0.02	0.86±0.00	0.86±0.00	0.86±0.00	0.85±0.01
β_a (mV/dec)	69±2	68±0	68±0	68±0	68±1

The α_{H^+} values are somewhat smaller from the theoretical value of 0.5, frequently considered for the hydrogen evolution on an iron surface [185]. Additionally, they are smaller than those obtained in this study so far for strong acid corrosion (~ 0.45) and CO_2 corrosion (~ 0.5). These differences suggest that the mechanism of H^+ ion reduction reaction on the steel surface in H_2S corrosion is somewhat different from those for strong acid and CO_2 corrosion.

The α_{H^+} was almost the same (~ 0.4) for all NaCl concentrations, indicating that the hydrogen evolution mechanism on the steel surface under the experimental conditions of this part of study (20^{o}C, ~ 1 bar $H_2S_{(g)}$, and pH 5) was not influenced by the presence of salt.

The α_{Fe} was almost 0.86 for all NaCl concentrations. Bockris *et al.* [185] proposed a theoretical value of 1.5 for active dissolution reaction of iron in acidic media without the presence of halides. In the presence of halides, there are studies that reported similar α_{Fe} values to those obtained in this part of study. McCafferty and Hackerman [178] reported a range of α_{Fe} from 0.7 to 1 for 6 N chloride solutions. Kuo and Nobe [195] measured 0.78 for α_{Fe} at pH 1.1 in solutions with chloride concentrations between 0.2 to 4 M. More details about these two studies can be found in Table 5-2. However, the α_{Fe} values measured for the active dissolution reaction of iron in the presence of 1 bar $H_2S_{(g)}$ are different from those obtained for strong acid corrosion (1.2 to 1.3) and CO_2 corrosion (1.0 to 1.1). This difference could be due to a change in the mechanism of active iron dissolution in the presence of high $H_2S_{(g)}$ concentration. The α_{Fe} values reported in Table 11-1 for 100 ppm $H_2S_{(g)}$ balanced with $N_{2(g)}$ were close to those for strong acid corrosion. The mechanisms of iron dissolution in the active region in the presence of chloride and H_2S gas have been comprehensively explained in Chapter 5. However, further investigations are required on this topic.

Since, α_{Fe} did not change with increasing NaCl concentration, it leads to the conclusion that the mechanism of active dissolution of iron in H_2S corrosion was not affected by salt concentration. This is similar to the results obtained for CO_2

corrosion. However, for strong acid corrosion, it was shown that α_{Fe} values increased with increasing NaCl concentration.

The variation in the exchange current density (i_{o,H^+}) of the H^+ ion reduction reaction with respect to NaCl concentration is shown in Figure 11-20 A. The i_{o,H^+} is an indication of the rate of charge transfer for an electrochemical reaction (Chapter 5). The decreasing trend for i_{o,H^+} implies that the rate of H^+ ion reduction reaction in the charge transfer region decreased with increasing NaCl concentration. The decreasing trend for i_{o,H^+} with respect to NaCl concentration is very similar to that reported in strong acid and CO_2 corrosion experiments. This similarity in i_{o,H^+} trends for different types of corrosion verifies the accuracy and reliability of results for the effect of salt concentration on i_{o,H^+}. The decrease in i_{o,H^+} at higher NaCl concentrations can be related to the adsorption of Cl^- ions on the surface and blocking the surface areas required for H^+ ion adsorption and reduction reactions [171]. Hence, the decrease in i_{o,H^+} can be an explanation for the decreasing trend of the corrosion rate at high NaCl concentrations shown in Figure 11-16.

Figure 11-20

Variations in (A) the cathodic limiting current density (i_{Lim}) and the H^+ reduction exchange current density (i_{o,H^+}) and (B) the Fe oxidation exchange current density ($i_{o,Fe}$) with NaCl concentration. The current densities were extracted from the PD sweeps of X65 carbon steel RCE specimen with a rotational speed of 1000 rpm exposed to H_2S-saturated aqueous solutions at 20°C, 1 bar total pressure, and pH 5. The error bars represent the minimum and maximum values obtained in two repeated experiments. The reference temperature was 20°C.

(A)

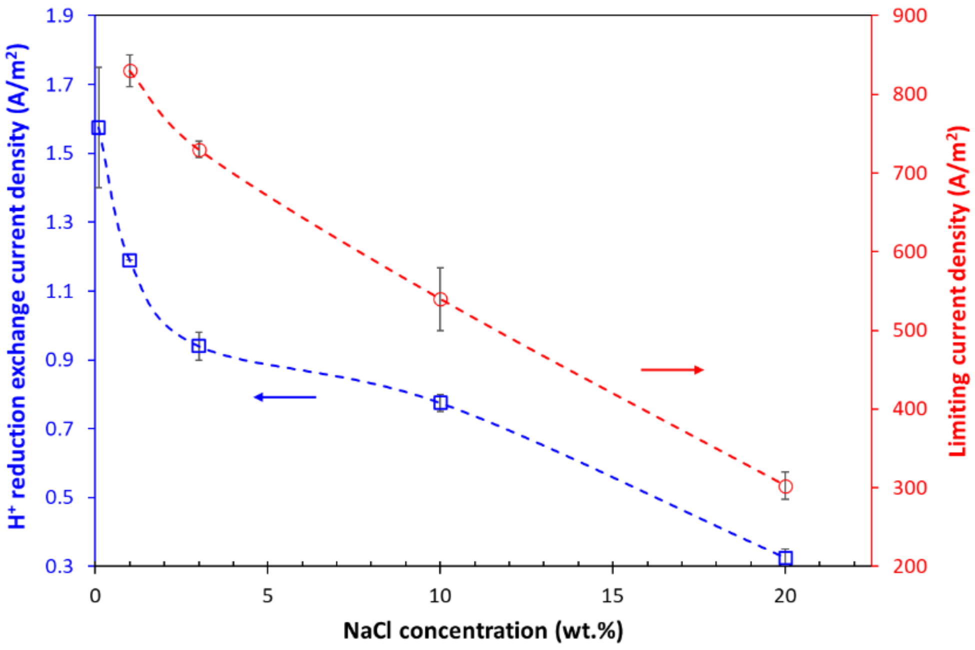

(B)

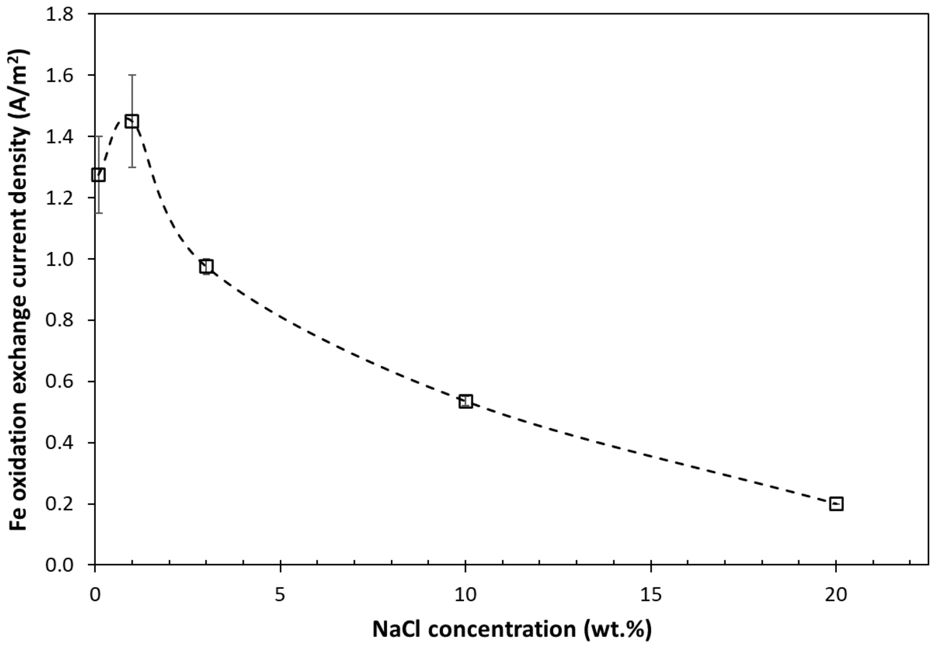

The trend observed for i_{o,H^+} in Figure 11-20 A can be modeled by using a correlation similar to Equation (5-23):

$$i_{o,H^+} = i_{o,H^+}^{ref} \left(\frac{a_{H^+,b}}{a_{H^+,b}^{ref}}\right)^{n_{H^+}^{H^+}} \left(\frac{a_{Cl^-,b}}{a_{Cl^-,b}^{ref}}\right)^{n_{Cl^-}^{H^+}} e^{-\frac{E_{a,H^+}}{R}\left(\frac{1}{T}-\frac{1}{T_{ref}}\right)} \qquad (11\text{-}8)$$

where, i_{o,H^+}^{ref} is the reference current density in A/m^2 at T_{ref} (293.15 K) and -685 mV *vs.* Ag/AgCl, $a_{H^+,b}$ is the bulk activity of H$^+$ ion in molarity concentration, $a_{H^+,b}^{ref}$ is the reference bulk activity of H$^+$ ion (= 10^{-4} M), $n_{H^+}^{H^+}$ is the reaction order of the H$^+$ ion reduction reaction with respect to H$^+$ ion activity, $a_{Cl^-,b}$ is the bulk activity of Cl$^-$ ion in molarity concentration, $a_{Cl^-,b}^{ref}$ is the reference bulk activity of Cl$^-$ ion (= 1 M), $n_{Cl^-}^{H^+}$ is the reaction order of the H$^+$ ion reduction reaction with respect to Cl$^-$ ion activity, E_{a,H^+} is the activation energy for the H$^+$ ion reduction reaction (= 59860 J/mol), T is solution temperature in K, and R is the gas constant in J/mol/K. Since the solution pH was constant in the experiments, the activity of H$^+$ ion was constant as well[97] (Figure 11-14 C). This means that x_{H^+} cannot be determined from this set of data points and experiments at different pH values are required to obtain that. However, a value of 0.5 obtained from the literature [96,185,207] is considered for $n_{H^+}^{H^+}$ in this study. By fitting Equation (10-11) with the experimental data presented in Figure 11-20 A, $n_{Cl^-}^{H^+}$ is determined to be ~ -0.2 and i_{o,H^+}^{ref} is equal to 2.2 A/m^2. The negative sign found for $n_{Cl^-}^{H^+}$ confirms the inhibition effect of Cl$^-$ ion activity (concentration) on the charge transfer rate for the H$^+$ ion reduction reaction.

---

[97] The changes in molarity-based activity due to changes in density with NaCl concentration is ignored.

The variation of $i_{o,Fe}$ as a function of NaCl concentration is shown in Figure 11-20 B. $i_{o,Fe}$ represents the rate of the anodic dissolution of Fe in the active region. $i_{o,Fe}$ increased between 0.1 wt.% and 1 wt.% NaCl concentrations and then reversed trend and decreased at NaCl concentrations greater than 1 wt.%. This behavior for $i_{o,Fe}$ in H_2S corrosion experiments has been observed in strong acid and CO_2 corrosion experiments as well. This consistency in $i_{o,Fe}$ trends for different type of corrosion confirms that the results for the effect of salt concentration on $i_{o,Fe}$ are accurate and can be trusted. Similar to strong acid corrosion, and unlike CO_2 corrosion, the maximum in the corrosion rate was observed at NaCl concentrations around 1 wt.%, The influence of $i_{o,Fe}$ on the H_2S corrosion will discussed in the following text where the Evans diagram is presented.

The trend presented for $i_{o,Fe}$ in Figure 11-20 B can be justified by considering the changes in the activities of OH^- ion, Cl^- ion, and H_2O with respect to NaCl concentration. According to Figure 11-14, the activities of OH^- ion and H_2O steadily decreases with increasing NaCl concentration, while the activity of Cl^- ion steadily increases. Similar to Equation (5-22), $i_{o,Fe}$ can be expressed in terms of activities of OH^- ion, Cl^- ion, and H_2O as follows:

$$i_{o,Fe} = i^{ref}_{o,Fe}\left(\frac{a_{OH^-,b}}{a^{ref}_{OH^-,b}}\right)^{n^{Fe}_{OH}}\left(\frac{a_{Cl^-,b}}{a^{ref}_{Cl^-,b}}\right)^{n^{Fe}_{Cl^-}}\left(\frac{a_{H_2O,b}}{a^{ref}_{H_2O,b}}\right)^{n^{Fe}_{H_2O}}\left(\frac{a_{H_2S,b}}{a^{ref}_{H_2S,b}}\right)^{n^{Fe}_{H_2S}} e^{-\frac{E_{a,Fe}}{R}\left(\frac{1}{T}-\frac{1}{T_{ref}}\right)} \quad (11\text{-}9)$$

where, $i^{ref}_{o,Fe}$ is the reference current density in A/m^2 at T_{ref} (293.15 K) and -685 mV *vs.* Ag/AgCl, $a_{OH^-,b}$ is the bulk activity of OH^- ion in molarity concentration, $a^{ref}_{OH^-,b}$ is the reference bulk activity of OH^- ion (= 10^{-10} M), n^{Fe}_{OH} is the reaction order of the

Fe oxidation reaction with respect to OH$^-$ ion activity, $a_{Cl^-,b}$ is the bulk activity of Cl$^-$ ion in molarity concentration, $a_{Cl^-,b}^{ref}$ is the reference bulk activity of Cl$^-$ ion (= 1 M), $n_{Cl^-}^{Fe}$ is the reaction order of the Fe oxidation reaction with respect to Cl$^-$ ion activity, $a_{H_2O,b}$ is the bulk activity of liquid water in molarity unit, $a_{H_2O,b}^{ref}$ is the reference bulk activity of liquid water (= 55.42 M), $n_{H_2O}^{Fe}$ is the reaction order of the Fe oxidation reaction with respect to H_2O, $a_{H_2S,b}$ is the bulk activity of $H_2S_{(aq)}$ in molarity unit, $a_{H_2S,b}^{ref}$ is the reference bulk activity dissolved $H_2S_{(aq)}$ (= 0.104 M), and $E_{a,Fe}$ is the activation energy for the Fe oxidation reaction in the active region (= 25398 J/mol), T is solution temperature in K, and R is the gas constant in J/mol/K. By comparing the PD sweeps at 100 ppm and ~ 1 bar $H_2S_{(g)}$, it was found that H_2S has a considerable effect on the rate of the anodic dissolution of iron. This has been discussed more in Section 12.1. Therefore, the effect of H_2S is included in Equation (11-9)

Lorenz [174] and McCafferty and Hackerman [178] reported different $n_{Cl^-}^{Fe}$ values for different range of Cl$^-$ activities (concentrations), as mentioned in Table 5-2. This indicates that the Fe dissolution reaction might proceed through different pathways depending on the activity of Cl$^-$ ion in the solution. From the $i_{o,Fe}$ trend presented in Figure 11-20 B, it can be assumed that at low NaCl concentrations below 1 wt.%[98], Cl$^-$ ions speeds up the anodic dissolution reaction by playing a catalytic role in iron dissolution, similar to that of OH$^-$ ions [172,194,195]. However, at NaCl concentrations above 1 wt.%, Cl$^-$ ions impedes the Fe dissolution reaction by being adsorbed on the surface and blocking the active sites (surface imperfections) required

---

[98] It can be any NaCl concentration between 1 wt.% and 3 wt.%, as the experimental NaCl resolution was not small enough to determine the exact maximum.

for the Fe dissolution reaction to happen [173,174,178,192]. Therefore, the $i_{o,Fe}$ curve is divided into two sections: below and above 1 wt.%. The reaction orders and $i_{o,Fe}^{ref}$ values for each region can be obtained by fitting Equation (11-9) using the bulk activity values calculated with the MSE model to the experimental $i_{o,Fe}$ values. Obtaining n_{OH}^{Fe} value needs experimentation at different solution pH. This means that n_{OH}^{Fe} cannot be found from the data presented in Figure 11-20 B. Therefore, a value of 1 was chosen for n_{OH}^{Fe} for the whole range of NaCl concentration according to the Bockris *et al.* [185,186] consecutive mechanism and reports by other scientists [174,195] (see Table 5-2). For NaCl $\leq$ 1 wt.%, $n_{Cl^-}^{Fe}$= 0.06, $n_{H_2O}^{Fe}$ = 0, and $i_{o,Fe}^{ref}$ = 0.24 and for NaCl $>$ 1, $n_{Cl^-}^{Fe}$= -0.4, $n_{H_2O}^{Fe}$ = 2, and $i_{o,Fe}^{ref}$ = 0.096. A reaction order of zero for H_2O at NaCl $\leq$ 1 means that the Fe dissolution reaction process is independent of H_2O activity in this NaCl concentration range. For $n_{H_2O}^{Fe}$ at high NaCl concentrations, the value found in this study is similar to the values (a range of 1.6-1.9) reported by Smart *et al.* [190,198]. $n_{H_2S}^{Fe}$ is found to be 0.3.

The last parameter in the PD sweeps for which the effect salt concentration needs to be discussed is i_{Lim}. Figure 11-20 A shows that i_{Lim} decreased monotonously when NaCl concentration was increased from 1 wt.% to 20 wt.%. Unlike the maximum reported for i_{Lim} at 1 wt.% NaCl in strong acid and CO_2 corrosion experiments, there was no maximum in i_{Lim} for H_2S corrosion. This is because i_{Lim} at 0.1 wt.% could not be measured. Otherwise, there could be a maximum in i_{Lim} for H_2S corrosion at 1 wt.% NaCl.

In H_2S corrosion, i_{Lim} is an indication of the rate of the H^+ ion reduction reaction that is controlled by the combination of the relatively slow rate of $H_2S_{(aq)}$

dissociation reaction and the rate of the mass transfer of species to the metal surface. i_{Lim} mainly depends on a_{H^+} and a_{H_2S}. This is explained in detail in Chapter 12. The experiments were carried out in an open system. Therefore, a_{H_2S} was constant for all NaCl concentrations. a_{H^+} was constant for all NaCl concentrations because the solution pH was adjusted at 5.00 in the experiments. Thus, a_{H^+} and a_{H_2S} cannot be the reason for the decrease in i_{Lim} with NaCl concentration. In addition, i_{Lim} depends on diffusion coefficients of H^+ ion and H_2S as well as their activity coefficients. Out of these parameters, the contribution of H^+ diffusion coefficient and its activity coefficient in the total i_{Lim} value is dominant. i_{Lim} is directly related to H^+ ion diffusion coefficient and inversely depends on H^+ ion activity coefficient. The decreasing trend for i_{Lim} when NaCl was increased from 1 wt.% to 20 wt.% is primarily due to the increase in H^+ ion activity coefficients as well as the decrease in the diffusion coefficient of H^+ ion. The decrease in i_{Lim} with NaCl concentration is and an additional possible reason for the decreasing trend seen for the H_2S corrosion rate in Figure 11-16.

Three possible reasons listed for the decrease in the H_2S corrosion rate at 20°C, pH 5 and ~ 1 bar $H_2S_{(g)}$ when NaCl concentration was increased from 0.1 wt.% to 20 wt.%: the variations in i_{o,H^+}, $i_{o,Fe}$, and i_{Lim} with increasing NaCl concentration. To find out which of these three parameters are dominant in changes in the H_2S corrosion rate as a function of NaCl concentration, the Evans diagram is deployed.

Figure 11-6 presents the Evans diagrams for 0.1 wt.%, 1 wt.%, and 20 wt.% NaCl concentrations at the experimental conditions used for this set of experiments. The H_2S corrosion process was under pure charge transfer control for the entire range of NaCl concentrations. When NaCl concentration was increased from 0.1 wt.% to 1 wt.%, shown in Figure 11-6 A, the anodic Fe dissolution reaction was accelerated, while the cathodic H^+ ion reduction reaction was retarded. The magnitude of the decrease in the rate of the cathodic H^+ ion reduction reaction was greater than the increase in the rate of the anodic Fe dissolution reaction. Therefore, the H_2S corrosion rate decreased with increasing NaCl concentration from 0.1 wt.% to 1 wt.%. This suggests that for H_2S corrosion at ~ 1 bar $H_2S_{(g)}$ partial pressure and NaCl concentrations below 1 wt.%, salt concentration influences the charge transfer part of the cathodic H^+ ion reduction reaction more than the anodic Fe dissolution reaction and i_{Lim}.

When NaCl concentration was increased from 1 wt.% to 20 wt.%, presented in Figure 11-6 A, both anodic Fe dissolution reaction and cathodic H^+ ion reduction reaction were retarded. The H_2S corrosion rate decreased in this NaCl range due to retardation of both iron dissolution reaction and the charge transfer part of the H^+ ion reduction reaction. The limiting current density had no effect on the rate of uniform H_2S corrosion under the experimental conditions of this part of study.

Figure 11-21

The Evans diagrams for the effect of NaCl concentration on uniform H_2S corrosion of X65 carbon steel RCE specimen with a rotational speed of 1000 rpm at 20°C, ~1 bar H_2S, pH 5, and 1000 rpm rotational speed. E_{corr} is the corrosion potential (OPC), i_{corr} is the corrosion current density (Green: 0.1 wt.% NaCl, Blue: 1 wt.% NaCl, and red: 20 wt.% NaCl). A and B do not have the same axis scale.

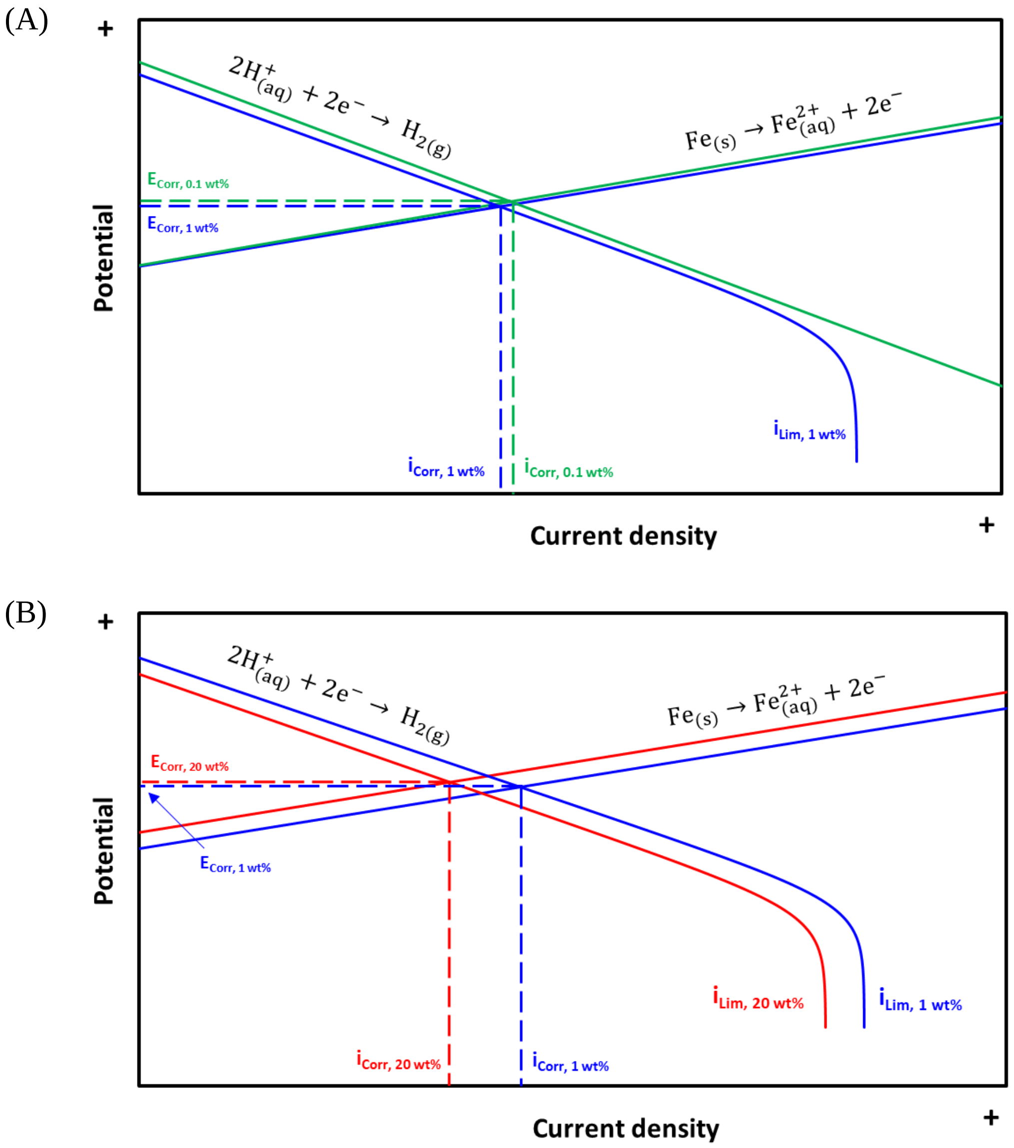

11.3.2.3 Surface analysis

The pictures of the long RCE specimens at 1 wt.% and 20 wt.% NaCl just after retrieval from the solution, after rinsing with water, and after acid washing are shown in Figure 11-22. After acid washing in the Clarke solution (Figure 11-22 III), the specimen surface became shiny as it was a freshly polished, uncorroded surface. Thus, it can be postulated that at both NaCl concentrations a layer was formed on the surface after the specimen was exposed for 5hr to the solution. These observations justify the need for more analytical surface analyses.

Figure 11-22

Pictures of X65 carbon steel RCE with a rotational speed of 1000 rpm exposed for 5 h to aqueous NaCl solutions at 20^{o}*C, ~1 bar* $H_2S_{(g)}$*, and pH 5:(A) 1 wt.% NaCl and (B) 20 wt.% NaCl. "Before pickling, no rinse" means just after retrieval before rinsing with DI water. "Before pickling, rinsed" means after retrieval and rinsing with DI water. "After pickling" means after acid washing and rinsing with DI water.*

(A) 1 wt.% NaCl

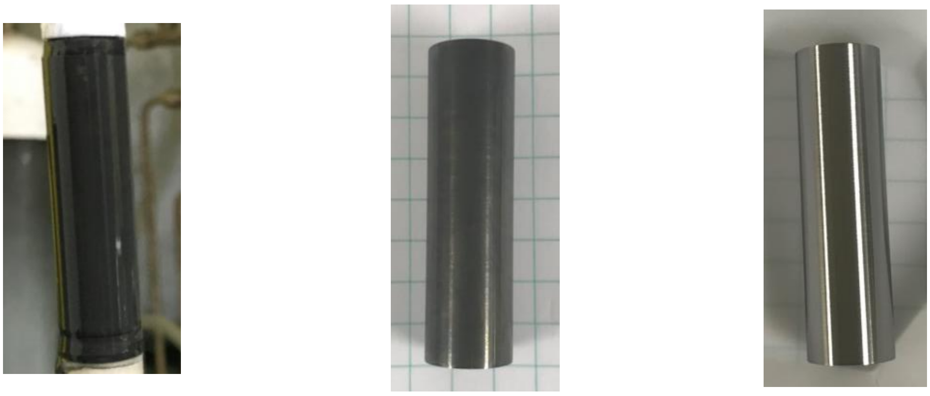

(I) Before pickling, no rinse (II) Before pickling, rinsed (III) After pickling

(B) 20 wt.% NaCl

(I) Before pickling, no rinse (II) Before pickling, rinsed (III) After pickling

Figure 11-23 shows the SEM images at 100X and 2000X magnifications of the corroded surface in 1 wt.% and 20 wt.% NaCl aqueous solutions. The SEM image of a freshly polished specimen is shown in Figure 10-34 for reference. SEM images at 100X magnification show that the surface was corroded uniformly at both NaCl concentrations. The surface at 1 wt.% NaCl was partially covered by a network of corrosion product phase(s) as evident by a light gray color in the 2000X magnification SEM image. This is similar for the specimen surface at 20 wt.% NaCl. However, the density of the corrosion product phase(s) is much less in this case. EDS elemental composition analysis was done at spots marked by arrows in Figure 11-23 to identify the nature of the corrosion product phase(s) formed on the specimen surface at 1 wt.% and 20 wt.% NaCl concentrations**.**

Figure 11-23

SEM images of the corroded square specimen exposed for 5 h to aqueous NaCl solutions at 20^{o}*C, ~1 bar* $H_2S_{(g)}$*, and pH 5:(A) 1 wt.% NaCl and (B) 20 wt.% NaCl. The top images are taken at 100X magnification. The area in the black boxes in the top images is magnified to 2000X and shown in the bottom images. The arrows indicate spots where the EDS elemental composition analysis was done.*

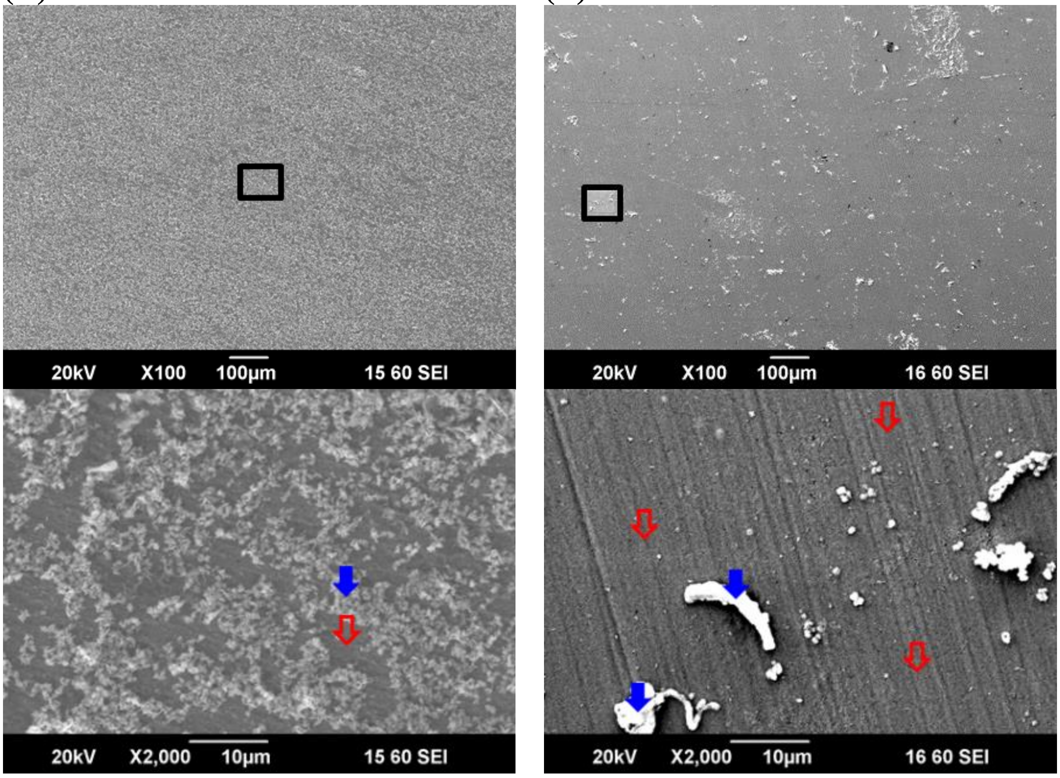

(A) 1 wt.% NaCl

(B) 20 wt.% NaCl

Figure 11-24 presents the elemental composition of the corroded surface by EDS analysis. The EDS analysis of a freshly polished specimen is provided in Figure 10-35 for comparison. The atomic concentrations of elements included in the analysis, Fe, C, S, Mn, Si, and N have been normalized to give a total of 100%. The elements: P, O, Cl, Ni, Cu, and Mo, which were found to be in trace amounts, are not listed in the elemental composition. Similarly, the main elements on the surface for both NaCl concentrations were Fe, C, S, and Mn. The elemental analyses of the dark gray phase (red hollow arrows in Figure 11-23) and the light gray phase (blue solid arrows in Figure 11-23) for each NaCl concentration shows that the concentration of Fe was higher and the concentration of S was lower in the dark gray phase compared to those for the light gray phase. This means that the gray background was mainly the steel matrix. However, it is possible that a very thin layer of iron sulfide covered the surface, particularly at 20 wt.% NaCl, because sulfur was also detected in the dark gray areas as well. Furthermore, the scattered phases on the surface with the light gray color were likely iron sulfides. To confirm the conclusions here, the EDS elemental mapping analysis was performed on the same spots on the specimen surface.

Figure 11-24

EDS elemental composition analysis of the corroded square specimen exposed for 5 h to aqueous NaCl solutions at 20°C, ~1 bar $H_2S_{(g)}$*, and pH 5:(A) 1 wt.% NaCl and (B) 20 wt.% NaCl. Arrows in top right side of the composition spectra correspond to the arrows in the SEM images in* Figure 11-23, *which show the location of EDS elemental composition analysis on the surface.*

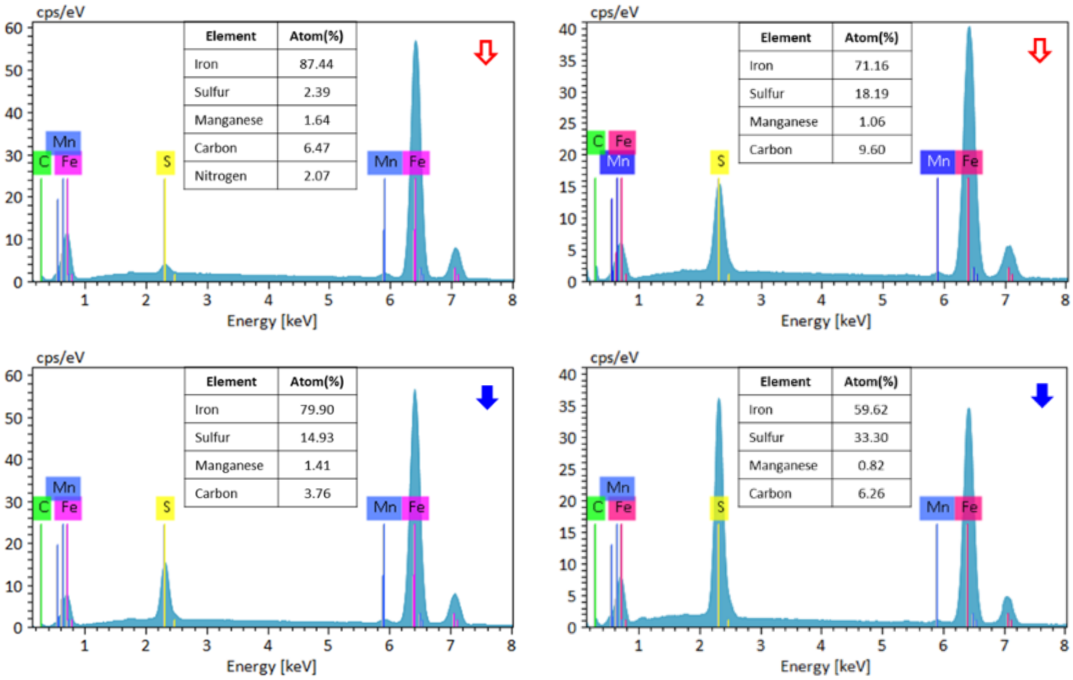

(A) 1 wt.% NaCl

(B) 20 wt.% NaCl

Element	Atom(%)
Iron	87.44
Sulfur	2.39
Manganese	1.64
Carbon	6.47
Nitrogen	2.07

Element	Atom(%)
Iron	71.16
Sulfur	18.19
Manganese	1.06
Carbon	9.60

Element	Atom(%)
Iron	79.90
Sulfur	14.93
Manganese	1.41
Carbon	3.76

Element	Atom(%)
Iron	59.62
Sulfur	33.30
Manganese	0.82
Carbon	6.26

Figure 11-25 shows the surface EDS elemental mapping analysis of the corroded square specimens. The EDS mapping analysis supports the elemental EDS results shown above. The light gray color phases scattered on the surface in both NaCl concentrations are high in sulfur content with little amounts of iron. Therefore, the EDS elemental mapping result confirms that the light gray color phases observed in Figure 11-23 on the specimen surface for both NaCl concentrations are iron sulfides. The EDS map at 1 wt.% NaCl in Figure 11-25 A shows that the dark gray phase is mainly Fe with probably small amounts of Mn. Yellow dots (indication of sulfur element) cover the entire EDS map at 20 wt.% NaCl in Figure 11-25 B, implying that a layer of iron sulfide(s) formed on the surface at this NaCl concentration.

Figure 11-25

SEM images and EDS elemental mapping analysis of the corroded square specimen exposed for 5 h to aqueous NaCl solutions at 20^{o}C, ~1 bar $H_2S_{(g)}$, and pH 5:(A) 1 wt.% NaCl and (B) 20 wt.% NaCl.

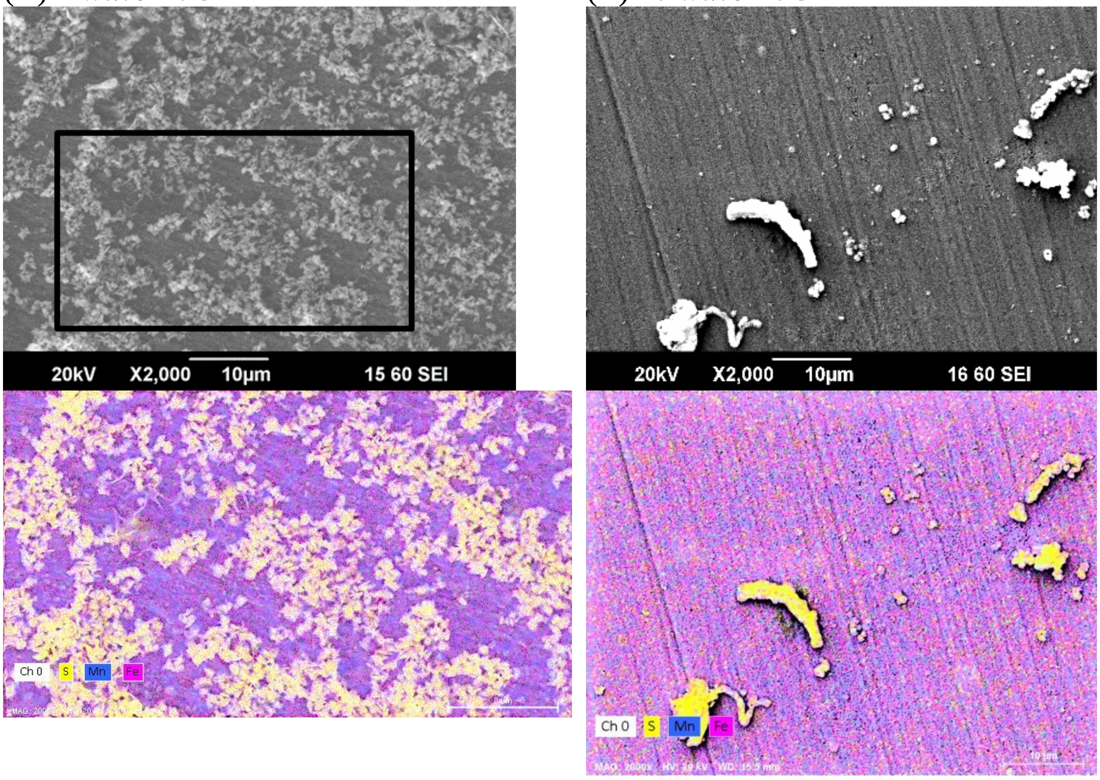

(A) 1 wt.% NaCl

(B) 20 wt.% NaCl

Figure 11-26 shows the cross-section SEM images of the corroded square specimens at different magnifications and different exposure times. In one of the experiments for 20 wt.% NaCl concentration, a square specimen was retrieved after 2 h from the beginning of the experiment to find out whether any layer forms on the surface in 2 h.

The uniform surface seen in the cross-section images at 100X magnification for both NaCl concentrations indicate that the surface was corroded evenly. The cross-section SEM images for 1 wt.% NaCl at 500X and 3000X magnifications show that no apparent uniform corrosion product layer formed on the surface at this NaCl concentration. However, some porous scattered corrosion products can be seen at the steel/epoxy interface at the left side of the 3000x magnification image for 1 wt.% NaCl.

Figure 11-26

Cross-section SEM images of the corroded square specimen exposed (A) 1 wt.% NaCl solution for 5 h, (B) 20 wt.% NaCl solution for 5 h, and (C) 20 wt.% NaCl solution for 2 h at 20°C, ~1 bar $H_2S_{(g)}$, and pH 5. The first, second, and third rows are taken at 100X, 500X, and 3000X magnifications, respectively.

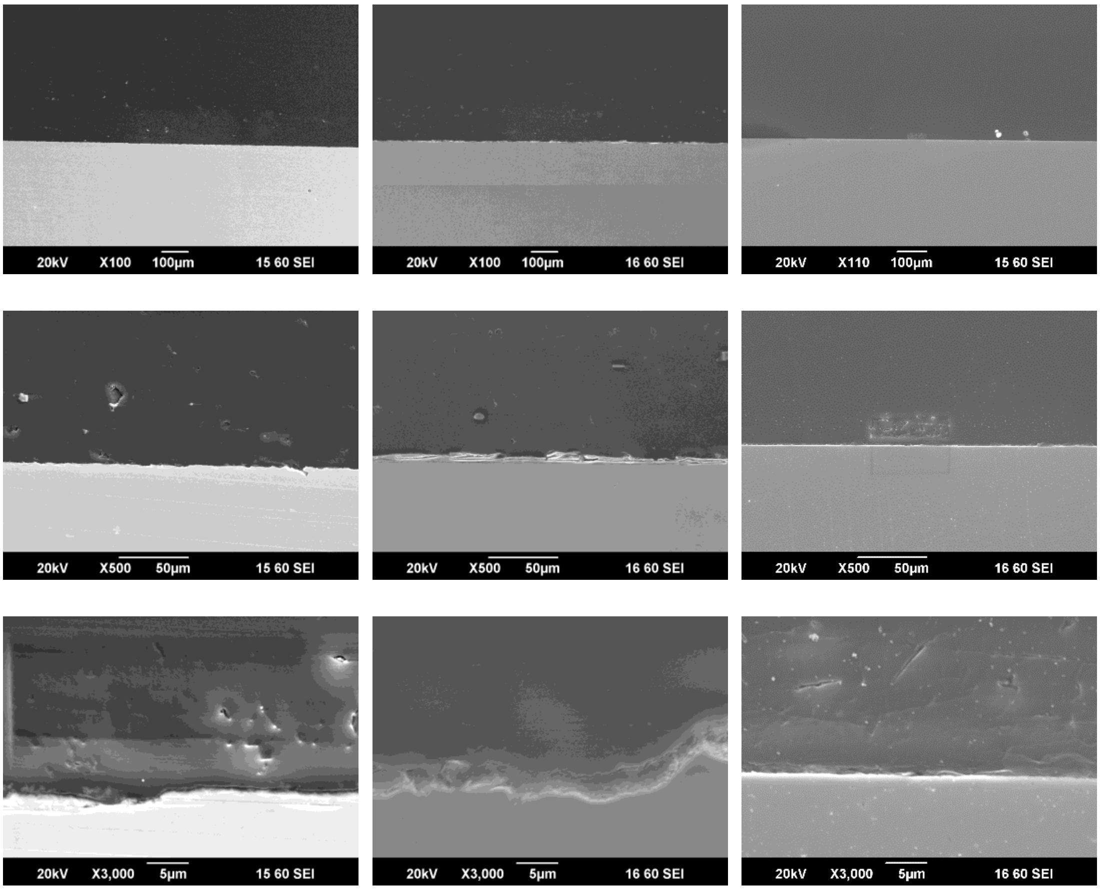

(A) 1 wt.%, After 5h (B) 20 wt.%, After 5h (C) 20 wt.%, After 2h

A continuous layer of corrosion products seems to cover the surface at 20 wt.% NaCl after 5h (the duration of corrosion rate experiments). However, after 2h (the duration of potentiodynamic polarization experiments) no layer, not even a thin discontinuous layer seems to form on the surface. The EDS elemental mapping analysis of the cross-section SEM images was performed to verify the chemical composition of the corrosion product(s) formed on the surface.

Figure 11-27

Cross section EDS mapping analysis of the corroded square specimen exposed for 5 h to aqueous NaCl solutions at 20°C, ~1 bar $H_2S_{(g)}$*, and pH 5:(A) 1 wt.% NaCl and (B) 20 wt.% NaCl.*

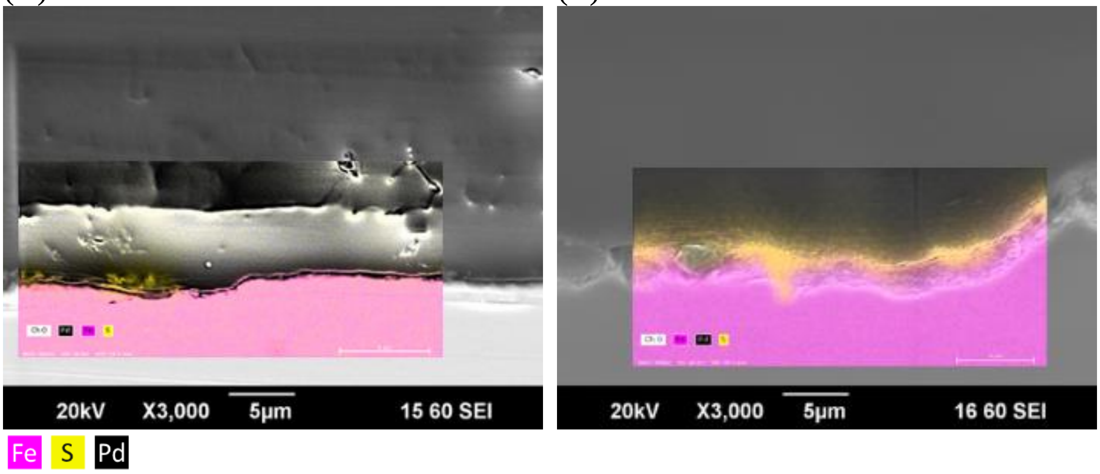
(A) 1 wt.% NaCl

(B) 20 wt.% NaCl

Figure 11-27 shows the EDS mapping analysis of the cross-section of the corroded square specimens in 1 wt.% and 20 wt.% NaCl concentrations. Pd was detected in the EDS mapping analysis because the cross-section samples were sputtered with Pd to provide electrical conductivity required for SEM/EDS analysis. The purple color across the surface shows the steel matrix for both NaCl concentrations. The chemical composition of the scattered phase(s) partially covered the surface at 1 wt.% NaCl as shown in Figure 11-26 A is high in sulfur content, indicating that at 1 wt.% NaCl the surface was partially covered with iron sulfide(s). There seems to be a very thin layer on the right side of the cross-section EDS map for 1 wt.% NaCl in Figure 11-27 A. However, that is the interface between the steel surface and the epoxy, and it is not a layer.

A continuous layer with a high amount of sulfur can be seen in the cross-section EDS map for 20 wt.% NaCl in Figure 11-27 B. This confirms the results observed earlier about the formation of a continuous layer of iron sulfide corrosion products on the surface at 20 wt.% NaCl after 5 hr. To characterize the nature of the iron sulfide(s) formed on the surface at 20 wt.% NaCl, Raman spectroscopy was performed with a laser beam of 10 mW in power and a wavelength of 785 nm with an aperture size of 1200 a.

Figure 11-28 shows the Raman spectrum for the corroded surface of the square specimen in 20 wt.% NaCl solution. Comparing the locations of peaks with those reported by Bourdoiseau *et al.* [313], reveals that the corrosion product layer formed on the surface in 20 wt.% NaCl was mackinawite. It is expected that the iron sulfide phase partially covered the surface of the 1 wt.% NaCl specimen was mackinawite as well.

Figure 11-28

Raman spectrum of the corroded square specimen exposed for 5 h to aqueous NaCl solutions at 20°C, ~1 bar $H_2S_{(g)}$*, pH 5, and 20 wt.% NaCl.*

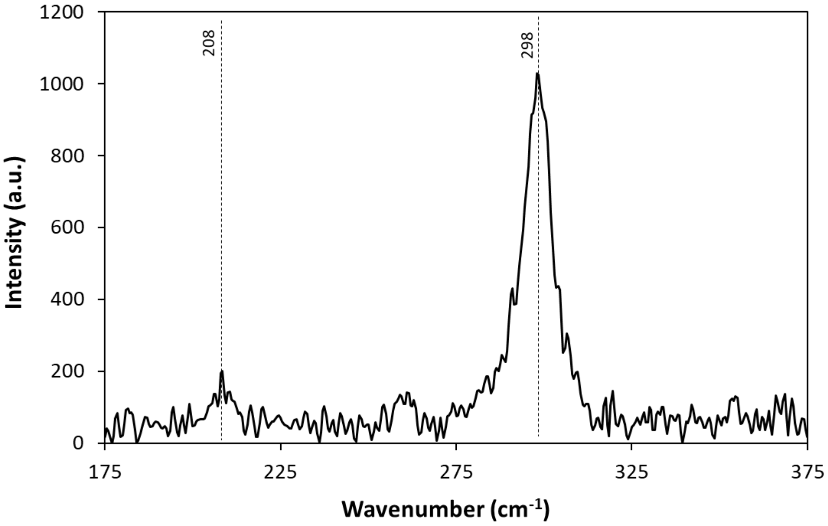

Surface profilometry was carried out to ensure that the surface was corroded uniformly at the experimental conditions used in this part of the study. The advantage of surface profilometry over SEM/EDS analysis is that it can cover a larger surface area, and therefore, it is more a more effective way in identifying localized corrosion (or pits) across the entire surface of a specimen. Figure 11-29 shows the one-dimensional (1D) and two-dimensional (2D) surface roughness profiles of the corroded square specimens exposed to 1wt.% and 20 wt.% NaCl solutions. The purple color seen on the corners of the 2D profiles was due to uneven polishing of the surface during the specimen preparation. 1D profiles show no sudden change in the surface roughness at both NaCl concentrations, which confirm that H_2S corrosion occurred uniformly on the steel surface under the experimental conditions used in this part of the study. The 2D surface profiles also show uniform surfaces, supporting the conclusion that the surface was corroded evenly.

Figure 11-29

1D and 2D surface roughness profilometry of the corroded square specimens exposed for 5 h to aqueous NaCl solutions at 20ºC, ~1 bar $H_2S_{(g)}$*, and pH 5:(A) 1 wt.% NaCl and (B) 20 wt.% NaCl. The length of the black scale bars is equivalent to 0.5 mm.*

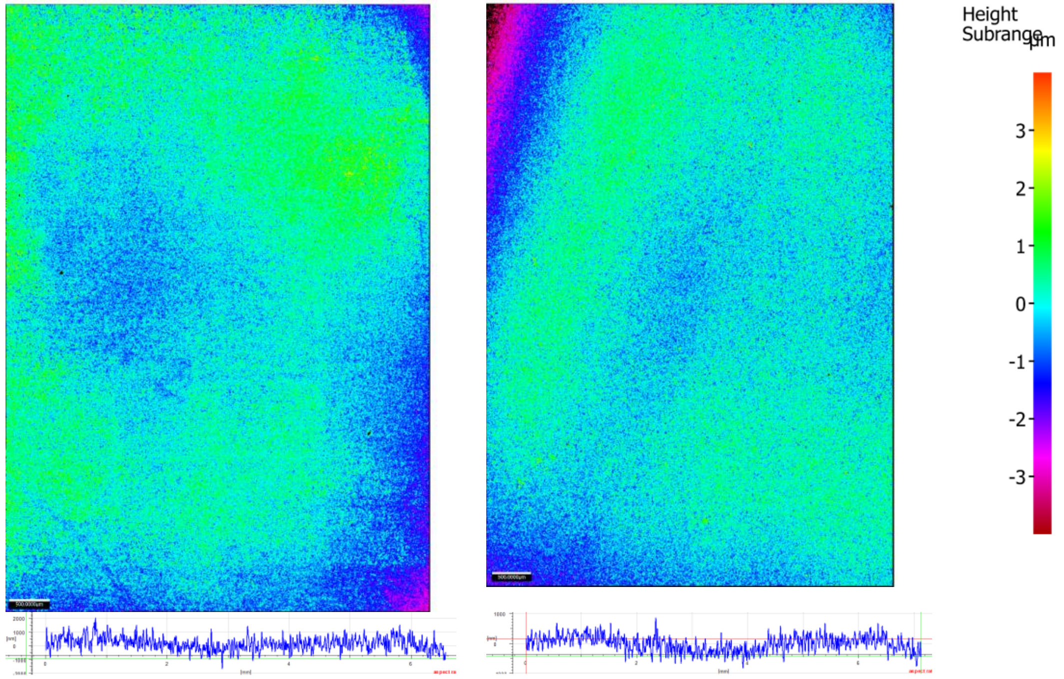
(A) 1 wt.% NaCl

(B) 20 wt.% NaCl

The surface analysis showed that after 5 h, the steel surface was covered partially or entirely with an iron sulfide layer. However, after 2 h, no layer was detected on the surface. This can explain the higher corrosion rates obtained in 2 h experiments compared to those in 5 h experiments, presented in Figure 11-16. The iron sulfide layer formed on the surface decreased the H_2S corrosion rate. The coherency of the iron sulfide layer at 20 wt.% NaCl compared to that for 1 wt.% NaCl might be another reason for the lower H_2S corrosion rate at 20 wt.% NaCl.

An interesting conclusion here is that 2 h can be recognized as an optimized experimental duration time for studying H_2S uniform corrosion in the absence of protective iron sulfide layers on the steel surface at these conditions.

11.3.3 Summary and Conclusions of RCE H_2S Corrosion Experiments at pH 5 and 1 bar $H_2S_{(g)}$

This set of experiments was done to understand the effect of salt concentration on aqueous uniform H_2S corrosion of carbon steel at high $H_2S_{(g)}$ concentrations. Experiments were carried out using X65 carbon steel specimens exposed to aqueous NaCl solutions, at 20°C and pH 5, saturated with ~ 1 bar $H_2S_{(g)}$. The following are the major conclusions reached in this set of experiments, when NaCl concentration was increased from 0.1 wt.% to 20 wt.%:

1. Similar to the CO_2-saturated solutions, the autogenous pH of solution decreased. The decrease in pH was attributed to the changes in the activity coefficient of H^+ ion with NaCl concentration.
2. The ionic strength-based speciation model (for the H_2O-NaCl-H_2S systems), introduced for the first time in this study, could predict the autogenous pH of solution with an acceptable accuracy.
3. The H_2S corrosion rate decreased continually.
4. The analysis of PD sweeps suggested that the mechanisms of the H^+ ion reduction reaction on the steel surface and the anodic dissolution of iron in H_2S corrosion differ somewhat from those for strong acid and CO_2 corrosion. However, salt concentration did not influence these mechanisms in H_2S corrosion at 1 bar $H_2S_{(g)}$.

5. The Evans diagrams showed that the H_2S corrosion process was under pure charge transfer control for the entire range of NaCl concentrations.
6. The Evans diagrams showed that at NaCl concentrations below 1 wt.%, salt concentration influenced the charge transfer part of the cathodic H^+ ion reduction reaction more than the anodic Fe dissolution reaction and i_{Lim}. This is the reason why the maximum in the CO_2 corrosion rate at low NaCl concentrations was not observed for in the H_2S corrosion trend.
7. For NaCl concentration between 1 wt.% to 20 wt.%, the H_2S corrosion rate decreased due to a decrease in the rates of both iron dissolution reaction and the charge transfer part of the H^+ ion reduction reaction.
8. Surface analysis revealed that the H_2S corrosion process occurred uniformly on the steel surface for NaCl concentrations between 1 wt.% to 20 wt.% under the experimental conditions

Chapter 12: Corrosion Rate Prediction Models for Uniform Strong acid Corrosion, Uniform CO_2 Corrosion, and Uniform H_2S Corrosion of Carbon Steel, Valid Across a Wide Range of Salt Concentration

At the beginning of this document, the key parameters involved in the aqueous corrosion process of carbon steels that can be affected by the variation in salt concentration were introduced (Figure 2-1). Then, in the following chapters, the effect of salt concentration on each of these parameters were discussed in detail. Models were presented for calculating solution density, solution viscosity, solution chemistry, and diffusion coefficient of dissolved species valid for a wide range of NaCl concentrations and different operational conditions. Next, the effect of salt concentration on the rate and electrochemistry of strong acid corrosion, CO_2 corrosion, and H_2S corrosion processes were studied. Finally, the kinetic properties required for developing a corrosion model for each type of corrosion were given. In this chapter, all the segments of information discussed in this document so far are put together to build corrosion rate prediction models for uniform strong acid corrosion, uniform CO_2 corrosion, and uniform H_2S corrosion applicable to a wide range of salt concentrations, temperature, pressure, and solution pH.

The corrosion rate prediction model described in this section is a combination of a speciation equilibrium model, empirical models for transport phenomena (density, viscosity, and diffusion coefficient), and an electrochemical model. The speciation model used in the corrosion rate prediction model is the MSE model described in Section 8.3.1. For the solution density, the Batzle and Wang [26] model in Section 3.1 is employed. A combination of Mao and Duan [31] and Islam and Carlson [45] models explained in Section 3.2 is used for calculating the solution viscosity. For the diffusion coefficients of dissolved species, the combination of the Smolyakov and the square root equations explained in Section 3.3 is implemented in the corrosion model. The electrochemical model as the core of the corrosion rate prediction model is a steady-state model based on bulk solution chemistry conditions. It is for uniform corrosion conditions. In other words, it does not account for the formation of any kind of surface corrosion product layers and their possible protectiveness effects. The electrochemical model and the implementation of the speciation equilibrium model and the transport phenomena models into the electrochemical model will be explained below.

As mentioned in Chapter 5, the main anodic reaction in the three types of corrosion is iron dissolution (Reaction (5-24)). The only cathodic reactions considered for the three types of corrosion (strong acid, CO_2, and H_2S) are the H^+ ion reduction (Reaction (5-66)) and the H_2O reduction (Reaction (5-67)) reactions. The former is considered as the main cathodic reactions, while the latter practically becomes an influencing factor at low partial pressures ($pCO_{2(g)}$ and $pH_2S_{(g)}$) <<1 and pH > 5 [200]. It has been shown that the direct reduction of H_2CO_3 (Reaction (5-79)) and H_2S (5-92)) reactions are not significant in the aqueous corrosion of carbon steel and they only act a source of H^+ ion for the H^+ ion reduction reaction [213,214,50].

The rate of electrochemical reactions in corrosion of carbon steel in aqueous solutions are usually controlled by one or a combination of the following steps: charge transfer, mass transfer, and chemical reaction. For the Fe dissolution reaction, the charge transfer step is almost always the controlling step. For the H^+ ion reduction reaction in strong acid corrosion, the charge transfer step or the mass transfer step or the combination of the two steps can control the rate of the reaction. In CO_2 corrosion, the charge transfer step, the combination of the CO_2 hydration chemical reaction step and the mass transfer step, or the combination of all three step can control the rate of the H^+ ion reduction reaction. For H_2S corrosion, the charge transfer step, the combination of the relatively slow H_2S dissociation reaction step and the mass transfer step, or the combination of all three steps can be controlling. For the H_2O reduction reaction, the charge transfer step is always the controlling step.

12.1 Charge Transfer Currents (i_{ct})

The rate of the Fe dissolution reaction, the H^+ ion reduction when it is under charge transfer controlled, and the rate of the H_2O reduction reaction can be calculated in the form of a current density (i) by using the following equations:

$$i_{ct,Fe} = i_{o,Fe} e^{\frac{\alpha_{Fe} F (E - E_{rev,Fe})}{RT}} \tag{12-1}$$

$$i_{ct,H^+} = -i_{o,H^+} e^{-\frac{\alpha_{H^+} F \left(E - E_{rev,H^+}\right)}{RT}} \tag{12-2}$$

$$i_{ct,\,H_2O} = -i_{o,H_2O} e^{-\frac{\alpha_{H_2O} F (E - E_{rev,H_2O})}{RT}} \tag{12-3}$$

The derivation of the above equations is explained in detail in Chapter 5. i_{ct} is called the charge transfer current density (rate) in A/m^2, α is the electron transfer coefficient, F is the Faraday's constant (= 96485.33 C/mol), E is the potential at electrode/electrolyte interface with respect to a reference electrode in V, E_{rev} is the reversible potential or the equilibrium potential of the half reaction in V, R is the gas constant (= 8.3145 J/mol/K), and T is the solution temperature in K. Theoretically, E_{rev} needs to be used in the charge-transfer current density equations. However, E_{rev} of each half reaction varies with the activities of its participating species. For example, E_{rev} for the H^+ ion reduction reaction is a function of H^+ ion activity or the solution pH [96]. Because E_{rev} is varying, it is difficult to use it for determining the reference current densities, which need to be done at a constant potential. To solve this problem, E_{rev} is assumed to be an arbitrary constant potential. The choice of potential does not change the final corrosion rate prediction results as far as it is kept constant for all modeling scenarios. In this study, E_{rev} for all three charge-transfer equations, Equation (12-1) to Equation (12-3), is -685 mV *vs*. Ag/AgCl, which is the reversible potential of X65 carbon steel at standard conditions.

The i_o in Equation (12-1) to Equation (12-3) is the exchange current density in A/m^2 and can be calculated from the following equations for the Fe oxidation, the H$^+$ ion reduction and the H_2O reduction reactions, respectively:

$$i_{o,Fe} = i_{o,Fe}^{ref}\left(\frac{a_{OH^-,b}}{a_{OH^-,b}^{ref}}\right)^{n_{OH}^{Fe}}\left(\frac{a_{Cl^-,b}}{a_{Cl^-,b}^{ref}}\right)^{n_{Cl^-}^{Fe}}\left(\frac{a_{H_2O,b}}{a_{H_2O,b}^{ref}}\right)^{n_{H_2O}^{Fe}} e^{-\frac{E_{a,Fe}}{R}\left(\frac{1}{T}-\frac{1}{T_{ref}}\right)} \tag{12-4}$$

$$i_{o,H^+} = i_{o,H^+}^{ref}\left(\frac{a_{H^+,b}}{a_{H^+,b}^{ref}}\right)^{n_{H^+}^{H^+}}\left(\frac{a_{Cl^-,b}}{a_{Cl^-,b}^{ref}}\right)^{n_{Cl^-}^{H^+}} e^{-\frac{E_{a,H^+}}{R}\left(\frac{1}{T}-\frac{1}{T_{ref}}\right)} \tag{12-5}$$

$$i_{o,H_2O} = i_{o,H_2O}^{ref}\left(\frac{a_{H^+,b}}{a_{H^+,b}^{ref}}\right)^{n_{H^+}^{H_2O}}\left(\frac{a_{Cl^-,b}}{a_{Cl^-,b}^{ref}}\right)^{n_{Cl^-}^{H_2O}}\left(\frac{a_{H_2O,b}}{a_{H_2O,b}^{ref}}\right)^{n_{H_2O}^{H_2O}} e^{-\frac{E_{a,H_2O}}{R}\left(\frac{1}{T}-\frac{1}{T_{ref}}\right)} \tag{12-6}$$

where, i_o^{ref} is the reference current density in A/m^2 at 293.15 K and -685 mV *vs.* Ag/AgCl, a_b is the bulk activity in molarity, a_b^{ref} is the reference bulk activity in molarity, E_a is the activation energy of the electrochemical reaction, n^{Fe}, n^{H^+}, and n^{H_2O} are the reaction orders for the Fe oxidation, the H$^+$ ion reduction, and the H_2O reduction reactions, respectively, and T_{ref} is the reference temperature (= 293.15 K). The values of a_b^{ref} and E_a are given in Table 12-1. The reference bulk activities are used just to make the activity terms in the exchange current density equations dimensionless and they can be any value. A different reference bulk activity results in a different reference current density. However, the final exchange current density value will be the same. All the bulk activities are calculated with the MSE model. Since the MSE model outputs are in mole fraction unit, they need to be converted to molarity unit for implementing into the above equations. For concentration unit conversion Equation (A-11) and for activity coefficient unit conversion Equation (P-10) in Appendix P can be used. The activity of water in molarity unit can be obtained using Equation (A-12) in Appendix A. The concentration, activity coefficient, and activity of H_3O^+ obtained from the MSE model are assumed to be equal to those for H^+ ion.

Table 12-1

The constant parameters required for the calculation of the exchange current densities in Equations (12-4) *to* (12-6).

Parameter	value	Unit	Ref.
$a_{H^+,b}^{ref}$	10^{-4}	Molarity	[314]
$a_{OH^-,b}^{ref}$	10^{-10}	Molarity	This study
$a_{Cl^-,b}^{ref}$	1	Molarity	This study
$a_{H_2O,b}^{ref}$	55.4[99]	Molarity	This study
$a_{H_2S,b}^{ref}$	0.104[100]	Molarity	This study
$E_{a,Fe}$	25398	J/mol/K	This study
E_{a,H^+}	59860	J/mol/K	This study
E_{a,H_2O}	24809	J/mol/K	This study

Table 12-2 and Table 12-3 summarize i_o^{ref} and n values in Equation (12-4) and Equation (12-5) obtained from the experimental results reported in Chapters 9, 10 and 11 for the Fe dissolution and the H^+ ion reduction reactions.

Comparing $i_{o,Fe}^{ref}$ values at 100 ppm and 1 bar H_2S in Table 12-2 shows that $i_{o,Fe}^{ref}$ increased almost one order of magnitude when the H_2S partial pressure was increased from 100 ppm (10^{-4} bar) to 1 bar. In Section 10.1.4, it was shown by comparing $i_{o,Fe}^{ref}$ values at zero and ~1 bar CO_2 partial pressures that the presence of

---

[99] It is the activity of pure water in molarity unit at 20°C and 1 bar pressure.
[100] It is the activity of dissolved H_2S in pure water at 20°C, ~1 bar pressure $H_2S_{(g)}$. This number is obtained by the MSE model.

CO_2 accelerated the Fe oxidation reaction. Yet, since the magnitude of changes was small, it was decided to ignore the CO_2 acceleration effect on the anodic dissolution of Fe. However, for H_2S corrosion magnitude of increase in $i_{o,Fe}^{ref}$ with increasing H_2S partial pressure is large. Therefore, it can be concluded that the presence of H_2S changes the rate of the anodic dissolution Fe. This needs to be considered in $i_{o,Fe}$ Equation (12-4). The new form of $i_{o,Fe}$ equation for H_2S corrosion with the effect of H_2S partial pressure included is given below:

$$i_{o,Fe} = i_{o,Fe}^{ref} \left(\frac{a_{OH^-,b}}{a_{OH^-,b}^{ref}}\right)^{n_{OH}^{Fe}} \left(\frac{a_{Cl^-,b}}{a_{Cl^-,b}^{ref}}\right)^{n_{Cl^-}^{Fe}} \left(\frac{a_{H_2O,b}}{a_{H_2O,b}^{ref}}\right)^{n_{H_2O}^{Fe}} \left(\frac{a_{H_2S,b}}{a_{H_2S,b}^{ref}}\right)^{n_{H_2S}^{Fe}} e^{-\frac{E_{a,Fe}}{R}\left(\frac{1}{T}-\frac{1}{T_{ref}}\right)} \tag{12-7}$$

where, n^{H_2S} is the reaction order for the Fe oxidation with respect to the $H_2S_{(aq)}$ bulk activity ($a_{H_2S,b}$ in molarity) and $a_{H_2S,b}^{ref}$ is the reference $H_2S_{(aq)}$ bulk activity given in Table 12-1. The rest of parameters have been defined earlier.

The water reduction line[101] of the PD sweeps in all the experiments was fitted with the same simple electrochemical model [96], used for modeling the Fe oxidation and the H^+ ion reduction reactions, to determine the kinetic parameters required for modeling the H_2O reduction reaction. The i_o^{ref} and n values in Equation (12-6) obtained from the fitting exercise are listed in Table 12-4. The information provided in Table 12-4 show that increasing NaCl concentration increased the rate of the H_2O reduction reaction.

---

[101] the short diagonal line appeared in all the PD sweeps at very negative potentials after the limiting current density region.

Table 12-2

The kinetic parameters for the iron oxidation reaction exchange current density in Equation (12-4) obtained in the experiments at total pressure of 1 bar and NaCl concentrations between 0.1 wt.% to 20 wt.%.

Atmosphere	p_{gas} (bar)	Setup	T (°C)	pH	NaCl	n_{OH}^{Fe}	$n_{Cl^-}^{Fe}$	$n_{H_2O}^{Fe}$	$i_{o,Fe}^{ref}$
N_2	~0.98	RDE	10	3	< 1 wt.%	1	0.48	0	0.51
N_2	~0.98	RDE	10	3	≥ 1 wt.%	1	-0.25	2	0.117
N_2	~0.98	RCE	20	3	< 1 wt.%	1	0.49	0	0.061
N_2	~0.98	RCE	20	3	≥ 1 wt.%	1	-0.24	2	0.0143
CO_2	~0.98	RDE	10	3	< 3 wt.%	1	0.57	0	0.82
CO_2	~0.98	RDE	10	3	≥ 3 wt.%	1	-0.4	2	0.30
CO_2	~0.97	RCE	30	3.73-4.01	< 3 wt.%	1	0.19	0	0.91
CO_2	~0.97	RCE	30	3.48-3.73	≥ 3 wt.%	1	-0.24	2	0.61
CO_2	~0.98	RCE	20	5	< 1 wt.%	1	0.22	0	0.21
CO_2	~0.98	RCE	20	5	≥ 1 wt.%	1	-0.26	2	0.084
H_2S	10^{-4}	RCE	20	5	≥ 1 wt.%	1	-0.4	2	0.01[102]
H_2S	~0.98	RCE	20	5	< 1 wt.%	1	0.06	0	0.24
H_2S	~0.98	RCE	20	5	≥ 1 wt.%	1	-0.4	2	0.096

---

[102] This value is not corrected for the effect of H2S partial pressure. The corrected value is given in Table 12-5.

Table 12-3

The kinetic parameters for the H^+ ion reduction reaction exchange current density in Equation (12-5) obtained in the experiments at total pressure of 1 bar and NaCl concentrations between 0.1 wt.% to 20 wt.%.

Atmosphere	p_{gas} (bar)	Setup	T (°C)	pH	$n_{H^+}^{H^+}$	$n_{Cl^-}^{H^+}$	i_{o,H^+}^{ref}
N_2	~0.98	RDE	10	3	0.5	-0.09	5.1
N_2	~0.98	RCE	20	3	0.5	-0.31	6.9
CO_2	~0.98	RDE	10	3	0.5	-0.23	11.9
CO_2	~0.97	RCE	30	3.48-4.01	0.5	-0.30	7.4
CO_2	~0.98	RCE	20	5	0.5	-0.23	5.1
CO_2	~0.90	RCE	50	5	N/A	N/A	1.3
CO_2	~0.57	RCE	80	5	N/A	N/A	1.2
H_2S	10^{-4}	RCE	20	5	N/A	N/A	0.7
H_2S	~0.98	RCE	20	5	0.5	-0.2	2.2

Table 12-4

The kinetic parameters for the H_2O reduction reaction exchange current density in Equation (12-6) *obtained in the experiments at total pressure of 1 bar and NaCl concentrations between 0.1 wt.% to 20 wt.%.*

Atmosphere	p_{gas} (bar)	Setup	T (°C)	pH	α_{H_2O}	$n_{H^+}^{H_2O}$	$n_{Cl^-}^{H_2O}$	$n_{H_2O}^{H_2O}$	i_{o,H_2O}^{ref}
N_2	~0.98	RDE	10	3	0.35-0.43	-0.5	1.2	2	2.0e-2
N_2	~0.98	RCE	20	3	0.50-0.60	-0.5	1.5	2	9.2e-4
CO_2	~0.98	RDE	10	3	0.75	N/A	N/A	N/A	9.0e-2
CO_2	~0.97	RCE	30	3.48-4.01	1.0-1.3	-0.5	0.6	2	5.9e-3
CO_2	~0.98	RCE	20	5	0.44-0.63	-0.5	0.4	2	5.6e-3
CO_2	~0.90	RCE	50	5	0.50-0.58	N/A	N/A	N/A	1.1e-3
CO_2	~0.57	RCE	80	5	0.50-0.53	N/A	N/A	N/A	3.4e-4
H_2S	10^{-4}	RCE	20	5	0.32-0.45	-0.5	1	2	5.0e-2
H_2S	~0.98	RCE	20	5	0.20-0.40	-0.5	1	2	1.4e-2

In all the experiments, the electron transfer coefficients for the Fe oxidation (α_{Fe}) and the H^+ ion reduction (α_{H^+}) reactions were almost constant when NaCl concentration was increased, except α_{H^+} in the strong acid experiments. It was shown in Table 9-3 and Table 9-6 that α_{H^+} increased with increasing NaCl concentration in strong acid solutions. To account for the variation of α_{H^+} in the strong acid solutions with NaCl concentration in the corrosion rate prediction model, an empirical correlation is proposed as follows:

$$\alpha_{H^+} = 0.5 + 0.0247 m_{NaCl} \tag{12-8}$$

where, m_{NaCl} is NaCl molality concentration.

Similarly, the electron transfer coefficient for the H_2O reduction reaction (α_{H_2O}) changed with NaCl concentration, not just in the strong acid solutions, but in all the experiments. In this study, α_{H_2O} is expressed as a function of α_{H^+}:

$$\alpha_{H_2O} = F_\alpha \alpha_{H^+} \tag{12-9}$$

where, F_α is an empirical correction factor defined as a function of NaCl molality concentration (m):

For strong acid and CO_2 corrosion:

$$F_\alpha = -0.0378 m_{NaCl} + 1.061 \tag{12-10}$$

For H_2S corrosion:

$$F_\alpha = -0.0284 m_{NaCl} + 0.630 \tag{12-11}$$

Equations (12-10) and (12-11) indicate that salt affects the mechanism of the H_2O reduction reaction. However, since this reaction does not contribute much to the aqueous corrosion of steel, changes its mechanism is not a concern in this study.

The final values of the kinetic parameters needed to calculate the charge transfer current densities in Equations (12-1) to (12-3) are listed Table 12-5 for each type of corrosion.

Table 12-5

The values of the kinetic parameters needed to calculate the charge transfer current densities in Equations (12-1) to (12-3) and Equation (12-7).

Parameter	Strong acid corrosion	CO_2 corrosion	H_2S corrosion
α_{Fe}	1.3	1.1	0.86
α_{H^+}	Eq. (12-8)	0.5	0.39
α_{H_2O}	Eq. (12-10)	Eq. (12-10)	Eq. (12-11)
$i_{o,Fe}^{ref}$ (NaCl $\leq$ 1 wt.%)	0.20	0.21	0.13
$i_{o,Fe}^{ref}$ (NaCl $>$ 1 wt.%)	0.020	0.084	0.068
n_{OH}^{Fe}	1	1	1
$n_{Cl^-}^{Fe}$ (NaCl $\leq$ 1 wt.%)	0.48	0.50	0.06
$n_{Cl^-}^{Fe}$ (NaCl $>$ 1 wt.%)	-0.25	-0.3	-0.4
$n_{H_2O}^{Fe}$ (NaCl $\leq$ 1 wt.%)	0	0	0
$n_{H_2O}^{Fe}$ (NaCl $>$ 1 wt.%)	2	2	2
$n_{H_2S}^{Fe}$	0	0	0.3
i_{o,H^+}^{ref}	5.2	10	2.2
$n_{Cl^-}^{H^+}$	-0.20	-0.23	-0.25
$n_{H^+}^{H^+}$	0.5	0.5	0.5
i_{o,H_2O}^{ref}	0.001	0.051	5.5e-4
$n_{Cl^-}^{H_2O}$	1.35	0.5	0.5
$n_{H^+}^{H_2O}$	-0.5	-0.5	-0.5
$n_{H_2O}^{H_2O}$	2	2	2

12.2 Limiting Current Densities (i_{Lim})

The rate of the H$^+$ ion reduction reaction, when it is controlled by the slow mass transfer step in strong acid corrosion, and when it is controlled by a combination of the slow homogenous chemical $CO_{2(aq)}$ hydration reaction step and the slow mass transfer step in CO_2 corrosion, and when it is controlled by the combination of the relatively slow $H_2S_{(aq)}$ dissociation step and the slow mass transfer step in H_2S corrosion, is expressed as a current density called the H$^+$ ion reduction reaction limiting current density (i_{Lim}). Equations have been developed for calculating i_{Lim} in CO_2 and H_2S corrosion. These equations in addition to the i_{Lim} equation for strong acid corrosion are given below:

I) *strong acid corrosion*

$$i_{Lim} = \frac{1000nFD_{H^+}c_{H^+,b}^{eq}}{\delta_{m,H^+}} \tag{12-12}$$

where, i_{Lim} is in A/m^2, n is the charge number of H$^+$ ion (= 1), D_{H^+} is the diffusion coefficient of H$^+$ ion in the solution in m^2/s, $c_{H^+,b}^{eq}$ is the equilibrium bulk concentration of H$^+$ ion in molarity (M), and δ_{m,H^+} is the thickness of mass transfer boundary layer for H$^+$ ion in m. δ_{m,H^+} calculation will be explained below. The derivation of i_{Lim} for strong acid corrosion is explained in Appendix U.

II) *CO_2 corrosion*

$$i_{Lim} = 1000nF\sqrt{D_{eff}k_{f,CO_2}\, a_{CO_2,b}^{eq}a_{H_2O,b}^{eq}\, a_{H^+,b}^{eq}}\ coth\left(\frac{\delta_{m,H^+}}{\delta_r}\right) \tag{12-13}$$

where,

$$D_{eff} = \frac{D_{H^+}}{\gamma_{H^+}^{c}} + \frac{a_{H_2CO_3,b}^{eq}}{a_{H^+,b}^{eq}}\frac{D_{H_2CO_3}}{\gamma_{H_2CO_3}^{c}} \tag{12-14}$$

$$\delta_r = \sqrt{\frac{D_{eff}a^{eq}_{H^+,b}}{k_{f,hyd}a^{eq}_{CO_2,b}a^{eq}_{H_2O,b}}} \quad (12\text{-}15)$$

where, i_{Lim} is in A/m^2, n is the charge number of the H$^+$ ion reduction reaction (= 1), F is the Faraday's constant (=96485.33 C/mol), D_{H^+} and $D_{H_2CO_3}$ are the diffusion coefficients of H$^+$ ion and $H_2CO_{3(aq)}$ in the solution, respectively, in m^2/s, D_{eff} is called the *effective diffusion coefficient* in m^2/s, $a^{eq}_{H^+,b}$, $a^{eq}_{CO_2,b}$, $a^{eq}_{H_2CO_3,b}$, and $a^{eq}_{H_2O,b}$ are the equilibrium bulk activities of H$^+$ ion, $CO_{2(aq)}$, and $H_2CO_{3(aq)}$, $H_2O_{(l)}$ in molarity (M), $\gamma^c_{H^+}$ and $\gamma^c_{H_2CO_3}$ are the activity coefficients for H$^+$ ion and $H_2CO_{3(aq)}$ in molarity basis, $k_{f,hyd}$ is the forward reaction rate constant for the CO_2 hydration reaction in 1/M/s, δ_{m,H^+} is the thickness of mass transfer boundary layer for H$^+$ ion in m and δ_r is the thickness of the chemical reaction boundary layer in m. The derivation of i_{Lim} equations for CO_2 corrosion is explained in Appendix V.

The $a^{eq}_{H^+,b}$, $a^{eq}_{CO_2,b}$, and $a^{eq}_{H_2O,b}$ are calculated with the MSE model. The MSE model outputs are in the mole fraction unit. They must be converted to the molarity unit. The mole fraction concentration unit can be converted to the molarity unit by using Equation (A-11). For water, to convert from the mole fraction unit to the molarity unit, Equation (A-12) can be used. The mole fraction activity coefficient can be transformed into the molarity basis by using Equation (P-10) in Appendix P. Finally, the product of the molarity concentration and the molarity-based activity coefficient gives the activity in the molarity unit. The $\gamma^c_{H^+}$ is considered equal to $\gamma^c_{H_3O^+}$ obtained from the MSE model. The $\gamma^c_{H_2CO_3}$ is assumed to be the same as $\gamma^c_{CO_2}$. $a^{eq}_{H_2CO_3,b}$ can be calculated by using the equilibrium equation for the $CO_{2(aq)}$ hydration Reaction (8-2):

$$a^{eq}_{H_2CO_3,b} = K_{hyd}a^{eq}_{CO_2,b}a^{eq}_{H_2O,b} \tag{12-16}$$

where, K_{hyd} is the equilibrium constant for the CO_2 hydration reaction in 1/M.

K_{hyd}, $k_{f,hyd}$, and $K_{b,hyd}$ can be calculated from the equations below:

$$K_{hyd} = \frac{6.62 \times 10^{-2} \exp\left(\frac{-9553}{RT}\right)}{a^{eq}_{H_2O,b}} \tag{12-17}$$

$$k_{f,hyd} = \frac{5.796 \times 10^{10} \exp\left(\frac{-69335}{RT}\right)}{a^{eq}_{H_2O,b}} \tag{12-18}$$

$$k_{b,hyd} = 8.755 \times 10^{11} \exp\left(\frac{-59782}{RT}\right) \tag{12-19}$$

where, K_{hyd} in 1/M is the equilibrium constant, $k_{f,hyd}$ in 1/M/s is the forward reaction rate constant, and $k_{b,hyd}$ in 1/s is the backward reaction rate constant for the CO_2 hydration Reaction (8-2). $a^{eq}_{H_2O,b}$ is the equilibrium bulk activity of water in M, R is the gas constant (= 8.3145 J/mol/K) and T is temperature in K. D_{H^+} and $D_{H_2CO_3}$ can be calculated based on information provided in Table 3-2, Table 3-3, and Table 3-4. δ_{m,H^+} equations for different flow geometry are given in Appendix X. The equation for K_{hyd} is taken from Kahyarian *et al.* [107]. The $k_{f,hyd}$ equation is obtained in this study by using the experimental results at pH 5 and 1 wt.% NaCl at 20°C, 50°C and 80°C. The $k_{b,hyd}$ equation is derived according to the $k_{b,hyd} = k_{f,hyd}/K_{hyd}$ relation.

III) H_2S corrosion

Four different equations have been developed in this study for the calculation of i_{Lim} in weak acid solutions including H_2S-satuarated solution (Appendix W). The two most accurate ones are presented here:

The theoretical two-section diffusion boundary layer equation:

$$i_{Lim} = -\frac{1000nFa_{H^+,b}^{eq}}{\frac{\delta_{m,H_2S}}{D_{eff}} + \frac{\gamma_{H^+}^{c}\delta_*}{D_{H^+}}} \tag{12-20}$$

where,

$$D_{eff} = \frac{D_{H^+}}{\gamma_{H^+}^{c}} + \frac{a_{H_2S,b}^{eq}}{a_{H^+,b}^{eq}}\frac{D_{H_2S}}{\gamma_{H_2S}^{c}} \tag{12-21}$$

$$\delta_r = \sqrt{\frac{D_{H^+}\, a_{H^+,b}^{eq}}{\gamma_{H^+}^{c} k_{f,H_2S}\, a_{H_2S,b}^{eq}}} \tag{12-22}$$

$$\delta_* = \delta_r \tanh\left(\frac{\delta_{m,H^+} - \delta_{m,H_2S}}{\delta_r}\right) \tag{12-23}$$

where, i_{Lim} is in A/m^2, n is the charge number of the H$^+$ ion reduction reaction (= 1), F is the Faraday's constant (=96485.33 C/mol), D_{H^+} and D_{H_2S} are the diffusion coefficients of H$^+$ ion and $H_2S_{(aq)}$ in m^2/s, D_{eff} is the effective diffusion coefficient in m^2/s, $a_{H^+,b}^{eq}$ and $a_{H_2S,b}^{eq}$ are the equilibrium bulk activities of H$^+$ ion and $H_2S_{(aq)}$ in M, $\gamma_{H^+}^{c}$ and $\gamma_{H_2S}^{c}$ are the activity coefficients for H$^+$ ion and $H_2S_{(aq)}$ in molarity basis, k_{f,H_2S} is the forward reaction rate constant for the H_2S dissociation Reaction (8-40) in 1/s, δ_{m,H^+} and δ_{m,H_2S} are the thickness of the mass transfer boundary layers for H$^+$ ion and $H_2S_{(aq)}$, δ_r is the thickness of the chemical reaction boundary layer in m, and δ_* is in m. The derivation of i_{Lim} equations for H_2S corrosion is explained in Appendix W.

The $a_{H^+,b}^{eq}$ and $a_{H_2S,b}^{eq}$ are calculated with the MSE model. As mentioned earlier, the MSE model outputs are in the mole fraction unit, and they must be converted to the molarity unit. Equation (A-11) can be used to convert the mole fraction concentration unit to the molarity concentration. For water, to convert from the mole fraction unit to the molarity unit, Equation (A-12) is given. The activity coefficients also need to be converted from the mole fraction basis to the molarity basis, using Equation (P-10) in Appendix P. Finally, the product of the molarity concentration and the molarity-based activity coefficient provides the activity in the molarity unit. The $\gamma_{H^+}^{c}$ is assumed identical to $\gamma_{H_3O^+}^{c}$ calculated from the MSE model. k_{f,H_2S} is equal to 6.24 × 10^3 1/s [315].

The semi-empirical two-section diffusion boundary layer equation:

$$i_{lim} = \frac{Fa_{H^+,b}^{eq}}{\dfrac{\delta_{m,H^+} - \delta_{m,H_sS}}{Factor\left(\dfrac{D_{H^+}}{\gamma_{H^+}^{c}}\right)} + \dfrac{\delta_{m,H_sS}}{D_{eff}}} \tag{12-24}$$

where, $Factor$ is an empirical factor:

$$Factor = \frac{a_{H^+,b}^{eq} + a_{H_2S,b}^{eq}}{a_{H^+,b}^{eq}} \tag{12-25}$$

other parameters have the same definition as those for the theoretical equation.

In the following, the calculated i_{Lim} values obtained by the above equations are compared with those measured in strong acid, CO_2, and H_2S corrosion experiments in this study.

Figure 12-1 compares the experimental i_{Lim} values obtained in the RDE and the RCE strong acid experiments in Sections 9.1 and 9.2 with those calculated with Equation (12-12). The model predictions of i_{Lim} are accurate for both sets of experimental data over the entire range of NaCl concentrations. Most of the predicted i_{Lim} values are within the 20% of the experimental results as presented by the Parity plot in Figure 12-2. This indicates that all the information and models used to calculate i_{Lim} are accurate, such as models for the solution density, the solution viscosity, the H^+ ion diffusion coefficient, the H^+ concentration, and the mass transfer boundary layers. The maximum seen in the model predictions at ~ 1 wt.% NaCl is due to the H^+ ion profile with respect to NaCl concentration (similar to Figure 10-17 C).

The comparison presented here helps to understand better the reasons for possible disagreements between i_{Lim} predictions and experimental i_{Lim} values for the CO_2 and H_2S corrosion.

Figure 12-1

The comparison of the calculated limiting current density values with those obtained from the measurements in (A) the RDE strong acid corrosion experiments at 10°C, pH 3, 1 bar $N_{2(g)}$, and 2000 rpm, and (B) the RCE strong acid corrosion experiments at 20°C, pH 3, 1 bar $N_{2(g)}$, and 1000 rpm.

(A)

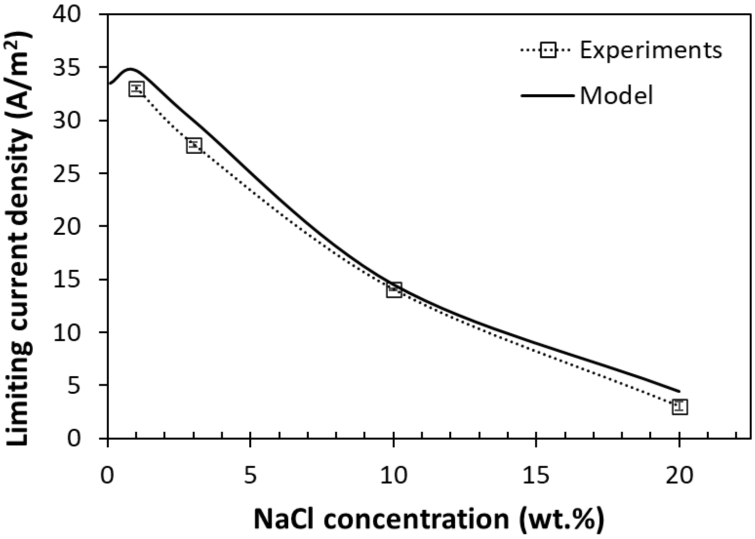

(B)

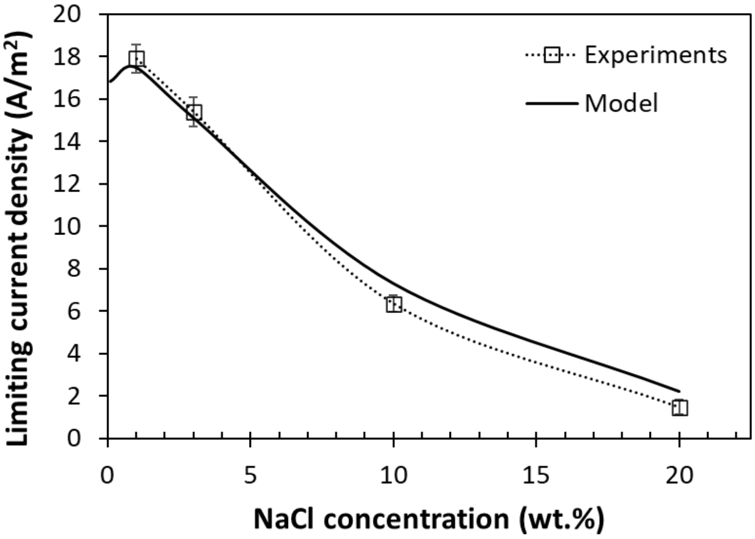

Figure 12-2

The Parity plot compares the predicted limiting current density (i_{Lim}) values with those measured in strong acid ($N_{2(g)}$) corrosion experiments.

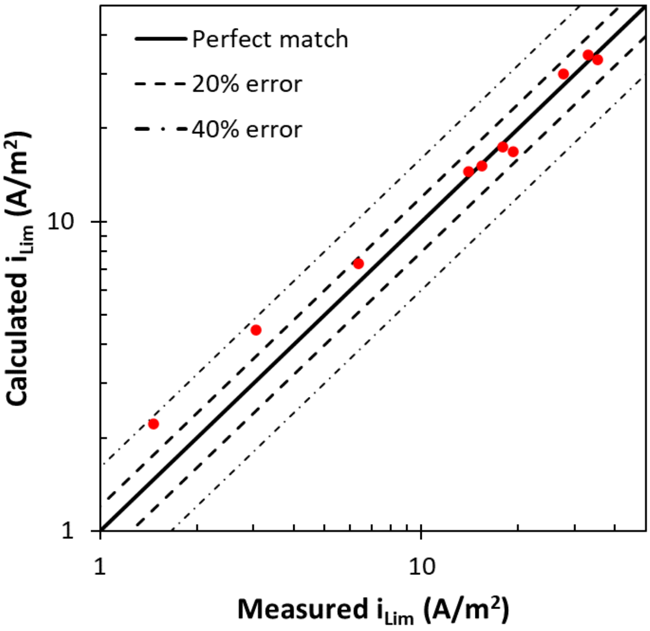

Figure 12-3 shows the comparisons between the experimental i_{Lim} values obtained in the RDE and the RCE CO_2 experiments in Sections 10.1 and 10.2 with those calculated with Equation (12-13). For Figure 12-3 A, the calculated i_{Lim} values are very close to the experimental values for the entire NaCl concentration range. At pH 3, the CO_2 buffering effect is negligible and similar i_{Lim} values are expected in the absence and presence of CO_2. This can be confirmed by comparing the experimental i_{Lim} results for strong acid corrosion in Figure 12-1 A with those reported in Figure 12-3 A. The predicted i_{Lim} values in CO_2 corrosion at 10°C and pH 3 are slightly larger than the predicted i_{Lim} values in strong acid under the same conditions. This shows that the buffering effect has a minor contribution in the overall i_{Lim}. Also, this comparison proves that the i_{Lim} equation for CO_2 corrosion works for strong acid conditions as well.

Figure 12-3

The comparison of the calculated limiting current density values with those obtained from the measurements in (A) the RDE CO_2 corrosion experiments at 10°C, pH 3, 1 bar $CO_{2(g)}$, and 2000 rpm, and (B) the RCE CO_2 corrosion experiments at 30°C, autogenous pH 3, 1 bar $CO_{2(g)}$, and 1000 rpm.

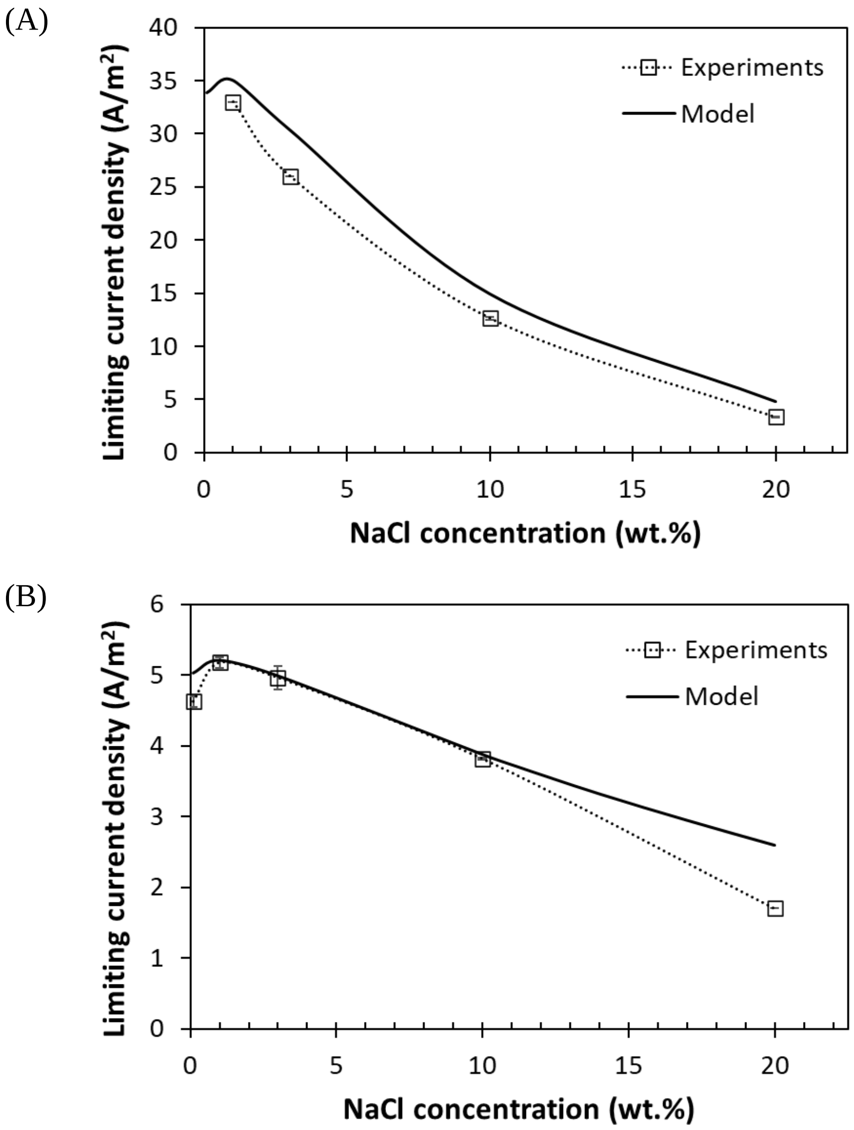

For the CO_2 corrosion experiments at 30°C and autogenous pH, the predicted i_{Lim} values in Figure 12-3 B matches very well with the experimental results up to 10 wt.% NaCl. However, the calculated i_{Lim} values at 20 wt.% NaCl deviates by ~ 0.8 A/m^2 for the measured i_{Lim} at this NaCl concentration. The reason can be found out by looking at D_{eff} and $a^{eq}_{H^+,b}$ trends with NaCl concentrations as these are the only parameters in i_{Lim} Equation (12-13) that change with NaCl concentration. The experiments in this study were done in an open system at a constant partial pressure of $CO_{2(g)}$, so $a^{eq}_{CO_2,b}$ was constant for all NaCl concentrations. $a^{eq}_{H_2O,b}$ in i_{Lim} Equation (12-13) is canceled out by that in $k_{f,hyd}$ Equation (12-18). At a constant solution pH, $a^{eq}_{H^+,b}$ is also constant and the only parameter that changes i_{Lim} with NaCl concentration is D_{eff}. Therefore, it is expected that at a constant pH the trends for i_{Lim} and D_{eff} with NaCl concentration be similar. This can be confirmed by comparing the i_{Lim} trend for the RCE CO_2 experiments at constant pH 3 in Figure 12-3 A by that for D_{eff} presented in Figure 12-4. However, for the case of autogenous solution pH, both $a^{eq}_{H_2O,b}$ and D_{eff} vary with NaCl concentration. As shown in Figure 12-4, D_{eff} decreases with increasing NaCl concentration. However, $a^{eq}_{H_2O,b}$ increases continually when NaCl concentration is increased, as reported in Figure 10-17 C. At NaCl concentrations greater than 10 wt.%, the slope of changes in $a^{eq}_{H_2O,b}$ with respect to NaCl concentration is greater than that for D_{eff} and because of that the i_{Lim} value at 20 wt.% NaCl is higher than the measured i_{Lim} value. This overprediction is not seen in the constant pH i_{Lim} calculations because of the nature of the i_{Lim} equation for CO_2 corrosion. In autogenous solution pH, $a^{eq}_{H_2O,b}$ is not constant and therefore the errors in calculating that with the solution chemistry model influence the i_{Lim} predictions. The overprediction of pH values at high NaCl concentrations obtained by the MSE model for 1 bar CO_2 and 30°C shown in Figure 10-16 is a proof for the above argument.

Figure 12-4

Changes in the H^+ ion effective diffusion coefficient (D_{eff}) with NaCl concentration in the presence of 1 $CO_{2(g)}$ at different solution pH and temperatures.

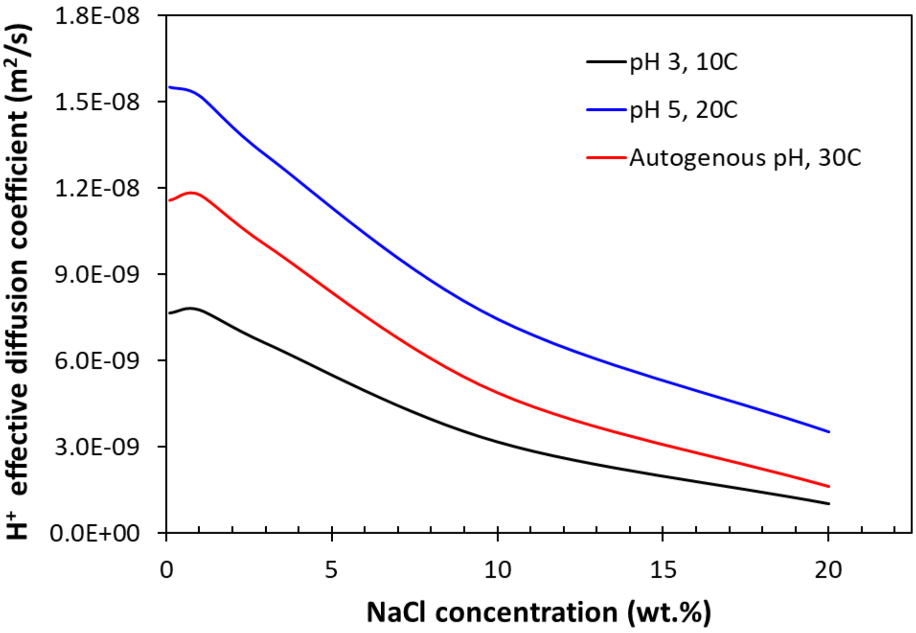

Figure 12-5 compares the experimental i_{Lim} values measured at 20°C, 50°C, and 80°C in the RCE CO_2 corrosion experiments in Sections 10.3 and 10.4 with those calculated with Equation (12-12)(12-13). At 1 wt.% NaCl concentration, the predicted i_{Lim} values are almost the same as the measured i_{Lim} values for all three temperatures. This is not a surprise as the $k_{f,hyd}$ equation proposed in this study was calibrated with these three data points. There is a slight underprediction for all three temperatures at high NaCl concentrations. The underprediction at 20 wt.% NaCl is ~ 15% for 20°C, 10% for 50°C, and ~17% for 80°C. Few reasons might be behind the underprediction in i_{Lim}.

Figure 12-5

The comparison of the calculated limiting current density values with those obtained from the measurements in the RCE CO_2 corrosion experiments at pH 5, 1 bar $CO_{2(g)}$, and 1000 rpm at 20°C, 50°C, and 80°C. The dotted lines are just to show the trend.

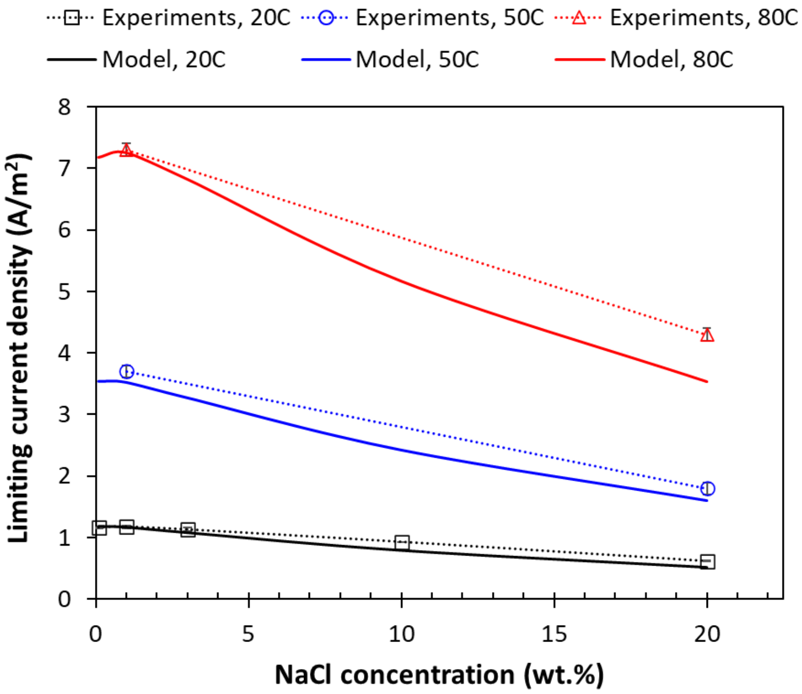

The $k_{f,hyd}$ has been always expressed as a function of temperature in the literature [107,267,298,316]. It is possible that $k_{f,hyd}$ changes with salt concentration as well. However, since at higher NaCl concentrations, the availability of free water molecules in the solution decreases, it is expected that $k_{f,hyd}$ decreases with increasing NaCl. This results in a lower i_{Lim} value and therefore does not solve the underprediction problem. Another possible reason is the activity coefficient and the diffusion coefficient of $H_2CO_{3(aq)}$ in the D_{eff} Equation (12-14). The activity coefficient of $H_2CO_{3(aq)}$ is assumed to be same as that for $CO_{2(aq)}$. At 20^{o}C, pH 5, 1 bar CO_2, and 20 wt.% NaCl the molality-based activity coefficient of $CO_{2(aq)}$ is ~ 2.3 (Figure 10-29 A). This number is around 1.7 for 1 bar $H_2S_{(aq)}$ (Figure 11-14 A). Both $CO_{2(aq)}$ and $H_2S_{(aq)}$ molecules are neutrals, the same as $H_2CO_{3(aq)}$. However, their molecular structures and weights are different, which are likely the reasons for their different activity coefficients at the similar conditions. Therefore, it would not be surprising if the activity coefficient of $H_2CO_{3(aq)}$ is different from that for $CO_{2(aq)}$. The salt concentration dependency of $H_2CO_{3(aq)}$ diffusion coefficient is also assumed to be same as that for $CO_{2(aq)}$ (Table 3-4). Therefore, uncertainty about $H_2CO_{3(aq)}$ activity coefficient and diffusion coefficient values might be another reason for the observed underprediction in i_{Lim}. The last possible reason is related to the inaccuracy of the MSE model at high NaCl concentrations used to calculate the activities for the i_{Lim} Equation (12-13).

The i_{Lim} predictions for CO_2 corrosion experiments with the proposed i_{Lim} equation show acceptable accuracy for most experimental conditions carried out in this study. Most i_{Lim} predictions are within the 20% of the measured i_{Lim} values as shown by Parity plot in Figure 12-6. Despite this, possible reasons for inaccuracies observed in the i_{Lim} predictions have been discussed for different experimental conditions. The predictions can become more accurate by improving the solution chemistry models and determining $H_2CO_{3(aq)}$ activity coefficient and diffusion coefficients for high salt concentrations.

Figure 12-6

The Parity plot compares the predicted limiting current density (i_{Lim}) values with those measured in CO_2 corrosion experiments.

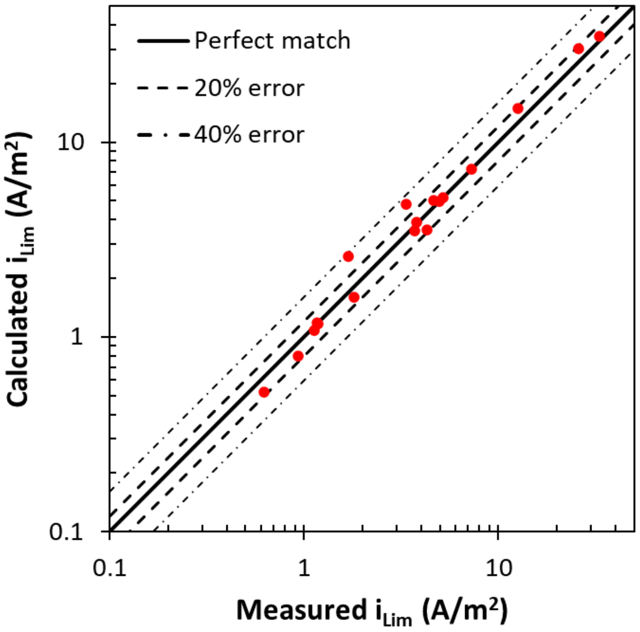

Figure 12-7 compares the experimental i_{Lim} values obtained in the RCE H_2S experiments in Sections 11.2 and 11.3 with those calculated with Equations (12-20) and (12-24). The semi-empirical Equation (12-24) predicts i_{Lim} at 100 ppm $H_2S_{(g)}$ more accurately than the theoretical Equation (12-20). At 100 ppm $H_2S_{(g)}$, $a^{eq}_{H_2S,b}$ is very small. This makes the second term on the D_{eff} Equation (12-21) negligible and the D_{eff} trend with NaCl concentration will be the mirror of the $\gamma^{c}_{H^+}$ trend (similar to Figure 11-14 C). Therefore, the theoretical i_{Lim} Equation shows a maximum at ~ 1 wt.% NaCl. The theoretical i_{Lim} Equation overpredicts considerably at 1 wt.% NaCl concentration. The reason for this overprediction could be due to the assumptions of constant $a^{eq}_{H_2S,b}$ in the outer part of the two-section mass transfer boundary layer or the constant $a^{eq}_{HS^-,b}$ over the entire thickness of the mass transfer boundary layer.

Figure 12-7

The comparison of the calculated limiting current density values with those obtained from the measurements in (A) the RCE H_2S corrosion experiments at 20°C, pH 5, 1 bar total pressure, 100 ppm $H_2S_{(g)}$, and 1000 rpm, and (B) the RCE H_2S corrosion experiments at 20°C, pH 5, 1 bar $H_2S_{(g)}$, and 1000 rpm.

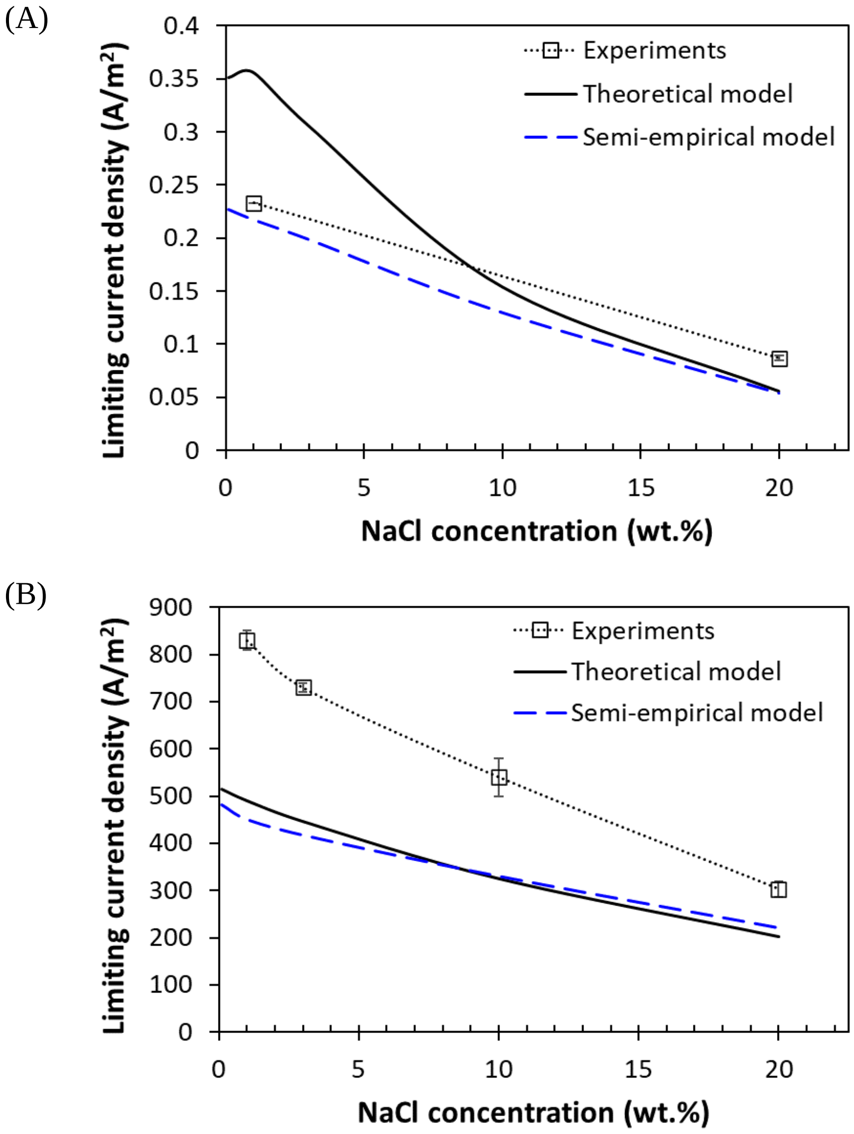

For the 1 bar H_2S corrosion experiments in Figure 12-7 B, both equations underpredict i_{Lim} for the whole range of NaCl concentrations. The first speculation about the reason is that the k_{f,H_2S} value is inaccurate. However, this cannot be correct as k_{f,H_2S} is not involved in the semi-empirical equation. Moreover, k_{f,H_2S} values up to 10^8 times of the original value were tested and no significant increase was observed in the predicted i_{Lim} values. Since the underprediction occurs for all NaCl concentrations, therefore the possible inaccuracies in the solution chemistry model and the H_2S diffusion coefficient cannot be the cause. The only reason left is the constant $a_{H_2S,b}^{eq}$ and $a_{HS^-,b}^{eq}$ assumptions made to derive the two i_{Lim} equation.

The underprediction reported here for i_{Lim} at 1 bar of H_2S does not impact the H_2S corrosion rate prediction, because the H_2S corrosion process at high H_2S partial pressures is controlled by the charge transfer processes, as shown by the Evans diagrams in Figure 11-21. For low H_2S partial pressures (below 0.1 bar), the semi-empirical equation showed very good accuracy when compared with the experimental data presented in this study and those reported by Zheng [49].

12.3 Corrosion Current Density (i_{Corr})

The charge-transfer current density equations for the H^+ ion reduction (i_{ct,H^+}), the Fe oxidation ($i_{ct,Fe}$), and H_2O reduction (i_{ct,H_2O}) reactions are given. The limiting current density equations for the H^+ ion reduction (i_{Lim}) are provided. The net current densities for the Fe oxidation (i_{Fe}) and the H_2O reduction (i_{H_2O}) reactions are equal to their charge-transfer current densities as the rate of these two reactions in carbon steel aqueous corrosion are controlled by the charge transfer processes:

$$i_{Fe} = i_{ct,Fe} \tag{12-26}$$

$$i_{H_2O} = i_{ct,H_2O} \tag{12-27}$$

For the H^+ ion reduction reaction to calculate the net current density (i_{H^+}) as a function of both charge transfer and limiting current densities, the following equation can be used:

$$i_{H^+} = \frac{i_{ct,H^+} i_{Lim}}{i_{ct,H^+} + i_{Lim}} \tag{12-28}$$

The Equation (12-28) is theoretically valid when the reaction order with respect to the activity of H^+ ion is one in i_{ct,H^+} Equation (12-5). However, it has been shown that Equation (12-28) matches well with the experimental results for all three types of corrosion, with an H^+ ion reaction order of 0.5, which is used in this study [96,317]. Kim [318] provided an analytical equation for i_{H^+} with an H^+ ion reaction order of 0.5.

The net current densities are calculated in small potential steps (for example every 1 mV) over a potential range that covers the corrosion potential (E_{corr} or OCP). For example, the OCP of X65 carbon steel in an aqueous solution is usually between -600 to -800 mV *vs.* Ag/AgCl reference electrode. All the current densities are in A/m^2 in this study. The calculated net current densities are commonly two straight lines (in semi-log potential *vs.* log(i) scale) for the Fe oxidation and the H_2O reduction reactions and an L-shape curve for the H^+ ion reduction reaction, as shown in Figure 12-8.

Figure 12-8

An example of the net current densities for Fe oxidation, H^+ *ion reduction, and* H_2O *reduction reactions as functions of the electrode potential for natural occurring corrosion of carbon steel in aqueous solutions.*

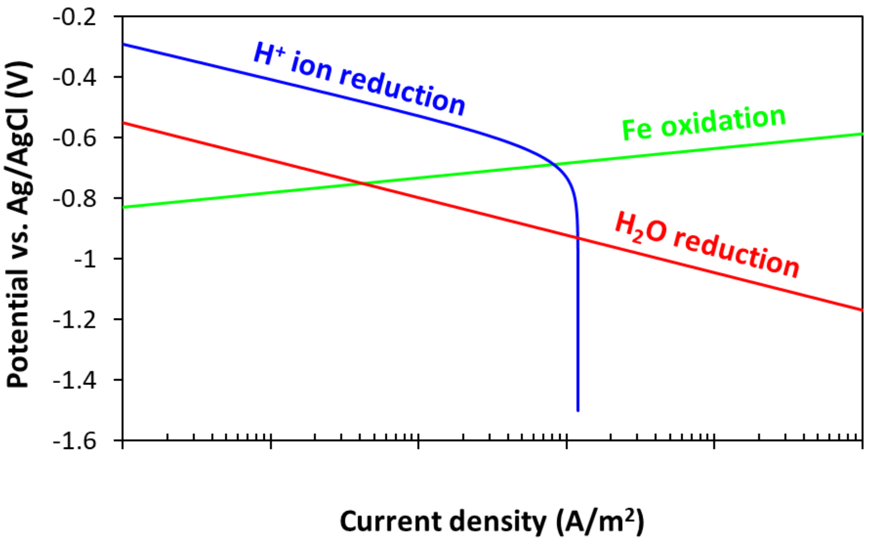

The corrosion current density can be obtained by implementing the charge balance equation at the metal surface [314][103]:

$$\sum_{1}^{n_a} i_a = \sum_{1}^{n_c} i_c \qquad (12\text{-}29)$$

where, n_a and i_a are the total number of anodic reactions and their corresponding net current densities, and n_c and i_c are the total number of cathodic reactions and their corresponding net current densities. The only anodic reaction in aqueous corrosion of carbon steel is Fe oxidation and the cathodic reactions are the H^+ ion reduction and

---

[103] The cathodic current is considered positive in this argument. It is also common to assume the cathodic current as a negative current (See Equation (2-3).

the H_2O reduction reactions. Therefore Equation (12-29) will be as follows for the case of aqueous corrosion of carbon steel:

$$i_{Fe} = i_{H^+} + i_{H_2O} \tag{12-30}$$

To obtain the net cathodic current density, i_{H^+} and i_{H_2O} need to be added up at any given potential over the entire potential range of interest. For i_{Fe}, since it is only one current density there is no need to do that. The corrosion current density (i_{Corr}) is the current density at which the net anodic current density is equal to the net cathodic current density. Or, in other words, i_{Corr} is the current density at which the subtraction of the net cathodic current density from the net anodic current density or *vice versa* is equal to zero. The corresponding electrode potential at which the corrosion current density occurs is the corrosion potential (E_{corr}) or the open circuit potential (OCP).

Figure 12-9 shows an example of the net anodic and the net cathodic current density curves. i_{Corr} and E_{corr} are the corresponding current density and the electrode potential at which the two curves intersect. Figure 12-9 shows the summation of curves presented in Figure 12-8.

.

Figure 12-9

An example of the net anodic and cathodic current densities as functions of the electrode potential for natural occurring corrosion of carbon steel in aqueous solutions. i_{Corr} *and* E_{corr} *are the corrosion current density and the corrosion potential, respectively.*

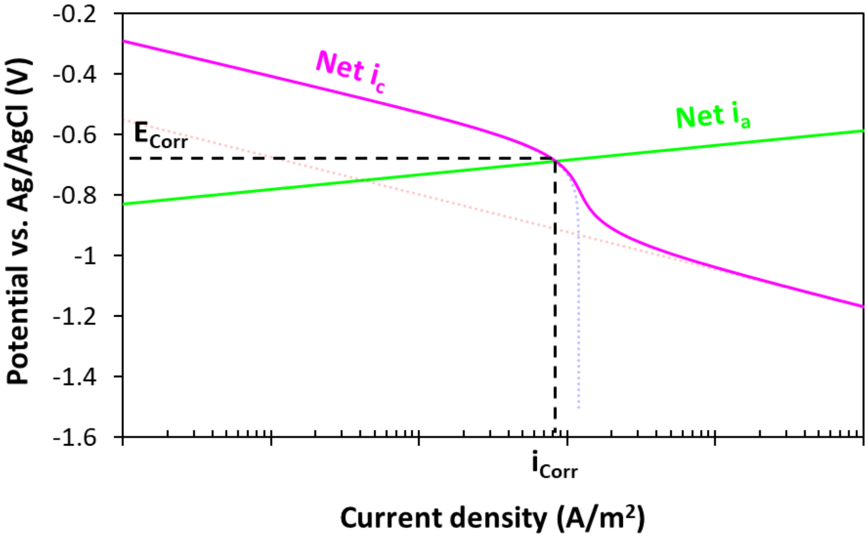

Finally, the calculated corrosion current density (i_{Corr}) can be converted to a corrosion rate (CR) in mm/y by using the equation below:

$$CR = 3.1536 \times 10^{10}\frac{M}{nFd}i_{Corr} \cong 1.16\ i_{Corr} \qquad (12\text{-}31)$$

where, i_{Corr} is A/m^2, M is the molecular weight of carbon steel (= 55.85×10^{-3} kg/mol), n is the number of electrons exchanged within the dissolution reaction (= 2), F is the Faraday's constant (= 96485.33 C/mol), d is the density of carbon steel (= 7870 kg/m^3).

12.4 Corrosion Rate Prediction Model Performance: Calculated Corrosion Rates vs. Measured Corrosion Rates

In this section the accuracy of the final corrosion rate prediction model is evaluated at different experimental conditions and NaCl concentrations. In Figure 12-10 to Figure 12-17, the corrosion rates measured at different NaCl concentrations in each set of experiments are compared at the same conditions with those calculated with the corrosion rate prediction model developed in this study. Also, the predicted PD sweeps at 1 wt.% and 20 wt.% NaCl concentrations are overlapped with the experimental sweeps at these NaCl concentrations to evaluate the performance of the model in capturing the effect of salt concentration on various kinetic features of the PD sweeps.

Generally, the predicted corrosion rates match very well with the measured ones for all sets of experiments. For those sets of experiments for which a maximum in the corrosion rate was observed at low NaCl concentrations, such as those in Figure 12-12, Figure 12-13, and Figure 12-14, the corrosion prediction model can capture the trend perfectly.

The predicted PD sweeps are also well-matched with the experimental PD sweeps. The only considerable deviation in the PD sweeps is related to the H_2O reduction reaction line. The reason for this deviation is the use of a single parameter for all types of corrosion.

Figure 12-10

The comparison of the calculated corrosion rate values and the PD sweeps with those obtained from the measurements in the RDE strong acid corrosion experiments at 10°C, pH 3, ~1 bar $N_{2(g)}$*, and 2000 rpm.*

(A)

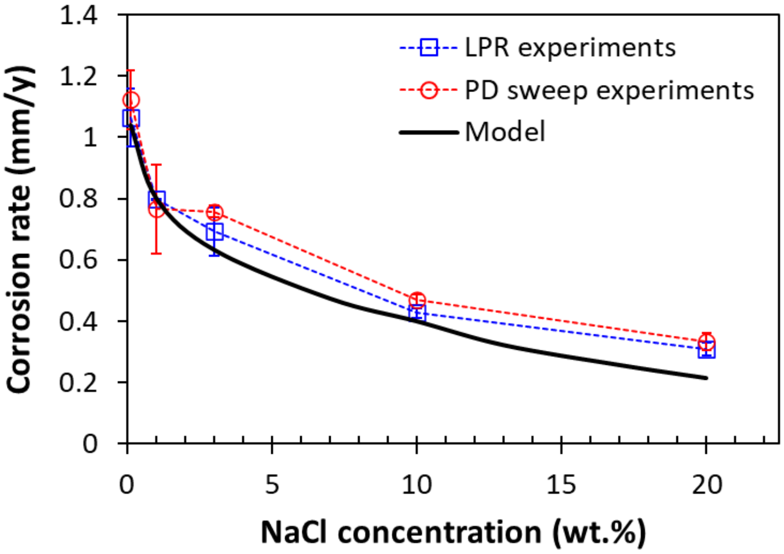

(B)

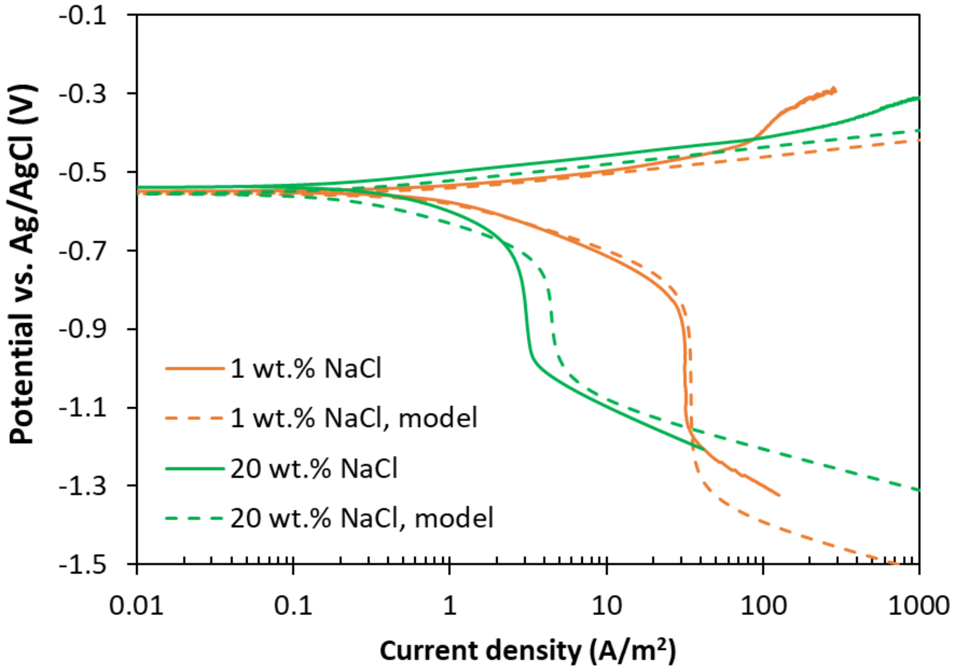

Figure 12-11

The comparison of the calculated corrosion rates and the PD sweeps with those obtained from the measurements in the RCE strong acid corrosion experiments at 20°C, pH 3, ~1 bar $N_{2(g)}$ *, and 1000 rpm.*

(A)

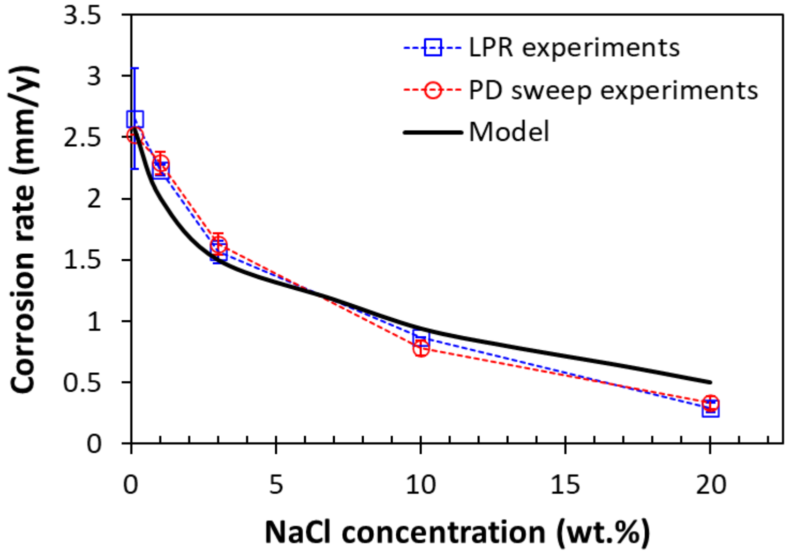

(B)

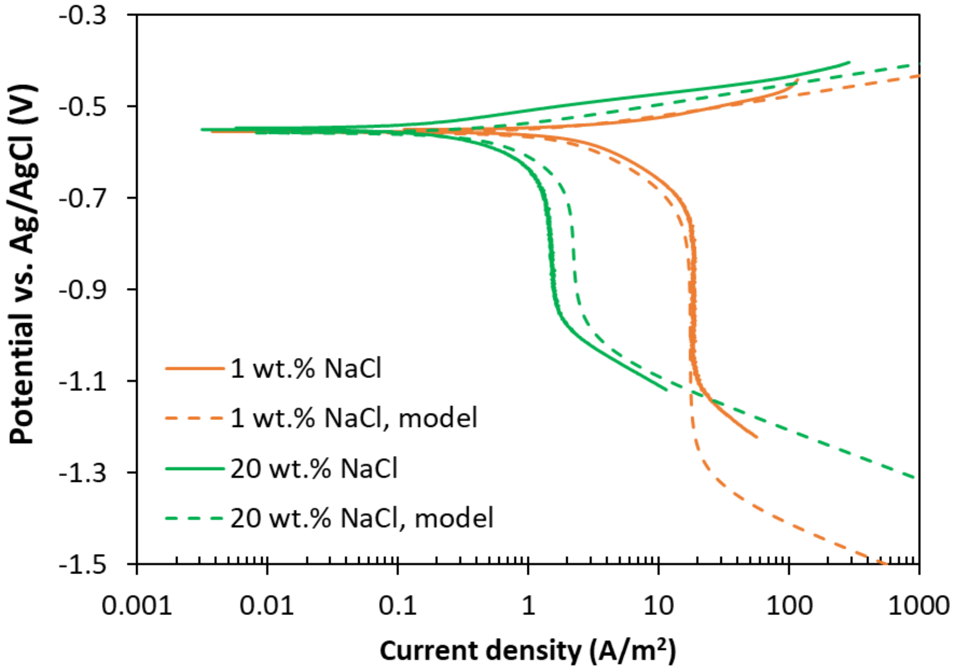

Figure 12-12

The comparison of the calculated corrosion rates and the PD sweeps with those obtained from the measurements in the RDE CO_2 corrosion experiments at 10°C, pH 3, ~1 bar $CO_{2(g)}$, and 2000 rpm.

(A)

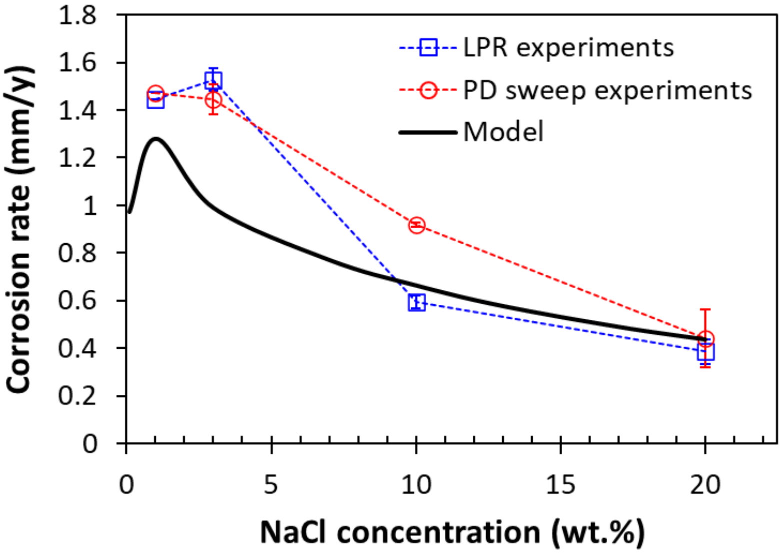

(B)

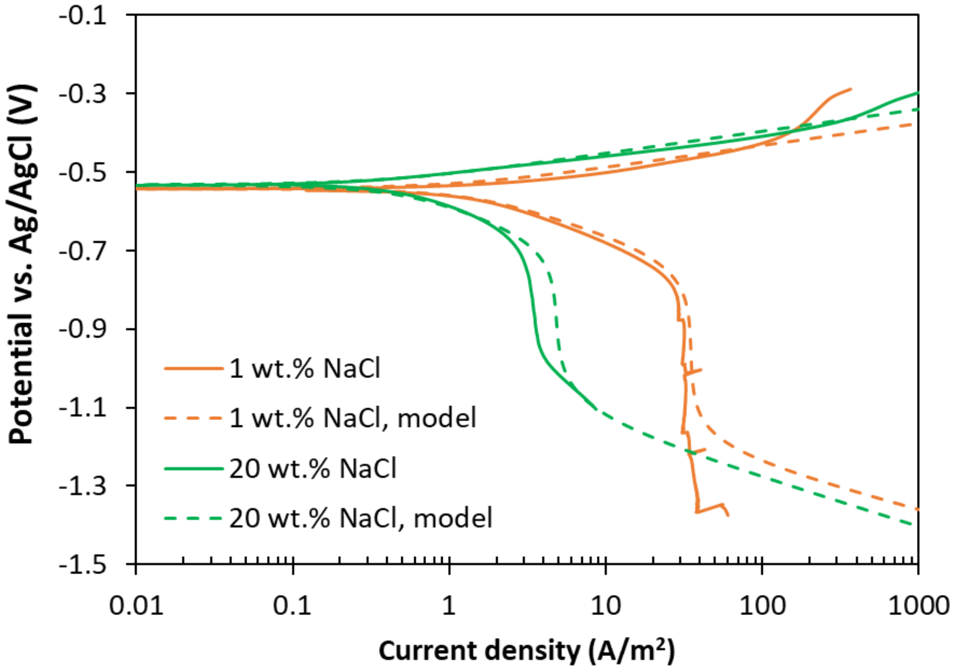

Figure 12-13

The comparison of the calculated corrosion rates and the PD sweeps with those obtained from the measurements in the RCE CO_2 corrosion experiments at 30^{o}C, autogenous pH, ~1 bar $CO_{2(g)}$, and 1000 rpm.

(A)

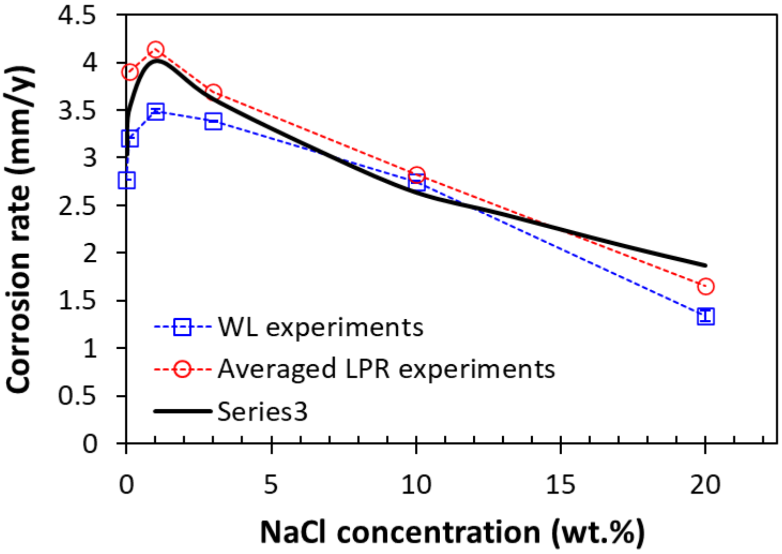

(B)

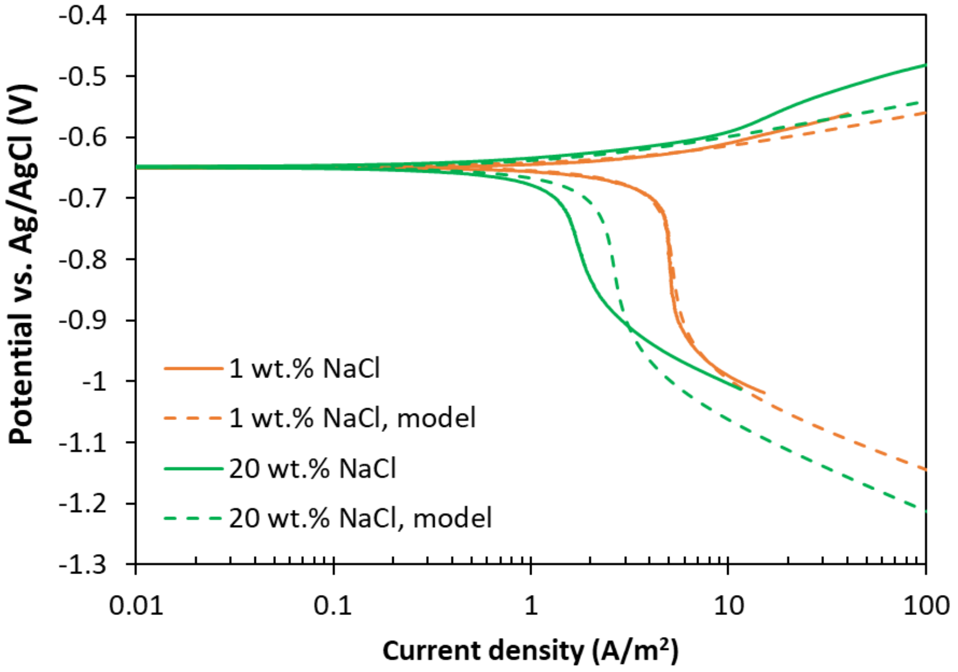

Figure 12-14

The comparison of the calculated corrosion rates and the PD sweeps with those obtained from the measurements in the RCE CO_2 corrosion experiments at 20°C, pH 5, ~1 bar $CO_{2(g)}$, and 1000 rpm.

(A)

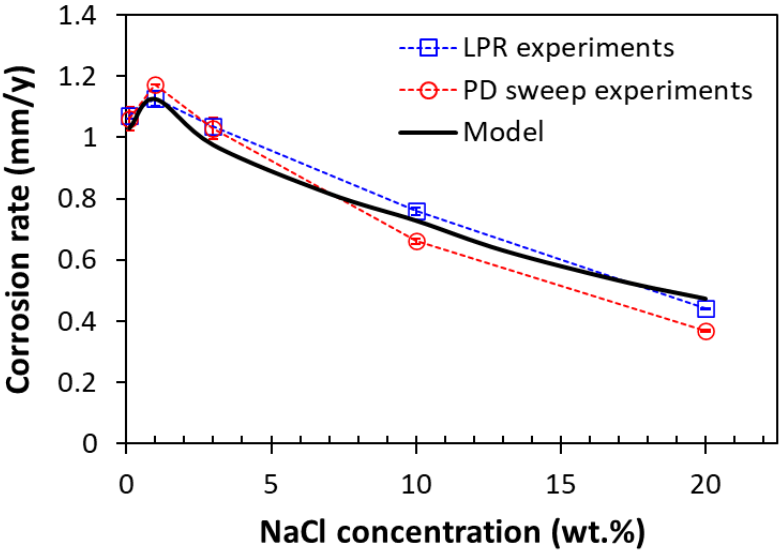

(B)

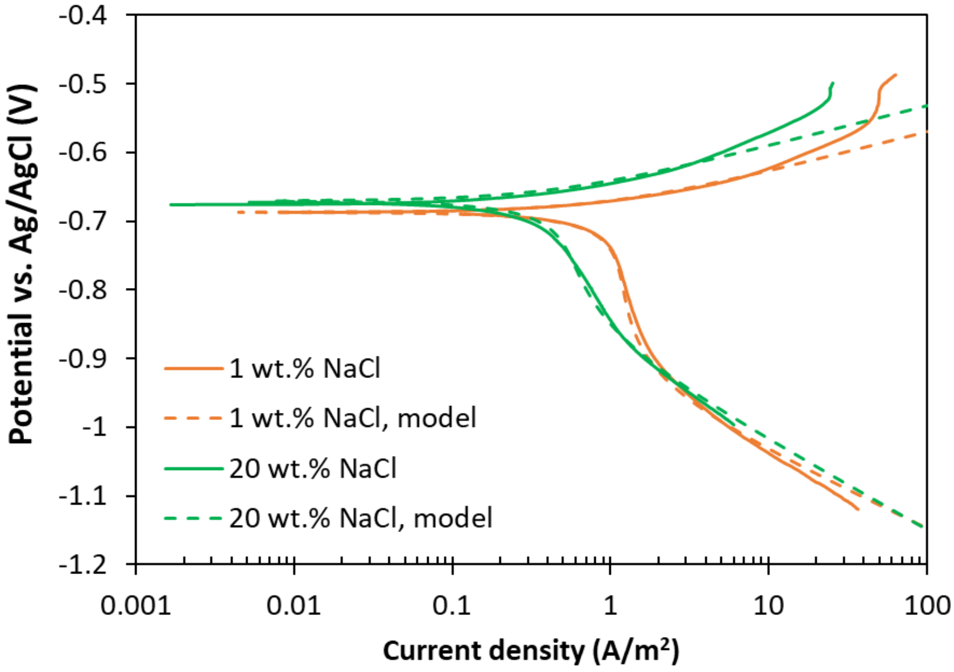

Figure 12-15

The comparison of the calculated corrosion rates with those obtained from the measurements in the RCE CO_2 *corrosion experiments at pH 5, 1 bar total pressure, 1000 rpm, and (A) 50°C and* $pCO_{2(g)} \cong 0.9$ *bar and (B) 80°C and* $pCO_{2(g)} \cong 0.57$ *bar.*

(A)

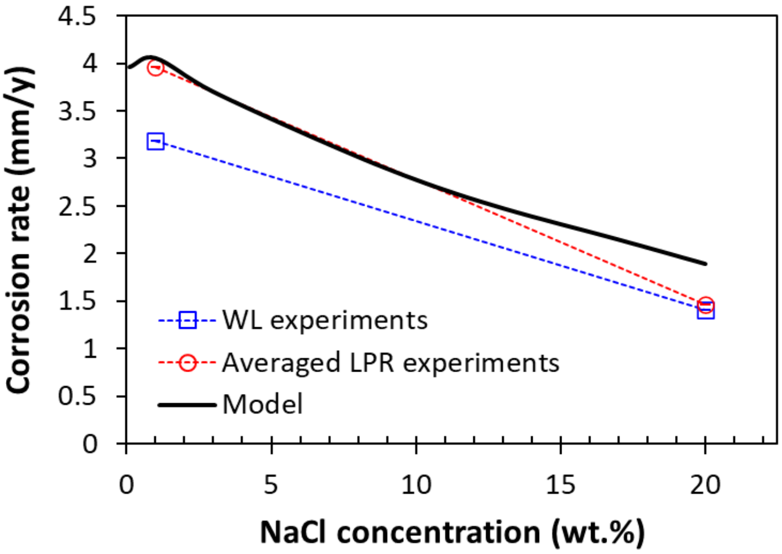

(B)

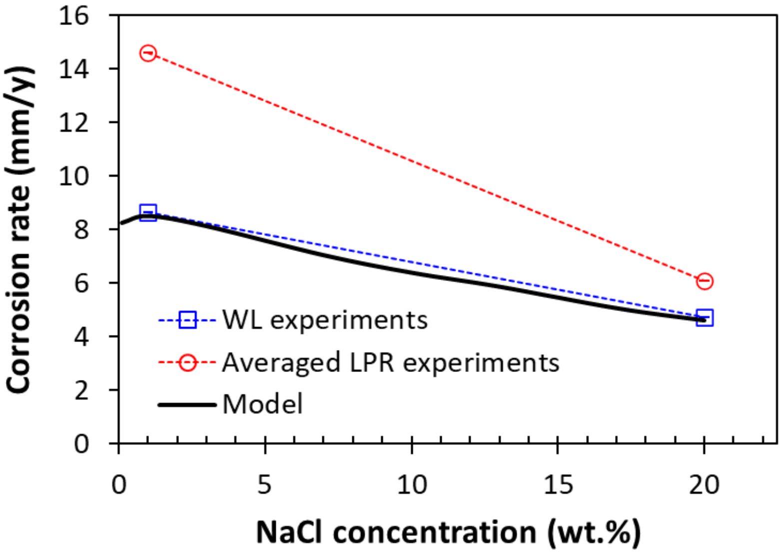

Figure 12-16

The comparison of the calculated corrosion rates and the PD sweeps with those obtained from the measurements in the RCE H_2S corrosion experiments at 20°C, pH 5, 1 bar total pressure, 100 ppm (10^{-4} bar) $H_2S_{(g)}$, and 1000 rpm.

(A)

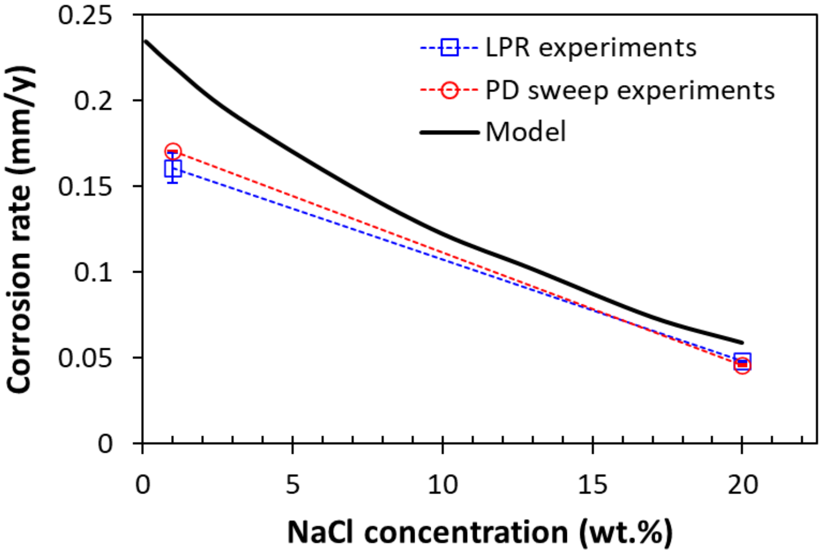

(B)

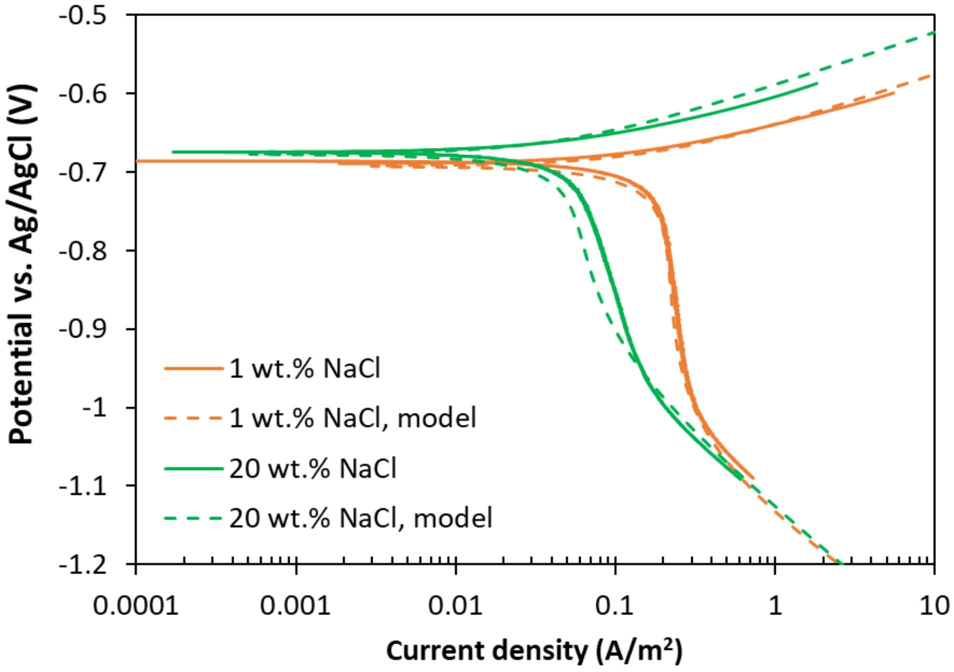

Figure 12-17

The comparison of the calculated corrosion rates and the PD sweeps with those obtained from the measurements in the RCE H_2S corrosion experiments at 20^oC, pH 5, ~1 bar $H_2S_{(g)}$, and 1000 rpm.

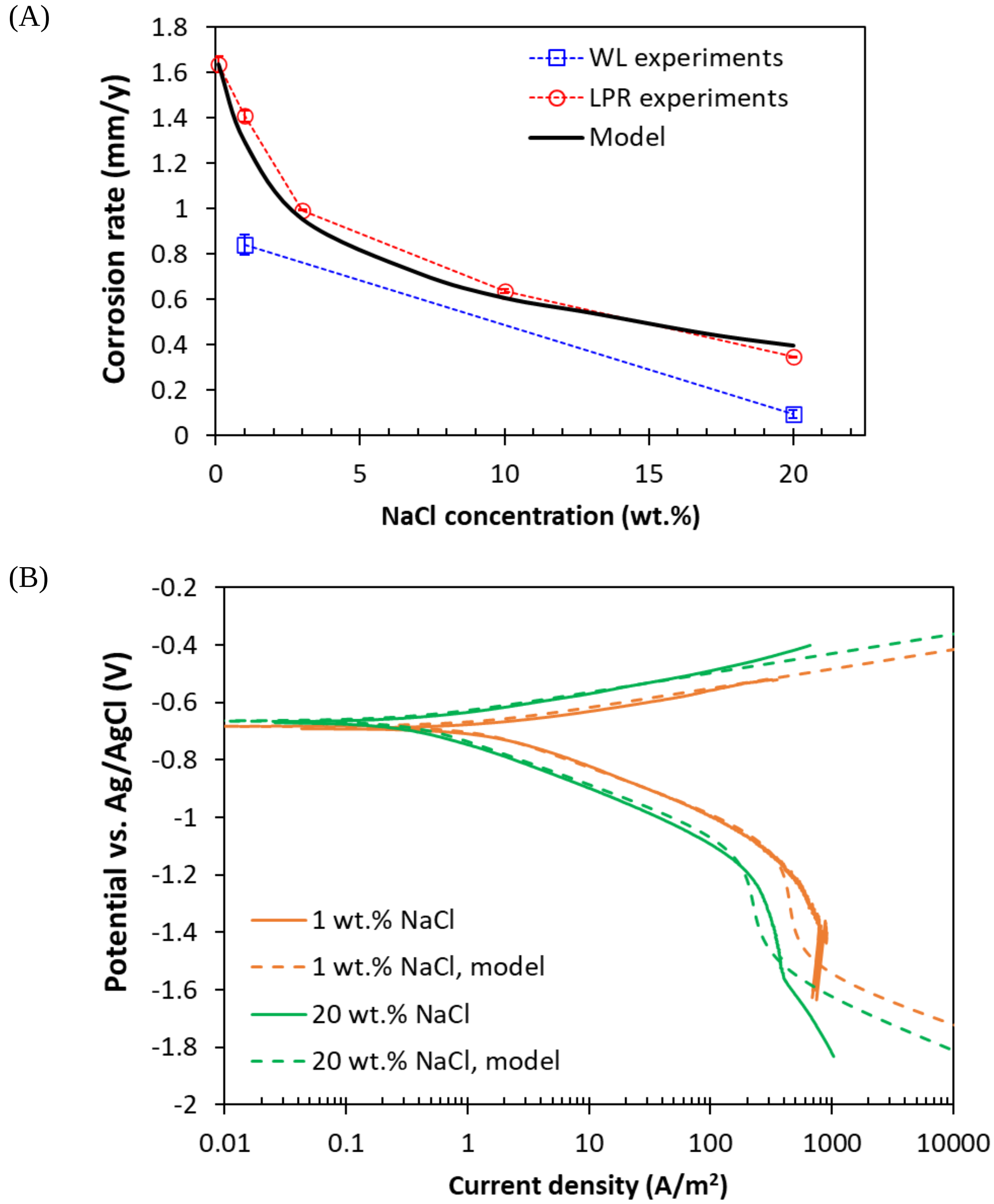

Figure 12-18 compares the calculated corrosion rates with the measured corrosion rates in this study in the form of a parity plot. For most of the data points, the errors in the predictions are less than 20%. For a better analysis of the corrosion rate prediction model performance the magnitude of the prediction errors is calculate for each data point.

Figure 12-18

A parity plot compares the calculated corrosion rates with those measured in this study in N_2-saturated solutions (strong acid corrosion), CO_2-saturated solution (CO_2 corrosion), and H_2S-saturated solutions (H_2S corrosion). Totally, 37 data points are compared.

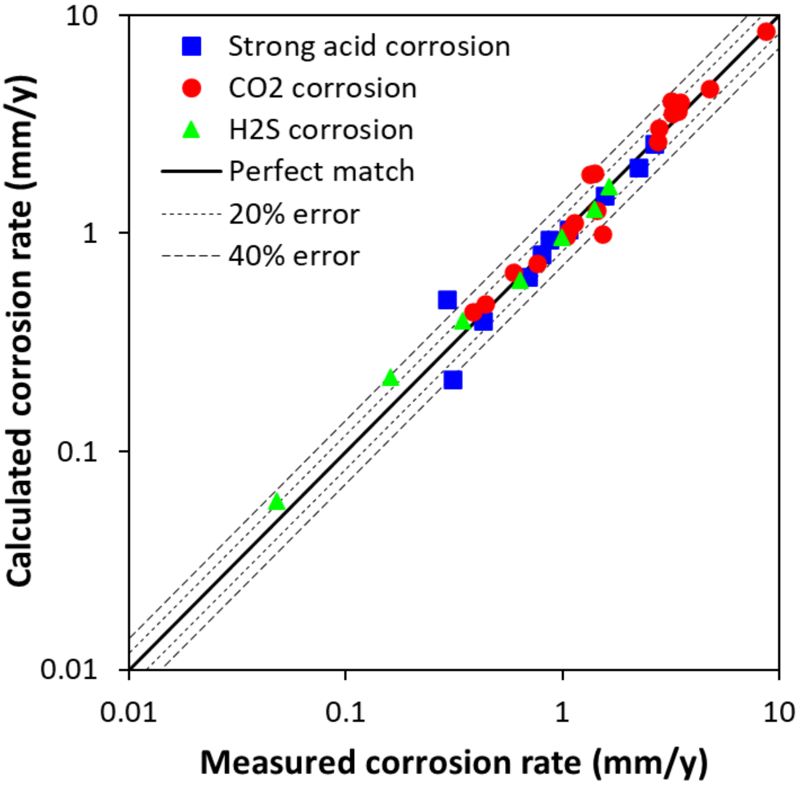

The average absolute errors[104] in the corrosion rate predictions for each type of corrosion rate data are presented in Figure 12 19. The corrosion rate prediction model performed better on CO_2 corrosion rate data followed by H_2S corrosion rate data. The corrosion rate predictions for strong acid corrosion has the least accuracy among the three. Although a broad range of conditions has been investigated in this study, it is possible to have different average errors if other conditions are entered into the model. However, the “Total” column, which covers the errors in the corrosion rate predictions for the all the experimental data, shows that the total average of the absolute errors in the corrosion rate predictions is around 13.5%. The standard deviation of the absolute errors for all the corrosion rate predictions in this study is 14.5%. This magnitude of absolute error can be considered quite pleasing when the complexity and the extent of information required to develop this corrosion rate prediction model are taken into account.

---

[104] Absolute error% = 100 × |measured corrosion rate-calculated corrosion rate| / measured corrosion rate

Figure 12-19

The average absolute errors obtained by comparing the corrosion rate predictions with the experimental corrosion rate data measured in this study for three types of corrosion. "Total" considers the errors in the corrosion rate predictions for the all the experimental data.

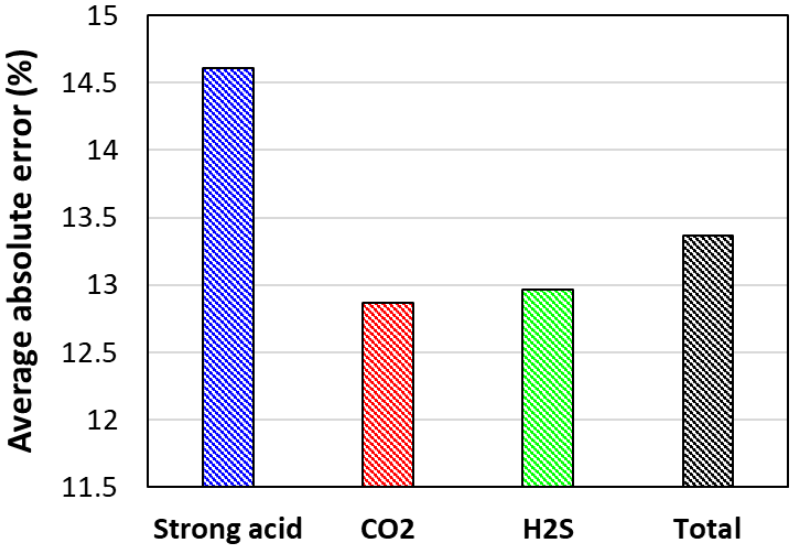

Figure 12-20 shows the scatters of errors obtained by the corrosion rate prediction model for each type of corrosion by a box and whisker plot. The scatters of errors are similar for CO_2 and H_2S corrosion rate predictions. The calculated corrosion rates for strong acid corrosion are more scattered than the other two with a maximum error of ~ 70%. The 70% error is related to the corrosion rate prediction in the strong acid RCE experiments at 20 wt.% NaCl, which seems to be very close to the measured corrosion rate shown Figure 12-11. The next largest error is around 40% for the CO_2 RCE experiments at 30°C, autogenous pH, and 20 wt.% NaCl.

The column “Total” in Figure 12-20 considers the errors in the corrosion rate predictions for all the experimental data in this study, *i.e.,* strong acid, CO_2, and H_2S corrosion all together. The “Total” column shows that the median of errors for the corrosion rate prediction model is approximately 8%. This mean that for half of the experimental conditions, the corrosion rate model was able to predict the corrosion rate with an accuracy of around 8%, which is an indication of the acceptable performance of the corrosion rate prediction model.

Figure 12-20

The box and whisker plot (min, quartile 1, median, quartile 3 and max) of the corrosion rate prediction errors for three types of experimental corrosion data measured in this study. “Total” considers the errors for all the measured data in this study.

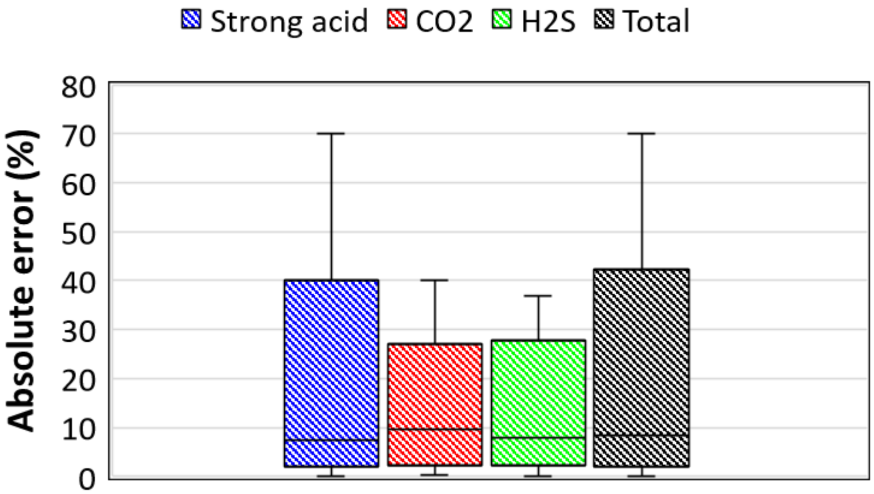

In summary, the average absolute accuracy of the corrosion rate prediction model is 13.5%. The median of the absolute errors is ~ 8% and the standard deviation of absolute errors is 14.5%.

12.5 Corrosion Rate Prediction Model Validation Range and Limitations

The corrosion rate prediction model developed in this study is valid for the H_2O-NaCl-CO_2-H_2S system, temperatures above the water freezing point and below the water boiling point, pressures up to few bars, solution pH values from 1.0 up to 6.5, and NaCl concentrations between zero to 20 wt.% (~4.3 m). The model is applicable to CO_2 and H_2S partial pressures between 0 bar to 1 bar as well. It is expected that the model works for higher pressures up to the critical pressure of $CO_{2(g)}$ (~ 73 bar).

In the proposed models, there are a few factors which are not taken into consideration. These factors need to be pointed out here to avoid any confusion or misuse of the model:

1. The current model is only valid for prediction uniform corrosion of carbon steel. It does not cover scenarios when corrosion product surface layers such as iron carbonate or iron sulfides are present or localized corrosion is expected. However, the model provides a solid foundation for constructing models for such scenarios.
2. The model is valid for the H_2O-NaCl-CO_2-H_2S system. The effects of oxygen, dissolved ferrous ion, elemental sulfur, and other dissolved species are not considered.
3. The model is only applicable to the water-rich phase. It is not designed for the dense gas-rich phase (dissolution of water phase into the dense gas phase).

4. The model is only valid for single-phase liquid flows. For multiphase flows appropriate empirical mass transfer correlations need to be integrated into the model. to couple with the current model.
5. The accuracy of the model at very low NaCl concentrations, between (0 wt.% to 0.1 wt.%) might be not as good as that for higher NaCl concentrations.

Chapter 13: Overall Summary and Conclusions

In the present dissertation study, the effect of salt (NaCl) concentration on aqueous uniform strong acid, CO_2, and H_2S corrosion of carbon steel is investigated. The key parameters in the corrosion process that are influenced by changing salt concentration are identified: transport phenomena (solution density, solution viscosity and diffusion coefficients of dissolved species), solution chemistry, and electrochemistry of underlying reactions. Models are reproduced or developed for accounting for the effect of salt concentration on transport phenomena and solution chemistry. The effect of salt concentration on electrochemistry of the corrosion processes was studied by preforming eight sets of experiments at different salt concentrations, with key conditions as follows:

<u>Strong acid corrosion</u>:

1. N_2-saturated solution, RDE, 10^oC, ~1 bar $pN_{2(g)}$, pH 3, 2000 rpm, 0.1-20 wt.% NaCl
2. N_2-saturated solution, RCE, 20^oC, ~1 bar $pN_{2(g)}$, pH 3, 1000 rpm, 0.1-20 wt.% NaCl

<u>CO_2 corrosion</u>:

3. CO_2-saturated solution, RDE, 10^oC, ~1 bar $pCO_{2(g)}$, pH 3, 2000 rpm, 1-20 wt.% NaCl
4. CO_2-saturated solution, RCE, 30^oC, ~1 bar $pCO_{2(g)}$, autogenous pH, 1000 rpm, 0-20 wt.% NaCl
5. CO_2-saturated solution, RCE, 20^oC, ~1 bar $pCO_{2(g)}$, pH 5, 1000 rpm, 0.1-20 wt.% NaCl

6. CO_2-saturated solution, RCE, 50°C and 80°C, total pressure of 1 bar, pH 5, 1000 rpm, 1 wt.% and 20 wt.% NaCl

H_2S corrosion:

7. H_2S-N_2 saturated solution, RCE, 20°C, total pressure of 1 bar, 100 ppm $H_2S_{(g)}$, pH 5, 1000 rpm, 1 wt.% and 20 wt.% NaCl
8. H_2S-saturated solution, RCE, 20°C, ~1 bar $pH_2S_{(g)}$, pH 5, 1000 rpm, 0.1-20 wt.% NaCl

The experimental results are used to quantify the effect of salt concentration on kinetic parameters needed for the development of an electrochemical model. The electrochemical model is completed with implementing the new limiting current density equations proposed in this study for the first time. Ultimately, the models for transport phenomena and solution chemistry are coupled with the electrochemical model to build the final corrosion rate prediction model. The major conclusions derived in this study are summarized and the performance of the corrosion rate prediction model is briefly described below:

1. Increase in salt concentration, increases solution density; and generally, increases solution viscosity; decreases diffusion coefficient of dissolved species.
2. The Smolyakov equation is chosen for correcting the diffusion coefficients for the effect of temperature. The square root equation (Kohlrausch law) is used for correcting the diffusion coefficients for the effect of salt concentration. The coefficients in both equations are modified in this study for correcting diffusion

coefficients of dissolved species important in aqueous corrosion of carbon steel, such as H^+ ion, carbonic acid ($H_2CO_{3(aq)}$) and hydrogen sulfide ($H_2S_{(aq)}$).

3. Gas solubility, including $CO_{2(g)}$ and $H_2S_{(g)}$ solubilities, decreases when salt is added to the solution. This is called the salting-out effect. Very accurate models have been reproduced for salting out of $CO_{2(g)}$ and $H_2S_{(g)}$ in aqueous NaCl solutions valid for a wide range of temperatures, pressures, and NaCl concentrations.
4. Increasing salt concentration changes interspecies interactions in the solutions. Also, it decreases the number of free water molecules in the solution. In the solution chemistry models (or water chemistry models or thermodynamic speciation equilibrium models), the changes in interspecies interactions are accounted for by activity coefficients. The change in number of free water molecules is considered by water activity or osmotic coefficient.
5. Two types of solution chemistry models are reproduced in this study and compared with one another: ionic strength-based models and activity coefficient-based models. The first group is simpler to reproduce; this only sometimes results in more accurate predictions of equilibrium concentrations and solution pH. However, the second group is often more accurate and has a broader validity range in terms of temperature, pressure, number of dissolved species, and concentration of dissolved species. The activity coefficient-based models can be valid for compositions extending from very dilute solutions, such as pure water, to fused salts.

6. The comparison of the solution chemistry models shows that the mixed solvent electrolyte (MSE) model is the most accurate model available in the literature for the H_2O-NaCl-CO_2-H_2S systems. The MSE model is chosen for the solution chemistry calculations in this study.
7. The pH measurements at 1 bar total pressure and temperatures below 80°C showed that the autogenous pH of aqueous CO_2- and H_2S-saturated solutions decreased with increasing NaCl concentration. However, when the solution was saturated with N_2 gas, the autogenous pH of solution increased. The reason for the decrease in the solution pH is attributed to the changes in the interactions between different species in the solution with increasing salt concentration. The solution chemistry models could predict the behavior of solution pH in CO_2- and H_2S-saturated solutions. However, the increasing trend of pH in N_2-saturated solutions could not be captured with these models.
8. The analysis of the PD sweeps in all sets of experiments showed that with increasing NaCl concentration the rate of the cathodic H^+ ion reduction reaction decreased continually, while the rate of the cathodic water reduction reaction generally increased. The rate of anodic dissolution of Fe in the active region increased at lower NaCl concentrations and then switched trend and decreased at higher NaCl concentrations.
9. The results of the experimental sets #1 and #2 in N_2-saturated solutions showed that with increasing NaCl concentration, the uniform strong acid corrosion rate decreased steadily; both cathodic (H^+ reduction) and anodic (iron dissolution)

charge transfer reactions were retarded; the limiting current density (i_{Lim}) for H^+ ion reduction decreased. Salt concentration seemed to have no effect on the mechanism of active dissolution of iron. However, it apparently altered the mechanism of H^+ ion reduction at the steel surface.

10. The results of the experimental sets #3 to #6 in CO_2-saturated solutions showed that the uniform CO_2 corrosion rate first increased between 1 wt.% and 3 wt.% and then switched trend and decreased continually between 3 wt.% and 20 wt.%. The increase in the CO_2 corrosion rate at low NaCl concentrations was due to the acceleration of the active dissolution reaction of iron. The decrease in the CO_2 corrosion rate at higher NaCl concentrations was attributed to retardation of both iron dissolution and charge transfer controlled reactions as well as the decrease in i_{Lim}. At low temperatures (*e.g.*, 20°C) and low solution pH values (*e.g.*, 3), the charge transfer iron dissolution and H^+ ion reduction reactions controlled the rate of the CO_2 corrosion process. However, at higher temperature (e.g., 50°C) and higher pH values the CO_2 corrosion process was under mixed control (charge transfer, mass transfer, and chemical reaction control). At 80°C and pH 5, and 1 wt.%, the CO_2 corrosion process was purely controlled by i_{Lim}, *i.e.*, a combination of mass transfer and chemical reaction control.
11. The results of the experimental sets #7 to #8 in H_2S-saturated solutions indicated that the uniform H_2S corrosion rate decreased monotonously with increasing NaCl concentration. Below 1 wt.%, NaCl, the decrease in the rate of the cathodic H^+ ion reduction reaction and above 1 wt.% NaCl in addition to that the decrease in the

rate of the iron dissolution reaction were the reasons for the decrease in the H_2S corrosion rate with NaCl concentration.

12. The analysis of PD sweeps suggested that in H_2S corrosion the mechanisms of cathodic H^+ ion reduction and anodic iron dissolution differ somewhat from those that occurring in strong acid and CO_2 corrosion. However, H_2S corrosion mechanisms at 1 bar $H_2S_{(g)}$ were unaffected by salt concentration. Additionally, the Evans diagrams demonstrated that the H_2S corrosion process at ~ 1 bar $H_2S_{(g)}$ was under pure charge transfer control for the entire range of NaCl concentrations.
13. The comparison of the exchange current density results in N_2-saturated solutions ($pCO_2 = 0$ bar) and CO_2-saturated solutions ($pCO_2 \cong 1$ bar) at 10^oC and pH 3 indicated that the rates of both charge transfer cathodic H^+ ion reduction and anodic iron dissolution reactions increased slightly with increasing NaCl concentration. This suggests that the presence of CO_2 influenced the charge transfer cathodic H^+ ion reduction and the anodic iron dissolution reactions. However, since the increase was within the experimental and the fitting procedure errors, this conclusion needs further investigation and is recommended as a priority for future work.
14. The comparison of the exchange current density results obtained for H_2S corrosion at two partial pressures of 10^{-4} bar and ~1 bar showed that the charge transfer H^+ ion reduction reaction was influenced very little by the presence of H_2S. However, the rate of the anodic iron dissolution increased almost 10 times

when pH_2S was increased from 10^{-4} bar to ~1 bar. Therefore, it is concluded that the presence of H_2S accelerates the anodic dissolution of iron, and this effect is included in the final corrosion rate prediction model.

15. Simple limiting current density equations were developed for CO_2 and H_2S corrosion, considering H^+ ion reduction as the only cathodic reaction. The equations are applicable to ideal, near ideal and non-ideal solutions with an acceptable accuracy.
16. The corrosion rate prediction model is valid for the H_2O-NaCl-CO_2-H_2S system, temperatures above the water freezing point and below the water boiling point, pressures up to a few bars, solution pH values from 1.0 up to 6.5, and NaCl concentrations between 0 wt.% to 20 wt.% (~4.3 m). The model is also applicable to CO_2 and H_2S partial pressures between 0 bar to 1 bar. It is expected that the model works for higher pressures up to the critical pressure of $CO_{2(g)}$ (~ 73 bar).
17. The corrosion rate prediction model could predict the experimental corrosion rates measured in this study with an average absolute accuracy of 13.5%.

Chapter 14: Recommendations for Future Work

Some recommendations for future work are listed as follows:

- Include more species such as Ca^{2+}, Mg^{2+}, Ba^{2+}, Fe^{2+}, SO_4^{2-}, N_2, CH_4, O_2, and iron complexes into the solution chemistry model.
- Improve the accuracy of the solution chemistry model for H_2S containing solutions by performing more pH measurement experiments at high temperatures, high pressures over a wide range of salt concentration.
- Although the major dissolved salt in groundwater is sodium chloride, it would be interesting to understand the effect of other ions such as Ca^{2+}, Mg^{2+}, Ba^{2+} and SO_4^{2-} on aqueous corrosion of carbon steel.
- Experiments at high partial pressures of CO_2 at different NaCl concentrations to improve the accuracy of the corrosion rate prediction model at these conditions.
- Experiments at high temperatures in H_2S-containing solutions to enhance the accuracy of the corrosion rate prediction model at these conditions.

References

[1] D.B. Burnett, Potential for beneficial use of oil and gas produced water, Global Petroleum Institute, Texas Water Resources Institute, Texas A&M University, 2004.

[2] C.E. Clark, J.A. Veil, Produced water volumes and management practices in the United States, U.S. Department of Energy, Office of Fossil Energy, National Energy Technology Laboratory, Argonne National Laboratory, 2009.

[3] G.N. Breit, USGS Produced Waters Database, U.S. Department of the Interior, 2002.

[4] K. Guerra, K. Dahm, S. Dundorf, Reclamation managing water in the west: oil and gas produced water management and beneficial use in the Western United States, US Department of the Interior Bureau of Reclamation, 2011.

[5] H. Fang, Low temperature and high salt concentration effects on general CO_2 corrosion for carbon steel, Master's thesis, Ohio University, 2006.

[6] H. Fang, S. Nesic, B. Brown, S. Wang, General CO_2 corrosion in high salinity brines, in: Corros. Conf., NACE International, San Diego, CA, 2006: p. No. 06372.

[7] J. Han, J.W. Carey, J. Zhang, Effect of sodium chloride on corrosion of mild steel in CO_2-saturated brines, J. Appl. Electrochem. 41 (2011) 741–749. https://doi.org/10.1007/s10800-011-0290-3.

[8] F.F. Eliyan, F. Mohammadi, A. Alfantazi, An electrochemical investigation on the effect of the chloride content on CO_2 corrosion of API-X100 steel, Corros. Sci. 64 (2012) 37–43. https://doi.org/10.1016/j.corsci.2012.06.032.

[9] J.L. Crolet, M.R. Bonis, pH measurements in aqueous CO_2 solutions under high pressure and temperature, CORROSION. 39 (1983) 39–46. https://doi.org/10.5006/1.3580813.

[10] G. Hinds, P. Cooling, A. Wain, S. Zhou, A. Turnbull, Technical note: measurement of pH in concentrated brines, CORROSION. 65 (2009) 635–638. https://doi.org/10.5006/1.3319089.

[11] Q.Y. Liu, L.J. Mao, S.W. Zhou, Effects of chloride content on CO_2 corrosion of carbon steel in simulated oil and gas well environments, Corros. Sci. 84 (2014) 165–171. https://doi.org/10.1016/j.corsci.2014.03.025.

[12] Z. Zeng, R.S. Lillard, H. Cong, Effect of salt concentration on the corrosion behavior of carbon steel in CO_2 environment, CORROSION. 72 (2016) 805–823. https://doi.org/10.5006/1910.

[13] S. Li, Z. Zeng, M.A. Harris, L.J. Sánchez, H. Cong, CO_2 corrosion of low carbon steel under the joint effects of time-temperature-salt concentration, Front. Mater. 6 (2019). https://doi.org/10.3389/fmats.2019.00010.

[14] S. Zhang, L. Hou, Y. Wei, H. Du, H. Wei, B. Liu, X. Chen, Dual functions of chloride ions on corrosion behavior of mild steel in CO_2 saturated aqueous solutions, Mater. Corros. 70 (2019) 888–896. https://doi.org/10.1002/maco.201810566.

[15] J.O. Bockris, A.K.N. Reddy, Modern Electrochemistry: An Introduction to an Interdisciplinary Area, A Plenum/Rosetta, Plenum Publishing Corporation, 1973.

[16] C. Wagner, W. Traud, Über die deutung von korrosionsvorgängen durch überlagerung von elektrochemischen teilvorgängen und über die potentialbildung an mischelektroden, Z. Für Elektrochem. Angew. Phys. Chem. 44 (1938) 391–402. https://doi.org/10.1002/bbpc.19380440702.

[17] Z. Ahmad, Principles of Corrosion Engineering and Corrosion Control, Elsevier Science, 2006.

[18] M.G. Fontana, Corrosion Engineering, 3rd edition, McGraw-Hill Book Company, New York, 1985.

[19] A. Anderko, Modeling of Aqueous Corrosion, in: Shreirs Corros., Elsevier, 2010: pp. 1585–1629. https://doi.org/10.1016/B978-044452787-5.00083-4.

[20] J.O. Bockris, A.K.N. Reddy, Modern Electrochemistry: An Introduction to an Interdisciplinary Area, A Plenum/Rosetta, Plenum Publishing Corporation, 1973. https://doi.org/10.1007/978-1-4615-8600-5.

[21] J. Newman, K.E. Thomas-Alyea, Electrochemical Systems, 3 edition, Wiley-Interscience, Hoboken, N.J, 2004.

[22] L. Meites, P. Zuman, H.W. Nurnberg, Recommended terms, symbols, and definitions for electroanalytical chemistry, Pure Appl. Chem. 57 (1985) 1491–1505. https://doi.org/10.1351/pac198557101491.

[23] F.G. Thomas, G. Henze, Introduction to Voltammetric Analysis: Theory and Practice, Csiro Publishing, 2001.

[24] R.H. Perry, D.W. Green, Perry’s Chemical Engineers’ Handbook, McGraw-Hill, 1999.

[25] P.S.Z. Rogers, K.S. Pitzer, Volumetric properties of aqueous sodium chloride solutions, J. Phys. Chem. Ref. Data. 11 (1982) 15–81. https://doi.org/10.1063/1.555660.

[26] M. Batzle, Z. Wang, Seismic properties of pore fluids, Geophysics. 57 (1992) 1396–1408. https://doi.org/10.1190/1.1443207.

[27] Y. Song, B. Chen, M. Nishio, M. Akai, The study on density change of carbon dioxide seawater solution at high pressure and low temperature, Energy. 30 (2005) 2298–2307. https://doi.org/10.1016/j.energy.2003.10.022.

[28] Z. Duan, J. Hu, D. Li, S. Mao, Densities of the CO_2–H_2O and CO_2–H_2O–NaCl Systems Up to 647 K and 100 MPa, Energy Fuels. 22 (2008) 1666–1674. https://doi.org/10.1021/ef700666b.

[29] Y. Song, Y. Zhan, Y. Zhang, S. Liu, W. Jian, Y. Liu, D. Wang, Measurements of CO_2–H_2O–NaCl solution densities over a wide range of temperatures, pressures, and NaCl concentrations, J. Chem. Eng. Data. 58 (2013) 3342–3350. https://doi.org/10.1021/je400459y.

[30] S. Mao, D. Zhang, Y. Li, N. Liu, An improved model for calculating CO_2 solubility in aqueous NaCl solutions and the application to CO_2–H_2O–NaCl fluid inclusions, Chem. Geol. 347 (2013) 43–58. https://doi.org/10.1016/j.chemgeo.2013.03.010.

[31] S. Mao, Z. Duan, The viscosity of aqueous alkali-chloride solutions up to 623 K, 1,000 bar, and high ionic strength, Int. J. Thermophys. 30 (2009) 1510–1523. https://doi.org/10.1007/s10765-009-0646-7.

[32] J.L.M. Poiseuille, Ann. Chim. Phys. 21 (1847) 76.

[33] M.P. Applebey, The viscosity of salt solutions, R. Soc. Chem. (1910) 2000–2025.

[34] G. Jones, M. Dole, The viscosity of aqueous solutions of strong electrolytes with special reference to barium chloride, J. Am. Chem. Soc. 51 (1929) 2950–2964. https://doi.org/10.1021/ja01385a012.

[35] P. Debye, E. Huckel, On the theory of electrolytes. I. Freezing point depression and related phenomena, Phys. Z. 24 (1923) 185–206.

[36] J.D. Bernal, R.H. Fowler, A theory of water and ionic solution, with particular reference to hydrogen and hydroxyl Ions, J. Chem. Phys. 1 (1933) 515. https://doi.org/10.1063/1.1749327.

[37] K.D. Collins, Charge density-dependent strength of hydration and biological structure, Biophys. J. 72 (1997) 65–76. https://doi.org/10.1016/S0006-3495(97)78647-8.

[38] H.T. Kwak, G. Zhang, S. Chen, The effects of salt type and salinity on formation water viscosity and NMR responses, in: Int. Symp. Soc. Core Anal., Toronto, Ca, 2005: p. No. SCA2005-51.

[39] H. Falkenhagen, M. Dole, The internal friction of electrolytic solutions and its interpretation according to debye theory, Z. Phys. 30 (1929) 611–616.

[40] H. Falkenhagen, E.L. Vernon, The viscosity of strong electrolyte solutions according to electrostatic theory, Lond. Edinb. Dublin Philos. Mag. J. Sci. 14 (1932) 537–565. https://doi.org/10.1080/14786443209462095.

[41] H.L. Zhang, S.J. Han, Viscosity and density of water + sodium chloride + potassium chloride solutions at 298.15 K, J. Chem. Eng. Data. 41 (1996) 516–520. https://doi.org/10.1021/je9501402.

[42] M. Kaminsky, The concentration and temperature dependence of the viscosity of aqueous solutions of strong electrolytes. III. KCl, K_2SO_4, $MgCl_2$, $BeSO_4$, and $MgSO_4$ solutions, Z. Phys. Chem. (1957) 206–231.

[43] J. Kestin, H.E. Khalifa, R.J. Correia, Tables of the dynamic and kinematic viscosity of aqueous NaCl solutions in the temperature range 20–150 °C and the pressure range 0.1–35 MPa, J. Phys. Chem. Ref. Data. 10 (1981) 71–88. https://doi.org/10.1063/1.555641.

[44] J.P. Spivey, W.D.Jr. McCain, R. North, Estimating density, formation volume factor, compressibility, methane solubility, and viscosity for oilfield brines at temperatures from 0 to 275 ° C, pressures to 200 MPa, and salinities to 5.7 mole/kg, J. Can. Pet. Technol. 43 (2004). https://doi.org/10.2118/04-07-05.

[45] A.W. Islam, E.S. Carlson, Viscosity models and effects of dissolved CO_2, Energy Fuels. 26 (2012) 5330–5336. https://doi.org/10.1021/ef3006228.

[46] W. Wagner, J.R. Cooper, A. Dittmann, J. Kijima, H.J. Kretzschmar, A. Kruse, R. Mares, K. Oguchi, H. Sato, I. Stocker, O. Sifner, Y. Takaishi, I. Tanishita, J. Trubenbach, Th. Willkommen, The IAPWS industrial formulation 1997 for the

thermodynamic properties of water and steam, J. Eng. Gas Turbines Power. 122 (2000) 150–184. https://doi.org/10.1115/1.483186.

[47] M. Afzal, M. Saleem, M.T. Mahmood, Temperature and concentration dependence of viscosity of aqueous electrolytes from 20.degree.C to 50.degree.C chlorides of (sodium(1+), potassium(1+), magnesium(2+), calcium(2+), barium(2+), strontium(2+), cobalt(2+), nickel(2+), copper(2+) and chromium(3+), J. Chem. Eng. Data. 34 (1989) 339–346. https://doi.org/10.1021/je00057a023.

[48] R.I. Pepinov, V.D. Yusufova, N.V. Lobkova, Thermodynamics of the viscous flow of aqueous solutions of sodium chloride, Russ. J. Phys. Chem. 53 (1979) 172–173.

[49] Y. Zheng, Electrochemical mechanism and model of H_2S corrosion of carbon steel, PhD, Ohio University, 2015.

[50] A. Kahyarian, B. Brown, S. Nesic, The unified mechanism of corrosion in aqueous weak acids solutions: a review of the recent developments in mechanistic understandings of mild steel corrosion in the presence of carboxylic acids, carbon dioxide, and hydrogen sulfide, Corrosion. 76 (2020) 268–278. https://doi.org/10.5006/3474.

[51] A. Kahyarian, M. Singer, S. Nesic, Modeling of uniform CO_2 corrosion of mild steel in gas transportation systems: A review, J. Nat. Gas Sci. Eng. 29 (2016) 530–549. https://doi.org/10.1016/j.jngse.2015.12.052.

[52] R. Mills, Diffusion in electrolytes, J. Electroanal. Chem. 1959. 9 (1965) 57–69. https://doi.org/10.1016/0022-0728(65)80065-1.

[53] H.J.V. Tyrrell, K.R. Harris, Diffusion in Liquids: A Theoretical and Experimental Study, Butterworth-Heinemann, 2013.

[54] R.A. Robinson, R.H. Stokes, Electrolyte Solutions: Second Revised Edition, Courier Corporation, 2002.

[55] J. Ahl, Tracer and interdiffusion measurements of some common salts in aqueous solutions and in porous ceramic media, PhD dissertation, Aalto University, 2014.

[56] A.C.F. Ribeiro, V.M.M. Lobo, L.R.C. Oliveira, H.D. Burrows, E.F.G. Azevedo, S.I.G. Fangaia, P.M.G. Nicolau, F.A.D.R.A. Guerra, Diffusion coefficients of chromium chloride in aqueous solutions at 298.15 K and 303.15 K, J. Chem. Eng. Data. 50 (2005) 1014–1017. https://doi.org/10.1021/je050003x.

[57] D.G. Miller, Estimation of tracer diffusion coefficients of ions in aqueous solution, Lawrence Livermore Laboratory, University of California, 1982.

[58] H.J.V. Tyrrell, K.R. Harris, Chapter 8 - Diffusion in electrolytes, in: H.J.V. Tyrrell, K.R. Harris (Eds.), Diffus. Liq., Butterworth-Heinemann, 1984: pp. 387–437. https://doi.org/10.1016/B978-0-408-17591-3.50012-5.

[59] P.W. Atkins, J.D. Paula, Elements of Physical Chemistry, 7th ed., Oxford University Press, 2017.

[60] J.C. Clunie, N.L. Burns, J.K. Baird, Nernst-Hartley evaluation of the interdiffusion coefficient of aqueous nickel sulfamate using new measurements of the equivalent conductances of the ions, J. Electroanal. Chem. 328 (1992) 317–320. https://doi.org/10.1016/0022-0728(92)80188-A.

[61] L. Onsager, R.M. Fuoss, Irreversible processes in electrolytes. diffusion, conductance and viscous flow in arbitrary mixtures of strong electrolytes, J. Phys. Chem. 36 (1932) 2689–2778. https://doi.org/10.1021/j150341a001.

[62] L. Onsager, Theories and problems of liquid diffusion, Ann. N. Y. Acad. Sci. 46 (1945) 241–265. https://doi.org/10.1111/j.1749-6632.1945.tb36170.x.

[63] L.J. Gosting, H.S. Harned, The application of the Onsager theory of ionic mobilities to self-diffusion, J. Am. Chem. Soc. 73 (1951) 159–161. https://doi.org/10.1021/ja01145a057.

[64] R. Mills, E.W. Godbole, Verification of the Onsager limiting law for trace-ion diffusion in electrolyte solutions, J. Am. Chem. Soc. 82 (1960) 2395–2396. https://doi.org/10.1021/ja01494a071.

[65] O. Bernard, W. Kunz, P. Turq, L. Blum, Self-diffusion in electrolyte solutions using the mean spherical approximation, J. Phys. Chem. 96 (1992) 398–403. https://doi.org/10.1021/j100180a074.

[66] S. Chapman, T.G. Cowling, The mathematical theory of non-uniform gases: an account of the kinetic theory of viscosity, thermal conduction and diffusion in gases, Cambridge University Press, 1990.

[67] R.L. Kay, J.L. Dye, The determination of the electrophoretic contribution to conductance from the concentration dependence of transference numbers, Proc. Natl. Acad. Sci. 49 (1963) 5–11. https://doi.org/10.1073/pnas.49.1.5.

[68] L. Onsager, The motion of Ions: principles and concepts, Science. 166 (1969) 1359–1364. https://doi.org/10.1126/science.166.3911.1359.

[69] N.D. Pinto, E.E. Graham, Evaluation of diffusivities in electrolyte solutions using Stefan-Maxwell equations, AIChE J. 32 (1986) 291–296. https://doi.org/10.1002/aic.690320216.

[70] A. Anderko, M.M. Lencka, Modeling self-diffusion in multicomponent aqueous electrolyte systems in wide concentration ranges, Ind. Eng. Chem. Res. 37 (1998) 2878–2888. https://doi.org/10.1021/ie980001o.

[71] P. Wang, A. Anderko, Modeling Self-Diffusion in Mixed-Solvent Electrolyte Solutions, Ind. Eng. Chem. Res. 42 (2003) 3495–3504. https://doi.org/10.1021/ie030050n.

[72] M. Jardat, B. Hribar-Lee, V. Dahirel, V. Vlachy, Self-diffusion and activity coefficients of ions in charged disordered media, J. Chem. Phys. 137 (2012) 114507. https://doi.org/10.1063/1.4752111.

[73] N.G. Pinto, E.E. Graham, Multicomponent diffusion in concentrated electrolyte solutions: effect of solvation, AIChE J. 33 (1987) 436–443. https://doi.org/10.1002/aic.690330309.

[74] R.T. Ferrell, D.M. Himmelblau, Diffusion coefficients of hydrogen and helium in water, AIChE J. 13 (1967) 702–708. https://doi.org/10.1002/aic.690130421.

[75] D.M. Himmelblau, Diffusion of dissolved gases in liquids, Chem. Rev. 64 (1964) 527–550. https://doi.org/10.1021/cr60231a002.

[76] K. Kigoshi, T. Hashitani, The self-diffusion coefficients of carbon dioxide, hydrogen carbonate ions and carbonate ions in aqueous solutions, Bull. Chem. Soc. Jpn. 36 (1963) 1372–1372. https://doi.org/10.1246/bcsj.36.1372.

[77] N. Haimour, O.C. Sandall, Molecular diffusivity of hydrogen sulfide in water, J. Chem. Eng. Data. 29 (1984) 20–22. https://doi.org/10.1021/je00035a009.

[78] A. Tamimi, E.B. Rinker, O.C. Sandall, Diffusion coefficients for hydrogen sulfide, carbon dioxide, and nitrous oxide in water over the temperature range 293-368 K, J. Chem. Eng. Data. 39 (1994) 330–332. https://doi.org/10.1021/je00014a031.

[79] D.R. Lide, CRC Handbook of Chemistry and Physics, 84th Edition, 84th ed., CRC Press, 2003.

[80] Y.H. Li, S. Gregory, Diffusion of ions in sea water and in deep-sea sediments, Geochim. Cosmochim. Acta. 38 (1974) 703–714. https://doi.org/10.1016/0016-7037(74)90145-8.

[81] V. Vitagliano, P.A. Lyons, Diffusion in aqueous acetic acid solutions, J. Am. Chem. Soc. 78 (1956) 4538–4542. https://doi.org/10.1021/ja01599a008.

[82] D.G. Leaist, P.A. Lyons, Diffusion in dilute aqueous acetic acid solutions at 25°C, J. Solut. Chem. 13 (1984) 77–85. https://doi.org/10.1007/BF00646041.

[83] W.J. Albery, A.R. Greenwood, R.F. Kibble, Diffusion coefficients of carboxylic acids, Trans. Faraday Soc. 63 (1967) 360–368. https://doi.org/10.1039/TF9676300360.

[84] M.J. Tham, R.D. Walker, K.E. Gubbins, Diffusion of oxygen and hydrogen in aqueous potassium hydroxide solutions, J. Phys. Chem. 74 (1970) 1747–1751. https://doi.org/10.1021/j100703a015.

[85] L.-K. Ju, C.S. Ho, Measuring oxygen diffusion coefficients with polarographic oxygen electrodes: I. Electrolyte solutions, Biotechnol. Bioeng. 27 (1985) 1495–1499. https://doi.org/10.1002/bit.260271015.

[86] M. Jamnongwong, K. Loubiere, N. Dietrich, G. Hébrard, Experimental study of oxygen diffusion coefficients in clean water containing salt, glucose or surfactant: Consequences on the liquid-side mass transfer coefficients, Chem. Eng. J. 165 (2010) 758–768. https://doi.org/10.1016/j.cej.2010.09.040.

[87] P.A. Witherspoon, D.N. Saraf, Diffusion of methane, ethane, propane, and n-butane in water from 25 to 43°, J. Phys. Chem. 69 (1965) 3752–3755. https://doi.org/10.1021/j100895a017.

[88] J.W. Mutoru, A. Leahy-Dios, A. Firoozabadi, Modeling infinite dilution and Fickian diffusion coefficients of carbon dioxide in water, AIChE J. 57 (2011) 1617–1627. https://doi.org/10.1002/aic.12361.

[89] C.R. Wilke, P. Chang, Correlation of diffusion coefficients in dilute solutions, AIChE J. 1 (1955) 264–270. https://doi.org/10.1002/aic.690010222.

[90] D.E. Bidstrup, C.J. Geankoplis, Aqueous molecular diffusivities of carboxylic acids., J. Chem. Eng. Data. 8 (1963) 170–173. https://doi.org/10.1021/je60017a004.

[91] G. Le Bas, The Molecular Volumes of Liquid Chemical Compounds, from the Point of View of Kopp, Longmans, Green, 1915.

[92] B.J. Krieg, S.M. Taghavi, G.L. Amidon, G.E. Amidon, In vivo predictive dissolution: transport analysis of the CO_2, bicarbonate in vivo buffer system, J. Pharm. Sci. 103 (2014) 3473–3490. https://doi.org/10.1002/jps.24108.

[93] E.G. Scheibel, Correspondence. liquid diffusivities. vscosity of gases., Ind. Eng. Chem. 46 (1954) 2007–2008. https://doi.org/10.1021/ie50537a062.

[94] R.E. Zeebe, On the molecular diffusion coefficients of dissolved CO_2,HCO_3^-, and CO_3^{2-} and their dependence on isotopic mass, Geochim. Cosmochim. Acta. 75 (2011) 2483–2498. https://doi.org/10.1016/j.gca.2011.02.010.

[95] A. Einstein, Über die von der molekularkinetischen Theorie der Wärme geforderte Bewegung von in ruhenden Flüssigkeiten suspendierten Teilchen, Ann. Phys. 322 (1905) 549–560. https://doi.org/10.1002/andp.19053220806.

[96] S. Nesic, J. Postlethwaite, S. Olsen, An electrochemical model for prediction of corrosion of mild steel in aqueous carbon dioxide solutions, CORROSION. 52 (1996) 280–294. https://doi.org/10.5006/1.3293640.

[97] M.S. Helal, H.A. Farag, M.S. Mansour, Y.O. Fouad, Experimental study of the diffusion-controlled corrosion of copper in the bottom of a jet stirred reactor, Braz. J. Chem. Eng. 35 (2018) 101–110. https://doi.org/10.1590/0104-6632.20180351s20160333.

[98] A. Anderko, M.M. Lencka, Computation of electrical conductivity of multicomponent aqueous systems in wide concentration and temperature ranges, Ind. Eng. Chem. Res. 36 (1997) 1932–1943. https://doi.org/10.1021/ie9605903.

[99] B.D. Cornish, R.J. Speedy, Proton conductivity in supercooled aqueous hydrochloric acid solutions, J. Phys. Chem. 88 (1984) 1888–1892. https://doi.org/10.1021/j150653a043.

[100] A.S. Quist, W.L. Marshall, Assignment of limiting equivalent conductances for single ions to 400°, J. Phys. Chem. 69 (1965) 2984–2987. https://doi.org/10.1021/j100893a027.

[101] W.J. Thomas, M.J. Adams, Measurement of the diffusion coefficients of carbon dioxide and nitrous oxide in water and aqueous solutions of glycerol, Trans. Faraday Soc. 61 (1965) 668–673. https://doi.org/10.1039/TF9656100668.

[102] M.J.W. Frank, J.A.M. Kuipers, W.P.M. van Swaaij, Diffusion coefficients and viscosities of CO_2 + H_2O, CO_2 + CH_3OH, NH_3 + H_2O, and NH_3 + CH_3OH Liquid Mixtures, J. Chem. Eng. Data. 41 (1996) 297–302. https://doi.org/10.1021/je950157k.

[103] A. Iverson, The measured resistivity of pure water and determination of the limiting mobility of OH_- from 5 to 55°, J. Phys. Chem. 68 (1964) 515–521. https://doi.org/10.1021/j100785a012.

[104] D.L. Wise, G. Houghton, The diffusion coefficients of ten slightly soluble gases in water at 10–60°C, Chem. Eng. Sci. 21 (1966) 999–1010. https://doi.org/10.1016/0009-2509(66)85096-0.

[105] P.T.H.M. Verhallen, L.J.P. Oomen, A.J.J.M. v. d. Elsen, J. Kruger, J.M.H. Fortuin, The diffusion coefficients of helium, hydrogen, oxygen and nitrogen in water determined from the permeability of a stagnant liquid layer in the quasi-s, Chem. Eng. Sci. 39 (1984) 1535–1541. https://doi.org/10.1016/0009-2509(84)80082-2.

[106] K.E. Gubbins, K.K. Bhatia, R.D. Walker, Diffusion of gases in electrolytic solutions, AIChE J. 12 (1966) 548–552. https://doi.org/10.1002/aic.690120328.

[107] A. Kahyarian, S. Nesic, On the mechanism of carbon dioxide corrosion of mild steel: experimental investigation and mathematical modeling at elevated pressures and non-ideal solutions, Corros. Sci. 173 (2020) 108719. https://doi.org/10.1016/j.corsci.2020.108719.

[108] J. Jun, G.S. Frankel, N. Sridhar, Effect of chloride concentration and temperature on growth of 1D Pit, J. Solid State Electrochem. 19 (2015) 3439–3447. https://doi.org/10.1007/s10008-015-2780-4.

[109] R.M. Katona, J. Carpenter, E.J. Schindelholz, R.G. Kelly, Prediction of maximum pit sizes in elevated chloride concentrations and temperatures, J. Electrochem. Soc. 166 (2019) C3364. https://doi.org/10.1149/2.0451911jes.

[110] M.V. Stackelberg, M. Pilgram, Diffusionskoeffizient des wasserstoffions in wässrigen KCl-lösungen, Collect. Czechoslov. Chem. Commun. 25 (1960) 2974–2976. https://doi.org/10.1135/cccc19602974.

[111] M. Stastny, F. Strafelda, Concentration dependence of the diffusion coefficient of hydrogen ions in aqueous solutions of alkali metal salts, Collect. Czechoslov. Chem. Commun. 34 (1969) 168–176.

[112] R.H. Stokes, L.A. Woolf, R. Mills, Tracer diffusion of iodide ion in aqueous alkali chloride solutions at 25°, J. Phys. Chem. 61 (1957) 1634–1636. https://doi.org/10.1021/j150558a016.

[113] L.A. Woolf, Tracer diffusion of hydrogen ion in aqueous alkali chloride solutions at 25°, J. Phys. Chem. 64 (1960) 481–484. https://doi.org/10.1021/j100833a027.

[114] Malgorzata. Ciszkowska, Zbigniew. Stojek, S.E. Morris, J.G. Osteryoung, Steady-state voltammetry of strong and weak acids with and without supporting electrolyte, Anal. Chem. 64 (1992) 2372–2377. https://doi.org/10.1021/ac00044a013.

[115] R.L. Miller, W.L. Bradford, N.E. Peters, Specific conductance; theoretical considerations and application to analytical quality control, Department of the Interior, 1988. https://doi.org/10.3133/wsp2311.

[116] H. Hikita, S. Asai, H. Ishikawa, M. Seko, H. Kitajima, Diffusivities of carbon dioxide in aqueous mixed electrolyte solutions, Chem. Eng. J. 17 (1979) 77–80. https://doi.org/10.1016/0300-9467(79)80008-8.

[117] C.N. Carter, Effect of pH and oxidizing agents on the rate of absorption of hydrogen sulfide into aqueous media, PhD dissertation, Lawrence University, 1966.

[118] C.A.J. Appelo, Solute transport solved with the Nernst-Planck equation for concrete pores with ‘free’ water and a double layer, Cem. Concr. Res. 101 (2017) 102–113. https://doi.org/10.1016/j.cemconres.2017.08.030.

[119] K.A. Snyder, X. Feng, B.D. Keen, T.O. Mason, Estimating the electrical conductivity of cement paste pore solutions from OH^-, K^+ and Na^+ concentrations, Cem. Concr. Res. 33 (2003) 793–798. https://doi.org/10.1016/S0008-8846(02)01068-2.

[120] N.K. Roberts, H.L. Northey, Hydrogen ion mobility in aqueous electrolyte solutions. Comparison of polarographic and diaphragm cell methods, J. Chem.

Soc. Faraday Trans. 1 Phys. Chem. Condens. Phases. 68 (1972) 1528–1532. https://doi.org/10.1039/F19726801528.

[121] S.P. Cadogan, G.C. Maitland, J.P.M. Trusler, Diffusion coefficients of CO_2 and N_2 in water at temperatures between 298.15 K and 423.15 K at pressures up to 45 MPa, J. Chem. Eng. Data. 59 (2014) 519–525. https://doi.org/10.1021/je401008s.

[122] N. Sato, Chemical Energy and Exergy: an introduction to chemical thermodynamics for engineers, 1st ed., Elsevier, 2004.

[123] J.P. O'Connell, J.M. Haile, Thermodynamics: Fundamentals for Applications, Cambridge University Press, 2005.

[124] M.R. Wright, An Introduction to Aqueous Electrolyte Solutions, John Wiley & Sons, 2007.

[125] K. Thomsen, Electrolyte Solutions: Thermodynamics, Crystallization, Separation methods, Technical University of Denmark, 2009.

[126] Z. Duan, R. Sun, An improved model calculating CO_2 solubility in pure water and aqueous NaCl solutions from 273 to 533 K and from 0 to 2000 bar, Chem. Geol. 193 (2003) 257–271. https://doi.org/10.1016/S0009-2541(02)00263-2.

[127] Z. Duan, R. Sun, R. Liu, C. Zhu, Accurate thermodynamic model for the calculation of H_2S solubility in pure water and brines, Energy Fuels. 21 (2007) 2056–2065. https://doi.org/10.1021/ef070040p.

[128] A.B.J. Atkinson, A model for the PTX properties of H_2O-NaCl, Master's thesis, Virginia Polytechnic Institute and State University, 2002.

[129] J.O. Bockris, H. Egan, The salting-out effect and dielectric constant, Trans. Faraday Soc. 44 (1948) 151–159. https://doi.org/10.1039/TF9484400151.

[130] A.M. Hyde, S.L. Zultanski, J.H. Waldman, Y.-L. Zhong, M. Shevlin, F. Peng, General principles and strategies for salting-out informed by the Hofmeister series, Org. Process Res. Dev. 21 (2017) 1355–1370. https://doi.org/10.1021/acs.oprd.7b00197.

[131] F.A. Long, W.F. McDevit, Activity coefficients of nonelectrolyte solutes in aqueous salt solutions, Chem. Rev. 51 (1952) 119–169. https://doi.org/10.1021/cr60158a004.

[132] P.K. Grover, R.L. Ryall, Critical appraisal of salting-out and its implications for chemical and biological sciences, Chem. Rev. 105 (2005) 1–10. https://doi.org/10.1021/cr030454p.

[133] N. Spycher, K. Pruess, A phasepartitioning model for CO_2–brine mixtures at elevated temperatures and pressures: application to CO_2-enhanced geothermal systems, Transp. Porous Media. 82 (2010) 173–196. https://doi.org/10.1007/s11242-009-9425-y.

[134] X. Shi, S. Mao, An improved model for CO_2 solubility in aqueous electrolyte solution containing Na^+, K^+, Mg^{2+}, Ca^{2+}, Cl^- and SO_4^{2-} under conditions of CO_2 capture and sequestration, Chem. Geol. 463 (2017) 12–28. https://doi.org/10.1016/j.chemgeo.2017.05.005.

[135] P. Wang, A. Anderko, R.D. Young, A speciation-based model for mixed-solvent electrolyte systems, Fluid Phase Equilibria. 203 (2002) 141–176. https://doi.org/10.1016/S0378-3812(02)00178-4.

[136] D. Li, Z. Duan, The speciation equilibrium coupling with phase equilibrium in the H_2O–CO_2–NaCl system from 0 to 250 °C, from 0 to 1000 bar, and from 0 to 5 molality of NaCl, Chem. Geol. 244 (2007) 730–751. https://doi.org/10.1016/j.chemgeo.2007.07.023.

[137] J. Ananthaswamy, G. Atkinson, Thermodynamics of concentrated electrolyte mixtures. 4. Pitzer-Debye-Hueckel limiting slopes for water from 0 to 100.degree.C and from 1 atm to 1 kbar, J. Chem. Eng. Data. 29 (1984) 81–87. https://doi.org/10.1021/je00035a027.

[138] R.H. Stokes, R.A. Robinson, Ionic hydration and activity in electrolyte solutions, J. Am. Chem. Soc. 70 (1948) 1870–1878. https://doi.org/10.1021/ja01185a065.

[139] K.S. Pitzer, Thermodynamics of electrolytes. I. Theoretical basis and general equations, J. Phys. Chem. 77 (1973) 268–277. https://doi.org/10.1021/j100621a026.

[140] K.S. Pitzer, Activity Coefficients in Electrolyte Solutions, 2nd ed., CRC Press, 2018. https://doi.org/10.1201/9781351069472.

[141] K.S. Pitzer, Electrolytes. From dilute solutions to fused salts, J. Am. Chem. Soc. 102 (1980) 2902–2906. https://doi.org/10.1021/ja00529a006.

[142] C.E. Harvie, N. Møller, J.H. Weare, The prediction of mineral solubilities in natural waters: The Na-K-Mg-Ca-H-Cl-SO_4-OH-HCO_3-CO_3-CO_2-H_2O system to high ionic strengths at 25°C, Geochim. Cosmochim. Acta. 48 (1984) 723–751. https://doi.org/10.1016/0016-7037(84)90098-X.

[143] A.R. Felmy, J.H. Weare, The prediction of borate mineral equilibria in natural waters: Application to Searles Lake, California, Geochim. Cosmochim. Acta. 50 (1986) 2771–2783. https://doi.org/10.1016/0016-7037(86)90226-7.

[144] C.-C. Chen, H.I. Britt, J.F. Boston, L.B. Evans, Extension and application of the pitzer equation for vapor-liquid equilibrium of aqueous electrolyte systems with molecular solutes, AIChE J. 25 (1979) 820–831. https://doi.org/10.1002/aic.690250510.

[145] P. de A. Pessôa Filho, G. Maurer, An extension of the Pitzer equation for the excess Gibbs energy of aqueous electrolyte systems to aqueous polyelectrolyte solutions, Fluid Phase Equilibria. 269 (2008) 25–35. https://doi.org/10.1016/j.fluid.2008.04.019.

[146] H.T. Kim, W.J. Frederick, Evaluation of Pitzer ion interaction parameters of aqueous electrolytes at 25.degree.C. 1. Single salt parameters, J. Chem. Eng. Data. 33 (1988) 177–184. https://doi.org/10.1021/je00052a035.

[147] H.T. Kim, W.J. Frederick, Evaluation of Pitzer ion interaction parameters of aqueous mixed electrolyte solutions at 25.degree.C. 2. Ternary mixing parameters, J. Chem. Eng. Data. 33 (1988) 278–283. https://doi.org/10.1021/je00053a017.

[148] J.A. Rard, A.M. Wijesinghe, Conversion of parameters between different variants of Pitzer’s ion-interaction model, both with and without ionic strength dependent higher-order terms, J. Chem. Thermodyn. 35 (2003) 439–473. https://doi.org/10.1016/S0021-9614(02)00377-4.

[149] N. Plummer, D.L. Parkhurst, G.W. Fleming, S.A. Dunkle, A computer program incorporating Pitzer's equations for calculation of geochemical reactions in brines, U.S. Geological Survey, 1988. https://doi.org/10.3133/wri884153.

[150] A.R. Felmy, G.T. MacLean, Development of an enhanced thermodynamic database for the Pitzer model in ESP: the fluoride and phosphate components, Battelle Pacific Northwest Division, Richland, Washington, USA, 2001.

[151] J.N. Brönsted, Studies on solubility. IV. the principle of the specific interaction of ions, J. Am. Chem. Soc. 44 (1922) 877–898. https://doi.org/10.1021/ja01426a001.

[152] E.A. Guggenheim, J.C. Turgeon, Specific interaction of ions, Trans. Faraday Soc. 51 (1955) 747–761. https://doi.org/10.1039/TF9555100747.

[153] George. Scatchard, Concentrated solutions of strong electrolytes., Chem. Rev. 19 (1936) 309–327. https://doi.org/10.1021/cr60064a008.

[154] R.M. Garrels, M.E. Thompson, A chemical model for sea water at 25 degrees C and one atmosphere total pressure, Am. J. Sci. 260 (1962) 57–66. https://doi.org/10.2475/ajs.260.1.57.

[155] F.J. Millero, D.R. Schreiber, Use of the ion pairing model to estimate activity coefficients of the ionic components of natural waters, Am. J. Sci. 282 (1982) 1508–1540. https://doi.org/10.2475/ajs.282.9.1508.

[156] C.-L. Lin, L.-S. Lee, H.-C. Tseng, Thermodynamic behavior of electrolyte solutions: Part I. Activity coefficients and osmotic coefficients of binary systems, Fluid Phase Equilibria. 90 (1993) 57–79. https://doi.org/10.1016/0378-3812(93)85004-6.

[157] X. Ge, X. Wang, M. Zhang, S. Seetharaman, Correlation and prediction of activity and osmotic coefficients of aqueous electrolytes at 298.15 K by the modified TCPC model, J. Chem. Eng. Data. 52 (2007) 538–547. https://doi.org/10.1021/je060451k.

[158] D.S. Abrams, J.M. Prausnitz, Statistical thermodynamics of liquid mixtures: A new expression for the excess Gibbs energy of partly or completely miscible systems, AIChE J. 21 (1975) 116–128. https://doi.org/10.1002/aic.690210115.

[159] G. Maurer, J.M. Prausnitz, On the derivation and extension of the UNIQUAC equation, Fluid Phase Equilibria. 2 (1978) 91–99. https://doi.org/10.1016/0378-3812(78)85002-X.

[160] M.H. Lietzke, R.W. Stoughton, The calculation of activity coefficients from osmotic coefficient data, J. Phys. Chem. 66 (1962) 508–509. https://doi.org/10.1021/j100809a032.

[161] C.W. Davies, Ion association., Butterworths, London, 1962.

[162] T.J. Wolery, EQ3NR, a computer program for geochemical aqueous speciation-solubility calculations: Theoretical manual, user`s guide, and related documentation (Version 7.0); Part 3, Lawrence Livermore National Lab. (LLNL), Livermore, CA (United States), 1992. https://doi.org/10.2172/138643.

[163] H.C. Helgeson, Thermodynamics of hydrothermal systems at elevated temperatures and pressures, Am. J. Sci. 267 (1969) 729–804. https://doi.org/10.2475/ajs.267.7.729.

[164] L.A. Bromley, Thermodynamic properties of strong electrolytes in aqueous solutions, AIChE J. 19 (1973) 313–320. https://doi.org/10.1002/aic.690190216.

[165] H.C. Helgeson, D.H. Kirkham, Theoretical prediction of the thermodynamic behavior of aqueous electrolytes at high pressures and temperatures; II, Debye-Huckel parameters for activity coefficients and relative partial molal properties, Am. J. Sci. 274 (1974) 1199–1261. https://doi.org/10.2475/ajs.274.10.1199.

[166] E.A. Guggenheim, L. The specific thermodynamic properties of aqueous solutions of strong electrolytes, Lond. Edinb. Dublin Philos. Mag. J. Sci. 19 (1935) 588–643. https://doi.org/10.1080/14786443508561403.

[167] E. Güntelberg, Untersuchungen über Ioneninteraktion, Z. Für Phys. Chem. 123U (1926) 199–247. https://doi.org/10.1515/zpch-1926-12312.

[168] H.F. Gibbard, G. Scatchard, Vapor-liquid equilibriums of synthetic seawater solutions from 25-100.deg., J. Chem. Eng. Data. 17 (1972) 498–501. https://doi.org/10.1021/je60055a008.

[169] V. Thurmond, F.J. Millero, Ionization of carbonic acid in sodium chloride solutions at 25°C, J. Solut. Chem. 11 (1982) 447–456. https://doi.org/10.1007/BF00647107.

[170] A.J. Bard, L.R. Faulkner, Electrochemical Methods: Fundamentals and Applications, 2 edition, Wiley, New York, 2000.

[171] L.J. Vracar, D.M. Drazic, Influence of chloride ion adsorption on hydrogen evolution reaction on iron, J. Electroanal. Chem. 339 (1992) 269–279. https://doi.org/10.1016/0022-0728(92)80457-F.

[172] K.E. Heusler, G.H. Cartledge, The Influence of Iodide Ions and Carbon Monoxide on the Anodic Dissolution of Active Iron, J. Electrochem. Soc. 108 (1961) 732. https://doi.org/10.1149/1.2428207.

[173] W.J. Lorenz, H. Yamaoka, H. Fisher, On the electrochemical behavior of iron in hydrochloric acid Solution, Ber Bunsenges Phys Chem. 67 (1963) 932–943.

[174] W.J. Lorenz, Der einfluss von halogenidionen auf die anodische auflösung des eisens, Corros. Sci. 5 (1965) 121–131. https://doi.org/10.1016/S0010-938X(65)90478-6.

[175] K.J. Vetter, Electrochemical Kinetics: Theoretical and Experimental Aspects, Academic Press, 1967.

[176] J.O. Bockris, S.U.M. Khan, Surface Electrochemistry: A Molecular Level Approach, Springer US, 1993. https://doi.org/10.1007/978-1-4615-3040-4.

[177] E. Gileadi, Electrode Kinetics for Chemists, Chemical Engineers, and Materials Scientists, Capstone, 1993.

[178] E. McCafferty, N. Hackerman, Kinetics of iron corrosion in concentrated acidic chloride solutions, J. Electrochem. Soc. 119 (1972) 999–1009. https://doi.org/10.1149/1.2404426.

[179] W.J. Lorenz, K.E. Heusler, Anodic dissolution of iron group metals, in: Corros. Mech. F Mansfeld, CRC Press, 1987: pp. 1–85.

[180] Y. Ishikawa, T. Yoshimura, T. Ozaki, Adsorption of water on the iron surface with reference to corrosion, Zair.--Kankyo. 40 (1991) 540–544. https://doi.org/10.3323/JCORR1991.40.540.

[181] M. Keddam, Anodic dissolution, in: Corros. Mech. Theory Pract., 3rd ed., CRC Press, 2011: pp. 149–215.

[182] G.M. Florianovich, L.A. Sokolova, Ya.M. Kolotyrkin, On the mechanism of the anodic dissolution of iron in acid solutions, Electrochimica Acta. 12 (1967) 879–887. https://doi.org/10.1016/0013-4686(67)80124-5.

[183] F. Hibert, Y. Miyoshi, G. Eichkorn, W.J. Lorenz, Correlations between the kinetics of electrolytic dissolution and deposition of iron: II . The cathodic deposition of iron, J. Electrochem. Soc. 118 (1971) 1927. https://doi.org/10.1149/1.2407869.

[184] G.S. Frankel, R.P. Frankenthal, eds., Corrosion science: a retrospective and current status in honor of Robert P. Frankenthal: proceedings of the international symposium, Electrochemical Society, Pennington, NJ, 2002.

[185] J.O. Bockris, D. Drazic, A.R. Despic, The electrode kinetics of the deposition and dissolution of iron, Electrochimica Acta. 4 (1961) 325–361. https://doi.org/10.1016/0013-4686(61)80026-1.

[186] J.O. Bockris, H. Kita, Analysis of galvanostatic transients and application to the iron electrode reaction, J. Electrochem. Soc. 108 (1961) 676. https://doi.org/10.1149/1.2428188.

[187] E.J. Kelly, The active iron electrode I . iron dissolution and hydrogen evolution reactions in acidic sulfate solutions, J. Electrochem. Soc. 112 (1965) 124–131. https://doi.org/10.1149/1.2423480.

[188] G. Eichkorn, W.J. Lorenz, L. Albert, H. Fischer, Einfluß der oberflächenaktivität auf die anodischen auflösungsmechanismen von eisen in sauren lösungen, Electrochimica Acta. 13 (1968) 183–197. https://doi.org/10.1016/0013-4686(68)80020-9.

[189] G.T. Burstein, D.H. Davies, The electrochemical behavior of scratched iron surfaces in aqueous solutions, J. Electrochem. Soc. 128 (1981) 33. https://doi.org/10.1149/1.2127383.

[190] N.G. Smart, J.O. Bockris, Effect of water activity on corrosion, CORROSION. 48 (1992) 277–280. https://doi.org/10.5006/1.3315933.

[191] L. Cavallaro, L. Felloni, G. Trabanelli, F. Pulidori, The anodic dissolution of iron and the behaviour of some corrosion inhibitors investigated by the potentiodynamic method, Electrochimica Acta. 9 (1964) 485–494. https://doi.org/10.1016/0013-4686(64)80022-0.

[192] N.A. Darwish, F. Hilbert, W.J. Lorenz, H. Rosswag, The influence of chloride ions on the kinetics of iron dissolution, Electrochimica Acta. 18 (1973) 421–425. https://doi.org/10.1016/0013-4686(73)80046-5.

[193] A.J. Arvia, J.J. Podestá, The kinetics of anodic dissolution of active iron in acid solutions containing high concentration of halides, Corros. Sci. 8 (1968) 203–205. https://doi.org/10.1016/S0010-938X(68)80202-1.

[194] R.J. Chin, K. Nobe, Electrodissolution kinetics of iron in chloride solutions III . acidic solutions, J. Electrochem. Soc. 119 (1972) 1457–1461. https://doi.org/10.1149/1.2404023.

[195] H.C. Kuo, K. Nobe, Electrodissolution kinetics of iron in chloride solutions VI . concentrated acidic solutions, J. Electrochem. Soc. 125 (1978) 853–860. https://doi.org/10.1149/1.2131567.

[196] JA.M. Kolotyrkin, Pitting corrosion of metals, Corrosion. 19 (1963) 261t–268t. https://doi.org/10.5006/0010-9312-19.8.261.

[197] G.T. Burstein, D.H. Davies, The effects of anions on the behaviour of scratched iron electrodes in aqueous solutions, Corros. Sci. 20 (1980) 1143–1155.

[198] N.G. Smart, M. Gamboa-Aldeco, J.O. Bockris, Corrosion mechanisms of iron in concentrated acidic zinc chloride media, Corros. Sci. 34 (1993) 759–777. https://doi.org/10.1016/0010-938X(93)90098-2.

[199] W.J. Lorenz, J.R. Vilche, Zur kinetik der anodischen eisenauflösung im neutralen medium, Corros. Sci. 12 (1972) 785–798. https://doi.org/10.1016/S0010-938X(72)90284-3.

[200] S. Nesic, R. Nyborg, A. Stangeland, M. Nordsveen, A mechanistic modeling for CO_2 corrosion with protective iron carbonate films, in: Corros. Conf., NACE International, Houston, TX, 2001: p. No. 01040.

[201] X. Gao, F. Madani Sani, Z. Ma, B. Brown, M. Singer, S. Nesic, A quantitative study of $FeCO_3$ solubility in non-ideal solutions, in: Corros. Conf., NACE International, Virtual, 2021: p. Paper No. 16964.

[202] T. Hurlen, S. Gunvaldsen, R. Tunold, F. Blaker, P.G. Lunde, Effects of carbon dioxide on reactions at iron electrodes in aqueous salt solutions, J. Electroanal. Chem. Interfacial Electrochem. 180 (1984) 511–526. https://doi.org/10.1016/0368-1874(84)83604-7.

[203] B.R. Linter, G.T. Burstein, Reactions of pipeline steels in carbon dioxide solutions, Corros. Sci. 41 (1999) 117–139. https://doi.org/10.1016/S0010-938X(98)00104-8.

[204] T. das Chagas Almeida, M.C.E. Bandeira, R.M. Moreira, O.R. Mattos, New insights on the role of CO_2 in the mechanism of carbon steel corrosion, Corros. Sci. 120 (2017) 239–250. https://doi.org/10.1016/j.corsci.2017.02.016.

[205] S. Nesic, N. Thevenot, J.-L. Crolet, D.M. Drazic, Electrochemical properties of iron dissolution in CO_2 solutions-basics revisited, in: NACE International, Houston, TX, 1996: p. No. 3.

[206] A. Więckowski, E. Ghali, M. Szklarczyk, J. Sobkowski, The behaviour of iron electrode in CO_2−saturated neutral electrolyte—II. Radiotracer study and corrosion considerations, Electrochimica Acta. 28 (1983) 1619–1626. https://doi.org/10.1016/0013-4686(83)85226-8.

[207] A. Kahyarian, Mechanism and prediction of mild Steel corrosion in aqueous solutions containing carboxylic acids, carbon dioxide, and hydrogen sulfide, Ohio University, 2018.

[208] A. Kahyarian, S. Nesic, A new narrative for CO_2 corrosion of mild steel, J. Electrochem. Soc. 166 (2019) C3048–C3063. https://doi.org/10.1149/2.0071911jes.

[209] L.G.S. Gray, B.G. Anderson, M.J. Danysh, P.R. Tremaine, Mechanisms of carbon steel corrosion in brines containing dissolved carbon dioxide At pH 4, in: NACE Int., 1989: p. No. 464.

[210] L.G.S. Gray, B.G. Anderson, M.J. Danysh, P.R. Tremaine, Effect of pH and temperature on the mechanism of carbon steel corrosion by aqueous carbon dioxide, in: NACE Int., 1990: p. No. 40.

[211] C. de Waard, D.E. Milliams, Carbonic acid corrosion of steel, Corrosion. 31 (1975) 177–181. https://doi.org/10.5006/0010-9312-31.5.177.

[212] C. de Waard, D.E. Milliams, Prediction of carbonic acid corrosion in natural gas pipelines., Int Conf Intern Extern. Prot Pipes. 1st (1975) F1-1-F1-8.

[213] E. Remita, B. Tribollet, E. Sutter, V. Vivier, F. Ropital, J. Kittel, Hydrogen evolution in aqueous solutions containing dissolved CO_2: Quantitative contribution of the buffering effect - ScienceDirect, Corros. Sci. 50 (2008) 1433–1440. https://doi.org/10.1016/j.corsci.2007.12.007.

[214] T. Tran, B. Brown, S. Nesic, Corrosion of mild steel in an aqueous CO_2 environment – basic electrochemical mechanisms revisited, in: Corros. Conf., NACE International, Dallas, TX, 2015: p. No. 5671.

[215] A. Kahyarian, B. Brown, S. Nesic, Mechanism of CO_2 Corrosion of Mild Steel: A New Narrative, in: Corros. Conf., NACE International, Phoenix, AZ, 2018: p. No. 11232.

[216] D. Rickard, An apparatus for the study of fast precipitation reactions, Mineral. Mag. 53 (1989) 527–530. https://doi.org/10.1180/minmag.1989.053.373.02.

[217] D. Rickard, Experimental concentration-time curves for the iron(II) sulphide precipitation process in aqueous solutions and their interpretation, Chem. Geol. 78 (1989) 315–324. https://doi.org/10.1016/0009-2541(89)90066-1.

[218] D. Rickard, Kinetics of FeS precipitation: Part 1. Competing reaction mechanisms, Geochim. Cosmochim. Acta. 59 (1995) 4367–4379. https://doi.org/10.1016/0016-7037(95)00251-T.

[219] D.R. Morris, L.P. Sampaleanu, D.N. Veysey, The Corrosion of Steel by Aqueous Solutions of Hydrogen Sulfide, J. Electrochem. Soc. 127 (1980) 1228. https://doi.org/10.1149/1.2129861.

[220] G.I. Ogundele, W.E. White, Some observations on corrosion of carbon steel in aqueous environments containing carbon dioxide, CORROSION. 42 (1986) 71–78. https://doi.org/10.5006/1.3584888.

[221] Z.A. Iofa, V.V. Batrakov, Cho-Ngok-Ba, Influence of anion adsorption on the action of inhibitors on the acid corrosion of iron and cobalt, Electrochimica Acta. 9 (1964) 1645–1653. https://doi.org/10.1016/0013-4686(64)80091-8.

[222] X.L. Cheng, H.Y. Ma, J.P. Zhang, X. Chen, S.H. Chen, H.Q. Yang, Corrosion of iron in acid solutions with hydrogen sulfide, Corrosion. 54 (1998) 369–376. https://doi.org/10.5006/1.3284864.

[223] H.Y. Ma, X.L. Cheng, S.H. Chen, G.Q. Li, X. Chen, S.B. Lei, H.Q. Yang, Theoretical interpretation on impedance spectra for anodic iron dissolution in acidic solutions containing hydrogen sulfide, Corrosion. 54 (1998) 634–640. https://doi.org/10.5006/1.3287641.

[224] H. Ma, X. Cheng, S. Chen, C. Wang, J. Zhang, H. Yang, An AC impedance study of the anodic dissolution of iron in sulfuric acid solutions containing hydrogen

sulfide, J. Electroanal. Chem. 451 (1998) 11–17. https://doi.org/10.1016/S0022-0728(98)00081-3.

[225] D.W. Shoesmith, P. Taylor, M.G. Bailey, D.G. Owen, The formation of ferrous monosulfide polymorphs during the corrosion of iron by aqueous hydrogen sulfide at 21°C, J. Electrochem. Soc. 127 (1980) 1007–1015. https://doi.org/10.1149/1.2129808.

[226] P.W. Bolmer, Polarization of Iron in H_2S-NaHS Buffers, CORROSION. 21 (1965) 69–75. https://doi.org/10.5006/0010-9312-21.3.69.

[227] J. Kittel, F. Ropital, F. Grosjean, E.M.M. Sutter, B. Tribollet, Corrosion mechanisms in aqueous solutions containing dissolved H_2S. Part 1: Characterisation of H</sub>2</sub>S reduction on a 316L rotating disc electrode, Corros. Sci. 66 (2013) 324–329. https://doi.org/10.1016/j.corsci.2012.09.036.

[228] S. Arzola, J. Genescá, The effect of H_2S concentration on the corrosion behavior of API 5L X-70 steel, J. Solid State Electrochem. 9 (2005) 197–200. https://doi.org/10.1007/s10008-004-0579-9.

[229] S. Arzola, J. Mendoza-Flores, R. Duran-Romero, J. Genesca, Electrochemical behavior of API X70 steel in hydrogen sulfide-containing solutions, Corrosion. 62 (2006) 433–443. https://doi.org/10.5006/1.3278280.

[230] A. Kahyarian, S. Nesic, H_2S corrosion of mild steel: A quantitative analysis of the mechanism of the cathodic reaction, Electrochimica Acta. 297 (2019) 676–684. https://doi.org/10.1016/j.electacta.2018.12.029.

[231] S.E. Drummond, Boiling and mixing of hydrothermal fluids: chemical effects on mineral precipitation, PhD dissertation, Pennsylvania State University, 1981.

[232] J.E. Oddo, M.B. Tomson, Simplified calculation of $CaCO_3$ Saturation at High temperatures and pressures in brine solutions, J. Pet. Technol. 34 (1982) 1583–1590. https://doi.org/10.2118/10352-PA.

[233] S.D. Cramer, Solubility of methane, carbon dioxide, and oxygen in brines from 0^o to 300^oC, U.S. Department of Energy Office of Scientific and Technical Information, 1982. https://www.osti.gov/biblio/6069408-solubility-methane-carbon-dioxide-oxygen-brines-from-sup-sup (accessed June 10, 2021).

[234] J.C. Peiper, K.S. Pitzer, Thermodynamics of aqueous carbonate solutions including mixtures of sodium carbonate, bicarbonate, and chloride, J. Chem. Thermodyn. 14 (1982) 613–638. https://doi.org/10.1016/0021-9614(82)90078-7.

[235] A. Battistelli, C. Calore, K. Pruess, The simulator TOUGH2/EWASG for modelling geothermal reservoirs with brines and non-condensible gas, Geothermics. 26 (1997) 437–464. https://doi.org/10.1016/S0375-6505(97)00007-2.

[236] J. Dubessy, A. Tarantola, J. Sterpenich, Modelling of liquid-vapour equilibria in the H_2O-CO_2-NaCl and H_2O-H_2S-NaCl Systems to 270°C, Oil Gas Sci. Technol. – Rev IFP. 60 (2005) 339–355.

[237] H. Zhao, M.V. Fedkin, R.M. Dilmore, S.N. Lvov, Carbon dioxide solubility in aqueous solutions of sodium chloride at geological conditions: Experimental results at 323.15, 373.15, and 423.15K and 150bar and modeling up to 573.15K and 2000bar, Geochim. Cosmochim. Acta. 149 (2015) 165–189. https://doi.org/10.1016/j.gca.2014.11.004.

[238] Y. Dadmohammadi, S. Gebreyohannes, A.M. Abudour, B.J. Neely, K.A.M. Gasem, Representation and prediction of vapor–liquid equilibrium using the Peng–Robinson equation of state and UNIQUAC activity coefficient model, Ind. Eng. Chem. Res. 55 (2016) 1088–1101. https://doi.org/10.1021/acs.iecr.5b03475.

[239] Y. Ji, X. Ji, X. Feng, C. Liu, L. Lü, X. Lu, Progress in the study on the phase equilibria of the CO_2-H_2O and CO_2-H_2O-NaCl systems., Chin. J. Chem. Eng. 15 (2007) 439–448. https://doi.org/10.1016/S1004-9541(07)60105-0.

[240] R.D. Springer, Z. Wang, A. Anderko, P. Wang, A.R. Felmy, A thermodynamic model for predicting mineral reactivity in supercritical carbon dioxide: I. Phase behavior of carbon dioxide–water–chloride salt systems across the H2O-rich to the CO2-rich regions, Chem. Geol. 322–323 (2012) 151–171. https://doi.org/10.1016/j.chemgeo.2012.07.008.

[241] R.D. Springer, P. Wang, A. Anderko, Modeling the properties of H_2S/CO_2/salt/water systems in wide ranges of temperature and pressure, SPE J. 20 (2015) 1,120-1,134. https://doi.org/10.2118/173902-PA.

[242] R. Sander, Compilation of Henry’s law constants (version 4.0) for water as solvent, Atmospheric Chem. Phys. 15 (2015) 4399–4981. https://doi.org/10.5194/acp-15-4399-2015.

[243] Z. Duan, N. Møller, J.H. Weare, An equation of state for the CH_4-CO_2-H_2O system: I. Pure systems from 0 to 1000°C and 0 to 8000 bar, Geochim. Cosmochim. Acta. 56 (1992) 2605–2617. https://doi.org/10.1016/0016-7037(92)90347-L.

[244] J. Setschenow, Über die Konstitution der Salzlösungen auf Grund ihres Verhaltens zu Kohlensäure, Z. Für Phys. Chem. 4U (1889) 117–125. https://doi.org/10.1515/zpch-1889-0409.

[245] A.A. Douabul, J.P. Riley, The solubility of gases in distilled water and seawater—V. hydrogen sulphide, Deep Sea Res. Part Oceanogr. Res. Pap. 26 (1979) 259–268. https://doi.org/10.1016/0198-0149(79)90023-2.

[246] A.H. Harvey, Semiempirical correlation for Henry’s constants over large temperature ranges, AIChE J. 42 (1996) 1491–1494. https://doi.org/10.1002/aic.690420531.

[247] N.F. Spycher, M.H. Reed, Fugacity coefficients of H_2, CO_2, CH_4, H_2O and of H_2O- CO_2-CH_4 mixtures: a virial equation treatment for moderate pressures and temperatures applicable to calculations of hydrothermal boiling, Geochim. Cosmochim. Acta. 52 (1988) 739–749. https://doi.org/10.1016/0016-7037(88)90334-1.

[248] G. Soave, Equilibrium constants from a modified Redlich-Kwong equation of state, Chem. Eng. Sci. 27 (1972) 1197–1203. https://doi.org/10.1016/0009-2509(72)80096-4.

[249] Z. Duan, D. Li, Coupled phase and aqueous species equilibrium of the H_2O–CO_2–NaCl–$CaCO_3$ system from 0 to 250°C, 1 to 1000bar with NaCl concentrations up to saturation of halite, Geochim. Cosmochim. Acta. 72 (2008) 5128–5145. https://doi.org/10.1016/j.gca.2008.07.025.

[250] Z. Duan, S. Mao, A thermodynamic model for calculating methane solubility, density and gas phase composition of methane-bearing aqueous fluids from 273 to 523K and from 1 to 2000bar, Geochim. Cosmochim. Acta. 70 (2006) 3369–3386. https://doi.org/10.1016/j.gca.2006.03.018.

[251] N. Spycher, K. Pruess, J. Ennis-King, CO_2-H_2O mixtures in the geological sequestration of CO_2. I. Assessment and calculation of mutual solubilities from 12 to 100°C and up to 600 bar, Geochim. Cosmochim. Acta. 67 (2003) 3015–3031. https://doi.org/10.1016/S0016-7037(03)00273-4.

[252] A.E. Markham, K.A. Kobe, The solubility of carbon dioxide and nitrous oxide in aqueous salt solutions, J. Am. Chem. Soc. 63 (1941) 449–454. https://doi.org/10.1021/ja01847a027.

[253] F.J. Millero, The thermodynamics and kinetics of the hydrogen sulfide system in natural waters, Mar. Chem. 18 (1986) 121–147. https://doi.org/10.1016/0304-4203(86)90003-4.

[254] F.J. Millero, J.P. Hershey, Thermodynamics and kinetics of hydrogen sulfide in natural waters, in: Biog. Sulfur Environ., American Chemical Society, 1989: pp. 282–313. https://doi.org/10.1021/bk-1989-0393.ch018.

[255] F.J. Millero, Thermodynamics of the carbon dioxide system in the oceans, Geochim. Cosmochim. Acta. 59 (1995) 661–677. https://doi.org/10.1016/0016-7037(94)00354-O.

[256] Z. Duan, N. Møller, J.H. Weare, Prediction of the solubility of H_2S in NaCl aqueous solution: an equation of state approach, Chem. Geol. 130 (1996) 15–20. https://doi.org/10.1016/0009-2541(95)00181-6.

[257] N.N. Akinfiev, V. Majer, Y.V. Shvarov, Thermodynamic description of H_2S–H_2O–NaCl solutions at temperatures to 573K and pressures to 40MPa, Chem. Geol. 424 (2016) 1–11. https://doi.org/10.1016/j.chemgeo.2016.01.006.

[258] O.M. Suleimenov, R.E. Krupp, Solubility of hydrogen sulfide in pure water and in NaCl solutions, from 20 to 320°C and at saturation pressures, Geochim. Cosmochim. Acta. 58 (1994) 2433–2444. https://doi.org/10.1016/0016-7037(94)90022-1.

[259] E.C.W. Clarke, D.N. Glew, Aqueous nonelectrolyte solutions. part VIII. deuterium and hydrogen sulfides solubilities in deuterium oxide and water, Can. J. Chem. 49 (1971) 691–698. https://doi.org/10.1139/v71-116.

[260] T.J. Barrett, G.M. Anderson, J. Lugowski, The solubility of hydrogen sulphide in 0–5 m NaCl solutions at 25°–95°C and one atmosphere, Geochim. Cosmochim. Acta. 52 (1988) 807–811. https://doi.org/10.1016/0016-7037(88)90352-3.

[261] H. Gamsjäger, P. Schindler, Löslichkeiten und Aktivitätskoeffizienten von H_2S in Elektrolytmischungen, Helv. Chim. Acta. 52 (1969) 1395–1402. https://doi.org/10.1002/hlca.19690520603.

[262] J. Kendall, J.C. Andrews, The solubilities of acids in aqueous solutions of other acids, J. Am. Chem. Soc. 43 (1921) 1545–1560. https://doi.org/10.1021/ja01440a016.

[263] P.G.T. Fogg, Hydrogen Sulfide in Aqueous Solvents, Department of Applied Chemistry and Life Sciences, Polytechnic of North london, Holloway, London, 1987.

[264] H. Gamsjäger, W. Rainer, P. Schindler, Löslichkeitskonstanten und freie Bildungsenthalpien von Metallsulfiden, 4. Mitt.: Die Löslichkeit von H_2S in $HClO_4$–$NaClO_4$–H_2O-Mischungen, Monatshefte Für Chem. Verwandte Teile Anderer Wiss. 98 (1967) 1793–1802. https://doi.org/10.1007/BF01167137.

[265] F.J. Millero, T.B. Graham, F. Huang, H. Bustos-Serrano, D. Pierrot, Dissociation constants of carbonic acid in seawater as a function of salinity and temperature, Mar. Chem. 100 (2006) 80–94. https://doi.org/10.1016/j.marchem.2005.12.001.

[266] F.J. Millero, F. Huang, T. Graham, D. Pierrot, The dissociation of carbonic acid in NaCl solutions as a function of concentration and temperature, Geochim. Cosmochim. Acta. 71 (2007) 46–55. https://doi.org/10.1016/j.gca.2006.08.041.

[267] D.A. Palmer, R. Van Eldik, The chemistry of metal carbonate and carbon dioxide complexes, Chem. Rev. 83 (1983) 651–731. https://doi.org/10.1021/cr00058a004.

[268] R.C. Patel, R.J. Boe, G. Atkinson, The CO_2-water system. I. Study of the slower hydration-dehydration step, J. Solut. Chem. 2 (1973) 357–372. https://doi.org/10.1007/BF00713250.

[269] W.L. Marshall, E.U. Franck, Ion product of water substance, 0–1000 °C, 1–10,000 bars New International Formulation and its background, J. Phys. Chem. Ref. Data. 10 (1981) 295–304. https://doi.org/10.1063/1.555643.

[270] I. Kron, S.L. Marshall, P.M. May, G. Hefter, E. Königsberger, The ionic product of water in highly concentrated aqueous electrolyte solutions, Monatshefte Für Chem. Chem. Mon. 126 (1995) 819–837. https://doi.org/10.1007/BF00811002.

[271] U.K. Deiters, R. Macías-Salinas, Calculation of densities from cubic equations of state: revisited, Ind. Eng. Chem. Res. 53 (2014) 2529–2536. https://doi.org/10.1021/ie4038664.

[272] G. Eriksson, K. Hack, ChemSage—A computer program for the calculation of complex chemical equilibria, Metall. Trans. B. 21 (1990) 1013–1023. https://doi.org/10.1007/BF02670272.

[273] C.W. Bale, P. Chartrand, S.A. Degterov, G. Eriksson, K. Hack, R. Ben Mahfoud, J. Melançon, A.D. Pelton, S. Petersen, FactSage thermochemical software and databases, Calphad. 26 (2002) 189–228. https://doi.org/10.1016/S0364-5916(02)00035-4.

[274] J.M. VanBriesen, M. Small, C. Weber, J. Wilson, Modelling chemical speciation: thermodynamics, kinetics and uncertainty., Model. Pollut. Complex Environ. Syst. Vol. 2. (2010) 135–151.

[275] A.M.M. Leal, M.J. Blunt, T.C. LaForce, Efficient chemical equilibrium calculations for geochemical speciation and reactive transport modelling, Geochim. Cosmochim. Acta. 131 (2014) 301–322. https://doi.org/10.1016/j.gca.2014.01.038.

[276] A.M.M. Leal, D.A. Kulik, W.R. Smith, M.O. Saar, An overview of computational methods for chemical equilibrium and kinetic calculations for geochemical and

reactive transport modeling, Pure Appl. Chem. 89 (2017) 597–643. https://doi.org/10.1515/pac-2016-1107.

[277] K.S. Pitzer, A thermodynamic model for aqueous solutions of liquid-like density, (1987). https://escholarship.org/uc/item/4tt1p617 (accessed June 20, 2021).

[278] Y.K. Kharaka, W.D. Gunter, P.K. Aggarwal, E.H. Perkins, J.D. DeBraal, SOLMINEQ.88; a computer program for geochemical modeling of water-rock interactions, U.S. Geological Survey, 1988.

[279] F.J. Millero, T. Plese, M. Fernandez, The dissociation of hydrogen sulfide in seawater, Limnol. Oceanogr. 33 (1988) 269–274. https://doi.org/10.4319/lo.1988.33.2.0269.

[280] F.J. Millero, W.H. Leung, Thermodynamics of seawater at one atmosphere, Am J Sci. 276 (1976) 1035–1077. https://doi.org/10.2475/ajs.276.9.1035.

[281] J.P. Hershey, T. Plese, F.J. Millero, The pK_1^* for the dissociation of H_2S in various ionic media, Geochim. Cosmochim. Acta. 52 (1988) 2047–2051. https://doi.org/10.1016/0016-7037(88)90183-4.

[282] NIST, NIST Chemistry WebBook, (n.d.). https://doi.org/10.18434/T4D303.

[283] A.D. Pelton, Phase Diagrams and Thermodynamic Modeling of Solutions, Academic Press, 2018.

[284] K.S. Pitzer, J.M. Simonson, Thermodynamics of multicomponent, miscible, ionic systems: theory and equations, J. Phys. Chem. 90 (1986) 3005–3009. https://doi.org/10.1021/j100404a042.

[285] B. Sander, Extended UNIFAC/UNIQUAC models for (1) gas solubilities and (2) electrolyte solutions, PhD dissertation, Technical University of Denmark, 1984.

[286] B. Sander, A. Fredenslund, P. Rasmussen, Calculation of vapour-liquid equilibria in mixed solvent/salt systems using an extended UNIQUAC equation, Chem. Eng. Sci. 41 (1986) 1171–1183. https://doi.org/10.1016/0009-2509(86)87090-7.

[287] B. Sander, P. Rasmussen, A. Fredenslund, Calculation of solid-liquid equilibria in aqueous solutions of nitrate salts using an extended UNIQUAC equation, Chem. Eng. Sci. 41 (1986) 1197–1202. https://doi.org/10.1016/0009-2509(86)87092-0.

[288] K. Thomsen, Aqueous Electrolytes Model Parameters and Process Simulation, PhD dissertation, Technical University of Denmark, 1997.

[289] S.L. Clegg, K.S. Pitzer, Thermodynamics of multicomponent, miscible, ionic solutions: generalized equations for symmetrical electrolytes, J. Phys. Chem. 96 (1992) 3513–3520. https://doi.org/10.1021/j100187a061.

[290] F. Opekar, P. Beran, Rotating disk electrodes, J. Electroanal. Chem. Interfacial Electrochem. 69 (1976) 1–105. https://doi.org/10.1016/S0022-0728(76)80129-5.

[291] F. Madani Sani, A. Afshar, M. Mohammadi, Evaluation of the simultaneous effects of sulfate reducing bacteria, soil type and moisture content on corrosion behavior of buried carbon steel API 5L X65, Int. J. Electrochem. Sci. 11 (2016) 3887–3907. https://doi.org/10.20964/110294.

[292] J.O. Bockris, J. McBreen, L. Nanis, The hydrogen evolution kinetics and hydrogen entry into a-iron, J. Electrochem. Soc. 112 (1965) 1025–1031. https://doi.org/10.1149/1.2423335.

[293] B.G. Levich, Physicochemical Hydrodynamics, Prentice-Hall, Inc, 1962.

[294] M. Eisenberg, C.W. Tobias, C.R. Wilke, Ionic mass transfer and concentration polarization at rotating electrodes, J. Electrochem. Soc. 101 (1954) 306–320. https://doi.org/10.1149/1.2781252.
[295] F. Madani Sani, B. Brown, S. Nesic, A mechanistic study on the effect of salt concentration on uniform corrosion rate of pipeline steel in acidic aqueous environments, in: Corros. Conf., NACE International, Virtual, 2021: p. No. 16788.
[296] C.W. Borgmann, Initial corrosion rate of mild steel influence of the cation, Ind. Eng. Chem. 29 (1937) 814–821. https://doi.org/10.1021/ie50331a018.
[297] L. Onyeji, G. Kale, Preliminary investigation of the corrosion behavior of proprietary micro-alloyed steels in aerated and deaerated brine solutions, J. Mater. Eng. Perform. 26 (2017) 5741–5752. https://doi.org/10.1007/s11665-017-3031-x.
[298] X. Wang, W. Conway, R. Burns, N. McCann, M. Maeder, Comprehensive study of the hydration and dehydration reactions of carbon dioxide in aqueous solution, J. Phys. Chem. A. 114 (2010) 1734–1740. https://doi.org/10.1021/jp909019u.
[299] F. Madani Sani, B. Brown, S. Nesic, An electrochemical study of the effect of high salt concentration on uniform corrosion of Carbon steel in aqueous CO_2 solutions, J. Electrochem. Soc. 168 (2021) 051501. https://doi.org/10.1149/1945-7111/abf5f9.
[300] ASTM International J01.01 Subcommittee, Guide for laboratory immersion corrosion testing of metals, ASTM International, 2004. https://doi.org/10.1520/G0031-21.
[301] D.C. Silverman, Technical note: on estimating conditions for simulating velocity-sensitive corrosion in the rotating cylinder electrode, CORROSION. 55 (1999) 1115–1118. https://doi.org/10.5006/1.3283948.
[302] D.R. Fincher, A.C. Nestle, A Review of corrosion monitoring techniques, in: SPE Symp. Handl. Oilfield Water, SPE International, Los Angeles, CA, 1972: p. No. SPE-4220-MS. https://doi.org/10.2118/4220-MS.
[303] SP0192-2012 Monitoring corrosion in oil and gas production with iron counts, NACE International, 2012.
[304] R.T. Foley, Role of the chloride ion in iron corrosion, CORROSION. 26 (1970) 58–70. https://doi.org/10.5006/0010-9312-26.2.58.
[305] M.E. Orazem, B. Tribollet, Electrochemical Impedance Spectroscopy, 2 edition, Wiley, Hoboken, New Jersey, 2017.
[306] G. Ilgenfritz, Theory and Simulation of Chemical Relaxation Spectra, in: I. Pecht, R. Rigler (Eds.), Chem. Relax. Mol. Biol., Springer Berlin Heidelberg, Berlin, Heidelberg, 1977: pp. 1–42. https://doi.org/10.1007/978-3-642-81117-3_1.
[307] G.A. Zhang, Y.F. Cheng, On the fundamentals of electrochemical corrosion of X65 steel in CO_2-containing formation water in the presence of acetic acid in petroleum production, Corros. Sci. 51 (2009) 87–94. https://doi.org/10.1016/j.corsci.2008.10.013.
[308] W.J. Lorenz, F. Mansfeld, Determination of corrosion rates by electrochemical DC and AC methods, Corros. Sci. 21 (1981) 647–672. https://doi.org/10.1016/0010-938X(81)90015-9.

[309] F.F. Eliyan, A. Alfantazi, Electrochemical investigations on the corrosion behavior and corrosion natural inhibition of API-X100 pipeline steel in acetic acid and chloride-containing CO_2-saturated media, J. Appl. Electrochem. 42 (2012) 233–248.

[310] S. Gao, B. Brown, D. Young, M. Singer, Formation of iron oxide and iron sulfide at high temperature and their effects on corrosion, Corros. Sci. 135 (2018) 167–176. https://doi.org/10.1016/j.corsci.2018.02.045.

[311] E.W.L. Chan, Magnetite and its galvanic effect on the corrosion of carbon steel under carbon dioxide environments, PhD, Curtin University, 2011.

[312] G01 Committee, ASTM G1-72: Practice for preparing, cleaning, and evaluating corrosion test specimens, ASTM International, 1972. https://doi.org/10.1520/G0001-03R17E01.

[313] J.-A. Bourdoiseau, M. Jeannin, R. Sabot, C. Rémazeilles, Ph. Refait, Characterisation of mackinawite by Raman spectroscopy: Effects of crystallisation, drying and oxidation, Corros. Sci. 50 (2008) 3247–3255. https://doi.org/10.1016/j.corsci.2008.08.041.

[314] M. Nordsveen, S. Nešić, R. Nyborg, A. Stangeland, A mechanistic model for carbon dioxide corrosion of mild steel in the presence of protective iron carbonate films—Part 1: theory and verification, CORROSION. 59 (2003) 443–456. https://doi.org/10.5006/1.3277576.

[315] M. Eigen, K. Kustin, The influence of steric factors in fast protolytic reactions as studied with HF, H_2 and substituted phenols, J. Am. Chem. Soc. 82 (1960) 5952–5953. https://doi.org/10.1021/ja01507a042.

[316] M.J. Welch, J.F. Lifton, J.A. Seck, Tracer studies with radioactive oxygen-15. Exchange between carbon dioxide and water, J. Phys. Chem. 73 (1969) 3351–3356. https://doi.org/10.1021/j100844a033.

[317] Y. Zheng, B. Brown, S. Nesic, Electrochemical study and modeling of H_2S corrosion of mild steel, in: Corros. Conf., NACE International, Orlando, FL, 2013: p. No. 2406. https://onepetro.org/NACECORR/proceedings/CORR13/All-CORR13/NACE-2013-2406/121504 (accessed September 23, 2021).

[318] Y.-J. Kim, Effect of variations in boiling water reactor water chemistry on type 304 stainless steel electrochemical corrosion potential, Corrosion. 58 (2002) 208–215. https://doi.org/10.5006/1.3279871.

[319] R.W. Potter, D.L. Brown, The volumetric properties of aqueous sodium chloride solutions from 0 degrees to 500 degrees C at pressures up to 2000 bars based on a regression of the available literature data, U.S. Geological Survey, 1975. https://doi.org/10.3133/ofr75636.

[320] J. Hu, Z. Duan, C. Zhu, I.-M. Chou, PVTx properties of the CO_2–H_2O and CO_2–H_2O–NaCl systems below 647 K: Assessment of experimental data and thermodynamic models, Chem. Geol. 238 (2007) 249–267. https://doi.org/10.1016/j.chemgeo.2006.11.011.

[321] H.C. Helgeson, D.H. Kirkham, Theoretical prediction of the thermodynamic behavior of aqueous electrolytes at high pressures and temperatures; I, Summary

of the thermodynamic/electrostatic properties of the solvent, Am. J. Sci. 274 (1974) 1089–1198. https://doi.org/10.2475/ajs.274.10.1089.

[322] W. Wagner, A. Pruss, The IAPWS formulation 1995 for the thermodynamic properties of ordinary water substance for general and scientific use, J. Phys. Chem. Ref. Data. 31 (2002) 387–535. https://doi.org/10.1063/1.1461829.

[323] R.G. Mortimer, Physical Chemistry, 3rd ed., Academic Press, 2008.

[324] J.W. Johnson, D. Norton, Critical phenomena in hydrothermal systems; state, thermodynamic, electrostatic, and transport properties of H_2O in the critical region, Am. J. Sci. 291 (1991) 541–648. https://doi.org/10.2475/ajs.291.6.541.

[325] E.L. Shock, E.H. Oelkers, J.W. Johnson, D.A. Sverjensky, H.C. Helgeson, Calculation of the thermodynamic properties of aqueous species at high pressures and temperatures. Effective electrostatic radii, dissociation constants and standard partial molal properties to 1000 °C and 5 kbar, J. Chem. Soc. Faraday Trans. 88 (1992) 803–826. https://doi.org/10.1039/FT9928800803.

[326] D.J. Bradley, K.S. Pitzer, Thermodynamics of electrolytes. 12. Dielectric properties of water and Debye-Hueckel parameters to 350.degree.C and 1 kbar, J. Phys. Chem. 83 (1979) 1599–1603. https://doi.org/10.1021/j100475a009.

[327] H.C. Helgeson, D.H. Kirkham, Theoretical prediction of the thermodynamic properties of aqueous electrolytes at high pressures and temperatures. III. Equation of state for aqueous species at infinite dilution, Am. J. Sci. 276 (1976) 97–240. https://doi.org/10.2475/ajs.276.2.97.

[328] E.L. Shock, H.C. Helgeson, Calculation of the thermodynamic and transport properties of aqueous species at high pressures and temperatures: Correlation algorithms for ionic species and equation of state predictions to 5 kb and 1000°C, Geochim. Cosmochim. Acta. 52 (1988) 2009–2036. https://doi.org/10.1016/0016-7037(88)90181-0.

[329] E.L. Shock, H.C. Helgeson, D.A. Sverjensky, Calculation of the thermodynamic and transport properties of aqueous species at high pressures and temperatures: Standard partial molal properties of inorganic neutral species, Geochim. Cosmochim. Acta. 53 (1989) 2157–2183. https://doi.org/10.1016/0016-7037(89)90341-4.

[330] J.C. Tanger, H.C. Helgeson, Calculation of the thermodynamic and transport properties of aqueous species at high pressures and temperatures; revised equations of state for the standard partial molal properties of ions and electrolytes, Am. J. Sci. 288 (1988) 19–98. https://doi.org/10.2475/ajs.288.1.19.

[331] R.H. Busey, R.E. Mesmer, The ionization of water in NaCl media to 300°C, J. Solut. Chem. 5 (1976) 147–152. https://doi.org/10.1007/BF00648896.

[332] Y. Shibue, Vapor pressures of aqueous NaCl and $CaCl_2$ solutions at elevated temperatures, Fluid Phase Equilibria. 213 (2003) 39–51. https://doi.org/10.1016/S0378-3812(03)00284-X.

[333] N. Moller, The prediction of mineral solubilities in natural waters: A chemical equilibrium model for the Na-Ca-Cl-SO_4-H_2O system, to high temperature and concentration, Geochim. Cosmochim. Acta. 52 (1988) 821–837. https://doi.org/10.1016/0016-7037(88)90354-7.

[334] Z. Duan, R. Sun, C. Zhu, I.-M. Chou, An improved model for the calculation of CO_2 solubility in aqueous solutions containing Na^+, K^+, Ca^{2+}, Mg^{2+}, Cl^-, and SO_4^{2-}, Mar. Chem. 98 (2006) 131–139. https://doi.org/10.1016/j.marchem.2005.09.001.

[335] G. Morrison, Effect of water on the critical points of carbon dioxide and ethane, J. Phys. Chem. 85 (1981) 759–761. https://doi.org/10.1021/j150607a007.

[336] Thermodynamic Tables Project, K.M. de Reuck, S. Angus, B. Armstrong, International thermodynamic tables of the fluid state: carbon dioxide, Pergamon Press, Oxford; New York, 1976.

[337] R.D. Goodwin, Hydrogen sulfide provisional thermophysical properties from 188 to 700K at pressures to 75 MPa, National Bureau of Standards, U.S. Department of Commerce, Boulder, CO, 1983.

[338] O. Sifner, Recommended values of critical parameters of ordinary and heavy water, Chem. Listy. 79 (1985) 199–200.

[339] G. Soave, S. Gamba, L.A. Pellegrini, SRK equation of state: Predicting binary interaction parameters of hydrocarbons and related compounds, Fluid Phase Equilibria. 299 (2010) 285–293. https://doi.org/10.1016/j.fluid.2010.09.012.

[340] G. Soave, Improving the treatment of heavy hydrocarbons by the SRK EOS, Fluid Phase Equilibria. 84 (1993) 339–342. https://doi.org/10.1016/0378-3812(93)85131-5.

[341] G. Soave, Extension of the classical mixing rules of the Redlich-Kwong equation of state, 2015. https://doi.org/10.13140/RG.2.1.3941.6806.

[342] A. Danesh, PVT and Phase Behaviour of Petroleum Reservoir Fluids, Elsevier Science, 1998.

[343] Thermodynamic Research Center (TRC), TRCE Thermodynamics Tables-Non-Hydrocarbons., Thermodynamics Research Center, Texas A & M University System, College Station, TX, 1989.

[344] H.F. Holmes, R.H. Busey, J.M. Simonson, R.E. Mesmer, D.G. Archer, R.H. Wood, The enthalpy of dilution of $HCl_{(aq)}$ to 648 K and 40 MPa thermodynamic properties, J. Chem. Thermodyn. 19 (1987) 863–890. https://doi.org/10.1016/0021-9614(87)90033-4.

[345] K.S. Pitzer, J.C. Peiper, R.H. Busey, Thermodynamic properties of aqueous sodium chloride solutions, J. Phys. Chem. Ref. Data. 13 (1984) 1–102. https://doi.org/10.1063/1.555709.

[346] R.T. Pabalan, K.S. Pitzer, Thermodynamics of $NaOH_{(aq)}$ in hydrothermal solutions, Geochim. Cosmochim. Acta. 51 (1987) 829–837. https://doi.org/10.1016/0016-7037(87)90096-2.

[347] D.A. Polya, E.M. Woolley, J.M. Simonson, R.E. Mesmer, The enthalpy of dilution and thermodynamics of $Na2CO3_{(aq)}$ and $NaHCO3_{(aq)}$ from T=298K to T=523.15K and pressure of 40 MPa, J. Chem. Thermodyn. 33 (2001) 205–243. https://doi.org/10.1006/jcht.2001.0754.

[348] K.S. Pitzer, Thermodynamics of electrolytes. V. effects of higher-order electrostatic terms, J. Solut. Chem. 4 (1975) 249–265. https://doi.org/10.1007/BF00646562.

[349] J.E. Mayer, E. Montroll, Molecular Distribution, J. Chem. Phys. 9 (1941) 2–16. https://doi.org/10.1063/1.1750822.
[350] J.E. Mayer, Statistical Mechanics, 2nd ed., Wiley, 1977.
[351] C. Christov, N. Moller, Chemical equilibrium model of solution behavior and solubility in the H-Na-K-OH-Cl-HSO_4-SO_4-H_2O system to high concentration and temperature, Geochim. Cosmochim. Acta. 68 (2004) 1309–1331. https://doi.org/10.1016/j.gca.2003.08.017.
[352] D.R. Gaskell, Introduction to the Thermodynamics of Materials, Fifth Edition, CRC Press, 2008.
[353] P. Wang, A. Anderko, Computation of dielectric constants of solvent mixtures and electrolyte solutions, Fluid Phase Equilibria. 186 (2001) 103–122. https://doi.org/10.1016/S0378-3812(01)00507-6.
[354] P.H. Rieger, Electrochemistry, 2nd ed., Springer Netherlands, 1994. https://doi.org/10.1007/978-94-011-0691-7.
[355] S. Nesic, B.F.M. Pots, J. Postlethwaite, N. Thevenot, Superposition of diffusion and chemical reaction controlled limiting currents- application to CO_2 corrosion, J. Corros. Sci. Eng. 1 (1995) No. 3.
[356] T. Tran, B. Brown, S. Nešić, B. Tribollet, Investigation of the electrochemical mechanisms for acetic acid corrosion of mild steel, Corrosion. 70 (2013) 223–229. https://doi.org/10.5006/0933.
[357] S. Navabzadeh Esmaeely, Galvanic localized corrosion of mild steel under iron sulfide corrosion product layers, PhD dissertation, Ohio University, 2018.
[358] M. Eigen, E.M. Eyring, Fast protolytic reactions in aqueous solutions of aminobenzoic acids, Ournal Am. Chem. Soc. 84 (1962) 3254–3256. https://doi.org/10.1021/ja00876a008.
[359] A. Kahyarian, A. Schumaker, B. Brown, S. Nesic, Acidic corrosion of mild steel in the presence of acetic acid: Mechanism and prediction, Electrochimica Acta. 258 (2017) 639–652. https://doi.org/10.1016/j.electacta.2017.11.109.
[360] R. Elgaddafi, R. Ahmed, S. Shah, Modeling and experimental studies on CO_2-H_2S corrosion of API carbon steels under high-pressure, J. Pet. Sci. Eng. 156 (2017) 682–696. https://doi.org/10.1016/j.petrol.2017.06.030.
[361] F.P. Berger, K.-F.F.-L. Hau, Mass transfer in turbulent pipe flow measured by the electrochemical method, Int. J. Heat Mass Transf. 20 (1977) 1185–1194. https://doi.org/10.1016/0017-9310(77)90127-2.
[362] C.A. Sleicher, M.W. Rouse, A convenient correlation for heat transfer to constant and variable property fluids in turbulent pipe flow, Int. J. Heat Mass Transf. 18 (1975) 677–683. https://doi.org/10.1016/0017-9310(75)90279-3.

Appendix A: Conversion between Concentration Units for Dissolved Species and Water

The definition of the weight percent unit used in this study:

$$wt = \frac{m_s}{m_s + m_w} \times 100 \tag{A-1}$$

where, m_s is the mass of salt and m_w is the mass of water.

The following unit conversions are for aqueous NaCl solutions. The equations are valid for other single salt solutions as well. However, for more than one dissolved salt (a pair of anion/cation), the additional anion/cation concentrations need to be accounted for in the conversion formulas.

NaCl weight percent (wt) to NaCl molality (m_{NaCl}):

$$m_{NaCl} = \frac{1000wt}{M_{NaCl}(100 - wt)} \tag{A-2}$$

where, M_{NaCl} is the molecular weight of NaCl (= 58.4428 g/mol).

NaCl weight percent (wt) to NaCl molarity (c_{NaCl}):

$$c_{NaCl} = \frac{wt \cdot \rho_{sol}}{100M_{NaCl}} \tag{A-3}$$

where, ρ_{sol} is the solution density in kg/m^3. ρ_{sol} for aqueous NaCl solutions can be calculated with the Batzle and Wang [26] model explained in Section 3.1.

NaCl molality (m_{NaCl}) to NaCl molarity (c_{NaCl}):

$$c_{NaCl} = \frac{m_{NaCl}\rho_{sol}}{1000 + m_{NaCl}M_{NaCl}} \tag{A-4}$$

NaCl molarity (c_{NaCl}) to NaCl molality (m_{NaCl}):

$$m_{NaCl} = \frac{1000c_{NaCl}}{\rho_{sol} - c_{NaCl}M_{NaCl}} \tag{A-5}$$

H_2O molarity concentration (c_w):

$$c_w = \frac{(100 - wt)\rho_{sol}}{100M_w} \tag{A-6}$$

For molarity concentration of other species (in general, species i) in the solution, it is necessary to assume that the concentrations of these species are low enough that they don't change the density of the aqueous NaCl. For example, for H_2O-NaCl-CO_2-H_2S mixtures, the concentration of dissolved species such as $CO_{2(aq)}$, $H_2S_{(aq)}$, H^+ ion, HCO_3^- ion, HS^- ion, *etc.* are usually low that they do not influence the solution density.

Molality of species i (m_i) to molarity of species i (c_i):

$$c_i = \frac{m_i\rho_{sol}}{1000 + m_{NaCl}M_{NaCl}} \tag{A-7}$$

NaCl mole fraction (x_{NaCl}) to NaCl molality (m_{NaCl}):

$$m_{NaCl} = \frac{1000x_{NaCl}}{x_wM_w} \tag{A-8}$$

where, x_w is the mole fraction of water and M_w is the molecular weight of water (= 18.01 g/mol).

Mole fraction of species i (x_i) to molality of species i (m_i)[105]:

$$m_i = \frac{1000x_i}{x_wM_w} \tag{A-9}$$

NaCl mole fraction (x_{NaCl}) to NaCl molarity (c_{NaCl}):

$$c_{NaCl} = \frac{x_{NaCl}\rho_{sol}}{x_wM_w + x_{NaCl}M_{NaCl}} \tag{A-10}$$

---

[105] The derivation is given in Appendix P.

Mole fraction of species i (x_i) to molarity of species i (c_i)

$$c_i = \frac{x_i \rho_{sol}}{(x_w M_w + x_{NaCl} M_{NaCl})} \qquad \text{(A-11)}$$

Other conversions can be obtained using the above formulas.

Conversion of the H_2O activity from the mole fraction basis to the molarity basis:

$$a_w^c = \frac{1000 x_w \rho_w \gamma_{H_2O}^{x,*}}{M_w} \qquad \text{(A-12)}$$

where, ρ_w is the density of water in g/cm^3. Models for calculating ρ_w are given in Appendix B. $\gamma_{H_2O}^{x,*}$ is the unsymmetrical mole fraction basis activity coefficient of water in dilute reference state. $\gamma_{H_2O}^{x,*}$ is explained in the MSE model and in Appendices O and P.

Appendix B: Density of Pure Water

There are several models in the literature for estimating the density of pure water at different pressures and temperatures [26,25,46,319–321]. Two models are explained in this section. The first model is by Hu and Duan [320], which is used for calculating the equilibrium dissociation constant of water in Appendix G. The second model is by Helgeson and Kirkham [321], which is applied in calculations related to the Born functions in Appendix F. The Hu and Duan model [320] is a straightforward model in the form of a single equation with empirical coefficients. On the other hand, the Helgeson and Kirkham model [321] is a complex model that involves several equations and requires iteration to obtain the water density. However, the Helgeson and Kirkham model [321] is reproduced because it is used in the HKF equation of state, which is an important part of the MSE speciation model reproduced in this study.

The Hu and Duan [320] water density model is an empirical model, which is reformatted in this study as follows:

$$V_w = \sum_{i=1}^{4} k_i P^{i-1} \tag{B-1}$$

$$k_i = \begin{cases} a_{i1}T^3 + a_{i2}T^2 + a_{i3}T + a_{i4} + a_{i5}T^{-1} & (i = 1, 2) \\ a_{i1}T^3 + a_{i2}T^2 + a_{i3} & (i = 3, 4) \end{cases} \tag{B-2}$$

where, V_w is the molar volume of liquid water in cm^3/mol, P is total pressure in bar, T is temperature in K, k_i are fit parameters as a function of temperature, and $a_{i\#}$ are constants listed in Table B-1. The density of water in g/cm^3 can be obtained by M_w/V_w, where M_w is the molecular weight of water (= 18.015 g/mol). Hu and Duan [320] claimed that their model is capable of reproducing the accurate complex IAPWS water density formulation by Wagner and Pruss [322] with an average deviation of 0.005% in a range from 0°C to 200°C and 0 bar to 2000 bar.

Table B-1

The coefficients used in Equation (B-2) for calculating the density of pure water according to Hu and Duan model [320].

$a_{i\#}$	Value	$a_{i\#}$	Value
a_{11}	3.27225e-7	a_{24}	3.5986e-2
a_{12}	-4.2095e-4	a_{25}	-3.55071e0
a_{13}	2.32594e-1	a_{31}	2.57241e-14
a_{14}	-4.1692e1	a_{32}	-1.24336e-11
a_{15}	5.71292e3	a_{33}	5.42707e-7
a_{21}	-2.32306e-10	a_{41}	-4.42028e-18
a_{22}	2.91138e-7	a_{42}	2.10007e-15
a_{23}	-1.49662e-4	a_{43}	-8.11491e-11

The Helgeson and Kirkham [321] water density model is a semi-empirical model that allows estimating water density by using the Helmholtz free energy. The Helgeson and Kirkham model [321] has the following form:

$$P = \rho_w RT\left(1 + \rho_w Q + \rho_w^2\left(\frac{\partial Q}{\partial \rho_w}\right)_T\right) \tag{B-3}$$

where, P is total pressure in bar, which is one of the model inputs, ρ_w is the density of water in g/cm^3, which needs to be determined, T is temperature in K and it is the other model input, Q is a function of temperature and density in cm^3/g, and $(\partial Q/\partial \rho_w)_T$ is the derivative of Q with respect to ρ_w at the constant temperature of T in g^2/cm^6. According to Helgeson and Kirkham [321], Q and $(\partial Q/\partial \rho_w)_T$ are expressed in terms of intermediate functions as below to ease the calculation procedure:

$$Q = x\sum_{j=1}^{7} y_j z_j \tag{B-4}$$

$$\left(\frac{\partial Q}{\partial \rho_w}\right)_T = x\sum_{j=1}^{7} y_j \left(\frac{\partial z_j}{\partial \rho_w}\right)_T \tag{B-5}$$

where,

$$x = \tau - \tau_c \tag{B-6}$$

$$y_j = (\tau - \tau_{aj})^{j-2} \tag{B-7}$$

$$z_j = u_j + \nu w_j \tag{B-8}$$

$$\left(\frac{\partial z_j}{\partial \rho_w}\right)_T = \left(\frac{\partial u_j}{\partial \rho_w}\right)_T + \nu\left(\frac{\partial w_j}{\partial \rho_w}\right)_T + w_j\left(\frac{\partial \nu}{\partial \rho_w}\right)_T \tag{B-9}$$

where,

$$\nu = \exp\left(-4.8\rho_w\right) \tag{B-10}$$

$$w_j = \sum_{i=9}^{10} A_{ij}\rho_w^{i-9} \tag{B-11}$$

$$u_j = \sum_{i=1}^{8} A_{ij}(\rho_w - \rho_{aj})^{i-1} \tag{B-12}$$

$$\left(\frac{\partial \nu}{\partial \rho_w}\right)_T = -4.8\nu \tag{B-13}$$

$$\left(\frac{\partial w_j}{\partial \rho_w}\right)_T = A_{10j} \tag{B-14}$$

$$\left(\frac{\partial u_j}{\partial \rho_w}\right)_T = \sum_{i=1}^{8}(i-1)A_{ij}(\rho_w - \rho_{aj})^{i-2} \tag{B-15}$$

where, $\tau = 1000/T$ (dimensionless), $\tau_c = 1000/T_c = 1.544912$ (dimensionless), $\tau_{aj} = \tau_c$ for $j = 1$[106] and $\tau_{aj} = 2.5$ for $j > 1$ (dimensionless), $\rho_{aj} = 0.634$ g/cm^3 for $j = 1$ and $\rho_{aj} = 1$ g/cm^3 for $j > 1$, and A_{ij} coefficients[107] are listed in Table B-2.

To find the density of water (ρ_w) at input conditions of constant pressure (P) and constant temperature (T), the following procedure is recommended:

1) Consider an initial guess for ρ_w
2) Compute P in Equation (B-3)
3) Compare the calculated P with the input P
4) If they are equal, then the initial guess is the desired ρ_w.
5) Otherwise, restart the procedure, until the condition in Step 4 is satisfied.

In this study, the “fsolve” MATLAB solver is used for the iterative procedure and calculating the water density. Molal volume[108] (cm^3/mol) of water at different temperature and pressure are provided in Table 3 of Helgeson and Kirkham [321].

---

[106] It is incorrectly written $j = i$ in the original publication [321].

[107] The unit for A_{ij} coefficients depends on the ρ exponent in Equations (B-11) and (B-12).

[108] Molal volume of pure water is the same as molar volume of that. Molar volume times molar mass gives density.

Table B-2

The A_{ij} *coefficients used in Equations (B-11), (B-12), (B-14), and (B-15) for calculating the density of pure water based on the Helgeson and Kirkham model* [321].

i	$j = 1$	$j = 2$	$j = 3$	$j = 4$	$j = 5$	$j = 6$	$j = 7$
1	29.492937	-5.1985860	6.8335354	-0.1564104	-6.3972405	-3.9661401	-0.69048554
2	-132.13917	7.7779182	-26.149751	-0.72546108	26.409282	15.453061	2.7407416
3	274.64632	-33.301902	65.326396	-9.2734289	-47.740374	-29.142470	-5.1028070
4	-360.93828	-16.254622	-26.181978	4.3125840	56.323130	29.568796	3.9636085
5	342.18431	-177.31074	0	0	0	0	0
6	-244.50042	127.48742	0	0	0	0	0
7	155.18535	137.46153	0	0	0	0	0
8	5.9728487	155.97836	0	0	0	0	0
9	-410.30848	337.31180	-137.46618	6.7874983	136.87317	79.847970	13.041253
10	-416.05860	-209.88866	-733.96848	10.401717	645.81880	399.17570	71.531353

Appendix C: Isothermal Compressibility ($\boldsymbol{\beta}$) and Isobaric Thermal Expansion ($\boldsymbol{\alpha}$) Coefficients of Water

The isothermal compressibility (β[109]) is a measure of the relative change in the volume (V) of a fluid or a solid due to a pressure (P) change at a constant temperature (T). β always has a positive value. This means that the volume of a system decreases with an increase in pressure [323]. The common definition of β is as follows [323]:

$$\beta \equiv -\frac{1}{V}\left(\frac{\partial V}{\partial P}\right)_T \tag{C-1}$$

The unit for β is 1/bar. At a constant mass, since the density (ρ_w) is inversely proportional to the volume, Helgeson and Kirkham [321] utilized the definition below for β:

$$\beta^{-1} = -\rho_w\left(\frac{\partial P}{\partial \rho_w}\right)_T \tag{C-2}$$

Differentiating Equation (B-3) with respect to ρ_w at a constant T results in an expression that can be used to calculate β:

$$\beta^{-1} = P + \rho_w^2 RT\left(Q + 3\rho_w^2\left(\frac{\partial Q}{\partial \rho_w}\right)_T + \rho_w^2\left(\frac{\partial^2 Q}{\partial \rho_w^2}\right)_T\right) \tag{C-3}$$

where, R is the gas constant (= 4.6151 $\mathrm{cm^3{\cdot}bar/g/K}$). It is assumed that P (bar) and T (K) are known as inputs. Q ($\mathrm{cm^3/g}$), $(\partial Q/\partial \rho_w)_T$, and ρ_w ($\mathrm{g/cm^3}$) for water can be obtained from Appendix B. Thus, only the second derivative of Q remains in Equation (C-3) to be

---

[109] It is usually shown by κ [323]. However, β is used in this study to be consistent with notations used in the Helgeson and Kirkham publication [321].

able to calculate β. The second derivative of Q can be calculated using the following equation [321]:

$$\left(\frac{\partial^2 Q}{\partial \rho_w^2}\right)_T = x \sum_{j=1}^{7} y_j \left(\frac{\partial^2 z_j}{\partial \rho_w^2}\right)_T \tag{C-4}$$

where,

$$\left(\frac{\partial^2 z_j}{\partial \rho_w^2}\right)_T = \left(\frac{\partial^2 u_j}{\partial \rho_w^2}\right)_T + 2\left(\frac{\partial \nu}{\partial \rho_w}\right)_T \left(\frac{\partial w_j}{\partial \rho_w}\right)_T + w_j \left(\frac{\partial^2 \nu}{\partial \rho_w^2}\right)_T \tag{C-5}$$

$$\left(\frac{\partial^2 u_j}{\partial \rho_w^2}\right)_T = \sum_{i=1}^{8} (i-1)(i-2) A_{ij} (\rho_w - \rho_{aj})^{i-3} \tag{C-6}$$

$$\left(\frac{\partial^2 \nu}{\rho_w^2}\right)_T = -4.8 \left(\frac{\partial \nu}{\partial \rho_w}\right)_T \tag{C-7}$$

x, y_j, $(\partial \nu / \partial \rho_w)_T$, w_j, $\left(\partial w_j / \partial \rho_w\right)_T$, ρ_{aj}, and A_{ij} are already given in Appendix B. Values of β at different temperatures and pressures are given in Table 8 of Helgeson and Kirkham [321].

The isobaric thermal expansion (α) describes the volume (V) of a fluid or a solid in response to temperature (T) change at constant pressure (P). α is usually positive, which indicates that the volume of the system increases with increasing temperature. However, some systems show negative α values. For example, water has a negative α between 0^{o}C to 3.98^{o}C [323]. α is usually formulated as below:

$$\alpha \equiv \frac{1}{V}\left(\frac{\partial V}{\partial T}\right)_P \tag{C-8}$$

The unit for α is 1/K. Similar to β, Helgeson and Kirkham [321] used a definition based on density (ρ_w):

$$\alpha = -\frac{1}{\rho_w}\left(\frac{\partial \rho_w}{\partial T}\right)_P \tag{C-9}$$

The following equation is suggested by Helgeson and Kirkham [321] to calculate α for water:

$$\alpha = \frac{\beta P}{T} + \rho_w RT\beta\left[\rho_w\left(\frac{\partial Q}{\partial T}\right)_{\rho_w} + \rho_w^2\left(\frac{\partial\left(\frac{\partial Q}{\partial \rho_w}\right)_T}{\partial T}\right)_{\rho_w}\right] \tag{C-10}$$

where,

$$\left(\frac{\partial Q}{\partial T}\right)_{\rho_w} = \frac{Q}{x}\left(\frac{\partial x}{\partial T}\right)_P + x\sum_{j=1}^{7} z_j\left(\frac{\partial y_j}{\partial T}\right)_P \tag{C-11}$$

$$\left(\frac{\partial\left(\frac{\partial Q}{\partial \rho_w}\right)_T}{\partial T}\right)_{\rho_w} = \frac{1}{x}\left(\frac{\partial Q}{\partial \rho_w}\right)_T\left(\frac{\partial x}{\partial T}\right)_P + x\sum_{j=1}^{7}\left(\frac{\partial y_j}{\partial T}\right)_P\left(\frac{\partial z_j}{\partial \rho_w}\right)_T \tag{C-12}$$

where,

$$\left(\frac{\partial x}{\partial T}\right)_P = -\frac{\tau}{T} \tag{C-13}$$

$$\left(\frac{\partial y_j}{\partial T}\right)_P = -\frac{(j-2)\tau y_j}{T(\tau - \tau_{aj})} \tag{C-14}$$

The rest of the functions, and parameters are given in Appendix B. Values of α for water at different temperatures and pressures are provided in Table 7 of Helgeson and Kirkham [321].

Appendix D: Dielectric Constant (Relative Permittivity) of Water

The dielectric constant—also called the relative permittivity—of water can be calculated by using the following equation suggested by Johnson and Norton [324]:

$$\varepsilon = \sum_{i=1}^{5} k_i ϼ^{i-1}$$

where, $ϼ = \rho_w/(1\,\frac{g}{cm^3})$, in which, ρ_w is the density of pure water in g/cm^3. k_i parameters are functions of temperature, given below:

$$k_1 = 1 \tag{D-1}$$

$$k_2 = e_1 \dagger^{-1} \tag{D-2}$$

$$k_3 = e_2 \dagger^{-1} + e_3 + e_4 \dagger \tag{D-3}$$

$$k_4 = e_5 \dagger^{-1} + e_6 \dagger + e_7 \dagger^{2} \tag{D-4}$$

$$k_5 = e_8 \dagger^{-2} + e_9 \dagger^{-1} + e_{10} \tag{D-5}$$

where, $\dagger = T/T_{ref}$, T is temperature in K, T_{ref} is the reference temperature (= 298.15 K) and e_i coefficients are presented in Table D-1. The values of dielectric constant of water at different temperatures and pressures are listed in Table C2 of Shock *et al.* [325].

Table D-1

The e_i coefficients used in Equations (D-2) to (D-5) for calculating the dielectric constant of water [324].

e_i	Value
e_1	0.1470333593e2
e_2	0.2128462733e3
e_3	-0.1154445173e3
e_4	0.1955210915e2
e_5	-0.8330347980e2
e_6	0.3213240048e2
e_7	-0.6694098645e1
e_8	-0.3786202045e2
e_9	0.6887359646e2
e_{10}	-0.2729401652e2

In Addition, the dielectric of water can be calculated by using Bradley and Pitzer equation [326]:

$$D = D_{1000} + C ln\left(\frac{B + P}{B + 1000}\right) \tag{D-6}$$

where, P is total pressure in bar, and D_{1000}, C, and B are temperature dependent parameters according to the equations below:

$$D_{1000} = a_1 \exp\,(a_2 T + a_3 T^2) \tag{D-7}$$

$$C = a_4 + \frac{a_5}{a_6 + T} \tag{D-8}$$

$$B = a_7 + \frac{a_8}{T} + a_9 T \tag{D-9}$$

T in Equations (D-7) to (D-9) is temperature in K, and a_i constants can be found in Table D-2.

Another model for calculating the dielectric of water has been proposed by Helgeson and Kirkham [321].

Table D-2

Constants used in Equations (D-7) to (D-9) for calculating the dielectric of water [326].

i	a_i
1	3.4279e2
2	-5.0866e-3
3	9.4690e-7
4	-2.0525e0
5	3.1159e3
6	-1.8289e2
7	-8.0325e3
8	4.2142e6
9	2.1417e0

Appendix E: Conventional Born Coefficient (ω)

The conventional Born coefficients ω and ω_{P_r,T_r} for the arbitrary aqueous ion, j can be calculated using the following equations [325]:

$$\omega_j = \eta Z_j\left(\frac{Z_j}{r_{e,j,P_r,T_r}+|Z_j|g}-\frac{1}{3.082+g}\right) \quad \text{(E-1)}$$

$$\omega_{j,P_r,T_r} = \eta Z_j\left(\frac{Z_j}{r_{e,j,P_r,T_r}}-\frac{1}{3.082}\right) \quad \text{(E-2)}$$

where, η is the Born constant (=1.066027$\times 10^5$ Å ·cal/mol) [327], Z_j refers to the charge number of ion j, r_{e,j,P_r,T_r} stands for the effective electrostatic radius of the ion j at P_r and T_r [327], g is a function of temperature and pressure independent of the identity of ion j, related to the solvent contribution to the effective electrostatic radius of ion j in Å. The equations to determine r_{e,j,P_r,T_r} are given in Shock *et al.* [328,329]. The r_{e,j,P_r,T_r} values for a large group of ions are provided in Shock and Helgeson [328]. The g function can be calculated from Appendix C of Tanger and Helgeson publication [330] and/or Shock *et al.* [325]. For temperatures below 150°C and pressures below 500 bar, g function and its partial derivatives are almost equal to zero ($g \approx 0$) [325,330]. Therefore, for most aqueous corrosion studies where operating temperatures and pressures are below the above ranges, ω_j and ω_{j,P_r,T_r} will be equal. For neutral species, ω_j is independent of temperature and pressure, *i.e.*, $g = 0$, and consequently, ω_j and ω_{j,P_r,T_r} are equal [325]. The values of ω_j and ω_{j,P_r,T_r} can be obtained by regression of the experimental data or sometimes by a correlation with respect to the standard partial molal entropy ($\bar{S}^o$) [329].

Appendix F: Born Function Y

The Born theory is rough and approximate model for estimating ion-solvent interactions during the dissolution process. In the Born model, the ion is considered as a rigid sphere with a charge z and solvent is assumed to be a structureless continuum. The ion-solvent interaction is described in terms of the free energy of solvation by calculating the work needs to be done to transfer the charges sphere from vacuum into the continuum. A comprehensive description of the Born theory is given by Bockris and Reddy [20]. Several functions have been defined as Born functions which describe the changes in the dielectric constant of solvent with respect to temperature and pressure. These functions are Q, Y, U, N, and X. The Born function, Q captures changes in the dielectric constant of solvent with a pressure change at a constant temperature. U and N are two derivatives of Q function. The Born function, Y is related to variations in the dielectric constant of solvent in response to a temperature change at a constant pressure. X is a derivative of Y Born function. The formulation for Born functions and their values at different temperatures and pressures are described in Helgeson and Kirkham [321,330].

The Born function, Y has the following form [321,330]:

$$Y \equiv -\left(\frac{\partial\left(\frac{1}{\varepsilon}\right)}{\partial T}\right)_P = \frac{1}{\varepsilon^2}\left(\frac{\partial \varepsilon}{\partial T}\right)_P \tag{F-1}$$

where, ε is the dielectric constant of water and can be calculated from Appendix D. The derivative of ε with respect to temperature (T) can be derived by using Equation (F-2)[110]:

---

[110] Equation C8 of Shock *et al.* [325] for $(\partial\varepsilon/\partial T)_P$ is missing i as the exponent of ρ.

$$\left(\frac{\partial \varepsilon}{\partial T}\right)_P = \sum_{i=1}^{5} \rho^{i-1}\left(\left(\frac{\partial k_i}{\partial T}\right)_P - \alpha(i-1)k_i\right) \qquad \text{(F-2)}$$

where, ρ is the density of solvent, water in this study, which is mentioned in Appendix B, ϯ, k_i, and the corresponding e_i coefficients are defined in Appendix D, and α is the isobaric thermal expansion coefficient of solvent. For water as the solvent, α calculation is explained in Appendix C. The $(\partial K_i/\partial T)_P$ terms corresponded to k_i functions given in Equations (F-3) to (F-7) are as follows[111]:

$$\left(\frac{\partial k_1(ϯ)}{\partial T}\right)_P = 0 \qquad \text{(F-3)}$$

$$\left(\frac{\partial k_2(ϯ)}{\partial T}\right)_P = -\frac{e_1 ϯ^{-2}}{T_{ref}} \qquad \text{(F-4)}$$

$$\left(\frac{\partial k_3(ϯ)}{\partial T}\right)_P = \frac{-e_2 ϯ^{-2} + e_4}{T_{ref}} \qquad \text{(F-5)}$$

$$\left(\frac{\partial k_4(ϯ)}{\partial T}\right)_P = \frac{-e_5 ϯ^{-2} + e_6 + 2e_7 ϯ}{T_{ref}} \qquad \text{(F-6)}$$

$$\left(\frac{\partial k_5(ϯ)}{\partial T}\right)_P = \frac{-2e_8 ϯ^{-3} - e_9 ϯ^{-2}}{T_{ref}} \qquad \text{(F-7)}$$

---

[111] Equations C11, C13, C15, and C17 for $(\partial K_1/\partial T)_P$, $(\partial K_2/\partial T)_P$, $(\partial K_3/\partial T)_P$, $(\partial K_4/\partial T)_P$, respectively, in Shock *et al.* [325] are missing T_{ref} in the denominator.

Appendix G: Equilibrium Dissociation Constant for Water (K_w)

The equation for dissociation constant of water proposed by Marshall and Franck [269] is as follows:

$$logK_w = a_1 + \frac{a_2}{T} + \frac{a_3}{T^2} + \frac{a_4}{T^3} + (a_5 + \frac{a_6}{T} + \frac{a_7}{T^2})log\rho_w \tag{G-1}$$

where, K_w is in (mol/kgH$_2$O)^2, ρ_w is the density of pure water in g/cm^3 and can be obtained from Appendix B, T is the solution temperature in K, and a_1 parameters are listed in Table G-1. To convert the unit to (mol/lit)^2, multiply the calculated K_w by ρ_w^2.

Table G-1

The coefficients used in Equation (G-1) for calculating the equilibrium dissociation constant for water.

i	1	2	3	4	5	6	7
a_i	-4.098	-3245.2	2.2362e5	-3.984e7	13.957	-1262.3	8.5641e5

A simpler equation proposed by Kharaka *et al.* [278] can be used as well:

$$logK_w = -29.3868 + 0.0737549T - 7.47881 \times 10^{-5}T^2 \tag{G-2}$$

where K_w is in (mol/lit)^2, and T is the solution temperature in K.

There are models [245,255,270,331] that consider the effect of salt concentration on dissociation constant of water.

Appendix H: Water Vapor Pressure in Aqueous NaCl Solutions

The Atkinson model [128] is proposed as a statistical model for water vapor pressure calculation in the H_2O-NaCl systems. It is valid from -21.2^{o}C to 1500^{o}C and for all compositions from pure water (0 wt.% NaCl) to pure NaCl (100 wt.% NaCl). Atkinson suggested three equations as a function of temperature and NaCl concentration for three temperature ranges of -21.2^{o}C to 300^{o}C, 300^{o}C to 484^{o}C, and 484^{o}C to 1500^{o}C. Each equation has a different set of coefficients estimated by fitting the equation with experimental data. For aqueous corrosion studies, the first temperature range will be sufficient, and therefore, the corresponding equation and coefficients for this temperature range are listed below:

$$
\begin{aligned}
log p_w = {} & \beta_{11} + \beta_{12}(\omega) + \beta_{14}(\omega)^3 + \beta_{15}(\omega)^4 + \beta_{16}(\omega)^5 + \beta_{17}(\omega)^6 \\
& + \beta_{18}(\omega)^7 + \beta_{21}\text{Ŧ} + \beta_{31}\text{Ŧ}^2 + \beta_{41}\text{Ŧ}^3 + \beta_{51}\text{Ŧ}^4 \\
& + \beta_{61}\text{Ŧ}^5 + \beta_{71}\text{Ŧ}^6 + \beta_{81}\text{Ŧ}^7 + \beta_{22}\text{Ŧ}(\omega) + \beta_{23}\text{Ŧ}(\omega)^2 \\
& + \beta_{24}\text{Ŧ}(\omega)^3 + \beta_{26}\text{Ŧ}(\omega)^5 + \beta_{27}\text{Ŧ}(\omega)^6 + \beta_{32}\text{Ŧ}^2(\omega) \\
& + \beta_{33}\text{Ŧ}^2(\omega)^2 + \beta_{34}\text{Ŧ}^2(\omega)^3 + \beta_{35}\text{Ŧ}^2(\omega)^4 + \beta_{36}\text{Ŧ}^2(\omega)^5 \\
& + \beta_{42}\text{Ŧ}^3(\omega) + \beta_{43}\text{Ŧ}^3(\omega)^2 + \beta_{44}\text{Ŧ}^3(\omega)^3 + \beta_{45}\text{Ŧ}^3(\omega)^4 \\
& + \beta_{53}\text{Ŧ}^4(\omega)^2 + \beta_{54}\text{Ŧ}^4(\omega)^3 + \beta_{62}\text{Ŧ}^5(\omega)
\end{aligned}
\qquad \text{(H-1)}
$$

where, p_w is the water vapor pressure in bar, Ŧ is the solution temperature in K divided by 100 (T/100), ω is NaCl weight percent divided by 100 (wt.%/100)[112], and β_{ij} are fit coefficients listed in Table H-1. For the other two temperature ranges, the reader is referred to the original publication [128]. By comparing the model with the experimental

---

[112] For example, if NaCl concentration in the solution is 3.5 wt.%, ω = 3.5/100

data, Atkinson showed that for 90% of the cases the prediction error is within ±5% of the experimental data [128]. Another model for calculating the water vapor pressure above aqueous NaCl solutions is proposed by Shibue [332]. This model is valid for 0^{o}C to 370^{o}C and NaCl concentrations up to 30 wt.% [332].

Table H-1

The coefficients used in Equation (H-1) for calculating the water vapor pressure in aqueous NaCl solutions [128].

i	j = 1	j = 2	j = 3	j = 4	j = 5	j = 6	j = 7	j = 8
1	-27.2444260945847	-3.43823854919821	-	49.6470810423974	284.920532084465	-671.468924936888	-306.420824097701	-476.3912831617690
2	19.6752698743832	2.94599944070388	-5.05958726370657	-78.057932502234	-	272.541674619991	191.281847960897	-
3	-6.03987279418686	-1.02712250242286	5.3605248349362	18.9371135629599	-27.5731923399911	-43.6261697756668	-	-
4	1.05318996126294	0.132241696257544	-1.43460393380215	-0.517812895404853	4.28981312806579	-	-	-
5	-0.107523830798341	-	0.115824432759682	-0.147543794540513	-	-	-	-
6	0.0063216048751384	-0.000792743415349166	-	-	-	-	-	-
7	-0.00020139101441089	-	-	-	-	-	-	-
8	0.0000029370853393422	-	-	-	-	-	-	-

Appendix I: Debye-Huckel Parameters or Debye-Huckel Limiting Slope Parameters

The Debye-Huckel parameter for osmotic coefficient in molality basis, A^{ϕ}, is defined as below [137,139]:

$$A_{\phi} = \frac{1}{3}\left(\frac{2\pi N_o \rho_w}{1000}\right)^{0.5}\left(\frac{e^2}{Dk_BT}\right)^{1.5} \tag{I-1}$$

where, A_{ϕ} is in $(\text{mol/kgH}_2\text{O})^{-0.5}$, π is the Pi number (= 3.14159), N_o is the Avogadro's number in 1/mol (= 6.022045×10^{23}), ρ_w is the density of pure water in g/cm^3, e is the charge of electron in $\text{g}^{0.5}\cdot\text{cm}^{1.5}/\text{s}$ (= 4.803242×10^{-10}), D is the dielectric of water (dimensionless), k_B is the Boltzmann constant in $\text{g}\cdot\text{cm}^2/\text{s}^2/\text{K}$ (= 1.38066×10^{-16}), and T is temperature in K. 1000 in Equation (I-1) has apparently a unit of g/kg. ρ_w can be calculated by the models given in Appendix B. Models for obtaining the dielectric of water (D) are provided in Appendix D. A_{ϕ} at 25^{o}C and 1 atm is 0.39145 [137]. There are simpler equations in the literature for A_{ϕ} calculation [125,333].

The Debye-Huckel parameter for osmotic coefficient in mole fraction basis, A_x, is given by:

$$A_x = \frac{1}{3}(2\pi N_o d_w)^{0.5}\left(\frac{e^2}{4\pi\varepsilon_o Dk_BT}\right)^{1.5} \tag{I-2}$$

where, A_x is dimensionless, π is the Pi number (= 3.14159), N_o is the Avogadro's number in 1/mol (= 6.022045×10^{23}), d_w is molar density of water in mol/m^3, e is the charge of electron in C (= 1.602177×10^{-19}), ε_o is the dielectric constant of vacuum in $\text{C}^2/\text{J/m}$ (= 8.8541878×10^{-12}), D is the dielectric of water (dimensionless), k_B is the Boltzmann constant in J/K (= 1.38066×10^{-23}), and T is temperature in K. The dielectric of water (D) can be determined by the models given in Appendix D. d_w can be obtained by using the following equation:

$$d_w = 10^6 \cdot \frac{\rho_w}{M_w} \tag{I-3}$$

where, ρ_w is the density of water in g/cm^3 presented in Appendix B, and M_w is the molecular weight of water in g/mol (= 18.015). A_x has a value of 2.916 at 25^{o}C and 1 atm.

Comparing A_ϕ and A_x equations indicates the relationship between the charge of electron with two different units used in Equation (I-1) and (I-2):

$$\sqrt{4\pi\varepsilon_o \times 10^{-9}} \times 4.803242 \times 10^{-10} = 1.602177 \times 10^{-19} \tag{I-4}$$

A_ϕ and A_x can be converted to each other by using the equation below:

$$A_x = \left(\frac{1000}{M_w}\right)^{0.5} A_\phi \tag{I-5}$$

Another form of the Debye-Huckel limiting slope is the Debye-Huckel coefficient for activity coefficient, A^γ. The relation between A_ϕ and A^γ is as follows:

$$A_\gamma = 3A_\phi \tag{I-6}$$

A_γ is in (mol/kgH$_2$O)$^{-0.5}$. A_γ at 25^{o}C and 1 atm is equal to 1.1743. Sometimes a value of 0.51 is reported for A_γ at 25^{o}C and 1 atm [118]. This is due to using a different definition for A_γ, which is proposed by Helgeson and Kirkham [137,165]. According to their definition:

$$A_{\gamma,10} = \frac{A_\phi}{ln10} \tag{I-7}$$

Therefore, $A_{\gamma,10}$ is equal to 0.51 at 25^{o}C and 1 atm.

Appendix J: An Equation of State and Fugacity Coefficient of Pure CO_2, H_2S, H_2O, and CH_4

The fugacity coefficients of pure CO_2, H_2S, H_2O, and CH_4 at pressure, P (bar), and temperature, T (K), can be calculated by using an equation of state developed by Duan *et al.* [243]. First, the reduced pressure, P_r, and the reduced temperature, T_r, are obtained according to Equations (J-1) and (J-2). The critical pressure, P_c (bar), and the critical temperature, T_c (K) for the above compounds are listed in Table J-1. Next, the reduced volume, V_r, is obtained in an iterative procedure by solving Equation (J-3) with the coefficients listed in Table J-2. The "fzero" solver in MATLAB was used to solve Equation (J-3) for V_r. Z in Equations (J-3) is the compressibility factor (dimensionless). Finally, the fugacity coefficient for each gas is determined by plugging T_r, V_r, Z, and appropriate a_i coefficients into Equation (J-4). Duan *et al.* [334] suggested an equation for the fugacity coefficient of CO_2 that does not require an iteration procedure to solve. However, a similar equation is not provided for H_2S, H_2O, and CH_4.

$$P_r = \frac{P}{P_c} \tag{J-1}$$

$$T_r = \frac{T}{T_c} \tag{J-2}$$

$$\begin{aligned} Z = \frac{P_r T_r}{V_r} = 1 + \frac{a_1 + \frac{a_2}{T_r^2} + \frac{a_3}{T_r^3}}{V_r} + \frac{a_4 + \frac{a_5}{T_r^2} + \frac{a_6}{T_r^3}}{V_r^2} + \frac{a_7 + \frac{a_8}{T_r^2} + \frac{a_9}{T_r^3}}{V_r^4} \\ + \frac{a_{10} + \frac{a_{11}}{T_r^2} + \frac{a_{12}}{T_r^3}}{V_r^5} + \frac{a_{13}}{T_r^3 V_r^2}\left(a_{14} + \frac{a_{15}}{V_r^2}\right) \exp\left(-\frac{a_{15}}{V_r^2}\right) \end{aligned} \tag{J-3}$$

$$ln\varphi(T,P) = Z - 1 - lnZ + \frac{a_1 + \frac{a_2}{T_r^2} + \frac{a_3}{T_r^3}}{V_r} + \frac{a_4 + \frac{a_5}{T_r^2} + \frac{a_6}{T_r^3}}{2V_r^2} + \frac{a_7 + \frac{a_8}{T_r^2} + \frac{a_9}{T_r^3}}{4V_r^4} + \frac{a_{10} + \frac{a_{11}}{T_r^2} + \frac{a_{12}}{T_r^3}}{5V_r^5} + \frac{a_{13}}{2T_r^3 a_{15}}\left[a_{14} + 1 - \left(a_{14} + 1 + \frac{a_{15}}{V_r^2}\right)\exp\left(-\frac{a_{15}}{V_r^2}\right)\right] \tag{J-4}$$

Table J-1

Critical pressure (P_c) and critical temperature (T_c) for CO_2, H_2S, and H_2O [243,335–338].

Critical properties	Unit	CO_2	H_2S	H_2O	CH_4
P_c	bar	73.825	89.70	220.64	46.41
T_c	Kelvin	304.2	373.4	647.14	190.6

The critical values are chosen according to the National Institute of Standards and Technology (NIST) Chemistry WebBook.

Table J-2

The a_i *coefficients used in an equation of state for* CO_2*,* H_2S*,* H_2O*, and* H_2O*, Equation* (J-3)*, as well as in Equation* (J-4) *for calculating the fugacity coefficient of pure* CO_2*,* H_2S*,* H_2O*, and* CH_4 [243,256].

a_i	CO_2	H_2S	H_2O	CH_4
a_1	8.99288497e-2	1.51743382e1	8.6444922e-2	8.72553928e-2
a_2	-4.94783127e-1	-7.06584137e1	-3.96918955e-1	-7.52599476e-1
a_3	4.77922245e-2	2.22560492e1	-5.73334886e-2	3.7519887e-1
a_4	1.03808883e-2	-2.97785078e2	-2.93893e-4	1.07291342e-2
a_5	-2.82516861e-2	9.45572292e2	-4.15775512e-3	5.4962636e-3
a_6	9.49887563e-2	2.49770630e2	1.99496791e-2	-1.84772802e-2
a_7	5.2060088e-4	1.42719562e3	1.18901426e-4	3.18993183e-4
a_8	-2.93540971e-4	-3.11004493e3	1.55212063e-4	2.11079375e-4
a_9	-1.77265112e-3	4.82481431e4	-1.06855859e-4	2.01682801e-5
a_{10}	-2.51101973e-5	-8.17715100e5	-4.93197687e-6	-1.65606189e-5
a_{11}	8.93353441e-5	2.71307041e4	-2.73739155e-6	1.19614546e-4
a_{12}	7.88998563e-5	-8.02424647e5	2.65571238e-6	-1.08087289e-4
a_{13}	-1.66727022e-2	-4.20778924e2	8.96079018e-3	4.48262295e-2
a_{14}	1.398	1	4.02	7.5397e-1
a_{15}	2.96e-2	200	2.57e-2	7.7167e-2

Appendix K: Calculation of Fugacity Coefficients of Gaseous Species in a Gas Mixture with Soave-Redlich-Kwong (SRK) Equation of State

The Soave-Redlich-Kwong (SRK) equation of state can provide an acceptable description of the liquid-vapor equilibrium behavior of systems composed of hydrocarbons and related compounds such as $N_{2(g)}$, $CO_{2(g)}$, and $H_2S_{(g)}$. The SRK equation of state has been widely used for process designs in the oil and gas industry [339]. The SRK equation of state is given below:

$$P = \frac{RT}{\upsilon - b} - \frac{\alpha}{\upsilon(\upsilon + b)} \tag{K-1}$$

where, P is pressure, R is the gas constant, T is temperature in K, υ is the specific volume, b is a volume constant depends on the gas type, and α is called the attractive parameter, which depends on temperature and the gas type [248,340].

The SRK equation can be expressed in a cubic form in terms of compressibility factor (Z) of the gas mixture [248]:

$$Z^3 - Z^2 + (A - B - B^2)Z - AB = 0 \tag{K-2}$$

where, A and B are dimensionless coefficients for the gas mixture formulated below [248]:

$$A = \frac{aP}{R^2T^2} \tag{K-3}$$

$$B = \frac{bP}{RT} \tag{K-4}$$

where, P is total pressure in atm, R is the gas constant in $cm^3 \cdot atm/K/mol$ (= 82.05746), and a and b are mixed-component parameters[113], which can be calculated using the classical quadratic mixing rules:

$$a_{ij} = \left(a_i a_j\right)^{0.5}(1 - k_{ij}) \tag{K-5}$$

$$a = \sum_{i=1}^{n}\sum_{j=1}^{n} y_i y_j\, a_{ij} \tag{K-6}$$

$$b = \sum_{i=1}^{n} y_i b_i \tag{K-7}$$

where, n is the number of gaseous species[114] in the gas mixture, y_i is the mole fraction of gaseous species i, a_{ij} is the mixing rule for mixed-component parameter a, k_{ij} is a binary correction factor (dimensionless) for the mixing rule a_{ij}, and a_i and b_i are pure-component parameters [241,248,339]. The mixing rules consider the interactions between different gas molecule types in the gas mixture. k_{ij} is defined as a function of temperature [241]:

$$k_{ij} = k_{ij}^{(0)} + \frac{k_{ij}^{(1)}}{T} \tag{K-8}$$

where, T is temperature in K, and $k_{ij}^{(0)}$ and $k_{ij}^{(1)}$ are the binary mixing-rule parameters[115] listed in Table K-1 for the H_2O-CO_2-H_2S gas mixture. a_i and b_i are pure-component parameters[116], which can be calculated by using the equations below [248]:

---

[113] In $cm^6 \cdot atm/mol^2$ and cm^3/mol, respectively.

[114] Three gaseous species in this study: $CO_{2(g)}$, $H_2S_{(g)}$, and $H_2O_{(g)}$

[115] $k_{ij}^{(0)}$ is dimensionless and $k_{ij}^{(1)}$ is in K.

[116] In $cm^6 \cdot atm/mol^2$ and cm^3/mol, respectively.

$$a_i = 0.42747\frac{R^2T_c^2}{P_c}\alpha_i \tag{K-9}$$

$$b_i = 0.08664\frac{RT_c}{P_c} \tag{K-10}$$

where, T_c is the critical temperature in K, P_c is the critical pressure in atm, and α_i is the attractive parameter (dimensionless) for gaseous species i. T_c, P_c, and α_i values for CO_2, H_2S, and H_2O are presented in Table K-2 [248]. The acentric factor (ω_i) (dimensionless) used in the α_i equation is a measure of the non-sphericity or centricity of molecules of gaseous species i. ω_i values or $CO_{2(g)}$, $H_2S_{(g)}$, and $H_2O_{(g)}$ are given in Table K-2.

To calculate the fugacity coefficients of gaseous species in an open system at a given temperature (T), total pressure (P), and mole fractions of gaseous species (y_i)[117], first, A and B coefficients in Equations (K-3) and (K-4) need to be determined by using Equations (K-5) to (K-10). Then, the SRK equation of state, Equation (K-2), will be solved for Z. The Cardano's method is used here to solve the cubic SRK equation of state [271]. The steps to this method are listed below [271]:

1) Match Equation (K-2) with the general form of a cubic equation with real coefficients as follows:

$$Z^3 + b_2Z^2 + b_1Z + b_0 = 0 \tag{K-11}$$

2) Form the following relations:

$$b_2 = -1 \tag{K-12}$$

---

[117] The mole fraction (y_i) and mole percent ($= y_i \times 100$) and partial pressure ($p_i = y_i \times P$) are equivalent. The mole fraction of $H_2O_{(g)}$ can be obtained from a water vapor pressure model (Appendix H). Therefore, for an open H_2O-CO_2-H_2S system, if the mole fraction of CO_2 or H_2S is known the other one can be calculated from $\sum y_i = 1$ equation ($y_{H_2O} + y_{H_2S} + y_{CO_2} = 1$).

$$b_1 = A - B - B^2 \tag{K-13}$$

$$b_0 = -AB \tag{K-14}$$

3) Calculate new parameters p and q:

$$p = b_1 - \frac{b_2^2}{3} \tag{K-15}$$

$$q = b_0 - \frac{b_1 b_2}{3} + \frac{2b_2^3}{27} \tag{K-16}$$

4) Calculate the discrimant d

$$d = \left(\frac{p}{3}\right)^3 + \left(\frac{q}{2}\right)^2 \tag{K-17}$$

5) If $d > 0$, all three real roots are the same and equal to Z:

$$Z = \sqrt[3]{-\frac{q}{2} + d^{0.5}} + \sqrt[3]{-\frac{q}{2} - d^{0.5}} - \frac{b_2}{3} \tag{K-18}$$

6) Otherwise, if $d \leq 0$, there will be three different real roots:

$$1^{st} Root = 2\sqrt{\frac{-p}{3}} \cos\left(\frac{\phi}{3}\right) - \frac{b_2}{3} \tag{K-19}$$

$$2^{nd} Root = 2\sqrt{\frac{-p}{3}} \cos\left(\frac{\phi + 2\pi}{3}\right) - \frac{b_2}{3} \tag{K-20}$$

$$3^{rd} Root = 2\sqrt{\frac{-p}{3}} \cos\left(\frac{\phi + 4\pi}{3}\right) - \frac{b_2}{3} \tag{K-21}$$

where,

$$\phi = \arccos\left(-\frac{q}{2}\sqrt{-\frac{27}{p^3}}\right) \tag{K-22}$$

7) If $d \leq 0$, Z is equal to the maximum value of the three roots:

$$Z = maximum\ (1^{st} Root, 2^{nd} Root, 3^{rd} Root) \tag{K-23}$$

After calculating Z, the following equation can be used to obtain the fugacity coefficient (φ) of gaseous species in the gas mixture [341,342]:

$$ln\varphi_i = \frac{b_i}{b}(Z-1) - \ln(Z-B) + \frac{A}{B}\left(\frac{b_i}{b} - 2\frac{\sum_{j=1}^{n} y_j a_{ij}}{a}\right)\ln\left(1+\frac{B}{Z}\right) \quad \text{(K-24)}$$

Table K-1

The binary parameters for the mixing-rule correction factor of the H_2O-CO_2-H_2S gas mixture [241].

Species i	Species j	$k_{ij}^{(0)}$	$k_{ij}^{(1)}$
$H_2O_{(g)}$	$CO_{2(g)}$	0.195736	47.0126
$H_2O_{(g)}$	$H_2S_{(g)}$	0.239679	0
$CO_{2(g)}$	$H_2O_{(g)}$	0.195736	47.0126
$CO_{2(g)}$	$H_2S_{(g)}$	0.0865454	0
$H_2S_{(g)}$	$H_2O_{(g)}$	0.239679	0
$H_2S_{(g)}$	$CO_{2(g)}$	0.0865454	0

Since $\sum_{i=1}^{n}\sum_{j=1}^{n} y_i y_j \left(a_i a_j\right)^{0.5}(1-k_{ij}) = \sum_{i=1}^{n}\sum_{j=1}^{n} y_j y_i \left(a_j a_i\right)^{0.5}(1-k_{ji})$, therefore, $k_{ij} = k_{ji}$.

Table K-2

The critical temperature (T_c), the critical pressure (P_c), the attractive parameter (α), and the acentric factor (ω) for gaseous species in the H_2O-CO_2-H_2S gas mixture [241].

Species	T_c (K)[§]	P_c (atm)[†]	α[‡]	ω[*]
$CO_{2(g)}$	304.2	72.86	$[1+(0.480+1.574\omega-0.176\omega^2)(1-T_r^{0.5})]^2$	0.231
$H_2S_{(g)}$	373.4	88.527	$[1+(0.480+1.574\omega-0.176\omega^2)(1-T_r^{0.5})]^2$	0.0827
$H_2O_{(g)}$	647.14	217.755	$[1+1.318711(1-T_r^{0.5})+2.304407(1-T_r^{0.5})^2]^2$	0.348

T_r is reduced temperature (dimensionless) and equal to $T_r = T/T_c$
α for $H_2O_{(g)}$ does not depend on ω.
[§] [282,335,337]
[†] [336–338]
[‡] [241,248]
[*] [241,343]

Appendix L: Modified Pitzer Equations and the Corresponding Parameters for H_2O-NaCl-CO_2 Systems

The modified Pitzer semi-empirical equations for calculating activity coefficients of species in an aqueous solution in addition to the osmotic coefficient of water as solvent are listed below [139,142,143,136]:

$$
\begin{aligned}
ln\gamma_X^m = z_X^2 F &+ \sum_{c=1}^{N_c} m_c(2B_{cX} + ZC_{cX}) \\
&+ \sum_{a=1}^{N_a} m_a\left(2\Phi_{Xa} + \sum_{c=1}^{N_c} m_c\psi_{Xac}\right) \\
&+ \sum_{c=1}^{N_c-1}\sum_{c'=c+1}^{N_c} m_c m_{c'}\psi_{cc'X} + |z_X|\sum_{c=1}^{N_c}\sum_{a=1}^{N_a} m_c m_a C_{ca} \\
&+ 2\sum_{n=1}^{N_n} m_n\lambda_{nX} + 6\sum_{n=1}^{N_n}\sum_{c=1}^{N_c} m_n m_c \zeta_{ncX}
\end{aligned} \tag{L-1}
$$

$$
\begin{aligned}
ln\gamma_M^m = z_M^2 F &+ \sum_{a=1}^{N_a} m_a(2B_{Ma} + ZC_{Ma}) \\
&+ \sum_{c=1}^{N_c} m_c\left(2\Phi_{Mc} + \sum_{a=1}^{N_a} m_a\psi_{Mca}\right) \\
&+ \sum_{a=1}^{N_a-1}\sum_{a'=a+1}^{N_a} m_a m_{a'}\psi_{aa'M} + |z_M|\sum_{c=1}^{N_c}\sum_{a=1}^{N_a} m_c m_a C_{ca} \\
&+ 2\sum_{n=1}^{N_n} m_n\lambda_{nM} + 6\sum_{n=1}^{N_n}\sum_{a=1}^{N_a} m_n m_a \zeta_{Mna}
\end{aligned} \tag{L-2}
$$

$$ln\gamma_N^m = 2\sum_{n=1}^{N_n} m_n\lambda_{Nn} + 2\sum_{c=1}^{N_c} m_c\lambda_{Nc} + 2\sum_{a=1}^{N_a} m_a\lambda_{Na} + \sum_{c=1}^{N_c}\sum_{a=1}^{N_a} m_c m_a \zeta_{Nca} \tag{L-3}$$

$$\begin{aligned}(\emptyset - 1) = \frac{2}{\sum_i m_i}\Bigg\{ & -\frac{A_\phi I_m^{1.5}}{1 + bI_m^{0.5}} \\ & + \sum_{c=1}^{N_c}\sum_{a=1}^{N_a} m_c m_a \left(B_{ca}^{\varphi} + ZC_{ca}\right) \\ & + \sum_{c=1}^{N_c-1}\sum_{c'=c+1}^{N_c} m_c m_{c'}\left(\Phi_{cc'}^{\varphi} + \sum_{a=1}^{N_a} m_a \psi_{cc'a}\right) \\ & + \sum_{a=1}^{N_a-1}\sum_{a'=a+1}^{N_a} m_a m_{a'}\left(\Phi_{aa'}^{\varphi} + \sum_{c=1}^{N_c} m_c \psi_{aa'c}\right) \\ & + \sum_{n=1}^{N_n}\sum_{c=1}^{N_c} m_n m_c \lambda_{nc} + \sum_{n=1}^{N_n}\sum_{a=1}^{N_a} m_n m_a \lambda_{na} \\ & + \sum_{n=1}^{N_n}\sum_{c=1}^{N_c}\sum_{a=1}^{N_a} m_n m_c m_a \zeta_{nca}\Bigg\}\end{aligned} \tag{L-4}$$

$$a_{H_2O} = \exp\left(-\frac{M_{H_2O}\cdot\emptyset}{1000}\cdot\sum_i m_i\right) \tag{L-5}$$

In Equations (L-1) to (L-5)[118], X, a, and c' refer to anions, M, c, and c' refer to cations, and N and n refer to neutral species, i, z_i denote the species of interest and its

---

[118] Equation (L-4) is reported incorrectly in Li and Duan [136] and Kahyarian and Nesic [107] publications.

corresponding charge, N_a, N_c, and N_n are the total number of anions, cations, and neutral[119] species in the solutions, respectively, m is molality concentration, γ_i^m represents the molality-based activity coefficient of species i, M_{H_2O} is the molecular weight of pure water in g/mol, $\emptyset$ and a_{H_2O} are the molal osmotic coefficient and activity of water (both dimensionless), A_ϕ is the Debye-Huckel parameter for osmotic coefficient (explained in Appendix I), and b is equal to 1.2 (mol/kgH$_2$O)$^{-0.5}$ [277]. F, C_{MX}, and Z are defined in the following forms [142,143]:

$$F = -A_\phi\left(\frac{I_m^{0.5}}{1+bI_m^{0.5}}+\frac{2}{b}\ln(1+bI_m^{0.5})\right)+\sum_{c=1}^{N_c}\sum_{a=1}^{N_a} m_c m_a B'_{ca} \tag{L-6}$$

$$+\sum_{c=1}^{N_c-1}\sum_{c'=c+1}^{N_c} m_c m_{c'} \Phi'_{cc'} + \sum_{a=1}^{N_a-1}\sum_{a'=a+1}^{N_a} m_a m_{a'} \Phi'_{aa'}$$

$$C_{MX} = \frac{C_{MX}^{\varphi}}{2|z_M z_x|^{0.5}} \tag{L-7}$$

$$Z = \sum_i |z_i| m_i \tag{L-8}$$

I_m is the solution ionic strength in molality basis. $\sum m_i$ in Equations (L-4), (L-5), and (L-8) covers all species: cations, anions, and neutral [142]. Other parameters in Equations (L-1) to (L-7) are the Pitzer interaction parameters, which will be explained in the following text. A brief description and example(s) of each parameter are given in Table L-1.

---

[119] Neutral in the Pitzer equations includes all neutral species except the solvent. For example, in H$_2$O-NaCl-CO$_2$ system, the only neutrals species is CO$_{2(aq)}$.

Table L-1

A summary of Pitzer interaction parameters and examples for the H_2O-NaCl-CO_2 system [136,142,143].

Pitzer parameter	Virial coefficient order	Interactions between	Example(s)
B_{MX}, B_{MX}^{φ}, B'_{MX}	Second	cation-anion	H-Cl, Na-OH
C_{MX}^{φ}	Third	cation-anion	H-OH, H-HCO_3
θ_{ij}	Second	cation-cation, anion-anion	Na-H, OH-Cl, Cl-HCO_3
Φ_{ij}, Φ_{ij}^{φ}, Φ'_{ij}	Second	cation-cation, anion-anion	Na-H, Cl-HCO_3, HCO_3-CO_3
ψ_{ijk}	Third	cation-cation-anion, anion-anion-cation	H-Na-HCO_3, Cl-CO_3-Na
λ_{ni}	Second	neutral-cation, neutral-anion	CO_2-HCO_3, CO_2-Na, CO_2-H
ζ_{nij}	Third	neutral-cation-anion	CO_2-Na-Cl
λ_{Nn}	Second	neutral-neutral	CO_2-CO_2

M: cation; X: anion; N and n: neutral; i, j, and k: either cations or anions

The tree types of second order virial coefficients, B, are functions of ionic strength and are defined as follows [142,143]:

$$B_{MX}^{\phi} = \beta_{MX}^{(0)} + \beta_{MX}^{(1)} e^{-\alpha_1\sqrt{I_m}} + \beta_{MX}^{(2)} e^{-\alpha_2\sqrt{I_m}} \tag{L-9}$$

$$B_{MX} = \beta_{MX}^{(0)} + \beta_{MX}^{(1)} g\left(\alpha_1\sqrt{I_m}\right) + \beta_{MX}^{(2)} g\left(\alpha_2\sqrt{I_m}\right) \tag{L-10}$$

$$B'_{MX} = \beta_{MX}^{(1)} \frac{g'\left(\alpha_1\sqrt{I_m}\right)}{I_m} + \beta_{MX}^{(2)} \frac{g'\left(\alpha_2\sqrt{I_m}\right)}{I_m} \tag{L-11}$$

where, function g and g' are defined as below [142,143]:

$$g(x) = \frac{2(1-(1+x)e^{-x})}{x^2} \tag{L-12}$$

$$g(x) = -2\frac{\left(1-\left(1+x+\frac{x^2}{2}\right)e^{-x}\right)}{x^2} \tag{L-13}$$

With $x = \alpha_1\sqrt{I_m}$ or $x = \alpha_2\sqrt{I_m}$. If either of cation (M) or anion (X) is univalent (*e.g.*, Na-Cl and H-CO_3 pairs), $\alpha_1 = 2$. For 2-2 or higher valence pairs (*e.g.*, Ca-CO_3), $\alpha_1 = 1.4$. For all types of electrolytes, $\alpha_2 = 12$. The unit for α_1 and α_2 are $(\mathrm{mol/kgH_2O})^{-0.5}$ [143]. $\beta_{MX}^{(2)}$ value is considered zero for all the pairs in the H_2O-NaCl-CO_2 system [136].

The values of $\beta_{MX}^{(0)}$, $\beta_{MX}^{(1)}$ and C_{MX}^{φ} for the existing pairs in the H_2O-NaCl-CO_2 system are given in Table L-2 to Table L-7.

Table L-2

The Pitzer second virial parameter for the H-Cl pair.

c_i	$\beta^{(0)}$	$\beta^{(1)}$	C^{φ}
c_1	0.17690	0.2973	7.24e-4
c_2	-9.14e-2	16.147	0
c_3	0	-1.7631e-2	0
c_4	-4.034e-4	0	-6.072e-5
c_5	6.20e-5	7.20e-4	0

$\beta_{MX}^{(0)} = \beta_{XM}^{(0)}$, $\beta_{MX}^{(1)} = \beta_{XM}^{(1)}$, $C_{MX}^{\varphi} = C_{XM}^{\varphi}$, T in K, and P in MPa
$Par(T,P) = c_1 + c_2 \ln(\rho_w/997) + c_3(\rho_w - 997) + c_4(T - 298.15) + c_5(P - 1)$
ρ_w is the density of pure water in kg/m^3 at temperature T and pressure P (given in Appendix B).
The coefficients and the equation are taken from [344].
The c_5 values for $\beta^{(0)}$ and $\beta^{(1)}$ are reported incorrectly in the Pitzer [277] and in the Li and Duan publications [136] probably due to a confusion in unit conversation from MPa to bar. If their coefficients are used and the unit for pressure is in bar instead of MPa, the last term in the Par equation should be $(P - 10)$.

Table L-3

The Pitzer second virial parameter for the Na-Cl pair.

c_i	$\beta^{(0)}$	$\beta^{(1)}$	C^{φ}	c_i	$\beta^{(0)}$	$\beta^{(1)}$	C^{φ}
c_1	-6.5681518e2	1.1931966e2	-6.1084589e0	c_{12}	8.6340233e-10	0	8.6926600e-11
c_2	2.4869130e1	-4.8309327e-1	4.0217793e-1	c_{13}	-4.1785962e-13	0	0
c_3	5.3812753e-5	0	2.2902837e-5	c_{14}	-1.5793660e0	-4.2345814	3.5310414e-1
c_4	-5.5887470e-8	0	0	c_{15}	2.2022821e-3	0	-4.3314252e-4
c_5	6.5893263e-12	0	0	c_{16}	-1.3105503e-7	0	0
c_6	-4.4640952e0	0	-7.5354649e-1	c_{17}	-6.3813683e-11	0	0
c_7	1.1109914e-2	1.4068095e-3	1.5317673e-4	c_{18}	9.7065780e0	0	-9.1871455e-2
c_8	-2.6573399e-7	0	-9.0550901e-8	c_{19}	-2.6860396e-2	0	5.1904777e-4
c_9	1.7460070e-10	0	0	c_{20}	1.5344744e-5	0	0
c_{10}	1.0462619e-14	0	0	c_{21}	-3.2153983e-9	0	0
c_{11}	-5.3070129e-6	0	-1.5386008e-8				

$\beta_{MX}^{(0)} = \beta_{XM}^{(0)}$, $\beta_{MX}^{(1)} = \beta_{XM}^{(1)}$, $C_{MX}^{\varphi} = C_{XM}^{\varphi}$, T in K, and P in bar.
$Par(T) = c_1/T + c_2 + c_3P + c_4P^2 + c_5P^3 + c_6 \ln T + (c_7 + c_8P + c_9P^2 + c_{10}P^3)T + (c_{11} + c_{12}P + c_{13}P^2)T^2 + (c_{14} + c_{15}P + c_{16}P^2 + c_{17}P^3)/(T - 227) + (c_{18} + c_{19}P + c_{20}P^2 + c_{21}P^3)/(680 - T)$
The coefficients and the equation are taken from [345].
The c_6 value for C^{φ} is reported incorrectly in the Pitzer [277] and in the Li and Duan publications [136].

Table L-4

The Pitzer second virial parameter for the Na-OH pair.

c_i	$\beta^{(0)}$	$\beta^{(1)}$	C^{φ}	c_i	$\beta^{(0)}$	$\beta^{(1)}$	C^{φ}
c_1	2.7682478e2	4.6286977e2	-1.6686897e1	c_7	7.1788733e-6	0	-1.0553037e-6
c_2	-2.8131778e-3	0	4.0534778e-4	c_8	-4.0218506e-5	-1.0795894e-4	2.3765786e-6
c_3	-7.3755443e3	-1.0294181e4	4.5364961e2	c_9	-5.8847404e-9	0	8.9893405e-10
c_4	3.7012540e-1	0	-5.1714017e-2	c_{10}	1.1931122e1	0	-6.8923899e-1
c_5	-4.9359970e1	-8.5960581e1	2.9680772e0	c_{11}	2.4824963e0	0	-8.1156286e-2
c_6	1.0945106e-1	2.3905969e-1	-6.5161667e-3	c_{12}	-4.8217410e-3	0	0

$\beta_{MX}^{(0)} = \beta_{XM}^{(0)}$, $\beta_{MX}^{(1)} = \beta_{XM}^{(1)}$, $C_{MX}^{\varphi} = C_{XM}^{\varphi}$, T in K, and P in bar

$Par(T,P) = c_1 + c_2 P + (c_3 + c_4 P)/T + c_5 \ln T + (c_6 + c_7 P)T + (c_8 + c_9 P)T^2 + c_{10}/(T - 227) + (c_{11} + c_{12} P)/(647 - T)$

The coefficients and the equation are taken from [346].

c_2 value for $\beta^{(0)}$ is reported in incorrectly in the Li and Duan publication [136].

Table L-5

The Pitzer second virial parameter for the Na-CO_3 and the Na-HCO_3 pairs.

	Na-CO_3			Na-HCO_3		
c_i	$\beta^{(0)}$	$\beta^{(1)}$	C^{φ}	$\beta^{(0)}$	$\beta^{(1)}$	C^{φ}
c_1	5.153e-1	2.044e0	-9.14e-2	6.61e-2	-4.116e0	0
c_2	-5.991e-4	-4.303e-3	0	0	6.309e-3	0
c_3	0	0	0	0	9.240e2	0
c_4	-2.581e1	-2.545e1	6.482e0	0	-5.202e1	0
c_5	-2.659e0	3.618e2	8.048e0	0	-8.026e1	0
c_6	0	0	0	3.75951e-8	0	0
c_7	8.750e-5	0	-2.890e-5	0	1.634e-4	0
c_8	-2.660e-8	0	0	0	-1.390e-7	0

$\beta_{MX}^{(0)} = \beta_{XM}^{(0)}, \beta_{MX}^{(1)} = \beta_{XM}^{(1)}, C_{MX}^{\varphi} = C_{XM}^{\varphi}, T$ in K, and P in bar

$$Par(T,P) = c_1 + c_2 T + c_3/T + c_4/(T-210) + c_5/(647-T) + c_6(T-443)^3/3 + c_7(P-1) + c_8(P-1)^2/2$$

The coefficients and the equation are taken from [347].

Table L-6

The Pitzer second virial parameter, λ, for the CO_2-CO_2 and the CO_2-Na pairs and the Pitzer third virial parameter, ζ, for the CO_2-Na-Cl triplet.

c_i	$\lambda_{CO_2-CO_2}$	λ_{CO_2-Na}	$\zeta_{CO_2-Na-Cl}$
c_1	-8.603471564e-1	-2.739092216e-1	-1.665719188e-2
c_2	3.297141654e-3	7.399855859e-4	1.3916186e-6
c_3	6.309267405e1	5.55213285e1	0
c_4	-4.0989605e-6	0	0
c_5	1.529493614e1	0	0
c_6	6.506644253e-3	0	0
c_7	-9.63797714e-4	0	0
c_8	-3.238222665e-1	5.683638727e-3	-1.873812115e-3
c_9	1.599113719e-2	-8.009093476e-4	-1.577400757e-3
c_{10}	0	0	0
c_{11}	-1.8867333e-5	-1.74562027e-5	0

$\lambda_{NM} = \lambda_{MN}$, $\zeta_{NMX} = \zeta_{NXM} = \zeta_{MNX} = \zeta_{MXN} = \zeta_{XNM} = \zeta_{XMN}$, T in K, and P in bar

$\lambda_{CO_2-Cl} = 0$

$$Par(T,P) = c_1 + c_2T + c_3/T + c_4T^2 + c_5/(630-T) + c_6P + c_7PlnT + c_8P/T + c_9P/(630-T) + c_{10}P^2/(630-T)^2 + c_{11}TlnP$$

The coefficients and the equation are taken from [136].

Table L-7

The Pitzer second virial parameter for the CO2-HCO3 and the CO2-CO3 pairs.

c_i	$\lambda_{CO_2-Na} + \lambda_{CO_2-HCO_3}$
c_1	0.35284
c_2	-27.85446
c_3	19.56109

$\lambda_{NM} = \lambda_{MN}$, $\lambda_{NX} = \lambda_{XN}$, T in K, and P in bar
$\lambda_{CO_2-CO_3} = 2\lambda_{CO_2-HCO_3}$
$Par(T,P) = c_1 + c_2/(T-210) + c_3/(P-100)$
The coefficients and the equation are taken from [136].

All three types of Pitzer second virial coefficients, Φ are functions of ionic strength. The equations for these coefficients are given below:

$$\Phi_{ij}^{\varphi} = \theta_{ij} + {}^{E}\theta_{ij}(I_m) + I\,{}^{E}\theta'_{ij}(I_m) \tag{L-14}$$

$$\Phi_{ij} = \theta_{ij} + {}^{E}\theta_{ij}(I_m) \tag{L-15}$$

$$\Phi'_{ij} = {}^{E}\theta'_{ij}(I_m) \tag{L-16}$$

θ_{ij} coefficients are given in Table L-8. ${}^{E}\theta_{ij}$ and ${}^{E}\theta'_{ij}$ are a function of ionic strength and the electrolyte pair. Pitzer [348] proposed the following equations, using the cluster-integral method [349,350], for computing ${}^{E}\theta_{ij}$ and ${}^{E}\theta'_{ij}$:

$${}^{E}\theta_{ij} = \frac{z_i z_j}{4I_m}\left(J(x_{ij}) - \frac{1}{2}J(x_{ii}) - \frac{1}{2}J(x_{jj})\right) \tag{L-17}$$

$${}^{E}\theta'_{ij} = -\frac{{}^{E}\theta_{ij}}{I_m} + \frac{z_i z_j}{8I_m^2}\left(x_{ij}J'(x_{ij}) - \frac{1}{2}x_{ii}J'(x_{ii}) - \frac{1}{2}x_{jj}J'(x_{jj})\right) \tag{L-18}$$

where, x_{ij} is a dimensionless parameter defined to simplify the integration calculations:

$$x_{ij} = 6z_i z_j A^{\phi} I_m^{0.5} \tag{L-19}$$

${}^{E}\theta_{ij}$ and ${}^{E}\theta'_{ij}$ are zero for 1-1 pairs such as H-Na, OH-Cl, Cl-HCO_3. They become important for 2-1, 3-1, and 4-1 mixing pairs [277].

The integral function J and its derivative, J' can be calculated from one of the following equations [348]:

- If $0.1 \leq x_{ij} \leq 80$

$$J(x) = -\frac{x^2(lnx)e^{-10x^2}}{6} + \left(\sum_{k=1}^{6} c_k x^{-k}\right)^{-1} \tag{L-20}$$

$$J'(x) = \frac{xe^{-10x^2}\left((20x^2 - 2)\ln(x) - 1\right)}{6} + \frac{x^5 \sum_{k=1}^{6} k c_k x^{(6-k)}}{(\sum_{k=1}^{6} c_k x^{(6-k)})^2} \tag{L-21}$$

- For other x_{ij} values

$$J(x) = x[4 + c_1 x^{-c_2} \exp(-c_3 x^{c_4})]^{-1} \tag{L-22}$$

$$J'(x) = \frac{x^{c_2}\exp(c_3 x^{c_4})\,[4x^{c_2}\exp(c_3 x^{c_4}) + c_1 c_3 c_4 x^{c_4} + c_1 c_2 + c_1]}{[4x^{c_2}\exp(c_3 x^{c_4}) + c_1]^2} \tag{L-23}$$

The values for J and J' at different x_{ij} are given by Pitzer [348]. The derivative functions, J' are derived in this study. Other methods have been proposed for calculating the integral function J and its derivative [277]. The c_k coefficients in Equations (L-20) to (L-23) are listed in Table L-9.

The rest of Pitzer parameters needed to build the Li and Duan model for the H_2O-NaCl-CO_2 system are given in Table L-10.

Table L-8

The Pitzer second virial parameter, θ, for the OH-Cl and the H-Na pairs and the Pitzer third virial parameter, ψ, for the OH-Cl-Na and the H-Na-Cl triplets.

c_i	θ_{OH-Cl}	θ_{H-Na}	$\psi_{OH-Cl-Na}$	$\psi_{H-Na-Cl}$
1	1.10485703e-1	4.81363462e-2	1.27601977e1	-1.45623335e-2
2	0	0	3.66503385e-3	0
3	0	0	0	3.59308925
4	0	0	0	0
5	-4.93613455e1	-4.05430635	-3.55227032e2	0
6	0	0	-2.2105122	0
7	0	0	3.23085637e-3	0
8	0	0	-2.71988632e1	0

$\psi_{XXM} = \psi_{MXX} = \psi_{XMX}$, $\psi_{MMX} = \psi_{XMM} = \psi_{MXM}$, T in K, and P in bar.
$Par(T) = c_1 + c_2T + c_3T^2 + c_4T^3 + c_5/T + c_6lnT + c_7/(T - 263) + c_8/(680 - T)$
The coefficients and the equation are taken from [351].
The Par equation in the Li and Duan publication [136] is reported differently.

Table L-9

Coefficients used in Equations (L-20) to (L-23) *for calculating the integral function J and its derivative J'.*

k	c_k in Equations (L-20) and (L-21)	c_k in Equations (L-22) and (L-23)
1	4.118	4.581
2	7.247	0.7237
3	-4.408	0.0120
4	1.837	0.528
5	-0.251	N/A
6	0.0164	N/A

The coefficient are taken from [348].
The equations for J', the derivative of the integral function, are derived in this study.

Table L-10

A part of Pitzer parameters used in the Li and Duan model for the H_2O-NaCl-CO_2 system [136].

Parameter	Value	Parameter	Value	Parameter	Value
λ_{CO_2-H}	0	$\psi_{OH-Cl-H}$	0	$\psi_{HCO3-CO_3-Na}$[a]	0.002
λ_{CO_2-OH}	0	ψ_{OH-HCO_3-H}	0	ζ_{CO_2-H-OH}	0
θ_{OH-HCO_3}	0	ψ_{OH-HCO_3-Na}	0	ζ_{CO_2-H-Cl}	0
θ_{OH-CO_3}[a]	0.1	ψ_{OH-CO_3-H}	0	$\zeta_{CO_2-H-HCO_3}$	0
θ_{Cl-HCO_3}[b]	0.0359	ψ_{OH-CO_3-Na}[a]	-0.017	$\zeta_{CO_2-H-CO_3}$	0
θ_{Cl-CO_3}[b]	-0.053	ψ_{Cl-HCO_3-H}	0	$\zeta_{CO_2-Na-OH}$	0
$\theta_{HCO_3-CO_3}$[a]	-0.04	ψ_{Cl-HCO_3-Na}[b, c]	-0.0143	$\zeta_{CO_2-Na-HCO_3}$	0
$\psi_{H-Na-OH}$	0	ψ_{Cl-CO_3-H}	0	$\zeta_{CO_2-Na-CO_3}$	0
$\psi_{H-Na-HCO_3}$	0	ψ_{Cl-CO_3-Na}[c]	0.016		
$\psi_{H-Na-CO_3}$	0	$\psi_{HCO3-CO_3-H}$	0		

[a][142], [b][234], [c][169]

Appendix M: Revised Helgeson-Kirkham-Flowers (HKF) Equation of State for Aqueous Ions and Electrolytes

The revised HKF equation of state allows to calculate the apparent standard-state partial molal enthalpy ($\Delta_f \overline{H}^o$) and Gibbs free energy ($\Delta_f \bar{G}^o$) of an aqueous species at a specific pressure and temperature using the standard partial molal volume ($\bar{V}^o$), the standard partial molal constant pressure heat capacity ($\bar{C}_P^o$), and the standard partial molal entropy ($\bar{S}^o$) of that aqueous species [328–330]. Each of $\bar{V}^o$, $\bar{C}_P^o$, and $\bar{S}^o$ parameters has two parts: the solvation part and the nonsolvation part. The solvation part depends on the dielectric constant of water, the conventional Born coefficient, and the Born function Q. The nonsolvation part depends on the characteristic of individual aqueous species [328].

The revised HKF equation of state for $\Delta_f \bar{G}^o$ at pressure, P, and temperature, T, is defined as below [329]:

$$\Delta_f \bar{G}^o(T, P) \equiv \Delta_f \bar{G}^o_{P_r,T_r} + \bar{G}^o_{P,T} - \bar{G}^o_{P_r,T_r} \tag{M-1}$$

$$\bar{G}^o_{P,T} - \bar{G}^o_{P_r,T_r} = -\bar{S}^o_{P_r,T_r}(T - T_r) - c_1\left[T ln\left(\frac{T}{T_r}\right) - T + T_r\right] \tag{M-2}$$

$$- c_2\left\{\left[\left(\frac{1}{T-\Theta}\right) - \left(\frac{1}{T_r-\Theta}\right)\right]\left(\frac{\Theta - T}{\Theta}\right)\right.$$

$$\left. - \frac{T}{\Theta^2}\ln\left(\frac{T_r(T-\Theta)}{T(T_r-\Theta)}\right)\right\} + a_1(P - P_r)$$

$$+ a_2\ln\left(\frac{\Psi + P}{\Psi + P_r}\right)$$

$$+ \left(\frac{1}{T-\Theta}\right)\left[a_3(P - P_r) + a_4\ln\left(\frac{\Psi + P}{\Psi + P_r}\right)\right]$$

$$+ \omega_{P,T}\left(\frac{1}{\varepsilon} - 1\right) - \omega_{P_r,T_r}\left(\frac{1}{\varepsilon_{P_r,T_r}} - 1\right)$$

$$+ \ \omega_{P_r,T_r}Y_{P_r,T_r}(T - T_r)$$

where, $\Delta_f\bar{G}^o_{P,T}$ is the apparent standard partial molal Gibbs free energy of formation of an aqueous species at pressure P (bar) and temperature T (K) in cal/mol; P_r is a reference pressure (= 1 bar); T_r is a reference temperature (= 298.15 K); $\Delta_f\bar{G}^o_{P_r,T_r}$ is the standard partial molal Gibbs free energy of formation of the species from the elements in their stable form at P_r and T_r in cal/mol; $\bar{G}^o_{P,T} - \bar{G}^o_{P_r,T_r}$ corresponds to the difference in the standard partial molal Gibbs free energy of formation of an aqueous species at P and T and that at P_r and T_r in cal/mol, $\bar{S}^o_{P_r,T_r}$ is the standard partial molal entropy at P_r and T_r in cal/mol/K; c_i stands for temperature- and pressure- independent integral constants for the nonsolvation part ($\Delta\bar{C}^o_{P,n}$) of $\bar{C}^o_P$, a_i represents temperature- and -pressure independent integral constants for the nonsolvation part ($\Delta\bar{V}^o_n$) of $\bar{V}^o$, Θ is a temperature constant characteristic of solvent (= 228 K), Ψ is a pressure constant characteristic of solvent (=

2600 bar), $\omega_{P,T}$ is the conventional Born coefficient at P and T in cal/mol, ω_{P_r,T_r} is the conventional Born coefficient at P_r and T_r in cal/mol; ε is the relative permittivity of water at P and T; ε_{P_r,T_r} is the dielectric constant of water at P_r and T_r; and Y is one of the Born functions at P_r and T_r in 1/K [329].

In the MSE model proposed by Springer *et al.* [241], ω_{j,P_r,T_r} values are determined by regression of the experimental data. As explained in Appendix E, ω_j and ω_{j,P_r,T_r} values are equal. ω_{j,P_r,T_r} values for different species are listed in Table M-1. The dielectric of water (ε) can be calculated using the equations in Appendix D. Y_{P_r,T_r} is the Born function Y at P_r and T_r. The calculation procedure for the Born function Y is explained in Appendix F.

The apparent[120] standard-state[121] partial molal Gibbs free energy of species i ($\Delta_f \bar{G}_i^o$) is equal to the molality based standard-state chemical potential of species i [125]:

$$\mu_i^{o,m} = (\frac{\partial G}{\partial n_i})_{P,T,n_{j\neq i}} = \Delta_f \bar{G}_i^o \qquad \text{(M-3)}$$

---

[120] The partial differentiation in Equation (M-3) means adding one type of ions, while keeping constant the concentrations for all other ions. This is not physically possible. Therefore, it is not feasible to measure the properties of a single ion independent of other ions. Therefore, what is measured is always the sum of the properties of an anion and a cation. To get numerical values of the standard-state properties of single ions, the properties of one ion are given fixed values. By convention, the standard state chemical potential of the hydrogen ion H^+ is 0 J/mol [125]. Thus, the standard-state properties of other ions are called apparent.

[121] Standard-state means for pure ion i (mole fraction of ion i is equal to one). It is not possible to have "pure ion i". Therefore, the standard-state is a hypothetical state to have the same definition for all ions identical to that for water [125].

Table M-1

The HKF parameters for the H_2O-NaCl-CO_2-H_2S system.

Species	$\Delta_f \bar{G}^o_{P_r,T_r}$ (cal/mol)	$\bar{S}^o_{P_r,T_r}$ (cal/mol/K)	a_1 cal/mol/bar	a_2 cal/mol	a_3 cal·K/mol/bar	a_4 cal·K/mole	c_1 cal/mol/K	c_2 cal·K/mol	ω_{P_r,T_r} cal/mol	Ref
$H_3O^+_{(aq)}$	-56686.1855	16.7290	0.451232	-21.2711	-8.64735	20487	14.6773	16976	-13672.5	[241]
$Na^+_{(aq)}$	-62591	13.96	0.1839	-228.5	3.256	-27260	18.18	-29810	33060	[328]
$OH^-_{(aq)}$	-37595	-2.6	-0.03899	434.6	13.37	-57770	4.15	-103460	172460	[328]
$Cl^-_{(aq)}$	-31379	13.56	0.4032	480.1	5.563	-28470	-4.40	-57140	145600	[328]
$HCO^-_{3(aq)}$	-140282	23.53	0.75621	115.05	1.2346	-28266	12.9395	-47579	127330	[328]
$CO^{2-}_{3(aq)}$	-126191[a]	-11.95	0.28524	-398.44	6.4142	-26143	-3.3206	-171917	339140	[328]
$HS^-_{(aq)}$	2856[a]	16.3	0.50119	497.99	3.4765	-29849	3.42	-62700	144100	[328]
$S^{2-}_{(aq)}$	21957.8991[a]	-2.7	0.25121	-164.77	-2.5371	-27109	-6.41	-179770	329520	[241]
$CO_{2(aq)}$	-92250	28.1	1.08886	0	-24.7708	0	40.0325	88004	-2000	[241]
$H_2S_{(aq)}$	-6636.95	31.7	0.694808	0	0	0	34.5689	-25509	0	[241]

[a] This value is reported incorrectly in the Springer *et al.* publication [241].

Appendix N: Molal Gibbs Free Energy of Formation of Liquid Water

Since water acts as the solvent in aqueous systems, the apparent standard-state partial molal[122] Gibbs free energy of formation of liquid water cannot be calculated with the HKF equation of state (Appendix M), which is for dissolved aqueous species. The apparent molal Gibbs free energy of formation of liquid water ($\Delta_f \bar{G}_w^o$) from its elements at pressure, P, and temperature, T, can be calculated from the equation below:

$$\Delta_f \bar{G}_w^o(T,P) = [\Delta G_{triple} + \psi - S_{triple}(T - T_{triple}) + \frac{0.1P}{\rho_w} - P_{triple} \times V_{triple}]M_w \quad \text{(N-1)}$$

where, $\Delta_f \bar{G}_w^o$ is in J/mol. ΔG_{triple} corresponds to the standard-state Gibbs free energy of formation of liquid water from its elements in their stable form at 298.15 K and 1 bar ($\Delta_f \bar{G}_{w,P_r,T_r}^o$) minus the change in the Gibbs free energy of liquid water caused by increasing the temperature and pressure from 273.16 K and 0.006113 bar at the triple point[123] to those at standard conditions[124] ($G_{P_r,T_r} - G_{triple}$). ΔG_{triple} is equal to -13073 J/g. S_{triple} stands for the molal third law entropy of liquid water at the triple point (= 3.5144 J/g/K). T_{triple} is temperature at the triple point (= 273.16 K). P_{triple} is pressure at the triple point (= 0.006113 bar). V_{triple} is the volume of water at the triple point (= 0.10002 J/g/bar). P is pressure in bar. ρ_w is the density of water in g/cm^3 (Appendix B).

---

[122] Molar is usually used in the literature. However, in the Helgeson and Kirkham publication [321] molal is used instead. Both units transfer the same meaning, which is when 1 mole of water is added to the system.

[123] The triple point of a substance is the temperature and the pressure at which its three states of solid, liquid, and gas coexist in a thermodynamic equilibrium.

[124] $\Delta G_{triple} = \Delta_f \bar{G}_{P_r,T_r}^{o,w} - (G_{P_r,T_r} - G_{triple})$

M_w is the molecular weight of water (= 18.0153 g/mol) [321]. ψ is a Helmholtz free energy function in J/g, which has the following form [321]:

$$\psi = \psi_o + RT(ln\rho_w + \rho_w Q) \tag{N-2}$$

where, R is the gas constant (= 0.46151 J/g/K), T is temperature in K, Q is in cm^3/g and explained in Appendix B, and:

$$\psi_o = \left(\sum_{i=1}^{6} \frac{C_i}{\tau^{i-1}}\right) + C_7 lnT + \frac{C_8 lnT}{\tau} \tag{N-3}$$

where, $\tau = 1000/T$ (dimensionless) and C_i coefficients are listed in Table N-1 [321].

The apparent standard-state partial molal Gibbs free energy of formation of liquid water ($\Delta_f \bar{G}_w^o$) is identical to the standard-state mole-fraction based chemical potential of water, μ_w^o [125]:

$$\mu_w^o = (\frac{\partial G}{\partial n_w})_{P,T,n_{i\neq w}} = \Delta_f \bar{G}_w^o \tag{N-4}$$

It is noteworthy to mention that μ_w^o is identical to the molality based standard-state chemical potential of water ($\mu_w^{o,m}$).

Table N-1

C_i *coefficients used in Equation* (N-3) *for calculating the Helmholtz function* ψ_o [321].

C_i	Values	C_i	Values
C_1	1857.065	C_5	-20.5516
C_2	3229.12	C_6	4.85233
C_3	-419.465	C_7	46.0
C_4	36.6649	C_8	-1011.249

Appendix O: Unsymmetrical Chemical Potential (μ^*) and Unsymmetrical Activity Coefficient (γ^*)

The chemical potential of water (μ_w) is defined as follows:

$$\mu_w = \mu_w^o + RTln(x_w\gamma_w^x) \tag{O-1}$$

where, μ_w^o is the standard-state chemical potential of water[125], R is the gas constant, T is temperature, x_w is the mole fraction of water, and γ_w^x is the mole-fraction based activity coefficient. When x_w approaches 1, it follows that $\gamma_w^x = 1$[125]. The reference in this case is *pure water* reference state (or sometimes called *pure fused salt* reference state) [135,289].

For convenience, Equation (O-1) is applied to aqueous dissolved species as well:

$$\mu_i = \mu_i^o + RTln(x_i\gamma_i^x) \tag{O-2}$$

where, i is an arbitrary aqueous species, μ_i^o is the mole fraction based standard-state chemical potential of species i, x_i is the mole fraction of species i, and γ_i^x is the mole fraction-based activity coefficient of species i. Using the same reference state as that for water means that when x_i comes close to 1, $\gamma_i^x = 1$. However, this is not physically possible as pure aqueous species i does not exist. Thus, a different reference state is required for aqueous dissolved species to be able to use the same chemical potential definition for all components [125]. This reference state is *infinite dilution*. In this reference state, the activity coefficient of the arbitrary aqueous species i becomes 1 when

---

[125] Since water acts as the solvent in aqueous solutions, the thermodynamic relationships involving the chemical potential (μ_w), activity and activity coefficient (usually osmotic coefficient instead of activity coefficient in molality basis) are given in mole fraction basis [289]. The molality based standard-state chemical potential of water is equal to the mole fraction based standard-state chemical potential ($\mu_w^o = \mu_w^{o,m}$).

$x_i \rightarrow 0$ [125,289]. This can be achieved by normalizing the activity coefficient at a relevant concentration, γ_i^x, with the activity coefficient at infinite dilution, $\gamma_i^{x,\infty}$, and defining a new activity coefficient as below [125]:

$$\gamma_i^{x,*} = \frac{\gamma_i^x}{\gamma_i^\infty} \tag{O-3}$$

It is obvious that at infinite dilution $\gamma_i^{x,*} = 1$. $\gamma_i^{x,*}$ is called the (rational) unsymmetrical activity coefficient. The term “unsymmetrical” indicates that the activity coefficient has a value of 1 at infinite dilution rather than in the pure state. On the other hand, γ_i^x is called a “symmetrical” activity coefficient because it is equal to 1, when species i is hypothetically in its pure state ($x_i = 1$) [125].

The new activity coefficient, can be integrated into Equation (O-2) to fix the problem with the reference state and to be able to use a similar formulation for the chemical potential to that for water [125]:

$$\begin{aligned} \mu_i &= \mu_i^o + RTln(x_i\gamma_i^x) \qquad \text{(O-4)} \\ &= \mu_i^o + RTln\gamma_i^{x,\infty} + RTln(x_i\gamma_i^{x,*}) \\ &= \mu_i^{o,*} + RTln(x_i\gamma_i^{x,*}) \end{aligned}$$

where, the (rational) unsymmetrical mole fraction based standard-state chemical potential is defined by [125]:

$$\mu_i^{o,*} \equiv \mu_i^o + RTln\gamma_i^{x,\infty} \tag{O-5}$$

Appendix P: Conversion between Mole Fraction-Based Standard-State Chemical Potential ($\mu_i^{o,*}$) and Activity Coefficient ($\gamma_i^{x,*}$), Molality Based Standard-State Chemical Potential ($\mu_i^{o,m}$) and Activity Coefficient (γ_i^{m}), and Molarity-Based Standard State Chemical Potential ($\mu_i^{o,c}$) and Activity Coefficient (γ_i^{c})

The relation between mole fraction (x_i) and molality concentration (m_i) of the arbitrary dissolved species i can be written as below[126]:

$$x_i = \frac{n_i}{n_T} = \frac{n_i}{\sum_j n_j + n_w} = \frac{n_i}{\sum_j n_j + n_w} \times \frac{M_w}{M_w} = \frac{n_i M_w}{n_w M_w (1 + \frac{\sum_j n_j}{n_w})}$$

$$= \frac{m_i}{1000} \times \frac{M_w n_w}{n_w + \sum_j n_j} = \frac{m_i}{1000} \times M_w \times \frac{n_w}{n_w + \sum_j n_j} \qquad \text{(P-1)}$$

$$= \frac{m_i M_w x_w}{1000}$$

where, n_T is the total number of moles, n_i is the number of moles of species i, $\sum_j n_j$ is the total number of moles of dissolved species, n_w is the number of moles of water, and M_w is the molecular weight of water (= 18.015 g/mol).

The chemical potential (μ_i) of the arbitrary aqueous species i in infinite dilution reference state in the mole fraction (x_i) basis can be expressed as below:

$$\mu_i = \mu_i^{o,*} + RTln\left(x_i \gamma_i^{x,*}\right) \qquad \text{(P-2)}$$

where, $\mu_i^{o,*}$ is the unsymmetrical mole fraction based standard-state chemical potential and $\gamma_i^{x,*}$ is the unsymmetrical mole fraction-based activity coefficient of species i in dilute reference state[127].

---

[126] $m_i = \frac{1000 n_i}{n_w M_w}$

[127] See Appendix O for details about the derivation of unsymmetrical properties.

If molality concentration is introduced from Equation (P-1) into Equation (P-2), the following equations can be obtained:

$$\mu_i = \mu_i^{o,*} + RTln\left(x_i\gamma_i^{x,*}\right) \tag{P-3}$$

$$= \mu_i^{o,*} + RTln\left(\frac{m_i M_w x_w \gamma_i^{x,*}}{1000}\right)$$

$$= \mu_i^{o,*} + RTln\left(\frac{M_w m_o}{1000}\right) + RTln\left(\frac{m_i x_w \gamma_i^{x,*}}{m_o}\right)$$

where, $m_o = 1$ mol/g is added to the final equation to make the terms in the natural logarithm dimensionless. However, m_o is usually omitted from the equation for simplicity:

$$\mu_i = \mu_i^{o,*} + RTln\left(\frac{M_w}{1000}\right) + RTln\left(m_i x_w \gamma_i^{x,*}\right) \tag{P-4}$$

The unsymmetrical molality based activity coefficient of species i (γ_i^m) is defined as [125]:

$$\gamma_i^m \equiv x_w \gamma_i^{x,*} \tag{P-5}$$

and the molality based standard-state chemical potential of species i ($\mu_i^{o,m}$) is defined as:

$$\mu_i^{o,m} \equiv \mu_i^{o,*} + RTln\left(\frac{M_w m_o}{1000}\right)$$

$$= \mu_i^{o,*} + RTln\left(\frac{M_w}{1000}\right) \tag{P-6}$$

Plugging Equations (P-5) and (P-6) into Equation (P-4) allows to express μ_i in terms of molality based standard-state chemical potential and the molality base activity coefficient[128] [125]:

$$\begin{aligned} \mu_i &= \mu_i^{o,m} + RTln\left(\frac{m_i\gamma_i^m}{m_o}\right) \\ &= \mu_i^{o,m} + RTln(m_i\gamma_i^m) \end{aligned} \tag{P-7}$$

$\mu^{o,m}$ is usually reported in the literature as the standard-state chemical potential of electrolyte species [125]. Equation (P-6) can be presented in the opposite way to obtain $\mu_i^{o,*}$ from $\mu_i^{o,m}$ [241]:

$$\begin{aligned} \mu_i^{o,*} &= \mu_i^{o,m} + \ RTln\left(\frac{1000}{M_w m_o}\right) \\ &= \mu_i^{o,m} + \ RTln\left(\frac{1000}{M_w}\right) \end{aligned} \tag{P-8}$$

The molarity based standard chemical potential of species i ($\mu_i^{o,c}$) can be related to mole fraction and molality based standard-state chemical potentials using the following equations:

$$\begin{aligned} \mu_i^{o,c} &= \mu_i^{o,m} + \ RTln\left(\frac{1000c_o}{m_o}\frac{1}{\rho_w}\right) \\ &= \mu_i^{o,*} + \ RTln\left(\frac{\gamma_i^{\infty} M_w c_o}{1000\rho_w}\right) \end{aligned} \tag{P-9}$$

where, c_o is a factor to make the natural logarithm dimensionless and equal to 1 mol/lit, ρ_w is the density of in kg/lit, and γ_i^{∞} is the symmetrical pure liquid reference state at

---

[128] The chemical potential of a species is independent of the reference state and the concentration unit. Therefore, the chemical potential (μ_i) in the mole fraction basis is equal to that in the molality basis.

infinite dilution (see Equation (8-95) and Appendix O). The relationship between the molarity-based activity coefficient and the molality-based and the mole fraction-based activity coefficients is given below:

$$\begin{aligned} \gamma_i^c &= \frac{m_i \rho_w}{c_i} \gamma_i^m \\ &= \frac{m_i \rho_w}{c_i} x_w \gamma_i^{x,*} \end{aligned} \qquad \text{(P-10)}$$

where, c_i is the molarity concentration of species i, mol/lit.

Appendix Q: Chemical Potential of Pure Gas i in the Ideal Gas State ($\mu_i^{g(o)}$)

The molality based chemical potential of pure gas i in the ideal gas state, $\mu_i^{g(o)}$ can be computed by using the heat capacity at constant pressure (C_P) of pure gas i. C_P is commonly expressed by a virial equation as a function of temperature:

$$C_P = a + bT + \frac{c}{T^2} + dT^2 + eT^3 \tag{Q-1}$$

where, the virial coefficients are specific to individual gas species. C_P unit here is J/mol/K. The virial coefficients for CO_2 and H_2S gases are listed in Table Q-1. To calculate $\mu_i^{g(o)}$, which is equivalent to the Gibbs free energy of formation ($\Delta_f \bar{G}^o$), the two equations below are integrated [352]:

$$\left(\frac{\partial \bar{S}^o}{\partial T}\right)_P = \frac{C_P}{T} \tag{Q-2}$$

$$\left(\frac{\partial \Delta_f \bar{G}^o}{\partial T}\right)_P = -\bar{S}^o \tag{Q-3}$$

$\bar{S}^o$ obtained from the integration of Equation (Q-2) is implemented into Equation (Q-3) to calculate $\Delta_f \bar{G}^o$. The standard-state molar entropy ($\bar{S}^o_{P_r,T_r}$) and the standard-state molar Gibbs free energy of formation ($\Delta_f \bar{G}^o_{P_r,T_r}$) at 1 bar and 25°C listed in Table Q-1 are utilized to obtained the integration constants for Equations (Q-2) and (Q-3), respectively [352]. The integrated equations are presented in the footnote of Table Q-1.

Table Q-1

The standard-state molar Gibbs free energy of formation, the standard-state molar entropy, and the virial coefficients for the heat capacity at constant pressure for calculating the molar Gibbs free energy of formation of CO_2 *and* H_2S *gases* [241].

Gas	$\Delta_f \bar{G}^o_{P_r,T_r}$ J/mol	$\bar{S}^o_{P_r,T_r}$ J/mol/K	a J/mol/K	b J/mol/K^2	c J$\cdot K$/mol	d J/mol/K^3	e J/mol/K^4
$CO_{2(g)}$	-394360	213.783	26.2022	0.051162	-169772	-2.9058e-5	6.20044e-9
$H_2S_{(g)}$	-33560	205.79	25.1348	0.026135	133554	-5.72502e-6	0

Reference pressure, P_r, (= 1 bar), reference temperature, T_r, (= 298.15).

$$\bar{S}^o = alnT + bT - \frac{c}{2T^2} + \frac{dT^2}{2} + \frac{eT^3}{3} + \left(\bar{S}^o_{P_r,T_r} - alnT_r - bT_r + \frac{c}{2T_r^2} - \frac{dT_r^2}{2} - \frac{eT_r^3}{3}\right)$$

$$\mu_i^{g(o)} = \Delta_f \bar{G}^o = \Delta_f \bar{G}^o_{P_r,T_r} - aT(lnT - 1) - \frac{bT^2}{2} - \frac{c}{2T} - \frac{dT^3}{6} - \frac{eT^4}{12} - \left(\bar{S}^o_{P_r,T_r} - alnT_r - bT_r + \frac{c}{2T_r^2} - \frac{dT_r^2}{2} - \frac{eT_r^3}{3}\right)T$$

$$+ aT_r(lnT_r - 1) + \frac{bT_r^2}{2} + \frac{c}{2T_r} + \frac{dT_r^3}{6} + \frac{eT_r^4}{12} + \left(\bar{S}^o_{P_r,T_r} - alnT_r - bT_r + \frac{c}{2T_r^2} - \frac{dT_r^2}{2} - \frac{eT_r^3}{3}\right)T_r$$

The units for $\mu_i^{g(o)}$ and $\bar{S}^o$ are J/mol and J/mol/K, respectively.

Appendix R: The Thermodynamic Equilibrium Constants for Vapor/Liquid and Dissociation Equilibria in H₂O-CO₂-H₂S System

For the following vapor/liquid equilibria:

$$CO_{2(g)} \overset{K_{sol}^{CO_2}}{\longleftrightarrow} CO_{2(aq)} \tag{R-1}$$

$$H_2S_{(g)} \overset{K_{sol}^{H_2S}}{\longleftrightarrow} H_2S_{(aq)} \tag{R-2}$$

The equilibrium constants can be computed by:

$$K_{sol}^{CO_2} = \exp\left(\frac{\mu_{CO_{2(g)}}^{g(o)} - \mu_{CO_{2(aq)}}^{l(o),m}}{RT}\right) \tag{R-3}$$

$$= \frac{x_{CO_{2(aq)}}\gamma_{CO_{2(aq)}}^{x,*}}{Py_{CO_{2(g)}}\varphi_{CO_{2(g)}}} \cdot \frac{1000}{M_w}$$

$$K_{sol}^{H_2S} = \exp\left(\frac{\mu_{H_2S_{(g)}}^{g(o)} - \mu_{H_2S_{(aq)}}^{l(o),m}}{RT}\right) \tag{R-4}$$

$$= \frac{x_{H_2S_{(aq)}}\gamma_{H_2S_{(aq)}}^{x,*}}{Py_{H_2S_{(g)}}\varphi_{H_2S_{(g)}}} \cdot \frac{1000}{M_w}$$

where, $\mu_i^{l(o),m}$ and $\mu_i^{g(o)}$ are the molality based standard-state chemical potential of species i in the liquid phase and the molality based chemical potential of pure gas i in the ideal gas state, respectively. $\mu_i^{l(o),m}$ and $\mu_i^{g(o)}$calculations are explained in Appendices M, N, and Q. R is the gas constant (= 8.3145 J/mol/K), and T is temperature in K.

For the dissociation equilibria:

$$CO_{2(aq)} + 2H_2O_{(l)} \overset{K_1^{CO_2}}{\longleftrightarrow} H_3O_{(aq)}^+ + HCO_{3(aq)}^- \tag{R-5}$$

$$HCO_{3(aq)}^{-} + H_2O_{(l)} \overset{K_2^{CO_2}}{\longleftrightarrow} H_3O_{(aq)}^{+} + CO_{3(aq)}^{2-} \tag{R-6}$$

$$H_2S_{(aq)} + H_2O_{(l)} \overset{K_1^{H_2S}}{\longleftrightarrow} H_3O_{(aq)}^{+} + HS_{(aq)}^{-} \tag{R-7}$$

$$HS_{(aq)}^{-} + H_2O_{(l)} \overset{K_2^{H_2S}}{\longleftrightarrow} H_3O_{(aq)}^{+} + S_{(aq)}^{2-} \tag{R-8}$$

$$2H_2O_{(l)} \overset{K_w}{\leftrightarrow} H_3O_{(aq)}^{+} + OH_{(aq)}^{-} \tag{R-9}$$

The equations to calculate the equilibrium constants are as follows:

$$K_1^{CO_2} = \exp\left(\frac{\mu_{CO_{2(aq)}}^{l(o),m} + 2\mu_w^{l(o),m} - \mu_{H_3O_{(aq)}^{+}}^{l(o),m} - \mu_{HCO_{3(aq)}^{-}}^{l(o),m}}{RT}\right) \tag{R-10}$$

$$= \frac{\left(x_{H_3O_{(aq)}^{+}}\gamma_{H_3O_{(aq)}^{+}}^{x,*}\right)\cdot\left(x_{HCO_{3(aq)}^{-}}\gamma_{HCO_{3(aq)}^{-}}^{x,*}\right)}{\left(x_{CO_{2(aq)}}\gamma_{CO_{2(aq)}}^{x,*}\right)\cdot\left(x_w\gamma_w^{x,*}\right)^2}\cdot\frac{1000}{M_w}$$

$$K_2^{CO_2} = \exp\left(\frac{\mu_{HCO_3^{-}}^{l(o),m} + \mu_{H_2O}^{l(o),m} - \mu_{H_3O^{+}}^{l(o),m} - \mu_{CO_3^{2-}}^{l(o),m}}{RT}\right) \tag{R-11}$$

$$= \frac{\left(x_{H_3O_{(aq)}^{+}}\gamma_{H_3O_{(aq)}^{+}}^{x,*}\right)\cdot\left(x_{CO_{3(aq)}^{2-}}\gamma_{CO_{3(aq)}^{2-}}^{x,*}\right)}{\left(x_{HCO_{3(aq)}^{-}}\gamma_{HCO_{3(aq)}^{-}}^{x,*}\right)\cdot\left(x_w\gamma_w^{x,*}\right)}\cdot\frac{1000}{M_w}$$

$$K_1^{H_2S} = \exp\left(\frac{\mu_{H_2S_{(aq)}}^{l(o),m} + \mu_w^{l(o),m} - \mu_{H_3O_{(aq)}^{+}}^{l(o),m} - \mu_{HS_{(aq)}^{-}}^{l(o),m}}{RT}\right) \tag{R-12}$$

$$= \frac{\left(x_{H_3O_{(aq)}^{+}}\gamma_{H_3O_{(aq)}^{+}}^{x,*}\right)\cdot\left(x_{HS_{(aq)}^{-}}\gamma_{HS_{(aq)}^{-}}^{x,*}\right)}{\left(x_{H_2S_{(aq)}}\gamma_{H_2S_{(aq)}}^{x,*}\right)\cdot\left(x_w\gamma_w^{x,*}\right)}\cdot\frac{1000}{M_w}$$

$$K_2^{H_2S} = \exp\left(\frac{\mu_{HS^-_{(aq)}}^{l(o),m} + \mu_w^{l(o),m} - \mu_{H_3O^+_{(aq)}}^{l(o),m} - \mu_{S^{2-}_{(aq)}}^{l(o),m}}{RT}\right) \tag{R-13}$$

$$= \frac{\left(x_{H_3O^+_{(aq)}}\gamma_{H_3O^+_{(aq)}}^{x,*}\right)\cdot\left(x_{S^{2-}_{(aq)}}\gamma_{S^{2-}_{(aq)}}^{x,*}\right)}{\left(x_{HS^-_{(aq)}}\gamma_{HS^-_{(aq)}}^{x,*}\right)\cdot\left(x_w\gamma_w^{x,*}\right)}\cdot\frac{1000}{M_w}$$

$$K_w = \exp\left(\frac{2\mu_w^{l(o),m} - \mu_{H_3O^+}^{l(o),m} - \mu_{OH^-_{(aq)}}^{l(o),m}}{RT}\right) \tag{R-14}$$

$$= \frac{\left(x_{H_3O^+_{(aq)}}\gamma_{H_3O^+_{(aq)}}^{x,*}\right)\cdot\left(x_{OH^-_{(aq)}}\gamma_{OH^-_{(aq)}}^{x,*}\right)}{\left(x_w\gamma_w^{x,*}\right)^2}\cdot\left(\frac{1000}{M_w}\right)^2$$

The $\frac{1000}{M_w}$ term comes into the equations when the chemical potentials are converted from mole fraction basis to molality basis according to Equation (P-6). $\mu_i^{l(o),m}$ calculation is explained in Appendices M and N.

Appendix S: Derivation of Long-Range Contribution of Mole-Fraction Based Activity Coefficient ($\boldsymbol{\gamma_{LR}^{x}}$) from Excess Gibbs Free Energy ($\boldsymbol{G_{LR}^{E}}$)

Pitzer [141] proposed the following equation for the contribution of long-range electrostatic ionic interactions to the excess Gibbs free energy:

$$\frac{G_{i,LR}^{E}}{RT} = -\left(\sum_{i} n_i\right)\left(\frac{1000}{M_w}\right)^{\frac{1}{2}}\left(\frac{4A_{\phi}I_x}{\rho}\right)\ln\left(1+\rho I_x^{\frac{1}{2}}\right) \tag{S-1}$$

Using A_{ϕ} and A_x conversion by Equation (I-5), the above equation can be written as below:

$$\frac{G_{i,LR}^{E}}{RT} = -\left(\sum_{i} n_i\right)\left(\frac{4A_xI_x}{\rho}\right)\ln\left(1+\rho I_x^{\frac{1}{2}}\right) \tag{S-2}$$

Equation (S-2) is in symmetrical pure liquid reference state, *i.e.*, when x_i approaches 1, $I_x = 0$, and therefore, $G_{i,LR}^{E} = 0$. To switch to an infinitely dilute reference state as it is desirable for electrolyte solutions ($x_i \to 0$, $\gamma_i = 1$) , the natural logarithm expression on the right-hand side of Equation (S-2) is divided (normalized) by $\sum_k x_k\,[1+\rho\left(I_{x,k}^{o}\right)^{\frac{1}{2}}]$ factor [135,289]:

$$\frac{G_{i,LR}^{E}}{RT} = -\left(\sum_{i} n_i\right)\left(\frac{4A_xI_x}{\rho}\right)\ln\left(\frac{1+\rho I_x^{\frac{1}{2}}}{\sum_k x_k\left[1+\rho\left(I_{x,k}^{o}\right)^{\frac{1}{2}}\right]}\right) \tag{S-3}$$

where, $I_{x,i}^{o}$ is the ionic strength of the system in pure condition and $I_{x,i}^{o} = (1/2)z_i^2$.

Following Equation (8-78) and taking the derivative of Equation (S-3) with respect to n_i gives:

$$ln\gamma_i^x = \left(\frac{\partial \frac{G_{i,LR}^E}{RT}}{\partial n_i}\right)_{T,P.n_{j\neq i}} \tag{S-4}$$

$$= -A_x\left[\frac{2z_i^2}{\rho}\ln\left(\frac{1+\rho I_x^{\frac{1}{2}}}{\sum_k x_k\left[1+\rho\left(I_{x,k}^0\right)^{\frac{1}{2}}\right]}\right)+\frac{I_x^{\frac{1}{2}}(z_i^2-2I_x)}{1+\rho I_x^{\frac{1}{2}}}\right]$$

$$-\frac{4A_xI_x}{\rho}\left\{\ln\left(\frac{1+\rho I_x^{\frac{1}{2}}}{\sum_k x_k\left[1+\rho\left(I_{x,k}^0\right)^{\frac{1}{2}}\right]}\right)\left(\sum_l n_l\right)\left[\frac{1}{2d_s}\frac{\partial d_s}{\partial n_i}-\frac{3}{2\varepsilon_s}\frac{\partial \varepsilon_s}{\partial n_i}\right]\right.$$

$$\left.-\frac{1+\rho\left(I_{x,i}^0\right)^{\frac{1}{2}}}{\sum_k x_k\left[1+\rho\left(I_{x,k}^0\right)^{\frac{1}{2}}\right]}+1\right\}$$

where, d_s is the molar density of solution in mol/m^3 and ε_s is the dielectric constant of solution [135]. ε_s can be obtained from a formulation proposed by Wang and Anderko [353].

The following two equations assist in performing the derivation of Equation (S-3):

$$\frac{\partial G_{i,LR}^E/RT}{\partial n_i} = \frac{G_{i,LR}^E/RT}{\frac{\partial n_i}{\sum_i n_i}\cdot\sum_i n_i} = \frac{G_{i,LR}^E/RT}{\partial x_i}\cdot\frac{1}{\sum_i n_i} \tag{S-5}$$

$$\frac{\partial I_x}{\partial n_i} = \frac{\partial I_x}{\partial x_i}\cdot\frac{1}{\sum_i n_i} = (\frac{1}{2}z_i^2 - I_x)\cdot\frac{1}{\sum_i n_i} \tag{S-6}$$

In this study, it is assumed that d_s and ε_s are for pure water and do not change with solution composition. Therefore, A_x does not change with solution composition and Equation (S-4) reduces to Equation (8-81).

Appendix T: Calculation of pH Based on Hydronium Ion ($\boldsymbol{H_3O^+_{(aq)}}$) Concentration

For the following reaction:

$$H_3O^+_{(aq)} \leftrightarrow H^+_{(aq)} + H_2O_{(l)} \tag{T-1}$$

It is assumed that the molar Gibbs free energy of reaction ($\Delta_r\bar{G}$) is equal to zero.

Therefore:

$$a^{x,*}_{H_3O^+_{(aq)}} = a^{x,*}_{H^+_{(aq)}} a^{x,*}_{w} \tag{T-2}$$

Where, $a^{x,*}_{H_3O^+_{(aq)}}$, $a^{x,*}_{H^+_{(aq)}}$, and $a^{x,*}_{w}$ are the mole fraction based activity of $H_3O^+_{(aq)}$, $H^+_{(aq)}$, and water in infinitely dilute reference state, respectively.

The activity of $H^+_{(aq)}$ in molality basis ($a^{m}_{H^+_{(aq)}}$) is related to $a^{x,*}_{H^+_{(aq)}}$ by:[129]

$$a^{m}_{H^+_{(aq)}} = \frac{1000 a^{x.*}_{H^+_{(aq)}}}{M_w} \tag{T-3}$$

where, M_w is the molecular weight of water in g/mol. Combining Equations (T-2) and (T-3) results in:

$$a^{m}_{H^+_{(aq)}} = \frac{1000}{M_w} \cdot \frac{a^{x,*}_{H_3O^+_{(aq)}}}{a^{x}_{w}} \tag{T-4}$$

The definition of pH is as follows:

$$pH \equiv -log_{10}\left(a^{m}_{H^+_{(aq)}}\right) \tag{T-5}$$

Plugging Equation (T-4) into Equation (T-5) provides the pH equation with respect to $H_3O^+_{(aq)}$ activity:

---

[129] From Equations (P-1) and (P-5) in Appendix P, $x_{H^+} = m_{H^+}M_w x_w/1000$ and $\gamma^{x,*}_{H^+} = \gamma^{m}_{H^+}/x_w$. Multiplying these two equations gives Equation (T-3).

$$pH = -log_{10}\left(\frac{a^{x,*}_{H_3O^+_{(aq)}}}{a^{x,*}_{w}}\right) - log_{10}\left(\frac{1000}{M_w}\right) \tag{T-6}$$

$$= -log_{10}\left(\frac{x_{H_3O^+_{(aq)}}\gamma^{x,*}_{H_3O^+_{(aq)}}}{x_w\gamma^{x,*}_{w}}\right) - log_{10}\left(\frac{1000}{M_w}\right)$$

Appendix U: Cathodic Limiting Current Density in Strong Acid Aqueous Solutions

In strong acid aqueous corrosion, the main cathodic reaction is the H$^+$ ion reduction reaction. Unlike weak acid corrosion, no homogenous chemical reaction is involved in the cathodic reaction in strong acid corrosion. The overall cathodic reaction in strong acid corrosion has the following form:

$$H^+_{(aq)} + e^- \rightarrow \frac{1}{2} H_{2(\mathrm{g})} \tag{U-1}$$

In the limiting current density situations, which usually occur at high temperatures and/or high solution pH values, the rate of H$^+$ ion reduction reaction is controlled only by diffusion of H$^+$ ions from the bulk to the surface. The diffusion occurs due to a chemical potential gradient between the bulk solution and the metal surface. As explained in Chapter 2, the rate of diffusion of species i in the absence of convection can be expressed in terms of a flux density (N) in mol/m^2/s as follows:

$$N_i = -u_i c_i \nabla \mu_i \tag{U-2}$$

where, u_i is the mobility of species i in m^2·mol/J/s, c_i is the concentration of species i in mol/m^3,and μ_i is the chemical potential of species i J/mol. Since aqueous corrosion occurs uniformly across the metal surface, the gradient (∇) of chemical potential for two directions (assume y and z) parallel to the metal surface will be zero. Therefore, Equation (U-2) can be written in one dimensional domain in x direction, normal to the metal surface.

$$N_i = -u_i c_i \frac{d\mu_i}{dx} \tag{U-3}$$

Expanding the chemical potential term gives [20]:

$$N_i = -u_i c_i \frac{d}{dx}\left(\mu_i^o + RTln(\gamma_i^c c_i)\right) \tag{U-4}$$

$$= -u_i c_i \frac{RT}{\gamma_i^c c_i}\frac{d}{dx}(\gamma_i^c c_i)$$

$$= -u_i \frac{RT}{\gamma_i^c}\frac{d}{dx}(\gamma_i^c c_i)$$

where, γ_i^c is the molarity-based activity coefficient of species i in the infinite dilution reference state (Appendix P), μ_i^o is the molarity based standard-state chemical potential of species i. According to Nernst-Einstein equation, the $u_i RT$ term is equal to the diffusion coefficient D_i (in m^2/s) [20]. The $\gamma_i^c c_i$ term is equal to activity of species i (a_i) in mol/m^3. Thus, the flux density transforms to the final form of:

$$N_i = -\frac{D_i}{\gamma_i^c}\frac{da_i}{dx} \tag{U-5}$$

Then, the conservation of mass (the Nernst-Planck equation) at steady-state conditions can be used across a diffusion boundary layer to calculate the H$^+$ ion reduction reaction limiting current density. The Nernst-Plank equation in the steady-state conditions in one dimensional domain in x direction is as follows [21]:

$$-\frac{dN_i}{dx} + R_i = 0 \tag{U-6}$$

where, the first term indicates the net input rate of species i into the diffusion boundary layer, and R_i denotes the rate at which species i produced by a homogenous chemical reaction in mol/m^3/s.

Since, there is no chemical reaction in strong acid corrosion, R_i in Equation (U-6) is equal to zero[130]. Plugging Equation (U-5) into Equation (U-6) and change species i to H^+ ion give:

$$-\frac{d}{dx}\left(-\frac{D_{H^+_{(aq)}}}{\gamma^c_{H^+_{(aq)}}}\frac{da_{H^+_{(aq)}}}{dx}\right)=0 \tag{U-7}$$

$D_{H^+_{(aq)}}$ and $\gamma^c_{H^+_{(aq)}}$ are assumed to be constant in the diffusion boundary layer. Equation (U-7) can be solved analytically by using appropriate boundary conditions as follows:

At the metal surface ($x = 0$),

$$a_{H^+_{(aq)}} = a_{H^+_{(aq),s}} \tag{U-8}$$

where, $a_{H^+_{(aq),s}}$ is the activity of H^+ ion at the surface;

And, at the edge of diffusion boundary layer for H^+ ion ($x = \delta_{m,H^+}$):

$$a_{H^+_{(aq)}} = a_{H^+_{(aq),b}} \tag{U-9}$$

where, $a_{H^+_{(aq),b}}$ is the equilibrium activity of H^+ ion in the bulk solution. δ_{m,H^+} unit is in m.

Integrating Equation (U-7) two times with respect to x and applying the boundary conditions:

$$a_{H^+_{(aq)}} = \left(\frac{a_{H^+_{(aq),b}} - a_{H^+_{(aq),s}}}{\delta_{m,H^+}}\right)x + a_{H^+_{(aq),s}} \tag{U-10}$$

---

[130] The contribution of water dissociation reaction in producing H^+ ion is negligible ($K_{H_2O} \cong 10^{-14}$ at 25°C), and therefore it is ignored in the calculations. Consequently, the activities of $H_2O_{(l)}$ and OH^- ion are assumed to be zero in the diffusion boundary layer.

Then, the net flux density of H$^+$ ion ($H^+_{(aq)}$) can be obtained by using Equations (U-5) and (U-10):

$$N_{H^+_{(aq)}} = -\frac{D_{H^+_{(aq)}}}{\gamma^c_{H^+_{(aq)}}}\left(\frac{a_{H^+_{(aq),b}} - a_{H^+_{(aq),s}}}{\delta_{m,H^+}}\right) \tag{U-11}$$

The H$^+$ ion flux density is related to the current density by the equation below [21,354][131]:

$$i = -nFN_{H^+_{(aq)}} \tag{U-12}$$

where, n is the number of electron transferred in H$^+$ ion reduction (= 1) and F is the Faraday's constant (= 96485.33 C/mol).

In limiting current controlling situations, the activity of H$^+$ ion at the metal surface approaches zero ($a_{H^+_{(aq),s}} \approx 0$) as all the H$^+$ ions arrive at the metal surface by slow diffusion are consumed almost instantaneously at the surface by a fast charge transfer process. Therefore, the current density at the surface in these situations is called the limiting current density (i_{Lim}) and is equal to:

$$i_{Lim} = \frac{FD_{H^+_{(aq)}}}{\gamma^c_{H^+_{(aq)}}}\frac{a_{H^+_{(aq),b}}}{\delta_{m,H^+}} \tag{U-13}$$

Equation (U-13) can be written in the following form if $\gamma^c_{H^+_{(aq)}}$ is removed from the equation:

$$i_{Lim} = FD_{H^+_{(aq)}}\frac{c_{H^+_{(aq),b}}}{\delta_{m,H^+}} \tag{U-14}$$

---

[131] The general equation is explained in Chapter 2. Since H$^+$ is consumed at the surface, i and N are opposite in sign [354].

where, i_{Lim} is in A/m^2, F is the Faraday's constant (= 96485.33 C/mol), $D_{H^+_{(aq)}}$ is m^2/s, $a_{H^+_{(aq),b}}$ and $c_{H^+_{(aq),b}}$ are in mol/m^3, $\gamma^c_{H^+_{(aq)}}$ is dimensionless, and δ_{m,H^+} is in m. A factor of 1000 needs to be multiplied to the right-hand side of Equations (U-13) and (U-14) for the molarity unit.

Appendix V: Cathodic Limiting Current Density in CO_2 Saturated Aqueous Solutions

Accurate calculation of the limiting current density becomes important in CO_2 corrosion, when the rate of the CO_2 corrosion process is close to the limiting current density. This occurs more at high pH values (> pH 5) and/or high temperatures. Examples were shown in Figure 10-42 for CO_2 corrosion experiments at pH 5 and 50^oC and 80^oC.

In CO_2-saturated solutions, dissolved $CO_{2(aq)}$ reacts with water and forms carbonic acid according to:

$$CO_{2(aq)} + H_2O_{(l)} \underset{k_{b,CO_2}}{\overset{k_{f,CO_2}}{\rightleftarrows}} H_2CO_{3(aq)} \tag{V-1}$$

$H_2CO_{3(aq)}$ subsequently dissociates partially through a relatively fast reaction and forms bicarbonate:

$$H_2CO_{3(aq)} \underset{k_{b,H_2CO_3}}{\overset{k_{f,H_2CO_3}}{\rightleftarrows}} HCO^-_{3(aq)} + H^+_{(aq)} \tag{V-2}$$

$HCO^-_{3(aq)}$ is a much weaker acid ($K_{HCO_3^-} \approx 10^{-11}$ M at 25^oC) compared to $H_2CO_{3(aq)}$ (with a ($K_{H_2CO_3} \approx 3 \times 10^{-5}$ M at 25^oC), so its dissociation and its contribution in buffering in aqueous CO_2 solutions can be ignored.

The H^+ ions, produced by the homogenous dissociation Reaction (V-2), diffuse to the metal surface:

$$H^+_{(aq)} \xrightarrow{diffusion} H^+|_{surface} \tag{V-3}$$

where they are reduced to evolve dissolved hydrogen gas according to:

$$H^+|_{surface} + e^- \rightarrow \frac{1}{2} H_{2(g)} \quad \text{(V-4)}$$

The overall hydrogen evolution reaction in aqueous CO_2 solution is then obtained as a summation of all these steps:

$$CO_{2(aq)} + H_2O_{(l)} + e^- \rightarrow HCO^-_{3(aq)} + \frac{1}{2} H_{2(g)} \quad \text{(V-5)}$$

In the past, it was assumed that in addition to the hydrogen ion reduction Reaction (V-4), there is a parallel hydrogen evolution reaction— the so-called direct reduction of carbonic acid:

$$H_2CO_{3(aq)} + e^- \rightarrow HCO^-_{3(aq)} + \frac{1}{2} H_{2(g)} \quad \text{(V-6)}$$

As mentioned in the main text in Section 5.2.2, the direct reduction of carbonic acid is shown to be insignificant in aqueous CO_2 corrosion. The main cathodic reaction in saturated CO_2 solutions is the H^+ ion reduction Reaction (V-4) and $H_2CO_{3(aq)}$ only acts as a source of H^+ ions for the main cathodic reaction. Therefore, the simple method of assuming two limiting current densities [96,212,355] (one for the H^+ ion reduction reaction and one for the direct reduction of $H_2CO_{3(aq)}$) for calculating the total limiting current density in CO_2 corrosion does not agree with the recent theories [213,356,214,208].

To be able to calculate the total limiting current density with only one reaction (H^+ ion reduction reaction), it is necessary to account simultaneously for co-diffusion of all participating species and the buffering by chemical Reactions (V-1) and (V-2) in the mass transfer boundary layer. This requires solving a system of six nonlinear differential equations for six species[132]: H^+ ion, $H_2CO_{3(aq)}$, HCO_3^- ion, $CO_{2(aq)}$, OH^- ion and $H_2O_{(l)}$, which involves complex numerical computations as reported in similar studies by Remita *et al.* [213], Tran *et al.* [214], and Kahyarian *et al.* [207,208]. Additionally, the numerical method does not result in an explicit expression for the limiting current density. However, with some assumptions the calculations can become much simpler and the total limiting current density can be expressed as explicit expressions.

The assumptions made here for calculating the cathodic H^+ ion reduction reaction limiting current density in CO_2-saturated aqueous solutions are as follows:

1. Mass transfer by convection can be ignored as the aqueous solution is chemically and thermally uniform.
2. Mass transfer by migration can be ignored as there is no external electrical field in naturally occurring corrosion. And, according to the mixed potential theory no potential gradient exists over the metal surface in natural uniform corrosion that causes migration of species.
3. Diffusion only occurs in one-dimensional along the x-axis perpendicular to the metal surface. The diffusion in the other two directions is considered zero.
4. The activities of water ($a_{H_2O_{(l)}}$) and aqueous carbon dioxide ($a_{CO_{2(aq)}}$) are constant across the mass transfer (diffusion) boundary layer and equal to the equilibrium bulk values.

$$a_{H_2O_{(l)}} \approx a^{eq}_{H_2O_{(l)},b} \equiv \ constant \qquad \text{(V-7)}$$

---

[132] CO_3^{2-} ion can be ignored as its activity is very small in conditions encountered in aqueous CO_2 corrosion.

$$a_{CO_{2(aq)}} \approx a^{eq}_{CO_{2(aq)},b} \equiv \ constant \tag{V-8}$$

This means that diffusion of $H_2O_{(l)}$ and $CO_{2(aq)}$ can be ignored in the calculations.

5. The activity of the bicarbonate, $a_{HCO^-_{3(aq)}}$ ion in the mass transfer boundary layer is constant and equal to the equilibrium bulk value.

$$a_{HCO^-_{3(aq)}} \approx a^{eq}_{HCO^-_{3(aq)},b} \equiv \ constant \tag{V-9}$$

This assumption may seem unreasonable, as from the dissociation Reaction (V-2) for every $H_2CO_{3(aq)}$ consumed, one H^+ ion and one $HCO^-_{3(aq)}$ are produced or vice versa. Therefore, any changes in their activities because of Reactions (V-2) must be the same:

$$|\Delta a_{H_2CO_3}| = |\Delta a_{HCO_3^-}| = |\Delta a_{H^+}| \tag{V-10}$$

However, substantial amount of dissolved CO_2 exists in the solution that pushes Reactions (V-1) and (V-2) to the right and since the latter is much faster than the former, most of $H_2CO_{3(aq)}$ molecules are converted to $HCO^-_{3(aq)}$. Thus, $a_{HCO^-_{3(aq)}}$ is considerably higher than $a_{H_2CO_{3(aq)}}$. Moreover, in the limiting current density controlling situations, the solution pH in the mass transfer boundary layer is always higher than pH 7 due to the fast consumption of H^+ ion at the metal surface. This indicates that $a_{H^+_{(aq)}}$ is very small. Consequently, $a_{HCO^-_{3(aq)}}$ is much larger than both $a_{H^+_{(aq)}}$ and $a_{H_2CO_{3(aq)}}$ in the mass transfer boundary layer. Therefore, for any given change in the activity (Δa),

$$\frac{|\Delta a_{HCO_3^-}|}{a_{HCO_3^-}} \ll \frac{\Delta a_{H^+}}{a_{H^+}} \tag{V-11}$$

$$\frac{|\Delta a_{HCO_3^-}|}{a_{HCO_3^-}} \ll \frac{\Delta a_{H_2CO_3}}{a_{H_2CO_3}} \tag{V-12}$$

So, the assumption about $a_{HCO_3^-}$ being constant in the mass transfer boundary layer is reasonably accurate. This assumption allows to ignore the contribution of $\mathrm{HCO_{3(aq)}^-}$ ion diffusion in the i_{Lim} calculation process.

6. Similar to assumption # 5, due to the high solution pH in the mass transfer boundary layer in the limiting current density controlling situations, the activity of OH$^-$ ion ($a_{OH^-_{(aq)}}$) is relatively high there as well, and its variation, and thereby its diffusion can be ignored in the calculations.
7. The dissociation Reaction (V-2) is near equilibrium in the mass transfer boundary layer as it is much faster than the CO_2 hydration Reaction (V-1).
8. $D_{H^+_{(aq)}}$ and $D_{H_2CO_{3(aq)}}$ are constant throughout the mass transfer boundary layer.
9. $\gamma^c_{H^+}$ and $\gamma^c_{H_2CO_3}$ are constant throughout the mass transfer boundary layer.

Consequently, only two species remain that their activities change in the mass transfer boundary layer: H$^+$ ion and $H_2CO_{3(aq)}$. The limiting current density can be calculated by solving the steady-state one-dimensional Nernst-Planck (mass conservation) equations [21] for the two remaining species as follows:

$$\frac{d}{dx}\left(\frac{D_{H^+}}{\gamma^c_{H^+}}\frac{\partial a_{H^+}}{\partial x}\right) + k_{f,H_2CO_3}\, a_{H_2CO_3} - k_{b,H_2CO_3}\, a_{H^+} a_{HCO_3^-} = 0 \tag{V-13}$$

$$\frac{d}{dx}\left(\frac{D_{H_2CO_3}}{\gamma^c_{H_2CO_3}}\frac{\partial a_{H_2CO_3}}{\partial x}\right) + k_{f,CO_2}\, a_{CO_2} a_{H_2O} - k_{b,CO_2} a_{H_2CO_3} - k_{f,H_2CO_3}\, a_{H_2CO_3} + k_{b,H_2CO_3}\, a_{H^+} a_{HCO_3^-} = 0 \tag{V-14}$$

The first terms in parentheses in both equations account for the molecular diffusion, while the other terms are related to production and consumption of species by the two chemical reactions. The use of activity and activity coefficient instead of concentration in the Nernst-Planck equation has been already explained in Appendix U. γ^c is the molarity-based activity coefficient in infinite dilution reference state (Appendix P).

The first step to solve Equations (V-13) and (V-14) simultaneously is to add them up, so that some of the chemical reaction kinetic terms cancel out:

$$\frac{d}{dx}\left(\frac{D_{H^+}}{\gamma^c_{H^+}}\frac{\partial a_{H^+}}{\partial x}\right)+\frac{d}{dx}\left(\frac{D_{H_2CO_3}}{\gamma^c_{H_2CO_3}}\frac{\partial a_{H_2CO_3}}{\partial x}\right)+k_{f,CO_2}\,a_{CO_2}a_{H_2O} - k_{b,CO_2}\,a_{H_2CO_3}=0 \tag{V-15}$$

Applying assumptions # 4, # 7, and # 8 results in:

$$\frac{D_{H^+}}{\gamma^c_{H^+}}\frac{d^2a_{H^+}}{dx^2}+\frac{D_{H_2CO_3}}{\gamma^c_{H_2CO_3}}\frac{d^2a_{H_2CO_3}}{dx^2}+k_{f,CO_2}\,a^{eq}_{CO_2,b}a^{eq}_{H_2O} - k_{b,CO_2}\,a_{H_2CO_3}=0 \tag{V-16}$$

The dissociation Reaction (V-2) is always near equilibrium in the mass transfer boundary layer because it is faster than the hydration Reaction (V-1). Following the equilibrium equation for Reaction (V-2):

$$a^{eq}_{H_2CO_3,b}=\frac{a^{eq}_{HCO_3^-,b}}{K_1}a^{eq}_{b,H^+} \tag{V-17}$$

$$a_{H_2CO_3}\approx\frac{a^{eq}_{HCO_3^-,b}}{K_1}a_{H^+} \tag{V-18}$$

where, K_1 is the equilibrium constant for Reaction (V-2). In transformation from Equation to (V-17) to Equation (V-18), assumption # 5 has been used.

Differentiating Equation (V-18) two times with respect to x and using Equation (V-17) give:

$$\frac{d^2 a_{H_2CO_3}}{dx^2} \approx \frac{a^{eq}_{HCO_3^-,b}}{K_1}\frac{d^2 a_{H^+}}{dx^2} = \frac{a^{eq}_{H_2CO_3,b}}{a^{eq}_{H^+,b}}\,\frac{d^2 a_{H^+}}{dx^2} \tag{V-19}$$

Plugging Equations (V-18) and (V-19) into Equation (V-15) results in:

$$\begin{gathered}\left(\frac{D_{H^+}}{\gamma^c_{H^+}} + \frac{D_{H_2CO_3}}{\gamma^c_{H_2CO_3}}\frac{a^{eq}_{H_2CO_3,b}}{a^{eq}_{H^+,b}}\right)\frac{d^2 a_{H^+}}{dx^2} + k_{f,CO_2}\, a^{eq}_{CO_2,b} \\ - \frac{k_{b,CO_2} a^{eq}_{HCO_3^-.b}}{K_1} a_{H^+} \ = 0\end{gathered} \tag{V-20}$$

The terms in the parentheses on the left-hand side of Equation (V-20) are defined as an *effective* diffusion coefficient, which accounts for the H^+ ion diffusion coefficient in the presence of $CO_{2(aq)}$:

$$D_{eff} = \frac{D_{H^+}}{\gamma^c_{H^+}} + \frac{D_{H_2CO_3}}{\gamma^c_{H_2CO_3}}\frac{a^{eq}_{H_2CO_3,b}}{a^{eq}_{H^+,b}} \tag{V-21}$$

For Reaction (V-1) at equilibrium, the forward reaction rate is equal to the backward reaction rate:

$$k_{f,CO_2}\, a^{eq}_{CO_2,b} a^{eq}_{H_2O,b} = k_{b,CO_2}\, a^{eq}_{H_2CO_3,b} \tag{V-22}$$

Plugging Equations (V-21) and (V-22) into Equation (V-20) gives:

$$D_{eff}\frac{d^2 a_{H^+}}{dx^2} + k_{b,CO_2}\, a^{eq}_{H_2CO_3,b}\left(1 - \frac{a^{eq}_{HCO_3^-.b}}{K_1 c^{eq}_{b,H_2CO_3}} a_{H^+}\right) = 0 \tag{V-23}$$

Recalling Equation (V-17), the term attached to a_{H^+} is equal to the equilibrium bulk activity of H^+ ion. Therefore:

$$D_{eff}\frac{d^2a_{H^+}}{dx^2}+k_{b,CO_2}\,a^{eq}_{H_2CO_3,b}\left(1-\frac{a_{H^+}}{a^{eq}_{H^+,b}}\right)=0 \tag{V-24}$$

Equation (V-24) can also be presented in the following form, using Equation (V-22):

$$D_{eff}\frac{d^2a_{H^+}}{dx^2}+k_{f,CO_2}\,a^{eq}_{CO_2,b}a^{eq}_{H_2O,b}\left(1-\frac{a_{H^+}}{a^{eq}_{H^+,b}}\right)=0 \tag{V-25}$$

After some rearrangement of Equation (V-25):

$$\frac{d^2}{dx^2}\left(\frac{a_{H^+}}{a^{eq}_{H^+,b}}\right)=\frac{1}{\dfrac{D_{eff}\,a^{eq}_{H^+,b}}{k_{f,CO_2}\,a^{eq}_{CO_2,b}a^{eq}_{H_2O,b}}}\left(\frac{a_{H^+}}{a^{eq}_{H^+,b}}-1\right)=0 \tag{V-26}$$

A new parameter called the *chemical reaction boundary layer* is defined to simplify Equation (V-26):

$$\delta_r=\sqrt{\frac{D_{eff}\,a^{eq}_{H^+,b}}{k_{f,CO_2}\,a^{eq}_{CO_2,b}a^{eq}_{H_2O,b}}}\equiv\sqrt{\frac{D_{eff}\,a^{eq}_{H^+,b}}{k_{b,CO_2}\,a^{eq}_{H_2CO_3,b}}} \tag{V-27}$$

This results in the following equation:

$$\frac{d^2}{dx^2}\left(\frac{a_{H^+}}{a^{eq}_{H^+,b}}\right)=\frac{1}{\delta_r^2}\left(\frac{a_{H^+}}{a^{eq}_{H^+,b}}-1\right)=0 \tag{V-28}$$

To further simply (V-28), a non-dimensional concentration ratio u is defined:

$$u=\frac{a_{H^+}}{a^{eq}_{b,H^+}} \tag{V-29}$$

Applying Equation (V-29) to Equation (V-28) gives the final simplified equation:

$$\frac{d^2u}{dx^2}=\frac{(u-1)}{\delta_r^2} \tag{V-30}$$

Equation (V-30) is a second order linear homogeneous differential equation, which can be solved analytically by choosing the appropriate boundary conditions as follows:

At the metal surface ($x = 0$),

$$u = u_s \tag{V-31}$$

where, $u_s = a_{H^+,s}/a^{eq}_{b,H^+}$;

At the edge of the diffusion boundary layer ($x = \delta_{m,H^+}$),

$$a_{H^+} = a^{eq}_{H^+,b} \;\Rightarrow u = 1 \tag{V-32}$$

The solution of Equation (V-30) with the above boundary conditions has the following form:

$$u(x) = (1{-}u_s)\left[\frac{exp\left(\frac{x}{\delta_r}\right)}{exp\left(\frac{2\delta_{m,H^+}}{\delta_r}\right) - 1} + \frac{exp\left(-\frac{x}{\delta_r}\right)}{exp\left(-\frac{2\delta_{m,H^+}}{\delta_r}\right) - 1}\right] + 1 \tag{V-33}$$

Similar to Equation (U-5), the flux density of H$^+$ ions at the metal surface ($x = 0$) is obtained as:

$$\begin{aligned} N|_{x=0} &= -D_{eff}\left.\frac{da_{H^+}}{dx}\right|_{x=0} \\ &\equiv -D_{eff}a^{eq}_{H^+,b}\left.\frac{du(x)}{dx}\right|_{x=0} \end{aligned} \tag{V-34}$$

So that:

$$N|_{x=0} = \frac{(1{-}u_s)D_{eff}\;a^{eq}_{H^+,b}}{\delta_r}\;\frac{1 + exp\left(\frac{2\delta_{m,H^+}}{\delta_r}\right)}{1 - exp\left(\frac{2\delta_{m,H^+}}{\delta_r}\right)} \tag{V-35}$$

Or, in terms of activities:

$$N|_{x=0} = \frac{\left(a^{eq}_{H^+,b} - a_{H^+,s}\right) D_{eff}}{\delta_r} \frac{1 + exp\left(\frac{2\delta_{m,H^+}}{\delta_r}\right)}{1 - exp\left(\frac{2\delta_{m,H^+}}{\delta_r}\right)} \qquad \text{(V-36)}$$

$$= -\frac{\left(a^{eq}_{H^+,b} - a_{H^+,s}\right) D_{eff}}{\delta_r} coth\left(\frac{\delta_{m,H^+}}{\delta_r}\right)$$

In limiting current controlling situations, when the rate of the overall electrochemical Reaction (V-6) is limited by the slow hydration Reaction (V-1), all the H^+ ions arrive at the metal surface are consumed almost instantaneously by the fast charge transfer Reaction (V-4); hence, the activity of H^+ ions at the metal surface approaches zero: $a_{H^+} \approx 0$. Thus, in limiting current case, $a_{H^+,s}$ can be assumed zero in Equation (V-36). Using Equation (U-12) the limiting current density for the diffusion of H^+ ions with buffering due the presence of $CO_{2(aq)}$ can be obtained:

$$i_{Lim} = \frac{FD_{eff} a^{eq}_{b,H^+}}{\delta_r} coth\left(\frac{\delta_{m,H^+}}{\delta_r}\right) = \frac{FD_{eff} a^{eq}_{b,H^+}}{\delta_r tanh\left(\frac{\delta_{m,H^+}}{\delta_r}\right)} \qquad \text{(V-37)}$$

Or in another form using, δ_r definition:

$$i_{Lim} = F\sqrt{D_{eff} k_{f,CO_2}\, a^{eq}_{CO_2,b} a^{eq}_{H_2O,b}\, a^{eq}_{H^+,b}}\; coth\left(\frac{\delta_{m,H^+}}{\delta_r}\right) \qquad \text{(V-38)}$$

where, i_{Lim} is in A/m^2, F is the Faraday's constant (= 96485.33 C/mol), D_{eff} is in m^2/s, k_{f,CO_2} is in m^3/mol/s, $a_{H^+,b}$, $a_{CO_2,b}$, $a_{H_2O,b}$ are in mol/m^3, and δ_{m,H^+} and δ_r are in m. In many cases, the $coth\left(\delta_{m,H^+}/\delta_r\right)$ term, which accounts for the effect of flow, is almost equal to 1; examples are stagnant solutions, low flow rates and high temperatures. Equation (V-38) without the $coth\left(\delta_{m,H^+}/\delta_r\right)$ term will be similar to i_{Lim} equation proposed by Vetter [175] for acetic acid containing solutions.

At zero partial pressure of $CO_{2(g)}$ or $a_{CO_2,b}^{eq} = 0$, δ_r comes close to infinity, which makes i_{Lim} equation for CO_2 corrosion, Equation (V-37), to transform to that for strong acid corrosion, Equation (U-13). This shows that the i_{Lim} equation for CO_2 corrosion works for very small partial pressures of $CO_{2(g)}$.

Equation (V-38) in molarity unit is:

$$i_{Lim} = 1000F\sqrt{D_{eff}k_{f,CO_2}\, a_{CO_2,b}^{eq} a_{H_2O,b}^{eq}\, a_{H^+,b}^{eq}}\ coth\left(\frac{\delta_{m,H^+}}{\delta_r}\right) \qquad \text{(V-39)}$$

where, i_{Lim} is in A/m^2, F is the Faraday's constant (= 96485.33 C/mol), D_{eff} is in m^2/s, k_{f,CO_2} is in 1/M/s, $a_{H^+,b}$, $a_{CO_2,b}$, $a_{H_2O,b}$ are in molarity, and δ_{m,H^+} and δ_r are in m.

Assuming ideal or near ideal conditions where the activity coefficients of aqueous species and the activity of water are close to unity, Equation (V-39) simplifies to:

$$i_{Lim} = F\sqrt{10^6 D_{eff}k_{f,CO_2}\, c_{CO_2,b}^{eq}\, c_{H^+,b}^{eq}}\ coth\left(\frac{\delta_{m,H^+}}{\delta_r}\right) \qquad \text{(V-40)}$$

where, i_{Lim} is in A/m^2, F is the Faraday's constant (= 96485.33 C/mol), D_{eff} is in m^2/s, k_{f,CO_2} is in 1/s, $c_{H^+,b}$ and $c_{CO_2,b}$ are in molarity, and δ_{m,H^+} and δ_r are in m.

Appendix W: Cathodic Limiting Current Density in H_2S Saturated Aqueous Solutions (Applicable to Other Weak Acids)

The limiting current density becomes important in electrochemical systems when the rate of an electrochemical reaction is affected by a homogenous chemical step producing species that subsequently diffuse and participate in a charge transfer step at the metal surface. An example is the corrosion process in H_2S-satuared aqueous solutions or solutions containing others weak acids such as acetic acid and formic acid when the rate of the H^+ ion reduction reaction is controlled by a combination of a preceding chemical dissociation reaction and H^+ diffusion to the metal surface. In this situation, the overall rate of the corrosion process will be equal to the H^+ ion reduction rate or in other words the limiting current density. The experimental result of this study in Chapter 11 and those reported by Yougui [49] and Navabzadeh Esmaeely [357] show that the controlling effect of the limiting current density on the overall H_2S corrosion rate becomes significant at low partial pressures of H_2S ($< 10^{-4}$ bar). At high partial pressures of $H_2S_{(g)}$ the cathodic reaction is controlled by the rate of the charge transfer process. The effects of high solution pH values and high temperatures on the rate of the H^+ ion reduction reaction seem to be much less comparing to the H_2S partial pressure.

Four different equations will be presented in this section for the limiting current density in H_2S-saturated aqueous solutions, which are applicable to other weak acid aqueous solutions such as acetic acid and formic acid solutions as well. All the equations are derived based on activities of species instead of their concentrations, which makes the limiting current density equations suitable for all ideal, near ideal and nonideal systems.

In H_2S containing aqueous solutions, the following homogenous chemical dissociation reaction occurs:

$$H_2S_{(aq)} \underset{k_{b,H_2S}}{\overset{k_{f,H_2S}}{\rightleftarrows}} H^+_{(aq)} + HS^-_{(aq)} \tag{W-1}$$

where k_{f,H_2S} and k_{b,H_2S} are respectively the forward and backward reaction rate for this reaction, called the $H_2S_{(aq)}$ dissociation reaction. Then, the produced H^+ ions diffuse to the metal surface:

$$H^+_{(aq)} \xrightarrow{diffusion} H^+|_{surface} \tag{W-2}$$

The H^+ ions at the surface are reduced and dissolved H_2 gas is produced:

$$H^+|_{surface} + e^- \rightarrow \frac{1}{2} H_{2(\mathrm{g})} \tag{W-3}$$

The overall cathodic reaction in H_2S corrosion has the following form:

$$H_2S_{(aq)} + e^- \rightarrow \frac{1}{2} H_{2(\mathrm{g})} \tag{W-4}$$

When the charge transfer Reaction (W-3) proceeds at very high rates, the combination of the slower preceding steps, *i.e.*, the chemical dissociation Reaction (W-1) and the diffusion step, Reaction (W-2), becomes rate limiting. The chemical dissociation reaction for $H_2S_{(aq)}$ (k_{f,H_2S} = 6.24 × 10^3 1/s [315]) is faster than carbonic acid dissociation reaction (k_{f,H_2S} = 0.037 1/s [298]) and slower than acetic acid dissociation reaction (k_{f,H_2S} = 8.7 × 10^5 1/s [358]). This means that the H_2S dissociation reaction is relatively slow.

Until several years ago, it was assumed that in H_2S containing aqueous solutions in addition to the H^+ ion reduction Reaction (W-3), there is a parallel hydrogen evolution reaction known as the direct reduction of $H_2S_{(aq)}$ [226,219,225,228,229,227,49]:

$$H_2S_{(aq)} + e^- \rightarrow HS^-_{(aq)} + \frac{1}{2}H_{2(g)} \tag{W-5}$$

However, recent studies showed that the direct reduction of weak acids including H_2S is insignificant in aqueous corrosion of mild steels [230,356,359]. The main cathodic reaction in weak acid solutions is the H^+ ion reduction Reaction (W-4) and in the case of H_2S saturated aqueous solutions, $H_2S_{(aq)}$ role is to only to provide more H^+ ions for the main cathodic reaction. Thus, the common method of assuming two limiting current densities [49,96,317,360]: one for H^+ ion reduction reaction and one for the direct reduction of $H_2S_{(aq)}$, for calculating the total limiting current density in H_2S corrosion is not acceptable.

Being able to calculate the total limiting current density with only one reaction (H^+ ion reduction reaction) requires accounting for co-diffusion of all participating species and the buffering by the chemical Reaction (W-1) in the mass transfer boundary layer. For this, solving a system of five nonlinear differential equations for five species[133]: H^+ ion, $H_2S_{(aq)}$, HS^- ion, OH^- ion and $H_2O_{(l)}$ is required, which involves complex numerical computations as reported by Kahyarian *et al.* [207,230]. Furthermore, the numerical method does not result in an explicit expression for the limiting current density. With some assumptions the calculations can be simplified and the total limiting current density can be expressed as explicit expressions.

The following assumptions are made for calculating the cathodic H^+ ion reduction reaction limiting current density in H_2S-saturated aqueous solutions:

---

[133] $S^{2-}_{(aq)}$ ion can be ignored as its activity is extremely small in conditions experienced in aqueous H_2S corrosion.

1. Mass transfer by convection can be ignored as the aqueous solution is chemically and thermally uniform.
2. Mass transfer by migration can be ignored as there is no external electrical field in naturally occurring corrosion. And, according to the mixed potential theory no potential gradient exists over the metal surface in natural uniform corrosion.
3. Diffusion only occurs in one-dimensional along the x-axis perpendicular to the metal surface. The diffusion in the other two directions is considered zero.
4. The activity of water ($a_{H_2O_{(l)}}$) is constant across the mass transfer (diffusion) boundary layer and equal to the equilibrium bulk values. This implies that diffusion of $a_{H_2O_{(l)}}$ can be ignored in the calculations.

$$a_{H_2O_{(l)}} \approx a^{eq}_{H_2O_{(l)},b} \equiv \ constant \tag{W-6}$$

5. The activity of the bisulfide ion ($a_{HS^-_{(aq)}}$) in the mass transfer boundary layer is constant and equal to the equilibrium bulk value.

$$a_{HS^-_{(aq)}} \approx a^{eq}_{HS^-_{(aq)},b} \equiv \ constant \tag{W-7}$$

This may appear to be erroneous, as from the dissociation Reaction (W-1) for every H^+ ion produced (or consumed), one HS^- ion is also produced (or consumed). Therefore, any changes in their activities because of Reactions (W-1) to (W-3) must be the same.

$$\Delta a_{HS^-} = \Delta a_{H^+} \tag{W-8}$$

Equation (W-8) argument seems to be contradicting the assumption that $a_{HS^-_{(aq)}}$ remains constant as a_{H^+} changes. However, in the limiting current controlling situations, where the pH in the mass transfer boundary layer is always greater than pH 7, $a_{HS^-} \gg a_{H^+}$. Therefore, for any given Δa_{H^+} that produces a significant change in a_{H^+}, the corresponding Δ_{HS^-} produces a very small change in a_{HS^-}. So, our assumption about a_{HS^-} being constant in the boundary layer is reasonably accurate.

$$\frac{\Delta a_{HS^-}}{a_{HS^-}} \ll \frac{\Delta a_{H^+}}{a_{H^+}} \tag{W-9}$$

The constant a_{HS^-} assumption means that the variation in a_{HS^-} in the mass transfer boundary layer can be ignored, and thereby allows to disregard the contribution of HS^- ion diffusion in the calculation process.

6. Similar to assumption # 5, due to the high solution pH in the mass transfer boundary layer in the limiting current density controlling situations, the activity of OH^- ion ($a_{OH^-_{(aq)}}$) is relatively high there as well, and its variation and thereby its diffusion can be ignored in the calculations.
7. $D_{H^+_{(aq)}}$ and $D_{H_2S_{(aq)}}$ are constant across the mass transfer boundary layer from the bulk to the metal surface.
8. $\gamma^c_{H^+}$ and $\gamma^c_{H_2S}$ are constant across the mass transfer boundary layer from the bulk solution to the metal surface.

Considering these assumptions, only two species remain that their activities change across the mass transfer boundary layer: H^+ ion and $H_2S_{(aq)}$. The limiting current density can be calculated by solving the steady-state one-dimensional Nernst-Planck (mass conservation) equations [21] for H^+ ion and $H_2S_{(aq)}$ as follows:

$$\frac{d}{dx}\left(\frac{D_{H^+}}{\gamma_{H^+}^c}\frac{da_{H^+}}{dx}\right)+k_{f,H_2S}\,a_{H_2S}-k_{b,H_2S}\,a_{HS^-}\,a_{H^+}=0 \qquad \text{(W-10)}$$

$$\frac{d}{dx}\left(\frac{D_{H_2S}}{\gamma_{H_2S}^c}\frac{da_{H_2S}}{dx}\right)-k_{f,H_2S}\,a_{H_2S}+k_{b,H_2S}\,a_{HS^-}\,a_{H^+}=0 \qquad \text{(W-11)}$$

The first terms in parentheses for both equations account for the molecular diffusion, while the other terms are related to production and consumption of species by H_2S chemical dissociation reaction. The use of activity and activity coefficient instead of concentration in the Nernst-Planck equation has been demonstrated in Appendix U. γ^c is the molarity-based activity coefficient in infinite dilution reference state (Appendix P).

Four different approaches haven been used in the present study to solve the coupled Equations (W-10) and (W-11). In the first two approaches, a single-section mass transfer boundary layer is considered, while in the last two approaches the mass transfer boundary layer is assumed to have two sections.

The first approach to solve the coupled Equations is to assume a single boundary layer (δ_m) across which the activity of both H^+ ion and H_2S change. The calculation procedure in this approach is very similar to that presented for the CO_2 corrosion limiting current density in Appendix V. Equations (W-10) and (W-11) are added to cancel out the terms related to the H_2S dissociation reaction. In this approach, it is assumed that the H_2S dissociation Reaction (W-12) is near equilibrium and this assumption is used to covert the second order derivative of a_{H_2S} to that for a_{H^+}. Then, the simple second order linear homogeneous differential Equation (W-12) is solved with two boundary conditions of at $x=0$, $a_{H^+}=a_{H^+,s}$ and at $x=\delta_m$, $a_{H^+}=a_{H^+,b}^{eq}$, where $a_{H^+,s}$ and $a_{H^+,b}^{eq}$ are the activity of H^+ ion at the metal surface and in the bulk solution, respectively.

$$\left(\frac{D_{H^+}}{\gamma_{H^+}^c}+\frac{D_{H_2S}}{\gamma_{H_2S}^c}\frac{a_{H_2S,b}^{eq}}{a_{H^+,b}^{eq}}\right)\frac{d^2a_{H^+}}{dx^2}=0 \qquad \text{(W-12)}$$

Then, the H$^+$ ion flux at $x=0$ is calculated and finally by using Equation of (U-12) the limiting current density can be obtained:

$$i_{Lim}=\frac{F}{\delta_m}\left(\frac{D_{H^+}}{\gamma_{H^+}^c}a_{H^+,b}^{eq}+\frac{D_{H_2S}}{\gamma_{H_2S}^c}a_{H_2S,b}^{eq}\right) \qquad \text{(W-13)}$$

Where, δ_m in Equation (W-13) can be either the H$^+$ diffusion boundary layer (δ_{m,H^+}) or the $H_2S_{(aq)}$ diffusion boundary layer (δ_{m,H_2S}), as these two are different in thickness due to a larger diffusion coefficient of H$^+$ ion compared to that for $H_2S_{(aq)}$ (Table 3-2). δ_{m,H^+} is about two times of δ_{m,H_2S} in thickness[134]. If δ_{m,H^+} is used in Equation (W-13), there will be underpredictions for i_{Lim} at high pH values and high H_2S partial pressures. On the other hand, if δ_{m,H_2S} is used in Equation (W-13), i_{Lim} will be overpredicted at low pH values and low H_2S partial pressures. Moreover, if δ_{m,H_2S} is used and the partial pressure of H_2S is equal to zero (*i.e.*, $a_{H_2S,b}^{eq}=0$), Equation (W-13) does not transform to i_{Lim} Equation (U-13) for the strong acid solutions.

In the second approach, a different mathematical approach is used to solve the co-diffusion mass balance equations. This approach is similar to that used by Rieger [354]. Rieger assumed ideal conditions and identical diffusion coefficients for the diffusing species. However, in this study, activities are used instead of concentrations and the diffusion coefficient of each diffusing species is implemented in i_{Lim} calculations. To

---

[134] The thickness of the diffusion boundary layer is proportional to the cubic root of the diffusion coefficient.

solve the coupled Equations (W-10) and (W-11) two variables are defined: A as the total activity of H^+ ion, $H_2S_{(aq)}$ and HS^- ion, and A' as the measure of departure of the H_2S dissociation Reaction (W-1) from equilibrium:

$$A = \frac{D_{H^+}}{\gamma^c_{H^+}} a_{H^+} + \frac{D_{H_2S}}{\gamma^c_{H_2S}} a_{H_2S} + \frac{D_{HS^-}}{\gamma^c_{HS^-}} a_{HS^-} \qquad \text{(W-14)}$$

$$A' = K_1 a_{H_2S} - a_{H^+} a_{HS^-} \qquad \text{(W-15)}$$

where, K_1 is the equilibrium constant for the H_2S dissociation Reaction (W-1) and equal to $k_{f,H_2S}/k_{b,H_2S}$.

Equations (W-10) and (W-11) are added up to cancel out the chemical reaction terms:

$$\frac{d}{dx}\left(\frac{D_{H^+}}{\gamma^c_{H^+}} \frac{da_{H^+}}{dx}\right) + \frac{d}{dx}\left(\frac{D_{H_2S}}{\gamma^c_{H_2S}} \frac{da_{H_2S}}{dx}\right) = 0 \qquad \text{(W-16)}$$

Since a_{HS^-} is assumed to be constant across the mass transfer boundary layer, its second derivative is equal to zero. Therefore, Equation (W-16) can be written as below:

$$\frac{d}{dx}\left(\frac{D_{H^+}}{\gamma^c_{H^+}} \frac{da_{H^+}}{dx}\right) + \frac{d}{dx}\left(\frac{D_{H_2S}}{\gamma^c_{H_2S}} \frac{da_{H_2S}}{dx}\right) + \frac{d}{dx}\left(\frac{D_{HS^-}}{\gamma^c_{HS^-}} \frac{da_{HS^-}}{dx}\right) = 0 \qquad \text{(W-17)}$$

Using assumption # 8, Equation (W-17) will be equivalent to:

$$\frac{d^2A}{dx^2} = 0 \qquad \text{(W-18)}$$

The second derivative of A' has the following form:

$$\frac{d^2A'}{dx^2} = K_1 \frac{d^2 a_{H_2S}}{dx^2} - a_{HS^-} \frac{d^2 a_{H^+}}{dx^2} - a_{H^+} \frac{d^2 a_{HS^-}}{dx^2} - 2 \frac{da_{H^+}}{dx} \frac{da_{HS^-}}{dx} \qquad \text{(W-19)}$$

a_{HS^-} is assumed to be constant. Thus, the last two terms in Equation (W-19) are equal to zero:

$$\frac{d^2A'}{dx^2} = K_1\frac{d^2a_{H_2S}}{dx^2} - a_{HS^-}\frac{d^2a_{H^+}}{dx^2} \tag{W-20}$$

From Equation (W-10) and (W-11) and using the definition of A', the following equations can be derived:

$$\frac{d^2a_{H_2S}}{dx^2} = \frac{k_{b,H_2S}\gamma^c_{H_2S}A'}{D_{H_2S}} \tag{W-21}$$

$$\frac{d^2a_{H^+}}{dx^2} = -\frac{k_{b,H_2S}\gamma^c_{H^+}A'}{D_{H^+}} \tag{W-22}$$

Plugging Equations (W-21) and (W-22) into Equation (W-20) gives:

$$\frac{d^2A'}{dx^2} = \left(\frac{k_{f,H_2S}\gamma^c_{H_2S}}{D_{H_2S}} + \frac{k_{b,H_2S}\gamma^c_{H^+}a_{HS^-}}{D_{H^+}}\right)A' \tag{W-23}$$

A new parameter called the chemical reaction boundary layer is defined (δ_r):

$$\delta_r = \sqrt{\frac{1}{\frac{k_{f,H_2S}\gamma^c_{H_2S}}{D_{H_2S}} + \frac{k_{b,H_2S}\gamma^c_{H^+}a_{HS^-}}{D_{H^+}}}} \tag{W-24}$$

where, δ_r is in m. Finally, the second mass balance equation becomes:

$$\frac{d^2A'}{dx^2} = \frac{A'}{\delta_r^2} \tag{W-25}$$

The first mass balance Equation (W-18) can be solved by the following boundary conditions:

At $x = \delta_m \Rightarrow \ A = A^{eq} = \frac{D_{H^+}}{\gamma^c_{H^+}}a^{eq}_{H^+} + \frac{D_{H_2S}}{\gamma^c_{H_2S}}a^{eq}_{H_2S} + \frac{D_{HS^-}}{\gamma^c_{HS^-}}a^{eq}_{HS^-}$;

At $x = 0 \Rightarrow \ A = A_s = \frac{D_{H^+}}{\gamma^c_{H^+}}a_{H^+,s} + \frac{D_{H_2S}}{\gamma^c_{H_2S}}a_{H_2S,s} + \frac{D_{HS^-}}{\gamma^c_{HS^-}}a^{eq}_{HS^-}$;

where, eq and s mean the equilibrium bulk and the surface activities, respectively. The solution of Equation (W-18) then is:

$$A = A_s + \left(\frac{A^{eq} - A_s}{\delta_m}\right) x \tag{W-26}$$

The second mass balance Equation (W-25) can be solved by the boundary conditions below:

At $x = \delta_m \Rightarrow \; A' = A'^{,eq} = K a^{eq}_{H_2S} - a^{eq}_{H^+} a^{eq}_{HS^-} = 0$;

At $x = 0 \Rightarrow \; A' = A'_s = K a_{H_2S,s} - a_{H^+,s} a^{eq}_{HS^-}$;

The solution to Equation (W-25) is:

$$A' = A'_s \frac{e^{\frac{\delta_m - x}{\delta_r}} - e^{-\frac{\delta_m - x}{\delta_r}}}{e^{\frac{\delta_m}{\delta_r}} - e^{-\frac{\delta_m}{\delta_r}}} \tag{W-27}$$

From the definitions of A and A', equations for the activities of H^+ ion and H_2S can be obtained as functions of A and A':

$$a_{H^+} = \frac{K_1 \left(A - \frac{D_{HS^-}}{\gamma^c_{HS^-}} a^{eq}_{HS^-}\right) - \frac{D_{H_2S}}{\gamma^c_{H_2S}} A'}{\frac{D_{H_2S}}{\gamma^c_{H_2S}} a^{eq}_{HS^-} + \frac{D_{H^+}}{\gamma^c_{H^+}} K_1} \tag{W-28}$$

$$a_{H_2S} = \frac{a^{eq}_{HS^-} \left(A - \frac{D_{HS^-}}{\gamma^c_{HS^-}} a^{eq}_{HS^-}\right) + \frac{D_{H^+}}{\gamma^c_{H^+}} A'}{\frac{D_{H_2S}}{\gamma^c_{H_2S}} a^{eq}_{HS^-} + \frac{D_{H^+}}{\gamma^c_{H^+}} K_1} \tag{W-29}$$

The fluxes for H^+ ion and H_2S at the surface are equal to:

$$\begin{aligned} N_{H^+}\big|_{x=0} &= -\frac{D_{H^+}}{\gamma^c_{H^+}} \frac{da_{H^+}}{dx}\bigg|_{x=0} \\ &= -\frac{\frac{D_{H^+}}{\gamma^c_{H^+}}}{\frac{D_{H_2S}}{\gamma^c_{H_2S}} a^{eq}_{HS^-} + \frac{D_{H^+}}{\gamma^c_{H^+}} K_1} \left[K_1 \frac{dA}{dx}\bigg|_{x=0} - \frac{D_{H_2S}}{\gamma^c_{H_2S}} \frac{dA'}{dx}\bigg|_{x=0} \right] \end{aligned} \tag{W-30}$$

$$N_{H_2S}\Big|_{x=0} = -\frac{D_{H_2S}}{\gamma^c_{H_2S}}\frac{da_{H_2S}}{dx}\Bigg|_{x=0}$$

$$= -\frac{\dfrac{D_{H_2S}}{\gamma^c_{H_2S}}}{\dfrac{D_{H_2S}}{\gamma^c_{H_2S}}a^{eq}_{HS^-} + \dfrac{D_{H^+}}{\gamma^c_{H^+}}K_1}\left[a^{eq}_{HS^-}\frac{dA}{dx}\bigg|_{x=0} + \frac{D_{H^+}}{\gamma^c_{H^+}}\frac{dA'}{dx}\bigg|_{x=0}\right] \tag{W-31}$$

From Equations (W-26) and (W-27) for A and A', the derivatives with respect to x at $x = 0$ can be calculated as follows:

$$\frac{dA}{dx}\bigg|_{x=0} = \frac{A^{eq} - A_s}{\delta_m} \tag{W-32}$$

$$\frac{dA'}{dx}\bigg|_{x=0} = -\frac{A'_s}{\delta_r \tanh\left(\dfrac{\delta_m}{\delta_r}\right)} \tag{W-33}$$

Implementing Equations (W-32) and (W-33) into Equations (W-30) and (W-31) gives:

$$N_{H^+}|_{x=0} = -\frac{\dfrac{D_{H^+}}{\gamma^c_{H^+}}}{\dfrac{D_{H_2S}}{\gamma^c_{H_2S}}a^{eq}_{HS^-} + \dfrac{D_{H^+}}{\gamma^c_{H^+}}K_1}\left[K_1\left(\frac{A^{eq} - A_s}{\delta_m}\right) + \frac{D_{H_2S}}{\gamma^c_{H_2S}}\left(\frac{A'_s}{\delta_r \tanh\left(\dfrac{\delta_m}{\delta_r}\right)}\right)\right] \tag{W-34}$$

$$N_{H_2S}\Big|_{x=0} = -\frac{\dfrac{D_{H_2S}}{\gamma^c_{H_2S}}}{\dfrac{D_{H_2S}}{\gamma^c_{H_2S}}a^{eq}_{HS^-} + \dfrac{D_{H^+}}{\gamma^c_{H^+}}K_1}\left[a^{eq}_{HS^-}\left(\frac{A^{eq} - A_s}{\delta_m}\right) - \frac{D_{H^+}}{\gamma^c_{H^+}}\left(\frac{A'_s}{\delta_r \tanh\left(\dfrac{\delta_m}{\delta_r}\right)}\right)\right] \tag{W-35}$$

Since the direct reduction of $H_2S_{(aq)}$ is insignificant in aqueous H_2S corrosion of carbon steel, the $H_2S_{(aq)}$ flux at the surface ($x = 0$), $N_{H_2S}\big|_{x=0}$ is equal to zero. This gives the following equation:

$$A'_s = \frac{\gamma^c_{H^+} a^{eq}_{HS^-}}{D_{H^+}} \left(\frac{A^{eq} - A_s}{\delta_m} \right) \delta_r \tanh\left(\frac{\delta_m}{\delta_r} \right) \qquad \text{(W-36)}$$

Substituting Equation (W-36) into the H^+ ion flux at the surface, Equation (W-34), results in:

$$\begin{aligned} N_{H^+}|_{x=0} &= -\frac{A^{eq} - A_s}{\delta_m} \\ &= -\frac{A^{eq} - \frac{D_{H^+}}{\gamma^c_{H^+}} a_{H^+,s} - \frac{D_{H_2S}}{\gamma^c_{H_2S}} a_{H_2S,s} - \frac{D_{HS^-}}{\gamma^c_{HS^-}} a^{eq}_{HS^-}}{\delta_m} \end{aligned} \qquad \text{(W-37)}$$

From the definition of A' at the surface, $x = 0$:

$$A'_s = K_1 a_{H_2S,s} - a_{H^+,s} a^{eq}_{HS^-} \qquad \text{(W-38)}$$

By equating Equations (W-36) and (W-38) for A'_s and solving for $a_{H_2S,s}$:

$$\begin{aligned} &a_{H_2S,s} \\ &= \frac{\frac{D_{H^+}}{\gamma^c_{H^+}} a^{eq}_{H^+} a^{eq}_{HS^-} + \frac{D_{H_2S}}{\gamma^c_{H_2S}} a^{eq}_{H_2S} a^{eq}_{HS^-} + (\lambda - 1) \frac{D_{H^+}}{\gamma^c_{H^+}} a_{H^+,s} a^{eq}_{HS^-}}{\lambda K_1 \frac{D_{H^+}}{\gamma^c_{H^+}} + \frac{D_{H_2S}}{\gamma^c_{H_2S}} a^{eq}_{HS^-}} \end{aligned} \qquad \text{(W-39)}$$

where, λ is called the kinetic parameter and is defined as:

$$\lambda = \frac{\delta_m}{\delta_r \tanh\left(\frac{\delta_m}{\delta_r} \right)} \qquad \text{(W-40)}$$

Substituting Equation (W-39) into Equation (W-37) gives:

$$N_{H^+}|_{x=0} = -\frac{\lambda K_1 \frac{D_{H^+}}{\gamma_{H^+}^c} A^{eq} - \lambda \frac{D_{H^+}}{\gamma_{H^+}^c}\left(\frac{D_{H_2S}}{\gamma_{H_2S}^c} a_{HS^-}^{eq} + \frac{D_{H^+}}{\gamma_{H^+}^c} K_1\right) a_{H^+,s} - \lambda K_1 \frac{D_{H^+}}{\gamma_{H^+}^c} \frac{D_{HS^-}}{\gamma_{HS^-}^c} a_{HS^-}^{eq}}{\delta_m \left(\frac{D_{H_2S}}{\gamma_{H_2S}^c} a_{HS^-}^{eq} + \frac{D_{H^+}}{\gamma_{H^+}^c} \lambda K_1\right)} \qquad \text{(W-41)}$$

In the limiting current situation, $a_{H^+,s}$ is equal to zero at the surface. Using Equation (U-12), the H$^+$ ion flux in Equation (W-41) can be converted to the limiting current density:

$$i_{Lim} = \frac{1000 F D_{H^+}}{\gamma_{H^+}^c}\left(\frac{\lambda K_1 \left(\frac{D_{H_sS}}{\gamma_{H_sS}^c} a_{H_sS,b}^{eq} + \frac{D_{H^+}}{\gamma_{H^+}^c} a_{H^+,b}^{eq}\right)}{\left(\frac{D_{H_sS}}{\gamma_{H_sS}^c} a_{HS^-,b}^{eq} + \frac{D_{H^+}}{\gamma_{H^+}^c} \lambda K_1\right) \delta_m}\right) \qquad \text{(W-42)}$$

where, i_{Lim} is in A/m^2, a_b^{eq} is the equilibrium bulk activity in M, the molarity-based activity coefficients (γ^c) are dimensionless, K_1 is the equilibrium constant for the H_2S dissociation reaction in M, diffusion coefficients (D_i) are in m^2/s, and δ_m is in m. δ_m in Equation (W-42) can be either δ_{m,H^+} or δ_{m,H_2S}. A factor of 1000 is multiplied to the right-hand side of Equation (W-42) for conversion from mol/m^3 unit to the molarity unit.

If δ_{m,H^+} is used in Equation (W-42), i_{Lim} will be underpredicted at high pH values and high H_2S partial pressures. On the other hand, if δ_{m,H_2S} is used in Equation (W-42), there will be overpredictions for i_{Lim} at low pH values and low H_2S partial pressures. Another problem is that when δ_{m,H_2S} is used and the partial pressure of H_2S is equal to zero (*i.e.*, $a_{H_2S,b}^{eq} = 0$), Equation (W-42) does not transform to i_{Lim} Equation (U-13) for the strong acid solutions. Despite this, the accuracy of Equation (W-42) is better than that for Equation (W-13).

For ideal and near ideal conditions where activity coefficients are close to one and concentrations can be used instead of activities, Equation (W-42) is simplified to:

$$i_{Lim} = 1000FD_{H^+}\left(\frac{\lambda K_1\left(D_{H_sS}c^{eq}_{H_sS,b} + D_{H^+}c^{eq}_{H^+,b}\right)}{\left(D_{H_sS}c^{eq}_{HS^-,b} + D_{H^+}\lambda K_1\right)\delta_m}\right) \qquad \text{(W-43)}$$

where, c_b^{eq} is the equilibrium bulk concentration in M.

To void problems originated from the choice between δ_{m,H^+} and δ_{m,H_2S} in Equations (W-13) and (W-42), a diffusion boundary layer with two sections is assumed that works for both low and high H_2S partial pressures as well as low and high pH values. The schematic of the two-section diffusion boundary layer and the activity profile of H^+ ion and $H_2S_{(aq)}$ is depicted in Figure W-1. The two mass balance equations are solved for each part.

Figure W-1

The schematic of a two-section diffusion boundary layer used for calculating the limiting current density in aqueous H_2S corrosion.

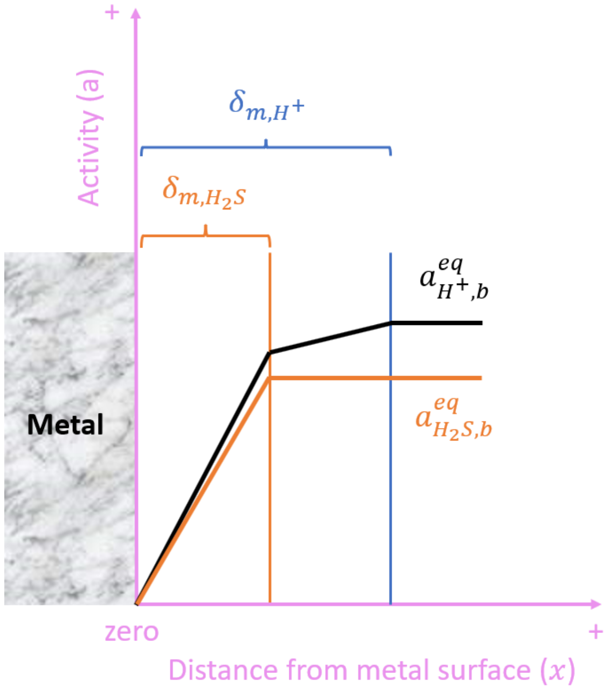

In the outer part, *i.e.*, between δ_{m,H_2S} and δ_{m,H^+}, it is assumed that a_{H_2S} variation is negligible; so, $\partial a_{H_2S}/\partial x \approx 0$ and $\partial^2 a_{H_2S}/\partial x^2 \approx 0$ and the only species diffusing are the H^+ ions. Therefore, for that outer part of the mass transfer boundary layer only the H^+ ion diffusion equation needs to be solved:

$$\frac{D_{H^+}}{\gamma^c_{H^+}}\frac{d^2 a_{H^+}}{dx^2} + k_{f,H_2S}\, a_{H_2S} - k_{b,H_2S}\, a_{HS^-}\, a_{H^+} = 0 \qquad \text{(W-44)}$$

Assumptions # 7 and # 8 have been applied to Equation (W-44). Since both a_{H_2S} and a_{HS^-} are assumed to be constant in the outer part of the diffusion boundary layer, they are equal to their equilibrium values in the bulk solution:

$$a_{H_2S} \approx c^{eq}_{H_2S,b} \equiv constant \tag{W-45}$$

$$a_{HS^-} \approx a^{eq}_{HS^-,b} \equiv constant \tag{W-46}$$

Therefore, Equation (W-44) can be written as below:

$$\frac{D_{H^+}}{\gamma^c_{H^+}} \frac{d^2 a_{H^+}}{dx^2} + k_{f,H_2S}\, a^{eq}_{H_2S,b} - k_{b,H_2S}\, a^{eq}_{HS^-,b}\, a_{H^+} = 0 \tag{W-47}$$

The equilibrium equation for Reaction (W-1) is used to simplify Equation (W-47):

$$k_{f,H_2S}\, a^{eq}_{H_2S,b} = k_{b,H_2S}\, a^{eq}_{HS^-,b} a^{eq}_{H^+,b} \tag{W-48}$$

So, Equation (W-48) can be presented as:

$$\frac{D_{H^+}}{\gamma^c_{H^+}} \frac{d^2 a_{H^+}}{dx^2} + k_{f,H_2S}\, a^{eq}_{H_2S,b} \left(1 - \frac{1}{\frac{K_{H_2S}\, a^{eq}_{H_2S,b}}{a^{eq}_{HS^-,b}}}\, a_{H^+} \right) = 0 \tag{W-49}$$

where, K_{H_2S} is the equilibrium constant for Reaction (W-1) and equal to ($k_{f,H_2S}/k_{b,H_2S}$). The term in the denominator is the equilibrium bulk activity of H$^+$ ions a^{eq}_{b,H^+}. Thus:

$$\frac{D_{H^+}}{\gamma^c_{H^+}} \frac{d^2 a_{H^+}}{dx^2} + k_{f,H_2S}\, a^{eq}_{H_2S,b} \left(1 - \frac{a_{H^+}}{a^{eq}_{H^+,b}} \right) = 0 \tag{W-50}$$

Both sides of Equation (W-50) are divided by $a^{eq}_{H^+,b}$, and dimensionless activity ratio (u) is defined:

$$u = \frac{a_{H^+}}{a^{eq}_{H^+,b}} \tag{W-51}$$

The diffusion Equation (W-50) takes the following form:

$$\frac{\partial^2 u}{\partial x^2} = \frac{(u-1)}{\delta_r^2} \tag{W-52}$$

where, δ_r is defined as the chemical reaction boundary layer and is equal to:

$$\delta_r = \sqrt{\frac{D_{H^+}\, a^{eq}_{H^+,b}}{\gamma^c_{H^+} k_{f,H_2S}\, a^{eq}_{H_2S,b}}} \qquad \text{(W-53)}$$

Equation (W-52) is a linear, 2nd order, non-homogenous, differential equation that can be solved by using the following boundary conditions:

At $x = \delta_{m,H_2S} \Rightarrow\ u = u_*$;

where, $u_* = a_{H^+,*}/a^{eq}_{H^+,b}$ is the non-dimensional activity of H^+ ions at the edge of the H_2S mass transfer boundary layer.

And, at $x = \delta_{m,H^+} \Rightarrow\ u = 1$.

The general solution of Equation (W-52) is as follows:

$$u\ = c_1 e^{\frac{x}{\delta_r}} + c_2 e^{-\frac{x}{\delta_r}} + 1 \qquad \text{(W-54)}$$

After finding the c_1 and c_2 constants by applying the boundary conditions, the final solution is derived:

$$u\ = (u_* - 1)\left[\frac{e^{\frac{x}{\delta_r}}}{e^{\frac{\delta_{m,H_2S}}{\delta_r}} - e^{\frac{2\delta_{m,H^+} - \delta_{m,H_2S}}{\delta_{r,H^+}}}} + \frac{e^{-\frac{x}{\delta_r}}}{e^{-\frac{\delta_{m,H_2S}}{\delta_r}} - e^{-\frac{2\delta_{m,H^+} - \delta_{m,H_2S}}{\delta_r}}}\right] + 1 \qquad \text{(W-55)}$$

Plugging back a_{H^+} into Equation (W-55) gives:

$$a_{H^+} = a^{eq}_{H^+,b} - \left(a^{eq}_{H^+,b} - a_{H^+,*}\right)\left[\frac{e^{\frac{x}{\delta_r}}}{e^{\frac{\delta_{m,H_2S}}{\delta_{r,}}} - e^{\frac{2\delta_{m,H^+} - \delta_{m,H_2S}}{\delta_r}}} + \frac{e^{-\frac{x}{\delta_r}}}{e^{-\frac{\delta_{m,H_2S}}{\delta_r}} - e^{-\frac{2\delta_{m,H^+} - \delta_{m,H_2S}}{\delta_r}}}\right] \tag{W-56}$$

The flux of H$^+$ ion at $x = \delta_{m,H_2S}$ is equal to:

$$N_{x=\delta_{m,H_2S}} = -\frac{D_{H^+}}{\gamma^c_{H^+}}\frac{da_{H^+}}{dx}\bigg|_{x=\delta_{m,H_2S}}$$

$$= \frac{D_{H^+}}{\gamma^c_{H^+}}\frac{\left(a^{eq}_{H^+,b} - a_{H^+,*}\right)}{\delta_r}\left[\frac{e^{\frac{\delta_{m,H_2S}}{\delta_r}}}{e^{\frac{\delta_{m,H_2S}}{\delta_r}} - e^{\frac{2\delta_{m,H^+} - \delta_{m,H_2S}}{\delta_r}}} - \frac{e^{-\frac{\delta_{m,H_2S}}{\delta_{r,H^+}}}}{e^{-\frac{\delta_{m,H_2S}}{\delta_{r,H^+}}} - e^{-\frac{2\delta_{m,H^+} - \delta_{m,H_2S}}{\delta_{r,H^+}}}}\right] \tag{W-57}$$

After some simplifications of the terms inside the brackets:

$$N_{x=\delta_{m,H_2S}} = \frac{D_{H^+}}{\gamma^c_{H^+}}\frac{\left(a^{eq}_{H^+,b} - a_{H^+,*}\right)}{\delta_r}\left[\frac{1}{1 - e^{\frac{2\left(\delta_{m,H^+} - \delta_{m,H_2S}\right)}{\delta_r}}} - \frac{1}{1 - e^{-\frac{2\left(\delta_{m,H^+} - \delta_{m,H_2S}\right)}{\delta_r}}}\right] \tag{W-58}$$

The terms inside the brackets are equal to $-\coth\left(\frac{\delta_{m,H^+} - \delta_{m,H_2S}}{\delta_r}\right)$. Therefore:

$$N_{x=\delta_{m,H_2S}} = -\frac{D_{H^+}}{\gamma^c_{H^+}}\frac{\left(a^{eq}_{H^+,b} - a_{H^+,*}\right)}{\delta_r}\coth\left(\frac{\delta_{m,H^+} - \delta_{m,H_2S}}{\delta_r}\right) \tag{W-59}$$

A new parameter is defined as follows:

$$\delta_* = \delta_r \tanh\left(\frac{\delta_{m,H^+} - \delta_{m,H_2S}}{\delta_r}\right) \tag{W-60}$$

Applying δ_* to Equation (W-59) results in the final equation for H$^+$ ion flux at $x = \delta_{m,H_2S}$:

$$N_{x=\delta_{m,H_2S}} = -\frac{D_{H^+}}{\gamma_{H^+}^c}\frac{\left(a_{H^+,b}^{eq} - a_{H^+,*}\right)}{\delta_*} \tag{W-61}$$

In the inner part of the mass transfer boundary layer, *i.e.*, between the metal surface and $\delta_{m,HAc}$ (Figure W-1), both H$^+$ and $H_2S_{(aq)}$ species diffuse, and their activities change with distance from the surface. Adding the two mass balance Equations (W-10) and (W-11) for the two species together, eliminates the chemical reaction terms:

$$\frac{d}{dx}\left(\frac{D_{H^+}}{\gamma_{H^+}^c}\frac{da_{H^+}}{dx}\right) + \frac{d}{dx}\left(\frac{D_{H_2S}}{\gamma_{H_2S}^c}\frac{da_{H_2S}}{dx}\right) = 0 \tag{W-62}$$

The equilibrium equation for Reaction (W-1) can be used to estimate the second derivative of a_{HAc} in the inner part of the mass transfer boundary layer:

$$\frac{d^2 a_{H_2S}}{dx^2} \approx \frac{a_{HS^-,b}^{eq}}{K_{H_2S}}\frac{d^2 a_{H^+}}{dx^2} = \frac{a_{H_2S,b}^{eq}}{a_{H^+,b}^{eq}}\frac{d^2 a_{H^+}}{dx^2} \tag{W-63}$$

Substituting Equation (W-63) into (W-62) and using assumptions # 7 and # 8 to pull out the D/γ^c terms from the parentheses give:

$$\left(\frac{D_{H^+}}{\gamma_{H^+}^c} + \frac{a_{H_2S,b}^{eq}}{a_{H^+,b}^{eq}}\frac{D_{H_2S}}{\gamma_{H_2S}^c}\right)\frac{d^2 a_{H^+}}{dx^2} = 0 \tag{W-64}$$

The terms in the parentheses are defined as the effective diffusion (D_{eff}):

$$D_{eff} = \frac{D_{H^+}}{\gamma_{H^+}^{c}} + \frac{a_{H_2S,b}^{eq}}{a_{H^+,b}^{eq}} \frac{D_{H_2S}}{\gamma_{H_2S}^{c}} \tag{W-65}$$

D_{eff} indicates the diffusion coefficient of H^+ in the presence of H_2S buffering effect. Therefore, the final mass balance equation will be as follows:

$$D_{eff} \frac{d^2 a_{H^+}}{dx^2} = 0 \tag{W-66}$$

Equation (W-66) is a linear 2-order homogenous differential equation that can be solved analytically with the following boundary conditions:

At $x = 0 \Rightarrow a_{H^+} = a_{H^+,s}$;

where, $a_{H^+,s}$ is the activity of H^+ ion at the metal surface.

At $x = \delta_{m,H_2S} \Rightarrow a_{H^+} = a_{H^+,*}$;

The final solution of Equation (W-66) has the following form:

$$a_{H^+} = a_{H^+,s} + \frac{a_{H^+,*} - a_{H^+,s}}{\delta_{m,H_2S}} x \tag{W-67}$$

The H^+ ion flux at $x = \delta_{m,H_2S}$ can be obtained from Equation (W-67):

$$\begin{aligned} N_{x=\delta_{m,H_2S}} &= -D_{eff} \frac{da_{H^+}}{dx}\bigg|_{x=\delta_{m,H_2S}} \\ &= -\frac{D_{eff}}{\delta_{m,H_2S}} \left(a_{H^+,*} - a_{H^+,s}\right) \end{aligned} \tag{W-68}$$

The H^+ ion fluxes at $x = \delta_{m,H_2S}$ calculated by Equations (W-61) and (W-68) must be equal. Using this constrain, $a_{H^+,*}$ can be derived as follows:

$$a_{H^+,*} = \frac{\frac{D_{eff}}{\delta_{m,H_2S}} a_{H^+,s} + \frac{D_{H^+}}{\gamma_{H^+}^{c}\delta_*} a_{H^+,b}^{eq}}{\frac{D_{eff}}{\delta_{m,H_2S}} + \frac{D_{H^+}}{\gamma_{H^+}^{c}\delta_*}} \qquad \text{(W-69)}$$

The H^+ ion flux at the surface can be calculated by plugging $a_{H^+,*}$ from (W-69) into Equation (W-68):

$$N_{x=0} = -\frac{1}{\frac{\delta_{m,H_2S}}{D_{eff}} + \frac{\gamma_{H^+}^{c}\delta_*}{D_{H^+}}}\left(a_{H^+,b}^{eq} - a_{H^+,s}\right) \qquad \text{(W-70)}$$

In limiting current controlling situations, $a_{H^+,s}$ can be assumed zero in Equation(W-70). Using Equation (U-12), the limiting current density (i_{Lim}) for the diffusion of H^+ ions with buffering due the presence of $H_2S_{(aq)}$ can be obtained by:

$$i_{Lim} = \frac{F a_{H^+,b}^{eq}}{\frac{\delta_{m,H_2S}}{D_{eff}} + \frac{\gamma_{H^+}^{c}\delta_*}{D_{H^+}}} \qquad \text{(W-71)}$$

where, i_{Lim} is in A/m^2, F is the Faraday's constant (= 96485.33 C/mol), $a_{H^+,b}^{eq}$ is in mol/m^3, D_{H^+} and D_{eff} are in m^2/s, and δ_{m,H_2S} and δ_* are in m. δ_m equations for different flow geometries are given in Appendix X. δ_* is given in Equation (W-60). D_{eff} can be calculated using Equation (W-65).

Equation (W-71) in molarity unit is:

$$i_{Lim} = \frac{1000 F a_{H^+,b}^{eq}}{\frac{\delta_{m,H_2S}}{D_{eff}} + \frac{\gamma_{H^+}^{c}\delta_*}{D_{H^+}}} \qquad \text{(W-72)}$$

where, i_{Lim} is in A/m^2, F is the Faraday's constant (= 96485.33 C/mol), $a_{H^+,b}^{eq}$ is in M, D_{H^+} and D_{eff} are in m^2/s, and δ_{m,H_2S} and δ_* are in m. The 1000 factor is added to Equation (W-72) for conversion from mol/m^3 to molarity.

A unique feature of Equation (W-71) is that it works for strong acid solutions too. At zero H_2S partial pressure (*i.e.*, strong acid solutions), $a_{H_2S,b}^{eq}$ is equal to zero and δ_r approaches infinity. Therefore, $D_{eff} = D_{H^+}/\gamma_{H^+}^{c}$ and $\delta_* = \delta_{m,H^+} - \delta_{m,H_2S}$. Substituting new D_{eff} and δ_* equations into Equation (W-71) results in i_{Lim} equation for strong acid solutions, Equation (U-13).

For ideal and near ideal solutions, the activity coefficients are close to one, and therefore concentration can be used instead of activity in i_{Lim} equations. Thus, for ideal and near ideal solutions, Equation (W-71) can be written as below:

$$i_{Lim} = \frac{1000 F c_{H^+,b}^{eq}}{\frac{\delta_{m,H_2S}}{D_{eff}} + \frac{\delta_*}{D_{H^+}}} \tag{W-73}$$

where,

$$\delta_r = \sqrt{\frac{D_{H^+}\, c_{H^+,b}^{eq}}{k_{f,H_2S}\, c_{H_2S,b}^{eq}}} \tag{W-74}$$

$$D_{eff} = D_{H^+} + \frac{c_{H_2S,b}^{eq}}{c_{H^+,b}^{eq}} D_{H_2S} \tag{W-75}$$

The fourth limiting current density equation developed in this study is a semi-empirical equation. It is a two-section boundary layer equation. For the outer part of the mass transfer boundary layer (*i.e.*, between δ_{m,H_sS} and δ_{m,H^+}), it is assumed that no chemical H_2S dissociation reaction occurs and only H^+ ions diffuse across this part of the layer. This assumption gives a mass balance equation as follows:

$$\frac{D_{H^+}}{\gamma_{H^+}^{c}}\frac{d^2 a_{H^+}}{dx^2} = 0 \tag{W-76}$$

Equation (W-76) can be solved effortlessly by using the same boundary conditions as those chosen for Equation (W-47). For the inner part, both H^+ ion diffusion and the buffering due the chemical H_2S dissociation reaction are assumed to occur concurrently. For this part of the layer, Equation (W-62) with the same boundary conditions can be solved.

Following the same procedure used for the derivation of the two-section boundary layer Equation (W-71) and including an empirical factor in the final equation gives the final i_{Lim} equation as below:

$$i_{lim} = \frac{1000 F a_{H^+,b}^{eq}}{\frac{\delta_{m,H^+} - \delta_{m,H_sS}}{Factor\left(\frac{D_{H^+}}{\gamma_{H^+}^{c}}\right)} + \frac{\delta_{m,H_sS}}{D_{eff}}} \tag{W-77}$$

where,

$$D_{eff} = \frac{D_{H^+}}{\gamma_{H^+}^{c}} + \frac{a_{H_2S,b}^{eq}}{a_{H^+,b}^{eq}}\frac{D_{H_2S}}{\gamma_{H_2S}^{c}} \tag{W-78}$$

$$Factor = \frac{a_{H^+,b}^{eq} + a_{H_2S,b}^{eq}}{a_{H^+,b}^{eq}} \tag{W-79}$$

$Factor$ is an empirical factor that added to Equation (W-77) for accurate estimation of i_{Lim}. Without the $Factor$, Equation (W-77) would underpredicts i_{Lim} values.

The four equations presented in this section for i_{Lim} in weak acid solutions are summarized in Table W-1. Figure W-2 compares the performance of different i_{Lim} equations in H_2S containing solutions in the form of a parity plot. Most calculated i_{Lim} values are within the 40% error region. For a better comparison between the i_{Lim} equations the average absolute error and the scatter of absolute errors are plotted in Figure W-3. The experimental data used for these comparisons cover an H_2S partial pressure range of 0 to ~ 1 bar, a temperature range of 20^{o}C to 80^{o}C, a pH range of 2 to 5, NaCl concentrations between 1 wt.% to 20 wt.%, and RCE rotational speeds between 200 to 4000 rpm [49].

Table W-1

A summary of equations proposed for calculating i_{Lim} in weak acid solutions.

Equation #	Description	Applicability
(W-13)	Theoretical one-section boundary layer	Weak acids
(W-42)	Theoretical one-section boundary layer	Weak acids
(W-72)	Theoretical two-section boundary layer	Strong and weak acids
(W-77)	Semi-empirical two-section boundary layer	strong and weak acids

Figure W-2

The Parity plot compares the predicted limiting current density (i_{Lim}) values with those measured in H_2S containing solutions. Experimental measurements, totally 25, are taken from [49] *and the present study. Old model refers to the summation of limiting current densities when the direct reduction of H_2S is considered as another cathodic reaction. δ_{m,H_2S} is used in Equation (W-42).*

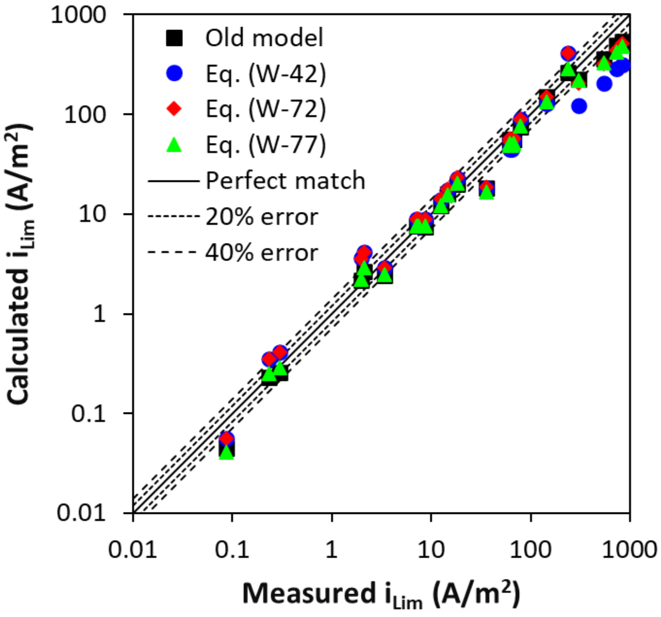

The semi-empirical Equation (W-77) shows a better performance comparing to the other two equations. It has a lower average absolute error, and the scatter of the absolute errors is smaller for that in comparison to the other two equations. The old model preforms better than all the equations proposed in this study. However, the old model has this problem that considers the direct reduction of H_2S as one of the cathodic reaction, which is believed to be insignificant in aqueous H_2S corrosion of carbon steel.

Figure W-3

(A) the average absolute errors and (B) the box and whisker plot (min, quartile 1, median, quartile 3 and max) of errors obtained by comparing the predicted i_{Lim} *values with those measured in* H_2S *containing solutions. Experimental measurements, totally 25, are taken from* [49] *and the present study. Old model refers to the summation of limiting current densities when the direct reduction of* H_2S *is considered as another cathodic reaction.* δ_{m,H_2S} *is used in Equation (W-42).*

(A)

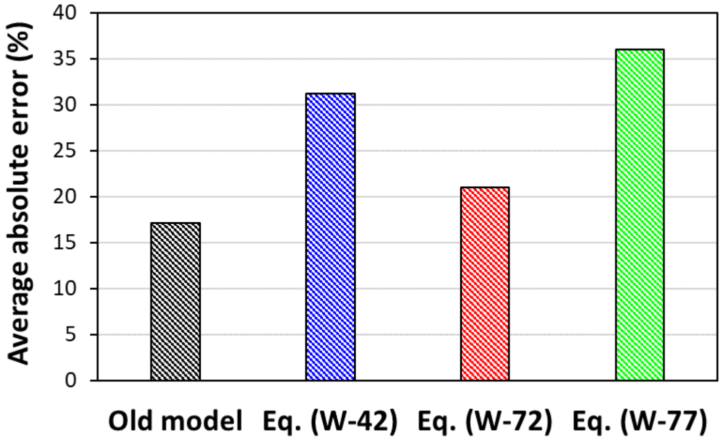

(B)

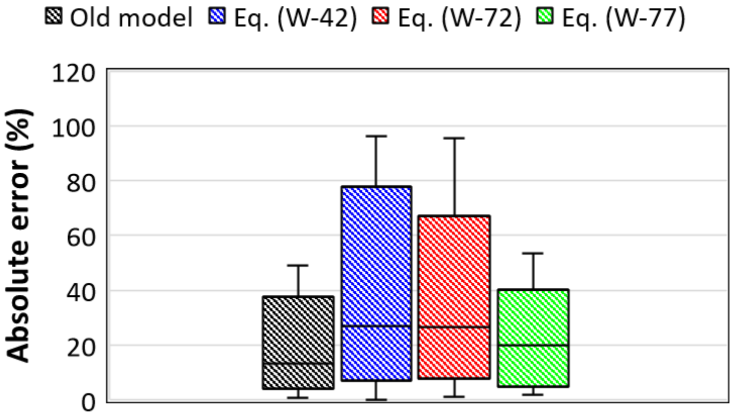

Appendix X: Mass Transfer (Diffusion) Boundary Layer (δ_m) Equations for Various Flow Geometries

1. Rotating disk in a laminar flow regime [290,293]:

$$\delta_{m,i} = \frac{4.975}{rpm^{0.5}}\left(\frac{\mu_{sol}}{\rho_{sol}}\right)^{1/6} D_i^{1/3} \tag{X-1}$$

2. Rotating cylinder in a turbulent flow regime [294]:

$$\delta_{m,i} = \frac{99.64}{d^{0.4}rpm^{0.7}}\left(\frac{\mu_{sol}}{\rho_{sol}}\right)^{0.344} D_i^{0.356} \tag{X-2}$$

where, $\delta_{m,i}$ is the thickness of mass transfer boundary layer for species i in m, μ_{sol} is the dynamic viscosity of solution in kg/m/s, ρ_{sol} is the solution density in kg/m^3, rpm is the rotational speed in revolutions per minute, d is the rotating cylinder diameter in m, and D_i is the diffusion coefficient of species i dissolved in the solution in m^2/s.

3. Pipe in a turbulent flow regime [361]:

$$\delta_{m,i} = \frac{60.606 d^{0.14} \mu_{sol}^{0.53} D_i^{0.33}}{V^{0.86} \rho_{sol}^{0.53}} \tag{X-3}$$

where, $\delta_{m,i}$ is the thickness of mass transfer boundary layer for species i in m, μ_{sol} is the dynamic viscosity of solution in kg/m/s, ρ_{sol} is the solution density in kg/m^3, D_i is the diffusion coefficient of species i dissolved in the solution in m^2/s, d is the pipe diameter in m, and V is the average flow velocity in the pipe in m/s.

4. Thin duct channel in a turbulent flow regime [362][135]:

$$\delta_{m,i} = \frac{H}{5 + 0.015\left[H^a V^a D_i^{-b}\left(\frac{\mu_{sol}}{\rho_{sol}}\right)^{b-a}\right]} \tag{X-4}$$

---

[135] Assume that the width is much larger than the height (H).

where,

$$a = 0.88 - \frac{0.24}{4 + \frac{\mu_{sol}}{\rho_{sol} D_i}} \tag{X-5}$$

$$b = \frac{1}{3} + 0.5 \exp\left(-0.6 \frac{\mu_{sol}}{\rho_{sol} D_i}\right) \tag{X-6}$$

where, $\delta_{m,i}$ is the thickness of mass transfer boundary layer for species i in m, μ_{sol} is the dynamic viscosity of solution in kg/m/s, ρ_{sol} is the solution density in kg/m^3, D_i is the diffusion coefficient of species i dissolved in the solution in m^2/s, H is the height of the thin channel in m, and V is the average flow velocity in the thin channel in m/s.

The solution density (ρ_{sol}) can be calculated using Equation (3-2) [26]. Models for the solution viscosity (μ_{sol}) are provided in Section 3.2. The diffusion coefficient (D_i) can be calculated based on information provided in Table 3-2, Table 3-3, and Table 3-4.